Title

Controls on inorganic calcite growth from the nano to field scale

Author

Mills, Jennifer Victoria

Publication Date

2021

Controls on inorganic calcite growth from the nano to field scale

By

Jennifer Victoria Mills

A dissertation submitted in partial satisfaction of the

requirements of the degree of

Doctor of Philosophy

in

Environmental Science, Policy and Management

in the

Graduate Division

of the

University of California, Berkeley

Committee in charge:

Professor Laura N. Lammers, Chair
Professor Ronald Amundson
Professor Donald J. DePaolo

Summer 2021

Controls on inorganic calcite growth from the nano to field scale

by

Jennifer Victoria Mills

Abstract

Controls on inorganic calcite growth from the nano to field scale

by

Jennifer Victoria Mills

Doctor of Philosophy in Environmental Science, Policy and Management

University of California, Berkeley

Professor Laura N. Lammers, Chair

This dissertation focuses on two aspects of biogeochemical cycling essential for our understanding of future carbon cycle trajectories and carbon dioxide removal strategies: carbonate crystal growth and soil carbon cycling. In the first two chapters, I develop the use of calcium isotopes as molecular probes that shed light on the complicated suite of processes occurring at the fluid-mineral interface during crystal growth. The solution stoichiometry dependence of calcium isotope fractionation is first investigated as a direct test of classical ion-by-ion models of isotope partitioning during calcite growth (Chapter 2). Fractionations measured through a series of constant-composition calcite growth experiments are well-captured by an ion-by-ion model that incorporates the influence of surface speciation. This provides strong supporting evidence for the model of calcium isotope discrimination driven by Ca exchange at kink sites on the growing crystal surface and yields much-needed constraints on the solution chemistry dependence of $\Delta^{44/40}$Ca, critical for the interpretation of Ca isotopes in natural systems. Model predictions of the relationship between $\Delta^{44/40}$Ca and growth inhibition in the presence of impurity ions then lay the theoretical groundwork for the use of Ca isotopes to probe interfacial processes during carbonate crystal growth.

In Chapter 3, I operationalize this new tool, employing calcium isotope fractionation to help elucidate the mechanism by which two divalent cations with starkly contrasting compatibility, magnesium and manganese, interact with the growing calcite surface and are ultimately incorporated into the mineral lattice. Invariant $\Delta^{44/40}$Ca with increasing ${}^{\{Mn^{2+}\}}/_{\{Ca^{2+}\}}$ and ${}^{\{Mg^{2+}\}}/_{\{Ca^{2+}\}}$, despite more than an order of magnitude decline in growth rate, is indicative of a dominantly kink blocking inhibition mechanism. For Mg^{2+}, experimental trends are consistent with inhibition driven by slow Mg^{2+}-aquo complex dehydration relative to Ca^{2+}, but large Mn^{2+} partition coefficients cannot be explained by desolvation rate-limited attachment of Mn^{2+}. Instead, I argue that the dominant Mn^{2+} species interacting with kink sites is not the free ion in solution but instead an ion pair, hydrated species, or possibly larger polynuclear cluster and that growth kinetics are limited by a carbonate-based kink blocking mechanism. These findings raise questions about the prevalence and broader ramifications of non-monomer trace constituent incorporation during otherwise classical crystal growth.

In the second half of the dissertation, I turn to carbon cycling at the field scale, investigating the controls on soil carbon cycling and soil-atmosphere CO_2 exchange in the Mojave Desert. Arid soils can contain significant concentrations of inorganic carbon in the form of

pedogenic carbonate, but the short-timescale dynamics of the soil inorganic carbon system and its impact on CO_2 fluxes remains poorly constrained. I present results from a multi-year field campaign, including two years of continuous measurements of meteorological and soil conditions from a series of soils along a climate/elevation gradient. In Chapter 4, I focus on unpacking the primary controls on CO_2 production in these highly water-limited ecosystems, and develop quantitative models to describe how the sensitivity of CO_2 production to environmental conditions varies with depth in the soil profile and spatially on scales of meters to kilometers. Significant nighttime CO_2 pulse events observed in near-surface soils of the more densely vegetated, higher elevation, sites are also explored and provisionally linked to microbial activity stimulated by the delivery of non-rainfall moisture to the litter layer and surficial soils.

In Chapter 5, I discuss the causes and consequences of two types of CO_2 consumption documented at the lowest elevation, most arid site: periods of frequent negative nighttime surface fluxes during the dry season and acute episodes of CO_2 uptake following rain events. The negative surface fluxes are driven by almost continuous nighttime CO_2 consumption in shallow soil layers (0-15cm depth), the magnitude of which is strongly dependent on the amplitude of the diurnal soil temperature oscillation. Quantitative evaluation of potential driving mechanisms suggests that thermal impacts on the soil carbonate system alone cannot produce the magnitude of consumption observed, and that temperature-dependent CO_2 adsorption to soil minerals may also contribute to an abiotic diurnal cycle of CO_2 uptake and release in these desert soils. In contrast, the CO_2 uptake observed following rain events is consistent with CO_2 consumption due to carbonate mineral dissolution, potentially augmented by near-surface biotic carbon fixation. I end with a discussion of the broader implications of the documented inorganic CO_2 fluxes for the interpretation of carbon dynamics in arid ecosystems.

Contents

Contents **i**

List of Figures **vi**

List of Tables **x**

1 Introduction **1**

1.1 Carbonate crystal growth: why do we care? 1

1.2 Soil carbon cycling in arid ecosystems 2

2 The influence of Ca^{2+}:$CO_3{}^{2-}$ stoichiometry on Ca isotope fractionation **4**

Abstract 4

2.1 Introduction 5

2.1.1 Calcium isotope fractionation during calcite precipitation from aqueous solution: causes and consequences 5

2.1.2 Ion by ion model framework predicts strong solution stoichiometry dependence on $\Delta^{44/40}$Ca 7

2.1.3 Investigation goals 9

2.2 Methods 9

2.2.1 Constant composition growth experiments 9

2.2.1.1 Experimental Setup 9

2.2.1.2 Materials and solution preparation 11

2.2.1.3 Experimental run 11

2.2.2 Analytical techniques 12

2.2.3 Growth rate determination 13

2.2.4 Calculation of calcium isotope fractionation 13

2.2.5 Ion-by-ion model of calcite growth and $\Delta^{44/40}$Ca 15

2.3 Results 17

2.3.1 Morphology of precipitated calcite 17

2.3.2 Calcite precipitation kinetics 19

2.3.2.1 Growth rate as a function of solution stoichiometry: seeded experiments 19

2.3.2.2 Unseeded experiments: influence of solution stoichiometry on nucleation dynamics 20

2.3.3 Ca isotope fractionation variation with solution stoichiometry 21

2.4 Discussion 23
  2.4.1 Comparison to ion-by-ion model predictions: Original formulation overpredicts $\Delta^{44/40}Ca$ stoichiometry dependence 23
  2.4.2 Interrogating damped solution stoichiometry effect 25
    2.4.2.1 Influence of non-equivalent calcite steps 25
    2.4.2.2 Influence of surface speciation 27
  2.4.3 Model predictions for bulk growth rate and implications for $\Delta^{44/40}Ca$ - growth rate relationship 32
  2.4.4 Additional potential controls on $\Delta^{44/40}Ca$-solution stoichiometry relationship 33
  2.4.5 Implications for the interpretation of Ca isotopes in natural systems . 35
  2.4.6 Stable Ca isotopes as probes of crystal growth: Predicted influence of impurity ions 36
2.5 Conclusions 38

3 Ca isotope insights into Mn^{2+} and Mg^{2+} inhibition of calcite growth 39
Abstract 39
3.1 Motivation: towards predicting growth dynamics in complicated solutions . . 40
  3.1.1 Understanding how impurities impact calcite growth: Mn vs. Mg as a case study 41
  3.1.2 Investigation goals 43
3.2 Methods 45
  3.2.1 Constant composition growth experiments 45
    3.2.1.1 Experimental Setup 45
    3.2.1.2 Materials and solution preparation 45
    3.2.1.3 Experimental run 48
  3.2.2 Analytical techniques 49
  3.2.3 Growth rate determination 50
  3.2.4 Partition coefficient calculation 50
  3.2.5 Calculation of calcium isotope fractionation 52
  3.2.6 Ion-by-ion modeling of calcite growth and trace element + isotope partitioning 53
    3.2.6.1 Solid solution thermodynamic data 54
    3.2.6.2 Potential influence of surface speciation 55
    3.2.6.3 Complicating factor: influence of impurity ions on step density 55
    3.2.6.4 Baseline model assumptions 58
3.3 Results 58
  3.3.1 Crystal morphology in the presence of Mn and Mg 58
  3.3.2 XRD: precipitation of $(Mn,Ca)CO_3$ and $(Mg,Ca)CO_3$ solid-solution series 65
    3.3.2.1 $(Ca,Mn)CO_3$ series powder XRD results 65
    3.3.2.2 $(Ca,Mg)CO_3$ series powder XRD results 65
  3.3.3 Growth rate inhibition 68
    3.3.3.1 Initially slow growth rate observed in high-Mn solutions . . 70
  3.3.4 Trace element partitioning 71

3.3.5 Ca isotope fractionation 72
3.4 Discussion 74
3.4.1 Mn and Mg kinetic data 74
3.4.2 Mn and Mg incorporation dynamics 75
3.4.2.1 Mn partitioning 75
3.4.2.2 Mg partitioning 78
3.4.3 Invariant $\Delta^{44/40}$Ca points towards kink-blocking inhibition mechanism 80
3.4.4 Insights from ion-by-ion model 81
3.4.4.1 Mn inhibition of calcite growth: evidence for non-monomer incorporation 81
3.4.4.2 Mg inhibition of calcite growth: kink blocking...but how? . . 85
3.4.5 Implications for interpretation of $\Delta^{44/40}$Ca in natural systems 94
3.4.6 Expanding the microkinetic framework: non-monomer incorporation and beyond 95
3.5 Conclusions 96

4 Unpacking controls on soil CO_2 production along a climate gradient in the Mojave Desert 97
Abstract 98
4.1 Introduction 98
4.1.1 Investigation goals 99
4.2 Methods 100
4.2.1 Climate Transect in the Mojave National Preserve 100
4.2.2 Ex-situ soil analysis 102
4.2.2.1 Organic C, N content and isotope analysis 102
4.2.2.2 Carbonate content and isotopes 103
4.2.3 Data quality assurance and gap-filling 103
4.2.3.1 Correcting VWC measurement temperature dependence . . 103
4.2.4 CO_2 flux and production calculations 103
4.2.4.1 Identification of anomalous nighttime pulses of CO_2 105
4.2.5 Analysis of dominant controls on daily CO_2 production and anomalous nighttime CO_2 pulses: Decision trees 106
4.2.6 Production-diffusion model of CO_2 dynamics 107
4.3 Results and Discussion 109
4.3.1 Site and soil characteristics 109
4.3.2 Primary controls of daily CO_2 production 113
4.3.3 CO_2 production regression analysis 115
4.3.3.1 Features inconsistent with production-diffusion framework: CO_2 consumption and nighttime pulses of CO_2 119
4.3.3.2 Temperature and water sensitivity of shallow and deeper soils 119
4.3.4 Predictive modeling of CO_2 production throughout the soil profile . . 124
4.3.4.1 Reconciling the differential environmental sensitivity of shallow and deep production: Two respiration terms 125
4.3.4.2 Predictive modeling of CO_2 dynamics throughout the soil profile 126

4.3.5 Exploring nighttime pulses of CO_2: Respiration driven by non-rainfall moisture? 131
4.3.5.1 Frequency and magnitude of anomalous nighttime pulse events 133
4.3.5.2 Mechanism scoping: correlation with environmental variables 136
4.3.5.3 Insights from decision tree analysis 139
4.3.5.4 Summary and potential broader implications of nighttime pulse events 141
4.4 Conclusions 144

5 Magnitude and mechanism of CO_2 consumption in Mojave Desert soils 146

Abstract 146
5.1 Introduction: Complicated drivers of soil-atmosphere CO_2 exchange in arid systems 147
5.2 Methods 148
5.2.1 In-situ monitoring of Mojave Desert Climosequence 148
5.2.2 CO_2 flux and production calculations 149
5.2.3 Geochemical modeling of nighttime CO_2 consumption 149
5.2.3.1 CO_2 consumption due to temperature-sensitive carbonate system reactions 150
5.2.3.2 CO_2 adsorption to mineral surfaces 151
5.3 Results and Discussion 152
5.3.1 Negative nighttime surface fluxes 152
5.3.2 Acute CO_2 consumption following rain events 153
5.3.3 Potential drivers of nightly CO_2 consumption 155
5.3.3.1 Magnitude of CO_2 consumption 155
5.3.3.2 Spatial heterogeneity: bare soil versus under-canopy 157
5.3.3.3 Relationship to environmental predictors 162
5.3.4 Interrogation of potential mechanisms for nighttime consumption 166
5.3.4.1 Temperature-dependent carbonate system reactions 166
5.3.4.2 Temperature-dependent CO_2 adsorption to mineral surfaces 168
5.3.4.3 Alternative explanations: biologic carbon fixation and enhanced transport of CO_2 171
5.3.5 Interpretation of acute consumption following rain 172
5.3.6 Broader implications for measurements and predictions of CO_2 fluxes in these systems 174
5.4 Conclusions 175

References 176

Appendix A: Supplementary information for Chapter 2, The influence of Ca^{2+}:$CO_3{}^{2-}$ stoichiometry on Ca isotope fractionation 205

Appendix B: Supplementary information for Chapter 3, Ca isotope insights into Mn^{2+} and Mg^{2+} inhibition of calcite growth 216

Appendix C: Mojave climosequence soil characterization **224**

Appendix D: Supplementary information for Chapter 4, Unpacking controls on soil CO_2 production along a climate gradient in the Mojave Desert **234**

Appendix E: Supplementary information for Chapter 5, Magnitude and mechanism of CO_2 consumption in Mojave Desert soils **253**

List of Figures

2.1 Ion-by-ion model prediction of variation in $\Delta^{44/40}Ca_{calcite-fluid}$ with changing solution stoichiometry for a range of supersaturations. 8
2.2 Chemostat reactor setup for Ca^{2+}:$CO_3{}^{2-}$ calcite growth experiments 10
2.3 Key processes modeled in ion-by-ion growth models: the addition and removal of growth units from kink sites 16
2.4 Representative scanning electron microscope images of (A) precipitated solids in unseeded experiments, (B) precipitated solids in seeded experiments, and (C) initial calcite seed material. 19
2.5 Measured growth rates for seeded experiments 20
2.6 Nucleation and growth dynamics for unseeded (SI 0.8) experiments. 21
2.7 Ca isotope fractionation variation with solution stoichiometry 22
2.8 Ion-by-ion model prediction of $\Delta^{44/40}Ca$ for original parameterization of Nielsen et al. (2012) model and re-optimized endmember fractionations including the $\Delta^{44/40}Ca$ data from this study 24
2.9 Accounting for the influence of calcite growth hillock anisotropy on modeled calcium isotope fractionation. 28
2.10 Ion-by-ion model prediction of $\Delta^{44/40}Ca$ accounting for surface speciation. . 29
2.11 Extent of surface Ca exchange as a function of Ca^{2+}:$CO_3{}^{2-}$ activity ratio for A) Nielsen *et al.* (2012) ion-by-ion model and B) Wolthers *et al.* (2012) formulation which incorporates a surface complexation model. 31
2.12 Modeled bulk growth rates and $\Delta^{44/40}Ca$-growth rate relationship. 34
2.13 Influence of supersaturation and pH on predicted $\Delta^{44/40}Ca$. 37

3.1 Diagram demonstrating how the presence of impurities can influence calcite growth. 44
3.2 Chemostat reactor setup for Mn^{2+}, Mg^{2+} calcite growth experiments. 46
3.3 Example of Mn^{2+} concentrations coming to a quasi-steady state over the course of an experiment, potentially driven by a negative feedback between growth rate and Mn partitioning. 48
3.4 Comparison of calculated Mn partition coefficient using the measured solid overgrowth composition and titrant composition. 52
3.5 Importance of considering y_0 sensitivity to inhibitor ions. 57
3.6 Post-growth SEM images of Mn calcite inhibition experiments. 62
3.7 High-magnification SEM images of growth features on precipitated $(Mn,Ca)CO_3$. 63

3.8 Post-growth SEM images of precipitated solids from Mg^{2+} calcite inhibition experiments . . . 64
3.9 Powder XRD results for Mn^{2+} calcite growth experiments . . . 66
3.10 Changes in calcite lattice parameters with Mn content. . . . 67
3.11 Powder XRD results for Mg^{2+} calcite growth experiments . . . 69
3.12 Calcite growth rate inhibition by Mn^{2+} and Mg^{2+} . . . 70
3.13 Evolution in initial growth rate observed for high-Mn experiments. . . . 72
3.14 Manganese and magnesium partitioning . . . 73
3.15 Calcium isotope fractionation during Mn^{2+} and Mg^{2+} inhibition of calcite growth. . . . 74
3.16 Extent of calcite growth inhibition across studies and inhibitor systems. . . . 76
3.17 Mn^{2+} partitioning into calcite exhibits a strong log-linear inverse dependence on growth rate across a wide range of solution conditions. . . . 77
3.18 Literature compilation of Mg^{2+} partitioning results. . . . 78
3.19 Invariant $\Delta^{44/40}Ca$ with $\{Me^{2+}\}/\{Ca^{2+}\}$ draws observed fractionations off the pure calcite $\Delta^{44/40}Ca$-rate relationship. . . . 80
3.20 Ion-by-ion model prediction of bulk growth rate (A), Mn^{2+} partition coefficient (B), and $\Delta^{44/40}Ca_{calcite-fluid}$ (C) as a function of $\{Mn^{2+}\}/\{Ca^{2+}\}$ for Mn^{2+} inhibition of calcite growth driven by Mn^{2+} complex addition (allowing for $k_{Mn}>>k_{Ca}$) coupled to kink-blocking due to slow $CO_3{}^{2-}$ attachment at Mn^{2+} kink sites. . . . 83
3.21 Predicted sensitivity of Mn^{2+} growth rate inhibition and partitioning to supersaturation. . . . 86
3.22 Ion-by-ion model prediction of bulk growth rate (A), Mg^{2+} partition coefficient (B), and $\Delta^{44/40}Ca_{calcite-fluid}$ (C) as a function of $\{Mg^{2+}\}/\{Ca^{2+}\}$ for Mg^{2+} inhibition of calcite growth driven by Mg^{2+}-solvation driven kink blocking. . . 88
3.23 Predicted sensitivity of Mg^{2+} growth rate inhibition to supersaturation for the different inhibition mechanisms explored. . . . 90
3.24 Ion-by-ion model prediction of bulk growth rate (A), Mg^{2+} partition coefficient (B), and $\Delta^{44/40}Ca_{calcite-fluid}$ (C) as a function of $\{Mg^{2+}\}/\{Ca^{2+}\}$ for Mg^{2+} inhibition of calcite growth driven by Mg^{2+} complex addition and carbonate ion kink blocking. . . . 91
3.25 Variation in $\Delta^{26/24}Mg_{calcite-fluid}$ and $\Delta^{60/58}Ni_{calcite-fluid}$ with growth rate. . 93

4.1 Mojave study sites. . . . 100
4.2 Two years of in-situ monitoring data from the bare-soil profile at the most arid climosequence site, Creosote . . . 110
4.3 Two years of in-situ monitoring data from the bare-soil profile at the mid-elevation, Joshua Tree, site. . . . 111
4.4 Two years of in-situ monitoring data from the PJ-1 soil profile at the highest elevation, Pinyon Juniper, site. . . . 112
4.5 Overview of spatial heterogeneity in soil conditions across the climosequence sites. . . . 114
4.6 Regression trees predicting daily CO_2 production in shallow and deep soils in the vegetated profile of the mid-elevation, Joshua Tree site. . . . 116

4.7 Truncated regression trees predicting daily CO_2 production in shallow (2.5-15cm depth) and deep (15-37.5cm depth) soils from vegetated profiles across the Mojave climosequence. 117
4.8 Truncated regression trees predicting daily CO_2 production in shallow (2.5-15cm depth) and deep (15-37.5cm depth) soils from interspace profiles across the Mojave climosequence. 118
4.9 Regression results for shallow and deep CO_2 production, using a simple Arrhenius temperature dependence and Gompertz water content dependence. . 120
4.10 Regression results for shallow and deep CO_2 production, using a Lloyd and Taylor temperature dependence and an exponential-squared water content dependence. 121
4.11 Regression results for shallow (A-C) and deep (D-F) CO_2 production, using the best-fit temperature and water content dependence, allowing for the influence of antecedent water content. 124
4.12 Depth dependence of modeled CO_2 production functions. 126
4.13 CO_2 production-diffusion model results for the interspace profile at Creosote (C1) 128
4.14 CO_2 production-diffusion model results for the vegetated profile at Joshua Tree (JT2) 129
4.15 CO_2 production-diffusion model results for the mixed shrub/grass profile at Pinyon Juniper (PJ1) 130
4.16 Temperature and water content sensitivity of heterotrophic and autotrophic respiration derived from modeling CO_2 dynamics across the complete soil profile. 131
4.17 Observations of seemingly anomalous nighttime CO_2 pulses in shallow soils (5cm depth) of the vegetated profile of the Joshua Tree site. 134
4.18 Cross-plots of the nighttime pulse magnitude (ratio of maximum [CO_2] during the nighttime vs. preceding daytime interval) with potential predictor variables at the JT2 soil profile. 137
4.19 Time series of soil CO_2 concentration at 5cm depth, the difference between air temperature and the dew point, and relative humidity during intervals with a series of nighttime pulse events. 138
4.20 Cross-plots of the nighttime pulse magnitude (ratio of maximum [CO_2] during the nighttime vs. preceding daytime interval) with potential predictor variables at the PJ2 soil profile. 140
4.21 Decision trees predicting nighttime pulse events at the Joshua Tree vegetated profile (JT2). 142
4.22 Decision trees predicting nighttime pulse events at the Pinyon Juniper mixed shrub/grass profile (PJ2). 143

5.1 Calculation of conservative 'max production' term for quantifying the magnitude of CO_2 consumption. 150
5.2 Near-surface CO_2 dynamics during a winter drought interval (3 months without rain) at the Creosote site. 153
5.3 Monthly average diurnal pattern in CO_2 surface flux for four months from September 2017 - September 2018. 154

5.4 Acute CO_2 consumption in the intercanopy soil profile following rain events. 156
5.5 Daily integrated surface flux and shallow soil CO_2 production (upper 15cm) across the 2018-2019 seasonal cycle. 158
5.6 Time series of CO_2 production in upper 15cm of the bare soil profile, partitioned into daytime and nighttime intervals. 159
5.7 Spatial relationship between the monitored soil pits and 'island of fertility' generated by established creosote shrub. 161
5.8 Soil temperature and water dynamics in the vegetated and interspace profiles from September 2017-September 2019. 163
5.9 Cross-plots of daily mean CO_2 production in the upper 15cm of the bare soil profile with environmental parameters that could influence soil physiochemical conditions, broken into daytime (gold) and nighttime (blue) intervals. 165
5.10 Modeled potential nighttime CO_2 uptake from temperature-dependent carbonate system reactions. 169
5.11 Potential CO_2 consumption due to temperature-dependent adsorption to mineral surfaces. 171
5.12 Biocrusts observed at Creosote interspace profile. 173

List of Tables

2.1 Summary of experimental solution conditions and results. 18
2.2 Summary of post-growth SEM analysis of unseeded growth experiments and calcite seed material. 19
2.3 Fitted attachment/detachment coefficients and end member Ca isotope fractionations for the model parameterizations in the following analysis 26

3.1 Summary of experimental solution conditions. 59
3.2 Growth rate inhibition, Ca isotope fractionation, and partitioning results. . . 60
3.3 Solution conditions for Mn^{2+} and Mg^{2+} partitioning studies 77
3.4 Model parameters for Mn^{2+} inhibition of calcite growth. 82
3.5 Model parameters for Mg^{2+} inhibition of calcite growth. 87

4.1 Mojave climosequence site locations. 101
4.2 List of relationships between soil CO_2 production (generally CO_2 efflux) and soil temperature/moisture content previously applied in empirical models and tested here. 108
4.3 Mean annual meteorological conditions measured at the climosequence sites from September 2017-2019. 110
4.4 Calculated Q_{10} and water content threshold for the CO_2 production model fits presented. 122
4.5 Fitted parameters and calculated Q_{10} and water content threshold for the autotrophic and heterotrophic CO_2 production functions used to model the complete soil profile. 132
4.6 Number of nighttime CO_2 pulses identified at each site. 133
4.7 Contribution of nighttime pulse events to total surface flux. 135

5.1 Summary of CO_2 uptake in intercanopy soils following precipitation events. . 155
5.2 Monthly average CO_2 production and soil conditions in the Creosote bare soil profile for three representative dry intervals. 160
5.3 Soil temperature and water content (mean ± standard deviation) of Creosote soil profiles from September 2017-September 2019. 162
5.4 Results of single-variable regression analysis predicting mean nighttime CO_2 production, considering only nights where net CO_2 consumption occurs. . . . 164
5.5 Calculated maximum potential nighttime CO_2 uptake from temperature-dependent carbonate system reactions during three representative months. 170

Acknowledgements

First and foremost, I would like to thank my primary research advisor, Laura Lammers. Your support and guidance has been invaluable throughout this PhD journey. Thank you for always challenging me and encouraging my scientific curiosity, even when that curiosity led us down seemingly endless rabbit holes. I am also deeply indebted to Ron Amundson, who not only taught me everything I know about soil science, but has also been a constant source of inspiration throughout my time at Berkeley. Your zeal for science is infectious; thank you for welcoming me into your lab group, for your boundless energy and enthusiasm in the field, and for countless insightful discussions as I waded through the complexities of the desert carbon cycle. I am also grateful for the mentorship of Don DePaolo. Thank you for the multitude of thought-provoking conversations throughout the years, for encouraging my interest in carbon removal, and for always pushing me to think about the big picture.

I would also like to thank all of the members of the Lammers and Amundson research groups: Holly Barnhart, Liz Mitnick, Luis Anaya, Elliot Chang, Karol Kulasinski, Kathrin Schilling, Jian He, Marco Pfeiffer, Hannah Welsh, and Greg Maurer. Thank you for supporting me, laughing with me, and for always being so willing to act as a sounding board for my ideas. In particular, the Mn/Mg calcite inhibition study (Chapter 3) would not have been possible without the excellent laboratory assistance and constant camaraderie of Holly and the Mojave Carbon Project (including Chapters 4 and 5) was completely underpinned by Greg's expertise and efforts in implementing and maintaining our hugely ambitious series of in-situ monitoring installations. Thank you, Greg, for being a wonderful field companion, for the countless hours spent on the road and trekking through the Mojave, and for teaching me so much about ecohydrology. The Mojave project would also not have been possible without the help of Marco, Hannah and an intrepid group of undergraduate researchers: Lena Kallweit, Erika Cota, and Emily Stuart. Thank you for all of your help in the field and in the laboratory, including sieving and grinding what likely amounts to a literal ton of soil samples. Thank you also to Wenbo Yang and Stefania Mambelli for invaluable help with light stable isotope analyses.

Many thanks are also due to all of the members of the BES Geochemistry and Isotope Geochemistry groups. My time at Berkeley has been greatly enriched through conversations, collaborations, feedback from Ben Gilbert, John Christensen, Anna Clinger, Yijun Yang, Shaun Brown, Mike Whittaker, Harry Lisabeth, Piotr Zarzycki, Hang Deng, Claresta Joe-Wong, Sergio Carrero Romero, and Chris Colla. I'm particularly indebted to Shaun for guiding me so patiently through calcium isotope sample preparation and TIMS operation. I am also incredibly grateful for a Berkeley Fellowship and EPA-Marshall Scholarship, which provided funding for my first few years at Cal, and for research funding from the California Energy Commission under contract no. EPC-15-039 and from the DOE Office of Science, Basic Energy Sciences, Division of Chemical, Biological and Geological Sciences under contract no. DE-AC02-05CH11231.

Finally, I would like to thank my family. I simply would not have been able to do this without you.

Chapter 1

Introduction

This dissertation presents a series of studies that span the spatial scales of carbon cycling, from the microscopic reactions occurring at the fluid-mineral interface during carbonate crystal growth to the kinetics of processes that control landscape-scale CO_2 exchange. It is organized into two parts, the first of which focuses on fundamental studies of carbonate crystal growth and the development of calcium isotopes as molecular probes to tie observations of bulk growth phenomena to underlying molecular-scale mechanisms. The second focuses on using high spatial and temporal resolution measurements of soil CO_2 dynamics in desert ecosystems to elucidate the controls on carbon cycling and surface-atmosphere CO_2 exchange in these water-limited soil systems characterized by the accumulation of pedogenic carbonate. The two parts are linked first by the overarching theme of building a better mechanistic understanding of the controls on inorganic carbonate mineral precipitation/dissolution reactions across spatial scales. As developed in the following sections, the two halves also separately speak to aspects of carbon cycling of fundamental importance to our societal efforts to respond to the current climate crisis (IPCC, 2019; NASEM, 2019).

1.1 Carbonate crystal growth: why do we care?

I begin with two studies that probe the molecular-scale mechanisms of carbonate crystal growth, specifically targeting the development of a process-based understanding of calcium isotope fractionation during calcite precipitation and the application of that understanding to shed light on the interfacial reactions occurring during growth from complex solutions. Understanding the interplay between the physio-chemical conditions of the precipitating environment, carbonate mineral growth kinetics, and the partitioning of isotopes and trace elements into the mineral lattice has long been a key target of geochemists given the importance of carbonate-based paleoproxies to the reconstruction of Earth's climate history (e.g. Emiliani, 1955; Shackleton, 1967; Hoffman *et al.*, 1998; Ravizza and Zachos, 2003). Interest in developing predictive models of carbonate dissolution/precipitation reactions has increased in recent years because of the centrality of these reactions to the ocean's response to rising atmospheric CO_2 concentrations (Morse *et al.*, 2006) as well as a number of negative emissions technologies (NASEM, 2019). Ocean alkalinization (Renforth and Henderson, 2017), enhanced weathering (Renforth *et al.*, 2009; Beerling *et al.*, 2020), in-situ mineralization of basalts or peridotites (Kelemen *et al.*, 2011; Clark *et al.*, 2020), and engineered ex-situ mineralization of alkaline waste materials (Gerdemann *et al.*, 2007) are all increasingly attractive strategies for net CO_2 removal that rely on a detailed understanding of carbonate precipitation reactions in complex solutions. While carbonate precipitation and dissolution reactions have been studied extensively (c.f. Morse *et al.*, 2007 and references therein), we are only beginning to build a comprehensive understanding of mineral growth in simple electrolyte solutions and at relatively low aqueous supersaturations, let alone the complicated solutions encountered in natural systems.

To address this need, Chapter 2 tests a key prediction of classical ion-by-ion models of stable isotope partitioning during calcite growth (Nielsen *et al.*, 2012), and demonstrates that calcium isotope fractionation during calcite precipitation can be understood and mechanistically modeled in terms of the fluxes of monomer Ca^{2+} ions onto and off of kink sites on the growing crystal surface (Mills *et al.*, 2021). This in turn lays the groundwork for the use of calcium isotope fractionation as window into calcium surface dynamics during growth in more complicated solutions. Chapter 3 then operationalizes this new tool, employing calcium isotope fractionation to help elucidate the mechanism by which two representative impurity ions, magnesium and manganese, interact with the growing calcite surface and act to inhibit growth.

1.2 Soil carbon cycling in arid ecosystems

The second half of the dissertation turns to two studies which aim to unravel the complex controls on soil carbon cycling in arid ecosystems. Understanding how global soil carbon stocks and soil-atmosphere CO_2 fluxes will respond to changing environmental boundary conditions is imperative for effective climate change mitigation policy (Crowther *et al.*, 2016; Bradford *et al.*, 2016; Paustian *et al.*, 2016). Soils represent the largest terrestrial repository of organic carbon, with approximately 2400GtC to 2m depth, exceeding the total mass of carbon contained in vegetation and the atmosphere combined (Jobbágy and Jackson, 2000; Batjes, 2014). The storage of organic carbon in soils is dictated by the balance of carbon inputs via plant-derived biomass and carbon losses, largely through heterotrophic respiration (Amundson, 2001). Soils thus at once represent a substantial reservoir of carbon vulnerable to respiration and release (Hicks Pries *et al.*, 2017; Bond-Lamberty *et al.*, 2018; Plaza *et al.*, 2019), and a potential opportunity to sequester carbon on the scale of 0.5-1.4GtC/yr through changes in land management practices (Paustian *et al.*, 1997; Lal, 2004; Paustian *et al.*, 2016; Fuss *et al.*, 2018; Soussana *et al.*, 2019).

Dryland ecosystems cover approximately 40% of the terrestrial land surface (Schimel, 2010) and are increasingly recognized as important contributors to global carbon fluxes (Poulter *et al.*, 2014; Ahlström *et al.*, 2015; Jung *et al.*, 2017). Yet predicting CO_2 fluxes in these ecosystems remains highly uncertain, in part due to the tight linkages between biotic activity and water availability (Noy-Meir, 1973) and the non-negligible impact of abiotic processes on carbon cycling in these systems (Rey, 2015). Critically, organic carbon is not the sole, or oftentimes dominant, carbon phase present in arid soils (Schlesinger, 1982). Arid soils can contain significant concentrations of inorganic carbon in the form of pedogenic carbonate, and there is growing evidence that the soil carbonate system can exert a first-order control on CO_2 dynamics on timescales ranging from the diurnal cycle to annual CO_2 exchange (Parsons *et al.*, 2004; Kowalski *et al.*, 2008; Roland *et al.*, 2013; Wang *et al.*, 2020). Non-biological contributors to the breakdown of organic material, including photo- and thermal-degradation of litter, also complicate the measurement and predictive modeling of carbon fluxes in arid systems (Austin and Vivanco, 2006; Brandt *et al.*, 2009; Austin *et al.*, 2016; Gliksman *et al.*, 2017).

The final two chapters present results from a multi-year field campaign aimed at interrogating the primary controls on soil carbon cycling in the Mojave Desert (Mills *et al.*, 2020). Two years of continuous monitoring of meteorological and soil conditions (CO_2 concentration, water content, and temperature to 125cm depth) at a series of sites along an elevation gradient provide a spatially and temporally rich view of the interplay between environmental conditions and CO_2 dynamics throughout the soil profile. Chapter 4 focuses on unpacking the primary controls of soil CO_2 production and how those controls vary across space and time. Models are developed to describe the temperature and water sensitivity of soil respiration, and the causes and consequences of substantial nighttime pulses of CO_2 observed at the more densely vegetated, higher elevation sites are explored. Chapter 5, in turn, targets observations of regular soil CO_2 consumption at the most arid site and analyzes the potential mechanistic underpinnings as well as the broader ramifications of this CO_2 uptake through the lens of abiotic contributors to CO_2 exchange.

Chapter 2

The influence of Ca^{2+}:$CO_3{}^{2-}$ stoichiometry on Ca isotope fractionation: Implications for process-based models of calcite growth

Abstract

The solution stoichiometry dependence of calcium isotope fractionation during calcite precipitation was investigated as a direct test of the conceptual model of calcium isotope discrimination driven by Ca exchange at surface sites during growth. Classical ion-by-ion models of calcite growth predict a strong solution stoichiometry influence on $\Delta^{44/40}Ca_{calcite-fluid}$: In low Ca^{2+}:$CO_3{}^{2-}$ solutions, $\Delta^{44/40}Ca$ is predicted to approach a kinetic limit (∼-2 to -4‰), while in high Ca^{2+}:$CO_3{}^{2-}$ solutions, exchange at dominantly Ca-occupied kink sites drives $\Delta^{44/40}Ca$ towards the equilibrium fractionation (near 0‰). To test this prediction, a series of seeded and unseeded constant composition calcite growth experiments were performed in which all aspects of solution chemistry were held constant and the Ca^{2+}:$CO_3{}^{2-}$ activity ratio was varied. Experiments were performed at pH 8.5, ionic strength 0.1M (adjusted with KCl), and calcite saturation index (SI = $\log_{10}\left(\{Ca^{2+}\}\{CO_3{}^{2-}\}/K_{sp}\right)$) of either 0.5 or 0.8.

Calcium isotope fractionation is found to be weakly stoichiometry dependent. The expected trend of larger magnitude fractionations at lower Ca^{2+}:$CO_3{}^{2-}$ is observed, but the magnitude of change in $\Delta^{44/40}Ca$ over the solution stoichiometries studied (Ca^{2+}:$CO_3{}^{2-}$ = 1-250) is only ∼0.35‰. Similar trends in $\Delta^{44/40}Ca$ with Ca^{2+}:$CO_3{}^{2-}$ are observed at SI = 0.5 and 0.8, with smaller magnitude fractionations at lower supersaturation. This yields an inverse correlation between $\Delta^{44/40}Ca$ and growth rate, confirming the $\Delta^{44/40}Ca$-rate relationship for inorganic calcite growth observed by Tang et al. (2008). The ion-by-ion model framework captures measured $\Delta^{44/40}Ca$ only when a surface complexation model is incorporated, highlighting the role of surface speciation in dictating Ca attachment/detachment dynamics. The model captures observed trends with Ca^{2+}:$CO_3{}^{2-}$ using best-fit kinetic and equilibrium fractionations consistent with end-members observed in natural systems (α_{kinetic} ~ 0.9978, α_{eq} ~ 0.9998). This result implies a total possible range in $\Delta^{44/40}Ca$ of 2‰ and

suggests that for most carbonate precipitating environments, solution supersaturation will be a stronger determinant of $\Delta^{44/40}Ca$ than stoichiometry. The demonstrated importance of surface speciation, however, implies a strong pH influence on $\Delta^{44/40}Ca$, independent of its influence on carbonate ion activity, that requires further investigation.

The results of this study provide strong evidence supporting the model of kink-exchange driven Ca isotope fractionation and suggest that calcite grows by a dominantly classical mechanism over the solution conditions investigated. Model predictions regarding the relationship between $\Delta^{44/40}Ca$ and growth inhibition in the presence of impurity ions lay the foundation for the use of Ca isotopes as molecular tracers of carbonate crystal growth pathways.

This chapter was previously published in Mills *et al.* (2021).

2.1 Introduction

2.1.1 Calcium isotope fractionation during calcite precipitation from aqueous solution: causes and consequences

The partitioning of isotopes and trace elements into carbonate minerals underpins the carbonate-based paleoproxies used to reconstruct Earth's climate and major element cycles throughout geologic time (Emiliani, 1955; Shackleton, 1967; Hoffman *et al.*, 1998). The calcium isotope composition of carbonates in particular has been used to reconstruct modern and ancient calcium (and by implications, carbon) cycles (Rocha and DePaolo, 2000; Fantle and DePaolo, 2005; Farkaš *et al.*, 2007; Sime *et al.*, 2007; Blättler *et al.*, 2012; Blättler and Higgins, 2017), as a temperature proxy (cf. Hippler *et al.* 2006; Gussone *et al.* 2009), to study weathering and pedogenic processes (Tipper *et al.*, 2006; Ewing *et al.*, 2008; Hindshaw *et al.*, 2011), and as a window into the diagenetic history of carbonate sediments (Ahm *et al.*, 2018; Higgins *et al.*, 2018). Interpretation of the calcium isotopic composition of carbonate minerals, however, requires a predictive understanding of the interplay between physio-chemical conditions and calcium isotope fractionation during mineral precipitation.

The lighter ^{40}Ca isotope is preferentially incorporated into calcite during precipitation from aqueous solution with $\Delta^{44/40}Ca_{calcite-fluid}$ ranging from 0‰ to ~-2‰ (DePaolo, 2004). Initial interpretations explained this partitioning either in terms of an equilibrium fractionation (Lemarchand *et al.*, 2004; Marriott *et al.*, 2004) or kinetic fractionation driven by mass-dependent diffusion rates of Ca^{2+}-aquocomplexes in solution (Gussone *et al.*, 2003). Laboratory inorganic precipitation experiments have demonstrated that $\Delta^{44/40}Ca$ is strongly dependent on growth rate (though contrasting dependencies have been observed (Lemarchand *et al.*, 2004; Tang *et al.*, 2008; AlKhatib and Eisenhauer, 2017b)), temperature (Marriott *et al.*, 2004; Gussone *et al.*, 2005; Tang *et al.*, 2008), and weakly dependent on ionic strength (Tang *et al.*, 2012). Although the temperature dependence is consistent with an equilibrium isotope effect, the strong growth rate dependence and lack of fractionation observed in natural systems where calcite precipitates close to equilibrium (deep sea pore fluids (Fantle and DePaolo, 2007) and terrestrial aquifers (Jacobson and Holmden, 2008)) suggest most of the variability in $\Delta^{44/40}Ca$ is driven by kinetic effects. DePaolo (2011) proposed a unifying framework for predicting $\Delta^{44/40}Ca$ in different growth regimes dictated by the relative rates of precipitation and diffusive transport through solution. During surface-reaction limited growth, Ca isotope fractionation is modeled as a balance between kinetic and equilibrium endmember fractionations, dictated by the amount of calcium exchange during growth (forward versus reverse flux of Ca from the surface):

$$\alpha_p = \frac{\alpha_f}{1 + \frac{R^b_{Ca}}{R^f_{Ca}}\left(\frac{\alpha_f}{\alpha_{eq}} - 1\right)} \tag{2.1.1}$$

where α_p is the net fractionation during calcite precipitation ($^{44/40}\mathrm{R}_{\mathrm{calcite}}/^{44/40}\mathrm{R}_{\mathrm{fluid}}$), α_{eq} is the equilibrium fractionation, and α_f is the kinetic isotope fractionation associated with Ca addition at the surface. Ion attachment at the growing crystal surface occurs through a multistep process: solvated ions must first diffuse through solution to the fluid-mineral interface and adsorb at the surface before being incorporated into the crystal lattice (Nielsen, 1984). Diffusion through aqueous solutions exhibits mass-dependent kinetic isotope fractionations (Richter *et al.*, 2006; Bourg and Sposito, 2007), but experimental and simulation studies suggest that the largest possible calcium isotope fractionation due to diffusion through water is ~-0.4‰ (Bourg *et al.*, 2010). Instead, the kinetic fractionation during Ca attachment is likely driven by the mass dependence of Ca desolvation kinetics during incorporation at a kink site (Hofmann *et al.*, 2012; Lammers *et al.*, 2020).

Nielsen *et al.* (2012) extended the conceptual framework of DePaolo (2011), incorporating Ca isotope fractionation into a process-based ion-by-ion model for calcite growth. Ion-by-ion models, formalized for a NaCl structure crystal by Zhang and Nancollas (1998), describe growth kinetics in terms of the addition and removal of monomer ions at kink sites on the growing crystal surface. Derived from classical crystal growth theory (Burton *et al.*, 1951), the ion-by-ion framework of Zhang and Nancollas (1998) accounts for both kink nucleation (Zhang and Nancollas, 1990) and propagation dynamics to describe the rate of step movement along the surface and thus net growth normal to the surface (Figure 2.3). Wolthers *et al.* (2012) and Nielsen et al. (2012; 2013) applied the Zhang and Nancollas (1998) model to calcite growth, accounting for surface speciation, stable isotope fractionation, and trace element partitioning, respectively.

The expression for α_p derived by Nielsen *et al.* (2012) simplifies to the DePaolo (2011) model (Eq. 2.1.1) but critically casts the relative rates of Ca attachment to and removal from the surface in terms of solution chemistry. The ion-by-ion model thus provides a predictive framework for understanding calcium isotope fractionation in terms of the chemistry of the precipitation environment, which is crucial for the interpretation of the calcium isotope composition of modern and ancient carbonates (Nielsen *et al.*, 2012; Druhan *et al.*, 2013; Nielsen and DePaolo, 2013). However, the interpretation of $\Delta^{44/40}Ca$ may be further complicated by aspects of surface structure and solution speciation that can also influence Ca isotope discrimination. Watkins *et al.* (2013) demonstrated that accounting for surface speciation and explicitly differentiating HCO_3^- and CO_3^{2-} interaction with the calcite surface (Wolthers *et al.*, 2012) is required to capture kinetic oxygen isotope fractionation during calcite growth. AlKhatib and Eisenhauer (2017b) further hypothesized that aqueous complexation effects, in their case the formation of Ca^{2+}-NH_3 complexes with strong covalent character, could lead to equilibrium isotope effects that overprint the Ca kinetic isotope fractionation due to surface processes. Differences in local bonding environments and surface structure could also lead to distinct isotopic fractionation factors, as proposed for Ca fractionation into the different vicinal faces of gypsum by Harouaka *et al.* (2014).

The ion-by-ion framework thus requires rigorous testing before it can be applied broadly to the interpretation of Ca isotope fractionation in natural systems. More fundamentally, if this conceptual model holds and $\Delta^{44/40}Ca$ is indeed controlled by Ca exchange at the surface during growth, predictive modeling of $\Delta^{44/40}Ca$ could be used to probe the molecular mechanisms underlying crystal growth. Our understanding of crystal growth has evolved rapidly over the past two decades; non-classical growth mechanisms (e.g. pre-nucleation cluster formation and growth by particle attachment) are increasingly recognized to be pervasive in both abiotic precipitation and biomineralization (Gebauer *et al.*, 2008; De Yoreo *et al.*, 2015). The mass-dependent partitioning of isotopes thus potentially represents a powerful tool for deciphering the complicated suite of processes occurring at the fluid-mineral interface during crystal growth.

2.1.2 Ion by ion model framework predicts strong solution stoichiometry dependence on $\Delta^{44/40}$Ca

One of the strongest predictions from the ion-by-ion model for Ca isotope fractionation (eq 2.2.17) is that α_p (equivalently $\Delta^{44/40}Ca_{calcite-fluid}$) should exhibit a strong dependence on solution stoichiometry (Figure 2.1). For a given supersaturation, at high Ca^{2+}:CO_3^{2-}, $\Delta^{44/40}Ca$ should trend towards the equilibrium fractionation (thought to be near-zero (Fantle and DePaolo, 2007; Jacobson and Holmden, 2008)) because most of the kink sites are occupied by calcium and can thus undergo significant exchange with solution. Conversely, in low Ca^{2+}:CO_3^{2-} solutions there is a paucity of calcium-occupied kinks, which limits the possibility of exchange and drives $\Delta^{44/40}Ca$ towards the kinetic endmember fractionation. The fractionation is also saturation dependent; larger fractionations are expected from higher supersaturation solutions (Figure 2.1).

Numerous studies have investigated the dependence of calcite growth rate on solution stoichiometry, both through bulk growth experiments (Nehrke *et al.*, 2007; Gebrehiwet *et al.*, 2012) and in-situ (or post-growth) AFM measurements (Perdikouri *et al.*, 2009; Hong and Teng, 2014; Sand *et al.*, 2016; Larsen *et al.*, 2010; Davis, 2008; Stack and Grantham, 2010; Bracco *et al.*, 2012). In the bulk growth studies, growth rates are observed to be highest at a Ca^{2+}:CO_3^{2-} slightly higher than 1 (R_{max} ~2 Nehrke *et al.* (2007), R_{max}~3,Gebrehiwet *et al.* (2012)) with relatively symmetric declines in growth rate at higher and lower Ca^{2+}:CO_3^{2-}. Step velocity data provide a more nuanced view of kink propagation dynamics and allow for independent observation of the non-equivalent acute and obtuse calcite steps. The shape of the step velocity curve as a function of Ca^{2+}:CO_3^{2-} varies between acute and obtuse steps and as a function of supersaturation (Sand *et al.*, 2016) and pH (Hong and Teng, 2014). For obtuse steps, the maximum step velocity is observed at a Ca^{2+}:CO_3^{2-} of 1 or higher, consistent with rate limitation by Ca addition due to slower cation desolvation kinetics (Stack and Grantham, 2010). Conversely, the maximum step velocity for acute steps is generally observed at a Ca^{2+}:CO_3^{2-} < 1 ($0.2<Ca^{2+}$:$CO_3^{2-}<0.6$ (Sand *et al.*, 2016)), which suggests that CO_3^{2-} is the limiting ion for the more sterically confined step (potentially due

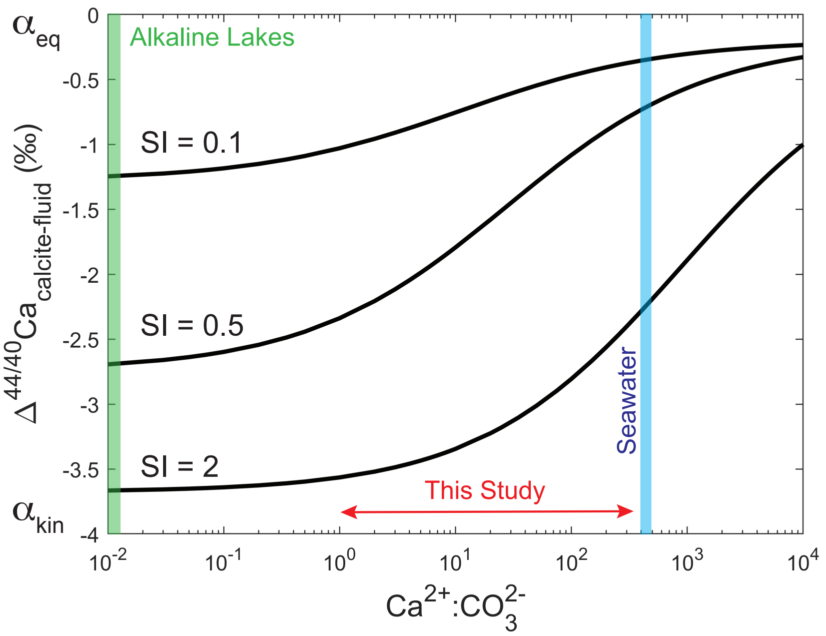

Figure 2.1 – Ion-by-ion model prediction of the variation in $\Delta^{44/40}Ca_{calcite-fluid}$ with changing solution stoichiometry for a range of supersaturations. Model parameterized with step velocities and end member isotopic fractionations from Nielsen et al. (2012) for optimization to Davis (2008) step velocities.

to stronger water adsorption on the acute step (Ruiz-Agudo *et al.*, 2011b; Lardge *et al.*, 2010) or slow CO_3^{2-} re-orientation kinetics during surface diffusion (Hong and Teng, 2014)). More broadly, molecular dynamics simulations suggest that the acute and obtuse steps exhibit different water exchange dynamics, including the density of water molecules at the surface and distribution of water residence times, the kinetic implications of which remain under investigation (Lardge *et al.*, 2010; Wolthers *et al.*, 2013; De La Pierre *et al.*, 2016, 2017).

Comparable systematic data does not exist for the dependence of Ca isotope fractionation on solution stoichiometry. Interrogating this dependence using natural samples is difficult because there are limited carbonate-precipitating environments which span a wide range of $Ca^{2+}:CO_3^{2-}$ under otherwise comparable solution conditions. Seawater ($Ca^{2+}:CO_3^{2-}$~500 (Berner, 1965)) and alkaline lakes ($Ca^{2+}:CO_3^{2-} << 1$) provide high and low $Ca^{2+}:CO_3^{2-}$ end-member scenarios (Figure 2.1), but represent radically different carbonate precipitating environments. Calcium isotope fractionations measured at Mono Lake ($Ca^{2+}:CO_3^{2-}$ 0.0001 - 1) hint at a solution stoichiometry dependence: larger magnitude fractionations are observed in lower $Ca^{2+}:CO_3^{2-}$ solutions, but the fractionations observed do not differ significantly from those observed in seawater (Nielsen and DePaolo, 2013). Moreover, most experimental inorganic calcite growth studies of Ca isotope fractionation are performed with a large aqueous Ca reservoir (Lemarchand *et al.*, 2004; Marriott *et al.*, 2004; Tang *et al.*, 2008; AlKhatib and Eisenhauer, 2017b), resulting in high $Ca^{2+}:CO_3^{2-}$ (500+) and limiting our understanding of Ca isotope discrimination near the kinetic limit.

2.1.3 Investigation goals

In this study we explicitly test the model of kink-exchange driven stable isotope fractionation by investigating the solution stoichiometry (Ca^{2+}:$CO_3{}^{2-}$ activity ratio) dependence of $\Delta^{44/40}Ca$. We present results from a series of constant-composition inorganic calcite growth experiments where all aspects of solution conditions are held constant while Ca^{2+}:$CO_3{}^{2-}$ is varied. These experiments target the low to intermediate Ca^{2+}:$CO_3{}^{2-}$ conditions where $\Delta^{44/40}$Ca is predicted to show a strong solution stoichiometry dependence, but laboratory measurements of $\Delta^{44/40}$Ca are lacking (Figure 2.1). The experimentally determined calcium isotope fractionations provide much-needed constraints on both the solution chemistry dependence of $\Delta^{44/40}$Ca and the magnitude of kinetic and equilibrium endmember fractionations, critical for the interpretation of Ca isotopes in natural systems. More fundamentally, the results allow for a critical assessment of process-based models of calcite growth and pave the way for the use of Ca isotopes as molecular tracers to inform our understanding of the complicated suite of processes occurring at the fluid-mineral interface during crystal growth.

2.2 Methods

2.2.1 Constant composition growth experiments

2.2.1.1 Experimental Setup

Constant composition calcite growth experiments with varied Ca^{2+}:$CO_3{}^{2-}$ stoichiometry were performed using the chemostat reactor shown in Figure 2.2 (adapted from Watkins *et al.* (2013)). Although more difficult to implement than batch (closed system) experiments, the chemostat setup allows us to examine steady-state calcite growth under nearly constant solution conditions. In closed reactors or even most pH stat experiments, changing solution chemistry will lead to dynamically evolving conditions at the fluid-mineral interface, which makes it challenging if not impossible to isolate the effects of different chemical variables on crystal growth and isotope partitioning. The setup consists of a 2L Pyrex growth chamber contained within a fixed-temperature water bath maintained at 25°C by a heater and chiller. An automated titration system controlled by solution pH measurement is used to maintain constant solution conditions in the growth chamber. As calcite precipitates over the course of an experiment, the decrease in solution pH (eq. 2.2.1) triggers the addition of equimolar $CaCl_2$ and K_2CO_3 titrant solutions (0.25M) to return the pH to the set point (8.5), thus replacing the growth units removed from solution through precipitation.

$$Ca^{2+} + HCO_3^- \rightarrow CaCO_3 + H^+ \tag{2.2.1}$$

The titration system consists of two Titronic universal burettes and an IoLine pH combination electrode (Schott Instruments, calibrated with pH 7 and 10 NIST-traceable buffers), interfaced with a multitasking titration system (Multi_T, Jensen Systems). Experiments were run using 1.8L of growth solution to minimize head space volume and potential degassing (problematic only for the high-alkalinity, low Ca^{2+}:$CO_3{}^{2-}$ experiments). The growth solution was stirred at 250rpm with a 3-inch basal stir bar. An important consideration in running these types of experiments is ensuring rapid solution homogenization following

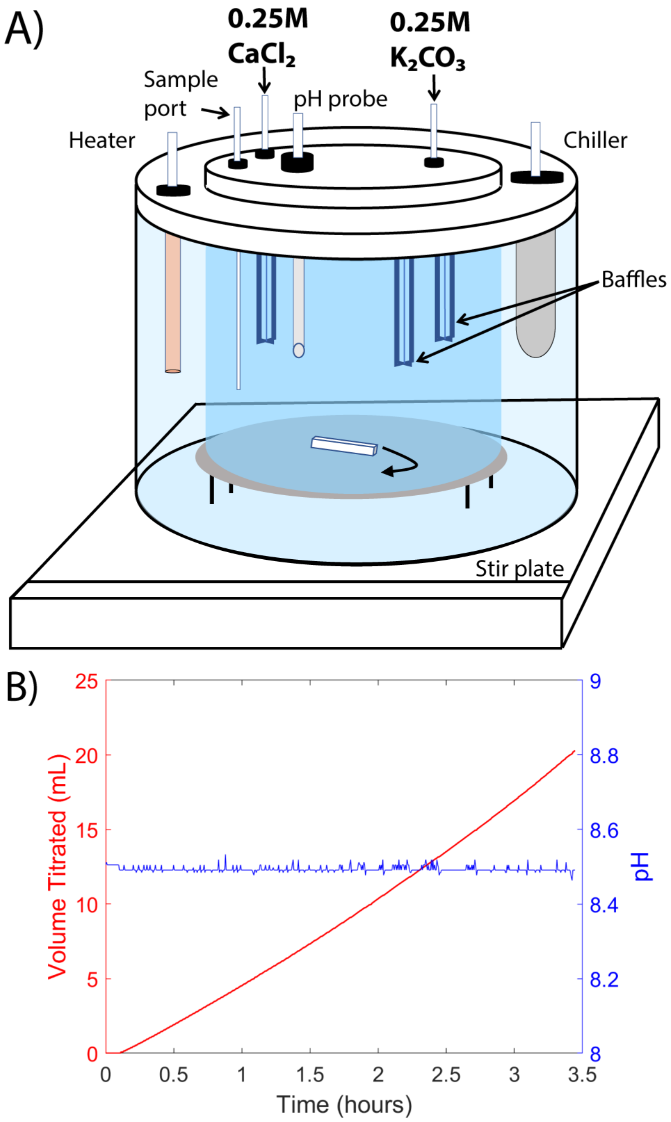

Figure 2.2 – Experimental setup. A) Schematic of chemostat reactor. The Pyrex growth chamber (2L volume) is contained within a fixed-temperature water bath. Constant solution conditions are maintained by auto-titration of K_2CO_3 and $CaCl_2$ to replace the growth units removed from solution by precipitation (titration triggered by pH measurement). B) Representative titration curve showing titrant addition (left axis, red line) in response to measured pH (right axis, blue line) over the course of an experiment.

titrant addition. The $CaCl_2$ and K_2CO_3 titrant inlet ports are located on opposite sides of the growth chamber (Figure 2.2A), and it was initially assumed that the rapid stirring would disperse the titrant drops rapidly enough to prevent calcite nucleation or growth under locally-high supersaturation conditions near the titrant inlet. Initial testing demonstrated that stirring with a basal stir bar was not sufficient to disperse the titrant droplets (which became entrained in the laminar flow) and baffles were added to the growth chamber to disrupt the laminar flow and ensure rapid solution homogenization. The baffles consisted of 3, 10mL pipette tips suspended from the lid of the growth chamber (Figure 2.2A).

2.2.1.2 Materials and solution preparation

Three suites of constant-composition calcite growth experiments were performed (Table 2.1). To isolate the influence of solution stoichiometry on Ca isotope fractionation, all experiments were run at a fixed solution pH (8.5 +/- 0.1), ionic strength (0.1M, adjusted with KCl), temperature (25 ± 0.5°C), and calcite saturation (SI = 0.5 or 0.8), where

$$SI = log_{10}\left(\frac{(Ca^{2+})(CO_3^{2-})}{K_{sp}}\right) \tag{2.2.2}$$

Solution speciation and calcite saturation were determined using PhreeqC, with the phreeqC.dat thermodynamic database and calcite equilibrium constant $K_{sp} = 10^{-8.48}$ (Plummer and Busenberg, 1982). Throughout this work we use Ca^{2+}:$CO_3{}^{2-}$ to denote the Ca^{2+} to $CO_3{}^{2-}$ activity ratio.

In each suite of experiments, the Ca^{2+}:$CO_{3^{2-}}$ activity ratio was varied from 1-100 or 250. Two sets of seeded experiments were performed, at SI 0.5 and 0.8, using Baker-analyzed calcite as seed material. Approximately 100mg of seed was used in the SI 0.5 experiments and 500mg used in the SI 0.8 experiments. The seed material was used directly as obtained from the manufacturer and not treated prior to the experiments. A third set of experiments was run unseeded at SI 0.8 to test the robustness of the experimental setup and determine whether calcite nucleation influences Ca isotope fractionation.

Growth and titrant solutions were prepared by dissolving ACS reagent grade chemicals (Sigma-Aldrich) in ultrapure water (18.2MΩ, Milli-Q). All Ca solutions were prepared using the same 1M $CaCl_2{\bullet}2H_2O$ stock solution; a new stock solution was made before the unseeded experiments (experiment 12, Table 2.1). Titrant solutions (0.25M $CaCl_2$, 0.25M K_2CO_3) were prepared at the start of a suite of experiments and stored in gas-tight Tedlar bags (Sigma-Aldrich). Separate 0.9L cation ($CaCl_2$) and anion ($KHCO_3$ + KCl) growth solutions were prepared at the start of each experiment. The $KHCO_3$ solution was prepared and pH-adjusted with 0.1M KOH just before the start of an experiment to minimize potential loss of dissolved inorganic carbon via CO_2 degassing.

2.2.1.3 Experimental run

Each experiment was started by combining the $CaCl_2$ and $KHCO_3$ + KCl solutions in the growth chamber and attaching the chamber lid (sealed with an o-ring). The solution pH was adjusted to 8.5 using 0.1M KOH and the automated titration program was started. For the seeded experiments, the calcite seed was then added through a port in the chamber lid to initiate precipitation. Solution conditions were monitored throughout the course an experiment by taking 5-20mL fluid aliquots through the sample port at regular intervals. Samples were passed through $0.2\mu m$ syringe filters to remove any calcite; aliquots for cation concentration analysis were immediately acidified with 15N HNO_3 while aliquots for alkalinity analysis were stored (unacidified) in 15mL falcon tubes with minimal headspace until analysis. Alkalinity was measured within 1 hour of sampling. This measurement provided an external check on solution pH, which can drift slightly due to calcite precipitation on the pH probe. The average calcite supersaturation and Ca^{2+}:$CO_3{}^{2-}$ reported in Table 2.1 account for this pH drift. At the end of an experiment, the solution was vacuum filtered through a $0.45\mu m$ nylon membrane filter to collect the precipitated calcite, which was rinsed 3x with Milli-Q H_2O before being dried at room temperature in a fume hood. Experimental duration was dictated by the type of experiment (seeded vs. unseeded) and titration volume required for the determination of Ca isotope fractionation (Section 2.2.2). Unseeded experiments were kept as short as possible to minimize the impact of calcite nucleation and growth on the pH probe.

2.2.2 Analytical techniques

Changes in growth solution Ca concentration over the course of an experiment were measured by ICP-OES (Perkin Elmer 5300 DV, uncertainty ~5% based on repeat analysis of standards). Precise elemental Ca concentrations for initial and end fluid samples were obtained from isotope-dilution measurements (uncertainty ~1%) during Ca isotope analysis. Alkalinity was measured by Gran-titration with calibrated 0.01M H_2SO_4. The morphology of the solids precipitated was examined using scanning electron microscopy (SEM, Zeiss EVO-10 Variable Vacuum). The surface area of the calcite seed material was measured as the N_2 BET surface area at 77K (3Flex, Micromeritics).

Calcium isotope ratios and elemental Ca concentrations were measured with a Finnigan TRITON thermal ionization mass spectrometer (TIMS) using the double spike method (^{42}Ca + ^{48}Ca). Aliquots of fluid samples (or $CaCO_3$ solid samples dissolved in 1M acetic acid) containing 30μg of Ca were spiked with 10μL of double spike per μg Ca added. Calcium separation was performed via column chemistry using Ca-specific DGA resin (Eichrom). The columns were loaded with approximately 300uL resin, and rinsed with 2mL double deionized (DDI) H_2O and 1mL 3M HNO_3. The spiked sample was loaded on the column in 3M HNO_3 and rinsed with 200, 400, and 800uL 3M HNO_3. Ca was then eluted from the column with 1.5mL DDI H_2O (400, 400, 700μL step wise addition). The eluted Ca was dried down and re-suspended in a few drops of concentrated HNO_3 and 40% hydrogen peroxide and left overnight. The samples were dried down once more and resuspended in 10μL, 3M nitric acid. The purified Ca sample was then loaded on outgassed zone-refined Re double filaments (3μg Ca loaded with 40% phosphoric acid) and its Ca isotopic composition was analyzed on the TIMS. All Ca isotope ratios are expressed in standard delta notation relative to bulk silicate earth (BSE - ^{44}Ca/^{40}Ca = 0.0212035) as:

$$\delta^{44/40}Ca = \left(\frac{(^{44}Ca/^{40}Ca)_{sample}}{(^{44}Ca/^{40}Ca)_{BSE}} - 1 \right) 1000 \tag{2.2.3}$$

The NIST SRM 915a reference material was measured 3x per turret and used to determine external errors on $\delta^{44/40}$Ca measurements. SRM 915a measurements averaged to -0.92‰ with an external 2σ reproducibility of ±0.15‰ (n = 18).

2.2.3 Growth rate determination

The calcite growth rate in mol/s was determined from the experimental titration curve (Figure 2.2B):

$$R(mol/s) = C * \frac{dV}{dt} \tag{2.2.4}$$

where C is the titrant concentration (0.25M) and $\frac{dV}{dt}$ is the slope of the titrant volume versus time curve (Figure 2.2B). To obtain surface-normal growth rates (mol/m^2/s), this rate must be normalized by an estimate of the reactive surface area (m^2). Reactive surface area is difficult to quantify as it is scale-dependent and can evolve over the course of an experiment as new crystals nucleate from solution and subsequently ripen. For the seeded experiments, we used the BET surface area of the seed crystal (specific surface area, SSA = 0.21 ± 0.1 m^2/g) to calculate the reactive surface area (m^2 = SAA*grams calcite) and calculated the slope of the titration curve from the first 0.5-2.5mL titrated. This constrained the growth rate calculation to the interval in which the reactive surface area is best defined - before the onset of nucleation when the vast majority of surface area is provided by the seed crystal. When the same amount of seed was used in replicate experiments, calculated surface-normal growth rates were within 3% but relative differences up to 10% were observed in experiments run with different amounts of seed material. We thus assign a 10% error to the absolute surface-normal growth rates measured.

For the unseeded experiments, the reactive surface area was estimated from the geometric surface area calculated from post-growth SEM images (Figure 2.4), calculating the surface area of a regular rhombohedron as:

$$SA = (d_1 * d_2) + 4 * \left(\left(\frac{d_1}{2}\right)^2 + \left(\frac{d_2}{2}\right)^2\right) \tag{2.2.5}$$

where d$_1$ and d$_2$ are the diagonals of the rhombic face. Given that this surface area was derived from post-growth analysis, the slope of the titration curve was taken from the final 2mL titrated in each experiment. For comparison to growth rates calculated with the BET surface area, the geometric surface area was scaled by the ratio of the geometric surface area calculated for the seed crystals (0.39 m^2/g) to the BET surface area (0.21 m^2/g). However, we present these geometric surface areas as qualitative estimates only and focus on the surface-normalized growth rates measured for the two suites of seeded experiments. The induction time for the unseeded experiments was also estimated as the time before the onset of titrant addition and thus calcite growth following nucleation from solution.

2.2.4 Calculation of calcium isotope fractionation

The calcium isotope fractionation factor between the solid and aqueous solution (eq 2.2.6) was calculated using a Ca isotope box model, where Ca is added to the growth solution through titration and removed through calcite precipitation (eqs 2.2.7-2.2.11). This accounts for variations in the size of the Ca reservoir. Initial Ca concentrations vary by a factor of 20 across the experiments presented here, which changes how the isotopic composition of the growth solution changes through time. In low Ca^{2+}:CO_3^{2-} ratio solutions, $\delta^{44}Ca_{fluid}$ evolves to much heavier values over the course of an experiment (as the system approaches isotopic steady-state, where $\delta^{44}Ca_{in} = \delta^{44}Ca_{calcite}$) than in high calcium solutions.

$$\Delta^{44/40}Ca_{calcite-fluid} = \delta^{44}Ca_{calcite} - \delta^{44}Ca_{fluid} \approx 1000 ln\alpha_p \tag{2.2.6}$$

For a non-steady state mass, the change in Ca over time is:

$$\frac{dCa_{fluid}}{dt} = F_{in} - F_{out} \tag{2.2.7}$$

where F_{in} is the flux of Ca into the growth solution (i.e. titration rate - mol/s) and F_{out} is the flux of Ca out of solution via precipitation. The change in $\delta^{44}Ca_{fluid}$ over time can similarly be modeled by tracking ^{40}Ca and ^{44}Ca separately:

$$\frac{d^{44}Ca_{fluid}(t)}{dt} = \frac{R_{in}}{R_{in}+1}F_{in}(t) - \frac{R_{calcite}(t)}{R_{calcite}(t)+1}F_{out}(t) \tag{2.2.8}$$

$$\frac{d^{40}Ca_{fluid}(t)}{dt} = \frac{1}{R_{in}+1}F_{in}(t) - \frac{1}{R_{calcite}(t)+1}F_{out}(t) \tag{2.2.9}$$

$$R_{fluid}(t) = \frac{^{44}Ca_{fluid}(t)}{^{40}Ca_{fluid}(t)} \tag{2.2.10}$$

$$R_{calcite}(t) = \alpha_p R_{fluid}(t) \tag{2.2.11}$$

where $R_{in,}$ R_{fluid}(t), and $R_{calcite}$(t) are the 44/40 ratio of the $CaCl_2$ titrant solution (constant), growth solution, and precipitated calcite at a given point of time, respectively. Equations 2.2.7-2.2.11 were solved numerically by finite difference in Matlab. This allowed any changes in the size of the Ca reservoir due to titrant offset (even a 1% difference between the $CaCl_2$ and K_2CO_3 titrants can lead to substantial changes in [Ca^{2+}] for the lowest Ca^{2+}:CO_3^{2-} experiments) to be taken into account. The total change in Ca concentration over the course of an experiment was <5% for all experiments (usually <2%) with the exception of the Ca^{2+}:CO_3^{2-} $=$ 1 experiments, where [Ca] decreased by 11% and 13% in experiments 1 and 11, respectively (Table 2.1). Maintaining constant [Ca] in experiments where Ca^{2+}:CO_3^{2-} $\leq$ 1 is particularly difficult due to the small size of the Ca reservoir and higher potential for CO_2 degassing associated with the high carbonate alkalinity.

For the unseeded experiments, this full time-dependent box model was used to track the evolution of $\delta^{44}Ca_{fluid}$ and $\delta^{44}Ca_{calcite}$ over the course of each experiment (the final solid $\delta^{44}Ca_{calcite}$ is the $\delta^{44}Ca_{calcite}$(t) integrated over time), using the experimental titration curve to set F_{in}. $\Delta^{44/40}Ca_{calcite-fluid}$ was calculated from the range of α_p that yielded measured $\delta^{44}Ca_{fluid}$ (final + intermediate time points) and $\delta^{44}Ca_{calcite}$ (final) values within 2σ error. For the seeded experiments, $\Delta^{44/40}Ca_{calcite-fluid}$ was calculated from the evolution of the fluid reservoir exclusively. In this case, $\Delta^{44/40}Ca_{calcite-fluid}$ from the full time-dependent model was well-approximated by that calculated from a simplified, steady-state box model:

$$\Delta^{44/40}Ca_{calcite-fluid} = \frac{\delta^{44/40}Ca_{fluid,initial} - \delta^{44/40}Ca_{fluid,final}}{1 - e^{-(moles\,Ca\,titrated/moles\,Ca\,growth\,solution)}} \tag{2.2.12}$$

In all cases, 2σ error for $\Delta^{44/40}Ca_{calcite-fluid}$ was calculated through formal error propagation.

2.2.5 Ion-by-ion model of calcite growth and $\Delta^{44/40}$Ca

The process-based model of Nielsen *et al.* (2012) was used as the baseline description of calcite growth kinetics and $\Delta^{44/40}Ca$ as a function of solution chemistry. Calcium isotope fractionation was also incorporated into the Wolthers *et al.* (2012) ion-by-ion model of calcite growth to explore the influence of surface speciation (cf. Watkins *et al.* 2013). Key equations for the two models are summarized in Table A1 (Appendix A). In brief, the net growth rate is dictated by the rate at which monomer ions are added and removed from kink sites on the growing crystal surface:

$$R_{net}(m/s) = \left(\frac{h}{y_0}\right) v_{st} = \frac{\rho u h a}{y_0} \tag{2.2.13}$$

where h is the step height (m), y_0 is the step spacing (m), v_{st} is the step velocity (m/s), ρ is the kink density (unitless), u is the kink propagation rate (s^{-1}), and a is the kink depth (m) (Figure 2.3). The growing steps on the surface can be thought to consist of two types of kink sites – ‘A’ kinks where B ions attach, and ‘B’ kinks where A ions attach. In the case of calcite, A and B are Ca^{2+} and CO_3^{2-}. Thus, the rate of propagation of an A kink is the rate at which A ions are incorporated at kink sites (dictated by the attachment rate $k_A\{A\}$ and the probability a given kink site is a B kink – P_B) relative to the rate at which they are removed from kink sites (dictated by the detachment frequency v_A and the probability a given kink site is an A kink):

$$u_A = k_A\{A\}P_B - v_A P_A \tag{2.2.14}$$

The same is true for a B kink:

$$u_B = k_B\{B\}P_A - v_B P_B \tag{2.2.15}$$

The overall kink propagation rate is then the sum of A and B kink propagation rates:

$$u = u_A + u_B \tag{2.2.16}$$

Accounting for the $^{44/40}Ca$ fractionation during attachment at (α_f) and removal from (α_b) a kink site yields (Nielsen *et al.*, 2012):

$$\alpha_p = \frac{\alpha_f k_A[A]P_B}{k_A[A]P_B + v_A P_A\left(\frac{\alpha_f}{\alpha_{eq}} - 1\right)} \tag{2.2.17}$$

where the equilibrium fractionation arises from the difference between Ca fractionation during attachment and detachment ($\alpha_{eq} = {}^{\alpha_f}/_{\alpha_b}$).

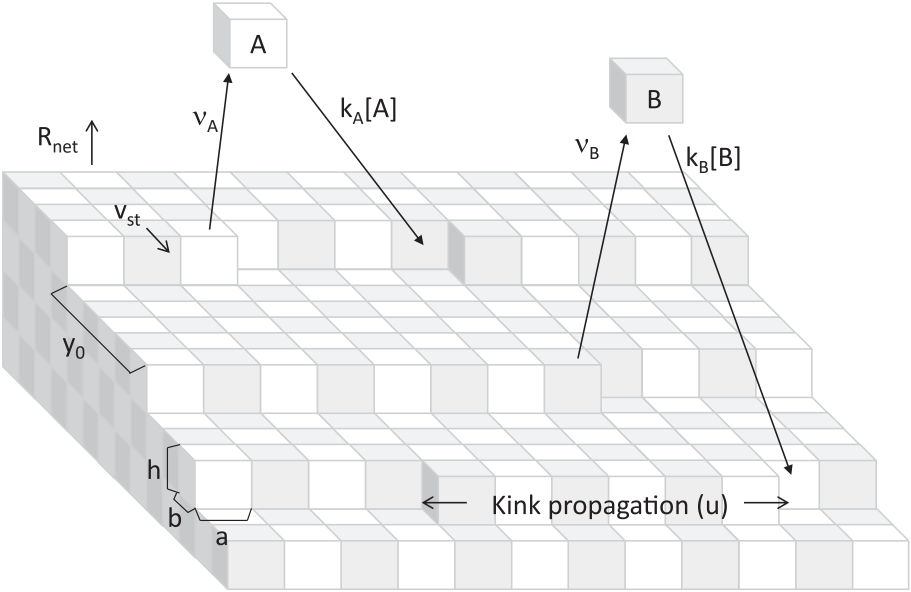

Figure 2.3 – Key processes modeled in ion-by-ion growth models: the addition and removal of growth units from kink sites. Figure modified from Nielsen *et al.* (2012).

The primary differences between the two ion-by-ion formulations are that bicarbonate is explicitly modeled as a third growth unit (B_2) in the Wolthers formulation, and the kink site probabilities do not sum to 1. Instead, the fraction of available growth sites (χ) for a given solution composition is calculated from the surface complexation model of Wolthers et al. (2008). Watkins et al. (2013) demonstrated that differentiating between bicarbonate and carbonate is required to model oxygen isotope fractionation during calcite growth but did not invoke a solution chemistry dependent χ. Both model formulations contain two sets of free parameters: attachment/detachment coefficients, which dictate kink propagation rates and their stoichiometry dependence, and endmember Ca isotope fractionations. Attachment/detachment coefficients were fit to available step velocity data (Davis, 2008; Larsen *et al.*, 2010; Stack and Grantham, 2010; Bracco *et al.*, 2012; Hong and Teng, 2014; Sand *et al.*, 2016). For the Nielsen model, the Ca^{2+} and CO_3^{2-} detachment frequencies were assumed to be equal (given that the same bond is broken for either species to detach from a kink site) and k_A, k_B were fit to the step velocity data. For the Wolthers formulation, we followed the assumptions from that study, assuming k_B=2k_A, and fitting k_A and ν_A (Table A1). Kinetic and equilibrium endmember Ca isotope fractionations were fit to the data from this study and the 25°C dataset from Tang et al. (2008). All optimizations were performed by least-squares optimization using fminsearchbnd.m in Matlab. For the Ca isotope fractionations, the residual was weighted by the experimental variance ($1/\sigma^2$). Fitted model parameters for all available step velocity measurements are provided in Table A2 and Figure A1 in Appendix A; for simplicity we only show models fit to Davis (2008) step velocity measurements here. Optimization for the other step velocity measurements yielded comparable results.

To calculate surface area normalized growth rates from modeled step velocities, an expression for the average step spacing (y_0) is needed (Eq. 2.2.13). Step nucleation during classical calcite growth at low supersaturations typically occurs at single screw dislocations, generating spiral growth hillocks. However, step nucleation can also occur on hillocks with more complicated morphologies (via multiple dislocation sources) as well as by 2D-nucleation at higher supersaturations (Teng *et al.*, 2000). Although each of these mechanisms gives a distinct dependence of y_0 on aqueous supersaturation, they do not influence the relative rates of ion exchange on the step. Notably, as long as growth occurs by classical ion-by-ion addition to kink sites, Ca isotope fractionation at a given set of solution conditions (Eq. 2.1.1 and 2.2.17) should be independent of growth morphology. Assumptions regarding the growth mechanism are critical, however, for modeling the $\Delta^{44/40}Ca$-growth rate relationship.

Here we calculate the bulk growth rate assuming step nucleation occurs at single screw dislocations forming spiral growth hillocks but also consider the implications of growth by 2D nucleation (Table A1). Equation 2.2.13 describes the bulk growth rate for the case of single spiral growth. In order to scale-up calculated step velocities, the step spacing (y_0) for the given solution conditions must be estimated. Previous ion-by-ion formulations have relied on a thermodynamic representation of y_0, which is sensitive only to the assumed step edge free energy and supersaturation ((Teng *et al.*, 1998):

$$y_0 = \frac{16ha^2\gamma}{k_bT\sigma} \tag{2.2.18}$$

where γ is the step-edge free energy per unit step height (~1.4 J/m^2(Teng *et al.*, 2000)). However, it has been demonstrated that the step width is sensitive to solution stoichiometry at a constant supersaturation (Bracco *et al.*, 2013; Davis, 2008). Bracco *et al.* (2013) found that the step width decreases with increasing Ca^{2+}:$CO_3{}^{2-}$ while Davis (2008) found that y_0 increases with increasing Ca^{2+}:$CO_3{}^{2-}$. We examine the implications of both here.

For the Davis y_0 relationship, we calculated the step width at Ca^{2+}:$CO_3{}^{2-} = 1$ using eq. 2.2.18 and then scaled y_0 with Ca^{2+}:$CO_3{}^{2-}$ as:

$$y_0(i) = y_{0,Ca:CO_3=1}\left(0.3364\log_{10}\left(\frac{\{Ca^{2+}\}}{\{CO_3^{2-}\}}\right) + 1.05\right) \tag{2.2.19}$$

For the Bracco y_0 relationship, we used the empirical relationship between step density (1/step width), SI and Ca^{2+}:$CO_3{}^{2-}$ derived in that publication:

$$\frac{1}{y_0}(\mu m^{-1}) = 1.8 * SI + 0.42\log_{10}\left(\frac{\{Ca^{2+}\}}{\{CO_3^{2-}\}}\right) + 1.47 \tag{2.2.20}$$

In all cases, the obtuse step velocity was used to calculate the bulk growth rate. Rates calculated from either the acute or obtuse step must be equivalent given geometric constraints (Nielsen et al., 2012), but more step width data are available for obtuse steps.

2.3 Results

2.3.1 Morphology of precipitated calcite

Rhombohedral calcite was the only morphology observed to have precipitated in all experiments (Figure 2.4); no morphological evidence of the other crystalline $CaCO_3$ polymorphs

Exp.	Calcite seed	$[Ca]_0$	$[Ca]_{end}$	$\text{Alkalinity}_{\text{avg}}{}^{*}$	$\text{SI}_{\text{avg}}{}^{\dagger}$	$\{Ca^{2+}\}\,/\,\{CO3^{2-}\}_{avg}{}^{\dagger}$	Growth rate	$\Delta^{44/40}Ca_{calcite-fluid}$	2σ error
units	g	mM	mM	meq/L			mol/m^2/s	‰	
1	0.10	1.36	1.34	1.88	0.49	26.0	1.04E-06	-0.87	0.12
2	0.10	0.30	0.28	9.20	0.49	1.0	1.18E-06	-1.25	0.09
3	0.10	0.89	0.90	2.97	0.53	10.0	1.16E-06	-1.11	0.14
4	0.10	2.67	2.67	0.99	0.53	92.9	9.55E-07	-0.97	0.13
5	0.10	1.36	1.36	1.90	0.53	23.8	1.01E-06	-0.97	0.12
6	0.49	0.43	0.38	12.89	0.76	1.0	3.00E-06	-1.54	0.07
7	0.50	1.22	1.22	4.20	0.78	10.3	3.10E-06	-1.41	0.09
8	0.51	1.98	1.91	2.72	0.81	24.9	2.86E-06	-1.43	0.14
9	0.50	3.79	3.69	1.41	0.79	100.5	2.45E-06	-1.22	0.21
10	0.50	6.00	5.76	0.92	0.79	242.3	2.16E-06	-1.23	0.22
11	1.00	5.97	5.66	0.93	0.76	265.9	2.41E-06	-1.30	0.19
12	-	0.42	0.37	13.20	0.78	0.90		-1.62	0.09
13	-	1.19	1.15	4.27	0.83	8.3		-1.47	0.05
14	-	1.88	1.83	2.81	0.84	21.3		-1.46	0.16
15	-	3.64	3.70	1.49	0.86	81.9		-1.14	0.10
16	-	3.70	3.68	1.44	0.84	87.2		-1.31	0.15

Table 2.1 – Summary of experimental solution conditions and results. *Average alkalinity is the average between initial and final measured alkalinity. †Average saturation index (SI) and Ca^{2+}:$CO_3{}^{2-}$ activity ratio reflect the average between the initial and final Ca^{2+} and $CO_3{}^{2-}$ $CO_3{}^{2-}$ activities, after accounting for any pH drift due to calcite precipitation on the pH probe. Additional data on solution conditions and $\delta^{44}Ca$ results are provided in Table A5.

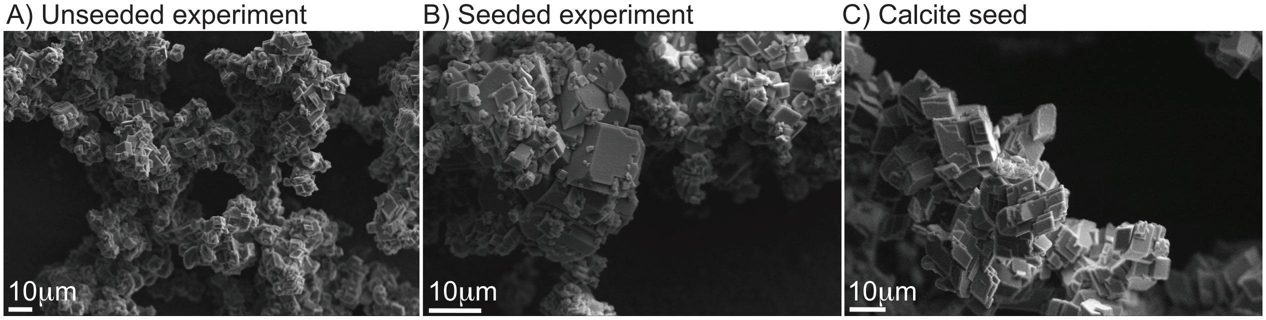
A) Unseeded experiment B) Seeded experiment C) Calcite seed

Figure 2.4 – Representative scanning electron microscope images of (A) precipitated solids in unseeded experiments, (B) precipitated solids in seeded experiments, and (C) initial calcite seed material. Scale bar = 10μm.

Exp	Ca^{2+}:CO_3^{2-}	Exp duration	Induction time	$CaCO_3$ precipitated	Geometric SA	Growth rate
units		hours	hours	g	m^2/g	$mol/m^2/s$
12	0.9	10.5	5.2	0.263	1.08	1.59E-06
13	8.3	9	4.7	0.272	1.06	2.39E-06
14	21.3	9.8	4.3	0.193	0.82	2.83E-06
15	81.9	7.7	3.7	0.203		2.25E-06
16	87.2	7.3	3.7	0.157	1.6	2.45E-06
seed					0.39	

Table 2.2 – Summary of post-growth SEM analysis of unseeded growth experiments and calcite seed material.

vaterite or aragonite was observed. In the unseeded experiments, average particle size ranged from $1.9\pm0.8\mu m$ - $3.2\pm1.1\mu m$, with the smallest particles and thus highest geometric surface area observed for the Ca^{2+}:CO_3^{2-} = 100 experiment that ran for the shortest amount of time (Table 2.2). This was considerably smaller than the average particle size of $6.4\pm2.2\mu m$ observed for the calcite seed material (Figure 2.4C).

2.3.2 Calcite precipitation kinetics

2.3.2.1 Growth rate as a function of solution stoichiometry: seeded experiments

Consistent with previous reports (Nehrke *et al.*, 2007; Gebrehiwet *et al.*, 2012), calcite growth rate varies systematically with the Ca^{2+}:CO_3^{2-} activity ratio, with the maximum growth rate occurring somewhere between a ratio of 1 and 10 and declining growth rates as the Ca^{2+}:CO_3^{2-} increases (Figure 2.5). Figure 2.5A shows absolute surface-normal growth rates for the two suites of seeded experiments. In Figure 2.5B, those growth rate data are normalized by the measured rate at Ca^{2+}:CO_3^{2-} =1 for each set of experiments to examine how the relative growth rate varies as a function of Ca^{2+}:CO_3^{2-}. The same seed material was used throughout these experiments, so the normalized data highlight the relationship between

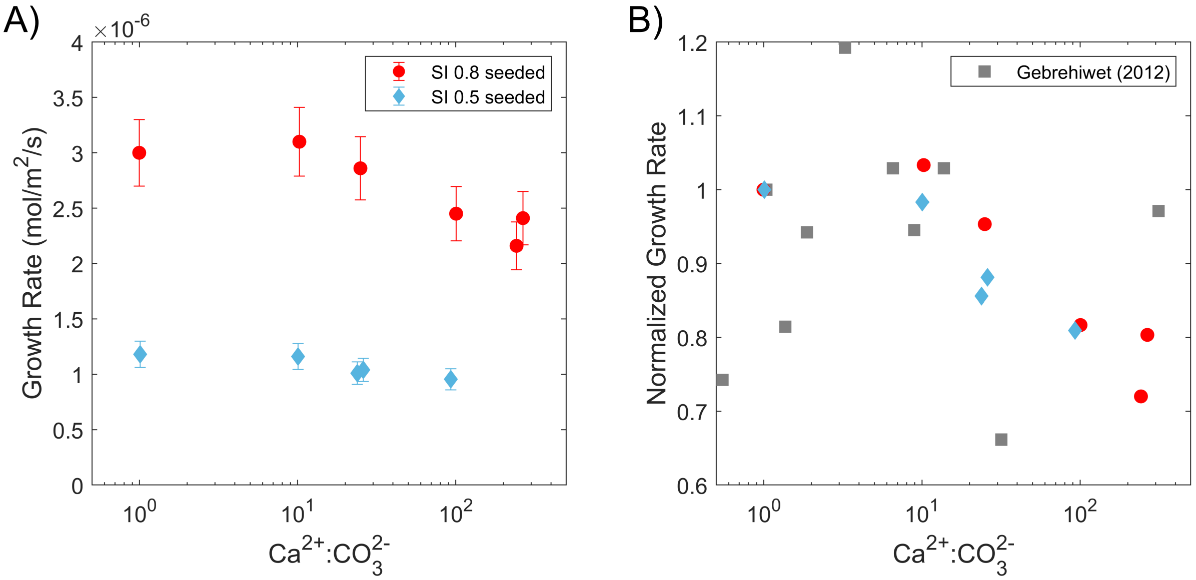

Figure 2.5 – Measured growth rates for seeded experiments at SI = 0.5 (blue diamonds) and SI = 0.8 (red circles). A) Surface-normal growth rates. B) Relative growth rates, normalized by the surface-normal growth rate at Ca^{2+}:$CO_3{}^{2-}$ = 1 for each supersaturation. Growth rates from Gebrehiwet et al. (2012), normalized by the growth rate at Ca^{2+}:$CO_3{}^{2-}$ = 1 from that study, are shown as grey squares.

growth rate and solution stoichiometry independent of the aqueous supersaturation with respect to calcite. Data from the seeded growth experiments from this study are plotted alongside bulk growth rate data from Gebrehiwet *et al.* (2012), normalized by the growth rate at Ca^{2+}:$CO_3{}^{2-}$ =1 from that study. The seeded calcite growth experiments in Gebrehiwet *et al.* (2012) were performed at the same pH (8.5) used here and a slightly higher SI (0.9). Although Gebrehiwet et al. assumed a much higher reactive surface area (1.3 m^2/g) and thus report lower growth rates at SI = 0.9 than we measure at SI = 0.8, the relative change in growth rate as a function of solution stoichiometry is consistent with our findings (Figure 2.5B). Bulk growth rates are low at low Ca^{2+}:$CO_3{}^{2-}$, increase to a maximum at a ratio of ~3-5, and then decrease with increasing Ca^{2+}:$CO_3{}^{2-}$.

2.3.2.2 Unseeded experiments: influence of solution stoichiometry on nucleation dynamics

As discussed in Section 2.2.3, determining absolute growth rates for unseeded experiments is challenging given the uncertainty surrounding the reactive surface area and its evolution through time. Estimating specific surface area from SEM images (and scaling to reflect the BET specific surface area 2.2.3) yields surface-normal growth rates for the unseeded experiments roughly equivalent to that observed in the seeded experiments (Figure 2.6A). However, the same rate dependence on solution stoichiometry is not observed - apparent maximum growth rates are observed at Ca^{2+}:$CO_3{}^{2-}$ = 25 in the unseeded experiments, while maximum growth rates occur between Ca^{2+}:$CO_3{}^{2-}$ = 1-10 in both the seeded experiments in this study and other seeded bulk-growth studies (Gebrehiwet *et al.*, 2012; Nehrke *et al.*,

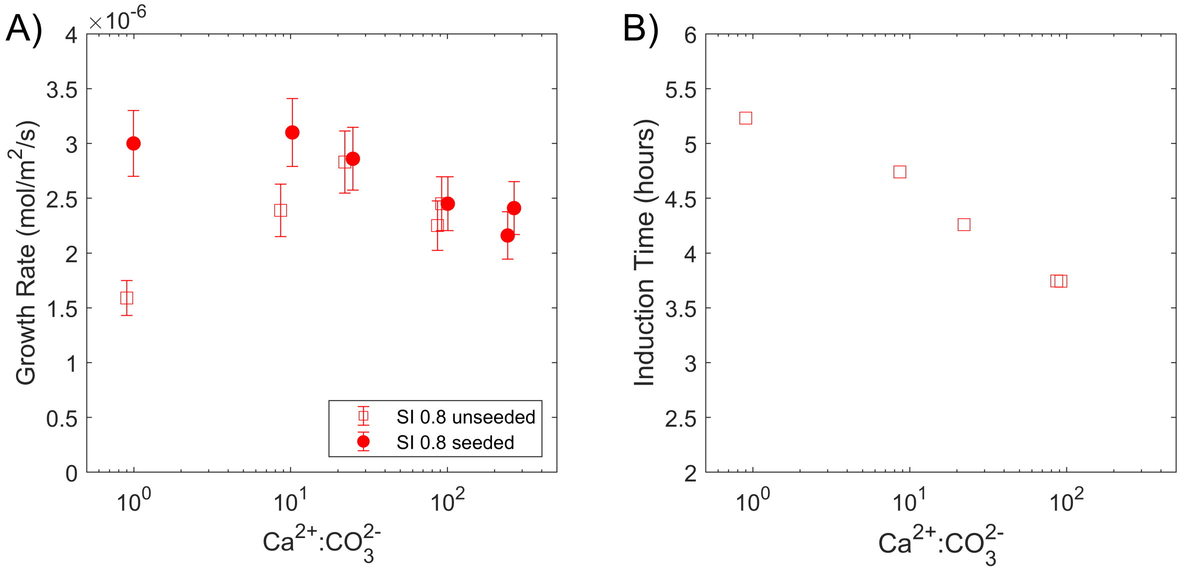

Figure 2.6 – Nucleation and growth dynamics for unseeded (SI 0.8) experiments. A) Estimated surface-normal growth rates for unseeded experiments (exps 12-16, hollow squares) plotted alongside growth rates for the SI 0.8 seeded experiments (exps 6-11, filled circles). See Section 2.2.3 for details of the growth rate calculation for the two suites of experiments; in each case, the growth rate was calculated from the time interval in which the reactive surface area is best constrained (first 0.5-2.5mL for seeded experiments, final 2mL for the unseeded experiments). B) Observed induction time as a function of Ca^{2+}:$CO_3{}^{2-}$ in the unseeded experiments.

2007). This is likely due to particle nucleation dynamics and differences in specific surface area that are not well-represented by estimates of geometric surface area from post-growth SEM images. Indeed, a systematic trend in calcite induction time (*i.e.* time before the onset of calcite growth via heterogeneous nucleation) with Ca^{2+}:$CO_3{}^{2-}$ is observed (Figure 2.6B). While these should be considered qualitative estimates, the measured induction times decrease monotonically with increasing Ca^{2+}:$CO_3{}^{2-}$, suggesting that the barrier to nucleation decreases with increasing Ca^{2+}:$CO_3{}^{2-}$. The lower nucleation rates in low Ca^{2+}:$CO_3{}^{2-}$ solutions may be responsible for the offset between surface-normal growth rates calculated for the seeded and unseeded experiments (Figure 2.6).

2.3.3 Ca isotope fractionation variation with solution stoichiometry

Calcium isotope fractionation is found to be weakly dependent on solution stoichiometry (Figure 2.7). Examining the results from the SI = 0.8 experiments (red circles and squares, Figure 2.7A), the expected trend of larger fractionations at lower Ca^{2+}:$CO_3{}^{2-}$ is observed, but the magnitude of the change in $\Delta^{44/40}Ca$ over the solution stoichiometries studied is only ~0.35‰, shifting from $\Delta^{44/40}Ca$ = -1.6‰ at Ca^{2+}:$CO_3{}^{2-}$=1 to ~-1.25‰ at Ca^{2+}:$CO_3{}^{2-}$ = 250. Nearly identical fractionations are measured in the seeded and unseeded suites of experiments. This lends confidence that the chemostat growth experiments are highly reproducible and suggests that nucleation does not measurably impact $\Delta^{44/40}Ca$. This is perhaps not surprising given the length scales over which a freshly nucleated calcite particle could

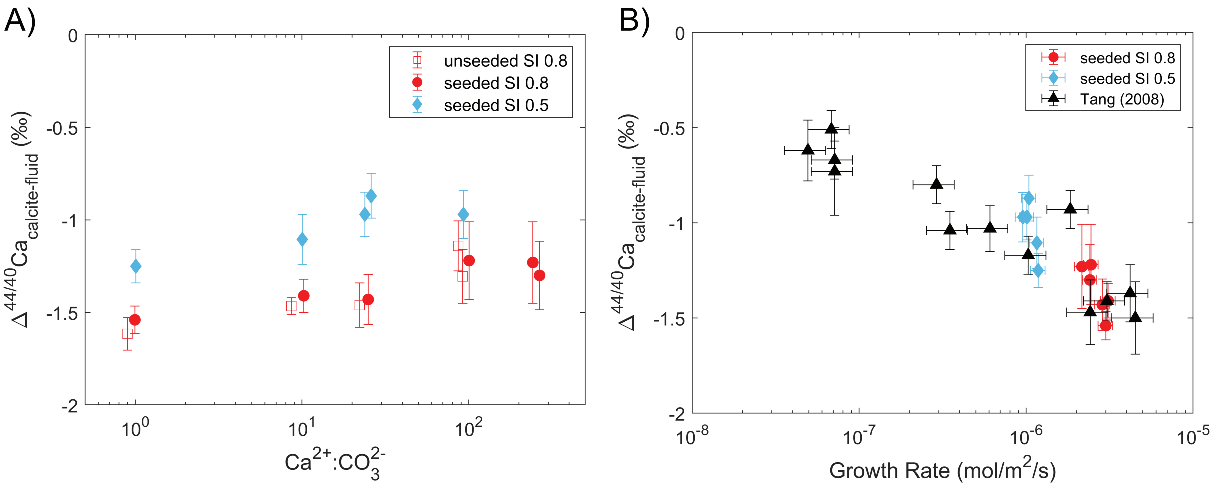

Figure 2.7 – Calcium isotope fractionation as a function of A) Ca^{2+}:$CO_3{}^{2-}$ activity ratio and B) surface-normal growth rate for SI = 0.8 unseeded (red squares), SI = 0.8 seeded (red circles), and SI = 0.5 seeded (blue diamonds) experiments. In B, the 25°C data from Tang et al. (2008) are plotted as black triangles.

be considered structurally distinct from bulk calcite. Assuming that a calcite nucleus is representative of the bulk structure once the bulk structure contribution to the free energy change during precipitation is greater than the surface free energy contribution, a particle >10nm should reflect the bulk under the conditions investigated here. This assumes a cubic nucleus, interfacial energy of 0.12J/m^2 (Söhnel and Mullin, 1978, 1982), and SI 0.5. The average particle size observed by post-growth SEM analysis of the unseeded experiments was between 2 and $3\mu m$ (Section 2.3.1). Thus, the volume fraction of material representative of the calcite nucleus versus that representative of bulk material is on the order of 1e-7. The good agreement between the seeded and unseeded results should thus not be interpreted to suggest that $\Delta^{44/40}Ca$ during calcite nucleation is identical to that during bulk growth; instead these results highlight the reproducibility of the experiments and suggest that $\Delta^{44/40}Ca$ reflects steady-state bulk growth conditions in both sets of experiments.

In the lower supersaturation experiments (SI = 0.5), a similar trend in fractionation as a function of Ca^{2+}:$CO_3{}^{2-}$ is observed, shifted to more positive values of $\Delta^{44/40}Ca$ (blue diamonds, Figure 2.7). Smaller magnitude Ca isotope fractionations in lower supersaturation solutions are consistent with both the conceptual framework of Ca isotope discrimination driven by Ca-exchange at kink sites (Eq. 2.2.17 and Figure 2.1) and the inorganic calcite growth experiments of Tang *et al.* (2008). Our findings confirm the trend that $\Delta^{44/40}Ca$ becomes more negative with increasing growth rate, in line with the growth rate dependence reported by Tang *et al.* (2008) and the 37.5°C data of AlKhatib and Eisenhauer (2017b), but not the lower temperature results of AlKhatib and Eisenhauer (2017b) or those of Lemarchand *et al.* (2004).

2.4 Discussion

2.4.1 Comparison to ion-by-ion model predictions: Original formulation over-predicts $\Delta^{44/40}Ca$ stoichiometry dependence

Comparing these results to ion-by-ion model predictions, we find that the original parameterization of the Nielsen et al. (2012) model predicts a much stronger solution stoichiometry influence on Ca isotope discrimination than observed here. With attachment/detachment coefficients fit to Davis (2008) step velocities and endmember Ca isotope fractionations fit to the Tang et al. (2008) 25°C dataset, the model substantially over-estimates $\Delta^{44/40}Ca$ at low Ca^{2+}:$CO_3{}^{2-}$ (Figure 2.8A,B). Notably, the Tang et al. (2008) experiments were performed in high Ca^{2+}:$CO_3{}^{2-}$ solutions (Ca^{2+}:$CO_3{}^{2-}$ 450-1750), leaving the kinetic endmember fractionation poorly constrained. In order to capture the Tang et al. (2008) data with an equilibrium endmember fractionation of -0.2‰ (Fantle and DePaolo, 2007), optimized kinetic endmember fractionations ranged from -3.7‰ for attachment coefficient fit to Davis (2008) step velocities to -8‰ for attachment coefficients fit to step velocity data from Larsen et al. (2010) (Nielsen et al., 2012). The model thus predicted larger magnitude fractionations at low Ca^{2+}:$CO_3{}^{2-}$ than have been observed in natural systems (DePaolo, 2004). The total range of $\Delta^{44/40}Ca$ of Holocene marine carbonates falls within 2‰ of average $\Delta^{44/40}Ca_{\text{seawater}}$ (Fantle and Tipper, 2014). Reported $\Delta^{44/40}Ca$ for biomineralized calcite typically ranges from -0.6 to -1.6‰ (DePaolo, 2004; Gussone *et al.*, 2005; Steuber and Buhl, 2006; Gussone *et al.*, 2007; Mejía *et al.*, 2018) and a similar range in $\Delta^{44/40}Ca$ has been reported for calcite precipitation stimulated by microbial alkalinity production (Henderson *et al.*, 2006; Druhan *et al.*, 2013; Bradbury *et al.*, 2020). The largest magnitude $\Delta^{44/40}Ca$ thus far observed for fully inorganic calcite growth is -2.4‰ (measured at 7°C, $\Delta^{44/40}Ca$ varied from -1.8 to -2.3‰ at 25°C), reported by Reynard *et al.* (2011) in cave-analog experiments where precipitation was driven by rapid CO_2 degassing. Even in highly alkaline Mono Lake (Ca^{2+}:$CO_3{}^{2-}$ 0.0001-1), the most negative $\Delta^{44/40}Ca_{calcite-fluid}$ observed was -1.8‰ (Nielsen and DePaolo, 2013).

Optimizing endmember isotope fractionations to the $\Delta^{44/40}Ca$ data from this study and Tang et al. (2008) yields model predictions that qualitatively match the observed $\Delta^{44/40}Ca$ dependence on solution stoichiometry (Figure 2.8C,D). Note that attachment coefficients were again fit to Davis (2008) step velocities, but a lower kink formation energy was used following Nielsen *et al.* (2013) (Table 2.3). The model fit broadly captures both our and the Tang et al. (2008) data with endmember fractionations more consistent with those observed in the natural environment ($\alpha_f = 0.9976$, $\alpha_{eq} = 0.9995$, Table 3). However, the best fit requires a lower equilibrium endmember fractionation than is generally accepted based on studies of deep-sea pore fluids and long residence time carbonate aquifers where precipitation rates are many orders of magnitude slower than the slowest laboratory growth experiments (eq = 1.0000 ± 0.0001 (Fantle and DePaolo, 2007; Jacobson and Holmden, 2008)). In a more recent analysis of similar pore fluids, Bradbury and Turchyn (2018) suggest that a fractionation of $\alpha = 0.9995$ is required to explain observed depth profiles of $\Delta^{44/40}Ca$, so we consider this to be an absolute lower limit on the equilibrium Ca isotope fractionation. More problematically, the model systematically under-predicts fractionations at intermediate solution stoichiometries (Ca^{2+}:$CO_3{}^{2-}$ 100-1000). Although a clear dependence of calcium

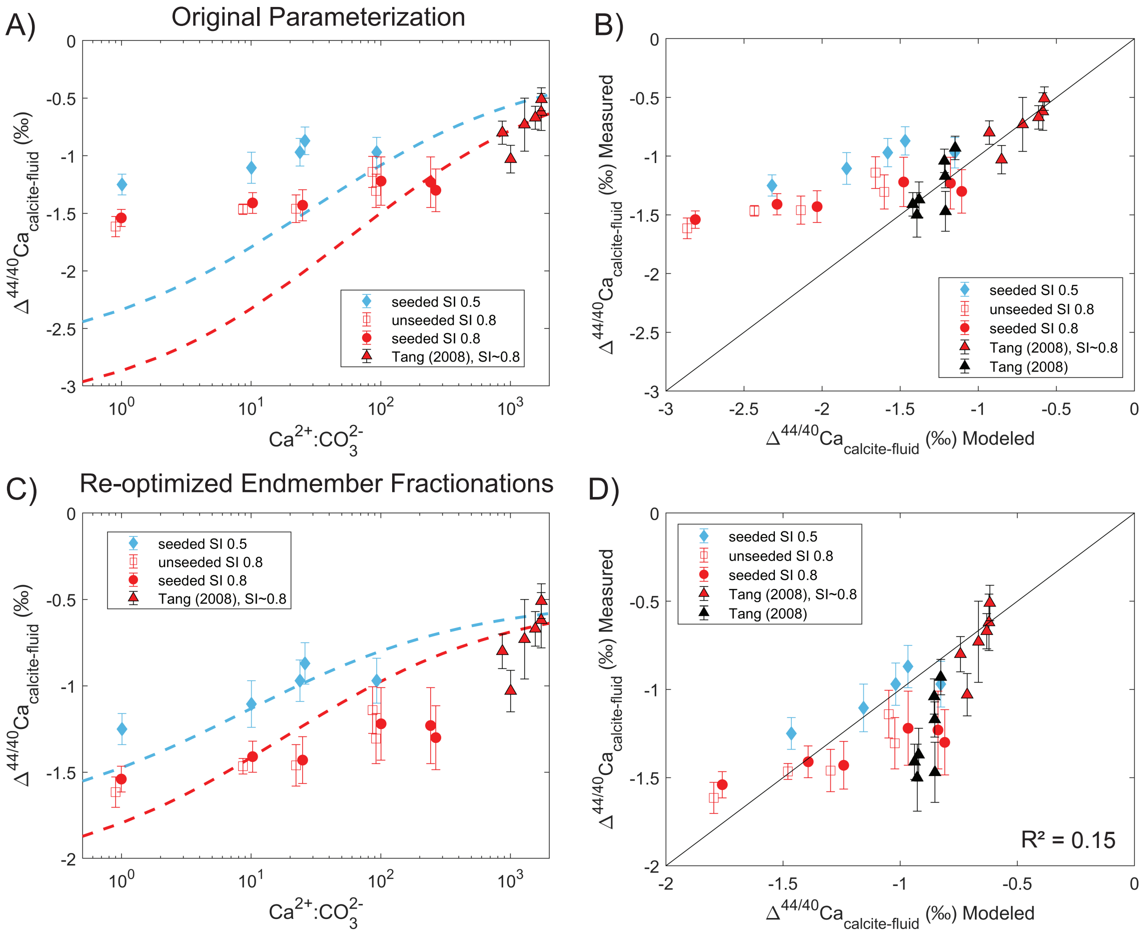

Figure 2.8 – Ion-by-ion model prediction of $\Delta^{44/40}Ca$ for A,B) original parameterization of Nielsen et al. (2012) and C,D) re-optimized endmember fractionations including the $\Delta^{44/40}Ca$ data from this study. In both cases, attachment/detachment frequencies were fit to Davis (2008) step velocities. In A and C, model predictions for the range of $Ca^{2+}:CO_3^{2-}$ at SI 0.5 (blue) and SI 0.8 (red) are shown as dashed lines, plotted with measured $\Delta^{44/40}Ca$ from this study and experiments from Tang et al. (2008) where $0.65<SI<0.95$. Panels B and D show modeled vs. measured $\Delta^{44/40}Ca$ for the exact solution conditions of each experiment from this study and the full 25°C dataset of Tang et al. (2008).

isotope fractionation on solution stoichiometry is identified here, the poor fit at intermediate Ca^{2+}:$CO_3{}^{2-}$ suggests either that the Nielsen et al. (2012) model framework does not fully capture how the extent of Ca isotope exchange at kink sites varies with solution chemistry, or that Ca isotope discrimination is influenced by additional processes not considered in the ion-by-ion framework. We explore these possibilities in turn.

2.4.2 Interrogating damped solution stoichiometry effect

Working first from the assumption that Ca isotope fractionation during calcite precipitation is controlled only by Ca exchange at kink sites, the model offset at intermediate Ca^{2+}:$CO_3{}^{2-}$ implies that the ion-by-ion framework does not properly capture how the ratio of Ca detachment from versus addition to kink sites $\left(\frac{R_{b,Ca}}{R_{f,Ca}}\right)$ varies with solution stoichiometry (Eq. 2.1.1). Note, this assumes that the kinetic isotope effect associated with Ca attachment at a kink site (α_f) is independent of solution conditions, an assumption we discuss in Section 2.4.4. In the following we consider two mechanisms that could change the $\frac{R_{b,Ca}}{R_{f,Ca}}$- Ca^{2+}:$CO_3{}^{2-}$ dependence: hillock anisotropy and surface speciation. Explicit treatment of surface and solution bicarbonate species is required to capture kinetic oxygen isotope fractionation during calcite precipitation (Watkins *et al.*, 2013).

2.4.2.1 Influence of non-equivalent calcite steps

The $(10\bar{1}4)$ calcite face displays two non-equivalent step structures, termed acute and obtuse based on the angle formed with the terrace below. As discussed in Section 2.1.2, the acute and obtuse calcite steps exhibit different growth rate-solution stoichiometry relationships; maximum growth rates for the acute step are observed at Ca^{2+}:$CO_3{}^{2-} < 1$ while maximum growth rates for the obtuse step occur at Ca^{2+}:$CO_3{}^{2-} \geq 1$ (Figure 2.9A, Hong and Teng 2014; Sand *et al.* 2016; Larsen *et al.* 2010; Davis 2008; Stack and Grantham 2010; Bracco *et al.* 2012). These v_{step}-Ca^{2+}:$CO_3{}^{2-}$ relationships suggest that $CO_3{}^{2-}$ is limiting on the acute step while Ca^{2+} is limiting on the obtuse step, which in turn implies that the two steps will undergo differing extents of Ca exchange at a given solution stoichiometry. The acute step should exhibit a higher proportion of Ca-occupied kink sites (P_{Ca}, Figure 2.9B), undergo higher rates of Ca exchange, and thus exhibit smaller magnitude Ca isotope fractionation than the obtuse step under comparable solution conditions (Figure 2.9C). Non-equivalent acute and obtuse steps can be incorporated into the ion-by-ion framework by fitting attachment/detachment coefficients for the obtuse and acute steps separately and calculating the bulk calcium isotope fractionation using a mixing model where the fraction of the surface covered by obtuse steps (f_{obtuse}) is dictated by the relative step velocities at a given solution stoichiometry (Nielsen *et al.* 2012):

$$f_{obtuse} = \frac{v_{obtuse}}{v_{obtuse} + v_{acute}} \tag{2.4.1}$$

$$\alpha_{p,bulk} = f_{obtuse}\alpha_{p,obtuse} + (1 - f_{obtuse})\,\alpha_{p,acute} \tag{2.4.2}$$

While this generates an interesting prediction that the acute and obtuse faces of a calcite growth hillock should express substantially different calcium isotope fractionations

Model	v_{step} dataset	Step	k_A ($s^{-1}M^{-1}$)	k_B ($s^{-1}M^{-1}$)	α_f*	α_{eq}*	SSE ($\Delta^{44/40}Ca$)†
Nielsen *et al.* (2012) best fit:							
Nielsen (2012)	Davis (2008)	Obtuse	1.32E8	1.77E8	0.9963	0.9998	
This study best fit:							
Nielsen (2012)	Davis (2008)	Obtuse	6.65E+05	1.87E+06	0.9976	0.9995	2.17
		Acute	1.86E+06	3.62E+05	0.9972	0.9995	2.36
		Step	k_A ($s^{-1}M^{-1}$)	ν_A (s^{-1})	α_f*	α_{eq}*	SSE
Wolthers (2012)	Davis (2008)	Obtuse	1.62E+07	3.43E+02	0.9979	0.9998	0.61
		Acute	1.08E+07	1.93E+03	0.9977	0.9997	0.60
		y_0	k_A ($s^{-1}M^{-1}$)	ν_A (s^{-1})	α_f*	α_{eq}*	SSE
Wolthers (2012) fit to bulk growth rates	This study	Davis (2008)	2.11E+08	9.86E+02	0.9983	1.0000	0.99
	This study	Bracco (2013)	4.67E+08	1.56E+04	0.9980	0.9995	0.78
	This study	thermo	1.41E+08	2.48E+03	0.9980	0.9998	0.54

Table 2.3 – Fitted attachment/detachment coefficients and end member Ca isotope fractionations for the model parameterizations discussed here. The Nielsen et al. (2012) best-fit used a kink formation energy of $\epsilon/(k_bT)$=7.775; for the rest of the fits a kink formation energy of $\epsilon/(k_bT)$=2.8 was used following Nielsen et al. (2013). *Fitted end member fractionations listed for the obtuse step represent models run only considering the obtuse step while those listed under the acute step account for hillock anisotropy and differing isotope discrimination between the two non-equivalent steps (Section 2.4.2.1). †SSE ($\Delta^{44/40}Ca$) is the sum-squared error of the best-fit Ca isotope fractionations $\left(\sum_i \left(\Delta^{44/40}Ca_{measured,i} - \Delta^{44/40}Ca_{modeled,i}\right)^2\right)$.

($\Delta^{44/40}Ca_{acute}$ ~0.5 higher than $\Delta^{44/40}Ca_{obtuse}$ for Ca^{2+}:$CO_3{}^{2-}$ = 1-100), integrating these separate contributions to the bulk isotope fractionation does not improve the model misfit at intermediate Ca^{2+}:$CO_3{}^{2-}$ (Figure 2.9D). Accounting for the smaller magnitude acute step fractionation leads to larger magnitude best-fit kinetic endmember fractionations ($\alpha_f = 0.9972$, Table 2.3), but the shape of the $\Delta^{44/40}Ca$ solution stoichiometry relationship is largely unchanged at intermediate to high Ca^{2+}:$CO_3{}^{2-}$. This is because the fraction of the surface covered in obtuse steps is largely constant for Ca^{2+}:$CO_3{}^{2-}$ > 10 (Figure 2.9B, grey dotted line), so the bulk $\Delta^{44/40}Ca$ exhibits the same solution stoichiometry dependence as modeling the obtuse step alone. We conclude that hillock anisotropy alone does not explain the observed muted $\Delta^{44/40}Ca$-Ca^{2+}:$CO_3{}^{2-}$ dependence relative to the ion-by-ion model prediction.

2.4.2.2 Influence of surface speciation

Another mechanism that could shift the extent of Ca exchange at a given solution stoichiometry is surface speciation. Kink sites on the growing calcite surface do not actually consistent solely of unoccupied $\equiv CaCO_3^-$ and $\equiv CO_3Ca^+$ sites. Instead, growth sites can be variably protonated, hydroxylated, and complexed by other species in solution (Wolthers *et al.*, 2008; Pokrovsky *et al.*, 2000; Van Cappellen *et al.*, 1993), which changes the density of CO_3 and Ca kink sites available for attachment and isotope exchange. Incorporating the influence of surface speciation following Wolthers *et al.* (2012) generates ion-by-ion model predictions of $\Delta^{44/40}Ca$ that fit the observed $\Delta^{44/40}Ca$-Ca^{2+}:$CO_3{}^{2-}$ dependence within error. Figure 2.10A,B shows model predictions considering only the obtuse step (k_A,ν_A fit to step velocities from Davis (2008)); Figure 2.10C,D shows model predictions when non-equivalent isotope partitioning into the acute and obtuse steps is considered (Section 2.4.2.1). In both cases, the best-fit $\Delta^{44/40}Ca$ dependence implies a kinetic endmember fractionation of around -2.2‰ ($\alpha_f = 0.9979$ when only the obtuse calcite step is considered, $\alpha_f = 0.9977$ when both steps are modeled, Table 2.3) and an equilibrium fractionation of around -0.2‰ ($\alpha_{eq} = 0.9998$ or 0.9997). These endmember fractionations are highly consistent with available estimates from natural systems and imply that the maximum range of $\Delta^{44/40}Ca$ expected from inorganic calcite precipitation under surface-controlled conditions is 2‰. The best-fit kinetic endmember fractionation is also quite similar to that estimated in a model of $\Delta^{44/40}Ca$ during coccolithophore biomineralization (α_f= 0.9982, (Mejía *et al.*, 2018)).

Incorporating surface complexation damps the $\Delta^{44/40}Ca$-Ca^{2+}:$CO_3{}^{2-}$ relationship (Figure 2.10) by shifting the extent of Ca surface exchange $\left(\frac{R_{b,Ca}}{R_{f,Ca}}\right)$ to higher values of Ca^{2+}:$CO_3{}^{2-}$ (Figure 2.11). The Wolthers *et al.* (2008) CD-MUSIC surface complexation model predicts that the fraction of available growth sites (χ) declines with increasing Ca^{2+}:$CO_3{}^{2-}$. Notably, the extent of Ca exchange at a given solution chemistry (pH, supersaturation, Ca^{2+}:$CO_3{}^{2-}$) is dictated only by the Ca attachment/detachment coefficients; $\frac{R_{b,Ca}}{R_{f,Ca}}$ and thus α_p is independent of χ for a given k_A, ν_A (see Appendix A for derivation). The χ term cancels out when considering the $\frac{R_{b,Ca}}{R_{f,Ca}}$ ratio, so α_p does not have an explicit χ dependence. This could lead one to conclude that accounting for surface complexation and a variable number of available growth sites is unimportant for predicting isotope discrimination. However, accounting for the solution chemistry dependence of χ yields best-fit Ca attachment/detachment coefficients that substantially change the $\frac{R_{b,Ca}}{R_{f,Ca}}$ - Ca^{2+}:$CO_3{}^{2-}$ relationship and bring it in line

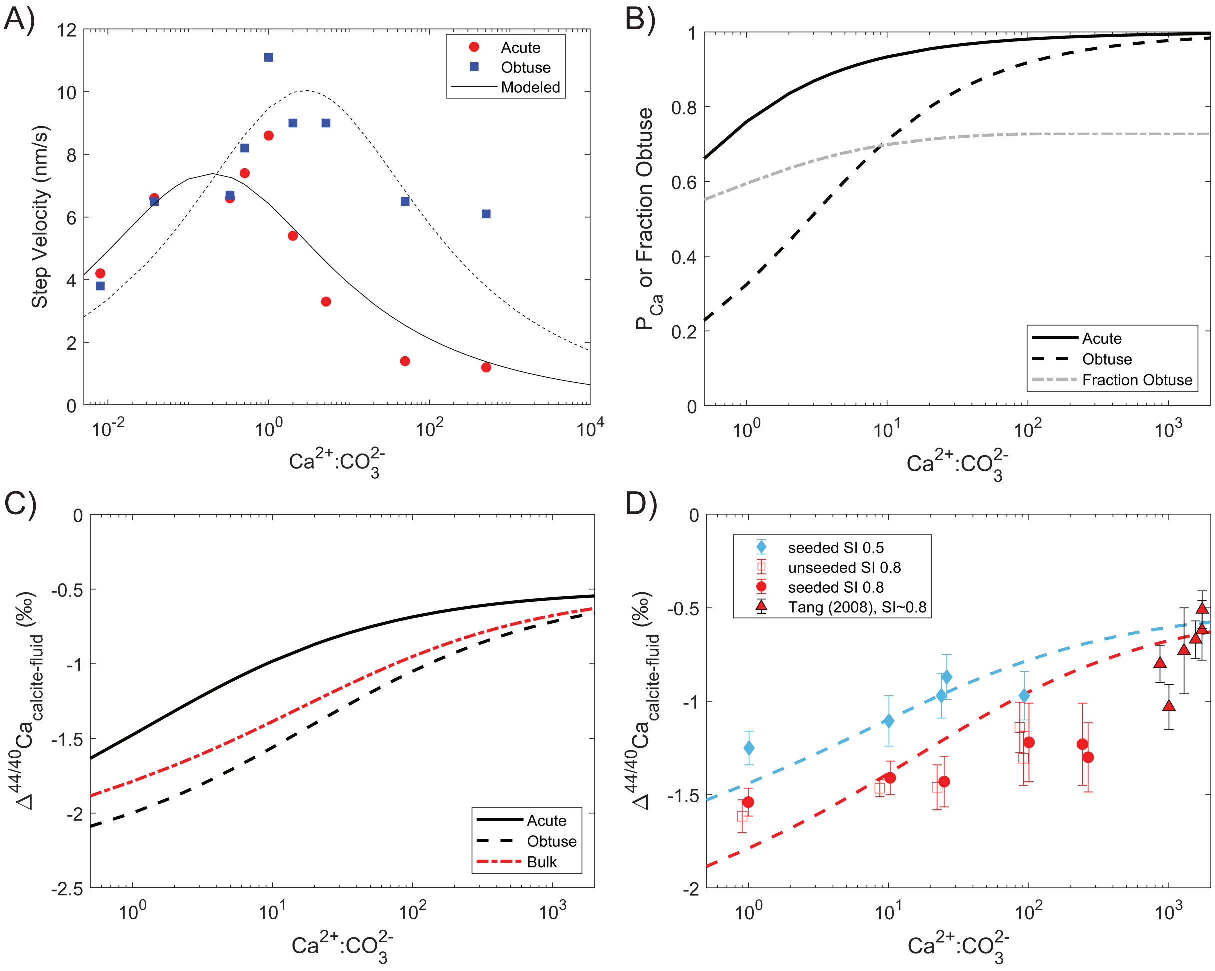

Figure 2.9 – Accounting for the influence of calcite growth hillock anisotropy on modeled calcium isotope fractionation. A) Measured (Davis, 2008) and modeled step velocities for acute (red, solid line) and obtuse (blue, dotted line) calcite steps. B) Ca kink site probability or fraction of the surface covered by obtuse steps (grey dotted line) as a function of Ca^{2+}:$CO_3{}^{2-}$. C) Calculated $\Delta^{44/40}Ca$ expressed on acute steps (solid black line), obtuse steps (dashed black line), and for the bulk solid (dotted red line) for SI = 0.8. D) Ion-by-ion model prediction of $\Delta^{44/40}Ca$ accounting for the non-equivalent acute and obtuse step fractionations. Model predictions for the range of Ca^{2+}:$CO_3{}^{2-}$ at SI 0.5 (blue) and SI 0.8 (red) are shown as dashed lines, plotted with measured $\Delta^{44/40}Ca$ from this study and experiments from Tang et al. (2008) where 0.65<SI<0.95.

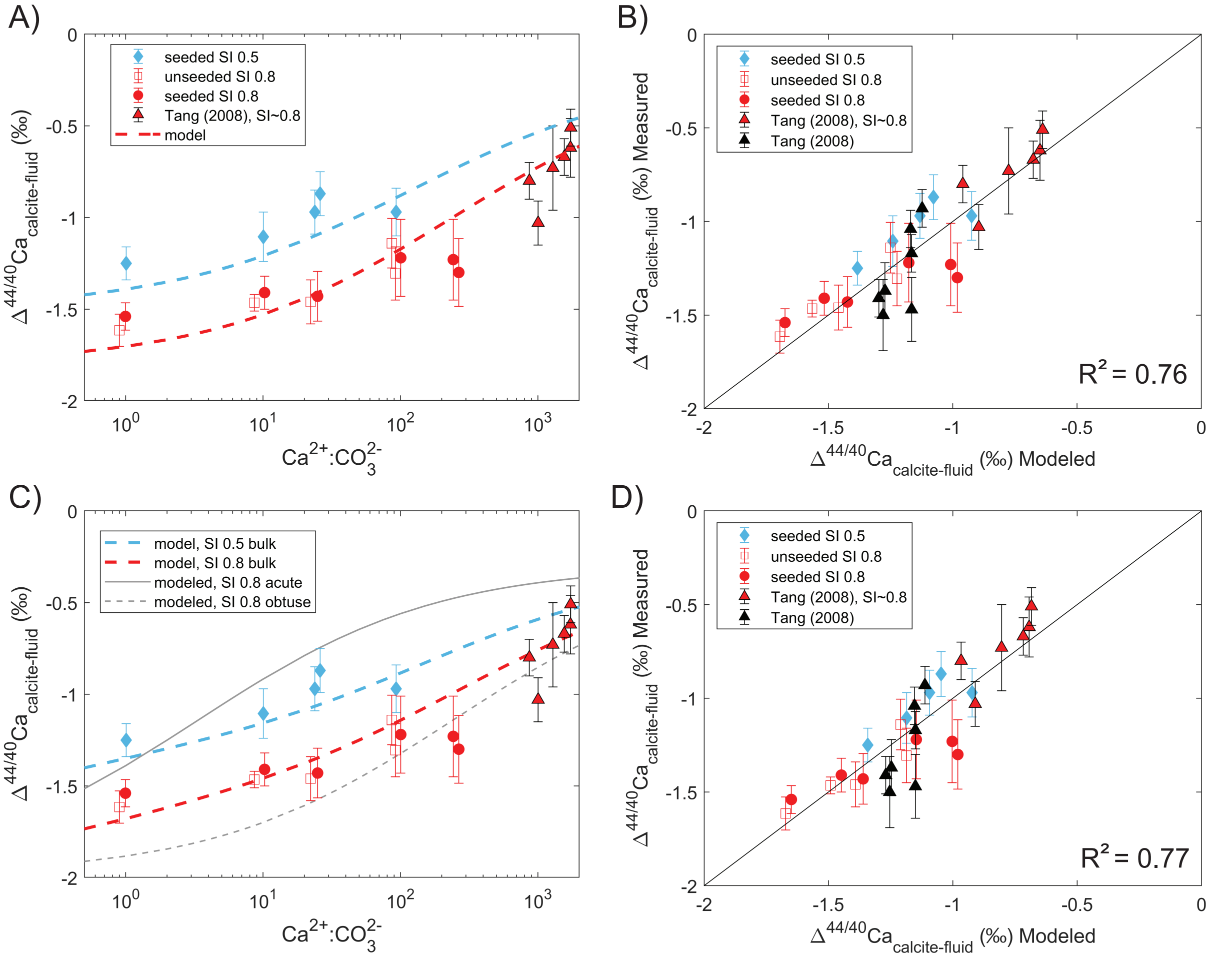

Figure 2.10 – Ion-by-ion model prediction of $\Delta^{44/40}Ca$ accounting for surface speciation (Wolthers *et al.*, 2012) considering only the obtuse calcite step (A,B) and allowing for different expressed fractionations on the acute and obtuse steps (C,D). In A and C, model predictions for the range of Ca^{2+}:$CO_3{}^{2-}$ at SI 0.5 (blue) and SI 0.8 (red) are shown as dashed lines, plotted with measured $\Delta^{44/40}Ca$ from this study and experiments from Tang *et al.* (2008) where $0.65<SI<0.95$. $\Delta^{44/40}Ca_{acute}$ and $\Delta^{44/40}Ca_{obtuse}$ for SI = 0.8 are shown in grey in C. Panels B and D show modeled vs. measured $\Delta^{44/40}Ca$ for the exact solution conditions of each experiment from this study and the full 25°C dataset of Tang *et al.* (2008).

with the $\Delta^{44/40}Ca$-Ca^{2+}:$CO_3{}^{2-}$ relationship observed (Figure A2). In particular, the solution chemistry dependent χ yields much lower Ca detachment rate coefficients (ν_A, Table A3), which leads to lower $\frac{R_{b,Ca}}{R_{f,Ca}}$ for a given Ca^{2+}:$CO_3{}^{2-}$ and larger magnitude $\Delta^{44/40}Ca$. Figure A2 demonstrates the influence of a surface complexation dependent χ on fitted step velocity measurements, $\frac{R_{b,Ca}}{R_{f,Ca}}$, and $\Delta^{44/40}Ca$. Although the variable χ only yields modest improvements in the goodness of fit to the step velocity measurements as noted by Sand *et al.* (2016), the resultant attachment/detachment coefficients vastly improve modeled $\frac{R_{b,Ca}}{R_{f,Ca}}$ and thus $\Delta^{44/40}Ca$ (Figure A2). Isotope discrimination is a much more sensitive tracer of relative surface ion exchange fluxes than is the bulk growth rate. This exemplifies the utility of using stable calcium isotope measurements to shed light on the calcite growth process and provide additional constraints for mechanistic models of crystal growth.

The finding that the Wolthers *et al.* (2012) ion-by-ion model formulation captures the observed trends in $\Delta^{44/40}Ca$ is further corroborated by model predictions using attachment/detachment coefficients fit to the surface-normal bulk growth rates measured in this study. Model predictions vary slightly depending on how the step width is calculated (Section 2.2.5), but in all cases the ion-by-ion prediction captures the observed trend in $\Delta^{44/40}Ca$ with Ca^{2+}:$CO_3{}^{2-}$ with best-fit endmember isotope fractionations very similar to those obtained when Ca attachment/detachment coefficients are fit to independent step velocity measurements (Table 2.3, Figure A3). In particular, the measured fractionations from this study and Tang *et al.* (2008) are best-fit by a thermodynamic representation of step width with endmember fractionations nearly identical to those obtained by fitting the Davis (2008) step velocity data. Thus, extrapolating growth dynamics from in-situ AFM step velocity measurements yields comparable results to observations from bulk-growth behavior. This suggests that bulk growth rate data from laboratory precipitation experiments may be sufficient to predict Ca attachment/detachment rate constants and thus $\Delta^{44/40}Ca$ for a given set of solution conditions if a realistic surface complexation model is available.

The implications of the good agreement between ion-by-ion model predictions and experimentally measured $\Delta^{44/40}Ca$ when solution speciation is taken into account are two-fold. Most fundamentally, it suggests that the conceptual framework of Ca isotope fractionation driven by Ca exchange at surface sites holds (DePaolo, 2011; Nielsen *et al.*, 2012). This further implies that calcium incorporation into calcite during steady-state growth (under the solution conditions studied here) occurs through largely classical crystal growth - via the incorporation of monomer growth units. Secondly, it suggests that accounting for surface complexation is key for interpreting isotope and by inference, trace element (Nielsen *et al.*, 2013), partitioning during calcite growth. The latter conclusion was demonstrated for oxygen isotopes in Watkins *et al.* (2013), but the influence of surface speciation on calcium isotopes has not been shown until now. Finally, while the Wolthers *et al.* (2008) CD-MUSIC model appears to adequately capture changes in surface speciation as a function of solution chemistry for the simple electrolyte solutions used here, improved surface complexation models that account for the influence of other ions in solution as well as variable dielectric properties at the electrical double layer (Heberling *et al.*, 2014; Song *et al.*, 2017; Sø *et al.*, 2012) may be required to predict or interpret isotope and trace element partitioning in complex solutions such as seawater.

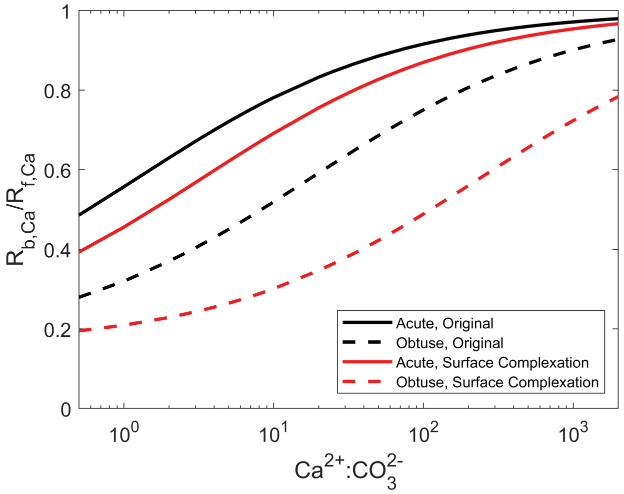

Figure 2.11 – Extent of surface Ca exchange (ratio of Ca detachment from versus attachment to kink sites) as a function of $Ca^{2+}:CO_3{}^{2-}$ activity ratio for an SI = 0.8, pH 8.5 solution using the Nielsen *et al.* (2012) ion-by-ion model (black lines) and Wolthers *et al.* (2012) formulation which incorporates a surface complexation model (red lines). Accounting for surface complexation damps the $\Delta^{44/40}Ca$-solution stoichiometry dependence by shifting the $\frac{R_{b,Ca}}{R_{f,Ca}}$ - $Ca^{2+}:CO_3{}^{2-}$ relationship: low relative rates of Ca exchange are maintained over a wider range of $Ca^{2+}:CO_3{}^{2-}$. Ca exchange on the obtuse step is the dominant control on bulk $\Delta^{44/40}Ca$ because the obtuse step velocity is higher for $Ca^{2+}:CO_3{}^{2-} > 1$ (Figure A2E), so more of the surface is covered by obtuse steps.

2.4.3 Model predictions for bulk growth rate and implications for $\Delta^{44/40}Ca$ - growth rate relationship

While the ion-by-ion framework appears to capture Ca-exchange dynamics well, significant uncertainty remains in modeling absolute fluxes and thus bulk growth rates. Figure 2.12 shows model predictions for A) bulk growth rates, and B) relative growth rates normalized by the rate at $Ca^{2+}:CO_3^{2-} = 1$ for the Wolthers model fit to Davis (2008) step velocities, using a thermodynamic representation of the hillock step spacing (y_0, Section 2.2.5). The step edge free energy per unit step height (γ) was scaled to capture the bulk growth rates observed. Figure 2.12C shows the resultant measured and modeled $\Delta^{44/40}Ca$-growth rate relationship. Note, as demonstrated by Nielsen *et al.* (2012), the dominantly higher supersaturation Tang *et al.* (2008) experiments are better fit with a 2D nucleation driven growth dependence and are modeled as such here while the SI = 0.5 and 0.8 experiments are modeled with a spiral growth rate dependence (Teng *et al.*, 2000). Two key observations are apparent. First, although the model adequately captures changes in relative growth rates with $Ca^{2+}:CO_3^{2-}$ (Figure 2.12B), modeled growth rates with a thermodynamic y_0 representation do not capture the observed supersaturation dependence well.

Supersaturation influences bulk growth rates in two ways: the relationship between step velocity and ion activity in solution, and the supersaturation dependence of the step width (y_0). Sand *et al.* (2016) reported that the Wolthers ion-by-ion framework struggled to capture the supersaturation dependence of observed step velocity measurements. In a subsequent analysis, Andersson *et al.* (2016) argued that the observed step velocity supersaturation dependence was better predicted by a microkinetic model where kink nucleation is initiated by ion pair or polynuclear complex addition. Hellevang *et al.* (2016) also suggested that ion pair formation could influence growth kinetics due to the different surface diffusion behavior of neutral complexes. It is thus possible that the assumptions regarding kink formation dynamics in the Wolthers and Nielsen ion-by-ion formulations simply do not realistically capture calcite growth dynamics. Notably, the Bracco *et al.* (2013) empirical relationship better captures the bulk growth rate supersaturation dependence observed here when attachment/detachment coefficients are fit to observed growth rate data (Figure A4), which suggests at least part of the offset between observed and modeled bulk growth rates is due to uncertainties associated with the solution chemistry dependence of y_0. The step width has been demonstrated to be sensitive to both solution stoichiometry (Bracco *et al.*, 2013; Davis, 2008) and impurity concentration (Davis *et al.*, 2000a; Wasylenki *et al.*, 2005a), underscoring the need to better understand the solution chemistry dependence of y_0 for scaling measured or modeled step velocities to bulk growth rates.

Second, a relatively low step edge free energy per unit step height ($\gamma = 0.18$ J/m^2) must be assumed in the thermodynamic calculation of y_0 in order to match the magnitude of the surface-normal growth rates observed (Figure 2.12A). This step edge free energy is quite similar to theoretical estimates of edge work by Nielsen (1984) (1.5E-20 J, equivalently 0.15 J/m^2) and estimates of interfacial tension from calcite nucleation experiments (~0.12 J/m^2 (Söhnel and Mullin, 1978, 1982)). The resultant step width (~22nm for SI = 0.5) is, however, lower than most measurements of step spacing from in-situ AFM measurements. For $Ca^{2+}:CO_3^{2-} \approx 1$, SI ≈ 0.4, Teng *et al.* (2000) measured step widths between 110-140nm (obtuse) and 50-72nm (acute) while Bracco *et al.* (2013) reported step widths on the order of

700nm for the obtuse step under the same conditions. Similarly, Cao *et al.* (2018) measured step widths of 86nm and 81nm for SI = 0.3 and 0.5 solutions, respectively, using vertical scanning interferometry. This significant spread in measured and modeled step widths further underscores the challenges associated with scaling step velocities to surface-normal growth rates.

2.4.4 Additional potential controls on $\Delta^{44/40}Ca$-solution stoichiometry relationship

Accounting for variations in surface speciation with solution stoichiometry recreates the observed variation in $\Delta^{44/40}Ca$ with reasonable end-member isotope fractionations within error, but it is possible that the ion-by-ion framework still somewhat under-predicts fractionations at intermediate to high Ca^{2+}:CO_3^{2-} (Figure 2.10). If that is the case, there are a few potential mechanisms that could lead to higher magnitude fractionations at Ca^{2+}:CO_3^{2-} ~250-1000 than the classical, ion-by-ion framework predicts. First, some fraction of Ca may be incorporated into the lattice through mechanisms other than monomer addition at kink sites. In the unseeded experiments, we observe what appears to be a systematic trend in induction time which suggests that the barrier to nucleation is lower in high Ca^{2+}:CO_3^{2-} solutions. This could indicate that clusters form more readily in higher Ca^{2+}:CO_3^{2-} solutions. The higher magnitude fractionations at intermediate Ca^{2+}:CO_3^{2-} could thus reflect the incorporation of preferentially light Ca due to non-monomer (polynuclear cluster) incorporation. We are just beginning to understand the influence of non-classical growth mechanisms in mineral systems that have long been assumed to adhere to classical crystal growth theory (De Yoreo *et al.* (2015) and references within), but existing evidence does not immediately support preferential incorporation of ^{40}Ca through non-monomer addition. Amorphous calcium carbonate, precipitated via non-classical pathways at very high supersaturations, exhibits small negative Ca isotope fractionations (~-0.25‰) (Niedermayr *et al.*, 2010; Gagnon *et al.*, 2010), and simulation studies have suggested that the heavy isotope preferentially partitions into both Ca (Moynier and Fujii, 2017) and Mg (Schott *et al.*, 2016) aqueous carbonate complexes. Thus, preferential incorporation of isotopically depleted Ca at high Ca^{2+}:CO_3^{2-} would require an as yet unrecognized cluster formation/incorporation pathway that exhibits large negative $\Delta^{44/40}Ca_{cluster-fluid}$, but the interactions between aqueous clusters and the growing calcite surface are just beginning to be explored (Andersson *et al.*, 2016; Hellevang *et al.*, 2016).

A second mechanistic explanation for larger magnitude fractionations at high Ca^{2+}:CO_3^{2-} than predicted by the model lies in the assumption that the kinetic isotope fractionation associated with Ca attachment at kink sites is independent of solution conditions. Molecular simulation studies have shown that the kinetic fractionation can be attributed to the mass dependence of Ca dehydration kinetics (Hofmann *et al.*, 2012) and that this kinetic effect is sensitive to the local water structure and calcium solvation environment (Lammers *et al.*, 2020). Given this fractionation mechanism, any aspect of solution chemistry that changes either the stability of the cation hydration shell or the structure of water at the calcite surface could exert an influence on the magnitude of Ca isotope discrimination. The presence of other ions in solution that can affect the bulk solution and surface hydration environ-

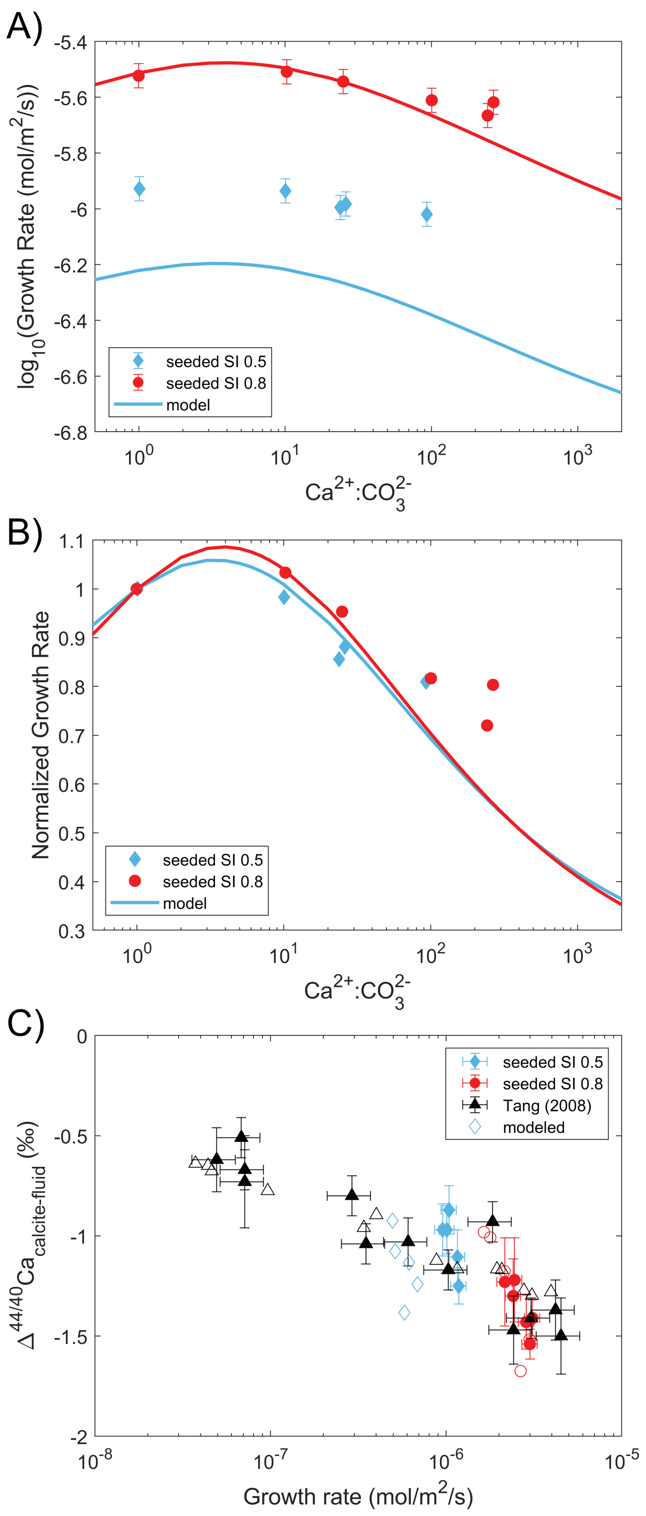

Figure 2.12 – Modeled bulk growth rates and $\Delta^{44/40}Ca$-growth rate relationship. Modeled absolute (A) and relative (B) bulk growth rates as a function of Ca^{2+}:CO$_3{}^{2-}$. In B, rates are normalized by the surface normal growth rate at Ca^{2+}:CO$_3{}^{2-}$ $= 1$. C) Measured (filled markers) and modeled (hollow markers) $\Delta^{44/40}Ca$-growth rate relationship. Tang *et al.* (2008) growth rates are modeled using a 2D-nucleation rate dependence (Nielsen *et al.*, 2012) while the SI $=$ 0.5 and 0.8 experiments from this study are modeled as spiral growth with $\gamma = 0.18$ J/m^2.

ment are known to influence calcite growth and dissolution dynamics (Ruiz-Agudo *et al.*, 2010, 2011b; Di Tommaso *et al.*, 2014). Ruiz-Agudo et al. (2011b) interpreted background electrolyte-specific effects on calcite step velocities in terms of their influence on cation and surface hydration, and ionic strength was found to have a weak but statistically significant influence on $\Delta^{44/40}Ca$ in the inorganic calcite growth experiments of Tang et al. (2012). The low $\Delta^{44/40}Ca$ observed at intermediate Ca^{2+}:$CO_3{}^{2-}$ observed here could thus hint at an increase in the magnitude of Ca isotope discrimination (lower α_f) with increasing surface potential, or more broadly reflect an α_f sensitive to solution conditions which influence Ca dehydration kinetics. This in turn raises the possibility that structurally distinct sites on the calcite surface could fractionate Ca isotopes differently. Molecular dynamics simulations have demonstrated that calcite surface sites can exhibit a wide range of water exchange frequencies (Wolthers *et al.*, 2013; De La Pierre *et al.*, 2016), with implications for site-specific isotope discrimination during Ca attachment and surface exchange (Lammers *et al.*, 2020). Future work is required to establish site-specific fractionation factors for both calcium and carbonate isotopologues during calcite growth (Watkins *et al.*, 2013).

2.4.5 Implications for the interpretation of Ca isotopes in natural systems

The updated ion-by-ion formulation and parameterization for $\Delta^{44/40}Ca_{calcite-fluid}$ implies a total possible range in $\Delta^{44/40}Ca$ of 2‰ with a maximum expressed kinetic isotope fractionation of -2.1 to -2.3‰ and an equilibrium fractionation of ~-0.2‰. While the model is consistent with a small equilibrium fractionation, it should not be interpreted as evidence of such; best-fit equilibrium endmember fractionations range ±0.2‰ depending on the details of the model fit. Moreover, for most carbonate precipitating environments, $\Delta^{44/40}Ca$ will be predominantly influenced by supersaturation and thus calcite growth rate (Figure 2.13A). For carbonate-dominated precipitation environments (Ca^{2+}:$CO_3{}^{2-} < 1$), $\Delta^{44/40}Ca$ is almost entirely dictated by supersaturation, and $\Delta^{44/40}Ca$ rises gradually between Ca^{2+}:$CO_3{}^{2-}$ = 10 to 1000.

Regarding the $\Delta^{44/40}Ca$-growth rate dependence, both the experimentally measured fractionations (Figure 2.7) and model predictions support an inverse dependence between $\Delta^{44/40}Ca$ and growth rate for classical calcite growth, where $\Delta^{44/40}Ca$ becomes more negative at higher growth rates (Figure 2.12C). This trend is consistent with that documented by inorganic calcite precipitation experiments in dilute $NH_4{}^+$ solutions (5mM NH_4Cl, (Tang *et al.*, 2008, 2012)), in *E. huxleyi* coccolithophores (Mejía *et al.*, 2018), and for monohydrocalcite precipitation stimulated by microbial sulfate reduction (Bradbury *et al.*, 2020). As argued by AlKhatib and Eisenhauer (2017b), the opposite trend observed in high $NH_4{}^+$ solutions (395mM NH_4Cl) observed by Lemarchand *et al.* (2004) and at 12.5°C and 25°C experiments of AlKhatib and Eisenhauer (2017b) is likely due either to the formation of NH_3-Ca^{2+} aqueous complexes enriched in ^{44}Ca, transport effects (DePaolo, 2011), or non-classical growth of amorphous calcium carbonate (ACC) in the high supersaturation solutions (Nielsen *et al.*, 2012).

The demonstrated importance of accounting for surface speciation leads to a further inference: $\Delta^{44/40}Ca$ should be sensitive to pH, independent of its influence on aqueous carbonate ion activity. Larger magnitude fractionations (more negative $\Delta^{44/40}Ca$) are predicted at lower pH (Figure 2.13B) due to the pH dependence of the effective Ca attachment coefficient ($\bar{k_A} = k_A \left(1 + 10^{8.6}10^{(-pH)}\right)$), Table A1). The effective Ca attachment frequency has a negative exponential dependence on pH due to changes in solution and surface bicarbonate activity while the Ca detachment frequency ($\bar{\upsilon_A}$) is pH independent. Thus, the Ca attachment flux increases relative to the Ca detachment flux as solution pH decreases, leading to higher magnitude $\Delta^{44/40}Ca$ (Eq. 2.1.1). While the predictions in Figure 2.13B should be considered qualitative estimates, as Ca attachment/detachment rate coefficients and even the magnitude of the kinetic fractionation associated with Ca incorporation into the lattice could be surface potential (and thus pH) dependent, there is some evidence to support the predicted pH trend. In an in-situ AFM study of calcite growth as a function of pH at fixed Ca^{2+}:$CO_3{}^{2-}$, Ruiz-Agudo *et al.* (2011a) reported a factor of 6 higher growth rates at pH 7.5 relative to pH 8.5, consistent with faster Ca attachment fluxes. A study of $\Delta^{44/40}Ca$ in cultured (calcite precipitating) planktic foraminifera also hints at an inverse pH dependence (Kisakürek *et al.*, 2011). In cultures of *Globigerinoides ruber*, the magnitude of $\Delta^{44/40}Ca$ decreases from pH = 7.9 to 8.4 despite accompanying increases in carbonate activity, though the documented shift in $\Delta^{44/40}Ca$ is within error (0.2‰) (Kisakürek *et al.*, 2011).

Accounting for this pH dependence yields estimates of $\Delta^{44/40}Ca$ from seawater-like solutions ($\{Ca^{2+}\}$ ~2.3e-3, $\{CO_3{}^{2-}\}$ ~4.8e-6, pH 8.1 (Berner, 1965)) of between -0.85‰ to -0.89‰. While the more complex surface complexation behavior of seawater is not accounted for in these estimates, they are in good agreement with $\Delta^{44/40}Ca$ measured for microbially-induced calcite precipitation from seawater solutions (-0.95±0.4‰ (Bradbury *et al.*, 2020)). Moreover, our estimates fall at the low end of typical $\Delta^{44/40}Ca$ during calcite biomineralization from seawater (DePaolo, 2004; Gussone *et al.*, 2005; Mejía *et al.*, 2018), consistent with seawater representing a minimum supersaturation and maximum Ca^{2+}:$CO_3{}^{2-}$ relative to the biogenic calcifying fluid.

Finally, our findings indicate that understanding how solution chemistry dictates surface speciation in complex solutions and resultant ion attachment/detachment rates is critical for predicting isotopic fractionations during surface-reaction controlled mineral precipitation.

2.4.6 Stable Ca isotopes as probes of crystal growth: Predicted influence of impurity ions

The ability of the Wolthers *et al.* (2012) ion-by-ion model formulation to capture observed trends in $\Delta^{44/40}Ca$ with Ca^{2+}:$CO_3{}^{2-}$ and rate provides strong supporting evidence for the process-based model of kink-exchange driven Ca isotope fractionation. This in turn lays the groundwork for using Ca isotope fractionation to probe carbonate crystal growth processes. Of particular interest is understanding the interplay between trace impurity incorporation and inhibition behavior (Morse *et al.*, 2007). Developing a predictive understanding of the link between solution chemistry, growth kinetics, and trace element uptake is essential for linking environmental conditions to partitioning behavior and for developing predictive models of growth kinetics in complex solutions. Importantly, Ca isotope fractionation could provide a window into the mechanism by which various inhibitors interact with the growing calcite surface and inhibit growth.

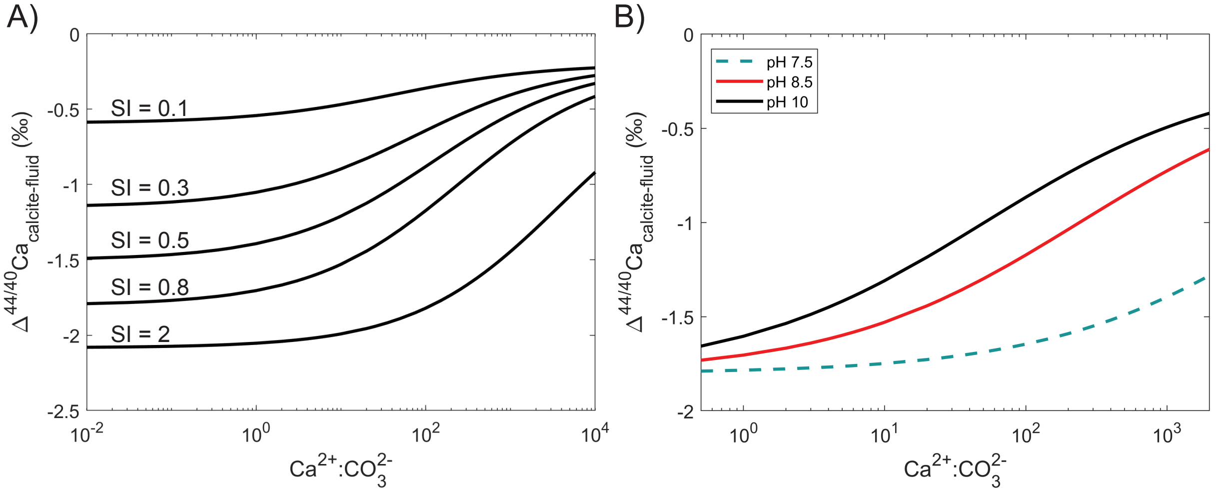

Figure 2.13 – Influence of supersaturation (A) and pH (B) on predicted $\Delta^{44/40}Ca$. In A, pH is fixed at 8.5 while the supersaturation is varied while in B, the supersaturation is held constant (SI 0.8) while pH is varied. In both, attachment/detachment coefficients fit to Davis (2008) obtuse step velocity are used to parameterize the Wolthers *et al.* (2012) ion-by-ion model (Table 2.3). Comparable plots allowing for different expressed fractionations on the acute and obtuse steps are shown in Figure A5.

Impurities can modify calcite growth through three primary mechanisms: step pinning, kink blocking, and incorporation (De Yoreo and Vekilov, 2003). For mechanisms that change the solubility of the solid phase through thermodynamic effects, the growth inhibition should be accompanied by a change in $\Delta^{44/40}Ca$. In particular, trace constituent incorporation that destabilizes the lattice and lowers the resultant solid solution supersaturation would lead to an increase in the flux of Ca off the surface at a given $\{Ca^{2+}\}$ and $\{CO_3^{2-}\}$, yielding a lower magnitude $\Delta^{44/40}Ca$. In contrast, if the inhibitor dominantly influences the rates of ion attachment at kink sites and subsequent kink propagation kinetics ('kink blocking'-type inhibition), $\Delta^{44/40}Ca$ is predicted to be invariant with impurity concentration and extent of inhibition. For example, Mg^{2+} is proposed to act as a kink-blocker due to its more strongly bound hydration waters and slow desolvation kinetics (Nielsen *et al.*, 2013). If this is the case, the ion-by-ion framework predicts that $\Delta^{44/40}Ca$ should be independent of Mg^{2+} under otherwise constant solution conditions. The slow attachment of Mg^{2+} and CO_3^{2-} on Mg^{2+}-occupied kinks slows kink propagation rates but does not change the relative rate of Ca addition and removal from kink sites because the dynamics of Ca-occupied kink sites are not affected. Growth rate inhibition by pure kink-blocking inhibitors is thus expected to decouple $\Delta^{44/40}Ca$ and rate, a prediction that can be tested with additional inorganic calcite growth experiments in the presence of representative trace elements (e.g. Mg^{2+}, Sr^{2+}, Ba^{2+}). The potential influence of step pinning on $\Delta^{44/40}Ca$ is less straight-forward. In step pinning, largely irreversible impurity adsorption to step edges blocks the advancement of steps such that step advance can only continue by growing around the impurities. Growth inhibition occurs through a thermodynamic effect; if the step curvature must exceed a critical radius in order to pass between the impurities, the step becomes undersaturated due to the curvature dependence of the Gibbs-Thomson equation. The step growth around the impurity sites likely leads to higher and more variable kink densities, which may influence gross forward and back fluxes of ions locally.

2.5 Conclusions

We report new measurements of the solution stoichiometry dependence of calcium isotope fractionation during inorganic calcite growth in order to test one of the key predictions of a classical ion-by-ion model of $\Delta^{44/40}Ca_{calcite-fluid}$ (Nielsen *et al.*, 2012). As predicted by the ion-by-ion framework, $\Delta^{44/40}Ca$ is stoichiometry dependent and the expected trend of larger fractionations at lower Ca^{2+}:$CO_3{}^{2-}$ is observed. However, $\Delta^{44/40}Ca$ is found to be less strongly influenced by solution stoichiometry than originally predicted; the magnitude of the change in $\Delta^{44/40}Ca$ over the solution stoichiometries studied (Ca^{2+}:$CO_3{}^{2-}$ = 1-250) is only ~0.4‰. An inverse correlation between $\Delta^{44/40}Ca$ and growth rate is also observed, confirming the $\Delta^{44/40}Ca$ -rate relationship observed by Tang *et al.* (2008).

Measured calcium isotope fractionations are consistent with the ion-by-ion model if a surface complexation model is incorporated that accounts for variations in the fraction of available kink sites with changes in solution chemistry (Wolthers *et al.*, 2012). The surface complexation-enabled model captures measured $\Delta^{44/40}Ca$ with best-fit kinetic and equilibrium endmember fractionations consistent with those observed in natural systems (α_{kinetic} ~ 0.9978, α_{eq} ~ 0.9998). This provides strong supporting evidence for the conceptual model of kink-exchange driven Ca isotope fractionation and suggests that calcite grows by a dominantly classical mechanism over the solution conditions investigated. Moreover, our findings indicate that understanding how solution chemistry dictates surface speciation in complex solutions and resultant ion attachment/detachment rates is critical for predicting isotopic fractionations during surface-reaction controlled mineral precipitation.

The updated model formulation and parameterization generates a number of predictions that can be tested to further our understanding of carbonate crystal growth processes:

- Expressed Ca isotope fractionation should vary between the obtuse and acute faces of a single calcite growth hillock, with smaller magnitude fractionations produced on the acute step.
- $\Delta^{44/40}Ca$ is pH dependent. Larger magnitude fractionations are predicted at lower pH for a given calcite supersaturation and Ca^{2+}:$CO_3{}^{2-}$.
- Calcium isotope fractionation can differentiate mechanisms of growth inhibition in the presence of impurities. Pure kink-blocking type inhibition should lead to invariant $\Delta^{44/40}Ca$ with growth rate while lattice destabilization due to impurity incorporation should yield smaller magnitude fractionations at lower growth rates.

Taken together, these predictions highlight the potential to use Ca isotopes as molecular tracers to inform our understanding of the complicated suite of processes occurring at the fluid-mineral interface during crystal growth.

Chapter 3

Ca isotope insights into Mn^{2+} and Mg^{2+} inhibition of calcite growth

Abstract

Impurity ion and isotope partitioning into carbonate minerals provide a window into the molecular processes occurring at the fluid-mineral interface during crystal growth. In Chapter 2 we demonstrated that calcium isotope fractionation during calcite precipitation can be understood and mechanistically modeled in terms of the fluxes of monomer Ca^{2+} ions onto and off of kink sites on the growing crystal surface. Here, we attempt to operationalize the use of stable isotopes as molecular probes of crystal growth, employing calcium isotope fractionation to help elucidate the mechanism by which two divalent cations with starkly contrasting compatibility, magnesium and manganese, inhibit calcite growth and are ultimately incorporated into the mineral lattice.

Independent seeded Mn-calcite and Mg-calcite growth experiments were run under different fluid metal to calcium ratios ($^{\{Mn^{2+}\}}/_{\{Ca^{2+}\}}$ $0.001 - 0.15$; $^{\{Mg^{2+}\}}/_{\{Ca^{2+}\}} = 0.01 - 2.6$) using a chemostat reactor. Calcite growth inhibition by Mg^{2+} is log-linear throughout the range of $^{\{Mg^{2+}\}}/_{\{Ca^{2+}\}}$ studied. Mn^{2+} exhibits much stronger log-linear growth rate inhibition at low Mn^{2+} concentrations (fluid $^{\{Mn^{2+}\}}/_{\{Ca^{2+}\}} = 0.001$–$0.02$). At higher Mn^{2+} concentrations, the extent of inhibition lessens and eventually reverses; faster growth rates are observed with increasing solution Mn^{2+} when solid phase Mn/Ca > 1. Mn^{2+} is readily incorporated into the calcite lattice, with large partition coefficients ($\mathrm{K_{Mn}}$ 4.6-15.6) inversely correlated to growth rate. In contrast, $\mathrm{K_{Mg}}$ is on the order of 0.02-0.03 for the solution conditions studied here.

For both Mn^{2+} and Mg^{2+}, calcium isotope fractionation is found to be invariant with $^{\{Me^{2+}\}}/_{\{Ca^{2+}\}}$ despite more than an order of magnitude decline in growth rate. Applying an ion-by-ion model for calcite growth, this invariant $\Delta^{44/40}Ca$ suggests that the presence of Mn^{2+} or Mg^{2+} does not significantly change the relative rates of Ca^{2+} attachment and detachment at kink sites during growth, indicative of a dominantly kink blocking inhibition mechanism. For Mg^{2+}, we demonstrate that this is broadly consistent with growth inhibition driven by slow Mg^{2+}-aquo complex dehydration relative to Ca^{2+} but argue that this mechanism likely represents one endmember scenario, seen in Mg-calcite growth at low su-

persaturations and net precipitation rates. During growth at faster net precipitation rates, some portion of Mg^{2+} is likely incorporated as a partially hydrated or otherwise complexed species, as proposed by Mavromatis *et al.* (2013) and Alvarez *et al.* (2021), but calcite growth remains significantly inhibited by the kinetics of CO_3^{2-} attachment at Mg^{2+} kink sites. In the case of Mn^{2+} inhibition of calcite growth, the large K_{Mn} observed at low solution Mn^{2+} cannot be explained by desolvation rate-limited attachment of Mn^{2+} at the kink. Instead, our findings suggest Mn^{2+} attaches to kink sites significantly faster than Ca^{2+}, which we interpret to represent non-monomer Mn^{2+} attachment as an ion pair, hydrated species, or possibly a larger polynuclear cluster. We propose that Mn^{2+} inhibits calcite growth by a novel carbonate-based kink blocking mechanism involving non-monomer Mn^{2+} attachment, rate limited by the kinetics of carbonate ion re-orientation to attach at Mn-occupied kink sites.

Taken together, these findings point to a hybrid mechanism of calcite growth whereby Ca^{2+} incorporates largely as a free ion at kink sites while Mn^{2+} (and some portion of Mg^{2+}) is incorporated via non-monomer attachment. We theorize that this may represent a broader trend relevant to crystal growth across mineral systems: that trace constituent cations with aquo-complex desolvation rates significantly slower than the mineral growth rate will be incorporated as a non-monomer species during otherwise classical crystal growth.

3.1 Motivation: towards predicting growth dynamics in complicated solutions

Mineral precipitation/dissolution reactions underpin a wide array of geochemical processes relevant to our understanding of both natural and engineered systems, from weathering rates and the long-term carbon cycle (Kump *et al.*, 2000), to water quality and contaminant remediation (Prieto *et al.*, 2013). Yet predicting reaction rates in natural systems remains frustratingly elusive given our limited knowledge of how the micro-scale chemical interactions that occur at mineral-fluid interfaces control the macro-scale kinetics of mineral dissolution and precipitation (Anbeek, 1993; Maher *et al.*, 2006, 2016). Understanding the growth kinetics and trace constituent partitioning behavior of carbonates is of particular interest given their fundamental importance to the paleo-proxy record (Ravizza and Zachos, 2003) and key role in climate change mitigation strategies such as geologic carbon storage (Bourg *et al.*, 2015). In particular, various forms of mineral carbonation, including in-situ mineralization of basalts or peridotites (Kelemen *et al.*, 2011; Clark *et al.*, 2020), ambient surficial weathering (Renforth *et al.*, 2009; McQueen *et al.*, 2020; Beerling *et al.*, 2020), and engineered ex-situ mineralization of alkaline waste materials (Gerdemann *et al.*, 2007), are increasingly attractive options for permanent storage of CO_2 (Kelemen *et al.*, 2020). Carbonate solid-solution formation is also a principal remediation technique for contaminants capable of being incorporated into the carbonate lattice (e.g. ^{90}Sr - Lukashev 1993; Achal *et al.* 2012).

Historically, studies of carbonate growth kinetics have focused on the development of empirical rate laws, generally calibrated with bulk precipitation experiments (c.f. Morse *et al.* 2007). While empirical rate laws are incredibly useful for describing reaction kinetics within the range of solution conditions measured and form the basis for nearly all reactive transport modeling, they provide no mechanistic information and often struggle to describe the influence of solution chemistry beyond saturation state. More recently, ion-by-ion models have been developed which describe carbonate growth kinetics in terms of the elementary reactions of ion addition and removal from the growing crystal surface (Nielsen *et al.*, 2012, 2013; Wolthers *et al.*, 2012). However, we are only beginning to build a comprehensive understanding of mineral growth in simple electrolyte solutions and at relatively low aqueous supersaturations, let alone the complex solutions encountered in natural systems. This effort has been complicated by the increasing recognition of non-classical growth mechanisms in systems long thought to fall squarely in the domain of classical crystal growth, including calcium carbonates (Gebauer *et al.*, 2008; Rodriguez-Navarro *et al.*, 2015; Zhu *et al.*, 2016).

In Chapter 2, we demonstrated that calcium isotope fractionation during calcite precipitation can be understood and mechanistically modeled in terms of the fluxes of monomer Ca^{2+} ions onto and off of kink sites on the growing crystal surface (DePaolo, 2011; Nielsen *et al.*, 2012). During surface reaction controlled, classical crystal growth, $\Delta^{44/40}Ca$ is dictated by the amount of Ca^{2+} exchange at kink sites on the growing crystal surface. Calcium isotope discrimination thus provides a window into calcium surface dynamics during growth and represents a potential new tool for interrogating the complicated suite of processes occurring at the fluid-mineral interface. Here, we put this tool to work to help elucidate calcite growth dynamics in more complex solutions, investigating calcite growth in the presence of manganese and magnesium as representative case studies of impurity ion interaction with the growing mineral lattice.

3.1.1 Understanding how impurities impact calcite growth: Mn vs. Mg as a case study

The presence of non-stoichiometric ions or molecules in solution can influence crystal growth through a number of different mechanisms (De Yoreo and Vekilov, 2003):

- In *step pinning,* largely irreversible impurity adsorption to a step edge 'pins' the step, meaning that step advancement can only continue by growing around the impurity (Cabrera and Vermilyea, 1958). For a given impurity concentration, this predicts a thermodynamic 'dead zone', or supersaturation below which growth ceases. This occurs when the step curvature must exceed a critical radius in order to pass between the impurities, and the step becomes undersaturated due to the curvature dependence of the Gibbs-Thomson equation.

- In *kink blocking*, adsorption of impurity ions at kink sites alters the rate of kink propagation, for example temporarily blocking the propagation of a kink due to slow desolvation kinetics.

- Foreign ion *incorporation* can also alter growth rates by modifying the stability of the mineral lattice and thus effective supersaturation.

Considering how the presence of foreign ions or molecules in solution can influence calcite growth, impurities can thus be categorized first on the basis of whether they are incorporating (capable of partitioning into the lattice) or not. Large organic molecules such as peptides or proteins cannot be incorporated into the lattice, except as inclusions, and their impact on growth is thus a fully surface-controlled phenomenon. Incorporating ions, on the other hand, are capable of replacing a stoichiometric growth unit in the lattice, and the influence of this partitioning on lattice stability must be accounted for.

Incorporating impurities can be further differentiated based on two parameters: 1) compatibility and 2) preferential partitioning into the acute or obtuse calcite step (Figure 3.1). Compatible elements are concentrated in the calcite lattice, with partition coefficients[1] greater than 1 while incompatible elements are depleted in the calcite lattice relative to the fluid, leading to $K_D < 1$. Similarly, the $(10\bar{1}4)$ calcite surface displays two non-equivalent step structures, termed acute and obtuse based on the angle formed with the terrace below (Figure 3.1A). In addition to the differences in step advancement kinetics discussed in Chapter 2 (Section 2.4.2.1), a number of trace elements have been shown to preferentially interact with and incorporate into either the acute or obtuse calcite step (Paquette and Reeder, 1995; Reeder, 1996; Temmam *et al.*, 2000; Wasylenki *et al.*, 2005b). This preferential partitioning, termed intrasectoral zoning by Paquette and Reeder (1990), can often be predicted based on the relative size of the substituting ion. Cations larger than Ca^{2+} (e.g. Sr^{2+}, Ba^{2+}, Paquette and Reeder (1995); Reeder (1996)) and anions larger than CO_3^{2-} (SO_4^{2-} and SeO_4^{2-}, Staudt *et al.* (1994)) tend to partition preferentially into the more geometrically 'open' obtuse step while cations smaller than Ca^{2+} (e.g. Mg^{2+} and Mn^{2+}, Paquette and Reeder (1995); Wasylenki *et al.* (2005b)) tend to partition preferentially into the more sterically confined acute step. A notable exception to this trend is Zn^{2+}, which partitions preferentially into the obtuse calcite step despite being considerably smaller than Ca^{2+}, possibly due to its electronic configuration (Reeder, 1996; Temmam *et al.*, 2000). While the original experiments by Reeder and colleagues were free-drift experiments performed in unstirred solutions where growth was potentially diffusion-limited, the later in-situ AFM study of Wasylenki *et al.* (2005b) confirmed that Mg^{2+} is preferentially incorporated into acute calcite steps during surface-reaction controlled growth.

Manganese and magnesium thus represent an interesting case-study of impurity interaction with the growing calcite surface. They are quite similar in many ways: both are cations smaller and more strongly hydrated than Ca^{2+} that partition preferentially into the acute step. The effective ionic radius of 6-coordinate Ca^{2+} is 1.0Å while those of Mg^{2+} and Mn^{2+} are 0.72Å and 0.83Å (high-spin state), respectively (Shannon, 1976). Water exchange frequencies among the three divalent cations are consistent with their differences in ionic potential: Helm and Merbach (1999) place the k_{wex} of Mg^{2+} at $6.7e5s^{-1}$ and Mn^{2+} at $2e7s^{-1}$ while the water exchange frequency of Ca^{2+} is greater than $2e8s^{-1}$. But Mg^{2+} and Mn^{2+} exhibit radically different compatibility with the calcite lattice. Mn^{2+} is highly compatible, with strongly rate-dependent partitioning; reported partition coefficients range from <5 to upwards of 30 (Pingitore *et al.*, 1988; Dromgoole and Walter, 1990b,a; Lorens, 1981). In contrast, Mg^{2+} is highly incompatible, with partition coefficients in the range of ~0.01-0.035 (Mucci and Morse, 1983; Mucci, 1987; Mavromatis *et al.*, 2013; Gabitov *et al.*, 2014).

As the major inhibitor cation in seawater, Mg^{2+} inhibition of calcite growth and concomitant partitioning behavior has been well-studied, both in seawater and simple elec-

---

[1] $K_D = {}^{(X/C)_{calcite}}/_{(\{X\}/\{C\})_{fluid}}$ where X is the impurity and C is the calcite growth unit it replaces in the lattice, Ca^{2+} for cations and CO_3^{2-} for anions

trolyte solutions (Berner, 1975; Mucci and Morse, 1983; Mucci, 1987; Davis *et al.*, 2000a; Wasylenki *et al.*, 2005b; Stephenson *et al.*, 2011; Mavromatis *et al.*, 2013; Gabitov *et al.*, 2014). However, the mechanism by which Mg^{2+} acts to inhibit calcite growth remains contested. Berner (1975) first argued that calcite growth inhibition by Mg^{2+} was driven by a largely solid solution thermodynamic effect, where Mg^{2+} incorporation yielded magnesian calcites considerably more soluble than pure calcite. Subsequent interpretations of bulk growth data invoked the stronger hydration of Mg^{2+} relative to Ca^{2+} to argue for a kink-blocking mechanism driven by Mg^{2+} adsorption followed by slow dehydration (Reddy and Wang, 1980; Mucci and Morse, 1983). Observations of near-linear declines in step velocity with increasing solution Mg^{2+} from in-situ AFM experiments were then interpreted as indicative of solid solution thermodynamic inhibition (Davis *et al.*, 2000a). A later in-situ AFM study by Astilleros *et al.* (2010), run at higher solution Mg/Ca, argued against this interpretation on the basis of existing calcite-magnesite solid solution thermodynamic data. Recent interpretations based on microkinetic models of calcite growth similarly argue for dominantly kink-blocking inhibition (Nielsen *et al.*, 2013; Dobberschütz *et al.*, 2018).

The interaction between Mn^{2+} and carbonate minerals is also of considerable geochemical interest; the Mn content of carbonates is often used to infer the redox conditions of the depositional environment (Barnaby and Rimstidt, 1989) and thus as a marker of diagenetic alteration (Brand and Veizer, 1980). While a number of studies have examined Mn^{2+} partitioning into calcite (Pingitore *et al.*, 1988; Dromgoole and Walter, 1990b,a; Lorens, 1981; Mucci, 1988), fewer well-controlled kinetic studies have been performed. By far the most extensive dataset was collected by Dromgoole and Walter (1990a; 1990b), who investigated Mn^{2+} inhibition of calcite growth and associated partitioning behavior as a function of temperature, P_{CO_2}, and ${}^{\{Mn^{2+}\}}/_{\{Ca^{2+}\}}$ in $CaCl_2$ solutions. They found that Mn^{2+} strongly inhibits calcite growth and that trends in the extent of inhibition with ${}^{\{Mn^{2+}\}}/_{\{Ca^{2+}\}}$ were roughly consistent with a Langmuir adsorption model (Dromgoole and Walter, 1990a). Notably, Mucci (1988) reported that in seawater solutions, the addition of Mn^{2+} actually increased calcite growth rates, potentially due to competitive adsorption with Mg^{2+} or $MgSO_4$ complexes (Nielsen *et al.*, 2016). While these observations could point towards a dominantly kink blocking inhibition mechanism, the extent to which changes in lattice solubility with considerable Mn^{2+} incorporation influence growth kinetics remains largely unconstrained. Predicting partitioning behavior based on mechanistic principles, particularly for highly compatible elements, also remains a key challenge. Previous studies have documented a strong kinetic control on Mn^{2+} partitioning into calcite (Dromgoole and Walter, 1990b; Lorens, 1981), the implications of which will be explored here.

3.1.2 Investigation goals

In Chapter 2, we introduced the concept that calcium isotope fractionation could differentiate between these different mechanisms of growth inhibition (Section 2.4.6). In brief, destabilization of the mineral lattice due to impurity incorporation should increase the flux of Ca off the surface at a given $\{Ca^{2+}\}$ and $\{CO_3{}^{2-}\}$ and thus decrease the magnitude of $\Delta^{44/40}Ca$. In contrast, $\Delta^{44/40}Ca$ is predicted to be invariant with impurity concentration for dominantly kink blocking inhibition, as inhibitor adsorption to kink sites and resultant modification of kink propagation kinetics will not change the *relative* rate of Ca attachment

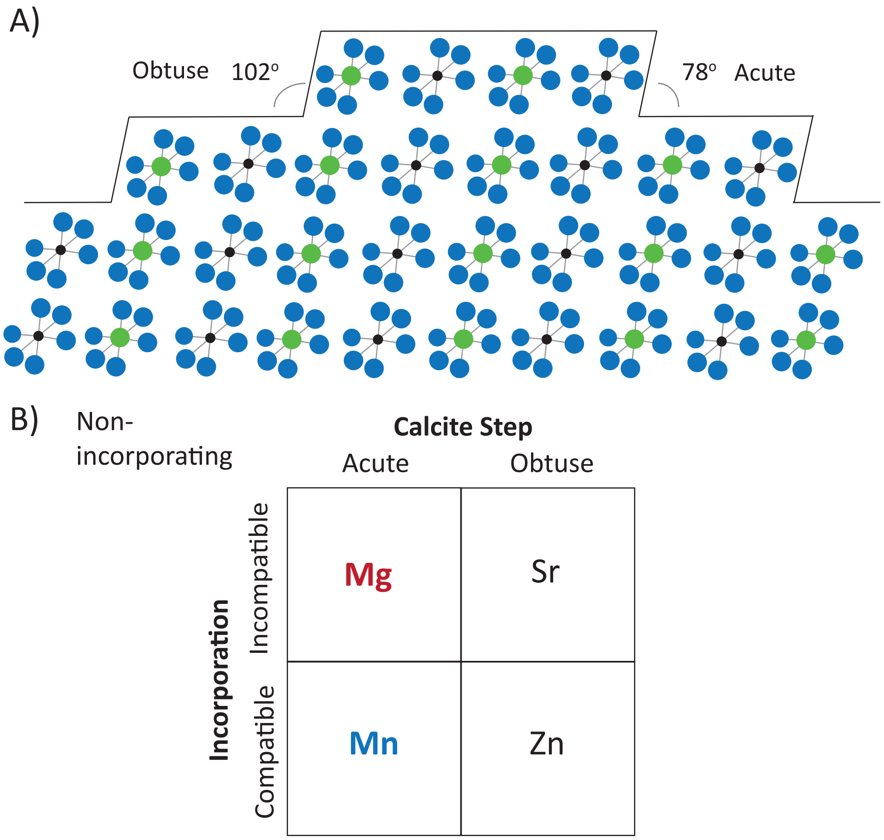

Figure 3.1 – Diagram demonstrating how the presence of impurities can influence calcite growth. A) The (10$\bar{1}$4) calcite face displays two non-equivalent step structures, termed acute and obtuse based on the angle formed with the terrace below. B) Impurities can be categorized first on the basis of whether they are incorporating (capable of partitioning into the lattice) or not; incorporating impurities can be further differentiated on the basis of two parameters: 1) compatibility and 2) preferential partitioning into the acute or obtuse calcite step.

to vs. removal from the surface.

Here, we attempt to operationalize the use of stable isotope isotopes as molecular probes of crystal growth, employing calcium isotope fractionation to help elucidate the mechanism by which two divalent cations with starkly contrasting compatibility, magnesium and manganese, interact with the growing calcite surface and inhibit growth. We present results from a series of constant-composition inorganic calcite growth experiments where all aspects of solution chemistry are held constant while $\{^{Me^{2+}}\}/\{_{Ca^{2+}}\}$ is varied. Observed trends in rate inhibition, trace element partitioning, and isotope fractionation are interpreted using an ion-by-ion kinetic framework to develop a molecular-level understanding of Mn^{2+} and Mg^{2+} inhibition of calcite growth.

3.2 Methods

A series of constant composition calcite growth experiments was undertaken to investigate the interplay between Mn and Mg inhibition of calcite growth, partitioning into the lattice, and Ca isotope fractionation. Independent seeded Mn-calcite and Mg-calcite growth experiments were run under different fluid metal to calcium (Me/Ca) ratios ($\{^{Mn^{2+}}\}/\{_{Ca^{2+}}\}$ 0.002 – 0.124; $\{^{Mg^{2+}}\}/\{_{Ca^{2+}}\} = 0.01 - 2.6$) using a chemostat reactor. A thorough description of the chemostat setup and protocol used is provided in Chapter 2; a summary which highlights challenges unique to performing constant composition experiments in the presence of impurity ions is provided here.

3.2.1 Constant composition growth experiments

3.2.1.1 Experimental Setup

Constant composition calcite growth experiments with varied Me/Ca ratios were performed using the chemostat reactor shown in Figure 3.2. An automated titration system controlled by solution pH measurement is used to maintain constant solution conditions in the growth chamber. As calcite precipitates over the course of an experiment, the decrease in solution pH triggers the addition of equimolar $(Me,Ca)Cl_2$ and K_2CO_3 titrant solutions (0.25M) to return the pH to the set point (8.0), thus replacing the growth units removed from solution through precipitation. The ratio of Mn/Ca or Mg/Ca in the 0.25M cation titrant solution is dictated by the Me/Ca distribution coefficient and can make running constant composition experiments with highly compatible elements quite challenging as discussed below.

3.2.1.2 Materials and solution preparation

Two suites of seeded, constant-composition calcite growth experiments were performed (Table 3.1) in which all aspects of solution chemistry were held constant except for the concentration of Mn or Mg in the growth solution. All experiments were run at a fixed solution pH (8.0 +/- 0.05), ionic strength (0.1M, adjusted with KCl), temperature (25 ± 0.5°C), and calcite saturation (SI = 0.8), where

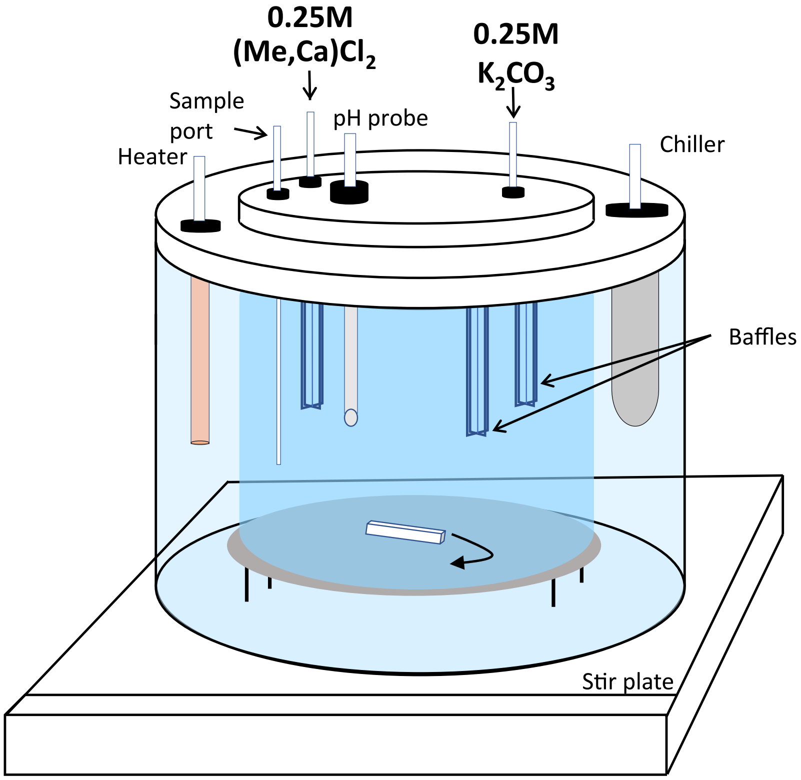

Figure 3.2 – Schematic of chemostat reactor. The pyrex growth chamber (2L volume) is contained within a fixed-temperature water bath (maintained at 25°C by a heater and chiller). Constant solution conditions are maintained by auto-titration of K_2CO_3 and $(Me,Ca)Cl_2$ to replace growth units removed from the solution by precipitation (titration triggered by pH measurement).

$$SI = log_{10}\left(\frac{\{Ca^{2+}\}\{CO_3^{2-}\}}{K_{sp}}\right) \tag{3.2.1}$$

Solution speciation and calcite saturation were determined using PhreeqC (Parkhurst and Apello, 2013), with the llnl.dat thermodynamic database and calcite equilibrium constant $K_{sp} = 10^{-8.48}$ (Plummer and Busenberg, 1982). Supersaturations are reported as calculated by PhreeqC based on the analytic expressions for the temperature dependence of calcite solubility. Measured values for Mn-(bi)carbonate ion pair stability constants as well as the K_{sp} for rhodochrosite span 2 orders of magnitude and this measurement spread is reflected in the geochemical thermodynamic databases (Figure B1). The choice of thermodynamic database thus has a non-negligible impact on calculated Mn speciation for the experimental solutions considered here. The llnl.dat database was used for speciation calculations throughout this study as it assumes a 'middle ground' rhodochrosite solubility ($K_{sp} = 10^{-10.5}$ (Morgan, 1967; Robie *et al.*, 1984; Johnson, 1982)) representative of the center of the normal distribution of reported values (Figure B1A) as well as ion pair stability constants consistent with existing measurements (Figure B1B,C).

The experiments were seeded using either 0.5g or 1g of Baker-analyzed calcite as seed material. A larger amount of seed was used in the higher Mn or Mg, slower-growing experiments to minimize the influence of pH drift and heterogeneous nucleation on the pH probe, which can become problematic in longer experiments (>1 day). Growth and titrant solutions were prepared by dissolving ACS reagent grade chemicals (Sigma-Aldrich) in ultrapure water (18.2MΩ, Milli-Q). All Ca solutions were prepared using the same 2M $CaCl_2 \bullet 2H_2O$ stock solution. A 1 or 0.1M $MgCl_2 \bullet 6H_2O$ stock solution was used to prepare Mg solutions; a new 1M $MgCl_2 \bullet 6H_2O$ solution was prepared before experiment Mg7 (Table 3.1). To prevent Mn^{2+} oxidation, all solutions were prepared with N_2-sparged water and fresh $MnCl_2 \bullet 4H_2O$ stock solutions were prepared just before every experiment. A solution pH of 8.0 was also chosen as a trade-off between slower Mn oxidation kinetics at low pH (Hem, 1963; Morgan, 2005) and maintaining a relatively low Ca^{2+}:CO_3^{2-} activity ratio (Ca^{2+}:CO_3^{2-} = 100; previous studies of Mn calcite growth inhibition used notably high Ca^{2+}:CO_3^{2-} (Lorens, 1981; Mucci, 1988; Dromgoole and Walter, 1990b,a)).

Titrant solutions (0.25M $(Me,Ca)Cl_2$, 0.25M K_2CO_3) were prepared at the start of each experiment and stored in gas-tight Tedlar bags (Sigma-Aldrich). The appropriate Me/Ca for the cation titrant solution is dictated by the trace constituent's distribution coefficient; in order to maintain constant solution conditions, the titrant Me/Ca should match the Me/Ca of the solid phase being precipitated. For highly incompatible elements such as Mg, a rough estimate of the partition coefficient (here, K_{Mg} ~ 0.02 was assumed) is adequate. So little Mg is removed from solution relative to the size of the growth solution Mg reservoir that even substantial deviations from the assumed K_d will not materially change solution Mg concentrations. For highly compatible elements such as Mn, it is much more difficult to maintain constant solution conditions. Slight offsets between the titrant concentration and solid Mn/Ca dictated by the distribution coefficient can lead to large changes in the growth solution Mn concentration given the small size of the growth solution Mn reservoir relative to that in the titrant. As discussed below, this is advantageous in that changes in growth solution [Mn] can be used to constrain the Mn partition coefficient. However, it also presents an

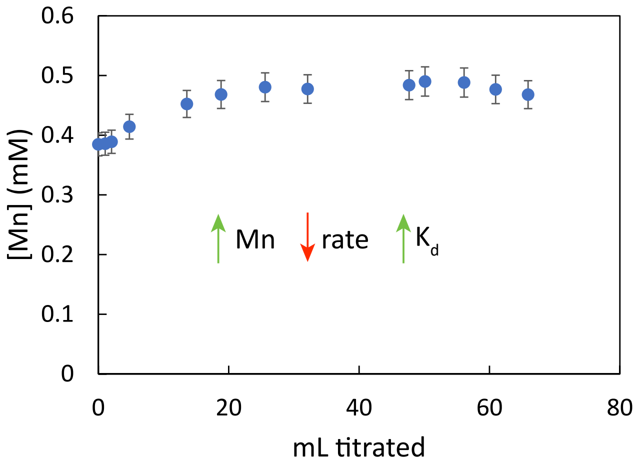

Figure 3.3 – Example of Mn^{2+} concentrations coming to a quasi-steady state over the course of an experiment (Exp Mn6, Table 3.1), potentially driven by a negative feedback between growth rate and Mn partitioning.

experimental challenge: one must either know the partition coefficient for a given set of solution conditions a-priori or dial-in the K_d through trial and error in successive experiments. Happily, initial testing revealed that as long as the titrant concentration was relatively close to that dictated by the K_d, solution Mn concentrations evolved to a steady-state over the course of an experiment (Figure 3.3). Most practically, this allowed us to run near-constant Mn concentration experiments with minimal trial-and error. In the steady-state region, the titrant Mn/Ca matches that being removed from solution, thus revealing the K_d for the steady-state solution $\{Mn^{2+}\}/\{Ca^{2+}\}$. A single replicate experiment with initial conditions adjusted to match the steady-state $\{Mn^{2+}\}/\{Ca^{2+}\}$ thus generally yielded solution Mn concentrations that varied $<10\%$ over the course of the experiment. More fundamentally, this self-stabilizing behavior observed in growth solution [Mn] is the first indication of a strong negative feedback between calcite growth rate and Mn partitioning (Section 3.3.4, Figure 3.3). If the titrant concentration over-predicts the partition coefficient, solution Mn concentrations will rise, thus decreasing growth rates. The fact that Mn concentrations stabilize instead of continuing to increase points towards a negative feedback between rate and K_d: the declining rates increase the partition coefficient until the Mn being removed through precipitation matches that being added via titration.

3.2.1.3 Experimental run

Each experiment was started by combining 0.9L cation ($(Me,Ca)Cl_2$) and anion ($KHCO_3 + KCl$) solutions in the growth chamber and purging the headspace with N_2 before attaching the chamber lid (sealed with an o-ring). The solution pH was adjusted to 8.0 with 0.1M KOH, the automated titration program was started, and calcite seed was then added through a port in the chamber lid to initiate precipitation. Solution conditions were monitored throughout the course an experiment by taking 5-20mL fluid aliquots through the sample port at regular intervals. Samples were passed through $0.2\mu m$ syringe filters to remove any calcite; aliquots for cation concentration analysis were immediately acidified by 15N

HNO_3 while aliquots for alkalinity analysis were stored (unacidified) in 15mL falcon tubes with minimal headspace until analysis. Alkalinity was measured within 1 hour of sampling. This measurement provided an external check on solution pH, which can drift slightly due to calcite precipitation on the pH probe. At the end of an experiment, the solution was vacuum filtered through a 0.45 μm nylon membrane filter to collect the precipitated material, which was rinsed 3x with Milli-Q H_2O before being dried at room temperature in a fume hood. Experimental duration was dictated by the titration volume (equivalently moles $(Me,Ca)CO_3$ precipitated) to achieve ~1 turnover of the Ca reservoir (Section 3.2.5). Importantly, for the Mn suite of experiments, this meant longer experiments and higher total titration volumes for high $\{Mn^{2+}\}$ experiments, as the $(Me,Ca)Cl_2$ titrant contained significantly less Ca (Table 3.1).

3.2.2 Analytical techniques

Changes in growth solution Ca, Mn, and Mg concentration over the course of an experiment and in resultant solids were measured by ICP-OES (Perkin Elmer 5300 DV, uncertainty ~5% based on repeat analysis of standards). Precise elemental Ca concentrations for initial and end fluids samples were obtained from isotope-dilution measurements (uncertainty ~1%) during Ca isotope analysis. Alkalinity was measured by Gran-titration with calibrated 0.01M H_2SO_4. The surface area of the calcite seed material was measured as the N_2 BET surface area at 77K (3Flex, Micromeritics). The morphology of the solids precipitated was examined using scanning electron microscopy (SEM, Zeiss EVO-10 Variable Vacuum). The mineralogy of the $(Me,Ca)CO_3$ precipitates was analyzed using powder X-Ray diffraction. The $(Mg,Ca)CO_3$ samples were analyzed on a PANalytical X-Pert Pro diffractometer equipped with a Co x-ray source; data was collected between 20° and 70° 2θ. The $(Mn,Ca)CO_3$ samples were analyzed on a Rigaku SmartLab diffractometer equipped with a Cu x-ray source; data was collected between 15° and 65° 2θ. Peak fitting and identification was performed with X'Pert HighScore Plus for the $(Mg,Ca)CO_3$ samples and QualX for the $(Mn,Ca)CO_3$ samples. GSAS-II was used for Reitveld refinement.

Calcium isotope ratios and elemental Ca concentrations were measured with a Finnigan TRITON thermal ionization mass spectrometer (TIMS) using the double spike method (^{42}Ca + ^{48}Ca). Aliquots of fluid samples (or $CaCO_3$ solid samples dissolved in 1M acetic acid) containing 30μg of Ca were spiked with 10μL of double spike per μg Ca added. Calcium separation was performed via column chemistry using Ca-specific DGA resin (Eichrom). The columns were loaded with approximately 300uL resin, and rinsed with 2mL double deionized (DDI) H_2O and 1mL 3M HNO_3. The spiked sample was loaded on the column in 3M HNO_3 and rinsed with 200, 400, and 800uL 3M HNO_3. Ca was then eluted from the column with 1.5mL DDI H_2O (400, 400, 700μL step wise addition). The eluted Ca was dried down and re-suspended in a few drops of concentrated HNO_3 and 40% hydrogen peroxide and left overnight. The samples were dried down once more and resuspended in 10μL, 3M nitric acid. The purified Ca sample was then loaded on zone-refined Re double filaments (3μg Ca loaded with 40% phosphoric acid) and its Ca isotopic composition was analyzed on the TIMS. All Ca isotope ratios are expressed in standard delta notation relative to bulk silicate earth (BSE - $^{44}Ca/^{40}Ca = 0.0212035$) as:

$$\delta^{44/40}Ca = \left(\frac{(^{44}Ca/^{40}Ca)_{sample}}{(^{44}Ca/^{40}Ca)_{BSE}} - 1 \right) 1000 \tag{3.2.2}$$

The NIST SRM 915a reference material was measured 3x per turret and used to determine external errors on $\delta^{44/40}$Ca measurements. SRM 915a measurements averaged to -0.94‰ with an external 2σ reproducibility of ±0.15‰ (n = 12).

3.2.3 Growth rate determination

The calcite growth rate in mol/s was determined from the experimental titration rate:

$$R(mol/s) = C * \frac{dV}{dt} \tag{3.2.3}$$

where C is the titrant concentration (0.25M) and $\frac{dV}{dt}$ is the slope of the titrant volume versus time curve (Figure 2.2B). To obtain surface-normal growth rates (mol/m^2/s), this rate must be normalized by an estimate of the reactive surface area (m^2). Here, we used the BET surface area of the seed crystal (specific surface area, SSA = 0.21 ± 0.01 m^2/g) to calculate the reactive surface area (m^2 = SAA*grams calcite). The raw growth rate (mol/s) was calculated for the 5-10mL titration interval for each experiment, constraining the growth rate calculation to the early stages of the experiment where reactive surface area is best defined (majority of surface area is provided by the seed crystal) but avoiding the first few mL titrated where Mn concentrations had not yet reached steady-state (Section 3.2.1.2, Figure 3.3). The grams of material precipitated over the 0-7.5mL titration interval were accounted for in the calculation of reactive surface area. The inter-experiment reproducibility, quantified as the average difference between near-replicates in the Mn suite of experiments, was 6.7%. Propagating this inter-experiment reproducibility with the 5% uncertainty on the BET surface area measurement yields an overall error of 8.4%. The impact of titration interval used to calculate the growth rate was also considered; calculating the growth rate based on different titration intervals within a single experiment (e.g. 5-10mL vs. 10-15mL) yielded an average relative difference of 3% for the Mn experiments and 6% for the Mg experiments. Error on the surface-normal growth rates measured was thus taken to be the larger of the 8.4% inter-experiment error and observed intra-experiment variability.

3.2.4 Partition coefficient calculation

Partition coefficients for manganese (K_{Mn}) and magnesium (K_{Mg}) were calculated as:

$$K_{Me} = \frac{(^{Me}/_{Ca})_{calcite}}{(^{\{Me^{2+}\}}/_{\{Ca^{2+}\}})_{fluid}} \tag{3.2.4}$$

where $(^{Me}/_{Ca})_{calcite}$ is the molar ratio of Me to Ca in the overgrowth and $(^{\{Me^{2+}\}}/_{\{Ca^{2+}\}})_{fluid}$ is the steady-state growth solution Me^{2+} to Ca^{2+} activity ratio. For comparison to literature datasets where sufficient data to calculate solution activities was not provided, $K_{Me,conc}$ is also presented using the fluid Me/Ca concentration ratio in the denominator.

The total Mn or Mg concentration in the experimental solids was determined by dissolving a weighed aliquot of the dried solid with 2% HNO_3 and measuring Mn, Mg, and Ca elemental concentrations via ICP-OES by the same method used for the experimental solutions (Section 3.2.2). The Me content of the bulk solid (seed + overgrowth) is almost exclusively derived from the overgrowth. The Baker-analyzed seed material used contained <0.01% Mn and Mg; the Mn content of bulk solids from the Mg experiments was never above instrument background and vice versa. The overgrowth composition was thus calculated as:

$$\left(\frac{Me}{Ca}\right)_{overgrowth} = \frac{\left(\frac{mol\,Me,bulk}{g,bulk}\right)(g,bulk)}{\left(\frac{mol\,Ca,bulk}{g,bulk}\right)(g,bulk) - mol\,Ca,seed} \tag{3.2.5}$$

where the moles Mn or Mg per gram of bulk solid $\left(\frac{mol\,Me,bulk}{g,bulk}\right)$ was derived directly from the ICP concentration measurement:

$$\left(\frac{mol\,Me,bulk}{g,bulk}\right) = \frac{[Me] * sample\,volume}{g\,sample} \tag{3.2.6}$$

and the total grams of bulk solid $(g,bulk)$ is the mass of seed material + the mass of overgrowth precipitated $(g,overgrowth)$, calculated as:

$$g,overgrowth = MW_{overgrowth} * [MeCl_{2,\,titrant} + MeCl_{2,\,titrant}] * volume\,titrated \tag{3.2.7}$$

For the Mg experiments, so little Mg is incorporated into the lattice that the solid solution molecular weight is approximately equal to that of calcite ($MW_{overgrowth} \sim MW_{calcite} =$ 100.08g/mol), while for the Mn experiments, $MW_{overgrowth}$ is estimated using the titrant Mn composition to generate an approximate mole fraction Mn ($MW_{overgrowth} \sim (X_{Mn} * MW_{rhodochrosite}) + ((1 - X_{Mn}) * MW_{calcite})$). The Mn overgrowth composition calculated in this manner is highly consistent with the changes in lattice parameters observed via powder XRD (Section 3.3.2.1, Figure 3.10). In all experiments, the overgrowth represented 40-60% of the bulk solid by weight.

For the Mn experiments, the partition coefficient can also be calculated directly from the evolution of growth solution Mn. As described in Section 3.2.1.2, fluid Mn concentrations were observed to approach a steady-state over the course of the experiment (Figure 3.3). In this steady-state region, a roughly equal number of moles of Mn are being added to and removed from solution, meaning that the titrant Mn/Ca matches the composition of the overgrowth. The partition coefficient can thus be calculated from the titrant Mn/Ca and the steady-state fluid activity ratio:

$$K_{Mn,fluid} = \frac{(^{Mn}/_{Ca})_{titrant}}{(\{^{Mn^{2+}}\}/\{_{Ca^{2+}}\})_{fluid}} \tag{3.2.8}$$

This fluid partition coefficient calculation homes in on the steady-state interval where $\{Mn^{2+}\}/\{Ca^{2+}\}$ is well-constrained ([Mn] varies up by 10% transiently before steady-state is achieved). Partition coefficients calculated from the solid and fluid data are compared in Figure 3.4. In all cases, K_{Mn} calculated using the two methods is within 5%, except for

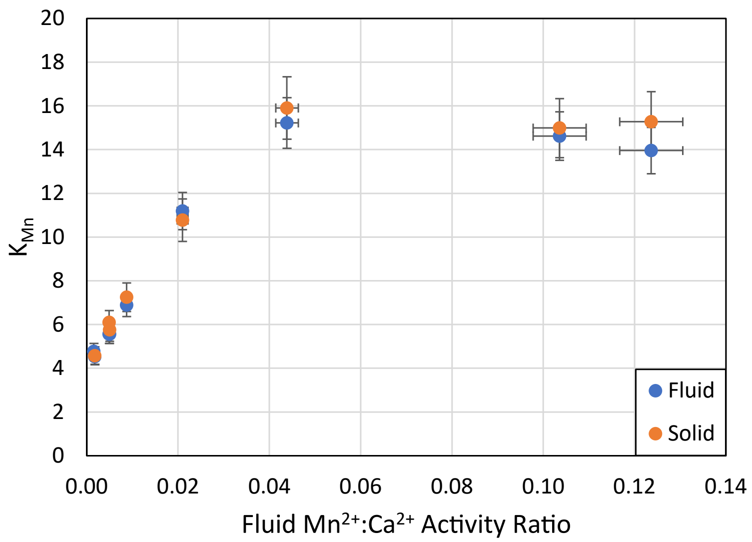

Figure 3.4 – Comparison of calculated Mn partition coefficient using the measured solid overgrowth composition (orange circles) and titrant composition (blue circles). In all cases, the resultant K_{Mn} calculated using the two methods is within 5%, except for the highest Mn experiment (Mn 13) where the partition coefficient calculated from the solid composition is 8.5% higher than that calculated from the fluids.

the highest Mn experiment (Mn 13) where the partition coefficient calculated from the solid composition is 8.5% higher than that calculated from the fluids (Table 3.2). In subsequent figures, we plot the average of the solid and fluid K_{Mn}.

3.2.5 Calculation of calcium isotope fractionation

The calcium isotope fractionation factor between the solid and aqueous solution (eq 3.2.9) was calculated using a Ca isotope box model as described in Mills et al. (2021) (Chapter 2), using the evolution of $\delta^{44}Ca_{fluid}$ over the course of an experiment to constrain $\Delta^{44/40}Ca_{calcite-fluid}$.

$$\Delta^{44/40}Ca_{calcite-fluid} = \delta^{44}Ca_{calcite} - \delta^{44}Ca_{fluid} \approx 1000ln\alpha_p \tag{3.2.9}$$

Briefly, for a non-steady state mass, the change in Ca over time is:

$$\frac{dCa_{fluid}}{dt} = F_{in} - F_{out} \tag{3.2.10}$$

where F_{in} is the flux of Ca into the growth solution (i.e. titration rate - mol/s) and F_{out} is the flux of Ca out of solution via precipitation. The change in $\delta^{44}Ca_{fluid}$ over time can similarly be modeled by tracking ^{40}Ca and ^{44}Ca separately:

$$\frac{d^{44}Ca_{fluid}(t)}{dt} = \frac{R_{in}}{R_{in}+1}F_{in}(t) - \frac{R_{calcite}(t)}{R_{calcite}(t)+1}F_{out}(t) \tag{3.2.11}$$

$$\frac{d^{40}Ca_{fluid}(t)}{dt} = \frac{1}{R_{in}+1}F_{in}(t) - \frac{1}{R_{calcite}(t)+1}F_{out}(t) \tag{3.2.12}$$

$$R_{fluid}(t) = \frac{^{44}Ca_{fluid}(t)}{^{40}Ca_{fluid}(t)} \tag{3.2.13}$$

$$R_{calcite}(t) = \alpha_p R_{fluid}(t) \tag{3.2.14}$$

where R_{in}, $R_{fluid}(t)$, and $R_{calcite}(t)$ are the 44/40 ratio of the $CaCl_2$ titrant solution (constant), growth solution, and precipitated calcite at a given point of time, respectively. Equations 3.2.10-3.2.14 were solved numerically by finite difference in Matlab. This allowed any changes in the size of the Ca reservoir due to titrant offset or CO_2 degassing to be taken into account. $\Delta^{44/40}Ca_{calcite-fluid}$ was calculated as the average of the range of α_p that yielded measured $\delta^{44}Ca_{fluid,final}$ within 2σ error. The error of calculated $\Delta^{44/40}Ca_{calcite-fluid}$ was taken to be the larger of 2σ error calculated through formal error propagation of a steady-state box model:

$$\Delta^{44/40}Ca_{calcite-fluid} = \frac{\delta^{44/40}Ca_{fluid,initial} - \delta^{44/40}Ca_{fluid,final}}{1 - e^{-(moles\,Ca\,titrated/moles\,Ca\,growth\,solution)}} \tag{3.2.15}$$

and the entire potential range of fractionations yielding measured final $\delta^{44}Ca_{fluid}$.

3.2.6 Ion-by-ion modeling of calcite growth and trace element + isotope partitioning

We employ the ion-by-ion growth model of Nielsen *et al.* (2013) to apply a mechanistic lens to the observed inhibition and trace constituent + isotope partitioning behavior. The Nielsen *et al.* (2013) builds upon the Nielsen *et al.* (2012) model described in Chapter 2 (Section 2.2.5, Table A1) by allowing for the presence of impurity ions. This requires a new type of growth unit and kink site (M – impurity) and the kink propagation rate and kink site probabilities must be amended accordingly. How those parameters must be amended depends on the type of impurity. The simplest case is that of *non-incorporating* impurities – molecules that will bind to kink sites but have no chance of being incorporated into the lattice. In this case, subsequent growth units cannot be attached to the impurity, so eventually the impurity will reach a steady-state concentration on the surface – meaning the kink propagation rate for the impurity is zero. Using that fact, one can calculate kink site probabilities that are complicated but dependent only on attachment/ detachment rate coefficients and ion activities in solution (Nielsen *et al.*, 2013).

The case for incorporating impurities like Mn^{2+} and Mg^{2+} is further complicated by the need to account for the lattice strain induced by incorporating a non-calcium or non-carbonate ion into the calcite lattice. Nielsen *et al.* (2013) implement this lattice strain effect by parameterizing kink detachment frequencies in terms of bulk equilibrium solid solution thermodynamics. This works from the premise that in the limit of infinitely slow growth, the kinetic model must be consistent with equilibrium solid solution thermodynamics and thus ion detachment frequencies must be related to the free energy of mixing. In practice, if the solid solution thermodynamics of the $CaCO_3$-$MeCO_3$ system are known, one can calculate the end member equilibrium ion activity products as:

$$[A]_{eq}[B]_{eq} = (1-x)K_{AB}\gamma_{AB} \tag{3.2.16}$$

$$[M]_{eq}[B]_{eq} = (x)K_{MB}\gamma_{MB} \tag{3.2.17}$$

where x is the mole fraction of $MeCO_3$; K_{AB} and K_{MB} are the calcite and $MeCO_3$ solubility products, respectively; and γ's are the solid-phase activity coefficients. Kink detachment frequencies can then be cast in terms of these equilibrium ion activity products:

$$\nu_A\nu_B = \frac{[A]_{eq}[B]_{eq}k_Ak_B}{1-x} \tag{3.2.18}$$

$$\nu_M\nu_{B-M} = \frac{[M]_{eq}[B]_{eq}k_Mk_{B-M}}{x} \tag{3.2.19}$$

3.2.6.1 Solid solution thermodynamic data

Implementing this lattice strain dependence for Mn^{2+} and Mg^{2+} thus requires a parameterization of calcite-rhodochrosite and calcite-magnesite solid solution thermodynamics, specifically a description of how solid-phase activity coefficients vary as a function of mole fraction $MeCO_3$. For Mg, we follow Lammers and Mitnick (2019), describing the Mg-Ca solid solution using a sub-regular model for binary solutions, with solid end-member activity coefficients given by:

$$RTln(\gamma_{AB}) = x^2\left[W_{12} + 2(W_{21} - W_{12})(1-x)\right] \tag{3.2.20}$$

$$RTln(\gamma_{MB}) = (1-x)^2\left[W_{21} + 2x(W_{12} - W_{21})\right] \tag{3.2.21}$$

where W_{12} and W_{21} are empirical interaction parameters. W_{21} is taken to be 8kJ/mol based on the temperature dependence reported by Lammers and Mitnick (2019). A value of 40kJ/mol for the W_{12} parameter was proposed in that study, based on calibration of the Nielsen *et al.* (2013) ion-by-ion model to fit data for Mg partitioning from seawater solutions (fluid [Mg]/[Ca] = 1-10 (Mucci and Morse, 1983)). Notably, the value of W_{12} dictates the sign of the K_{Mg}-$\{Mg^{2+}\}/\{Ca^{2+}\}$ relationship. Low values of W_{12} yield an increase in K_{Mg} with fluid $\{Mg^{2+}\}/\{Ca^{2+}\}$ while values of W_{12} greater than ~17kJ/mol cause the slope of the K_{Mg}-$\{Mg^{2+}\}/\{Ca^{2+}\}$ relationship to reverse (Lammers and Mitnick, 2019). We further explore the implications of the W_{12} parameter selection in Section 3.4.4.2.

A range of somewhat contradictory data exists on the solid solution thermodynamics of the calcite-rhodochrosite system (McBeath *et al.*, 1998). Here we use the low-temperature calorimetric data of Katsikopoulos *et al.* (2009) as our baseline description of the excess free energy of mixing (ΔG_{ex}). This data is consistent with both the earlier high-temperature calorimetric experiments of Capobianco and Navrotsky (1987) and recent computational studies (Wang *et al.*, 2011; Son *et al.*, 2019). Guggenheim parameters fit to the experimental ΔG_{ex} are used to calculate solid phase activity coefficients (Prieto, 2009):

$$\Delta G_{ex}(x) = x(1-x)RT\left[a_0 + a_1(2x-1) + a_2(2x-1)^2\right] \tag{3.2.22}$$

$$ln(\gamma_{AB}) = x^2 \left[a_0 - a_1(3 * (1-x) - x) + a_2 (1-2x) (5 * (1-x) - x)\right] \quad (3.2.23)$$

$$ln(\gamma_{MB}) = (1-x)^2 \left[a_0 + a_1(3x - (1-x)) + a_2 (2x-1) (5x - (1-x))\right] \quad (3.2.24)$$

where x is the mole fraction $MnCO_3$ and a_0, a_1, and a_2 are dimensionless fitting parameters.

3.2.6.2 Potential influence of surface speciation

In Chapter 2, we demonstrated that the solution stoichiometry dependence of Ca isotope fractionation is well-captured by an ion-by-ion framework that incorporates the influence of surface speciation (Mills *et al.*, 2021). The primary difference between the Nielsen *et al.* (2012, 2013) models and that employed in Chapter 2 (Wolthers *et al.*, 2012) is the addition of the solution chemistry-sensitive χ parameter, representative of the fraction of available growth sites. This adds additional solution chemistry sensitivity to the kink-site probabilities and kink nucleation dynamics, and yields different best-fit ion attachment coefficients (Section 2.2.5, 2.4.2.2).

We work with the Nielsen *et al.* (2013) framework here, without attempting to incorporate the influence of surface speciation, under the assumption that surface speciation would not substantially change our interpretations regarding inhibition mechanisms. Incorporating surface speciation in the presence of impurity ions is complicated by the fact that the *composition* of the surface is not known a-priori, but is instead a function of solution chemistry, and the surface complexation model would need to reflect this variation in solid solution composition. We leave that for future work, ideally informed by spectroscopic constraints on calcite-magnesite and calcite-rhodochrosite solid solution surface speciation as a function of solution chemistry.

3.2.6.3 Complicating factor: influence of impurity ions on step density

The model extensions described above address how the presence of impurities influence the step velocity (v_{st}). As discussed in Chapter 2, in order to scale measured or modeled step velocities to bulk growth rates, an additional solution chemistry dependent parameter is required: the step density. For the simplest case of growth on single growth hillocks, the bulk growth rate scales linearly with step density ($1/y_0$):

$$R_{net}(m/s) = \left(\frac{h}{y_0}\right) v_{st} \quad (3.2.25)$$

Most models rely on a thermodynamic representation of y_0, which is sensitive only to the assumed step edge free energy and supersaturation ((Teng *et al.*, 1998):

$$y_0 = \frac{16ha^2\gamma}{k_bT\sigma} \quad (3.2.26)$$

where γ is the step-edge free energy per unit step height (~1.4 J/m^2(Teng *et al.*, 2000)). We previously explored the implications of a solution-stoichiometry sensitive y_0 (Davis, 2008; Bracco *et al.*, 2013), but y_0 has also been demonstrated to vary with inhibitor concentration (Davis *et al.*, 2000a; Wasylenki *et al.*, 2005a), likely driven by changes in interfacial energy. The same holds for growth via 2D nucleation, where the bulk growth rate scales non-linearly with 2D nucleation frequency (which dictates the step density (van der Eerden, 1993)):

$$R_{net}(m/s) = 1.137h\left(Iv_{st}^2\right)^{1/3} \tag{3.2.27}$$

where I is the nucleation frequency ($m^{-2}s^{-1}$). Unlike y_0, the nucleation frequency of 2D islands is not an easy parameter to measure and is seldom reported. Yet it likely changes somewhat unpredictably with solution chemistry, as nucleation frequency is largely a function of the fluid-mineral interfacial energy (van der Eerden, 1993).

The importance of considering the influence of inhibitors on both step velocities and step density when interpreting bulk growth rate inhibition data is demonstrated in Figure 3.5. Figure 3.5A shows Sr^{2+} calcite growth inhibition data from Wasylenki *et al.* (2005a), using both measured step velocities and y_0 to calculate bulk growth rates; the step velocity inhibition data is down in Figure 3.5B. While high step velocities are maintained past a $\{Sr^{2+}\}/\{Ca^{2+}\}$ of 0.5 for most supersaturations (with step velocities slightly higher than the inhibitor-free solution in many cases as Sr^{2+} incorporation contributes to the net step propagation rate (Nielsen *et al.*, 2013)), the bulk growth rate is inhibited at low $\{Sr^{2+}\}/\{Ca^{2+}\}$ because y_0 increases substantially with increasing $\{Sr^{2+}\}/\{Ca^{2+}\}$.

Interpreting and modeling the bulk growth data obtained here thus requires knowledge of how y_0 varies with inhibitor concentration. For Mg^{2+}, Davis *et al.* (2000b) reported both step velocity and y_0 measurements over a range of $\{Mg^{2+}\}/\{Ca^{2+}\}$ and supersaturation (Figure 3.5C). A similar increase in y_0 with increasing $\{Mg^{2+}\}/\{Ca^{2+}\}$ was observed by Stephenson *et al.* (2008). Figure 3.5D demonstrates the influence of modeling y_0 using the thermodynamic representation (sensitive only to supersaturation - Eq. 3.2.26) vs. scaling y_0 using the slope of the y_0-$\{Mg^{2+}\}/\{Ca^{2+}\}$ relationship determined by Davis *et al.* (2000b). We use the SI = 0.61 data from Davis *et al.* (2000b) as it is closest to the SI = 0.8 conditions used here, but comparable results are obtained when considering the data from all supersaturations. Using the observed y_0-$\{Mg^{2+}\}/\{Ca^{2+}\}$ relationship yields a difference in y_0 and thus calculated bulk growth rate (Eq. 3.2.25) of up to a factor 3 at high $\{Mg^{2+}\}/\{Ca^{2+}\}$. We thus explicitly explore the implications of assumptions regarding y_0 when modeling Mg^{2+} inhibition of calcite growth, employing the y_0-$\{Mg^{2+}\}/\{Ca^{2+}\}$ relationship of Davis *et al.* (2000b) as our baseline assumption but including comparable model runs assuming an inhibitor-invariant y_0 (Section 3.4.4.2).

Comparable paired step velocity and y_0 measurements do not exist for Mn^{2+} inhibition of calcite growth. We thus must assume that the presence of Mn^{2+} influences y_0 solely through its influence on the solid solution supersaturation. This highlights the critical need to report and interpret measurements of step width in in-situ AFM studies in order to build predictive (ideally generalizable) models of y_0 as a function of solution chemistry. The lack of a comprehensive description of the sensitivity of step width to various solution parameters seriously hinders our ability to scale measured step velocities to bulk growth rates and compare data from in-situ AFM and bulk growth studies, let alone predictively

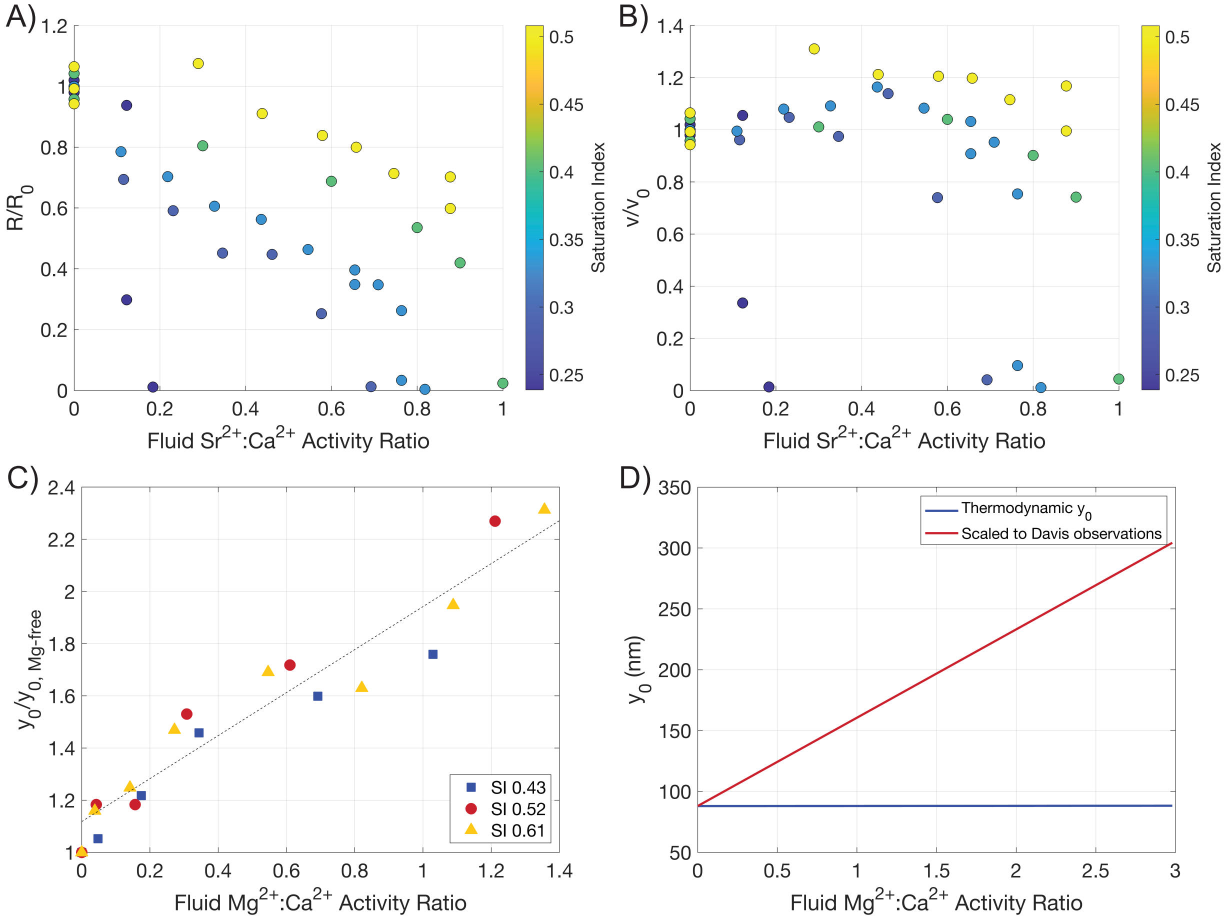

Figure 3.5 – Importance of considering y_0 sensitivity to inhibitor ions. Bulk growth rate (A) and step velocity (B) data for Sr^{2+} inhibition of calcite growth from Wasylenki *et al.* (2005a). C) Measured variation in y_0 with $\{Mg^{2+}\}/\{Ca^{2+}\}$ from Davis *et al.* (2000b). Dotted line is a linear regression through the SI = 0.61 data. D) Comparison of modeled y_0 for the solution conditions of the Mg^{2+} experiments, assuming either the thermodynamic representation of y_0 (blue) or scaling y_0 using the slope of the Davis *et al.* (2000b) y_0-$\{Mg^{2+}\}/\{Ca^{2+}\}$ relationship.

model mineral growth kinetics in natural solutions.

It should be emphasized that the rate dependence in Eq. 3.2.25 describes the growth of single spiral growth hillocks. Step nucleation and growth on the calcite surface can also occur on hillocks with more complicated morphologies as well as by 2D-nucleation (Teng *et al.*, 2000). There are thus significant open questions regarding the influence of growth *mechanism* on bulk growth behavior and inhibition in complex solutions. This is discussed briefly in Section 3.4.4.1, but elucidating the transition between spiral and 2D-nucleation driven growth as well as the solution chemistry dependence of nucleation frequency is left as a subject of future work.

3.2.6.4 Baseline model assumptions

Calcium and carbonate attachment/detachment coefficients fit to pH 8 data from Hong and Teng (2014) were used throughout the models presented here. Using coefficients fit to other step velocity datasets changes small details of the model fits (explored in Chapter 2) but does not change interpretations of inhibition mechanism. We do not differentiate between the acute and obtuse calcite steps here (Section 2.4.2.1) given our limited knowledge of preferential trace element partitioning as a function of solution chemistry and lack of step velocity data for calcite inhibition by Mn^{2+}. But this certainly represents a frontier worth pursuing in future investigations.

Following Nielsen *et al.* (2013), the Ca^{2+} and $CO_3{}^{2-}$ attachment coefficients (k_{Ca}, k_{CO3}) were scaled to match the magnitude of the inhibitor-free calcite growth rate measured here while maintaining a step edge free energy of 1.4 J/m^2(Teng *et al.*, 2000). As discussed in Section 2.4.3, a significantly lower step edge free energy was required to match the growth rate magnitude observed in the Ca^{2+}:$CO_3{}^{2-}$ study when using attachment/detachment coefficients fit to measured step velocity data. Scaling the step edge free energy and scaling the attachment coefficients yield nearly identical results. Finally, as discussed extensively in Chapter 2, the Nielsen et al. (2012, 2013) model formulation under-predicts Ca isotope fractionations at intermediate Ca^{2+}:$CO_3{}^{2-}$, including the Ca^{2+}:$CO_3{}^{2-}\sim$100 solutions studied here. Thus a slightly larger magnitude kinetic endmember fractionation is employed to bring the inhibitor-free $\Delta^{44/40}Ca$ in line with observations.

3.3 Results

Experimental solution conditions and results are summarized in Tables 3.1 and 3.2, respectively.

3.3.1 Crystal morphology in the presence of Mn and Mg

The Mn^{2+} calcite growth experiments yielded $(Mn,Ca)CO_3$ overgrowths with compositions ranging from 0-64 mol % $MnCO_3$ (Table 3.2). SEM images of these precipitates reveal irregular rhomobedra and changes in surface texturing with increasing solution and solid Mn/Ca (Figures 3.6, 3.7). The edges of the Mn-calcite rhombohedra begin to roughen in experiment Mn8 (fluid $\{Mn^{2+}\}\,/\,\{Ca^{2+}\} = 0.005$, 3% $MnCO_3$ - Figure 3.6 D, Figure 3.7B).

Exp.	Calcite			Steady-state concentration			Steady-state activity				$SI_{calcite}$	Titrant
	seed	$[Ca]_0$	$[Ca]_{end}$	$[Ca]$	$[Me]$	$Alkalinity$	$\{Ca^{2+}\}$	$\{Me^{2+}\}$	$\{Me^{2+}\} / \{Ca^{2+}\}$	$\{Ca^{2+}\} / \{CO3^{2-}\}$		$[Me]/[Ca]$
units	g	mM	mM	mM	mM	meq/L	mM	mM	-	--	-	-
Mn2	0.504	3.86	3.82	3.81	0.023	4.03	1.47	0.0072	0.0049	112.1	0.81	0.027
Mn3	0.502	3.86	3.53	3.63	0.039	4.06	1.40	0.012	0.0087	105.9	0.79	0.060
Mn5	1.001	3.85	3.70	3.73	0.201	4.02	1.42	0.062	0.044	109.9	0.79	0.67
Mn6	1.004	3.86	3.63	3.75	0.478	4.20	1.41	0.146	0.104	105.8	0.80	1.51
Mn7	1.001	3.84	3.67	3.76	0.097	4.08	1.43	0.030	0.021	108.8	0.80	0.23
Mn8	0.501	3.83	3.63	3.74	0.023	4.01	1.43	0.0072	0.0050	109.8	0.80	0.028
Mn9	0.500	3.82	3.62	3.66	0.0068	4.03	1.40	0.0022	0.0016	106.9	0.79	0.0074
Mn11	0.500	3.78	3.50	3.66	0	4.03	1.40	0	0	106.7	0.79	0
Mn12	0.502	3.79	3.60	3.68	0.008	4.05	1.40	0.0025	0.0018	106.9	0.79	0.0080
Mn13	1.001	3.77	3.69	3.72	0.567	4.23	1.39	0.172	0.124	104.1	0.80	1.73
Mg2	1.005	3.77	3.58	3.70	0.42	4.07	1.42	0.18	0.124	107.5	0.80	0.003
Mg3	1.001	3.79	3.62	3.70	4.22	4.10	1.43	1.78	1.243	110.1	0.80	0.026
Mg4	0.501	3.80	3.57	3.67	0.042	4.03	1.42	0.018	0.012	108.3	0.80	0.0004
Mg5	1.006	3.81	3.73	3.77	2.09	4.14	1.46	0.88	0.604	109.9	0.82	0.013
Mg7	1.007	3.82	3.63	3.75	8.90	4.31	1.47	3.81	2.589	110.1	0.82	0.064

Table 3.1 – Summary of experimental solution conditions.

Exp.	Growth					Distribution Coefficient				Solid Composition			
	rate	error	$\Delta^{44/40}Ca$	2σ error	$f_{OG}{}^{*}$	$K_D{}^{a}$	error	$K_D{}^{b}$	error	Mol % $MeCO_3{}^{a}$	error	Mol % $MeCO_3{}^{b}$	error
units	$mol/m^2/s$		‰										
Mn2	1.64E-06	1.37E-07			0.50	5.6	0.4	6.1	0.5	2.7	0.14	2.9	0.2
Mn3	1.40E-06	1.18E-07	-1.40	0.14	0.60	6.9	0.5	7.3	0.7	5.7	0.29	6.0	0.4
Mn5	1.94E-07	1.63E-08	-1.35	0.13	0.51	15.2	1.2	15.9	1.4	40.0	2.04	41.1	2.9
Mn6	2.53E-07	2.13E-08	-1.41	0.15	0.61	14.6	1.1	15.0	1.3	60.2	3.07	60.8	4.3
Mn7	4.25E-07	3.57E-08	-1.32	0.1	0.45	11.2	0.9	10.8	1.0	19.0	0.97	18.4	1.3
Mn8	2.01E-06	1.69E-07	-1.44	0.11	0.60	5.6	0.4	5.8	0.5	2.7	0.14	2.8	0.2
Mn9	2.80E-06	2.35E-07			0.60	4.8	0.4			0.74	0.04		
Mn11	2.92E-06	2.46E-07	-1.30	0.12	0.61	-	-	-	-	0.00	-	0.0	-
Mn12	2.70E-06	2.27E-07	-1.44	0.11	0.61	4.5	0.3	4.6	0.4	0.80	0.04	0.80	0.06
Mn13	3.38E-07	2.84E-08	-1.39	0.15	0.63	14.0	1.1	15.3	1.4	63.31	3.23	65.4	4.6
Mg2	2.67E-06	2.24E-07	-1.44	0.15	0.42	-	-	0.018	0.002	-	-	0.23	0.02
Mg3	8.74E-07	1.31E-07	-1.35	0.14	0.42	-	-	0.028	0.002	-	-	3.31	0.23
Mg4	2.77E-06	2.33E-07	-1.35	0.11	0.57	-	-	0.024	0.002	-	-	0.030	0.002
Mg5	1.89E-06	1.59E-07	-1.40	0.13	0.44	-	-	0.022	0.002	-	-	1.34	0.09
Mg7†	2.50E-07	2.10E-08	-1.35	0.14	0.42	-	-	0.032	0.003	-	-	7.6	0.3

Table 3.2 – Growth rate inhibition, Ca isotope fractionation ($\Delta^{44/40}Ca_{calcite-fluid}$), and partitioning results. *Fraction of the bulk solid represented by $(Me,Ca)CO_3$ overgrowth. [a]Mn partitioning calculated from the growth solution data exclusively (Eq. 3.2.8). [b]Mn partitioning calculated from the measured solid overgrowth composition (Section 3.2.4). †Aragonite is observed in the highest Mg experiment. See Section 3.3.2.2 for discussion of implications for the rate, partitioning, and isotope measurements.

At higher fluid $\{Mn^{2+}\}\,/\,\{Ca^{2+}\}$, two features emerge. First, jagged macro-steps appear, leading to an almost jigsaw puzzle effect of rough-edged lobes on the crystal face (Figure 3.7C). Then, the surface becomes textured by smaller, rounded domains and occasional, sub-μm elongate particles (Figure 3.7D-F). In interpreting these morphological differences, it is also important to recognize that the higher $\{Mn^{2+}\}\,/\,\{Ca^{2+}\}$ experiments were run for longer and to higher total titration volumes in order to achieve roughly the same turnover of the Ca reservoir for Ca isotope analysis. Thus more of the sample is composed of (Mn,Ca)CO_3 overgrowth in the higher Mn-content samples, though between 45-63% of the sample is overgrowth in all instances (Table 3.2).

In the sole in-situ AFM study of calcite growth in the presence of Mn^{2+}, Astilleros *et al.* (2002) observe similar changes in surface morphology with increasing solution Mn^{2+}. In the lowest Mn^{2+} concentration studied ($\{Mn^{2+}\} = 0.021$, roughly comparable to experiment Mn3 here, with $\{Mn^{2+}\} = 0.012$ and 6% $MnCO_3$), the initially straight calcite step edges become rounded and distorted, developing lobes during growth. At higher Mn ($\{Mn^{2+}\} = 0.096$), Astilleros *et al.* (2002) report a cessation of step advancement once the original calcite surface was fully coated and a transition to 2D nucleation-driven growth. In an in-situ scanning force microscopy study of calcite precipitation in the presence of PO_4^{3-}, Dove and Hochella (1993) observe a similar transition from straight to jagged, widely spaced steps in $10\mu M$ PO_4^{3-}, accompanied by the formation of rounded surface nuclei. The surface texturing observed here at fluid $\{Mn^{2+}\}\,/\,\{Ca^{2+}\}>0.02$ could thus be indicative of the formation of globular surface nuclei which grow by a 'birth and spread' mechanism but never fully coalesce to form a smooth surface.

Comparable surface texturing is not observed in the Mg^{2+} inhibition experiments (Figure 3.8) where far less Mg^{2+} was incorporated into the calcite lattice; overgrowth composition ranged from 0-7 mol % $MgCO_3$ (Table 3.2). Instead, the dominant morphological change with increasing fluid $\{Mg^{2+}\}\,/\,\{Ca^{2+}\}$ is the development of crystal faces not expressed in classical rhombohedral calcite (Figure 3.8C-F). As commonly observed for calcite grown in the presence of Mg^{2+}, the (110) and (100) calcite faces are progressively increasingly expressed over the (104) face with increasing fluid $\{Mg^{2+}\}\,/\,\{Ca^{2+}\}$ (Jiménez-López *et al.*, 2004; Zhang and Dawe, 2000; Davis *et al.*, 2004). Generally interpreted to represent selective interaction of Mg^{2+} with certain crystal faces (Folk, 1974; Zhang and Dawe, 2000), Davis *et al.* (2004) further interpreted the formation of such pseudo-facets in terms of preferential Mg incorporation into acute calcite steps (Paquette and Reeder, 1995; Wasylenki *et al.*, 2005b) and the accumulation of strain at the intersection of non-equivalent step types. In addition, aragonite needles are observed in the highest Mg experiment (Mg7, $\{Mg^{2+}\}\,/\,\{Ca^{2+}\}$=2.6, Figure 3.8F). A change in slope of the titration curve was observed after ~20 hours of growth (20 of 28mL titrated), likely indicative of aragonite nucleation late in the experiment. The implications of this aragonite formation for data interpretation are discussed in the following section.

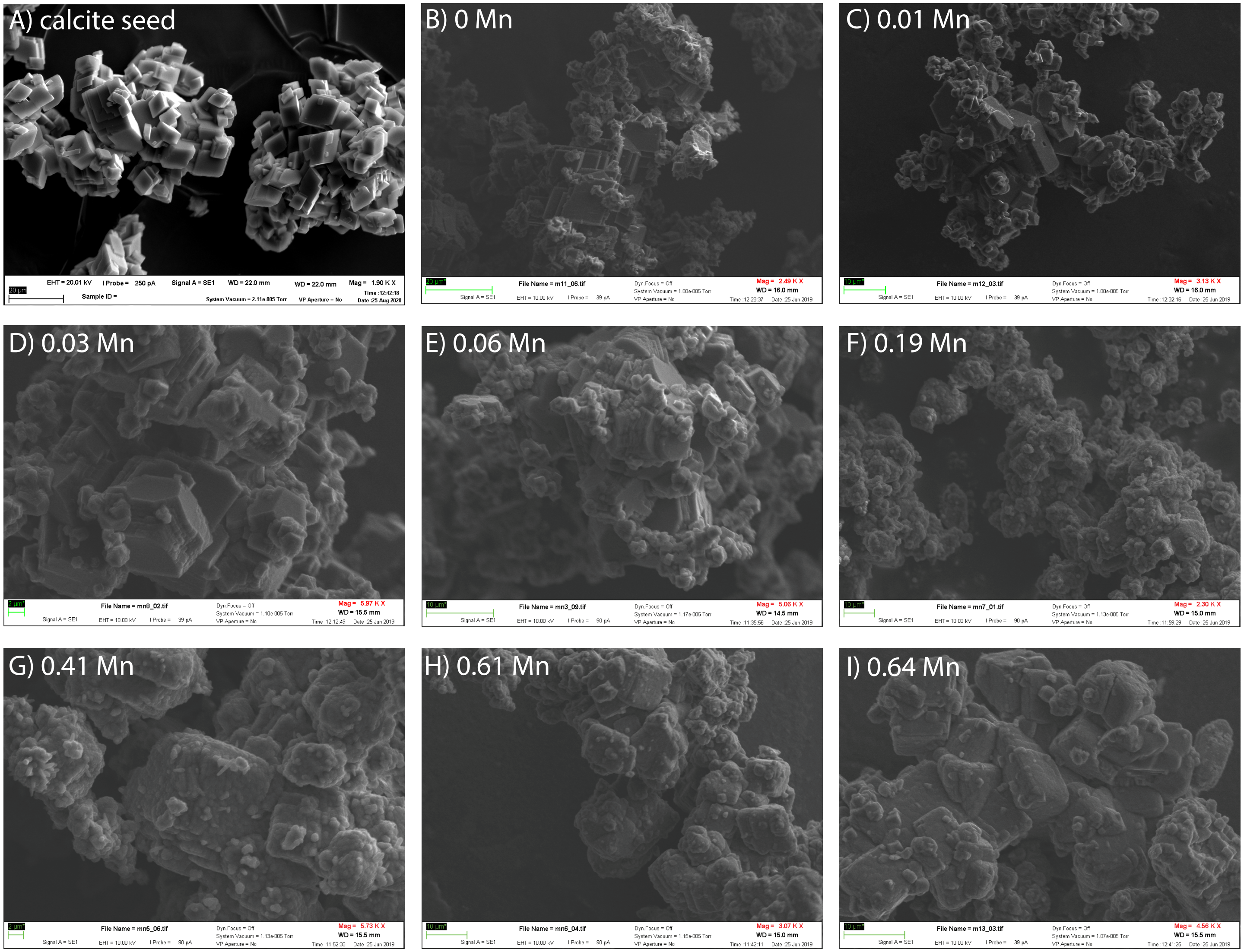

Figure 3.6 – Post-growth SEM images of precipitated solids from Mn^{2+} calcite inhibition experiments. Labeling denotes mole fraction $MnCO_3$ in the overgrowth. A) calcite seed, scale bar $= 20\mu m$; B) Mn11, scale bar $= 20\mu m$; C) Mn12, scale bar $= 10\mu m$; D) Mn8, scale bar $= 2\mu m$; E) Mn3, scale bar $= 10\mu m$; F) Mn7, scale bar $= 10\mu m$; G) Mn5, scale bar $= 2\mu m$; H) Mn6, scale bar $= 10\mu m$; I) Mn13, scale bar $= 10\mu m$.

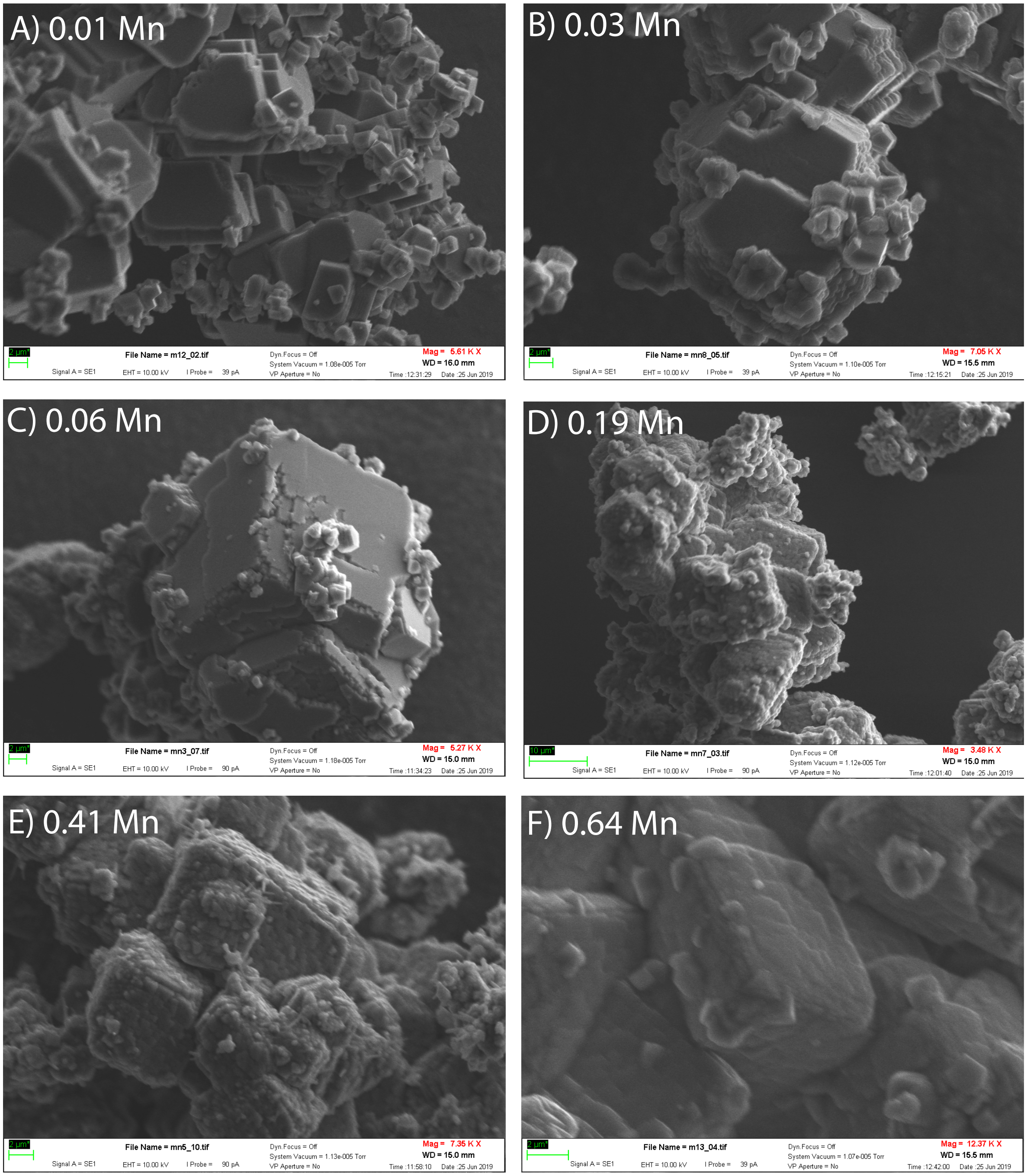

Figure 3.7 – High-magnification SEM images of growth features on precipitated (Mn,Ca)CO_3. Labeling denotes mole fraction $MnCO_3$ in the overgrowth. A) Mn12, scale bar $= 2\mu m$; B) Mn8, scale bar $= 2\mu m$; C) Mn3, scale bar $= 2\mu m$; D) Mn7, scale bar $= 10\mu m$; E) Mn5, scale bar $= 2\mu m$; F) Mn13, scale bar $= 2\mu m$.

A) Calcite seed

B) Mg/Ca = 0.012

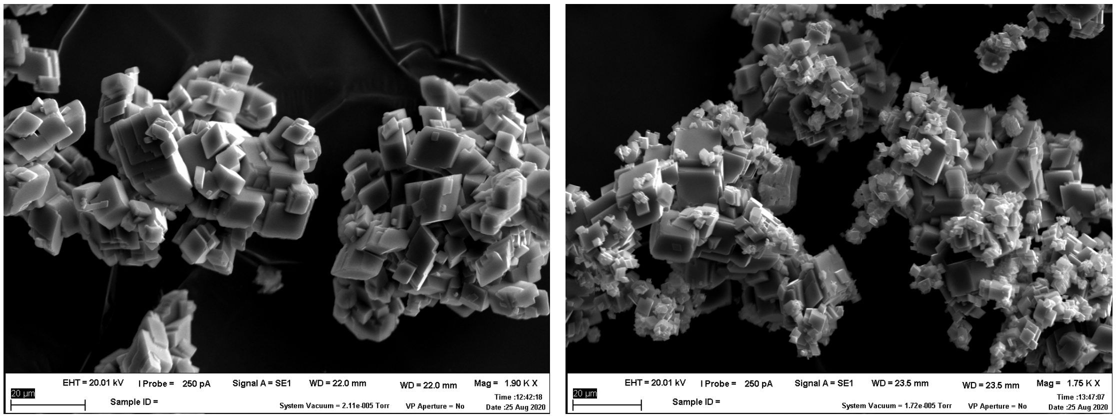

C) Mg/Ca = 0.12

D) Mg/Ca = 0.6

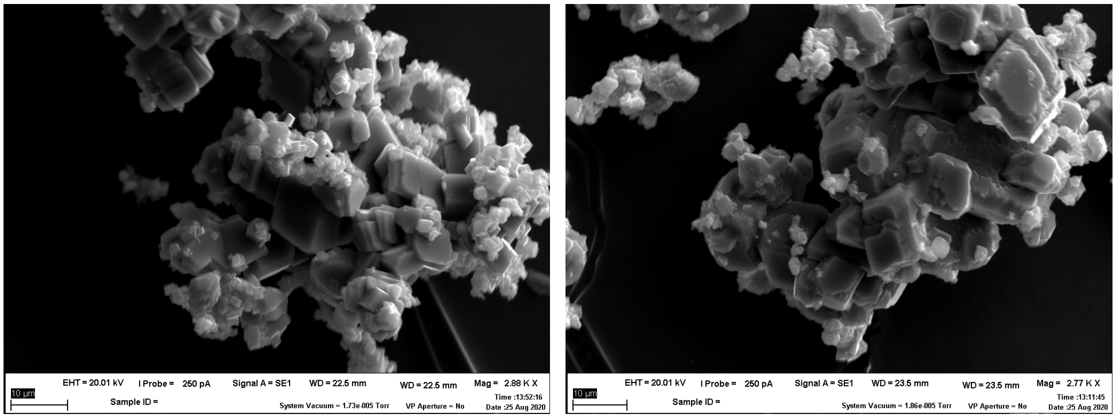

E) Mg/Ca = 1.2

F) Mg/Ca = 2.6

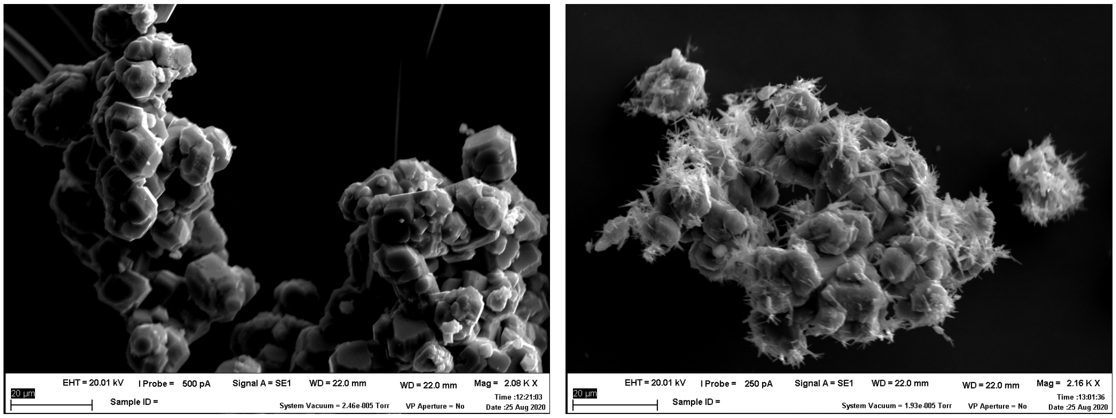

Figure 3.8 – Post-growth SEM images of precipitated solids from Mg^{2+} calcite inhibition experiments. Labeling denotes solution $\left\{Mg^{2+}\right\} / \left\{Ca^{2+}\right\}$. A) calcite seed material, scale bar $= 20\mu m$; B) Mg4, scale bar $= 20\mu m$; C) Mg2, scale bar $= 10\mu m$; D) Mg5, scale bar $= 10\mu m$; E) Mg3, scale bar $= 20\mu m$; F) Mg7, scale bar $= 20\mu m$.

3.3.2 XRD: precipitation of $(Mn,Ca)CO_3$ and $(Mg,Ca)CO_3$ solid-solution series

3.3.2.1 $(Ca,Mn)CO_3$ series powder XRD results

Powder XRD results for the Mn^{2+} inhibition experiments are shown in Figure 3.9. The calcite seed material produces pure-calcite peaks in all diffractograms. For overgrowths containing >6% $MnCO_3$, separated $(Mn,Ca)CO_3$ peaks shifted to higher 2θ are present, reflecting the decrease in d-spacing with substitution of the smaller Mn^{2+} ion. The progressive shift in the rhombohedral carbonate 104 peak between calcite and rhodochrosite endmembers is highlighted in Figure 3.9B and quantified in Figure 3.10B. As the Mn content of the overgrowth increases, the 2θ of the 104 peak increases linearly but no separate rhodochrosite phase is detected. Observed shifts in the overgrowth 104 and 110 d-spacing (Figure 3.10A,B) were used to calculate the a and c hexagonal unit cell parameters for the $(Mn,Ca)CO_3$ solid solutions precipitated (Figure 3.10C,D). The changes in unit cell parameters with solid Mn content observed here are in excellent agreement with the lattice parameter-Mn content relationships reported in previous calorimetric studies (Katsikopoulos *et al.* 2009; Capobianco and Navrotsky 1987, Figure 3.10C,D). The linear decline in unit cell length with increasing Mn content (Vegard's law) and close agreement between the solid composition derived from chemical analysis and changes in lattice parameters observed in other studies where the Mn-calcites were synthesized through different methods (including high-temperature recrystallization (Capobianco and Navrotsky, 1987)) suggest that dominantly homogeneous calcite-rhodochrosite solid solutions were precipitated in this study. Notably, the $(Mn,Ca)CO_3$ overgrowth peaks do exhibit some level of peak broadening (Figure 3.9). The full width half max (FWHM) of the pure calcite 104 peak is ~0.14° while comparable peaks for the well-separated $(Mn,Ca)CO_3$ overgrowth solid solutions exhibit FWHMs between 0.2-0.28°. This peak broadening could represent a degree of spatial heterogeneity or ordering in the lattice, but may also arise due to lattice strain effects or changes in crystallite size (Mittemeijer and Welzel, 2008). The high-Mn experiments were run for a longer duration to achieve the same turnover of the Ca reservoir for Ca isotope analysis (Section 3.2.5), likely resulting in more nucleation of small $(Mn,Ca)CO_3$ particles. The surface texturing observed in the higher Mn content samples ($\geq$19% $MnCO_3$, Figure 3.7) could also represent small crystallite domains. Higher resolution spatial analysis (e.g. HR-TEM) could help determine the cause and implications of the observed peak broadening.

3.3.2.2 $(Ca,Mg)CO_3$ series powder XRD results

Powder XRD results for the Mg^{2+} inhibition experiments are shown in Figure 3.11. For experiments Mg2-Mg5, the Mg content of the overgrowth was too low (mol % Mg $\leq$ 3.3) to detect separated $(Mg,Ca)CO_3$ peaks (3.11A). The magnesian-calcite overgrowth is visible in the diffractogram for the highest Mg experiment (Mg7, $\{Mg^{2+}\} / \{Ca^{2+}\} = 2.6$) as separated peaks shifted to higher 2θ, in addition a clear aragonite phase (3.11B,C). As discussed in Section 3.3.1, a change in slope of the titration curve after ~20 hours of growth and SEM evidence of aragonite needles formed on the exterior of clusters of Mg-calcite crystals point towards aragonite nucleation later in the experiment. Both Reitveld refinement and Reference Intensity Ratio (RIR) phase quantification indicate that approximately 19% of

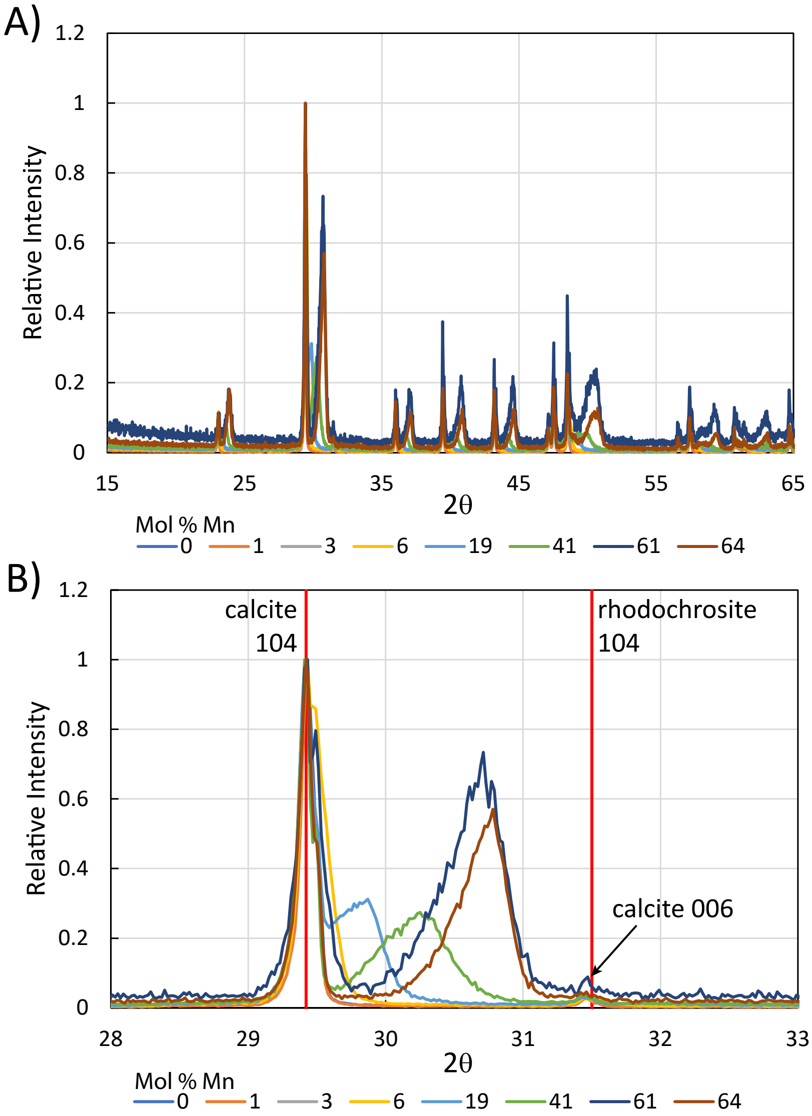

Figure 3.9 – Powder XRD results for Mn^{2+} calcite growth experiments (λ=1.5418Å, Cu K_α). A) Diffractograms of precipitated solids, normalized by the maximum intensity. B) Diffractograms zoomed in on the calcite 104 peak, highlighting the shift to higher 2θ with increasing mole % Mn in the overgrowth.

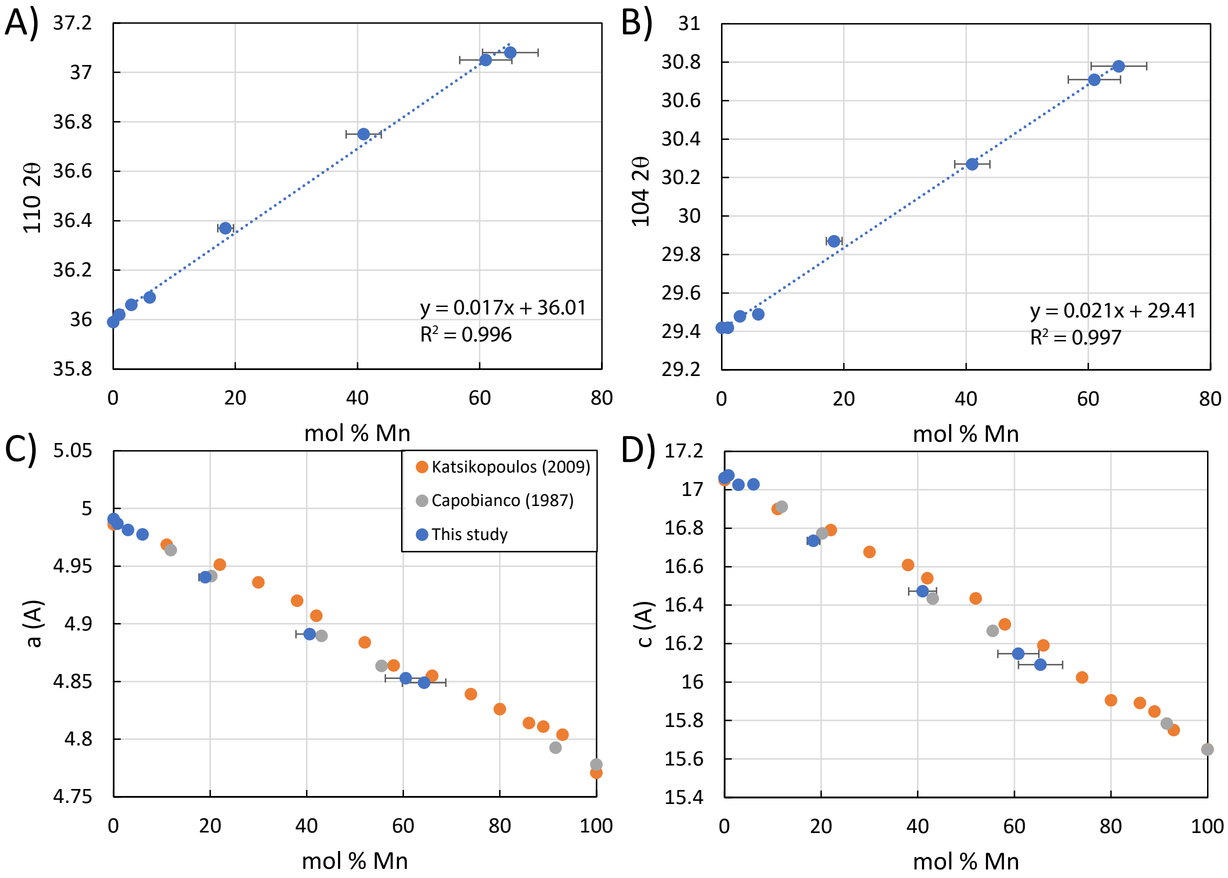

Figure 3.10 – Changes in calcite lattice parameters with Mn content. A) Linear shift in overgrowth 110 peak 2θ with increasing mol % Mn (solid composition from ICP analysis). B) Linear shift in overgrowth 104 peak 2θ. C) Variation in the calculated a hexagonal lattice parameter (Å) with increasing mol % Mn from this study (blue) and that reported by Katsikopoulos *et al.* (2009) (orange) and Capobianco and Navrotsky (1987) (grey). D) Variation in the calculated c hexagonal lattice parameter (Å) with increasing mol % Mn.

the bulk solid is aragonite, equivalent to 38% of the overgrowth. We thus do not use bulk chemical analysis as the primary constraint on the Mg content of the calcite overgrowth for experiment Mg7. Instead, the composition is calculated from the d-spacing of the magnesian calcite 104 and 110 peaks, employing the lattice parameter - Mg content relationships for inorganic calcite developed by Bischoff *et al.* (1983):

$$a = 4.9906 - 0.50x + 0.56x^2 \tag{3.3.1}$$

$$c = 17.069 - 2.27x + 2.1x^2 \tag{3.3.2}$$

$$c/a = 3.420 - 0.118x + 0.05x^2 \tag{3.3.3}$$

where x is the mole fraction $MgCO_3$. The average x derived from the a, c, and c/a relationships yields a mole fraction $MgCO_3$ of 0.076±0.003, thereby providing an estimate of Mg partitioning independent of the nucleated aragonite. We also include and interpret the growth rate calculated for Mg7 as the rate is calculated in the beginning stages of the experiment (5-10mL titrated, Section 3.2.3), before the titration data indicate probable aragonite nucleation. The presence of aragonite has the most significant impact on our interpretation of the calcium isotope fractionation results. We calculate $\Delta^{44/40}Ca_{calcite-fluid}$ assuming a constant fractionation throughout the course of an experiment (Section 3.2.5), yielding an integrated fractionation representative of the Ca isotope discrimination during both the aragonite and magnesian calcite precipitation. Larger magnitude Ca isotope fractionations are often observed during aragonite precipitation than calcite precipitation at a given temperature, particularly for biomineralized carbonates (Gussone *et al.*, 2005; Blättler *et al.*, 2012), but recent inorganic precipitation experiments reported largely indistinguishable $\Delta^{44/40}Ca_{calcite-fluid}$ and $\Delta^{44/40}Ca_{aragonite-fluid}$ (though the aragonite was generally grown at a slower rate, AlKhatib and Eisenhauer (2017a)). The Ca isotope fractionate-rate trend observed in the inorganic aragonite growth experiments of Gussone *et al.* (2003) also overlaps with that observed in the inorganic calcite growth experiments of Tang *et al.* (2008) and Mills *et al.* (2021) for rates in the ~10^{-6}-10^{-7}mol/m^2/s regime (Fantle and Tipper, 2014). It is thus not clear whether the nucleated aragonite would be expected to exhibit a measurably different Ca isotope fractionation than the magnesian calcite of interest here, so the Mg7 calcium isotope data is interpreted with caution (Section 3.3.5).

3.3.3 Growth rate inhibition

Both Mn^{2+} and Mg^{2+} strongly inhibit calcite growth (Figure 3.12). In the Mn experiments, log-linear rate inhibition is observed at low fluid Mn^{2+} concentrations; growth rates decline by almost an order of magnitude by $\{Mn^{2+}\} / \{Ca^{2+}\} = 0.02$ (Figure 3.12A). With increasing solution Mn^{2+}, the extent of inhibition begins to asymptote and eventually reverses. For $\{Mn^{2+}\} / \{Ca^{2+}\} > 0.1$, faster growth rates are observed with increasing solution Mn^{2+}. This growth rate inversion occurs when the Mn content of the precipitating solid surpasses approximately 50 mole %, transitioning into the regime of Ca-rich rhodochrosite solid solutions (Figure 3.12C). Log-linear rate inhibition is also observed in the presence of Mg^{2+}

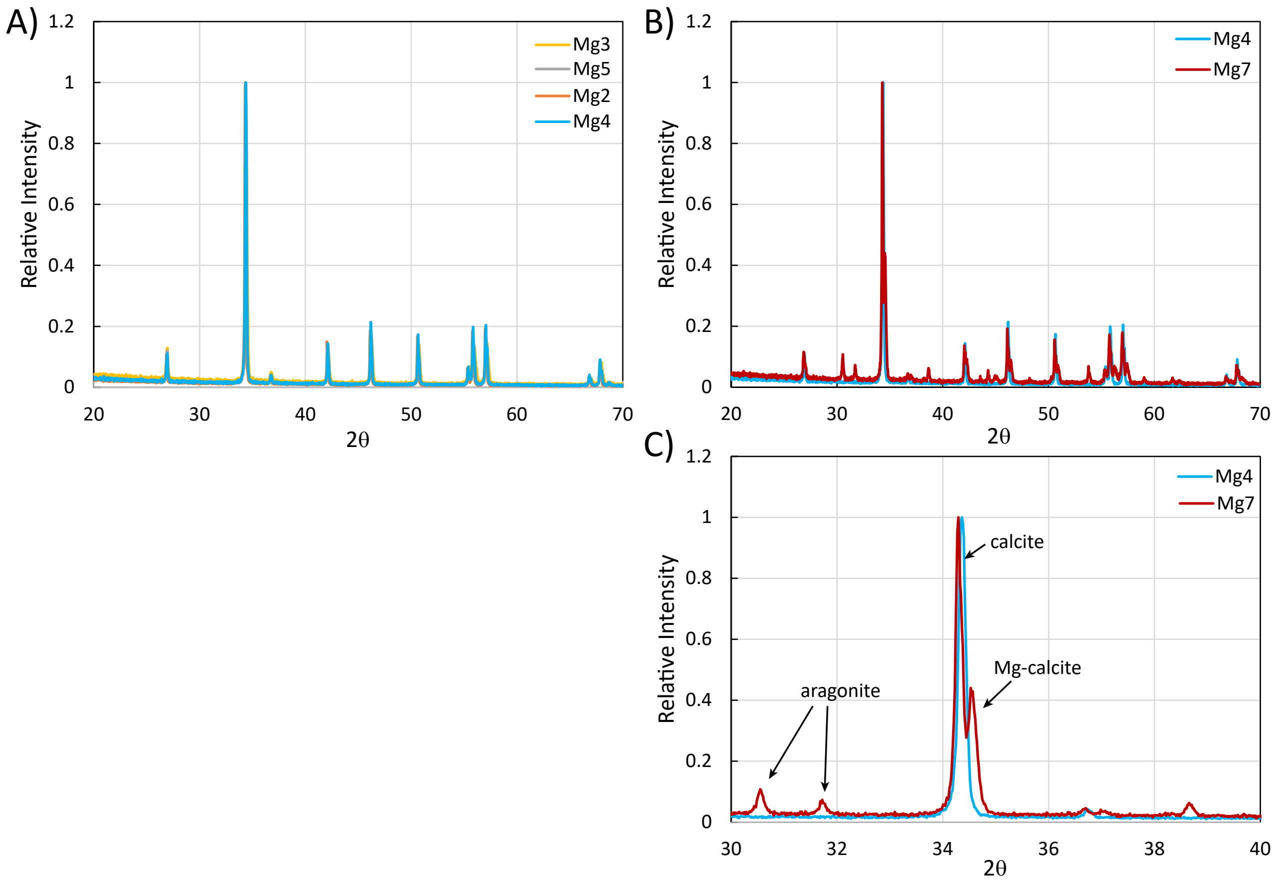

Figure 3.11 – Powder XRD results for Mg^{2+} calcite growth experiments (λ=1.79Å, Co K_α). A) Diffractograms of precipitated solids, normalized by the maximum intensity, for experiments Mg2-Mg5. B) Diffractograms of precipitated solids from Mg4 ($\{Mg^{2+}\}\,/\,\{Ca^{2+}\}$=0.01) and Mg7 ($\{Mg^{2+}\}\,/\,\{Ca^{2+}\}$=2.6). C) Diffractograms in B, zoomed to 2θ=30-40°, showing both the presence of aragonite and a distinct Mg-calcite phase in the overgrowth of experiment Mg7.

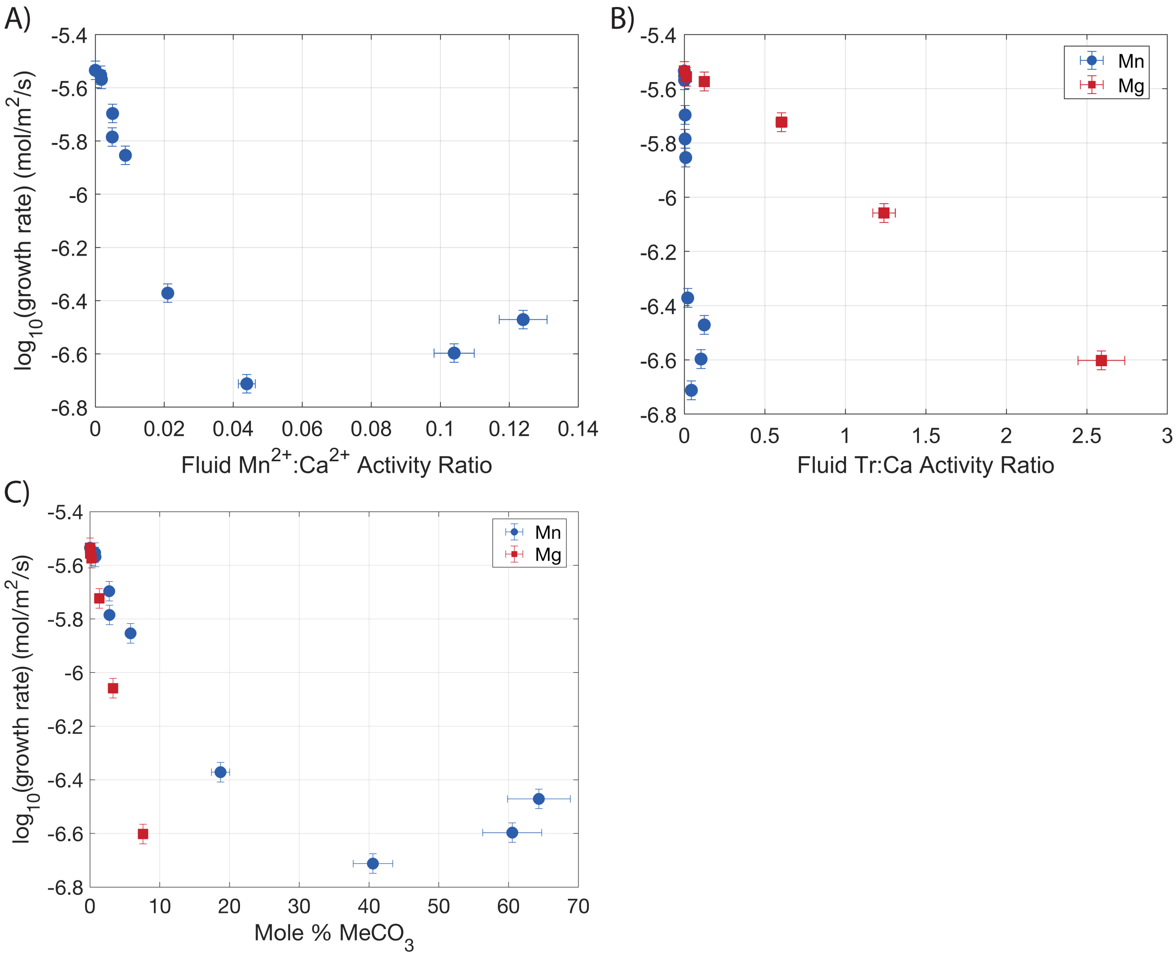

Figure 3.12 – Calcite growth rate inhibition by Mn^{2+}and Mg^{2+}. A) Surface-normal growth rate as a function of solution $\{Mn^{2+}\}/\{Ca^{2+}\}$. B) Data from A (blue circles) plotted alongside comparable growth rate data for Mg^{2+} (red squares). C) Surface-normal growth rates as a function of (Me,Ca)CO$_3$ solid composition.

but 100x higher inhibitor concentrations are required to achieve the same level of inhibition (Figure 3.12B). Thus for the solution chemistries studied here, Mn^{2+} is a far stronger inhibitor of calcite growth than Mg^{2+} when viewed through the lens of solution composition. However, when considering the amount of inhibitor ion incorporated into the lattice, Mg^{2+} exhibits higher levels of rate inhibition per mole incorporated (Figure 3.12C).

3.3.3.1 Initially slow growth rate observed in high-Mn solutions

Another notable pattern emerged in the initial growth rates for the Mn^{2+} experiments. While the growth rate data in Figure 3.12 reflect steady-state growth rates, in high-Mn solutions, the steady-state growth rate was not reached immediately. Instead, initial growth rates were markedly slower than the eventual steady-state growth rate and evolved to that rate over the first 0-1mL titrated (Figure 3.13). Moreover, the magnitude of the apparent additional inhibition at the start of the experiment scaled with Mn concentration: higher

$\{Mn^{2+}\}\,/\,\{Ca^{2+}\}$ experiments exhibited slower rates at the onset of the experiment (0-1mL titrated) relative to their steady-state growth rate. This is quantified in Figure 3.13A, where a roughly linear increase in the ratio of the growth rate calculated from 1-2mL titrated to the rate calculated from 0-1mL titrated is observed with increasing solution $\{Mn^{2+}\}\,/\,\{Ca^{2+}\}$. While a near-constant titration rate over the first few mL titrated is observed for experiments with $\{Mn^{2+}\}\,/\,\{Ca^{2+}\}$ $\leq$0.009 (equivalently solid $MnCO_3$ $\leq$6%), the rate observed at the onset of experiments with $\{Mn^{2+}\}\,/\,\{Ca^{2+}\}$ $\geq$0.04 is progressively slower than the rate achieved later in the experiment. The one outlier that deviates from this trend is experiment Mn7 (hollow circle, Figure 3.13A) where the rate calculated from 1-2mL titrated was slower than that at the onset of the experiment because the solution Mn^{2+} concentration increased by 10% over the first 2mL titrated, slowing the growth rate.

This phenomenon of slow initial rates at high-Mn is exemplified by comparing the titration curve for experiment Mn8 ($\{Mn^{2+}\}\,/\,\{Ca^{2+}\} = 0.005$) to that of experiment Mn13 ($\{Mn^{2+}\}\,/\,\{Ca^{2+}\} = 0.12$) (Figure 3.12B). As seen in the titration data for experiment Mn13, the sluggish initial rate is accompanied by an apparent induction period, where no measurable growth occurs following the addition of seed crystal for a period of 10's of minutes. Notably, these slow initial rates are observed for experiments where post-growth SEM images reveal a surface texturing reminiscent of rounded surface nuclei (Figure 3.7C-E). This is potentially consistent with the in-situ AFM observations of Astilleros *et al.* (2002) who report a complete cessation of step advancement once the original calcite surface has been coated by a monolayer of $(Mn,Ca)CO_3$ in high-Mn solutions and a transition to 2D-nucleation driven growth. Higgins and Hu (2005) observe a similar phenomenon for Mg-calcite growth on dolomite surfaces, and attribute slow growth rates in the *second* monolayer deposited to the formation of a highly strained initial monolayer. The induction time and initial slow growth rates observed here could thus represent impaired growth kinetics as 2D surface nuclei must form on a strained epitaxial layer of high-Mn solid solutions deposited on the pure calcite seed surface.

3.3.4 Trace element partitioning

Mn^{2+} inhibition of calcite growth is accompanied by a strong, kinetically controlled, concentration of Mn in the calcite lattice (Figure 3.14A,B). Large positive partition coefficients (K_{Mn} = 4-16) are observed at low solution $\{Mn^{2+}\}\,/\,\{Ca^{2+}\}$, and K_{Mn} increases with increasing Mn^{2+} until $\{Mn^{2+}\}\,/\,\{Ca^{2+}\} = 0.044$ (Figure 3.14A). Following the growth rate inversion observed when the precipitating solid solution exceeds 50 mole % $MnCO_3$ (Figure 3.12C), K_{Mn} ceases to rise with increasing solution Mn^{2+}, instead plateauing and even slightly declining to a value of ~15. This yields a strong log-linear inverse correlation between K_{Mn} and growth rate, with the largest partition coefficients observed in the slowest growing, most highly inhibited, experiments (Figure 3.14B). In contrast, the highly incompatible Mg^{2+} exhibits partition coefficients on the order of 0.02-0.03 (Figure 3.14C,D). The data do not support an exceptionally strong dependence of partitioning on $\{Mg^{2+}\}\,/\,\{Ca^{2+}\}$ and thus growth rate for the solution conditions studied here; while K_{Mg} tends to increase with increasing $\{Mg^{2+}\}\,/\,\{Ca^{2+}\}$, most of the variability falls within the measurement error.

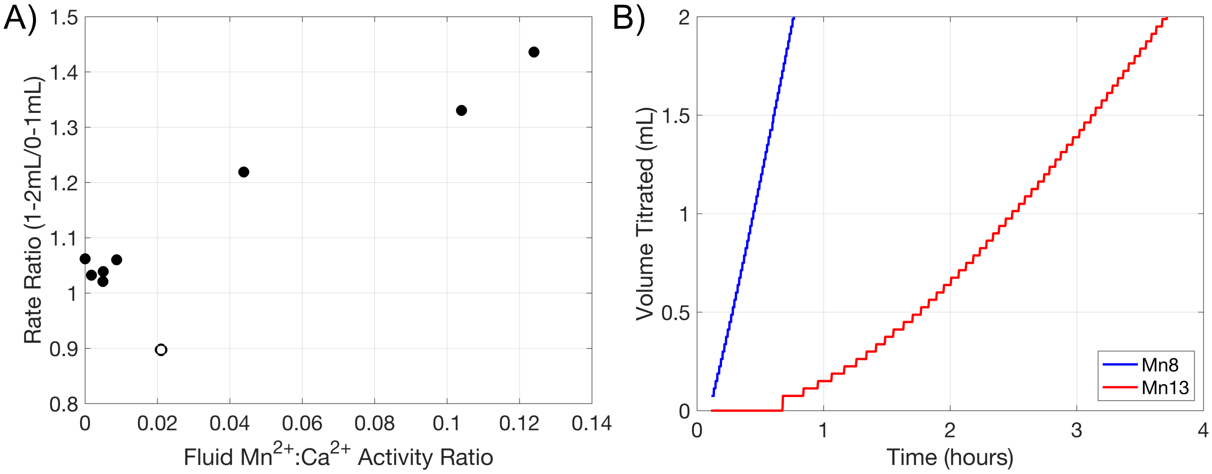

Figure 3.13 – Evolution in initial growth rate observed for high-Mn experiments. A) Ratio of growth rate calculated from 1-2mL titrated to the rate calculated from 0-1mL titrated as a function of solution $\{Mn^{2+}\}/\{Ca^{2+}\}$. The hollow circle is experiment Mn7, where solution Mn^{2+} concentration increased 10% over the first 2mL titrated (yielding a slower rate from 1-2mL). B) Titration curves for experiments Mn8 ($\{Mn^{2+}\}/\{Ca^{2+}\} = 0.005$, blue line) and Mn13 ($\{Mn^{2+}\}/\{Ca^{2+}\} = 0.124$, red line) highlighting the slow initial growth rate observed in high-Mn solutions.

3.3.5 Ca isotope fractionation

Calcium isotope fractionation is found to be largely invariant across all solution conditions examined here (Figure 3.15). In the presence of either Mn^{2+} or Mg^{2+}, large magnitude calcium isotope fractionations ($\Delta^{44/40}Ca_{calcite-fluid}$ = -1.3 to -1.44) are maintained, independent of $\{Me^{2+}\}/\{Ca^{2+}\}$ and associated kinetic inhibition. For both Mn^{2+} or Mg^{2+}, slightly larger magnitude fractionations are observed at low $\{Me^{2+}\}/\{Ca^{2+}\}$ (more specifically, low levels of rate inhibition, Figure 3.19) than inhibitor-free solutions and $\Delta^{44/40}Ca$ trends back towards the pure-calcite endmember with increasing $\{Me^{2+}\}/\{Ca^{2+}\}$. Although the difference between measurements falls within analytical error, a decrease in $\Delta^{44/40}Ca$ at low levels of inhibition could be driven by changes in hillock morphology due to preferential interaction of Mn^{2+} or Mg^{2+} with the acute calcite step. In-situ AFM observations have documented immediate roughening of the acute step at low Mg^{2+} while the obtuse step does not roughen until higher $\{Mg^{2+}\}/\{Ca^{2+}\}$ (Davis *et al.*, 2004). As explored in Chapter 2, a decline in the relative contribution of the acute step to the total expressed fractionation would likely yield larger magnitude $\Delta^{44/40}Ca$ as the acute step is predicted to exhibit smaller magnitude Ca isotope fractionations than the obtuse step under comparable solution conditions (Mills *et al.*, 2021).

Interestingly, nearly identical $\Delta^{44/40}Ca$ is observed in experiment Mg7, despite the precipitation of aragonite (Figure 3.15B, red asterisk). As discussed in Section 3.3.2.2, up to 40% of the precipitated solid may be aragonite, which is generally thought to exhibit larger magnitude Ca isotope fractionations. The comparable $\Delta^{44/40}Ca$ observed here suggests either that aragonite and Mg-calcite fractionate Ca isotopes similarly under these solution conditions (as discussed above (AlKhatib and Eisenhauer, 2017a; Fantle and Tipper, 2014))

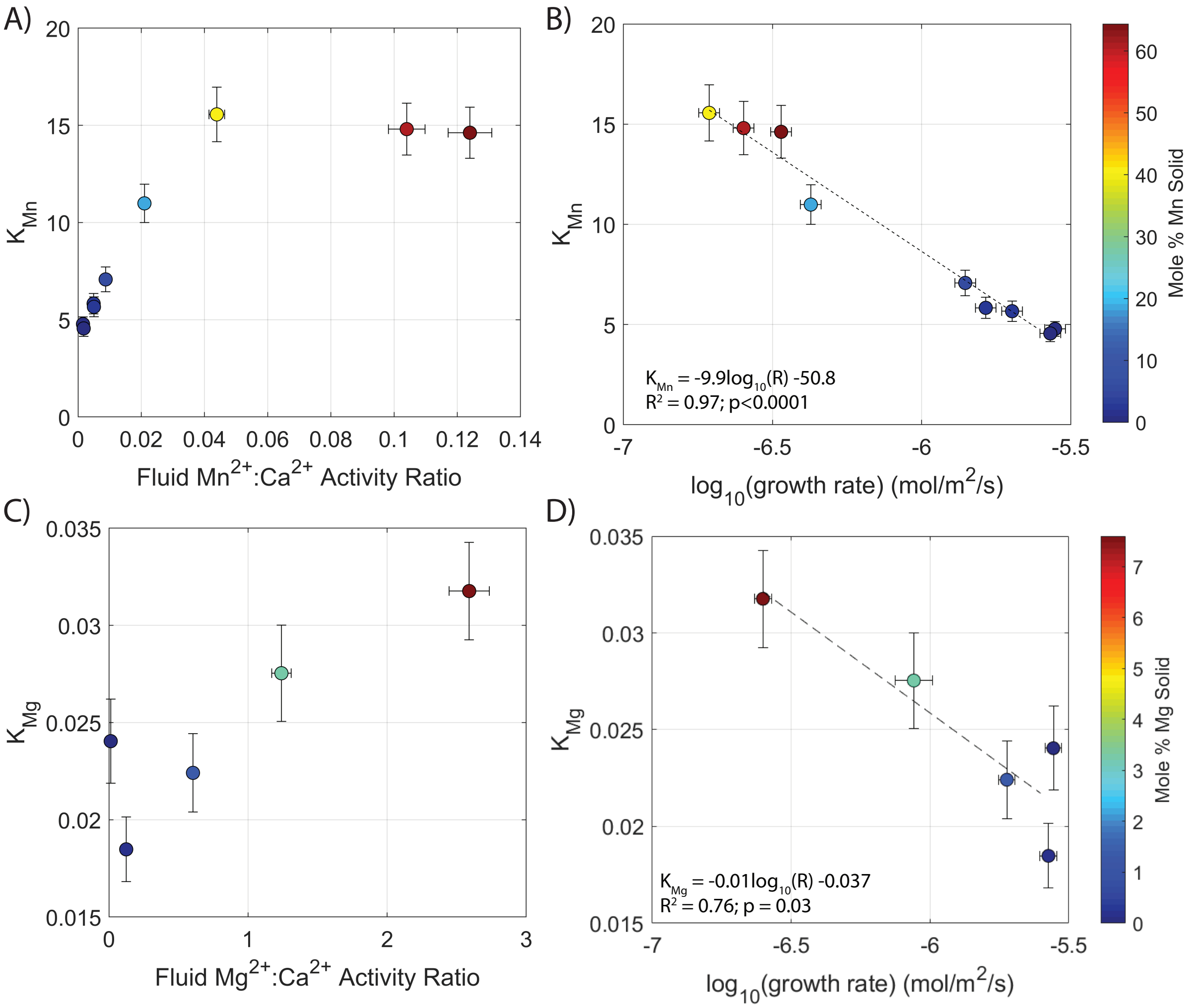

Figure 3.14 – Mn^{2+} and Mg^{2+} partition coefficients as a function of solution $\{Me^{2+}\}/\{Ca^{2+}\}$ (A,C) and growth rate (B,D).

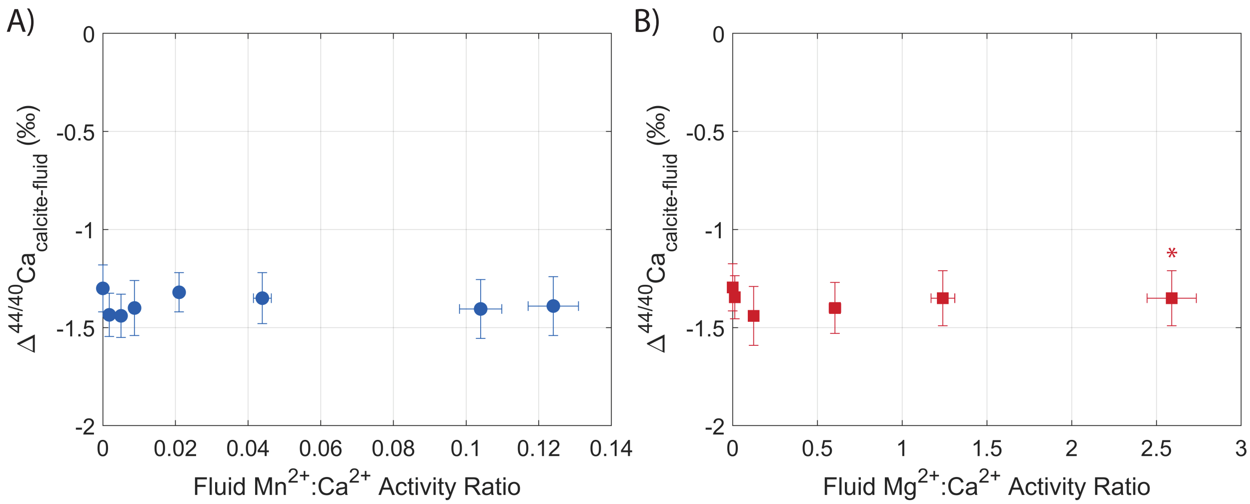

Figure 3.15 – Calcium isotope fractionation during Mn^{2+} and Mg^{2+} inhibition of calcite growth. Note, experiment Mg7 ($\{Me^{2+}\}/\{Ca^{2+}\} = 2.6$, red asterisk) contains aragonite as well as Mg-calcite in the overgrowth. See main text for discussion of implications for interpretation.

or that a larger magnitude aragonite fractionation could obscure a somewhat smaller magnitude $\Delta^{44/40}Ca_{calcite-fluid}$. The measured fractionation for Mg7 is thus considered a maximum estimate, but in the absence of unequivocal evidence to the contrary, we continue under the assumption that $\Delta^{44/40}Ca_{calcite-fluid}$ is independent of $\{Mg^{2+}\}/\{Ca^{2+}\}$.

3.4 Discussion

3.4.1 Mn and Mg kinetic data

Both Mn^{2+} and Mg^{2+} exhibit log-linear rate inhibition of calcite growth at low $\{Me^{2+}\}/\{Ca^{2+}\}$, with 100x stronger inhibition by Mn^{2+} when viewed through the lens of fluid inhibitor concentration. Importantly, at higher Mn^{2+} concentrations, the inhibition begins to plateau and growth rates eventually begin to increase with added Mn^{2+} while Mg^{2+} maintains a log-linear inhibition trend to high $\{Mg^{2+}\}/\{Ca^{2+}\}$. This is consistent with previous observations; Davis *et al.* (2000a) observe a log-linear decline in step velocities and bulk growth rate up to a $\{Mg^{2+}\}/\{Ca^{2+}\}$ of 2 and Astilleros *et al.* (2010) report continued inhibition up to $\{Mg^{2+}\}/\{Ca^{2+}\} = 5$.

The inhibition observed here can be directly compared to kinetic data from previous studies by examining how the extent of inhibition (${}^{(R_0-R)}/{}_{R_0}$, where R_0 is the pure calcite growth rate under comparable solution conditions) varies as a function of solution chemistry. Figure 3.16A and C compare the extent of calcite growth inhibition as a function of $\{Me^{2+}\}/\{Ca^{2+}\}$ for Mn^{2+} and Mg^{2+}, respectively, for bulk growth studies run at similar supersaturation with respect to calcite. The inhibition behavior documented here is in very good agreement with previous findings, despite other differences in solution chemistry. In particular, the extensive experiments of Dromgoole and Walter (1990a) confirm that calcite growth is highly inhibited at very low solution Mn^{2+} ($\{Mn^{2+}\} / \{Ca^{2+}\}$ <0.02) but that inhibition begins to plateau at higher $\{Mn^{2+}\} / \{Ca^{2+}\}$ (Figure 3.16A). Similarly for Mg^{2+}, the inhibition behavior observed here falls between the data of Lin and Singer (2009) and Nielsen *et al.* (2016), performed at lower and higher supersaturations, respectively (Figure 3.16C).

This in turn highlights another trend not evident from this study alone: both Mn^{2+} and Mg^{2+} inhibition of calcite growth is supersaturation dependent (Figure 3.16B,D). Comparing inhibition data both within single studies (Dromgoole and Walter (1990a) for Mn^{2+} and Davis *et al.* (2000a) for Mg^{2+}) and across studies demonstrates that lower supersaturation solutions exhibit a higher extent of inhibition for a given $\{Me^{2+}\} / \{Ca^{2+}\}$, a trend that has been documented by numerous other studies (Dromgoole and Walter, 1990a; Mucci and Morse, 1983; Davis *et al.*, 2000b). This supersaturation sensitivity is particularly strong at low $\{Mn^{2+}\} / \{Ca^{2+}\}$ during the log-linear inhibition phase (Figure 3.16B). That said, the magnitude of the supersaturation dependence is considerably lower for Mn^{2+} and Mg^{2+} than for Sr^{2+} (Wasylenki *et al.* (2005a), Figure 3.16E), interpreted to inhibit calcite growth through a dominantly solid solution thermodynamic effect by Nielsen *et al.* (2013). This observed supersaturation dependence thus represents a testable prediction for ground-truthing mechanistic interpretations in the ion-by-ion framework (Section 3.4.4).

3.4.2 Mn and Mg incorporation dynamics

3.4.2.1 Mn partitioning

The Mn^{2+} partitioning trend observed here demonstrates a strong inverse relationship between K_{Mn} and growth rate. K_{Mn} increases with increasing $\{Mn^{2+}\} / \{Ca^{2+}\}$ during the log-linear inhibition phase, then plateaus and even declines, mirroring the plateau in rate inhibition and growth rate inversion observed. This log-linear inverse dependence between K_{Mn} and growth rate holds over a wide range of solution conditions. Figure 3.17 shows the partitioning data from this study, plotted alongside data from Dromgoole and Walter (1990a) and Lorens (1981); solution conditions for the three studies are summarized in Table 3.3. The comprehensive suite of experiments of Dromgoole and Walter (1990a) targeted a similar range in $\{Mn^{2+}\} / \{Ca^{2+}\}$ to that investigated in this study, but were run at a significantly lower pH and thus high $\{Ca^{2+}\} / \{CO_3^{2-}\}$. In contrast, Lorens (1981) investigated Mn^{2+} partitioning using radioactive ^{54}Mn, thereby accessing orders of magnitude lower $\{Mn^{2+}\} / \{Ca^{2+}\}$ than traditional bulk-growth studies (Table 3.3). Despite these differences, all of the partitioning data falls along the same log-linear rate trend (Figure 3.17).

This is consistent with the surface kinetic model developed by DePaolo (2011), where trace element partitioning (like stable isotope fractionation) varies between kinetic and equilibrium endmembers, dictated by the amount of exchange occurring at the surface:

$$K_{Me} = \frac{K_f}{1 + \frac{R^b}{R^f}\left(\frac{K_f}{K_{eq}} - 1\right)} \tag{3.4.1}$$

where K_f is the forward kinetic fractionation factor for Me/Ca in the forward precipitation reaction; K_f is the equilibrium partition coefficient; and R^b, R^f are the back and

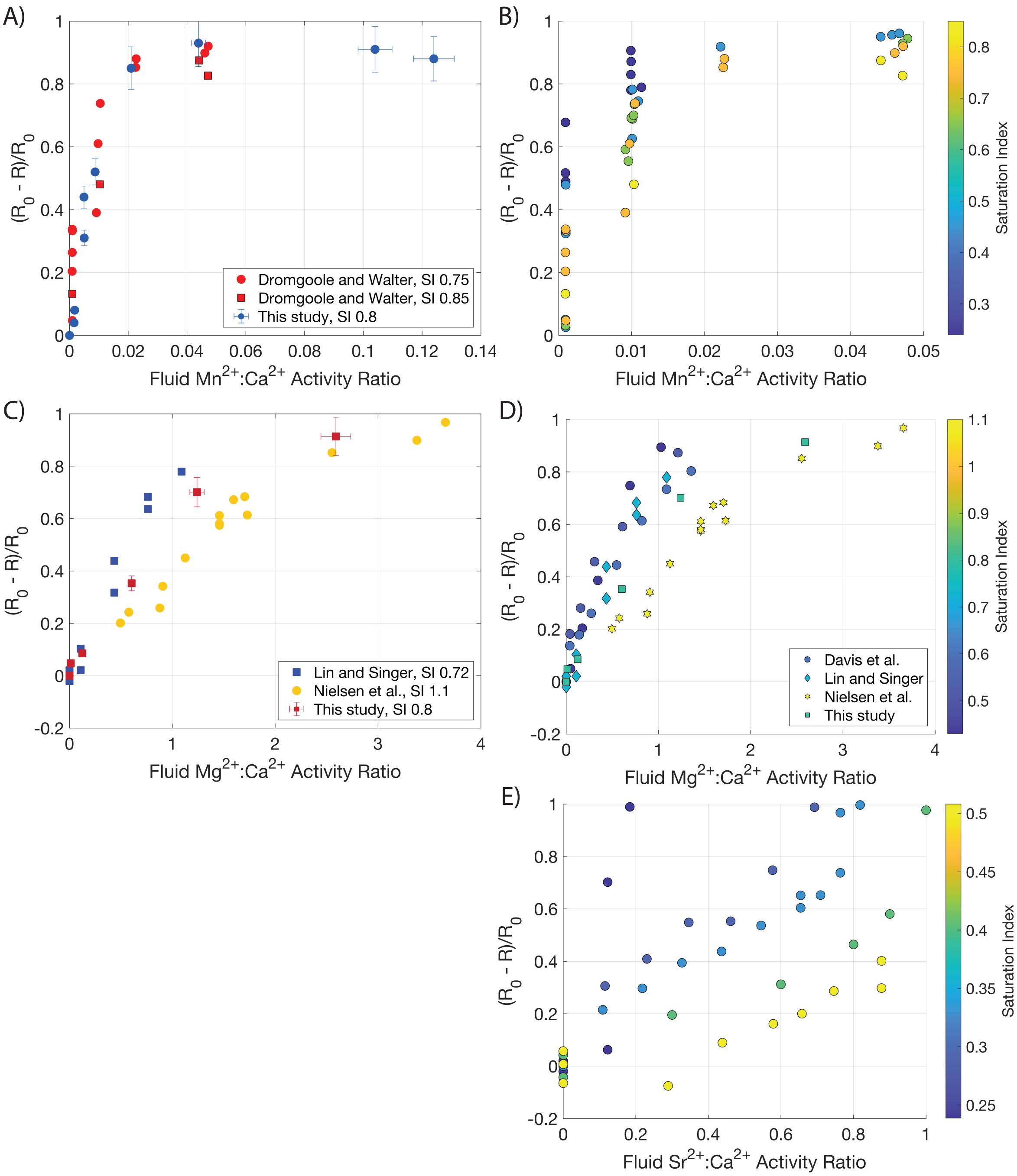

Figure 3.16 – Extent of calcite growth inhibition across studies and inhibitor systems. A) Extent of inhibition as a function of $\{Mn^{2+}\}/\{Ca^{2+}\}$ observed in this study and similar SI bulk growth experiments from Dromgoole and Walter (1990a). B) Data from Dromgoole and Walter (1990a), segmented by SI range, demonstrating higher extent of inhibition for a given $\{Mn^{2+}\}/\{Ca^{2+}\}$ at lower SI. C) Extent of inhibition as a function of $\{Mg^{2+}\}/\{Ca^{2+}\}$ observed in this study and similar SI bulk growth experiments from Lin and Singer (2009) and Nielsen *et al.* (2016). D) Literature compilation of Mg^{2+} bulk growth rate inhibition data, segmented by SI. A higher extent of inhibition is observed in lower SI solutions both within individual studies (Davis *et al.*, 2000a) and across studies (Davis *et al.*, 2000a; Lin and Singer, 2009; Nielsen *et al.*, 2016). E) Comparable extent of inhibition data for calcite inhibition by Sr^{2+} from Wasylenki *et al.* (2005a), showing much higher sensitivity to SI.

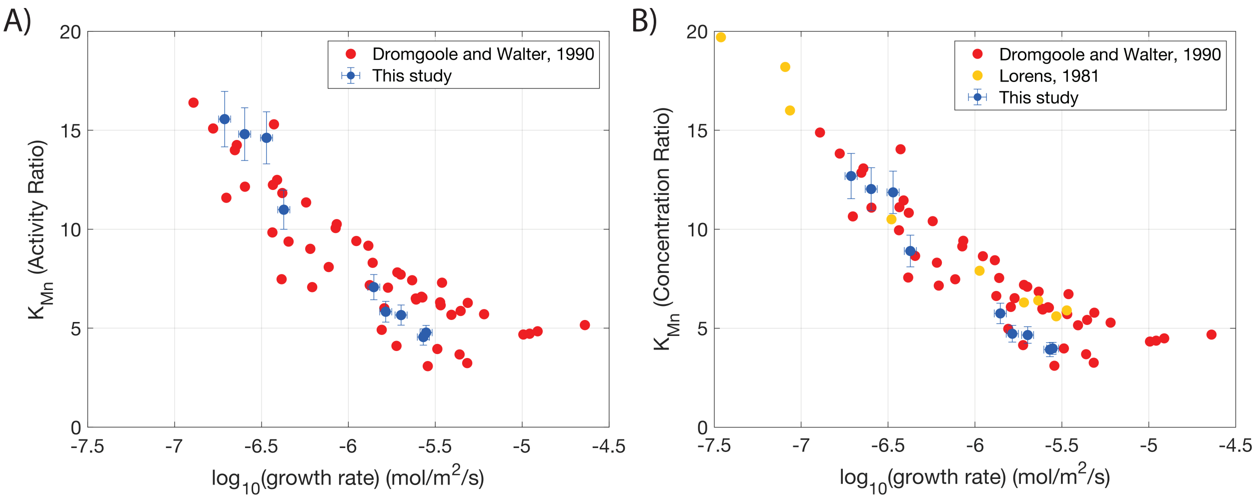

Figure 3.17 – Mn^{2+} partitioning into calcite exhibits a strong log-linear inverse dependence on growth rate across a wide range of solution conditions. K_{Mn} calculated using solution activity ratio (A) and concentration ratio (B) vs. growth rate for data from this study, Dromgoole and Walter (1990a), and Lorens (1981). Note, only data from experiments performed in milli-Q water from Lorens (1981) are included. See Table 3.3 for a summary of solution conditions used in each study.

forward precipitation fluxes (the net growth rate, $R^p = R^f - R^b$ where R^b is assumed to be 6e-7 mol/m^2/s based on the calcite dissolution study of Chou *et al.* (1989)). In this simplified framework, the Mn^{2+} partitioning data across studies is consistent with an equilibrium partition coefficient of ~55 and kinetic endmember of 4, the lowest value observed here. Although we will explore this partitioning in greater detail using the full mechanistic ion-by-ion model in Section 3.4.4.1, the common trend observed here highlights that Mn^{2+} partitioning is highly kinetically controlled. Mn^{2+} partitioning and calcite growth rate respond to solution conditions in a remarkably consistent manner.

Experiment	SI	$\{Me^{2+}\}/\{Ca^{2+}\}$	pH	$\{Ca^{2+}\}/\{CO_3^{2-}\}$	Ionic strength
Mn^{2+} studies					
This study	0.8	0.001-0.14	8.0	110	0.1M KCl
Dromgoole and Walter (1990a)	0.3-1.0	0.001-0.05	~6	10^3-10^5	~0.3M
Lorens (1981)	~0.1-0.8	~10^{-10}	7.5	300-1400	0.7M NaCl
Mg^{2+} studies					
This study	0.8	0.01-2.6	8.0	110	0.1M KCl
Mavromatis *et al.* (2013)	0.1-0.5	0.2-1.4	~6.2	10^3-10^4	0.1-0.6M NaCl
Nielsen *et al.* (2016)	0.8	0.5-3.5	8.3	~50	0.1M NaCl

Table 3.3 – Solution conditions for Mn^{2+} and Mg^{2+} partitioning studies

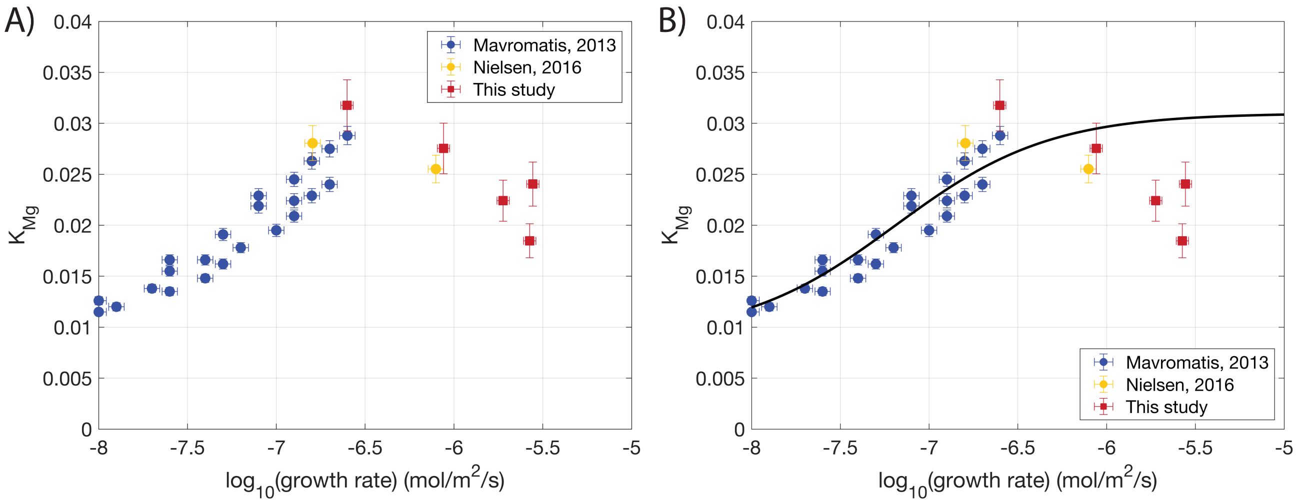

Figure 3.18 – Literature compilation of Mg^{2+} partitioning results. A) The results from this study (red squares) and Nielsen *et al.* (2016) depart from the strong log-linear trend observed by Mavromatis *et al.* (2013). Notably, the Mavromatis *et al.* (2013) experiments were run at a much lower pH and thus higher $\left\{Ca^{2+}\right\} / \left\{CO_3^{2-}\right\}$; see Table 3.3 for a summary of solution conditions. B) As in A but with DePaolo (2011) model prediction of K_{Mg} (see text for discussion).

3.4.2.2 Mg partitioning

In contrast to the highly consistent partitioning-rate trend observed for Mn^{2+}, comparing Mg^{2+} partitioning data across experiments reveals a marked divergence in the relationship between K_{Mg} and growth rate (Figure 3.18). While the dataset of Mavromatis *et al.* (2013) exhibits a strong positive correlation between K_{Mg} and rate, where higher partition coefficients are observed at faster rates, the K_{Mg} measured in this study and the similar bulk-growth study of Nielsen *et al.* (2016) depart from that trend. However, the three datasets overlap in the $10^{-6.5}$-10^{-7} mol/m^2/s growth rate regime, making it unclear whether they represent a single cohesive trend with a rate inversion at ~$10^{-6.5}$-10^{-7} mol/m^2/s or if fundamentally different rate dependencies are observed under different solution conditions. A single cohesive dataset that spans the $10^{-5.5}$ to $10^{-7.5}$ mol/m^2/s growth rate range under controlled solution conditions is required to definitively interpret these Mg^{2+} partitioning observations, but we explore some potential explanations here.

Considering first the possibility that the datasets represent fundamentally different K_{Mg}-rate behavior. The experiments of Mavromatis *et al.* (2013) were run at lower pH, higher $\left\{Ca^{2+}\right\} / \left\{CO_3^{2-}\right\}$, and lower supersaturation than used in this study and Nielsen *et al.* (2016) (Table 3.3), raising the possibility that the deviation from the positive log-linear trend could represent a pH or supersaturation effect. The literature is mixed here. Mucci and Morse (1983) report a trend of declining K_{Mg} with increasing $\left\{Mg^{2+}\right\} / \left\{Ca^{2+}\right\}$ and declining growth rate in seawater solutions (pH 7.7-8.2, SI 0.6-1.2), in line with the Mavromatis *et al.* (2013) trend. But Gabitov *et al.* (2014) found that K_{Mg} declines with increasing growth rate in a study of Mg^{2+} partitioning into single calcite crystals grown in NH_4Cl solutions (pH ~8, SI ~0.3).

Another possibility stems from the observation that Mavromatis *et al.* (2013) did not report any changes in calcite morphology following the precipitation of their magnesian calcite overgrowths, in contrast to the increasing expression of (110) and (100) calcite faces with increasing $\{Mg^{2+}\} \,/\, \{Ca^{2+}\}$ observed here (Section 3.3.1). Perhaps the inverse rate dependence observed here is driven by differences in preferential Mg^{2+} interaction with specific faces (Zhang and Dawe, 2000; Reeder and Grams, 1987) or steps (Davis *et al.*, 2004; Paquette and Reeder, 1995). In particular, the experiments in this study are run with a KCl background electrolyte (0.1M ionic strength) while the Nielsen *et al.* (2016) and Mavromatis *et al.* (2013) studies were run in NaCl, with a total ionic strength of 0.1M and 0.1-0.6M, respectively. Importantly, in NaCl solutions, the obtuse calcite step propagates substantially faster (2-4x) than the acute step while roughly equal obtuse/acute step velocities are observed in KCl solutions (Stephenson *et al.*, 2011; Hong and Teng, 2014; Ruiz-Agudo *et al.*, 2011b). Stephenson *et al.* (2011) also report that increasing ionic strength suppresses Mg^{2+} uptake in a background electrolyte-specific manner. It is thus possible that the trend of increasing K_{Mg} with increasing $\{Mg^{2+}\} \,/\, \{Ca^{2+}\}$ observed here stems from the background electrolyte used; perhaps relatively more Mg^{2+} is incorporated into the lattice at high $\{Mg^{2+}\}$ in KCl solutions because there is less interaction between the 'background' electrolyte and the acute calcite step where Mg^{2+} is preferentially incorporated.

Finally, as alluded to above (Section 3.2.6.1), in the ion-by-ion model framework, the slope of the K_{Mg}-${}^{\{Mg^{2+}\}}/_{\{Ca^{2+}\}}$ relationship is sensitive to assumptions regarding calcite-magnesite solid solution thermodynamics. Lower values of the W_{12} parameter in the subregular solid solution model yield increasing K_{Mg} with ${}^{\{Mg^{2+}\}}/_{\{Ca^{2+}\}}$ as observed here while higher values yield the opposite relationship as observed by Mavromatis *et al.* (2013) and Mucci and Morse (1983) (Lammers and Mitnick, 2019, Figure B7). Ordering has been shown to strongly influence the excess enthalpy of mixing for both Mg^{2+} (Lammers and Mitnick, 2019; Navrotsky and Capobianco, 1987; Burton and Van de Walle, 2003) and Mn^{2+} (Wang *et al.*, 2011). Different levels of Mg/Ca ordering within the calcite lattice could thus also conceivably influence the K_{Mg}-${}^{\{Mg^{2+}\}}/_{\{Ca^{2+}\}}$ and thus rate relationship.

Turning now to the possibility that the data from this study, Mavromatis *et al.* (2013), and Nielsen *et al.* (2016) all represent a cohesive trend in K_{Mg} vs. growth rate. Again working from the DePaolo (2011) surface kinetic framework (Eq. 3.4.1), in order to achieve a plateau in the K_{Mg} vs. rate relationship at ~$10^{-6.5}$ mol/m^2/s as observed, R^b must be a factor of 30x slower than that assumed from calcite dissolution studies (Chou *et al.*, 1989; DePaolo, 2011). A low Mg^{2+} back flux (equivalently, Mg^{2+} detachment rate) is potentially consistent with observations that the far from equilibrium dissolution rate for magnesite is between 100-1000x slower than that of calcite under a wide range of conditions (Chou *et al.*, 1989; Pokrovsky *et al.*, 2009). Figure 3.18B shows predicted K_{Mg}, assuming R^b=1.88e-8 mol/m^2/s, K_f=0.031, and K_{eq}=0.0089. Note that this model does not explain all of the observed partitioning behavior - nothing in the DePaolo (2011) framework would predict the decline in K_{Mg} observed at faster rates in our experiments. But a plateau in K_{Mg} at ~$10^{-6.5}$ mol/m^2/s is qualitatively consistent with the Nielsen et al. (2016) experiments run with a NaCl background electrolyte and the DePaolo (2011) surface kinetic framework hints that this may be explained in part due to slow Mg removal from the calcite surface. As further explored using the ion-by-ion modeling framework in Section 3.4.4.2, a sluggish Mg removal flux is consistent with other observations, including the supersaturation sensitive inhibition behavior described above (Section 3.4.1). We thus posit that slow Mg^{2+} detachment from

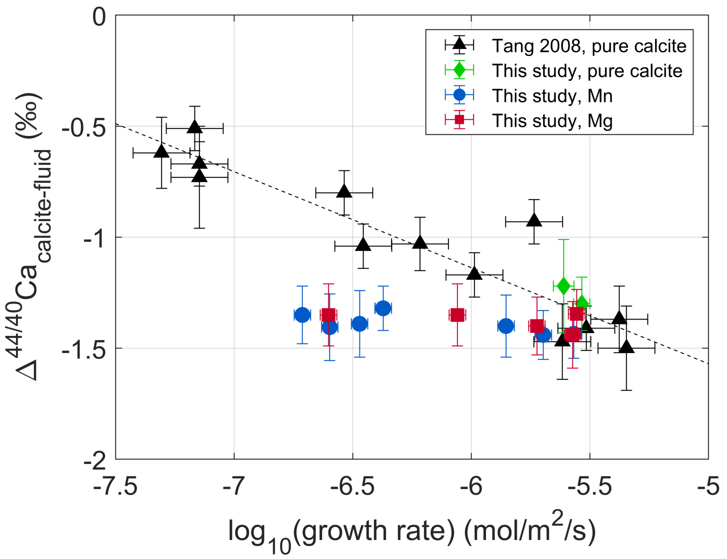

Figure 3.19 – Invariant $\Delta^{44/40}Ca$ with $\{Me^{2+}\}/\{Ca^{2+}\}$ draws observed fractionations off the pure calcite $\Delta^{44/40}Ca$-growth rate relationship and suggests that Mn^{2+} and Mg^{2+} inhibit calcite growth through a dominantly kink-blocking mechanism. Data from the Mn^{2+} (blue circles) and Mg^{2+}(red squares) experiments are plotted alongside data from inhibitor-free inorganic calcite growth experiments: 25°C dataset from Tang *et al.* (2008) (black triangles with linear regression shown as the dotted line) and $\{Ca^{2+}\}/\{CO_3^{2-}\}$=100, SI = 0.8 data from the current study and Mills *et al.* (2021).

the calcite surface may contribute to the observed apparent inconsistencies between Mg^{2+} partitioning datasets, but again caution that additional data is required from a single cohesive dataset that spans the $10^{-5.5}$ to $10^{-7.5}$ mol/m^2/s growth rate range to further elucidate these observations.

3.4.3 Invariant $\Delta^{44/40}$Ca points towards kink-blocking inhibition mechanism

Inorganic calcite growth experiments performed in the absence of inhibitors exhibit an inverse, log-linear relationship between calcium isotope fractionation and growth rate (Mills *et al.*, 2021; Tang *et al.*, 2008). The invariant $\Delta^{44/40}Ca$ during calcite inhibition by Mg^{2+} and Mn^{2+} draws the fractionations observed here off the pure calcite $\Delta^{44/40}Ca$-rate relationship, with high magnitude fractionations maintained despite more than an order of magnitude decline in growth rate (Figure 3.19). In Chapter 2, we verified both the conceptual framework of calcium isotope discrimination driven by Ca exchange at kink sites during growth and the process-based ion by ion framework that casts the expressed fractionation in terms of solution chemistry. The invariant $\Delta^{44/40}Ca$ thus indicates that calcite growth inhibition by Mg^{2+} and Mn^{2+} does not change the *relative* rate of Ca addition vs. removal from kink sites. As developed in Section 2.4.6, this is consistent with kink-blocking type inhibition, where the inhibitor dominantly influences the rates of ion attachment at kink sites and subsequent kink propagation kinetics but does not substantially destabilize the calcite lattice (which would increase the back flux of Ca).

This is consistent with inhibition driven by slow inhibitor cation desolvation kinetics, as has been proposed by Astilleros *et al.* (2010) and Nielsen *et al.* (2013) for the case of Mg^{2+}. The smaller Mg^{2+} ion is much more strongly hydrated than Ca^{2+}; the water exchange frequency for Mg^{2+} is >3 orders of magnitude lower than that of Ca^{2+} (Helm and Merbach, 1999). Magnesium may thus inhibit calcite growth by attaching at kink sites and literally blocking their propagation because it is slow to shed its hydration waters, impeding both Mg^{2+} attachment at the kink and subsequent $CO_3{}^{2-}$ attachment at Mg^{2+}-occupied kinks. Considering Mn^{2+}, the picture becomes a bit murkier. While Mn^{2+} should also dehydrate more slowly than Ca^{2+}, with an approximately 1 order of magnitude lower water exchange frequency (Helm and Merbach, 1999), it should shed its hydration waters far faster than Mg^{2+}. Thus despite the nearly identical behavior in $\Delta^{44/40}Ca$ as a function of growth rate and similar log-linear inhibition observed at low ${}^{\{Mn^{2+}\}}/_{\{Ca^{2+}\}}$, it appears difficult to explain the much stronger inhibition by Mn^{2+} at low solution inhibitor concentrations in terms of cation desolvation rate-limited kink blocking alone. We now turn to the classical ion-by-ion modeling framework to explore this discrepancy and potential mechanistic explanations for the observed trends in inhibition, trace element partitioning, and isotope fractionation.

3.4.4 Insights from ion-by-ion model

In searching for a mechanistic driver for calcite inhibition by Mg^{2+} and Mn^{2+}, a number of trends must be explained:

- From the perspective of solution inhibitor concentration, Mn^{2+} is an ~100x stronger inhibitor of calcite growth than Mg^{2+} but exhibits a similar log-linear inhibition trend at low ${}^{\{Mn^{2+}\}}/_{\{Ca^{2+}\}}$.
- Inhibition by both Mn^{2+} and Mg^{2+} is sensitive to supersaturation; a higher extent of inhibition is observed at lower supersaturation for a given ${}^{\{Me^{2+}\}}/_{\{Ca^{2+}\}}$.
- Large positive Mn^{2+} partition coefficients are observed at low ${}^{\{Mn^{2+}\}}/_{\{Ca^{2+}\}}$ and K_{Mn} is strongly inversely correlated to growth rate.
- K_{Mg} is on the order of 0.02-0.03 and increases with ${}^{\{Mg^{2+}\}}/_{\{Ca^{2+}\}}$ over the solution conditions studied here.
- $\Delta^{44/40}Ca$ is invariant with ${}^{\{Mn^{2+}\}}/_{\{Ca^{2+}\}}$ and ${}^{\{Mg^{2+}\}}/_{\{Ca^{2+}\}}$ despite more than an order of magnitude decline in growth rate.

In the following sections we employ the ion-by-ion model of Nielsen *et al.* (2013) to explore the mechanistic implications of this suite of observations.

3.4.4.1 Mn inhibition of calcite growth: evidence for non-monomer incorporation

We begin with Mn^{2+} inhibition of calcite growth. The first inhibition mechanism that can be categorically ruled out is cation desolvation driven kink blocking. Figure B2 shows

Ca^{2+} kinetic parameters				
	k_{Ca} ($s^{-1}M^{-1}$)	k_{CO_3} ($s^{-1}M^{-1}$)	$\nu_{Ca,0}$ (s^{-1})	$\nu_{CO_3,0}$ (s^{-1})
	3.75e6	2.2e7	523	523
Mn^{2+} kinetic parameters				
Mechanism	k_{Mn} ($s^{-1}M^{-1}$)	k_{CO_3Mn} ($s^{-1}M^{-1}$)	$\nu_{Mn,0}$ (s^{-1})	$\nu_{CO_3Mn,0}$ (s^{-1})
Cation desolvation driven kink blocking	$0.001{*}k_{Ca}$	$1e\text{-}5{*}k_{Ca}$	4.5e-4	0.002
Complex addition + carbonate kink blocking	$12{*}k_{Ca}$	$0.033{*}k_{Ca}$	3	13.6
Solid solution thermodynamic parameters				
Guggenheim parameters	a_0	a_1	a_2	K_{sp}, $MnCO_3$*
	1.5	-1.1	0	$10^{-11.13}$
Endmember calcium isotope fractionations				
	α_f	0.9967	α_{eq}	0.9995

Table 3.4 – Model parameters for Mn^{2+} inhibition of calcite growth. *Following Katsikopoulos *et al.* (2009)

modeled growth rate, K_{Mn}, and $\Delta^{44/40}Ca$ as a function of solution $\{Mn^{2+}\}/\{Ca^{2+}\}$ for growth inhibition driven by slow attachment of Mn^{2+} at $CO_3{}^{2-}$ kink sites and $CO_3{}^{2-}$ at Mn^{2+} kink sites (Table 3.4). In order to achieve the level of inhibition observed at low $\{Mn^{2+}\}/\{Ca^{2+}\}$, Mn^{2+} addition must be so slow that virtually no manganese is incorporated into the calcite lattice (Figure B2B). Thus although kink blocking driven by sluggish Mn^{2+} attachment kinetics is consistent with the invariant $\Delta^{44/40}Ca$ observed (Figure B2C), the large positive K_{Mn} at low $\{Mn^{2+}\}/\{Ca^{2+}\}$ observed rules out this inhibition mechanism.

In fact, in order to capture the Mn^{2+} incorporation behavior observed, Mn^{2+} must attach substantially *faster* than Ca^{2+} ($k_{Mn}>>k_{Ca}$, Table 3.4). Considering the water exchange frequencies of Mn^{2+} and Ca^{2+}, this proposition does not make much sense if manganese is attaching at kink sites as free Mn^{2+} ions; the desolvation rate and thus attachment rate of Mn^{2+} should be lower than that of Ca^{2+} (Helm and Merbach, 1999). This requisite fast attachment of Mn^{2+} thus points towards non-monomer incorporation of Mn^{2+}, where the dominant Mn^{2+} species interacting with kink sites is not the free ion in solution but instead an ion pair, hydrated species, or possibly a larger polynuclear cluster. In turn, if the kinetics of Mn^{2+} attachment are rapid, the dominantly kink blocking-type inhibition indicated by the invariant $\Delta^{44/40}Ca$ must be driven by slow carbonate attachment at Mn^{2+} kink sites.

Figure 3.20 shows modeled growth rate, K_{Mn}, and $\Delta^{44/40}Ca$ as a function of solution $\{Mn^{2+}\}/\{Ca^{2+}\}$ for a scenario where Mn^{2+} readily attaches at the calcite surface ($k_{Mn}=12k_{Ca}$) and growth inhibition is driven by slow attachment of $CO_3{}^{2-}$ at Mn^{2+} kink sites (Table 3.4). This mechanism captures both the magnitude of growth rate inhibition and manganese partitioning, while predicting very little change in $\Delta^{44/40}Ca$ with increasing $\{Mn^{2+}\}/\{Ca^{2+}\}$. The Mn^{2+} partitioning behavior, in particular the shape of the K_{Mn}-$\{Mn^{2+}\}/\{Ca^{2+}\}$ relationship (Figure 3.20B) is highly sensitive to assumptions regarding calcite-rhodochrosite solid solu-

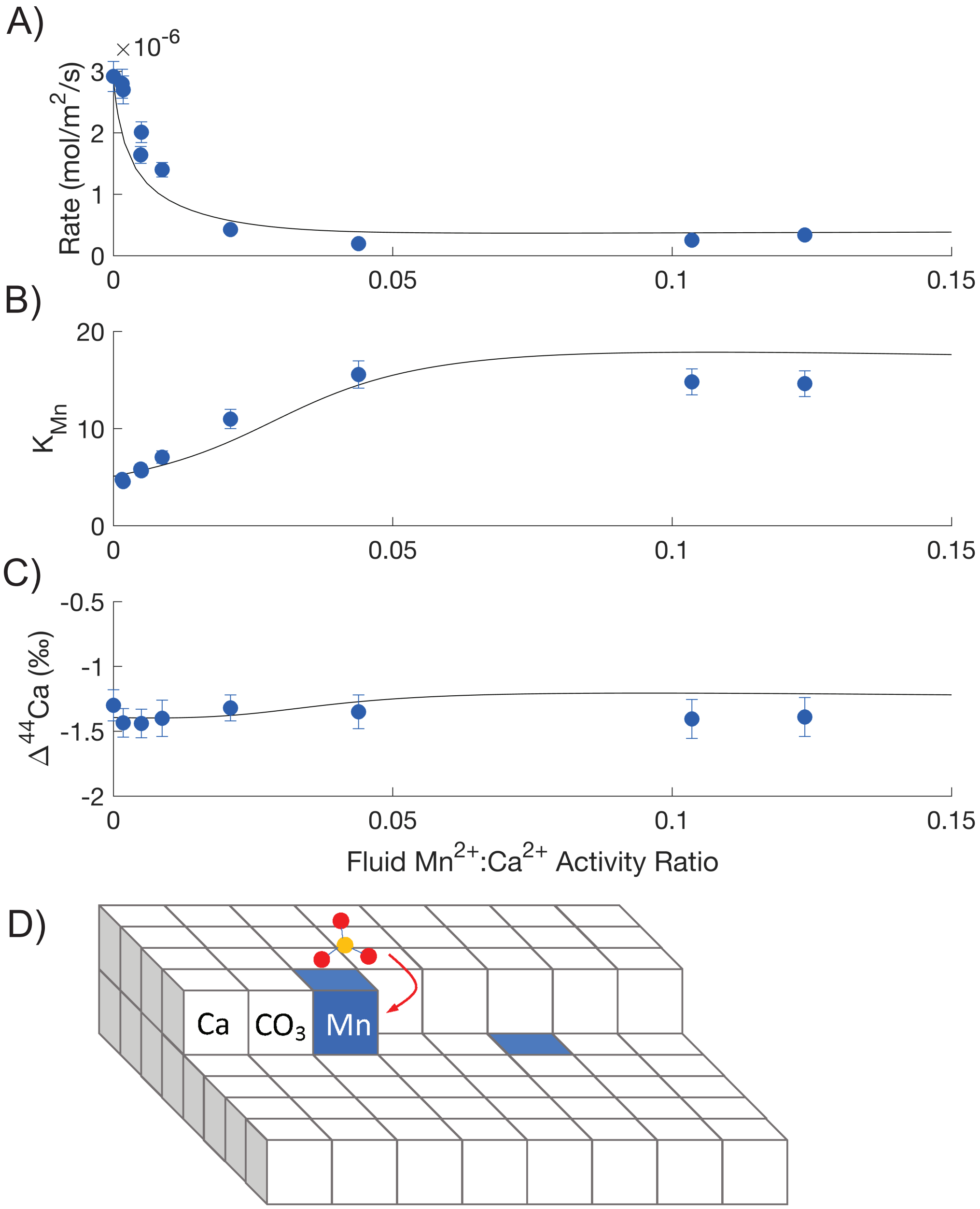

Figure 3.20 – Ion-by-ion model prediction of bulk growth rate (A), Mn^{2+} partition coefficient (B), and $\Delta^{44/40}Ca_{calcite-fluid}$ (C) as a function of $\{Mn^{2+}\}/\{Ca^{2+}\}$ for Mn^{2+} inhibition of calcite growth driven by Mn^{2+} complex addition (allowing for $k_{Mn}>>k_{Ca}$) coupled to kink-blocking due to slow CO_3^{2-} attachment at Mn^{2+} kink sites. See Table 3.4 for model parameters. D) Schematic of proposed carbonate based kink-blocking mechanism: slow re-orientation kinetics of carbonate ions that have formed an inner-sphere complex with Mn^{2+} at the surface but must reorient to incorporate into the lattice.

tion thermodynamics. We find the partitioning trends observed here are best described with an excess free energy of mixing with positive deviations from ideality, consistent with but not identical to the calorimetric measurements of Katsikopoulos *et al.* (2009) and Capobianco and Navrotsky (1987) (Figure B3). Notably, the model does predict a slight decrease in the magnitude of $\Delta^{44/40}Ca$ at higher ${Mn^{2+}}/{Ca^{2+}}$, as Ca is destabilized in the lattice (ν_{Ca} increases) at intermediate $(Mn_xCa_{1-x})CO_3$ solid solution compositions. While we do not measure more positive $\Delta^{44/40}Ca$ values at high ${Mn^{2+}}/{Ca^{2+}}$, the stabilization of the solid solution implied by the increasing growth rates measured here at ${Mn^{2+}}/{Ca^{2+}}$ >0.1 suggests that the model may be slightly over-estimating the ν_{Ca} increase at high ${Mn^{2+}}/{Ca^{2+}}$ for the solution conditions studied here. At lower supersaturations, the model captures the growth rate inversion (Figure 3.21), which would be associated by a trend back to slightly larger magnitude $\Delta^{44/40}Ca$.

But what could drive slow carbonate attachment at Mn^{2+} kink sites? We propose that the apparent carbonate kink blocking could arise from slow re-orientation kinetics of carbonate ions that have formed an inner-sphere complex with Mn^{2+} at the surface but must reorient to incorporate into the lattice (Figure 3.20D) . Unlike the spherical cations, the planar carbonate molecule can only be incorporated into the calcite lattice when the C-O-C plane is perpendicular to the C-axis of calcite. Hong and Teng (2014) argued that the rate limiting step in the propagation of acute calcite steps is the surface adsorption and reorientation of CO_3^{2-} ions based on observations of the differential response of acute and obtuse steps to changes in pH and Ca^{2+}:CO_3^{2-} solution stoichiometry. Mn^{2+} also forms ion pairs in solution much more readily than Ca^{2+} or Mg^{2+}; most estimates of the thermodynamic stability constant (logk) for the $MnCO_3^0$ ion pair formation reaction range from 4-5 (Luo and Millero (2003); Turner *et al.* (1981); Langmuir (1979); Wolfram and Krupp (1996), Figure B1) while the logk's for Ca^{2+} and Mg^{2+} carbonate ion pair formation reactions are 3.2 (Plummer and Busenberg, 1982) and 2.9, respectively (Reardon and Langmuir, 1974). Thus, a potential mechanism for the inhibition observed here is that interaction with surface Mn^{2+}, concentrated on the acute steps (Paquette and Reeder, 1995), further inhibits carbonate reorientation and leads to severely impeded CO_3^{2-} attachment at Mn^{2+} kink sites. Another possibility is that CO_3^{2-} attachment could be kinetically hindered by slow surface desolvation of Mn at kink sites on the current step and potentially even the step below, which can be quite Mn-rich.

We now turn to the question of whether this inhibition mechanism is consistent with the broader range of observations across a wide range of solution conditions (Sections 3.4.2.1, 3.4.1). First, examining how K_{Mn} varies with ${Mn^{2+}}/{Ca^{2+}}$ for a range of supersaturations (Figure 3.21C), we find that larger partition coefficients are predicted for a given ${Mn^{2+}}/{Ca^{2+}}$ in lower supersaturation (and thus slower growth rate) solutions. This is consistent with the inverse correlation between K_{Mn} and growth rate observed across experiments (Figure 3.17). Considering the sensitivity of inhibition to supersaturation, Figure 3.21A shows the supersaturation dependence of the inhibition intensity for the solution conditions examined here. Unlike that observed by Dromgoole and Walter (1990a), a lower extent of inhibition is observed at lower supersaturations for a given ${Mn^{2+}}/{Ca^{2+}}$. Notably, the Dromgoole and Walter (1990a) experiments were run at very high ${Ca^{2+}}/{CO_3^{2-}}$ (Table 3.3); implementing a comparably high ${Ca^{2+}}/{CO_3^{2-}}$ in the ion-by-ion model yields a lower sensitivity to supersaturation (Figure 3.21B) but does not capture the trend of higher inhibition at lower supersaturations. Importantly, without in-situ AFM measurements, we have no indication of how the presence of Mn^{2+} influences hillock step spacing (y_0, Section 3.2.6.3), leaving a key parameter in the scaling of modeled step velocities to bulk growth rates highly uncertain. A higher extent of inhibition at low ${Mn^{2+}}/{Ca^{2+}}$ for low supersaturation solutions could be driven by relatively larger changes in y_0 with increasing ${Mn^{2+}}/{Ca^{2+}}$ at low supersaturation. Calcite inhibition by Sr^{2+} exhibits this pattern (Figure 3.5). Wasylenki *et al.* (2005a) reported that y_0 increases by a factor of 3 between ${Sr^{2+}}/{Ca^{2+}}=0$ and ${Sr^{2+}}/{Ca^{2+}}=0.8$ in SI = 0.33 solutions, but y_0 only increases by a factor of 1.5 over a comparable range of ${Sr^{2+}}/{Ca^{2+}}$ in SI = 0.51 solutions. This leads to markedly stronger bulk growth rate inhibition than step velocity inhibition at lower supersaturations, particularly at low ${Me^{2+}}/{Ca^{2+}}$ where Mn^{2+} inhibition is also observed to be most sensitive to supersaturation (Figure 3.5A,B).

If future measurements reveal that the trend in inhibition sensitivity to supersaturation observed by Dromgoole and Walter (1990a) cannot be explained by changes in step spacing, the model presented here would need to be critically re-evaluated to consider whether aspects of the model framework are more sensitive to supersaturation than currently assumed, or if the framework is missing fundamental processes such as 2D step nucleation inhibition. Most obviously, the inhibition mechanism proposed here requires Mn^{2+} to attach at kink sites as a non-monomer species, which is not considered in classical growth models but may be incorporated into process-based models. Expanding such process-based models to incorporate non-classical processes (Section 3.4.6) as well as exploring the implications of changes in growth mechanism due to the presence of inhibitors, for example a transition to 2D nucleation driven growth (Section 3.3.1), are important avenues for future investigation.

3.4.4.2 Mg inhibition of calcite growth: kink blocking...but how?

In contrast to Mn^{2+}, our observations of calcite growth inhibition by Mg^{2+} are consistent with a classical cation desolvation driven kink blocking mechanism. Figure 3.22 shows modeled growth rate, K_{Mg}, and $\Delta^{44/40}Ca$ as a function of solution ${Mg^{2+}}/{Ca^{2+}}$ for growth inhibition driven by slow attachment of Mg^{2+} at CO_3^{2-} kink sites and CO_3^{2-} at Mg^{2+} kink sites (Table 3.5, Scenario 1). The model captures the key characteristics of Mg^{2+} inhibition observed: log-linear rate inhibition that continues to high ${Mg^{2+}}/{Ca^{2+}}$; K_{Mg} on the order of 0.02-0.03 that increases with ${Mg^{2+}}/{Ca^{2+}}$; and invariant $\Delta^{44/40}Ca$. It is also worth noting the large difference in requisite Mg^{2+} attachment rate in models that assume a constant y_0 (dictated only by solution supersaturation) and a step width that increases with ${Mg^{2+}}/{Ca^{2+}}$ following the observations of Davis *et al.* (2000b) (as shown in Figure 3.22). Assuming that step width is also sensitive to inhibitors leads to a factor of 4 increase in k_{Mg} as the rising y_0 further damps bulk growth rates at high ${Mg^{2+}}/{Ca^{2+}}$ (Table 3.5, Section 3.2.6.3). This further highlights the importance of better constraining the solution chemistry dependence of y_0 and investigating how changes in growth mechanism could influence inhibition dynamics.

While the model captures the trends in rate inhibition, partitioning, and calcium isotope discrimination observed here, the predicted extent of inhibition exhibits the wrong supersaturation dependence (Figure 3.23A). While observations both within single experiments (Davis *et al.*, 2000a) and from across the literature (Figure 3.16D) demonstrate that experiments run at a lower supersaturation are more strongly inhibited at a given ${Mg^{2+}}/{Ca^{2+}}$, the opposite trend is predicted here. Within the ion-by-ion modeling framework employed here

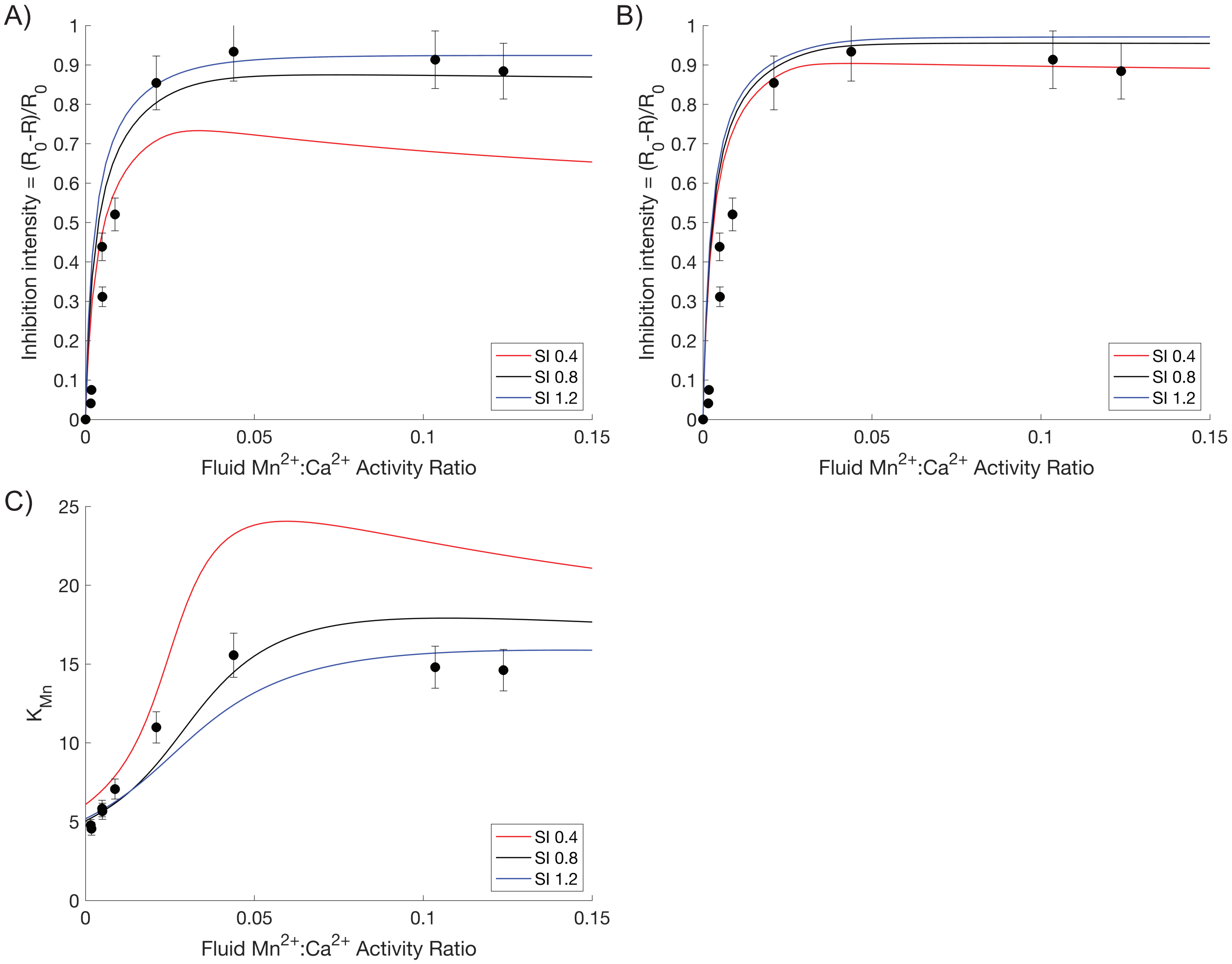

Figure 3.21 – Predicted sensitivity of Mn^{2+} growth rate inhibition and partitioning to supersaturation. A) Predicted extent of inhibition as a function of fluid $^{\{Mn^{2+}\}}/_{\{Ca^{2+}\}}$ for different supersaturation solutions, using the solution chemistry studied here. B) As in A, but using a $^{\{Ca^{2+}\}}/_{\{CO_3^{2-}\}}$ ratio of 3e4, representative of the conditions studied by Dromgoole and Walter (1990a). C) Predicted Mn^{2+} partition coefficient as a function of fluid $^{\{Mn^{2+}\}}/_{\{Ca^{2+}\}}$ for different supersaturation solutions, using the solution chemistry studied here.

Ca^{2+} kinetic parameters					
		k_{Ca} (s^{-1}M^{-1})	k_{CO_3} (s^{-1}M^{-1})	$\nu_{Ca,0}$ (s^{-1})	$\nu_{CO_3,0}$ (s^{-1})
		3.75e6	2.2e7	523	523
Mg^{2+} kinetic parameters: Cation desolvation driven kink blocking					
Scenario	y_0	k_{Mg} (s^{-1}M^{-1})	k_{CO_3Mg} (s^{-1}M^{-1})	$\nu_{Mg,0}$ (s^{-1})	$\nu_{CO_3Mg,0}$ (s^{-1})
1	thermo	0.05*k_{Ca}	0.05*k_{Ca}	8	1800
	Davis scaled	0.2*k_{Ca}	0.2*k_{Ca}	150	1500
2	thermo	0.008*k_{Ca}	0.024*k_{Ca}	0.001	0.001
	Davis scaled	0.008*k_{Ca}	0.12*k_{Ca}	0.01	1
3	Davis scaled	0.025*k_{Ca}	0.125*k_{Ca}	6	3000
Mg^{2+} kinetic parameters: Carbonate kink blocking					
Mechanism	y_0	k_{Mg} (s^{-1}M^{-1})	k_{CO_3Mg} (s^{-1}M^{-1})	$\nu_{Mg,0}$ (s^{-1})	$\nu_{CO_3Mg,0}$ (s^{-1})
Complex addition +	thermo	15*k_{Ca}	0.0135*k_{Ca}	1075	1075
carbonate kink blocking	Davis scaled	5.5*k_{Ca}	0.055*k_{Ca}	1300	1300
Solid solution thermodynamic parameters					
Interaction parameters	W_{12} (kJ/mol)	W_{21} (kJ/mol)	K$_{sp}$, MgCO$_3$*		
	8	8	$10^{-7.795}$		
Endmember calcium isotope fractionations					
		α_f	0.9967	α_{eq}	0.9995

Table 3.5 – Model parameters for Mg^{2+} inhibition of calcite growth.* Bénézeth *et al.* (2011)

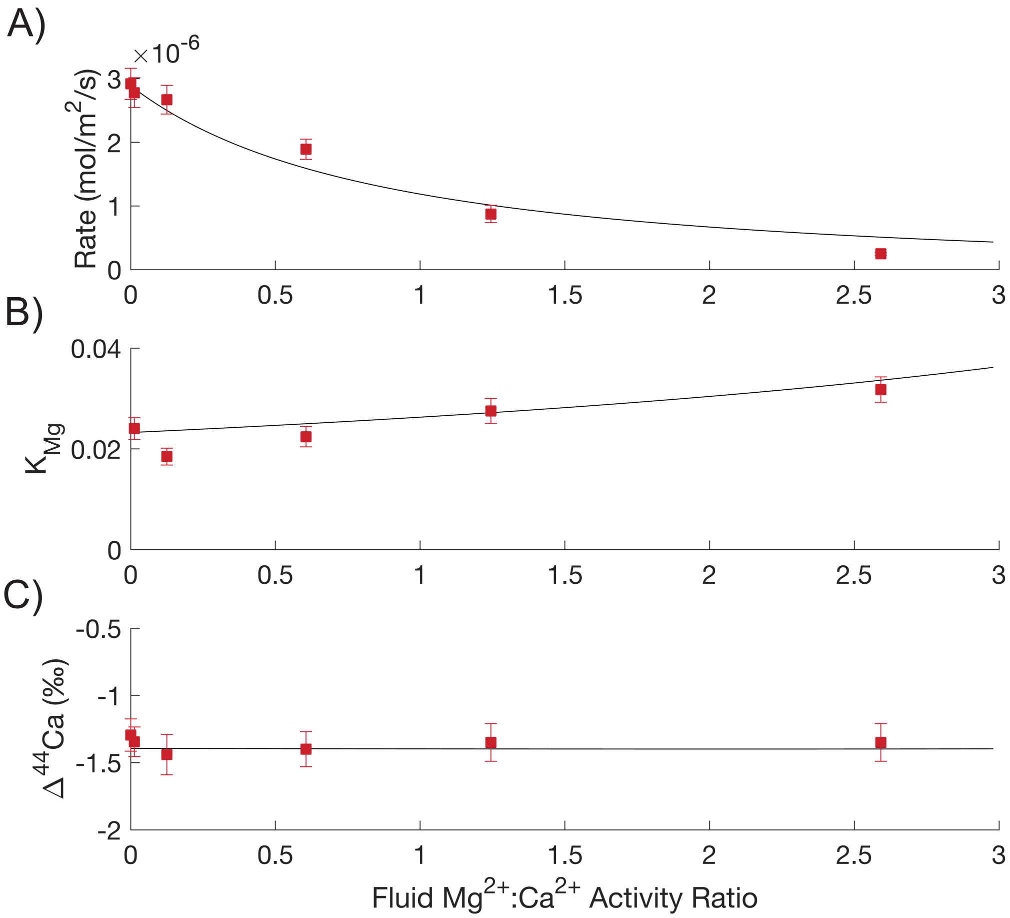

Figure 3.22 – Ion-by-ion model prediction of bulk growth rate (A), Mg^{2+} partition coefficient (B), and $\Delta^{44/40}Ca_{calcite-fluid}$ (C) as a function of ${}^{\{Mg^{2+}\}}/_{\{Ca^{2+}\}}$ for Mg^{2+} inhibition of calcite growth driven by Mg^{2+}-desolvation limited kink blocking. See Table 3.5 for model parameters (Scenario 1 with y_0 scaled to the observations of Davis *et al.* (2000b)).

(Nielsen *et al.*, 2013), the only mechanism we could identify that would both capture the measured data and predict stronger inhibition at lower supersaturation was cation-desolvation driven kink blocking, coupled to negligible Mg^{2+} detachment rates (Figure B4, 3.23B, Table 3.5, Scenario 2). This was achieved in the ion-by-ion framework by disconnecting ν_{Mg} from calcite-magnesite solid solution thermodynamics, and dictating that $\nu_{Mg} <<< \nu_{Ca}$ (Table 3.5). Sluggish Mg^{2+} detachment kinetics could be caused by kinetic constraints on Mg^{2+} hydration as it leaves the kink site and are potentially consistent with the 100-1000x slower dissolution rate of magnesite relative to calcite as previously discussed (Chou *et al.*, 1989; Pokrovsky *et al.*, 2009). However, forcing negligible Mg^{2+} detachment yields Mg partitioning behavior inconsistent with that observed across studies (Figure 3.18, B6B). While all other mechanisms explored here exhibit higher K_{Mg} at higher solution supersaturations, consistent with the growth rate trend documented by Mavromatis *et al.* (2013), turning off Mg^{2+} detachment yields the opposite trend (Figure B6). As previously discussed (Section 3.4.2.2), at a given supersaturation, the slope of the K_{Mg}-${}^{\{Mg^{2+}\}}/_{\{Ca^{2+}\}}$ relationship predicted by the ion-by-ion model is dictated by assumptions regarding the interaction parameters describing calcite-magnesite solid solution thermodynamics (Lammers and Mitnick, 2019, Figure B7). While a low W_{12} is consistent with the increasing K_{Mg} with ${}^{\{Mg^{2+}\}}/_{\{Ca^{2+}\}}$ observed here, the opposite trend is predicted when a higher W_{12} is assumed (Section 3.2.6.1).

In reality, cation-desolvation driven kink blocking by Mg^{2+} would likely resemble something in between the endmember scenarios represented by scenarios 1 and 2 (Table 3.5), were ν_{Mg} is low as suggested by the slow magnesite dissolution kinetics, but still linked to the solubility of the calcite lattice. This inhibition pathway is depicted by scenario 3 (Figure B5), achieved in the ion-by-ion framework by assuming that $\nu_{CO_3,Mg} >> \nu_{Mg}$ (Table 3.5). Assuming a low Mg^{2+} detachment flux yields growth rate inhibition that is largely insensitive to supersaturation (Figure 3.23C) but Mg^{2+} partitioning that exhibits the supersaturation dependence observed by Mavromatis *et al.* (2013) (Figure B6C). As will be discussed in more detail below, the lower sensitivity to inhibition in higher supersaturation solutions observed experimentally could be linked to processes not accounted for in the ion-by-ion framework such as incomplete dehydration of Mg^{2+} at faster growth rates, so we avoid making mechanistic deductions based on the inhibition supersaturation dependence alone.

We have thus far demonstrated that our observations of Mg-calcite precipitation dynamics can be captured by an ion-by-ion model of calcite growth in which growth is limited by Mg^{2+} desolvation kinetics and that assuming Mg^{2+} also exhibits slow detachment kinetics from kink sites brings the modeled inhibition supersaturation sensitivity closer to that observed experimentally. Importantly, the inhibition and partitioning behavior observed here can also be captured by a carbonate kink blocking mechanism similar to that invoked for Mn^{2+}. Figure 3.24 shows modeled growth rate, K_{Mg}, and $\Delta^{44/40}Ca$ as a function of solution ${}^{\{Mg^{2+}\}}/_{\{Ca^{2+}\}}$ for growth inhibition driven by fast attachment of Mg^{2+}, coupled to slow $CO_3{}^{2-}$ attachment at Mg^{2+} kink sites, potentially due to slow surface dehydration of Mg^{2+}. Using a step width that increases with ${}^{\{Mg^{2+}\}}/_{\{Ca^{2+}\}}$ following the observations of Davis *et al.* (2000b), Mg^{2+} must attach a factor of 5.5x faster than Ca^{2+}, and $CO_3{}^{2-}$ must attach a factor of 100x slower than Mg^{2+} (Table 3.5). This model scenario does an exceptionally good job of capturing the bulk growth rate inhibition observed here (Figure 3.24A).

While faster attachment of Mg^{2+} than Ca^{2+} is inconsistent with free Mg^{2+} in solution needing to fully dehydrate before attaching at a $CO_3{}^{2-}$ kink site, slow $CO_3{}^{2-}$ attachment

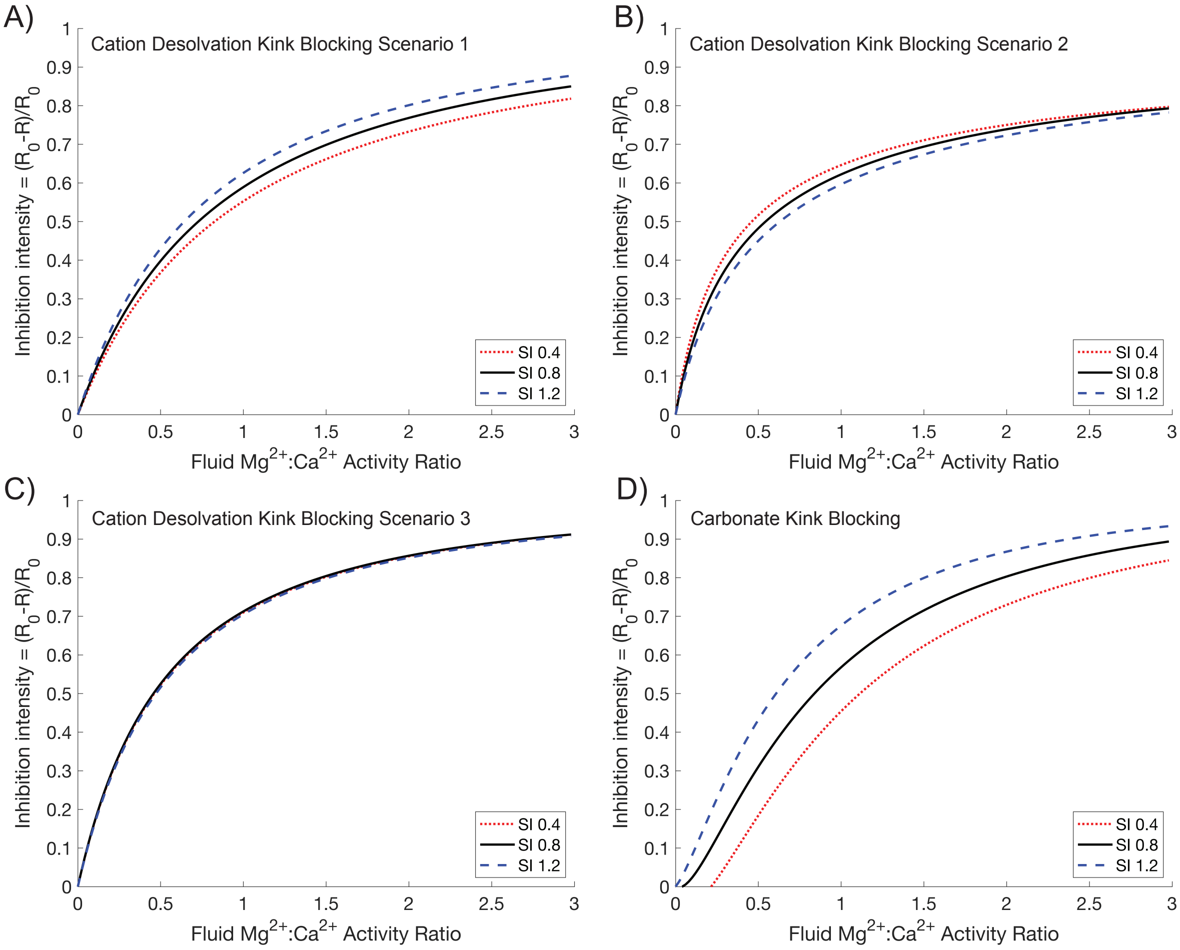

Figure 3.23 – Predicted sensitivity of Mg^{2+} growth rate inhibition to supersaturation for the different inhibition mechanisms explored. Inhibition intensity as a function of ${}^{\{Mg^{2+}\}}/_{\{Ca^{2+}\}}$ for inhibition modeled as cation-desolvation driven kink blocking for A) scenario 1 (y_0 scaled to Davis *et al.* (2000b)), B) scenario 2 (thermodynamic y_0), C) scenario 3 (y_0 scaled to Davis *et al.* (2000b)), and D) inhibition modeled as Mg^{2+} complex addition + carbonate kink blocking (y_0 scaled to Davis *et al.* (2000b)). See Table 3.5 for model parameters.

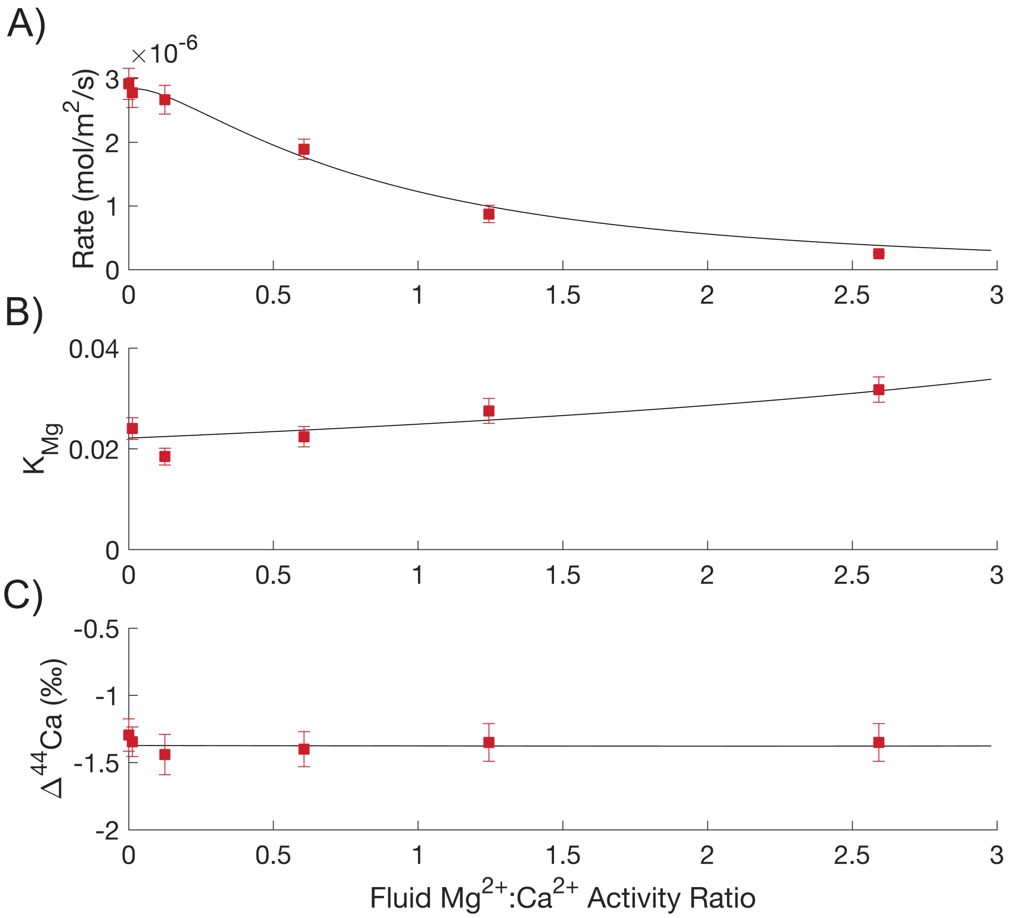

Figure 3.24 – Ion-by-ion model prediction of bulk growth rate (A), Mg^{2+} partition coefficient (B), and $\Delta^{44/40}Ca_{calcite-fluid}$ (C) as a function of ${}^{\{Mg^{2+}\}}/_{\{Ca^{2+}\}}$ for Mg^{2+} inhibition of calcite growth driven by Mg^{2+} complex addition and carbonate ion kink blocking. See Table 3.5 for model parameters (y_0 scaled to the observations of Davis *et al.* (2000b)).

on Mg^{2+} kinks is consistent with recent atomistic simulations that emphasize the likelihood of exceptionally slow Mg^{2+} dehydration on the calcite surface. In simulating the surface hydration dynamics of calcite, dolomite, and magnesite, Reischl *et al.* (2019) found that while Ca sites on the calcite surface exhibited a mean water residence time of ~2ns, not a single exchange of a water molecule in the first hydration layer was observed over the Mg sites of dolomite or magnesite over a 200ns long simulation. It is thus highly likely that at least part of the kink blocking inhibition indicated by the invariant $\Delta^{44/40}Ca$ is driven by slow CO_3^{2-} attachment on Mg^{2+} kinks due to surface dehydration rate limitation. In all scenarios investigated here, k_{CO_3Mg} must be smaller than k_{Ca} by a factor of 5-100 (Table 3.5).

Regarding the possibility that Mg^{2+} could attach faster than Ca^{2+} (at least under some conditions), we turn to observations of Mg isotope fractionation during calcite growth. In inhibitor-free solutions, the magnitude of calcium isotope fractionation increases with increasing growth rate (Figure 3.19). This trend is echoed by stable Sr^{2+} (AlKhatib and Eisenhauer, 2017b) and Ba^{2+} (Mavromatis *et al.*, 2020; von Allmen *et al.*, 2010) fractionation during calcite precipitation. In contrast, both Mg^{2+} (Mavromatis *et al.*, 2013) and Ni^{2+} (Alvarez *et al.*, 2021) exhibit the opposite trend, with the largest magnitude fractionations measured at the slowest growth rates (Figure 3.25). Like Mg^{2+}, Ni^{2+} is considerably more strongly hydrated than Ca^{2+}; the water exchange frequency for the Ni^{2+}-aquo ion is 5 orders of magnitude slower than that of Ca^{2+}. Mavromatis *et al.* (2013) and Alvarez *et al.* (2021) interpret this rate dependence to represent the progressive incorporation of more hydrated Mg^{2+} species at faster growth rates, working from the premise that the incorporation of incompletely dehydrated cations would lead to substantially less isotope discrimination. This argument could be expanded to included the incorporation of Mg-complexes more broadly, as density functional theory calculations suggest that the heavy ^{26}Mg isotope partitions preferentially into aqueous Mg-carbonate complexes (Schott *et al.*, 2016). Notably, in the Mavromatis *et al.* (2013) dataset, the ionic strength co-varies with supersaturation and growth rate, raising the possibility that some of the trend towards smaller magnitude fractionations at faster growth rates could be driven by changes in the magnitude of $^{26/24}Mg$ discrimination during Mg^{2+} attachment (smaller magnitude α_f) in higher ionic strength solutions (Figure 3.25). However, the Alvarez *et al.* (2021) experiments were run at a constant ionic strength of 0.2M and the observed $\Delta^{60/58}Ni$ rate dependence is markedly similar to the $\Delta^{26/24}Mg$ rate dependence observed by Mavromatis *et al.* (2013) (Figure 3.25).

This raises the possibility that at least some portion of Mg^{2+} is incorporated as a partially hydrated or otherwise complexed species and that the proportion of complexed Mg^{2+} increases with precipitation rate. It is important to emphasize that the ion-by-ion framework does not currently allow for this possibility; only the incorporation of fully dehydrated monomer ions is considered. Thus the 'carbonate kink blocking' scenario modeled in Figure 3.24 does not represent the variably hydrated impurity cation mechanism proposed by Mavromatis *et al.* (2013) and Alvarez *et al.* (2021) but instead exemplifies an endmember scenario in which all Mg^{2+} attaches rapidly at carbonate kink sites in the absence of the kinetic barrier of complete Mg^{2+}-aquo complex dehydration. Notably, the supersaturation dependence of inhibition predicted by this model scenario is again opposite to that observed experimentally (Figure 3.23D). However, if the Mg^{2+} and Ni^{2+} isotope trends are truly indicative of higher levels of partially hydrated cation incorporation at faster growth rates,

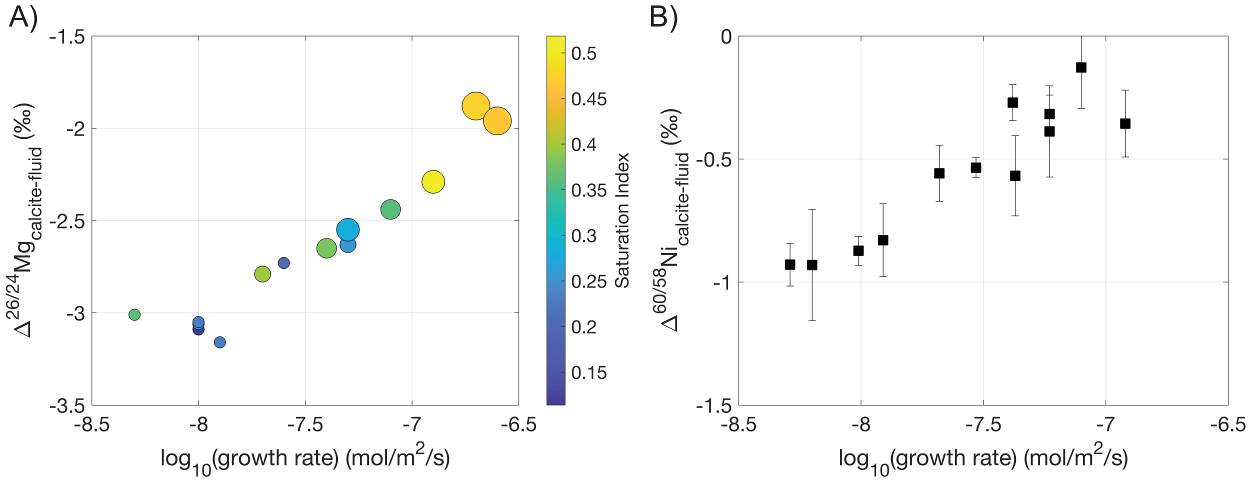

Figure 3.25 – Variation in $\Delta^{26/24}Mg_{calcite-fluid}$ (A) and $\Delta^{60/58}Ni_{calcite-fluid}$ (B) with growth rate from inorganic calcite precipitation experiments of Mavromatis *et al.* (2013) and Alvarez *et al.* (2021), respectively. In A, the marker size denotes solution ionic strength, which varied between 0.1-0.6M; larger markers correspond to higher ionic strengths. Both $\Delta^{26/24}Mg_{calcite-fluid}$ and $\Delta^{60/58}Ni_{calcite-fluid}$ exhibit a log-linear correlation with growth rate, opposite to that observed for $\Delta^{44/40}Ca_{calcite-fluid}$. Smaller magnitude fractionations are observed at *faster* growth rates.

this also has important ramifications for the supersaturation dependence of inhibition by Mg^{2+}. For a given $^{\{Mg^{2+}\}}/_{\{Ca^{2+}\}}$, in lower supersaturation solutions we would expect that a smaller proportion of Mg^{2+} is incorporated as a hydrated species, meaning that the full kink-blocking potential of Mg^{2+} is expressed - kink propagation is inhibited by slow Mg^{2+} desolvation of both the aquo-complex and the subsequent Mg^{2+} kink site. But at the faster growth rates experienced in higher supersaturation solutions, the incorporation of partially hydrated Mg^{2+} circumvents the kinetic bottleneck of aquo-complex desolvation, leading to lower levels of rate inhibition. Thus the incorporation of varying levels of partially hydrated Mg^{2+} could help explain the inhibition sensitivity to supersaturation observed experimentally (Figure 3.16D).

In all, the experimental observations and modeling undertaken here demonstrate that Mg^{2+} inhibits calcite growth through a dominantly kink-blocking mechanism, but that mechanism is likely not as simple as ’the Mg^{2+}-aquo complex dehydrates slowly relative to Ca^{2+}’. Instead, this likely represents one endmember scenario, seen in Mg-calcite growth at low supersaturations and net precipitation rates, where the kink-blocking potential of Mg^{2+} is fully expressed. Kink propagation is limited by Mg^{2+} desolvation both during cation attachment and subsequent desolvation of the Mg^{2+} kink site for CO_3^{2-} attachment. But under other solution conditions, Mg^{2+} desolvation during attachment at kink sites may not be kinetically limiting due to the incorporation of hydrated Mg^{2+} complexes. This would lessen the extent of inhibition and magnitude of Mg^{2+} isotope discrimination, but calcite growth would remain significantly inhibited by the kinetics of CO_3^{2-} attachment at Mg^{2+} kink sites. Further elucidation of the nuances of this inhibition mechanism will require a combination of molecular modeling, studies of paired isotope measurements under controlled solution conditions, and extension of our kinetic modeling frameworks to explicitly allow for non-monomer impurity incorporation (Section 3.4.6).

3.4.5 Implications for interpretation of $\Delta^{44/40}$Ca in natural systems

There is significant interest in using measurements of $\delta^{44/40}Ca$ in sedimentary carbonations to reconstruct the isotopic and chemical characteristics of the precipitating fluid (Fantle and Tipper, 2014). This requires knowledge of how various aspects of solution chemistry dictate the magnitude of calcium isotope fractionation as well as a broader understanding of the geochemical context in which the minerals were precipitated, including potential vital effects, closed vs. open-system behavior, and any subsequent recrystallization (Ahm *et al.*, 2018; Higgins *et al.*, 2018; Gussone *et al.*, 2020). In Chapter 2, we demonstrated that $\Delta^{44/40}Ca_{calcite-fluid}$ is less sensitive to solution stoichiometry than originally predicted, which lends more confidence to interpretations of calcite saturation state and associated growth rate from observed fractionations. In this chapter, we have demonstrated that, under the solution conditions investigated here, inhibition of calcite growth through a dominantly kink-blocking mechanism does not measurably influence $\Delta^{44/40}Ca$. Indeed, for a given supersaturation $\Delta^{44/40}Ca$ is independent of inhibition by Mg^{2+} or Mn^{2+}. Calcium isotope fractionation may thus be a useful tool for interpreting calcite supersaturation state, independent of growth rate, in natural systems.

An important caveat is that most natural fluids are significantly more complicated than the solution chemistries investigated here. $\Delta^{44/40}Ca_{calcite-fluid}$ is predicted to be independent of growth rate inhibition only if the inhibition is driven by a mechanism that does not substantially alter the solubility of the calcite lattice (thus increasing the Ca detachment flux). The formation of more complex solid solutions could destabilize the mineral lattice in ways that are difficult to predict. Unpacking how interactions between inhibitor ions (e.g. Mg^{2+} and SO_4^{2-} (Nielsen *et al.*, 2016)) influence calcite growth mechanics also remains an open area of investigation. Fortunately, the results of this work highlight that calcium isotope fractionation, and more broadly stable isotope fractionation, can be used to interrogate the mechanism by which these inhibitors act to inhibit growth - both alone and as part of more complex solution chemistries.

The invariant $\Delta^{44/40}Ca$ with increasing Mg^{2+} leads to two further inferences. First, the difference in $\Delta^{44/40}Ca$ between different calcite faces is likely to be small. Increasing fluid and solid Mg led to progressive expression of the (110) and (100) calcite faces over the (104) face (Figure 3.8) but did not yield measurably different $\Delta^{44/40}Ca$. This is in contrast to the face-specific $\Delta^{44/40}Ca$ in gypsum proposed by Harouaka *et al.* (2014). Second, the consistent $\Delta^{44/40}Ca$ observed here for experiment Mg7 despite significant precipitation of aragonite may suggest that the $\Delta^{44/40}Ca_{calcite-fluid}$ and $\Delta^{44/40}Ca_{aragonite-fluid}$ are more similar during inorganic precipitation than previously believed. Additional data from well-controlled experiments where calcite and aragonite are grown under identical solution conditions is required to further elucidate the differences or lack thereof between calcium isotope fractionation into calcite and aragonite.

3.4.6 Expanding the microkinetic framework: non-monomer incorporation and beyond

The Mn^{2+} and Mg^{2+} partitioning and inhibition patterns observed here point towards non-monomer incorporation of impurity ions during what appears to be otherwise largely classical calcite growth. This implies that our kinetic frameworks need to explicitly include species other than monomer growth units interacting with and ultimately being incorporated into the mineral lattice. Specifically, our results suggest that for Mn^{2+} and Mg^{2+}, cations more strongly hydrated than Ca^{2+}, the species being incorporated at kink sites may be an ion pair, a variably hydrated aquo-complex, or even a larger polynuclear cluster. In the context of the ion-by-ion framework, this will most obviously influence the calculation of kink-site probabilities but could also have important implications for kink nucleation dynamics as well as the magnitude of stable isotope fractionation given our current understanding of cation-desolvation driven mass discrimination (Lammers *et al.*, 2020).

Our observations regarding the importance of understanding y_0 sensitivity to inhibitor concentration as well as the apparent changes in growth mechanism with increasing solution and solid Mn^{2+} also highlight the need to better constrain feedbacks between solution chemistry, interfacial energy, and step density. While it is more straightforward to predict step velocities, scaling step velocities to bulk growth behavior hinges upon assumptions regarding growth mechanism (i.e. simple spiral or 2D nucleation driven growth (Teng *et al.*, 2000)) and step density. Both y_0 and 2D nucleation rate are sensitive to the fluid-mineral interfacial energy. Better parameterizing links between solution chemistry and interfacial energy is thus a key component of linking micro-scale processes at the fluid-mineral interface to bulk behavior and should be a significant focus of future work.

Finally, while we have demonstrated the utility of primary growth unit stable isotope partitioning as a tracer of crystal growth processes, much more could be learned from the fractionation behavior of trace constituents. The potential utility of using Mg^{2+} isotopes to differentiate between inhibition mechanisms was alluded to here, but there are numerous other cations and anions whose both inhibition and isotope fractionation behavior are of geochemical interest, including Ni^{2+} (Alvarez *et al.*, 2021), Ba^{2+}(Mavromatis *et al.*, 2020), Sr^{2+} (Böhm *et al.*, 2012; AlKhatib and Eisenhauer, 2017b), Zn^{2+}(Mavromatis *et al.*, 2019), and ${SO_4}^{2-}$(Barkan *et al.*, 2020). Developing a comprehensive kinetic framework to describe the fractionation of both primary growth units and trace constituents would both provide a stronger theoretical foundation for interpreting the solution chemistry dependence of those calcite-based proxies and provide important additional constraints on crystal growth dynamics. Explicitly modeling multiple isotope systems at once would provide additional windows into the surficial dynamics in complex solutions and help unravel interactions between inhibitor species. As described above, this will be complicated by the apparent need to account for varying degrees of complexed species interaction with the growing calcite surface, but additional experimental constraints including coupled bulk-growth and in-situ AFM studies in addition to FTIR quantification of water incorporation could by help circumvent these complications.

3.5 Conclusions

The experimental observations reported here shed light on fundamental aspects of calcite growth in complex solutions. Invariant calcium isotope fractionation during both manganese and magnesium inhibition of calcite growth is indicative of dominantly kink-blocking inhibition behavior. For both cations, which are notably more strongly hydrated than Ca^{2+}, trends in inhibition, partitioning, and isotope fractionation are best explained by non-monomer incorporation of the trace constituent.

The strong growth rate inhibition coupled to large positive K_{Mn} observed at low ${\{Mn^{2+}\}}/{\{Ca^{2+}\}}$ cannot be explained by desolvation rate-limited attachment of Mn^{2+}. Instead, our findings suggest Mn^{2+} attaches to kink sites significantly faster than Ca^{2+}, a pattern inconsistent with the slower desolvation kinetics of the Mn^{2+}-aquo complex. We thus posit that the dominant Mn^{2+} species interacting with kink sites is not the free ion in solution but instead an ion pair, hydrated species, or possibly larger polynuclear cluster. Growth kinetics are then limited by a carbonate-based kink blocking mechanism, driven by slow re-orientation kinetics of carbonate ions that have formed an inner-sphere complex with Mn^{2+} at the surface but must reorient to incorporate into the lattice and/or slow surface desolvation of Mn-occupied kink sites.

For Mg^{2+}, we find that experimental trends are broadly consistent with growth inhibition driven by slow Mg^{2+}-aquo complex dehydration relative to Ca^{2+}. However, that mechanistic explanation likely represents one endmember scenario, seen in Mg-calcite growth at low supersaturations and net precipitation rates. During growth at faster net precipitation rates, our findings are consistent with the incorporation of partially hydrated or otherwise complexed Mg^{2+}, as proposed by Mavromatis *et al.* (2013) and Alvarez *et al.* (2021) to explain the rate dependence of Mg^{2+} and Ni^{2+} isotope fractionation during calcite growth. Under these solution conditions, Mg^{2+} desolvation during attachment at kink sites may not be kinetically limiting due to the incorporation of Mg^{2+} complexes, but calcite growth would remain significantly inhibited by the kinetics of CO_3^{2-} attachment at Mg^{2+} kink sites.

Taken together, these findings are evocative of a larger potential trend: that trace constituent cations with aquo-complex desolvation rates significantly slower than the mineral growth rate will be incorporated as a non-monomer species. Additional systematic studies of divalent cation partitioning, inhibition, and stable isotope fractionation behavior of inhibitor cations spanning a range of hydration strengths (e.g. Ni^{2+} to Ba^{2+}) for both calcite and other mineral systems (e.g. sulfate and phosphates) will help test and refine this hypothesis. If supported by findings in other mineral systems, this behavior would have major implications not only for our understanding of the isotopic fractionation of trace species but also fundamental aspects of crystal growth, from defect formation to the controls on the transition from classical to non-classical growth pathways.

Chapter 4

Unpacking controls on soil CO_2 production along a climate gradient in the Mojave Desert

Abstract

Carbon cycling in dryland ecosystems is increasingly recognized as an important component of global carbon fluxes yet significant uncertainty remains regarding the primary controls on surface-atmosphere CO_2 exchange in these ecosystems. Here, we report measurements of two years of meteorological and soil conditions (CO_2 concentration, water content, and temperature to 125cm depth) from soils along an elevation gradient in the Mojave Desert. Observations include both inter- and under-canopy soils. We analyze this spatially and temporally rich dataset of CO_2 measurements in a production-diffusion framework to investigate how the sensitivity of CO_2 production to environmental conditions varies with depth in the soil profile and spatially on scales of meters to kilometers. We find that the sensitivity of CO_2 production to temperature and water availability is not constant across the soil profile: shallow soil layers (2.5-15cm depth) are significantly more water sensitive than deeper portions of the soil profile. The sensitivity of soil CO_2 production to temperature and water availability also varies with elevation: CO_2 production at the highest temperature, lowest elevation site is substantially less temperature sensitive than the higher elevation sites, particularly in shallow regions of the soil profile (Q_{10} 1.65-1.9 at the lowest elevation site vs. 2.7-3.5 at the mid- and high-elevation sites).

We demonstrate that soil CO_2 production is generally well-described by temperature and water content-dependent functions of shallow heterotrophic respiration that declines exponentially with depth and autotrophic respiration that follows the root distribution profile. Production-diffusion models driven by measured soil temperature and water content capture CO_2 dynamics throughout the soil profile, reflecting the soil carbon cycle response to both transient intervals of enhanced moisture availability and seasonal changes in environmental boundary conditions. However, we also document repeated episodes of significant nighttime CO_2 production in the shallowest soils of the more densely vegetated, higher elevation sites, that are not associated with any measurable change in water content. We interrogate poten-

tial mechanistic drivers for these nighttime CO_2 pulses and argue that they may be driven by the delivery of liquid water to the litter layer and surficial soils via water vapor deposition and potentially dew formation, which stimulates microbial respiration in the uppermost centimeters of the soil profile. Altogether, these results highlight the highly dynamic nature of soil respiration in arid ecosystems and provide important quantitative constraints on the response of soil CO_2 production to changing environmental conditions.

Parts of this chapter were previously published in Mills *et al.* (2020).

4.1 Introduction

Understanding how global soil carbon stocks and soil-atmosphere CO_2 fluxes will respond to both long-term climate change and shorter-term perturbations from land use change is imperative for effective climate change mitigation policy (Crowther *et al.*, 2016; Bradford *et al.*, 2016; Paustian *et al.*, 2016). Soils represent the largest terrestrial repository of organic carbon, with approximately 2400Pg C, equivalent to roughly 3 times the amount of carbon currently contained in the atmosphere as CO_2 (Jobbágy and Jackson, 2000; Batjes, 2014). It has been estimated that 133Pg C has been lost from the top 2m of soil due to agricultural land use over the course of human history (Sanderman *et al.*, 2017), resulting in a large 'carbon debt' that is the target of efforts to increase soil carbon stocks as a negative emissions strategy (Paustian *et al.*, 1997; Lal, 2004; Paustian *et al.*, 2016; Soussana *et al.*, 2019). The storage of organic carbon in soils is determined by the balance of carbon inputs, generally as plant biomass, and carbon losses, largely through heterotrophic respiration (Amundson, 2001). The response of heterotrophic respiration to rapidly changing environmental boundary conditions in both managed and natural systems is thus a critical but highly uncertain component of modeling future carbon cycle trajectories (Exbrayat *et al.*, 2013; Bradford *et al.*, 2016; Bond-Lamberty *et al.*, 2018).

Dryland soils are not particularly organic carbon-rich, but because they cover approximately 40% of the terrestrial land surface (Schimel, 2010) they are potentially an underappreciated contributor to the Earth's carbon and climate system. For example, recent global biome model studies have demonstrated that the inter-annual variability in atmospheric CO_2 concentration is correlated to biosphere-atmosphere CO_2 exchange in arid and semi-arid regions (Poulter *et al.*, 2014; Ahlström *et al.*, 2015). Much of this year-to-year variability is thought to be driven by temperature and water availability effects on productivity and respiration in drylands (Jung *et al.*, 2017).

Testing and improving upon existing quantitative frameworks for modeling the interplay between soil carbon cycling and environmental conditions in arid systems is thus an important component of improving projections of climate-carbon feedbacks and future biosphere-atmosphere CO_2 exchange. But developing predictive models of carbon cycling in such highly water-limited ecosystems is complicated by a number of factors. Biogeochemical cycling in dryland systems is tightly linked to ephemeral episodes of substantial moisture availability (Noy-Meir, 1973), meaning that small shifts in the magnitude and timing of precipitation can lead to large changes in carbon dynamics (Reed *et al.*, 2012). Dryland ecosystems are also known for their spatial heterogeneity, where 'islands of fertility' formed under shrub canopies due to the preferential accumulation of carbon and nutrients (Charley and West, 1975; Schlesinger *et al.*, 1996; Pointing and Belnap, 2012) can have significant impacts on localized soil respiration and CO_2 fluxes (Wang *et al.*, 2015; Tucker and Reed, 2016). In addition, it is important to recognize that organic carbon is not the sole, and oftentimes not the dominant, carbon phase present in arid soils (Schlesinger, 1982). Inorganic carbon in the form of pedogenic carbonate comprises approximately 38% of the total global soil carbon pool (Lal, 2004; Eswaran *et al.*, 2000; Hirmas *et al.*, 2010), and is concentrated in arid regions. The interplay between soil organic and inorganic carbon cycling and specifically the influence of the soil carbonate system on CO_2 dynamics is increasingly recognized as a critical aspect of interpreting CO_2 fluxes in arid systems (Parsons *et al.*, 2004; Kowalski *et al.*, 2008; Roland *et al.*, 2013; Rey, 2015; Wang *et al.*, 2020).

4.1.1 Investigation goals

The second half of this thesis is part of a larger effort to build a predictive understanding of coupled organic-inorganic carbon cycling in arid systems (Mills *et al.*, 2020). This study centers around a series of soils along a climate gradient in the Mojave Desert, termed a climosequence (Jenny, 1941), which we equipped for long-term monitoring of meteorological and soil conditions in January 2017. The Mojave Desert, located in the far southwestern region of North America, is the smallest and driest of the North American deserts (Thomey *et al.*, 2014) and is experiencing rapid and widespread environmental change. Significant warming has occurred over the past 100 years in the southwestern U.S., most markedly in the Mojave region (Anderegg and Diffenbaugh, 2015). The aridification of western North America is expected to proceed and accelerate in the next century, perhaps most severely in the southwestern U.S. (Seager *et al.*, 2013; Cook *et al.*, 2015). Additionally, open shrubland vegetation in the Mojave Desert region is being converted to solar energy facilities and other developed landcover types (Soulard and Sleeter, 2012; Hernandez *et al.*, 2015), accompanied by substantial perturbations to soils, vegetation, and biogeochemical cycling. The potential ramifications of this development are just beginning to be understood.

Our overarching goal with this work was to build a predictive understanding of how the organic and inorganic carbon cycles in Mojave Desert soils will respond to both 21st century climate change and acute land-use change perturbations. In this chapter, I focus on interrogating the primary controls of soil CO_2 production in these systems and developing a quantitative framework to describe the sensitivity of soil respiration to environmental conditions. In particular, I focus on developing a predictive understanding of CO_2 production throughout the soil profile, as well the meter- and kilometer-scale spatial heterogeneity of that production. Historically, studies have primarily focused on monitoring CO_2 fluxes at the soil surface, which provide an integrated measurement of subsurface processes. Here, we implement in-situ monitoring of soil temperature, water content, and CO_2 concentration to 125cm depth to investigate the controls on CO_2 dynamics throughout the full soil profile. We find that variations in CO_2 concentration with depth and through time are well-described using a CO_2 production-diffusion model driven by temperature and water-content dependent heterotrophic and autotrophic respiration functions, but also identify and discuss anomalous episodes of nighttime CO_2 production that may have important implications for our understanding of the short-timescale dynamics of soil biogeochemical cycling in these highly water-limited ecosystems.

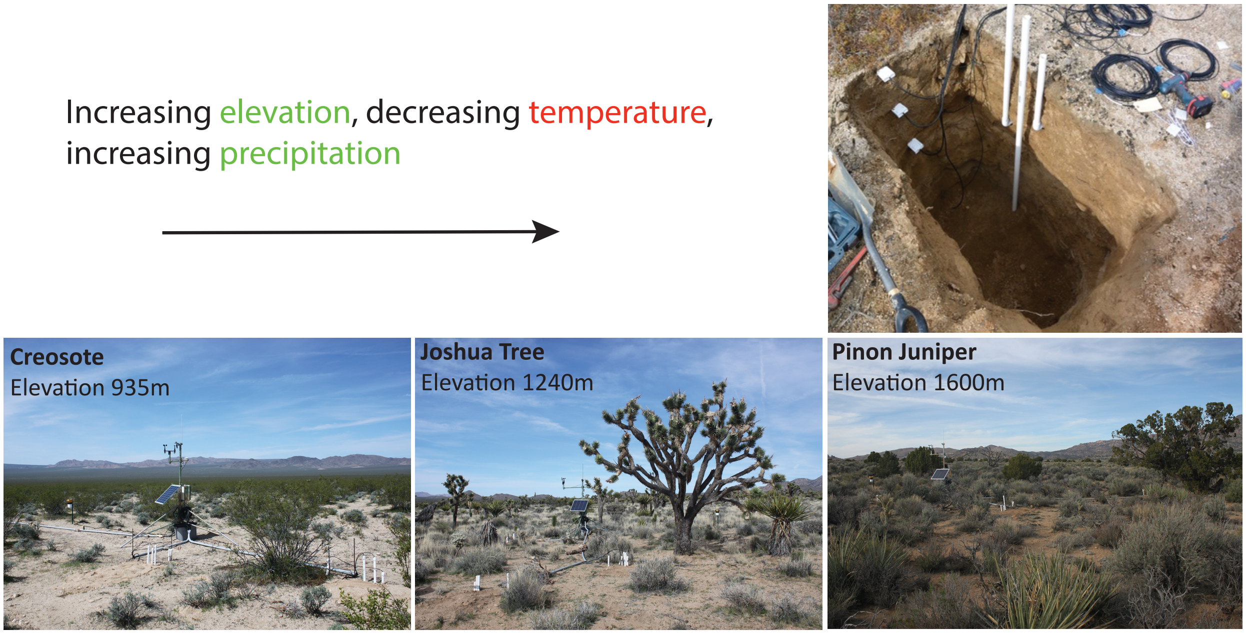

Figure 4.1 – Mojave study sites. Top: soil pit showing in-situ monitoring instrumentation. Bottom: Climosequence sites along an elevation gradient spanning the three major Mojave ecological zones.

4.2 Methods

4.2.1 Climate Transect in the Mojave National Preserve

In order to capture the spatial and temporal variability in soil carbon cycling in the Mojave, in January of 2017, a series of sites along a climate/elevation gradient in the Mojave National Preserve was sampled and instrumented for long-term monitoring of meteorological and soil conditions. The sites are all located on late-Pleistocene granitic alluvium and encompass the three major vegetation/ecosystem types in the Mojave: low elevation Creosote shrubland, mid-elevation Joshua tree dominated shrubland, and a high elevation mixed Pinyon/Juniper woodland (Figure 4.1). The lowest-elevation site is the hottest and driest site; mean annual precipitation increases with elevation while temperature decreases with elevation (Table 4.1).

Each site was instrumented with a weather station recording measurements of air temperature, pressure (278, Setra, Boxborough, MA, USA), relative humidity (HMP60, Vaisala Helsinki Finland), solar radiation (PQS 1, Kipp and Zonen, Delft, The Netherlands), windspeed and direction (03002, R.M. Young, Traverse City, MI, USA), and precipitation (TR-525M, Texas Electronics, Dallas, TX, USA) at 10 minute intervals. Three soil pits were excavated to a depth of >1.3m at each site - one directly adjacent to the dominant vegetation (i.e. next to a creosote bush or joshua tree) such that in-situ sensors would record the rhizosphere in close proximity to the above-ground biomass, and two on patches of intercanopy bare soil. Soil horizons were identified and characterized in the field for root, gravel, and carbonate content, after which approximately 2kg of soil from each horizon was collected for further analysis. Soil samples were collected in ziploc bags, sealed in the field and brought back to the laboratory. A bulk density core was taken at 5cm, 25cm, 50cm,

Site	Latitude	Longitude	Elevation (m)	MAP (mm)†	MAT (°C)†
Creosote	35.10613	-115.55074	935.4	156	18.3
Joshua Tree	35.16912	-115.480106	1252.7	185	16.4
Pinon-Juniper	35.195799	-115.347572	1601.1	224	14.5

Site	Profile	Vegetation	Notes
Creosote	1	Interspace	Adjacent to intact biological soil crust
	2	Vegetated (primary)	Adjacent to the canopy of a large creosote shrub
	3	Mixed	No CO_2 measurement
Joshua Tree	1	Interspace	Deepest measurement at 80cm due to the presence of an indurated layer at 90cm
	2	Vegetated (primary)	Adjacent to the canopy of a joshua tree.
	3	Mixed	No CO_2 measurement
Pinyon Juniper	1	Mixed	Not true interspace; adjacent to small shrubs and annual grasses
	2	Mixed	Not true interspace; adjacent to small shrubs and annual grasses
	3	Vegetated (primary)	Adjacent to the canopy of a juniper shrub. No CO_2 measurement.

Table 4.1 – Climosequence site locations and profile descriptions. †Climate data are 1991-2020 normals generated with the ClimateNA v.7.00 software package, available at http://tinyurl.com/ClimateNA (Wang *et al.*, 2016).

and 125cm. Vegetation cover and composition were quantified with five 50m random line-intercept transects. Field descriptions as well as complete characterizations of soil physical and chemical properties can be found in Appendix C.

Each soil pit was then equipped with in-situ sensors for volumetric water content, electrical conductivity, temperature (CS615, Campbell Scientific, Logan, UT, USA), and soil water potential (MPS6, Meter, Pullman, WA, USA) at depths of 5cm, 25cm, 50cm, and 125cm. These sensors were installed directly into the exposed wall of the soil pit where the soil surface remained undisturbed. For two pits at each site, soil CO_2 sensors were also installed at the same depths. A cylindrical cavity was excavated 20cm into the exposed pit face to accommodate a length of 1 inch diameter PVC tubing, which was coupled to a vertical length of PVC tubing running to the soil surface by a 90-degree elbow. The pits were then backfilled with soil and solid-state soil CO_2 sensors (GMP 252, Vaisala Inc., Vantaa, Finland) were lowered to the PVC elbow. The vertical PVC tubing was capped and sealed with silicone sealant above the soil surface. Meteorological and in-situ soil sensor data were logged at ten minute intervals with a Campbell Scientific data logger (CR1000, Campbell Scientific, Inc., Logan UT, USA).

4.2.2 Ex-situ soil analysis

Soil samples were dried in a 50°C oven and sieved to separate the gravel size fraction from the <2mm size fraction. Soil physical characteristics (water content, gravel content, and bulk density) were measured for every soil pit. Creosote 1, Joshua Tree 3, and Pinyon Juniper 1 were selected as sparsely vegetated profiles at each site for further analysis. For these pits, particle size distribution, bulk mineralogy, organic carbon and nitrogen content and isotopic composition, carbonate content and isotopic composition, and soil water chemistry (via saturated paste extracts) were characterized for each horizon.

Aliquots from the <2mm size fraction were ground to a fine powder in a mortar and pestle. Bulk mineralogy was characterized using powder X-Ray diffraction. Samples were analyzed on a PANalytical X-Pert Pro diffractometer equipped with a Co x-ray source; data was collected between 3° and 100° 2θ. Peak fitting and identification was performed with X'Pert HighScore Plus and phase abundance was estimated via the Reference Intensity Ratio (RIR). Particle size distribution and saturated paste extracts were analyzed by the UC Davis Analytical Lab using standard techniques.

4.2.2.1 Organic C, N content and isotope analysis

An aliquot of the ground sample was soaked in 0.5M HCl for 24 hours to remove any carbonate and subsequently vacuum filtered (0.45mm nylon membrane filter) and washed 3x with deionized water. Decarbonated samples were then oven dried at 50°C. Soil organic C and N content and isotopic composition were measured by continuous flow dual isotope analysis using a CHNOS Elemental Analyzer (vario ISOTOPE cube, Elementar, Hanau, Germany) interfaced to an IsoPrime 100 mass spectrometer (Isoprime Ltd, Cheadle, UK) at the Center for Stable Isotope Biogeochemistry at the University of California, Berkeley. Carbon and nitrogen isotopic compositions are reported in standard delta notation as per mil (‰)

deviations from Vienna Pee Dee Belemnite (VPDB) and atmospheric N_2, with an external precision of ± 0.10‰ and ± 0.20‰, respectively for $^{13}C_{organic}$ and $^{15}N_{organic}$.

4.2.2.2 Carbonate content and isotopes

Soil carbonate content and isotopic composition were measured using a MultiCarb system in line with a GV IsoPrime mass spectrometer in Dual Inlet at the Center for Stable Isotope Biogeochemistry at the University of California, Berkeley. Carbon and oxygen isotopic compositions are reported in standard delta notation as per mil (‰) deviations from VPDB, with an external precision of ± 0.05‰ and ± 0.07‰, respectively for $^{13}C_{carb}$ and $^{18}O_{carb}$.

4.2.3 Data quality assurance and gap-filling

Soil pits were excavated and in-situ monitoring commenced in January, 2017 but the first 6 months of data were discarded as the soil returned to quasi steady-state after the excavation disturbance and re-compacted, and initial issues with data collection were resolved. In cases of subsequent instrument failure, we gap filled select data streams based on data from other sites or profiles. For gaps in precipitation, soil temperature, volumetric water content, and air temperature that were longer than one day, missing data were estimated using linear regressions to equivalent measurements at the nearest site.

For the Creosote and Joshua Tree sites, we constrained our quantitative interpretation of CO_2 dynamics to September 2017-January 2019, when CO_2 concentration measurements were best calibrated and available throughout the profile. Robust CO_2 measurements were maintained through September 2019 at the Pinyon Juniper site, so two full years of data were considered, accounting for a measurement gap from July 15, 2018 - August 22, 2018 due to instrument failure. CO_2 dynamics were considered from August 1, 2017 - July 15, 2018 and September 1, 2018 - September 1, 2019 at that site.

4.2.3.1 Correcting VWC measurement temperature dependence

The volumetric water content sensors employed here are reflectometers that measure changes in the dielectric permittivity of the soil (water is the main contributor to the bulk dielectric permittivity). But the permittivity of water changes with temperature, so the VWC measurement is also somewhat temperature sensitive. A single, well-defined correction for this temperature dependence does not exist; the effect of temperature on the soil permittivity is related to soil-specific properties such as porosity and permittivity. Here, we follow Saito *et al.* (2009) and use the diurnal fluctuation in temperature and $\text{VWC}_{\text{measured}}$ during periods where VWC is not changing rapidly to calibrate $\frac{dVWC}{dT}$ as a function of water content. A temperature-corrected VWC was then produced by subtracting $\frac{dVWC}{dT}(VWC)$*(T-25) from the raw VWC data.

4.2.4 CO_2 flux and production calculations

Assuming that CO_2 production and transport via molecular diffusion are the dominant processes controlling CO_2 concentrations in a soil profile, the change in $[CO_2]$ with time at a given depth z can be expressed as:

$$\varepsilon(z,t)\frac{\partial C(z,t)}{\partial t} = D_s(z,t)\frac{\partial^2 C(z,t)}{\partial z^2} + P(z,t) \tag{4.2.1}$$

where C is the molar CO_2 concentration (mol/m^3), ε is the air-filled porosity, D_s is soil CO_2 diffusivity (m^2/s), and P is the CO_2 production rate (mol/m^3/s). Assuming the profile is at steady-state, the left hand size of Eq. 4.2.1 is zero, meaning that CO_2 production at every depth is matched by diffusion:

$$P(z) = -D_s(z)\frac{\partial^2 C(z)}{\partial z^2} \approx -D_s(z)\frac{C(z+\Delta z) + C(z-\Delta z) - 2C(z)}{\Delta z^2} \tag{4.2.2}$$

This allows for the calculation of a continuous CO_2 production profile with depth from continuous depth profiles of CO_2 concentration and diffusivity. It should be noted that the steady-state assumption does not hold generally, particularly during large transient CO_2 production events driven by precipitation, but we use this to derive an initial estimate of CO_2 production and relax the steady-state assumption in a forward, time-dependent model of CO_2 dynamics in Section 4.2.6. Moreover, this production-diffusion framework does not attempt to account for advective or convective transport of CO_2 or for inorganic carbon dynamics, assumptions that are considered in more detail in Chapter 5.

We calculate the soil CO_2 diffusivity ($D_s, m^2/s$) following Moldrup *et al.* (1999) (Eq. 7 in that work):

$$D_s = D_a\left(\phi^2\right)\left(\frac{\varepsilon}{\phi}\right)^{\beta * F_{cp}} \tag{4.2.3}$$

where ϕ is the porosity, ε is the air-filled porosity (ϕ-VWC), β is an empirically fitted parameter taken to be 2.9, F_{cp} is the sand and silt content of the <2mm size fraction ($0 \leq F_{cp} \leq 1$), and D_a is the diffusivity of CO_2 in air, corrected for temperature and pressure:

$$D_a = D_{a0}\left(\frac{T}{293.15}\right)^{1.75}\left(\frac{1.013 * 10^5}{P}\right) \tag{4.2.4}$$

where D_{a0} is 1.47*10-5 m^2/s (Jones, 1992), T is the temperature in K, and P is the pressure in Pa.

The CO_2 flux across various layers in the soil profile (including the surface) can also be calculated using flux gradient theory and Fick's first law of diffusion:

$$F = -D_s(z)\frac{\partial C(z)}{\partial z} \tag{4.2.5}$$

$$F_i = -\left(\frac{D_s(z_i) + D_s(z_{i+1})}{2}\right)\frac{C(z_i) - C(z_{i+1})}{z_{i+1} - z_i} \tag{4.2.6}$$

Once F_i has been calculated for multiple depths in the soil profile, CO_2 production can be calculated from the difference between the fluxes across adjacent layers as a flux divergence (Vargas *et al.*, 2010b):

$$P_i = \frac{F_i - F_{i+1}}{z_{i+1} - z_i} \tag{4.2.7}$$

where $\mathrm{P_i}$ is the soil CO_2 production rate (mol/m^3/s) between depths $\mathrm{z_i}$ and $\mathrm{z_{i+1}}$.

Two approaches can thus be taken to calculate CO_2 production: 1) a continuous CO_2 production function can be estimated from interpolated diffusivity and CO_2 concentration data or 2) production can be estimated for discrete intervals of the profile using the flux divergence method. Extensive testing was undertaken to determine whether various methods for interpolating our discrete depth measurements of CO_2 concentration and diffusivity could yield higher-quality estimates of CO_2 production than the flux divergence method. We determined that no interpolation scheme (e.g. cubic spline, pchip - peacewise cubic hermite interpolation, second or third order polynomial) could produce more reasonable estimates of continuous CO_2 concentrations with depth through time than simple linear interpolation (Figure D1). In particular, splines fits tended to add unrealistic curvature to the interpolated depth profile during periods of high production in shallow soils (e.g. following rain events) while polynomial functions acted to damp [CO_2] in the shallow profile during those intervals.

Moreover, the diffusive flux at depth z_i (and thus production with this steady-state assumption) is defined as the change in slope of the CO_2 concentration profile at z_i, divided by Δz. With a linear interpolation scheme, the slope is constant between discrete CO_2 measurements. Meaning that the calculated CO_2 production profile is zero everywhere except at the measured depths, where the calculated value of production is a function of Δz, i.e. how finely the profile is discretized. Thus to produce a meaningful CO_2 production value, the production calculated at the measured depths must be averaged out over a relevant depth interval, making calculation of CO_2 production from a linearly interpolated continuous profile practically equivalent to the flux divergence method. CO_2 production calculated for different soil depth intervals using the flux divergence method and interpolated profiles described above are compared in Figure D2. The flux divergence method and linear interpolation yield highly comparable results while the polynomial interpolation schemes vastly under-estimate production in the shallow regions of the soil profile. As a final check, we compared the CO_2 surface flux to these CO_2 production values, integrated over the measured portion of the soil profile (Figure D3). In this computational framework, depth-integrated production is equivalent to the net flux out of the soil, i.e. the CO_2 surface flux. Depth-integrated production is reasonably close to the calculated surface flux for all CO_2 production methods tested (Figure D3), but production calculated using the flux-divergence method yields total production values that most closely match the observed surface flux. We thus use the flux divergence method to estimate CO_2 production over discrete soil depth intervals (2.5-15cm, 15-37.5cm, and 37.5-87.5cm) throughout this study.

4.2.4.1 Identification of anomalous nighttime pulses of CO_2

As discussed in-depth in Section 4.3.5, at the higher elevation Joshua Tree and Pinyon Juniper sites, we observed repeated pulses of CO_2 in the shallowest soils (5cm depth) at night that were not associated with rain events. These nighttime pulse events could not be explained by our initial framework of CO_2 production driven by temperature and water-sensitive respiration functions (Section 4.2.6), as they occurred during the coldest part of the day and were not associated with any measurable change in water content. We thus developed an algorithm to identify and remove the seemingly anomalous nighttime pulses from the primary CO_2 production dataset, and analyze the pulse events separately in Section 4.3.5.

Anomalous nighttime pulses were identified by comparing integrated CO_2 production and maximum CO_2 production during the day (8am-8pm) vs. following night (8pm-8am) for every diurnal cycle. This was driven by the rationale that, all else being equal, CO_2 production and thus concentration at night should not be substantially higher than that during the day, due to the positive temperature dependence of both heterotrophic (Davidson and Janssens, 2006) and autotrophic (root) respiration (Palta and Nobel, 1989). Potential anomalous pulses were identified on nights when a) no precipitation was recorded during either the daytime or nighttime interval, and b) either the maximum night/day CO_2 production ratio was >1.1 or the ratio of integrated nighttime to daytime production was >1. These candidate pulses were then manually checked to remove any false positives or negatives and constrain the precise timing of the pulse event. The results of this nighttime pulse identification are shown in Figures D4 and D5 for the Joshua Tree 2 and Pinyon Juniper 2 soil profiles, respectively.

4.2.5 Analysis of dominant controls on daily CO_2 production and anomalous nighttime CO_2 pulses: Decision trees

We employed decision tree analysis to examine the first-order controls on CO_2 production and how those controls vary with depth at a single site and between sites along the elevation gradient (Safavian and Landgrebe, 1991; Vargas *et al.*, 2010a). Decision trees are a supervised machine learning method in which the value of the target variable is predicted based on a series of simple decision rules inferred from the predictor variables provided. A tree is constructed through an iterative process termed binary recursive partitioning in which the training dataset is split into distinct clusters based on the predictor variable and threshold that yield the largest information gain (or reduction in the chosen cost function) (Safavian and Landgrebe, 1991). This yields a hierarchical series of decisions that allows for interpretation of the explanatory nature of the predictor variables. Trees can be constructed to predict either continuous (regression trees) or categorical (classification trees) variables. Here, regression trees were trained to predict daily mean CO_2 production using daily mean values of soil temperature, volumetric water content, gross primary productivity (GPP, derived from the MODIS 8-day dataset linearly extrapolated to daily values (Robinson *et al.*, 2018)), and vapor pressure deficit. Trees were capped at a depth of 3 and minimum node size of 2 was used, meaning that a split would not occur unless 2 samples were contained in the resulting cluster. This small minimum node size was used to allow for prediction of transiently high values of CO_2 production with rain events.

Decision trees were also used to interrogate potential mechanistic drivers of the nighttime CO_2 pulses observed at higher elevation sites (Section 4.3.5). A classification tree was trained to predict the presence/absence of a nighttime pulse and a regression tree was trained to predict the magnitude of the nighttime/daytime CO_2 concentration ratio. In both, the following predictor variables were used: nighttime mean GPP, soil temperature at 5 and 25cm, soil volumetric water content at 5 and 25cm, days since the last rain, the magnitude of the last rain, days since the last major rain (≥10mm in a single day), the magnitude of the last major rain, as well as maximum, minimum, and mean values of the nighttime dew point temperature, relative humidity, air temperature, and the difference between air temperature and the dew point. Trees were capped at a depth of 3 with a minimum node size of 2 and the gini impurity was used as the split quality criterion. All decision tree analyses were performed using scikit-learn in Python (Pedregosa *et al.*, 2011).

4.2.6 Production-diffusion model of CO_2 dynamics

The full time series of CO_2 production over different depth intervals in the soil profile (at 10-minute time resolution) was analyzed in a regression framework to develop a predictive parameterization of CO_2 production as a function of soil conditions. Calculated CO_2 production was first fit to a quasi-mechanistic function that described production as a baseline respiration flux (R_0), scaled by functions of temperature and water content (Eq. 4.2.8):

$$R = R_0 * f(T) * f(\theta) \tag{4.2.8}$$

Functional forms that considered the influence of antecedent water content and primary productivity were also examined. CO_2 production calculated for shallow (2.5-15cm depth) and deeper (15-37.5cm) portions of the soil profile were considered independently. A large array of functional forms have been suggested to describe the sensitivity of soil respiration to environmental conditions (c.f. Sierra *et al.* (2015) and references therein). We thus tested 5 different functions for both the temperature and water content scaling factors, including making the temperature response sensitive to water availability and allowing for sensitivity to antecedent moisture (Table 4.2). It is important to note that we employed measurements of volumetric water content in this analysis as the indicator of soil moisture, instead of soil water potential, as we obtained more complete and interpretable measurements from the water content sensors. Models that employ both water content and potential have been utilized to predict respiration dynamics; reactive transport models with a soil physics subcomponent generally utilize soil water potential as unsaturated flow is modeled in terms of potentials (water flows from regions of high potential energy to lower potential energy) (Simunek and Suarez, 1993). Here, we utilize the more commonly reported water content (Vicca *et al.*, 2012) but note that using water content instead of potential may not fully represent the energy required for plants and microbes to extract water from the soil matrix when limited moisture is available (Moyano *et al.*, 2013; Sierra *et al.*, 2015). We leave a parameterization based on soil water potential for future work.

This yielded descriptions of the sensitivity of soil respiration to environmental conditions for discrete depth intervals in the soil profile. In order to generate continuous predictions of soil CO_2 dynamics with depth and through time, we then fed those respiration functions into a forward, time-dependent production-diffusion model of soil CO_2 concentrations, driven by measured temperature and water content data (Eq. 4.2.1). Importantly, the shallow and deeper soil CO_2 production were found to have distinct temperature and water content sensitivities (Section 4.3.3.2), so in order to capture CO_2 dynamics throughout the entire soil profile, two respiration terms were incorporated into the production-diffusion model (Section 4.3.4.1). The shallow-soil respiration function derived from fitting the 2.5-15cm CO_2

	Function*	Reference
Temperature Dependence		
Arrhenius	$f(T) = e^{\left(\frac{E_0(T-T_{20})}{RTT_{20}}\right)}$	Simunek and Suarez (1993)
Lloyd and Taylor	$f(T) = e^{E_0\left(\frac{1}{T_{10}-T_0} - \frac{1}{T-T_0}\right)}$	Lloyd and Taylor (1994)
Water-sensitive Lloyd and Taylor	$E_0 = E_b * \theta/\theta_{max}$	(Cable *et al.*, 2011)
Q_{10}	$f(T) = a^{(T-T_{10})/10}$	Davidson and Janssens (2006)
Sigmoid	$f(T) = a + \left(\frac{1}{b+c\left(\frac{T_{10}-T}{10}\right)}\right)$	Janssens *et al.* (2003)
Water Content Dependence		
Linear or curvilinear	$f(\theta) = bx + (1-b)x^2; x = \frac{\theta-\theta_0}{\theta_{max}-\theta_0}$	Myers *et al.* (1982)
Exponential	$f(\theta) = e^{(a*\theta)}$	Cable *et al.* (2011)
Exponential with squared term	$f(\theta) = e^{\left(a*\theta+b*\theta^2\right)}$	Tang *et al.* (2005)
Gompertz	$f(\theta) = e^{-e^{(a-b*\theta)}}$	Janssens *et al.* (2003)
Antecedent water content	$f(\theta) = e^{(a*moving\ average(\theta,b))}$	Cable *et al.* (2011)
Productivity Dependence		
Exponential	$f(GPP) = e^{(a*GPP)}$	

Table 4.2 – List of relationships between soil CO_2 production (generally CO_2 efflux) and soil temperature/moisture content previously applied in empirical models and tested here. *Fitted parameters are shown in red and further described in Table D1. In all cases, T is the soil temperature in Kelvin and θ is the volumetric water content (cm^3/cm^3).

production data was taken to be representative of dominantly heterotrophic respiration in the shallow layers of the soil profile, and assigned an exponentially declining depth dependence. This nominally heterotrophic respiration was supplemented with an autotrophic (plant root) respiration function with a depth dependence following the root distribution. The root distribution at each site was derived from field measurements of root density (Tables C1-C3), cross-checked against literature root distribution profiles for the dominant vegetation type at each site (Kemp *et al.*, 1997; Gutiérrez-Jurado *et al.*, 2006; Garcia *et al.*, 2011). The best-fit deeper soil CO_2 production function was used as the initial parameterization of the temperature and water content sensitivity of this autotrophic respiration. The fitted parameters were then re-optimized in the absence of a steady-state assumption using the full forward, time-dependent model in order to better account for CO_2 dynamics throughout the entire 1.25m profile, instead of only the top 40cm. All optimizations were performed by least-squares optimization using the scipy least_squares module in Python (Virtanen *et al.*, 2020); model performance was assessed using the coefficient of determination, root mean squared error, and Akaike Information Criterion (AIC). The CO_2 production-diffusion model (Eq. 4.2.1) was solved by finite difference in Python, using an atmospheric upper boundary condition of measured $[CO_{2,atm}]$ and a no-flux lower boundary.

4.3 Results and Discussion

4.3.1 Site and soil characteristics

Two years of continuous monitoring of meteorological and soil conditions shed light on the interplay between soil CO_2 dynamics and environmental drivers across space and time in Mojave Desert soils. Mean annual meteorological parameters for the September 2017-2019 monitoring interval for each of the climosequence sites are shown in Table 4.3. The first monitoring year captured a relatively warm, dry year compared to long-term climate normals (Table 4.1)[1] with extended dry periods between the winter and summer monsoon seasons while the second monitoring year captured a relatively cool, wet year with extended monsoon intervals. In-situ measurements of soil water content, temperature, and CO_2 concentration for interspace soil profiles at each of the climosequence sites are shown in Figures 4.2-4.4; comparable plots for the under-canopy profiles are shown in Figures D6-D8. Initial examination of this time series data reveals a number of general trends:

- Higher CO_2 concentrations are observed with depth and with elevation, especially at the more densely vegetated, higher elevation sites.
- CO_2 production more closely follows the seasonal temperature cycle at the higher elevation sites, particularly in deeper portions of the soil profile.
- Higher CO_2 fluxes are observed in under-canopy versus intercanopy profiles, particularly at the most arid Creosote site.

Now considering the mid-elevation, Joshua tree, site in further detail (Figure 4.3), we observe that in-situ CO_2 concentrations are tightly coupled to concurrent soil temperature and moisture availability. Moving forward in time from September 2017, CO_2 concentrations decline as the soil dries down over an extended (4-month) dry period, before rebounding with the onset of the winter monsoon rains. But the most significant episodes of CO_2 production and thus highest concentrations throughout the profile are not observed until the summer monsoon rains, at the peak of the seasonal temperature cycle. These data also highlight the fact that water availability in the uppermost portions of the soil profile is highly dynamic, with transiently high water contents in response to rain events followed by markedly low water contents ($<1\%$ VWC) over dry periods. In contrast, measured water content in the deeper portions of the soil profile remains relatively constant through time, maintaining higher VWC throughout the dry season but only receiving significant pulses of moisture during the largest rain events. This is coupled to a significantly damped diurnal temperature oscillation moving from surficial soils to >50cm depth. We quantitatively interrogate these patterns through the lens of building a predictive understanding of CO_2 production in arid soils in the following sections.

The high spatial resolution dataset produced here also allows us to examine how soil conditions vary both across sites (km-scale variability) and within sites (m-scale variability). Box and whisker plots of soil hourly temperature, water content, CO_2 concentration, and

---

[1] The high total precipitation for September 2017-2018 at the Creosote site is due to large rain events in early September 2017 and August 2018.

		Mean Annual Meteorological Conditions			
Site	Year	Air Temp. (°C)	Precipitation (mm)	RH	VPD (kPa)
Creosote	Sept 2017-2018	19.36	177.4	28.18	1.98
	Sept 2018-2019	18.24	133.5	33.08	1.86
Joshua Tree	Sept 2017-2018	17.61	142.65	30.83	1.7
	Sept 2018-2019	15.99	189.2	36.05	1.56
Pinyon Juniper	July 2017-2018	14.76	170.5	33.42	1.38
	Sept 2018-2019	13.16	272.1	40.09	1.25

Table 4.3 – Mean annual meteorological conditions measured at the climosequence sites from September 2017-2019. RH: relative humidity; VPD: vapor pressure deficit.

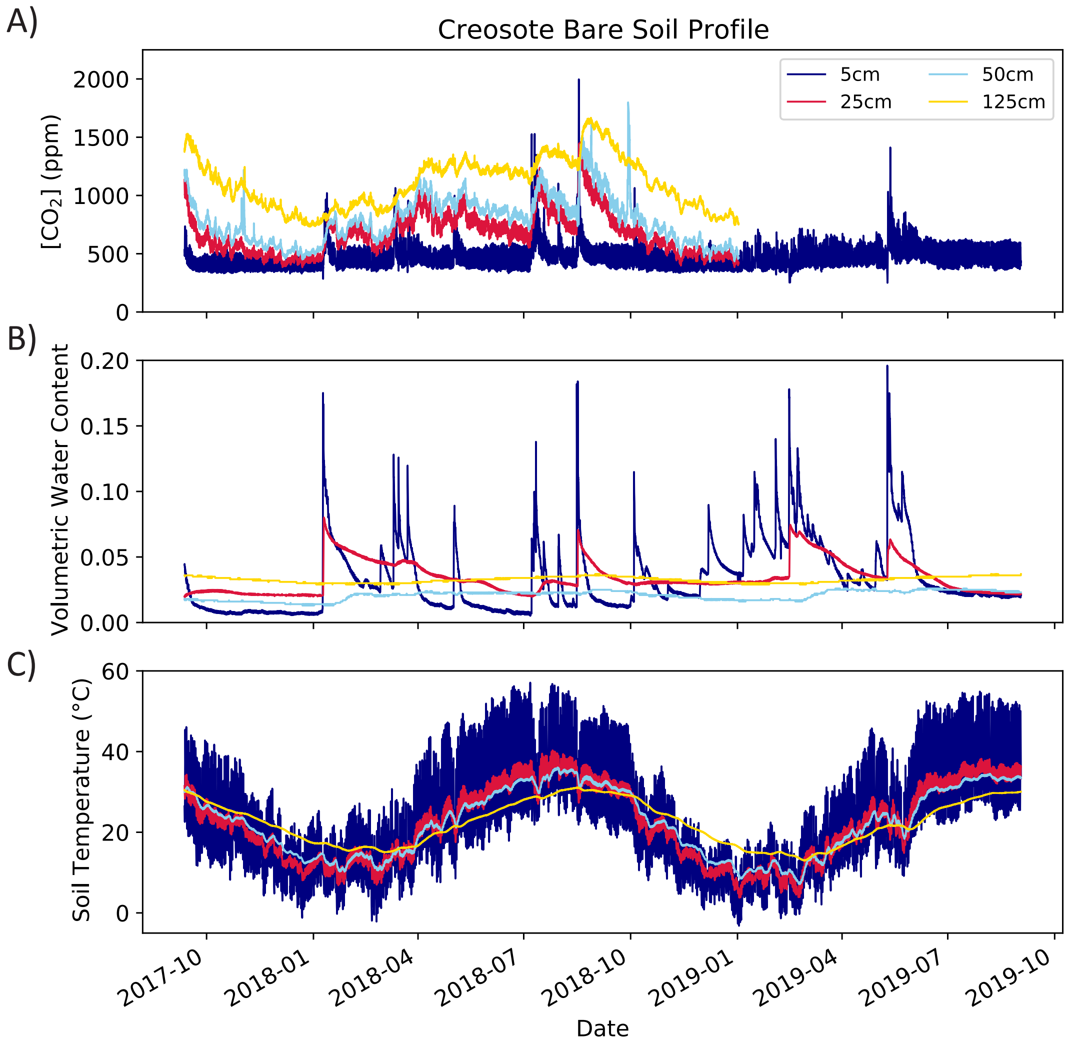

Figure 4.2 – Two years of in-situ monitoring data (10-minute resolution) from the bare-soil profile at the most arid climosequence site, Creosote: A) soil CO$_2$ concentration, B) volumetric water content, and C) temperature. Colors denote depth in soil profile. Data from the under-canopy soil profile at the same site is shown in Figure D6.

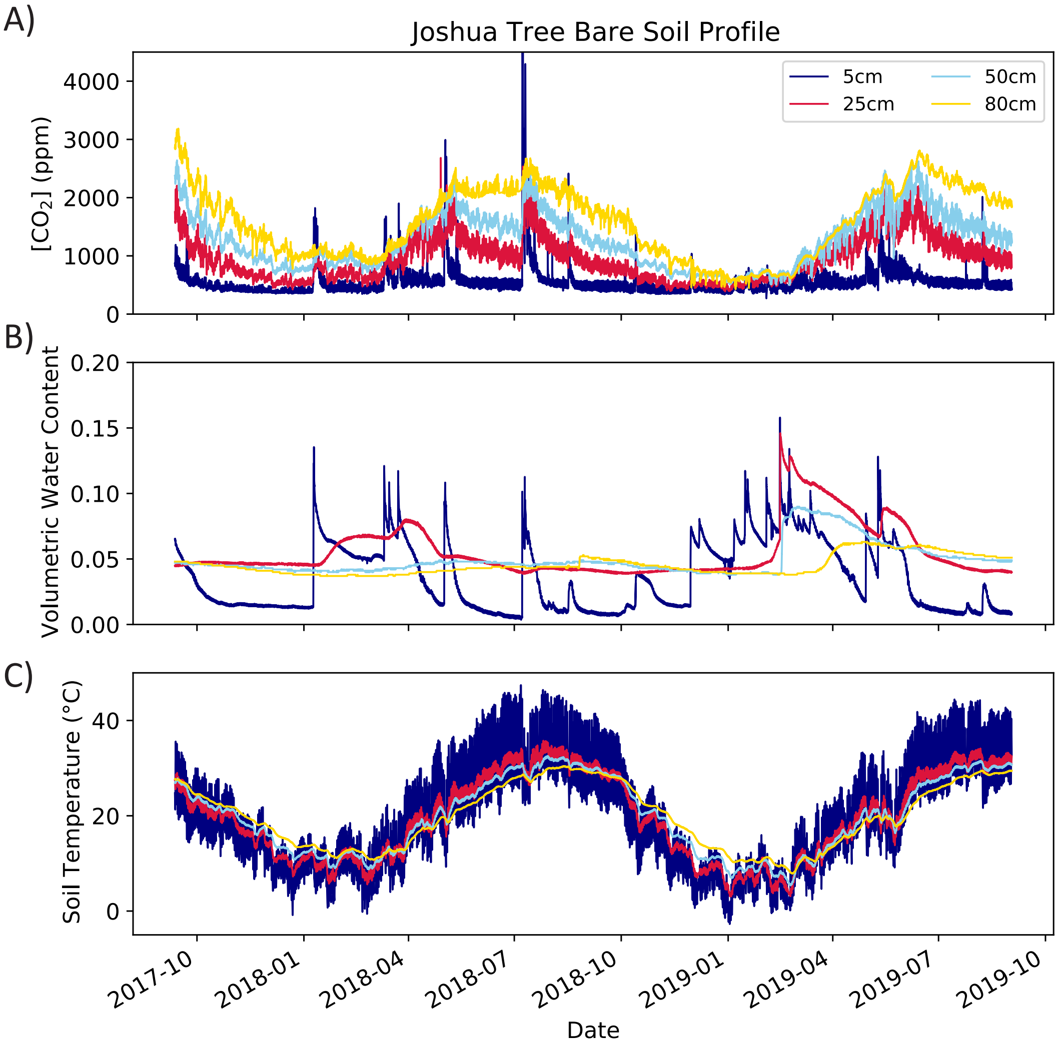

Figure 4.3 – Two years of in-situ monitoring data (10-minute increments) from the bare-soil profile at the mid-elevation, Joshua Tree, site: A) soil CO_2 concentration, B) volumetric water content, and C) temperature. Colors denote depth in soil profile. Note the lowest measurement depth in the soil profile is only 80cm due to the presence of a cemented hardpan which prevented excavation past 90cm. Data from the under-canopy soil profile at the same site is shown in Figure D7.

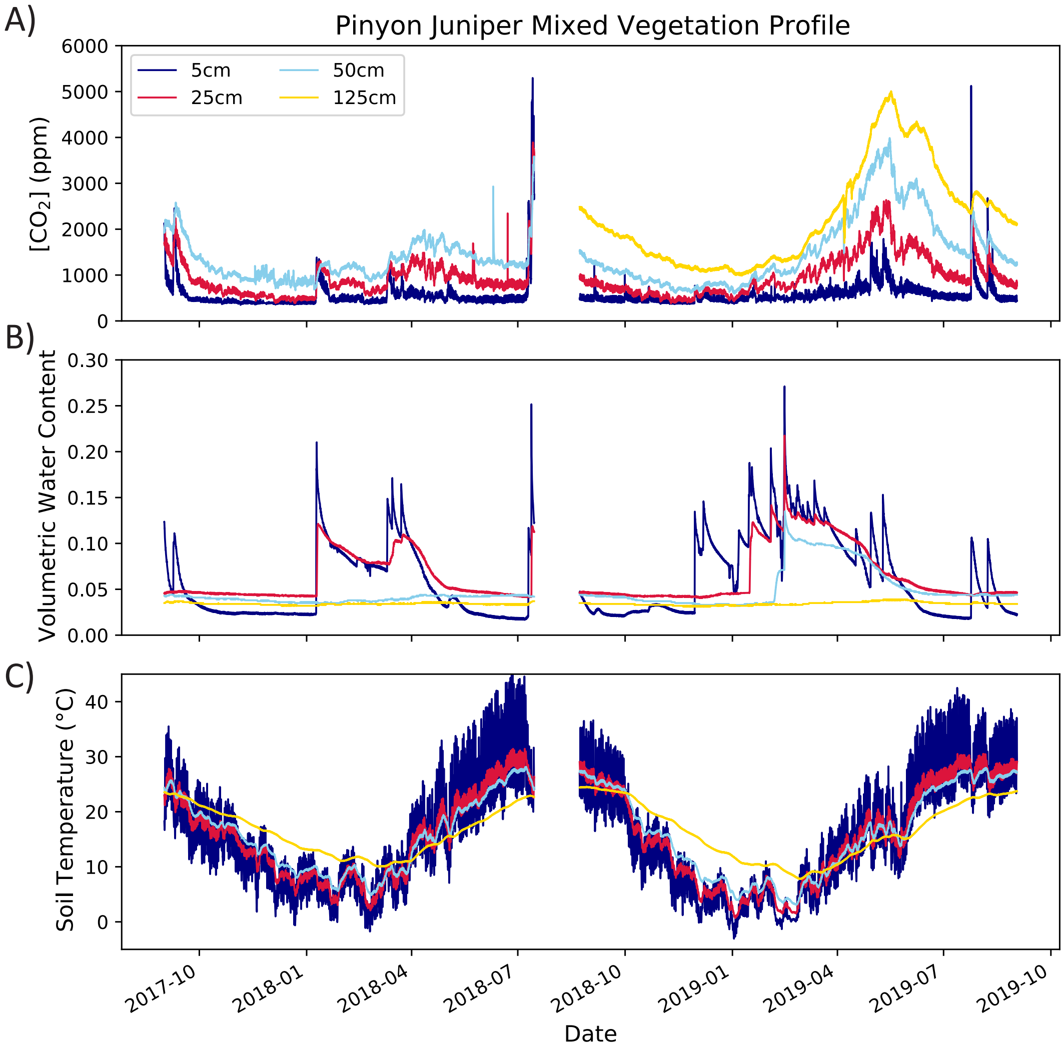

Figure 4.4 – Two years of in-situ monitoring data (10-minute increments) from the PJ-1 soil profile with mixed vegetation at the highest elevation, Pinyon Juniper, site: A) soil CO_2 concentration, B) volumetric water content, and C) temperature. Colors denote depth in soil profile. Data from the PJ-2 soil profile at the same site is shown in Figure D8.

the diurnal temperature range with depth for the 9 profiles monitored are shown in Figure 4.5. As expected, median soil temperatures decrease monotonically with elevation across the climosequence (Figure 4.5A) but remain relatively constant with depth and between profiles at a single site; only slightly higher temperatures are observed in shallow layers of under-canopy soil profiles. The magnitude of the diurnal temperature fluctuation (daily maximum - minimum temperature), however, exhibits strong inter- and intra-site variability, particularly in the shallow portions of the soil profile (Figure 4.5B). The daily temperature range declines with elevation but is also significantly smaller in under-canopy profiles than interspace or more sparsely vegetated sites. Intra-site differences in soil water content varies between sites (Figure 4.5C). At the most arid site, the median water content is lowest in the under-canopy profile, possibly due to root water uptake in the upper portions of the soil profile. In contrast, under-canopy profiles exhibit higher median water contents and a smaller range in VWC than interspace or more sparsely vegetated profiles at the higher elevation sites, perhaps due to the influence of shading on evaporation or hydraulic lift (Yoder and Nowak, 1999). Finally, as noted above, higher CO_2 concentrations are observed with increasing elevation and in under-canopy profiles, likely due to a combination of higher autotrophic respiration and the concentration of organic carbon and nutrients in 'islands of fertility' surrounding shrub canopies (Charley and West, 1975; Schlesinger *et al.*, 1996; Pointing and Belnap, 2012).

4.3.2 Primary controls of daily CO_2 production

In order to examine the first-order controls on CO_2 production and how those controls vary with depth at a single site and between sites along the elevation gradient, we trained regression trees to predict measured CO_2 production data on a daily timescale (Section 4.2.5). The goal of this exercise was to determine and visualize the key predictors of soil CO_2 production in the absence of assumptions regarding how various parameters influence net production. A regression tree represents a hierarchical series of decisions where the predictor variable and threshold that yield the largest information gain for predicting the target variable are identified in each successive branch. The initial branches thus represent the most 'information-rich' series of delineations, thereby providing a visual description of the key controls on CO_2 production in these soils.

Regression trees were trained to predict measured daily CO_2 production using soil temperature, water content, vapor pressure deficit (kPa), and primary productivity (GPP, units of $gC/m^2/8$-day) as predictor variables. Trees were trained for each soil profile individually, examining production in both shallow (2.5-15cm) and deeper (15-37.5cm) soil layers. Regression trees for the under-canopy soil profile at the mid-elevation Joshua Tree site are shown in Figure 4.6A,B; the resultant model predictions are compared to measured data in Figure 4.6C,D. In the shallow soil horizons (Figure 4.6A), water content is the first branch point - high levels of production are predicted only for soils with >7% VWC. A temperature filter is then applied in the next branch point: for moist soils, higher levels of production are seen when the soil temperature is above 24°C. Water availability then again dictates the production magnitude: production is highest when the soil temperature is above 24°C and water content is >8%. In contrast, primary productivity is the first branch point for the prediction of CO_2 production in deeper soils (Figure 4.6B). The highest levels of pro-

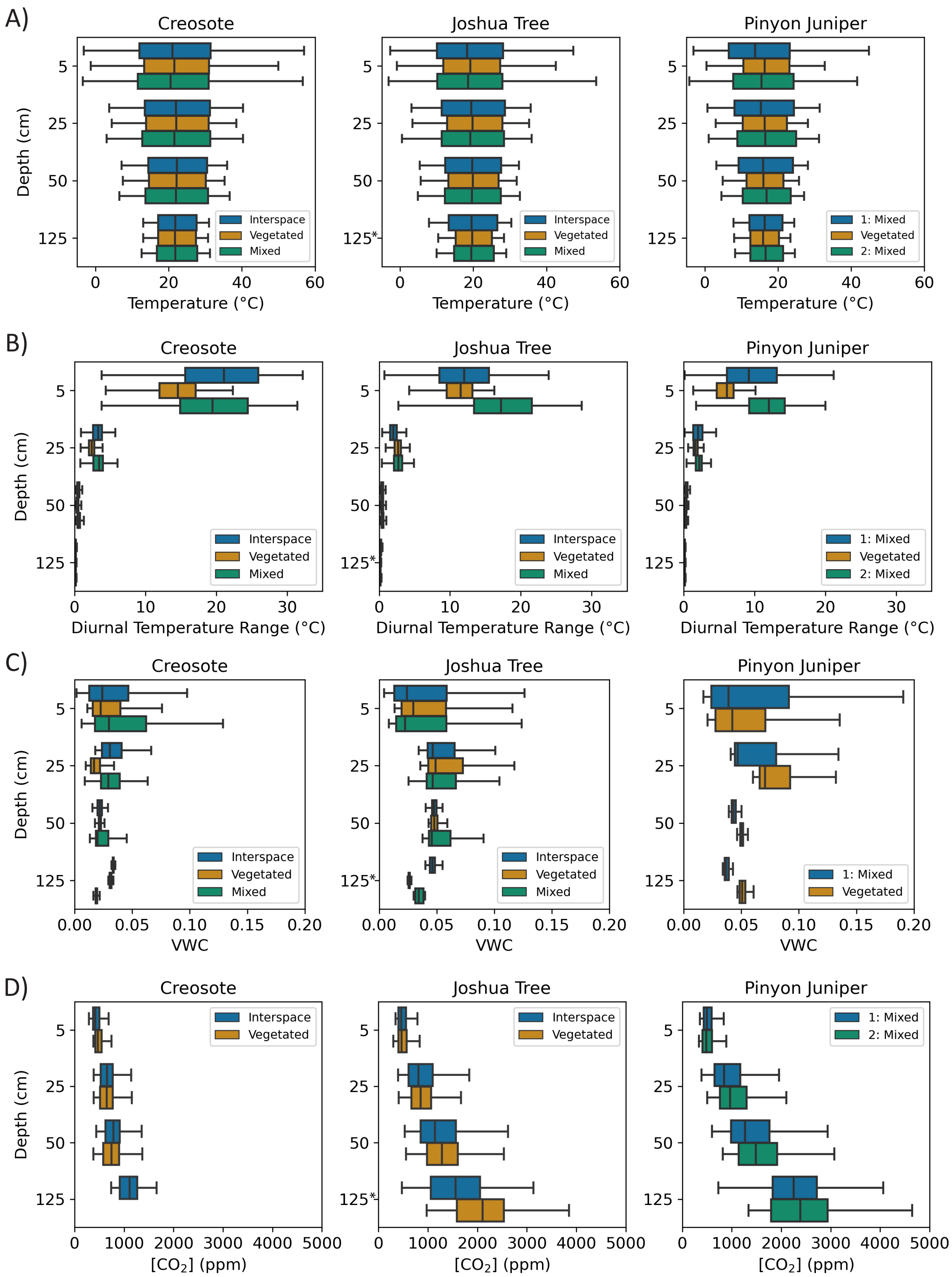

Figure 4.5 – Overview of spatial heterogeneity in soil conditions across the climosequence sites. Box and whisker plots of hourly measurements of A) soil temperature, B) the diurnal temperature range (daily maximum - minimum temperature), C) volumetric water content, and D) CO_2 concentration for two full seasonal cycles (date ranges in Table 4.3). *The deepest measurement for the Joshua Tree interspace soil is 80cm.

duction are predicted during high-productivity intervals (GPP $>$ 76gC/m^2/8-day) when the soil temperature is above 19.4°C. Water content is not invoked in a decision until the third branch point, where moderate levels of production are predicted for warm soils (temperature $>$ 20.7°C) with adequate moisture (VWC $>$ 5%).

This pattern is echoed across sites. Truncated trees showing just the first two branch points for vegetated and intercanopy soil profiles are shown in Figures 4.7 and 4.8, respectively. Water availability is always the first decision when predicting daily CO_2 production in shallow soils; higher levels of production are predicted when adequate moisture is present ($>$4.5-7% VWC). In contrast, soil temperature is the most important predictor of deeper soil CO_2 production at the most arid Creosote site, and GPP becomes an increasing important predictor for the higher elevation sites, particularly for the under-canopy soil profiles. The interspace profile at Joshua Tree is a notable exception to this trend, where deeper soil CO_2 production is best predicted by water availability (Figure 4.8).

These results demonstrate first that both seasonal trends in CO_2 dynamics and the transient pulses of production in response to transient moisture availability can be well-described by time-correlative measurements of soil and meteorological conditions, in addition to remotely-sensed indicators of primary productivity (Figure 4.6C,D). Moreover, the first-order controls on CO_2 production are not constant with depth in the soil profile. Water availability is always the most important determining factor for predicting CO_2 production in shallow layers of the soil profile. Moving deeper into the soil profile, concurrent water content loses that dominant status. Soil temperature and primary productivity are generally more predictive of CO_2 production in deeper portions of the soil profile, perhaps signaling a shift in the dominance of heterotrophic vs. autotrophic respiration with depth. The density of microorganisms is often substantially higher in surface horizons than at depth in the soil profile (Blume *et al.*, 2002; Fierer *et al.*, 2003b). Fierer *et al.* (2003b) reported microbial densities 1-2 orders of magnitude higher near the soil surface than at 2m depth in unsaturated mollisols; in some profiles the microbial density at 0-5cm depth was an order of magnitude higher than that at 15-25cm depth. The relative importance of autotrophic respiration vs. heterotrophic respiration almost undoubtedly changes with depth in these soils, particularly in the vicinity of deeply-rooted, drought-adapted plants characteristic of arid systems (Canadell *et al.*, 1996; Hartle *et al.*, 2006).

4.3.3 CO_2 production regression analysis

The decision tree analysis of CO_2 on a daily timescale provides insights into the primary controls on soil CO_2 production in these systems, and how those controls differ with depth in the soil profile. We now set out to utilize the high temporal resolution dataset (10-minutely measurements) to generate a continuous parameterization of CO_2 production as a function of soil conditions across the climosequence sites. We fit the calculated CO_2 production data for shallow (2.5-15cm depth) and deeper (15-37.5cm) portions of the soil profile to a respiration function that describes CO_2 production as a baseline respiration flux (R_0), scaled by physics-informed functions of environmental conditions (temperature, water availability, and primary productivity - Section 4.2.6). This section discusses the selection of functional forms to describe the sensitivity of respiration to soil conditions in these highly water-limited ecosystems and how the temperature and water content dependence varies spatially across

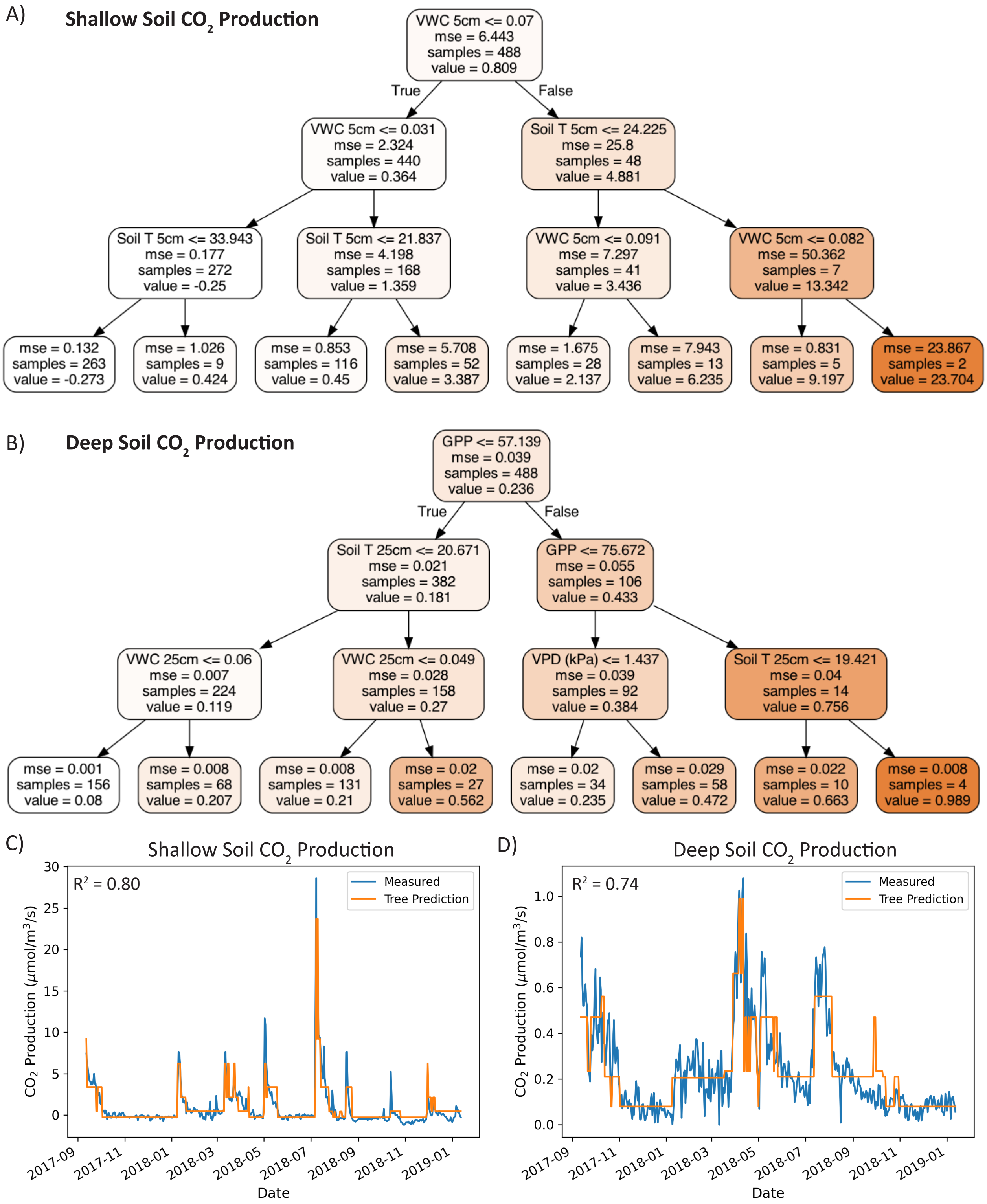

Figure 4.6 – Regression trees predicting daily CO_2 production in shallow (2.5-15cm depth, A) and deep (15-37.5cm depth, B) soils in the vegetated profile of the mid-elevation, Joshua Tree site. Orange coloration denotes higher predicted levels of CO_2 production. C and D) Model fits for the regression trees shown in A and B.

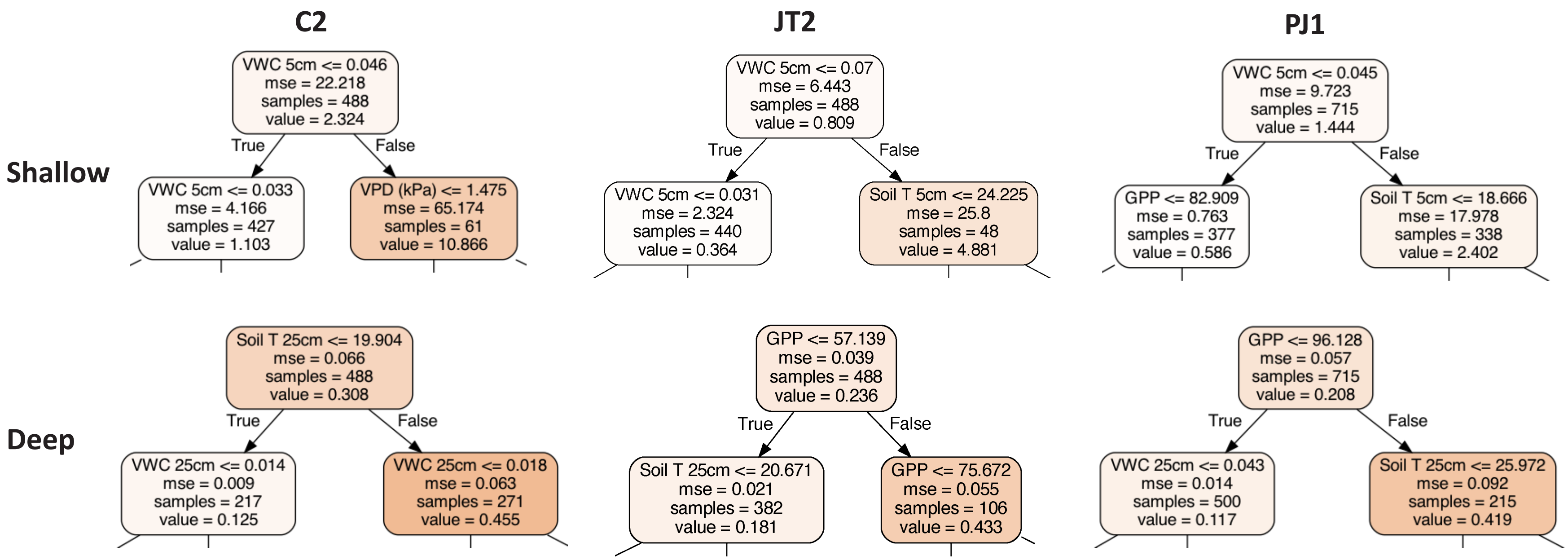

Figure 4.7 – Truncated regression trees predicting daily CO_2 production in shallow (2.5-15cm depth, A) and deep (15-37.5cm depth, B) soils from vegetated profiles across the Mojave climosequence. For clarity, only the first two branch points are shown; all trees have 3 branch points total. Orange coloration denotes higher predicted levels of CO_2 production.

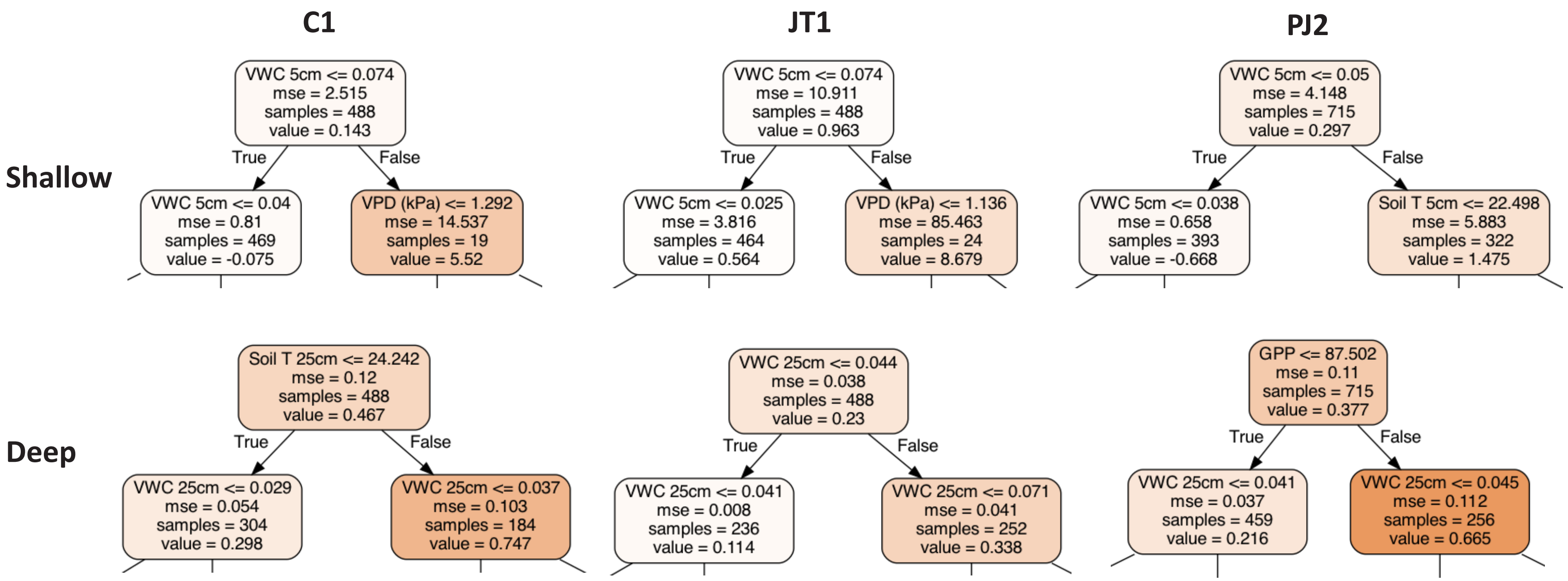

Figure 4.8 – Truncated regression trees predicting daily CO_2 production in shallow (2.5-15cm depth, A) and deep (15-37.5cm depth, B) soils from interspace profiles across the Mojave climosequence. For clarity, only the first two branch points are shown; all trees have 3 branch points total. Orange coloration denotes higher predicted levels of CO_2 production.

the climate gradient and with depth in the soil profile.

4.3.3.1 Features inconsistent with production-diffusion framework: CO_2 consumption and nighttime pulses of CO_2

The in-situ monitoring data revealed two patterns in CO_2 production that are not readily explained by the modeled temperature and water sensitive respiration functions: nighttime pulses of CO_2 at the mid to high elevation sites, and regular CO_2 consumption at the most arid site. At the Joshua Tree and Pinyon Juniper sites (less arid, more densely vegetated), we observed repeated pulses of CO_2 in the shallowest soils (5cm depth) at night, that were not associated with any measurable change in water content. Those nighttime pulses were removed from the dataset for the regression analysis presented here and are explored separately in Section 4.3.5. In contrast, at the lowest elevation site we document two types of regular CO_2 consumption, particularly in inter-canopy soils: periods of frequent negative nighttime surface fluxes during the dry season and acute episodes of CO_2 uptake associated with rain events. These observations are explored extensively in Chapter 5.

4.3.3.2 Temperature and water sensitivity of shallow and deeper soils

We first consider models for CO_2 production that are sensitive to concurrent temperature and water availability alone. Initial testing demonstrated that observed production dynamics were best described by functions with an Arrenhius-type temperature dependence and that the Lloyd and Taylor functional form generally yielded slightly better fits than a simple Arrhenius dependence (Table 4.2). A sigmoidal temperature dependence was found to yield the same quality of fit as Lloyd and Taylor, but the Arrhenius or modified Arrhenius functional forms require fewer and more physically interpretable fitting parameters so we did not further consider sigmoidal fits. The sensitivity of CO_2 production to water content was best captured by either a Gompertz or exponential-squared water content dependence. The temperature and water content scaling factors ($f(T)$, $f(\theta)$ in Eq. 4.2.8) for models fit with a simple Arrhenius temperature dependence and Gompertz water content dependence are shown in Figure 4.9; comparable results for Lloyd and Taylor temperature dependence shown in Figure D9. Fitted parameters and details on model goodness of fit are collated in Tables D2-D4.

The Gompertz functional form models the water sensitivity of CO_2 production as a true reduction function; the value of the water content scalar varies between 0 and 1, approaching those endmember values asymptotically (Figure 4.9B,D). An exponential water content dependence, specifically one with a θ^2 term in the exponential (Table 4.2), has been used to model CO_2 production in semiarid ecosystems where water availability is a critical control on carbon cycling (Tang *et al.*, 2005; Vargas *et al.*, 2010b). We found that models with an exponential-squared water content dependence did generally produce the best fits to the CO_2 production data (Tables D2-D4). However, that functional form yields extreme, likely over-fit water content scalars (Figure 4.10B,D). We thus employed a Gompertz water content dependence for the remainder of this analysis. Tucker and Reed (2016) also found that soil respiration in a dryland ecosystem in Eastern Utah was best-described by an Arrhenius temperature dependence (either simple exponential or Lloyd and Taylor) and a Gompertz

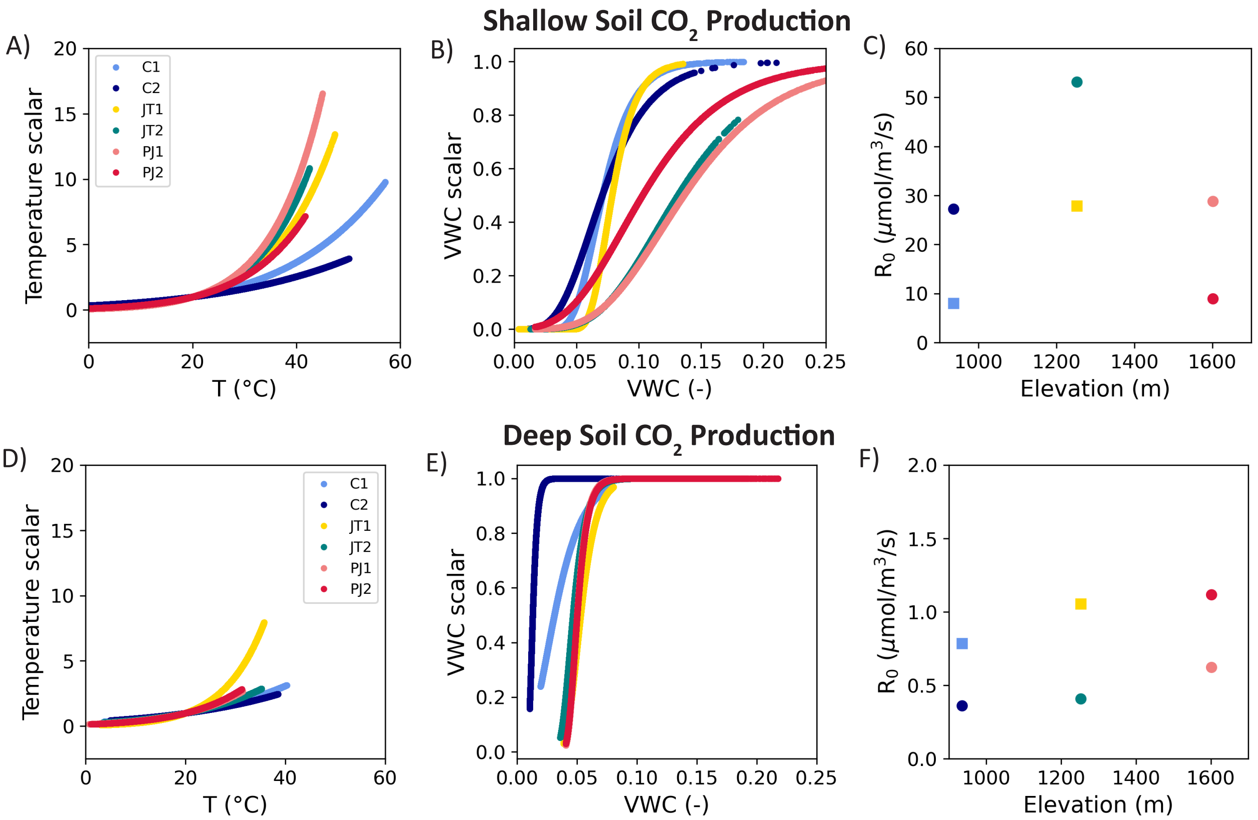

Figure 4.9 – Regression results for shallow (A-C) and deep (D-F) CO_2 production, using a simple Arrhenius temperature dependence and Gompertz water content dependence: temperature scaling factor (A,D), water content scaling factor (B,E), and baseline respiration (C,F). Colors denote the soil profile (Table 4.1).

water content dependence.

Examining the fitted respiration functions, we now introduce two metrics to compare the relationship between CO_2 production and environmental conditions across sites and with depth in the soil profile: Q_{10} and $\theta_{0.01}$. Q_{10}, the factor by which soil respiration increases in response to a 10°C increase in temperature, is a commonly reported index of temperature sensitivity (Fierer *et al.*, 2006; Bond-Lamberty and Thomson, 2010). For a given temperature, T_i, the Q_{10} for the Lloyd and Taylor temperature response function is given by:

$$Q_{10,i} = e^{E_0\left(\frac{1}{T_i-5-T_0} - \frac{1}{T_i+5-T_0}\right)} \tag{4.3.1}$$

Analogously, the Q_{10} for a simple Arrhenius temperature dependence is calculated as:

$$Q_{10,i} = e^{\frac{E_0}{R*T_{20}}\left(\frac{T_i+5-T_{20}}{T_i+5} - \frac{T_i-5-T_{20}}{T_i-5}\right)} \tag{4.3.2}$$

where i is an individual time point. We report the Q_{10} of the mean soil temperature over the time interval of interest but comparable results are obtained by computing the median Q_{10} for all observations i.

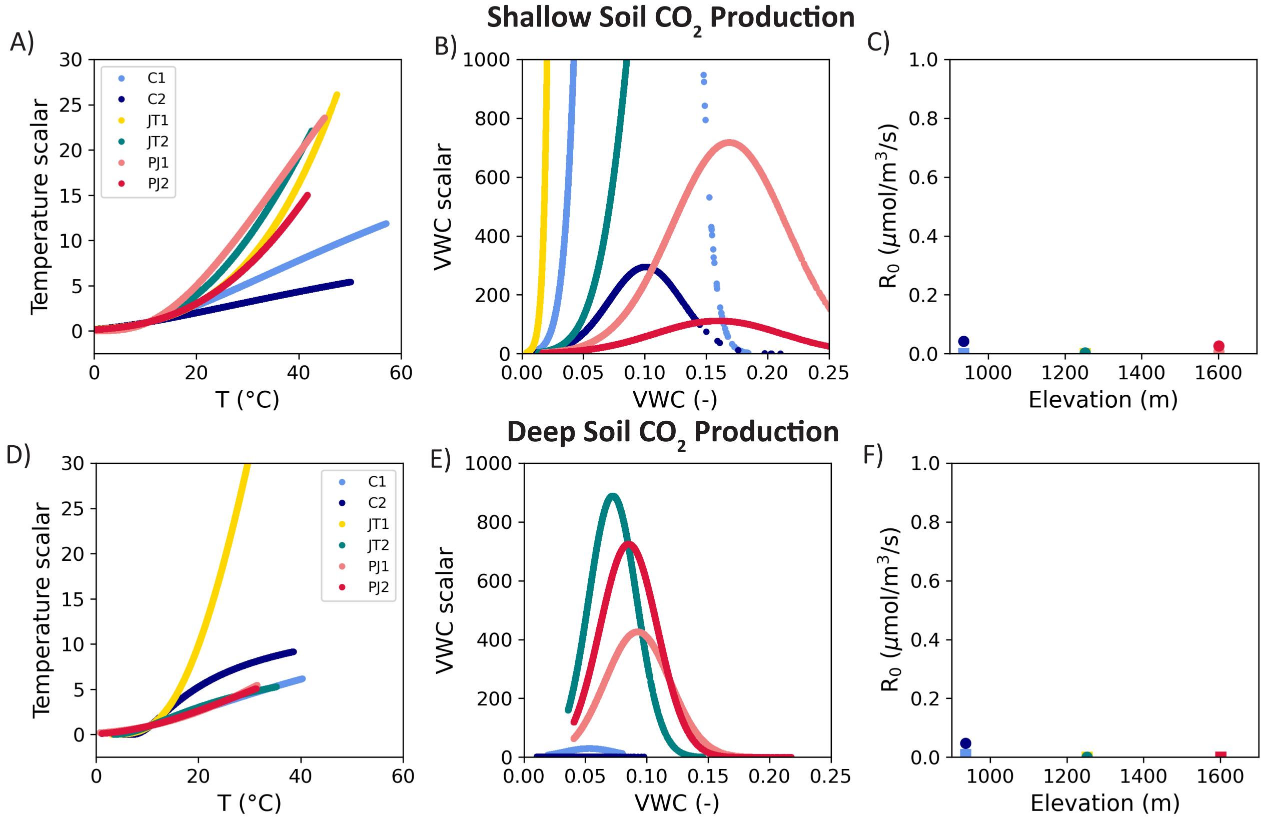

Figure 4.10 – Regression results for shallow (A-C) and deep (D-F) CO_2 production, using a Lloyd and Taylor temperature dependence and an exponential-squared water content dependence: temperature scaling factor (A,D), water content scaling factor (B,E), and baseline respiration (C,F). Colors denote the soil profile (Table 4.1).

Q_{10}

		Profile					
Model Fit	Depth	C1	C2	JT1	JT2	PJ1	PJ2
Arrhenius * Gompertz	shallow	1.99	1.64	2.84	3.14	3.52	2.72
	deep	1.81	1.66	4.03	2.07	2.51	2.66
LT * Gompertz	shallow	2.09	1.71	2.98	3.53	5.13	3.05
	deep	1.93	1.78	5.1	2.07	2.52	2.71
LT * $e^{\left(a*\theta+b*\theta^2\right)}$	shallow	2.13	1.71	2.95	3.35	5.65	3.13
	deep	1.92	1.81	5.59	2	2.64	2.6
LT * Gompertz*$f(antedecent\,\theta)$	shallow	2.09	1.61	1.98	2.61	2.31	2.06
	deep	2.01	1.84	3.86	3.86	3.43	2.53

θ at which VWC scalar < 0.01

Model Fit	Depth	C1	C2	JT1	JT2	PJ1	PJ2
Arrhenius * Gompertz	shallow	0.039	0.021	0.054	0.043	0.041	0.018
	deep	0.001	0.008	0.036	0.033	0.039	0.039
LT * Gompertz	shallow	0.036	0.02	0.054	0.046	0.036	0.017
	deep	0.001	0.008	0.034	0.032	0.039	0.038
LT * Gompertz*$f(antedecent\,\theta)$	shallow	0.036	0.021	0.053	0.029	0.035	0.017
	deep	0.001	0.008	0.035	0.03	0.041	0.039

Table 4.4 – Calculated Q_{10} and water content threshold ($\theta_{0.01}$) for the CO_2 production model fits presented. The water content threshold is the volumetric water content (θ) at which the Gompertz function becomes <0.01.

The threshold water content ($\theta_{0.01}$) for the Gompertz function is also reported as an indicator of the water content at which water availability severely limits CO_2 production. The Gompertz function approaches 0 asymptotically, meaning that the water content scalar never achieves a value of 0, so we define the threshold as the water content at which the value of the Gompertz function drops below 0.01 (reducing the baseline respiration by a factor of 100).

Focusing first on the temperature sensitivity, we find that for Arrhenius + Gompertz models, Q_{10} varies between 1.64-3.52 for shallow soil CO_2 production and 1.66-4.03 for deeper soil CO_2 production (Table 4.4). These values span the range of commonly reported Q_{10} for soil respiration (˜1.6-4.6, c.f Fierer *et al.*, 2006; Conant *et al.*, 2008). The Q_{10}'s calculated for the Creosote site ($\sim$1.65 for the vegetated profile, $\sim$1.9 for interspace soils) are in good agreement with the Q_{10} of $\sim$1.6 reported by Cable *et al.* (2011) for the Nevada FACE facility (Jordan *et al.*, 1999), located at a comparable elevation in the Mojave. Comparing the temperature sensitivity across sites, we find that CO_2 production at the highest temperature, lowest elevation site is substantially less temperature sensitive than the higher elevation sites, particularly for shallow soils (Figure 4.9A,D). This may reflect thermal adaptation of microbial respiration to the higher ambient temperatures experienced, as suggested by Dacal *et al.* (2019) in a recent incubation study of 110 dryland soils. We do not observe a significant difference in Q_{10} between shallow and deep soil CO_2 production when production is modeled solely as a function of concurrent temperature and water content.

Shallow and deep soil CO_2 production, however, exhibit starkly different water content sensitivities (Figure 4.9B,D). In the deeper soils, the water content scalar functionally acts as a binary switch. For most of the water content conditions experienced by the soil profile, the water content scalar is 1, meaning that water availability is not limiting (Figure 4.9D). As low water contents are approached, the scaling function declines steeply towards zero, yielding threshold water contents between $\theta_{0.01}$ = 0.1-4%. In contrast, shallow soil CO_2 production is sensitive to water content for the entire range of moisture conditions experienced (Figure 4.9B), indicating a much stronger dependence on water content than deeper soils. Intriguingly, for the lowest and mid-elevation sites, the threshold water content ($\theta_{0.01}$) is substantially higher in shallow soils than deeper soils (Table 4.4). This may again reflect a shift in the dominance of heterotrophic vs. autotrophic respiration with depth, if microbial activity becomes severely limited, either through desiccation or limitations in solute diffusion as the water-filled pore space becomes discontinuous at low water potentials, while drought-adapted plants are able to continue extracting water from the soil matrix (Manzoni *et al.*, 2012).

Adding sensitivity to GPP and antecedent water content to the CO_2 production model generally led to marginal improvements in model fit (Tables D2-D4). Figure 4.11 shows regression results for best-fit models incorporating the influence of antecedent water content. In shallow soil horizons, CO_2 production is best-fit by a negative exponential antecedent water content dependence at all sites (Figure 4.11C), meaning that *lower* levels of CO_2 production are predicted for soils that have experienced high water content conditions over the past 1-4 weeks. Previously high moisture conditions thus damp shallow soil CO_2 production, or conversely, the highest levels of CO_2 production in response to elevated water content occur following a previously dry period. This is consistent with 'Birch effect' pulses of CO_2 production in response to soil rewetting following drought conditions commonly observed in seasonally dry climates (Birch, 1964; Jarvis *et al.*, 2007; Unger *et al.*, 2010). In contrast, deeper soil CO_2 production is often best-fit by models with a positive antecedent water content dependence, implying that previously wet conditions enhance CO_2 production. This differential response to antecedent moisture conditions is again plausibly consistent with a shift from dominantly heterotrophic to autotrophic respiration with depth in the soil profile, as plant vitality and thus root respiration would be expected to be improved by previously wet conditions.

Incorporating the influence of antecedent moisture also modifies the modeled temperature sensitivity (Figure 4.11A,C), yielding lower predicted Q_{10} for the higher elevation sites. The Q_{10} for shallow soil CO_2 production falls between 1.6 and 2.6, bringing the temperature sensitivity of the highest elevation site largely in line with that of the lowest elevation profiles (Figure 4.11A). Deeper soil CO_2 production also exhibits significantly higher temperature sensitivities on average ($p = 0.034$, one-tailed t-test) than shallow soil production (Table 4.4). This is consistent with previous findings of more highly temperature sensitive heterotrophic respiration in subsurface soils (>20cm depth) relative to surficial soils (Fierer *et al.*, 2003a;

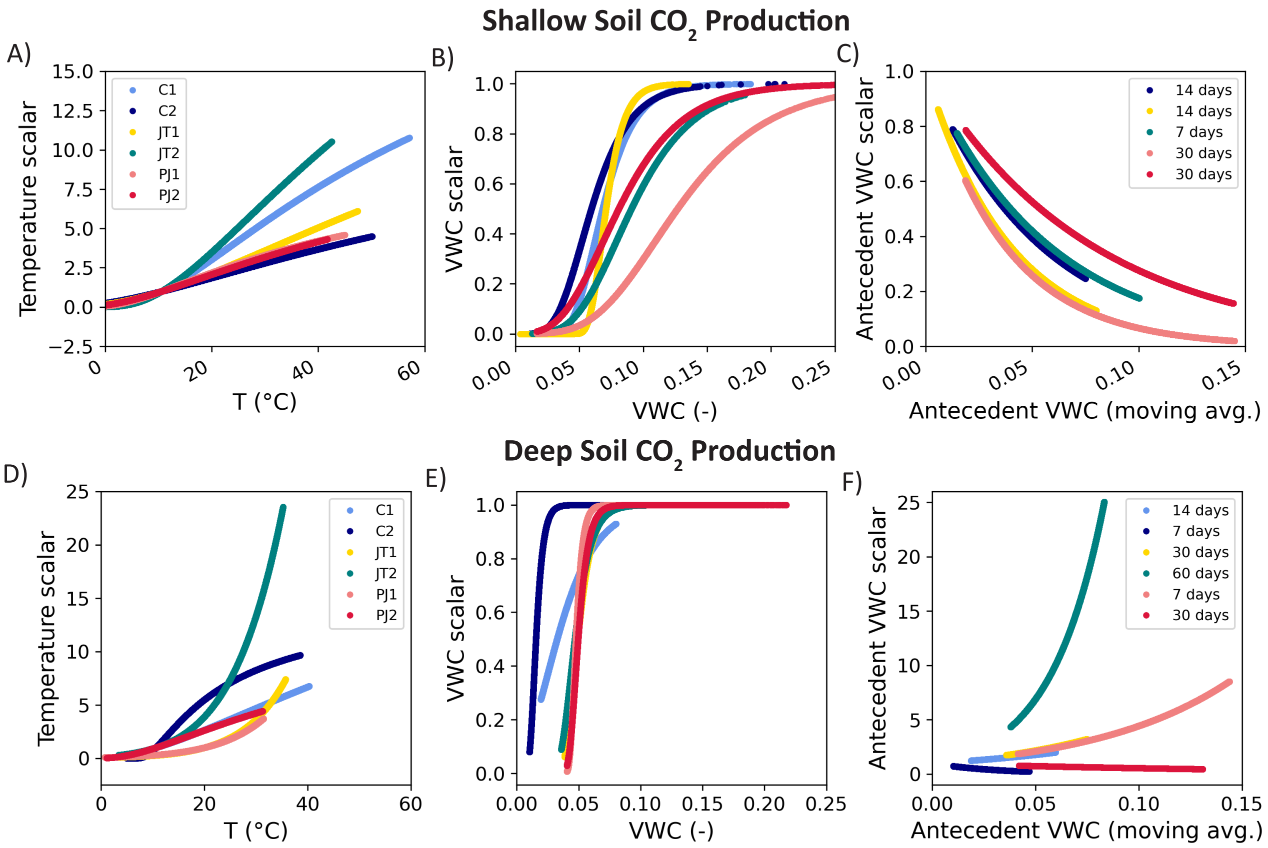

Figure 4.11 – Regression results for shallow (A-C) and deep (D-F) CO_2 production, using the best-fit temperature and water content dependence, allowing for the influence of antecedent water content: temperature (A,D), water content (B,E), and antecedent water content scaling factor (C,F). Colors denote the soil profile (Table 4.1) and legend in C and F indicates the length of the moving average window.

Yan *et al.*, 2017). Explanations for the shift in the temperature sensitivity of heterotrophic respiration include changes in the lability of the organic carbon pool (Conant *et al.*, 2008) and physio-chemical characteristics of the pedogenic environment (Matteodo *et al.*, 2018), but the higher temperature sensitivity of total CO_2 production observed here could also potentially reflect a higher Q_{10} for autotrophic respiration (Boone *et al.*, 1998).

4.3.4 Predictive modeling of CO_2 production throughout the soil profile

In the previous sections we demonstrated that the sensitivity of CO_2 production to environmental conditions varies with depth and developed quantitative descriptions of CO_2 production for discrete depth intervals of the soil profile. Here we build on that understanding to generate predictions of CO_2 dynamics over the entire soil profile through time. To do so, we incorporate the temperature and water sensitive CO_2 production functions derived in Section 4.3.3.2 into a forward, time-dependent production-diffusion model (Eq. 4.2.1), driven by measured temperature and water content data.

4.3.4.1 Reconciling the differential environmental sensitivity of shallow and deep production: Two respiration terms

The variable temperature and water sensitivity with depth presents a challenge - CO_2 dynamics throughout the entire profile cannot be modeled with a single production term. The model must account for the fact that the respiration which dominates surface soils is distinct from that of the deeper profile. We achieve this by positing that total soil CO_2 production is comprised of a shallow respiration component that declines exponentially with depth and a deeper respiration component that follows the root distribution profile. This is functionally assigning a heterotrophic and autotrophic respiration term, and for simplicity we will refer to the two CO_2 production terms as such, but it is important to note that we have not attempted to experimentally differentiate microbial vs. plant root-derived CO_2 (Hanson *et al.*, 2000). The autotrophic vs. heterotrophic distinction is simply used as a modeling framework here, though as discussed above, many of the patterns observed regarding the sensitivity of shallow vs. deeper soil CO_2 production to environmental conditions are consistent with surface soils dominated by highly water-sensitive heterotrophic respiration, accompanied by a shift to dominantly autotrophic respiration down profile. Microbial activity is often concentrated near the surface in desert soils (Fierer *et al.*, 2003b; Cable *et al.*, 2009; Pointing and Belnap, 2012) while autotrophic or plant-root respiration should follow the root distribution (Simunek and Suarez, 1993).

The shallow-soil respiration function derived from fitting the 2.5-15cm CO_2 production data was taken to be representative of dominantly heterotrophic respiration in the shallow layers of the soil profile, and assigned an exponentially declining depth dependence (Eq. 4.3.3, where $\bar{z}$=0.05m). For the purposes of this modeling effort, we utilize CO_2 production functions that are only sensitive to instantaneous temperature and water content at the given depth, as functions sensitive to present conditions were found to explain most of the variation in production (Tables D2-D4) and incorporating sensitivity to GPP or antecedent moisture led to only marginal improvements in model predictions.

$$R_{heterotrophic}(z,t) = R_0 * e^{-z/\bar{z}} * f(T(z,t)) * f(\theta(z,t)) \tag{4.3.3}$$

$$R_{autotrophic}(z,t) = R_0 * f(z) * f(T(z,t)) * f(\theta(z,t)) \tag{4.3.4}$$

where R_0 is the baseline respiration (μmol/m^3/s), z is the depth (m), $\bar{z}$ is the e-folding depth (m), $f(z)$ is the normalized root distribution profile, and $f(T)$ and $f(\theta)$ are the temperature and water content scaling factors, respectively (Table 4.2).

The autotrophic respiration function was parameterized initially with the temperature and water content sensitivity derived from fitting the deeper soil CO_2 production data and assigned a depth dependence following the normalized root distribution profile (Figure 4.12, Eq. 4.3.4). The fitted parameters for the temperature and water-content scaling functions of autotrophic respiration were then re-optimized using the full forward, time-dependent model in order to relax the steady-state assumption and better account for CO_2 dynamics throughout the entire 1.25m profile, instead of only the top 40cm.

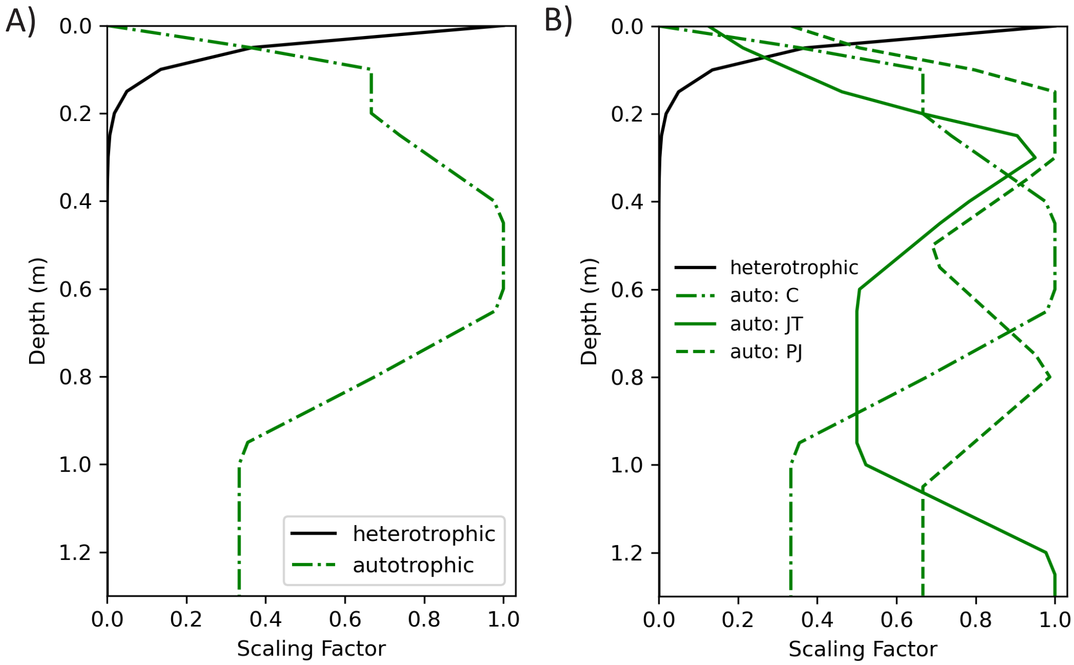

Figure 4.12 – Depth dependence of modeled CO_2 production functions. The shallow-soil heterotrophic respiration term declines exponentially with depth (Eq. 4.3.3) while the autotrophic respiration term follows the measured root distribution profile at each site.

In the following section, we use the time-dependent CO_2 production-diffusion model to examine how environmental conditions dictate CO_2 production and ultimately soil-atmosphere CO_2 exchange across space and time in these Mojave Desert soils.

4.3.4.2 Predictive modeling of CO_2 dynamics throughout the soil profile

Soil CO_2 dynamics throughout the soil profile are well-captured by the production-diffusion model driven by temperature and water-content sensitive respiration terms. Model results for a representative profile from each site are shown in Figures 4.13, 4.14, and 4.15 for the interspace Creosote profile, vegetated Joshua Tree profile, and mixed shrub/grass Pinyon Juniper profile (PJ1), respectively. Results for the vegetated Creosote profile and interspace Joshua Tree profile are shown in Figures D10 and D11. The PJ2 profile was not modeled further as a non-negligible percentage of total shallow-soil CO_2 production occurred during anomalous nighttime pulse events; this is further explored in Section 4.3.5. Fitted parameters and indicators of temperature and water content sensitivity are compiled in Table 4.5.

Examining results for the vegetated Joshua Tree profile in more detail (Figure 4.14), we find that the temperature and water content sensitive respiration functions replicate observed patterns in CO_2 concentration over time and with depth, capturing both the pulses of CO_2 following precipitation events and the longer-term seasonal cycle (Figure 4.14A). Figure 4.14B demonstrates how the modeled CO_2 production responds to seasonal environmental drivers. September 2017 - early January 2018 represents an extended dry period during which the soils dried down following the 2017 summer monsoon rains (Figure D7). During this interval, the highly water sensitive heterotrophic respiration in shallow soils (5cm depth) declined by 2 orders of magnitude before rebounding with the onset of winter monsoon rains in January 2018. This pattern is repeated throughout the year, as the re-wetting of near-surface soils drives (multiple) order of magnitude increases in CO_2 production via heterotrophic respiration. In contrast, the autotrophic respiration largely responsible for production throughout the rest of the profile is more consistent throughout the year, largely following the seasonal temperature signal.

Two additional general trends are apparent. First, the models tend to under-estimate the maximum magnitude of the CO_2 pulse in shallow soils following precipitation events. Fully capturing heterotrophic respiration dynamics during soil re-wetting likely requires a more explicit representation of soil organic carbon dynamics, including the accumulation of labile organic carbon over extended dry periods that can be readily accessed by microbes following moisture delivery (Zhang *et al.*, 2014). However, the simple framework presented here captures overall soil CO_2 dynamics well and requires knowledge of only 2 parameters: soil temperature and water content, both of which are regularly modeled. Second, the production-diffusion model does not capture the magnitude of the shallow soil diurnal CO_2 oscillation (5cm depth) during dry intervals, particularly at the most arid Creosote site (Figure 4.13A). This observation is explored through the lens of potential abiotic contributors to CO_2 exchange in Chapter 5.

The temperature and water content sensitivity of heterotrophic and autotrophic respiration derived from modeling CO_2 dynamics across the complete soil profile are compared in Figure 4.16. As observed above, heterotrophic respiration at the lowest elevation site is significantly less temperature sensitive than at the higher elevation sites, potentially due to thermal acclimation of soil microbial communities to the higher ambient temperatures experienced (Bradford *et al.*, 2019; Dacal *et al.*, 2019). The thermal sensitivity of autotrophic respiration, in contrast, is similar across sites (Figure 4.16B), with Q_{10}'s ranging from 1.63-2.36 (Table 4.5). However, the autotrophic respiration responsible for the bulk of respiration in the deeper portions of the soil profile is found to be less temperature sensitive than the dominantly surficial heterotrophic respiration at all sites. While some studies that have attempted to experimentally differentiate between heterotrophic and autotrophic respiration through field manipulations (e.g. trenching plots to exclude plant roots) have reported significantly higher temperature sensitivities for autotrophic respiration (e.g. Boone *et al.*, 1998), many others report negligible differences in the Q_{10}'s of heterotrophic and autotrophic respiration (Bhupinderpal-Singh *et al.*, 2003; Irvine *et al.*, 2005; Högberg, 2010; Schindlbacher *et al.*, 2009). In a seasonally dry Ponderosa pine plantation, Tang *et al.* (2005) find autotrophic respiration to be less temperature sensitive than heterotrophic respiration, a pattern they attribute to the thermal acclimation of root respiration (Atkin and Tjoelker, 2003). We thus note that while our observations are consistent with less temperature sensitive autotrophic respiration, experimental manipulations aimed at parsing apart the contributions of autotrophic and heterotrophic respiration (Hanson *et al.*, 2000) are required to definitively attribute the lower temperature sensitivity observed for deeper soils to root respiration.

The autotrophic and heterotrophic respiration functions derived here also differ substantially in their sensitivity to water content (Figure 4.16). As observed above, we find that the water content scaling function largely acts as an 'on/off' switch for the autotrophic respiration largely responsible for CO_2 production in deeper soils. Heterotrophic respiration is found to be sensitive to water availability over a wider range of water contents, particularly

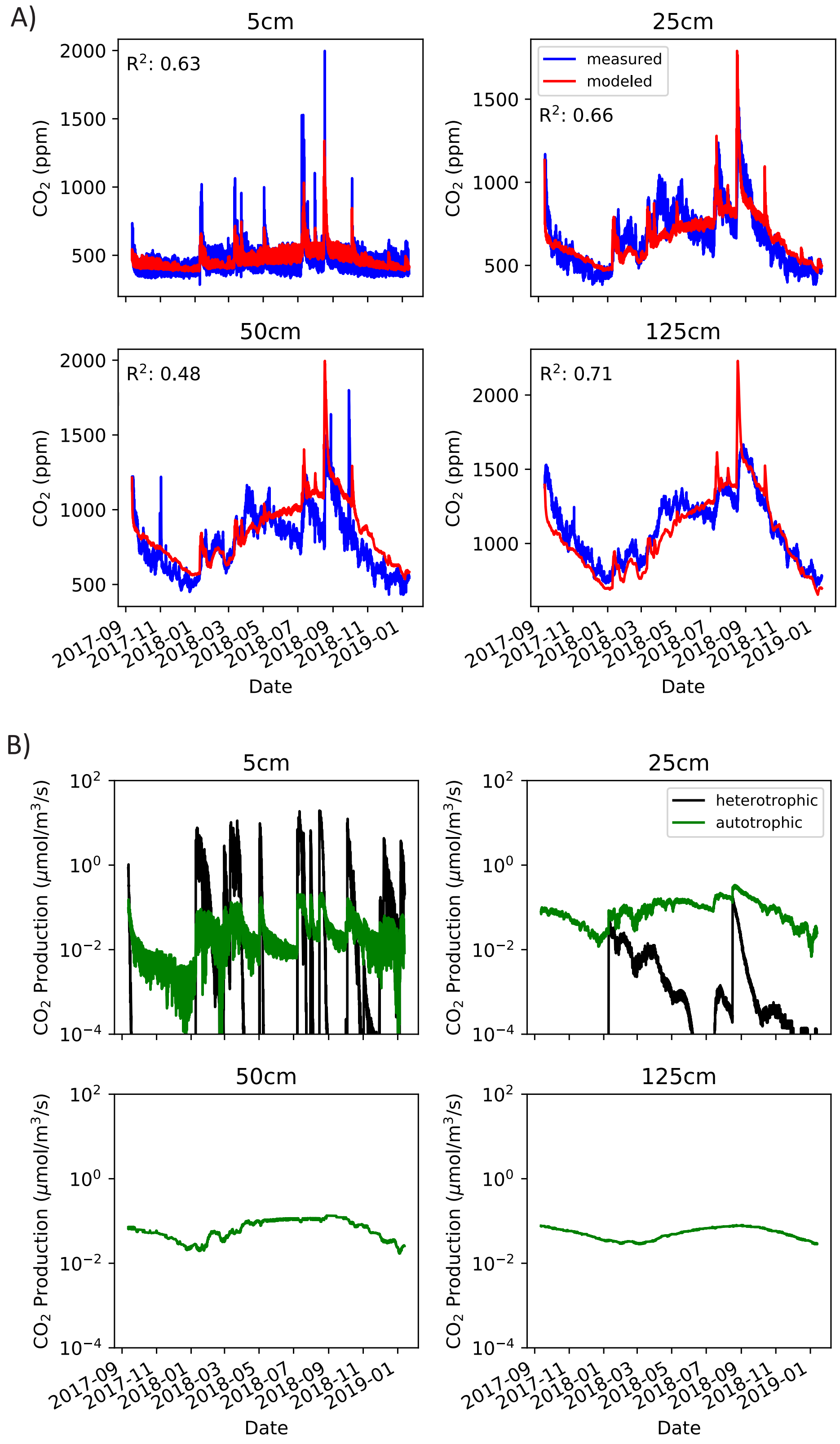

Figure 4.13 – CO_2 production-diffusion model results for the interspace profile at Creosote (C1): A) measured (blue) versus modeled (red) CO_2 concentrations and B) modeled heterotrophic (black) and autotrophic (green) respiration functions.

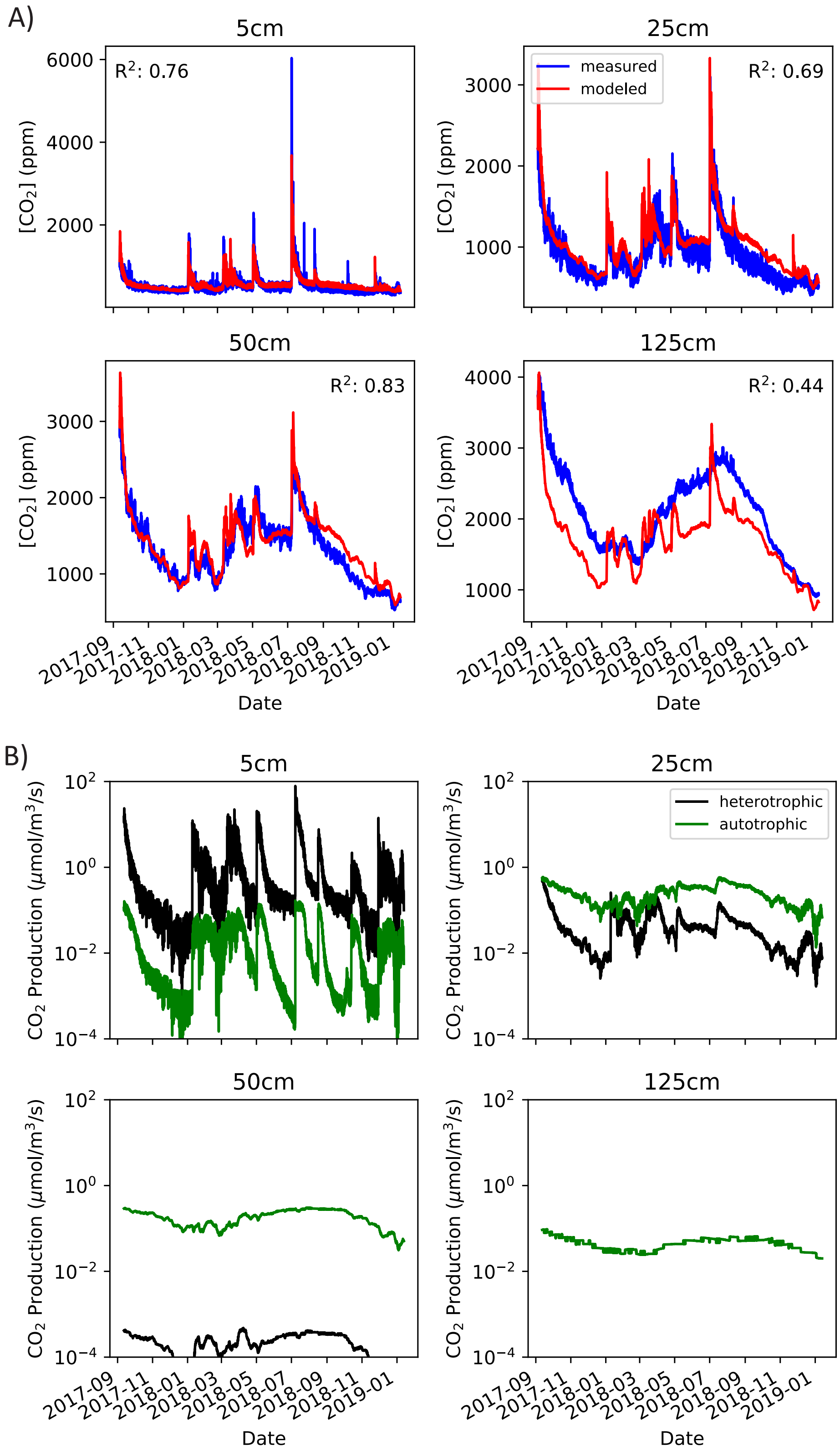

Figure 4.14 – CO$_2$ production-diffusion model results for the vegetated profile at Joshua Tree (JT2): A) measured (blue) versus modeled (red) CO$_2$ concentrations and B) modeled heterotrophic (black) and autotrophic (green) respiration functions.

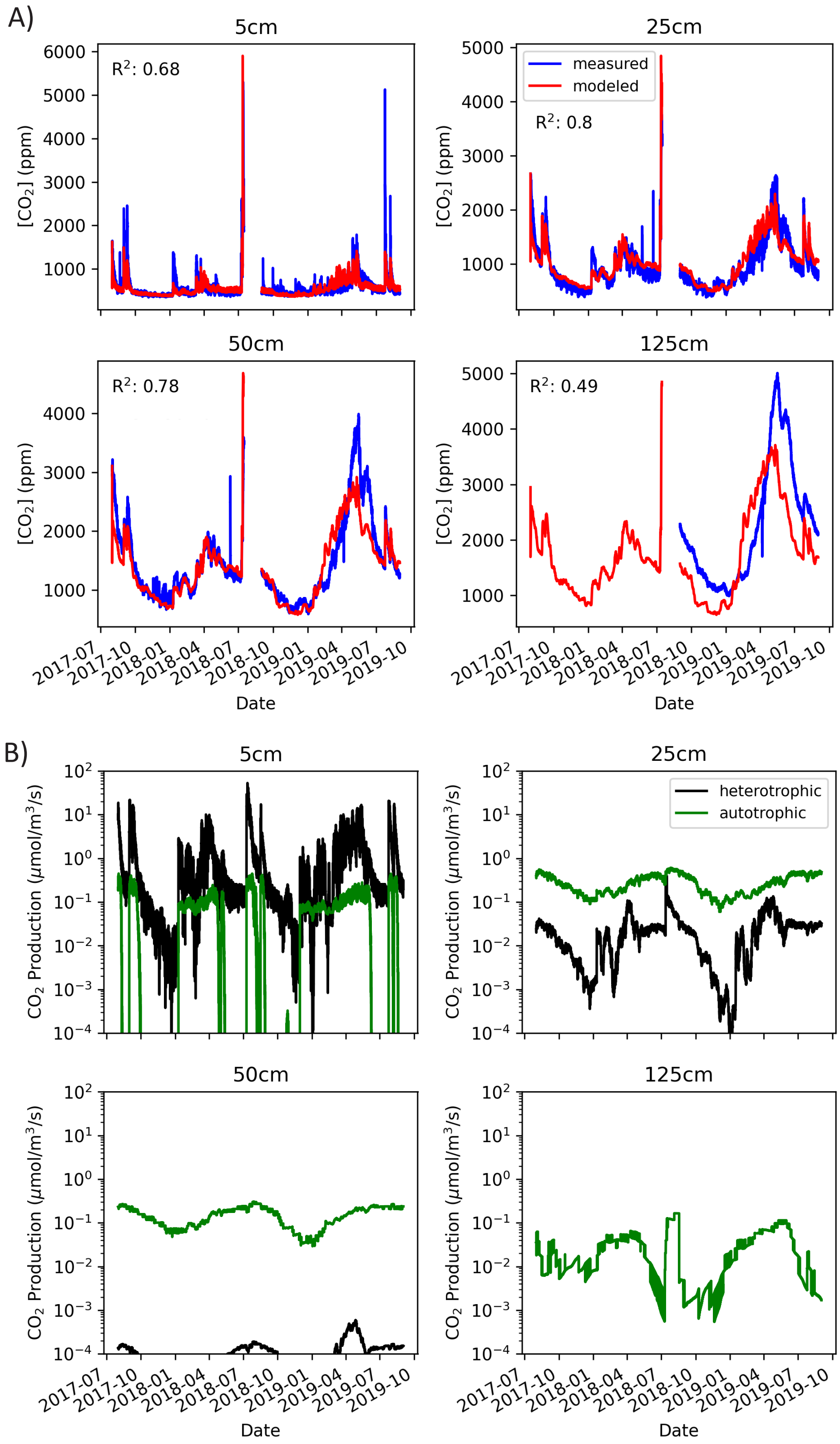

Figure 4.15 – CO_2 production-diffusion model results for the mixed shrub/grass profile at Pinyon Juniper (PJ1): A) measured (blue) versus modeled (red) CO_2 concentrations and B) modeled heterotrophic (black) and autotrophic (green) respiration functions.

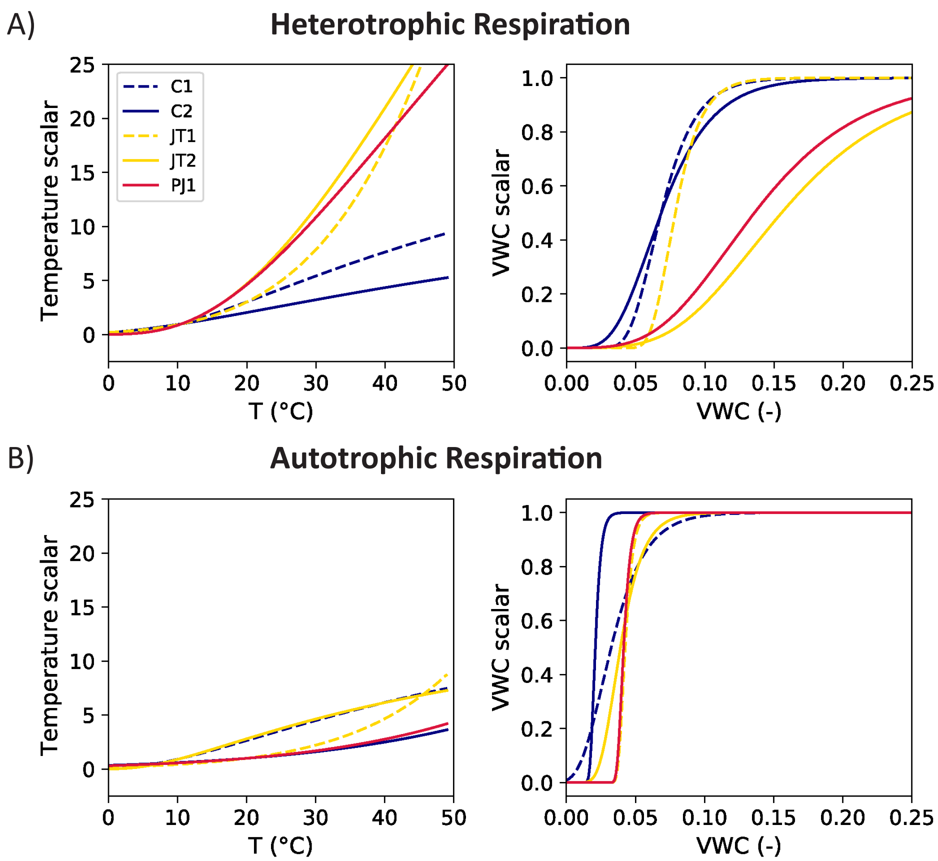

Figure 4.16 – Temperature and water content sensitivity of heterotrophic (A) and autotrophic (B) respiration derived from modeling CO_2 dynamics across the complete soil profile. Colors denote the climosequence site (Table 4.1).

at the higher elevation sites. Autotrophic respiration at the lowest elevation, most arid site is predicted to maintain non-negligible respiration rates to very low water contents (Table 4.5), in line with the ability of drought-adapted desert shrubs like *larrea tridentata* (creosote) to extract water from the soil matrix at very low pressure heads (up to -12MPa or -1200m (Pockman and Sperry, 2000)).

4.3.5 Exploring nighttime pulses of CO_2: Respiration driven by non-rainfall moisture?

In the previous sections we demonstrated that, in general, CO_2 dynamics across depth and time in these Mojave soils are well-described in a production-diffusion framework with temperature and water-content dependent microbial and root respiration terms. However, we also observed significant nighttime CO_2 pulse events at the higher elevation sites that are not predicted by the temperature and water-content sensitive model (Figure 4.17). The seemingly anomalous shallow-soil pulse events observed at the vegetated Joshua Tree profile are highlighted in Figure 4.17. There are a number of intervals, following rain events with a lag time of days to weeks, where large magnitude CO_2 production events are observed at

Shallow soil, heterotrophic respiration

		Parameters						
			Temperature scalar		VWC scalar		Q_{10}	$\theta_{0.01}$
Profile	Functional Form	R_0	E_0	T_0	a	b		
C1	LT * Gompertz	8.06	63.66	264.74	3.65	58.82	2.33	0.036
C2	LT * Gompertz	24.34	83.81	254.94	2.34	39.57	1.82	0.02
JT1	LT * Gompertz	20.48	965.79	197.65	5.65	76.70	2.92	0.054
	Arrhenius * Gompertz	69.73	74.03	-	5.70	77.28	2.83	0.054
JT2	LT * Gompertz	61.95	136.98	259.22	2.31	17.25	3.50	0.046
PJ1	LT * Gompertz	18.60	106.87	262.40	2.22	19.09	3.32	0.036

Deeper soil, autotrophic respiration

	Functional Form	R_0	E_0	T_0	a	b	Q_{10}	$\theta_{0.01}$
C1	LT * Gompertz	0.09	62.37	263.47	1.56	59.70	2.13	0.0006
C2	Arrhenius * Gompertz	0.10	34.97	-	7.01	352.72	1.63	0.016
JT1	Arrhenius * Gompertz†	0.43	58.76	-	10.81	262.77	2.36	0.035
	Arrhenius * Gompertz	0.46	61.20	-	9.52	228.84	2.36	0.035
JT2	LT * Gompertz	0.13	46.82	267.25	3.12	89.29	2.13	0.018
PJ1	Arrhenius * Gompertz	0.36	38.85	-	11.55	287.75	1.73	0.035

Table 4.5 – Fitted parameters and calculated Q_{10} and water content threshold ($\theta_{0.01}$) for the autotrophic and heterotrophic CO_2 production functions used to model the complete soil profile. †Autotrophic respiration for the JT1 soil profile using a simple Arrhenius temperature dependence when heterotrophic respiration is modeled with a Lloyd and Taylor temperature dependence.

Site	Date Range	Number of nighttime pulses identified	
		Bare soil profile	Vegetated profile
Creosote	9/12/2017 - 1/12/2019	0	0
Joshua Tree	9/12/2017 - 1/12/2019	7	25
Pinyon Juniper*	8/1/2017 - 9/1/2019	1 - PJ1	94 - PJ2

Table 4.6 – Number of nighttime CO_2 pulses identified at each site. *At the Pinyon Juniper site, both PJ1 and PJ2 soil profiles are located adjacent to mixed shrub/grass vegetation (Table 4.1).

5cm depth but the model predicts no increase in CO_2 concentrations (Figure 4.17A). Examining one of these pulse events more closely, it becomes evident that the model captures the regular diel cycle of CO_2 observed, with concentrations coming to a peak in the afternoon and then decreasing to a minimum near sunrise (Figure 4.17B). But on certain days, the regular diel pattern of shallow-soil $[CO_2]$ is followed by a large spike in $[CO_2]$ starting in the early evening and coming to a peak in the hours before sunrise. This behavior was initially quite puzzling, as $[CO_2]$ peaks when temperatures are near the daily minimum and the pulse events are not associated with a measurable change in water content at 5cm depth (Figure 4.17C). In the following sections we describe the frequency, magnitude, and thus relevance of these nighttime CO_2 production events to overall soil-atmosphere CO_2 exchange in these systems, and interrogate their predictability in the context of potential driving mechanisms.

4.3.5.1 Frequency and magnitude of anomalous nighttime pulse events

At each site, anomalous nighttime pulse events were identified based on an algorithm comparing integrated or maximum CO_2 production during the day vs. following night for each diurnal cycle (Section 4.2.4.1). Nighttime pulse events were only identified at the higher elevation sites; zero nighttime pulse events were observed over the 15-month monitoring interval at the lowest elevation Creosote site (Table 4.6). At the mid-elevation Joshua Tree site, nighttime pulse events were far more common in the vegetated soil profile (25 pulses identified) than the interspace profile (7 pulses identified). By far the most nighttime pulse events occurred in the PJ2 soil profile, with 94 pulse events identified over the 2-year monitoring period (Table 4.6). Notably, only 1 anomalous pulse event was recorded at the neighboring PJ1 profile, hinting at a highly spatially heterogeneous process.

The question then becomes: do these nighttime pulse events actually matter for our understanding of carbon cycling and CO_2 exchange in these systems? We approach this question first by quantifying the proportion of the total CO_2 surface flux over the monitoring interval that occurred during nighttime pulse events (Table 4.7). At the Joshua Tree site, the total integrated surface flux from the under-canopy soil profile (JT2) was slightly higher than that from the interspace profile (13.24 vs. 13.07 mol/m^2). However, 12.3% of the total surface flux from the under-canopy soils occurred during nighttime pulse events while only 3% of the surface flux from the interspace profile was derived from nighttime pulse events. At Pinyon Juniper, the total integrated surface flux was again similar between the PJ1 and PJ2 profiles, but 26% of that surface flux occurred during nighttime pulse events in the PJ2 profile.

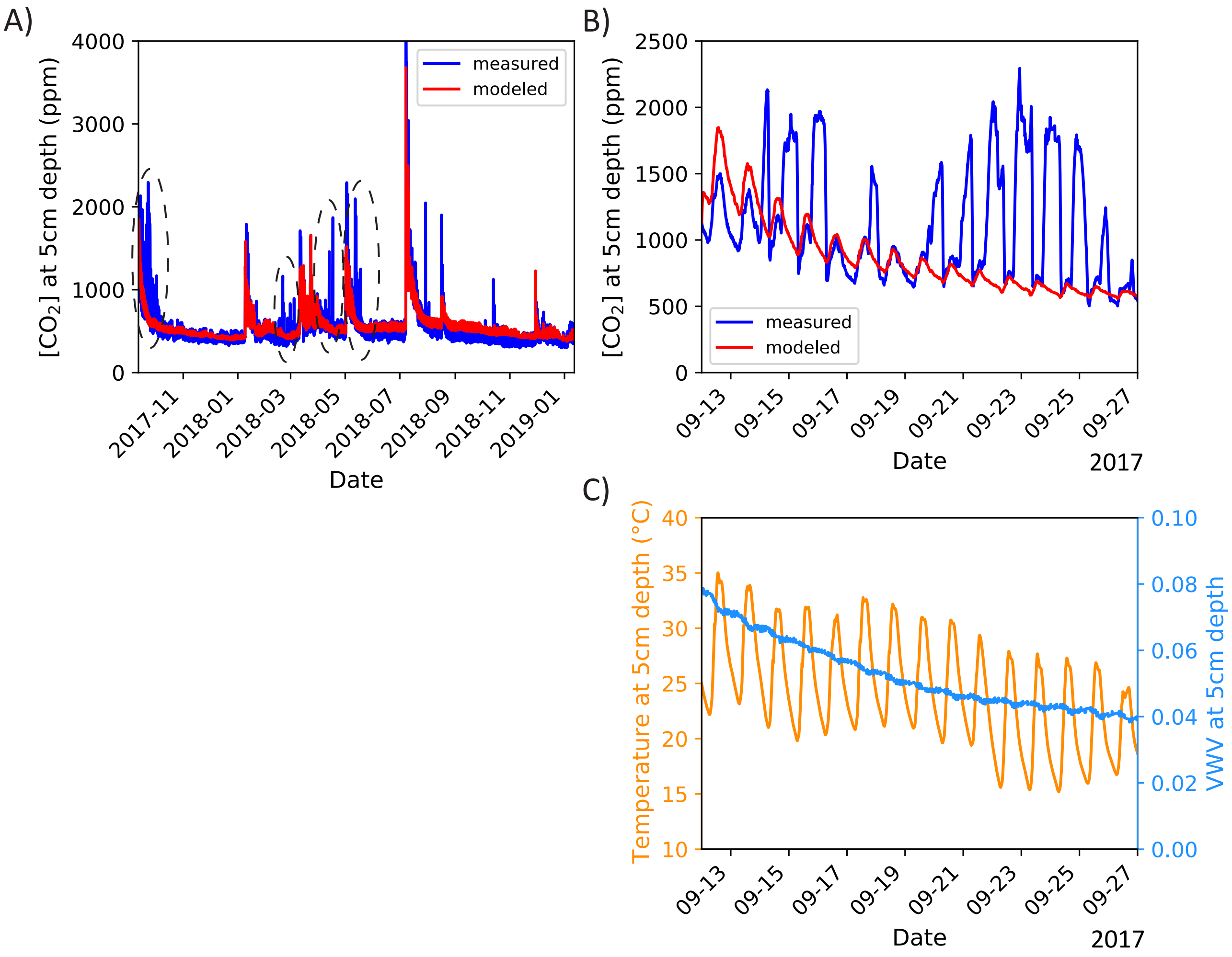

Figure 4.17 – Observations of seemingly anomalous nighttime CO_2 pulses in shallow soils (5cm depth) of the vegetated profile of the Joshua Tree site. A) Time series of measured (blue) vs. modeled (red) soil CO_2 concentration at 5cm depth, with intervals containing significant CO_2 production events not captured by the temperature and water content sensitive respiration model circled in black. B and C) Soil CO_2 concentration, temperature, and water content during the first interval highlighted in panel A.

Profile	Total CO_2 surface flux	Surface flux without nighttime pulses	Surface flux during pulse events
units	mol/m^2	mol/m^2	mol/m^2 (% of total)
Pinyon Juniper*			
PJ1	22.73	22.62	0.12 (0.5%)
PJ2	21.99	16.19	5.79 (26%)
Joshua Tree			
JT1	13.07	12.72	0.36 (3%)
JT2	13.24	11.61	1.63 (12.3%)
Creosote			
C1	5.3	5.3	0
C2	15.95	15.95	0

Table 4.7 – Contribution of nighttime pulse events to total surface flux. *Note, this reflects two full years of surface flux at the Pinyon Juniper site but only 15 months at the Joshua Tree and Creosote sites (Table 4.6). At Pinyon Juniper, the surface flux is integrated from August 1, 2017 - July 15, 2018 and September 1, 2018 - September 1, 2019 due to a gap in monitoring July-August 2018 due to instrumentation issues.

These observations lead to two initial inferences. First, they provide strong supporting evidence that the observed nighttime pulse events are a real phenomenon and not an instrument artifact. Without the nighttime pulse events, the integrated surface flux of the PJ2 profile would be 28% lower than the neighboring PJ1 profile, and that of the under-canopy profile would be 9% lower than of the interspace profile at Joshua Tree, an unlikely scenario given that soil respiration is often considerably higher adjacent to vegetation due to the concentration of carbon and nutrients as well as greater contribution from root respiration (c.f. Barron-Gafford *et al.*, 2011). Second, they suggest that the relevance of the nighttime pulse events is dictated by the time and spatial scale of interest. Understanding and predicting the frequency of the nighttime pulses appears to be of limited importance to the quantification of ecosystem CO_2 exchange or surface fluxes on an annual or seasonal timescale, if surface fluxes are continuously monitored. Integrated surface fluxes for the two profiles were within 1% and 3% at Joshua Tree and Pinyon Juniper, respectively, despite one profile at each site having a significantly higher incidence rate and total magnitude of CO_2 derived from nighttime pulse events. It is thus possible that the carbon being respired during these intervals is derived from labile organic matter in the litter layer or surficial soils that forms the basis of a readily reactive soil carbon pool with a high probability of being respired over the seasonal cycle. Meaning that transiently high CO_2 production during nighttime pulse events is compensated by lower production throughout the rest of the wet season due to the decline in the labile organic carbon pool, limiting the influence of nighttime CO_2 production on the total annual surface flux. However, the nighttime pulse events are critical for understanding high-frequency changes in soil solid, aqueous, and gas phase chemistry and the broader ramifications for biogeochemical cycling. For example, a nighttime CO_2 pulse generates very high P_{CO_2} conditions in near-surface soils at the coldest part of the day when carbonate minerals are most soluble. The frequency and magnitude of this nighttime CO_2 production thus has important implications for our understanding of soil carbonate chemistry and the dissolution/reprecipitation dynamics of carbonate minerals (Breecker *et al.*, 2009).

4.3.5.2 Mechanism scoping: correlation with environmental variables

We now turn to the question of the predictability and mechanism underpinning these nighttime pulse events. We begin by examining the incidence and magnitude of pulse events against potential explanatory environmental variables. The ratio of maximum CO_2 concentration during the nighttime vs. preceding daytime interval is used as a proxy for the nighttime pulse magnitude that is somewhat normalized against the influence of seasonal fluctuations in temperature and water availability. In the JT2 profile, this ratio of maximum nighttime/daytime [CO_2] indicates that nighttime pulse events occur in a relatively constrained parameter space (Figure 4.18): pulses occur during periods of high primary productivity, closely following rain events (not more than 20 days past, with an average of 12) when the nighttime air temperature draws closer to the dew point than average, and larger magnitude pulses are observed when there is higher nighttime relative humidity. Soil and meteorological conditions during nights with and without nighttime pulse events are compared in Table D5. Notably, nights where a nighttime CO_2 pulse occurred had a statistically significantly higher GPP; shorter time since the last rain event; lower vapor pressure deficit and higher relative humidity; and a lower air temperature and difference between air temperature and the dew point (Table D5). Indeed, examining the temporal evolution of shallow-soil [CO_2], air temperature, and relative humidity during a series of nighttime pulse events, we find that while no correlative changes in soil water content were observed over the course of a pulse event, the nighttime pulses occur as the air temperature drops and approaches the dew point (Figure 4.19A) and the magnitude of nighttime CO_2 production seemingly scales with relative humidity (Figure 4.19B).

These observations point towards a mechanistic driver increasingly recognized as a critical contributor to litter degradation and microbial carbon cycling in dryland ecosystems: the delivery of non-precipitation sources of water to the litter layer and surficial soils (Dirks *et al.*, 2010; McHugh *et al.*, 2015; Gliksman *et al.*, 2017; Evans *et al.*, 2020). It is well-known that in arid systems, precipitation can be so low relative to demand that water acts as the limiting nutrient for biological processes (Noy-Meir, 1973). In these water-limited ecosystems, non-precipitation sources of water can be a critical lifeline for biotic activity and a non-negligible component of the water budget (Agam and Berliner, 2006). There are three primary mechanisms through which water can be delivered to surface soils in the absence of precipitation: fog deposition, dew formation, and water vapor adsorption (Agam and Berliner, 2006). Fog is uncommon in dryland systems with the exception of coastal deserts, as atmospheric water vapor concentrations must reach saturation for fog to form. Dew on the other hand, is formed when surface temperatures drop below the dew point due to radiative cooling and has been suggested to be an important part of the water balance in some desert environments (Kidron *et al.*, 2002; Malek *et al.*, 1999). Water vapor adsorption can also occur anytime the relative humidity of the soil atmosphere is lower than the relative humidity of the overlying air (Agam and Berliner, 2006). With the current dataset, we lack measurements of soil surface temperature and the measured temperature at 5cm depth seldom drops below the air temperature. We thus lack the data required to determine if soil

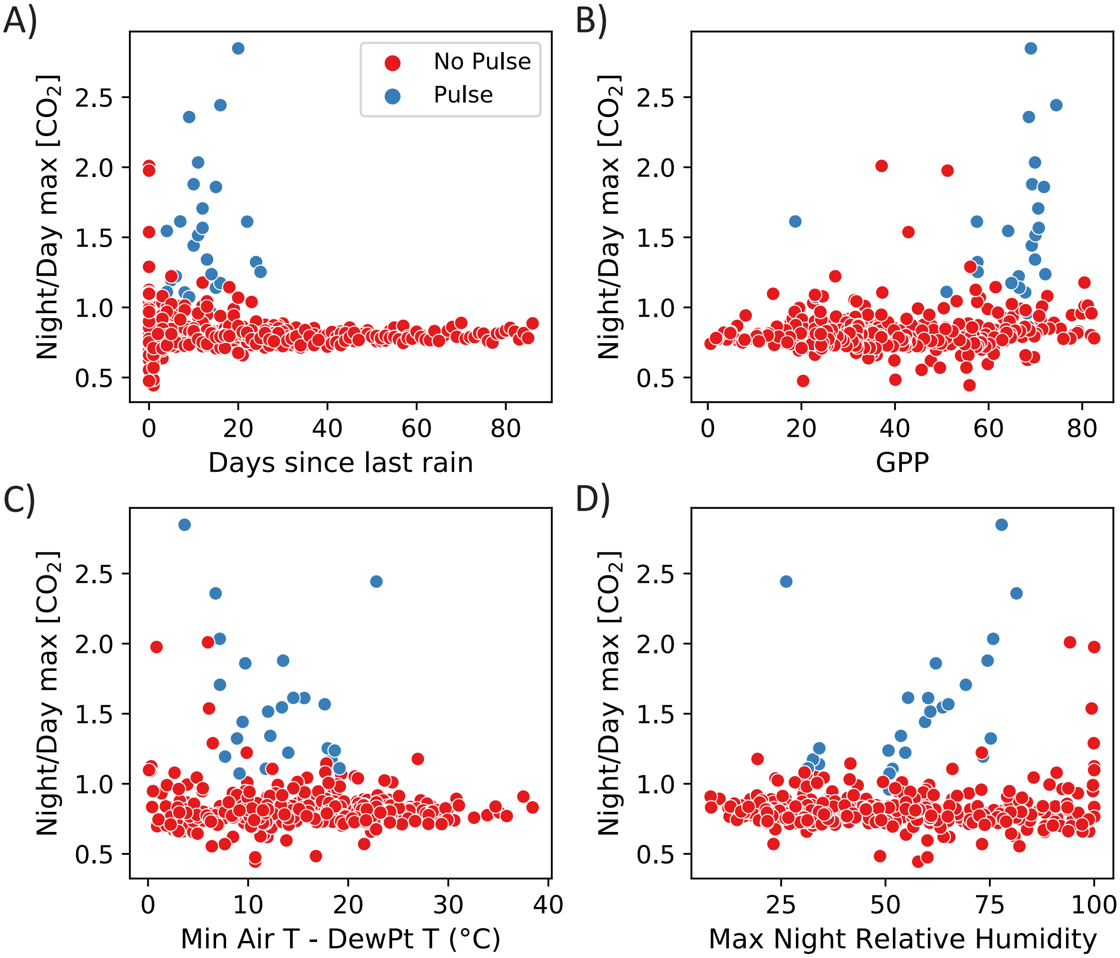

Figure 4.18 – Cross-plots of the nighttime pulse magnitude (ratio of maximum [CO$_2$] during the nighttime vs. preceding daytime interval) with potential predictor variables at the JT2 soil profile: A) number of days since the last rain event , B) gross primary productivity (gC/m^2/8-day), C) minimum nighttime difference between the air temperature and dew point, and D) maximum nighttime relative humidity.

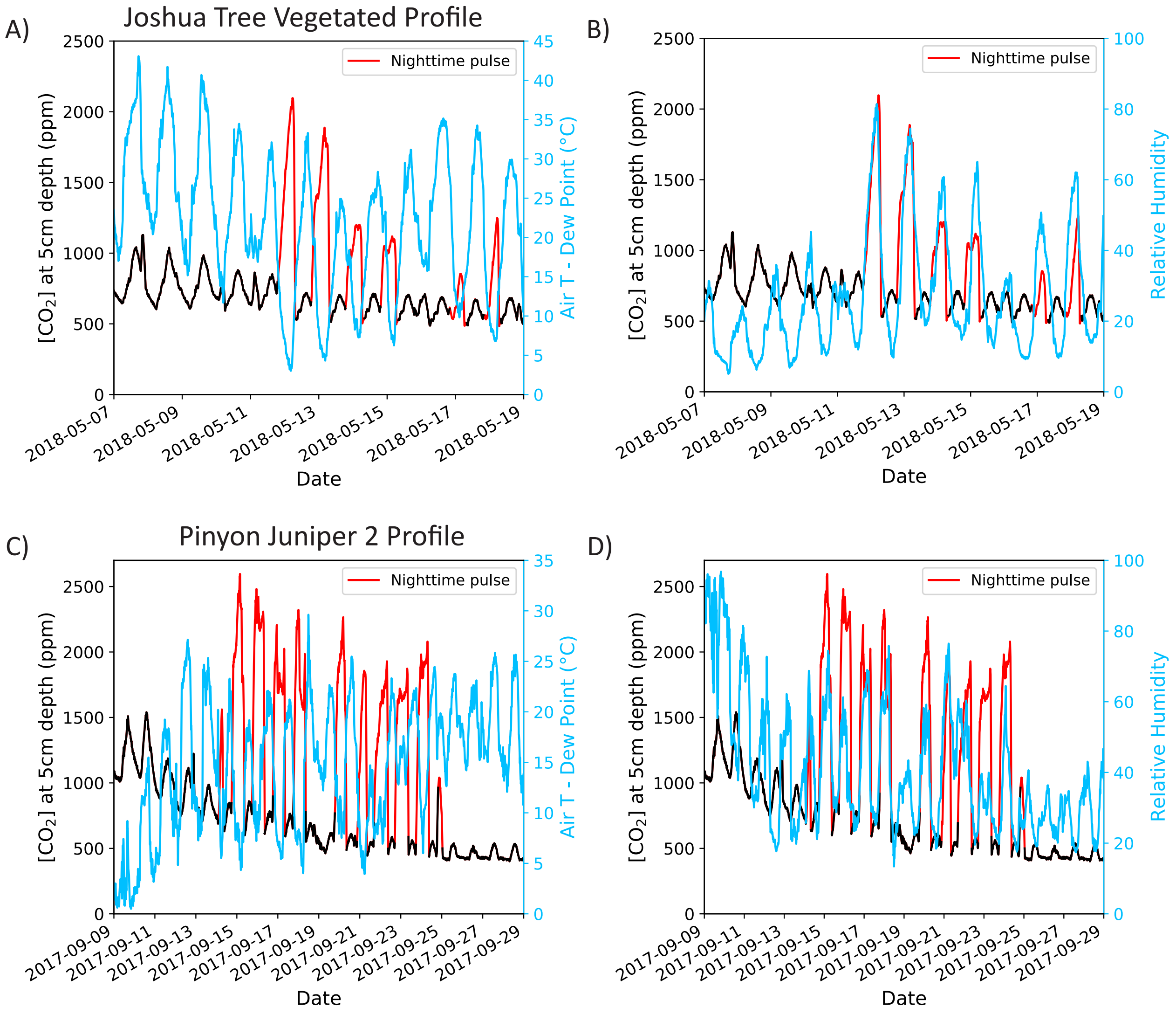

Figure 4.19 – Time series of soil CO_2 concentration at 5cm depth, the difference between air temperature and the dew point, and relative humidity during intervals with a series of nighttime pulse events at the JT2 (A,B) and PJ2 (C,D) profiles.

surface temperatures fall below the dew point during these nighttime CO_2 pulse episodes, and instead use the difference between air temperature and the dew point as a proxy for the probability that dew would form on the soil surface and/or that significant water vapor adsorption would deliver liquid water to surface soils.

Turning to the incidence of nighttime pulse events at the more densely vegetated Pinyon Juniper site, we find that the correlations between nighttime pulse formation and soil/meteorological conditions are not so straightforward (Figure 4.20). Nights where a nighttime pulse event occurred again exhibited a statistically higher GPP and shorter time since the last rain event than nights where no nighttime pulse was identified (Table D6). Pulses also occurred on nights with higher average soil temperature and water content (correlative with the higher primary productivity). However, nighttime pulse events were identified over a much broader range in parameter space than in the JT2 soil profile and the magnitude of nighttime CO_2 production was not as obviously correlated to relative humidity (Figure 4.20D, 4.19D). We thus further interrogate these patterns of nighttime pulse incidence rate and magnitude using decision tree analysis in the following section.

4.3.5.3 Insights from decision tree analysis

A classification tree was trained to predict the presence/absence of a nighttime pulse and a regression tree was trained to predict the magnitude of the nighttime/daytime CO_2 concentration ratio at each site using the predictor variables outlined in Section 4.2.5. Regression tree model fits are shown in Figure D12.

Mid-elevation Joshua Tree site The patterns identified above are further emphasized by the decision tree results at the Joshua Tree site. In the classification tree, primary productivity is the first branch point - nighttime pulses are more likely to occur during more productive times of the year (Figure 4.21A). The time since a major rain event ($\geq$10mm in a single day) then filters the pulse/no-pulse decision: the vast majority of pulse events occur within 16 days of a major rain event. These two predictors are potentially indicative of a concentration of labile organic carbon in surficial soils due to the ongoing elevated plant productivity and translocation of standing litter to the soil surface following a substantial rain event (Liu *et al.*, 2015a), coupled to relatively humid air in the presence of this near-surface litter layer. The final differentiator is the proximity to the dew point temperature. All pulse events in this main branch occur when the nighttime air temperature falls within 18.6°C of the dew point temperature, meaning that the nighttime CO_2 production occurs when conditions are amenable to water vapor adsorption and possibly dew formation. Outside of this main branch, pulse events are only predicted for very cool intervals (Figure 4.21A), again consistent with the delivery of non-rainfall water driven by falling temperatures.

A similar series of decisions predicts the magnitude of nighttime pulse events (Figure 4.21B). High nighttime CO_2 concentrations relative to the preceding day are predicted for high productivity intervals within approximately 2 weeks of a major rain event. The nighttime relative humidity then dictates the pulse magnitude: higher concentrations are predicted on nights where the relative humidity is above 61%. The highest magnitude pulse events are predicted during high-productivity intervals when the nighttime air temperature drops below 2°C. The 7 instances of significant nighttime CO_2 production observed at the interspace

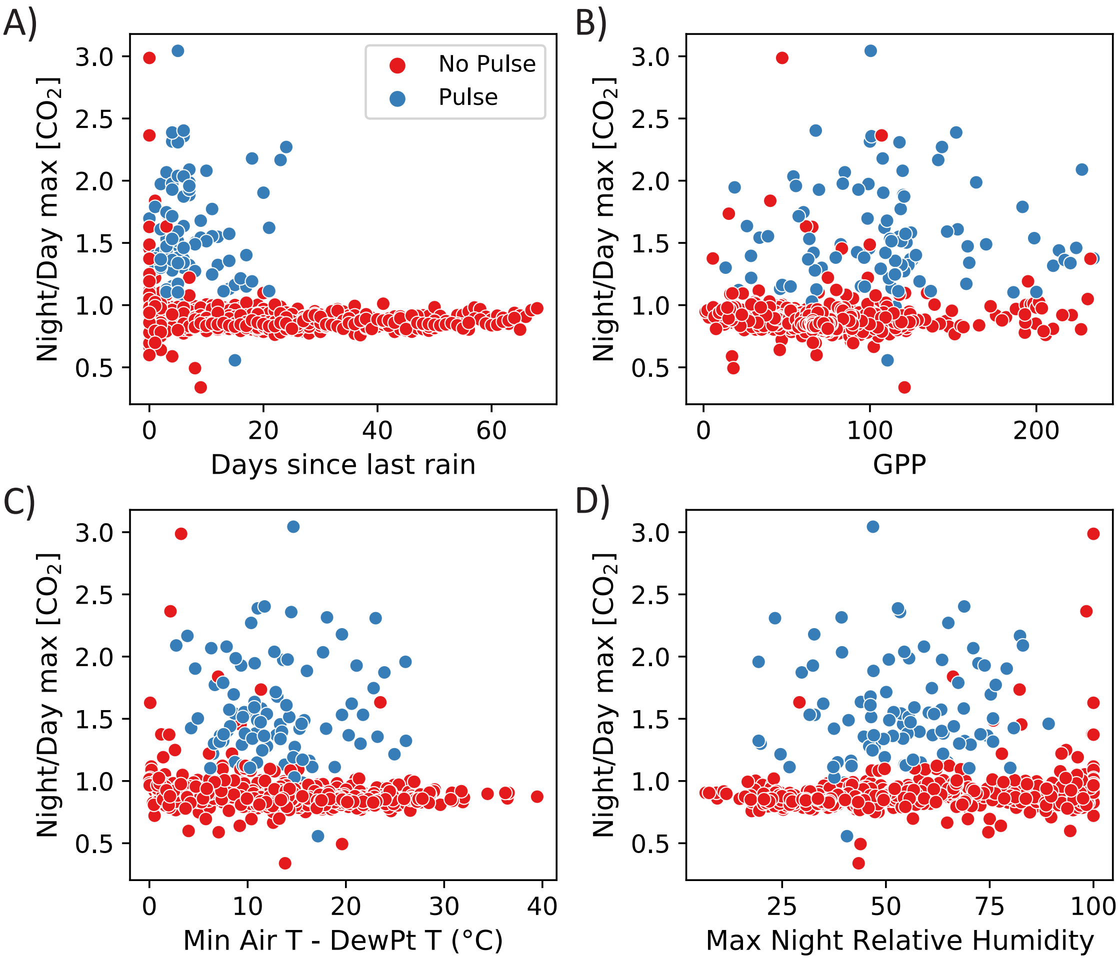

Figure 4.20 – Cross-plots of the nighttime pulse magnitude (ratio of maximum [CO_2] during the nighttime vs. preceding daytime interval) with potential predictor variables at the PJ2 soil profile: A) number of days since the last rain event, B) gross primary productivity (gC/m^2/8-day), C) minimum nighttime difference between the air temperature and dew point, and D) maximum nighttime relative humidity.

Joshua Tree profile (JT1) also support these trends (Figure D13).

High-elevation Pinyon Juniper site The story is more complicated at the high elevation Pinyon Juniper site. Most nighttime pulse events are identified during high productivity intervals when there is adequate moisture in near-surface soils (VWC at 5cm depth $> 4\%$) (Figure 4.22A). Relative humidity is then identified as a predictor of pulse formation, with a higher probability of an anomalous nighttime pulse event predicted when RH $< 83\%$. This potentially reflects a combination of the algorithm avoiding nighttime rain events which produce 'expected' pulses of CO_2 and the fact that radiative cooling is inhibited by high levels of atmospheric water vapor. The final pulse/no-pulse decision is dictated by the air temperature; there is a higher probability of a nighttime pulse event on cooler nights (Figure 4.22A). The regression tree analysis suggests that the highest nighttime CO_2 concentrations relative to the preceding day occur when near-surface soils are moist (VWC at 5cm depth $> 4\%$) and the relative humidity is high or near-surface soils are wet (VWC at 5cm depth $>$ 7%) and air temperatures are cool (Figure 4.22B). However, while a number of factors that correlate with a higher probability of pulse incidence and larger magnitude nighttime CO_2 production are consistent with moisture dynamics in the litter layer/surficial soils, it appears that nighttime CO_2 pulses simply occur much more readily in the PJ2 profile. Additional work is required to understand why the near-surface soils of the PJ2 profile are seemingly poised to generate significantly more nighttime CO_2 production than neighboring profiles (Table 4.6).

4.3.5.4 Summary and potential broader implications of nighttime pulse events

We hypothesize that the nighttime pulses of CO_2 documented here are driven by the delivery of non-precipitation sources of water to surficial soils, including the litter layer. This is consistent with our finding of highly water sensitive respiration in near-surface soils (Section 4.3.3.2) and a growing literature on the role of dew formation and water vapor adsorption in litter degradation in dryland systems (Dirks *et al.*, 2010; McHugh *et al.*, 2015; Gliksman *et al.*, 2017; Evans *et al.*, 2020). Dirks *et al.* (2010) and Gliksman *et al.* (2017) demonstrate that nighttime water vapor adsorption and dew deposition in the litter layer are the dominant drivers of litter decomposition during the extended dry season of Mediterranean shrub and grassland ecosystems in Israel. Gliksman *et al.* (2017) estimate that the majority of dry season litter CO_2 efflux is due to this nighttime microbial degradation, augmented by thermal- and photodegradation during the day (Brandt *et al.*, 2009; Austin *et al.*, 2016). Importantly, they found that nighttime litter decomposition driven by water vapor deposition could start in the early evening hours, as the relative humidity rose above 70%. This is highly similar to the timing of nighttime CO_2 production observed in the near-surface soils of the mid- and high-elevation climosequence sites (Figures 4.17, 4.19). McHugh *et al.* (2015) further demonstrated that the formation of liquid water in soil pores as a result of water vapor adsorption could stimulate microbial activity and CO_2 production in dryland soils.

The role of hyper-local microclimate and spatial variability in soil chemical characteristics and biotic activity in driving the nighttime CO_2 production requires further investigation. At the Joshua Tree site, the patterns of nighttime CO_2 production are consistent with the

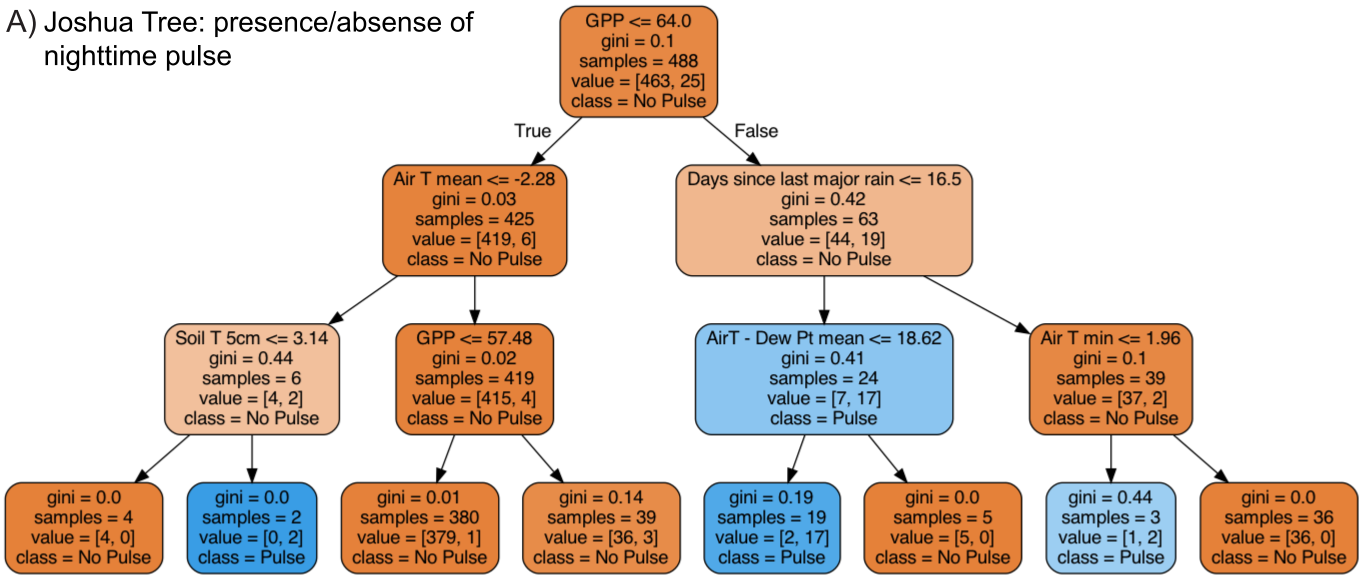
A) Joshua Tree: presence/absense of nighttime pulse

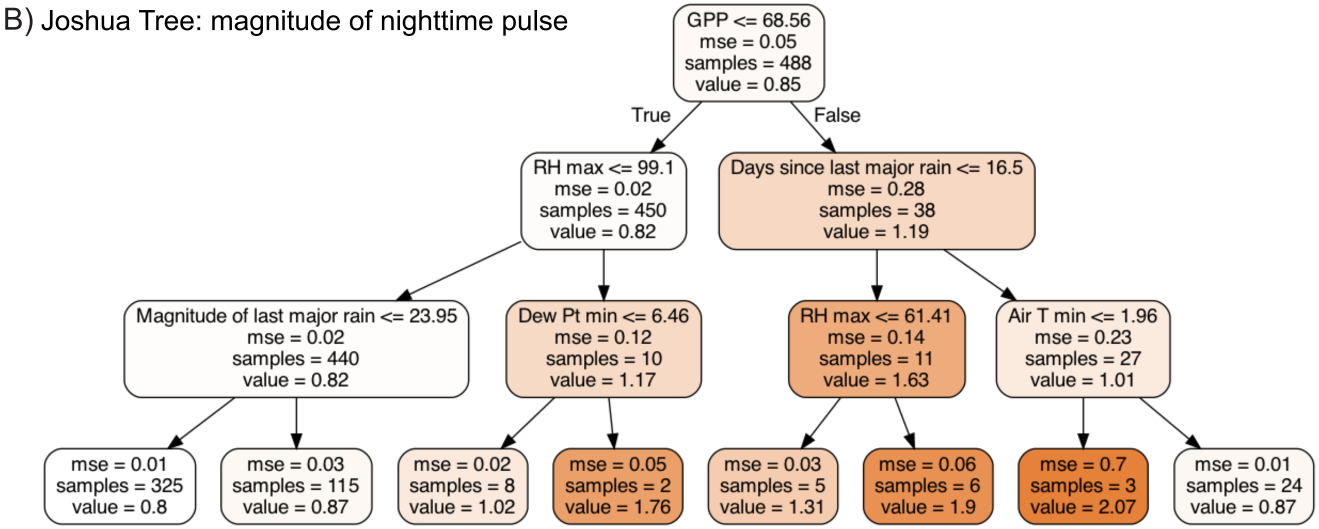
B) Joshua Tree: magnitude of nighttime pulse

Figure 4.21 – Decision trees predicting nighttime pulse events at the Joshua Tree vegetated profile (JT2). A) Classification tree predicting the presence/absence of a nighttime pulse. Blue coloration indicates the prediction of a nighttime pulse event. B) Regression tree predicting the magnitude of the nighttime pulse (ratio of maximum [CO_2] during the nighttime vs. preceding daytime interval). Orange coloration denotes a higher predicted nighttime CO_2 concentration relative to the preceding day.

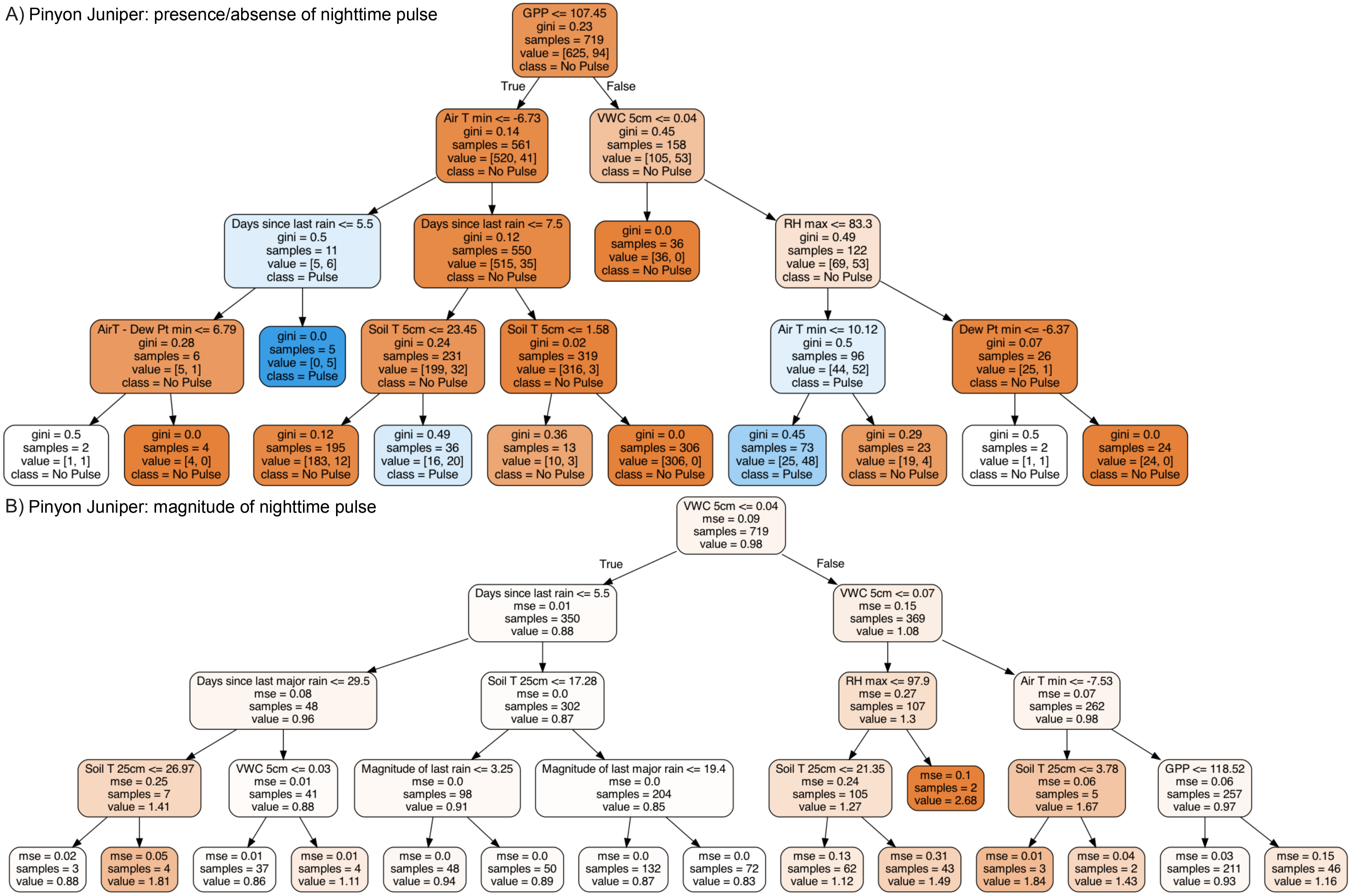

Figure 4.22 – Decision trees predicting nighttime pulse events at the Pinyon Juniper mixed shrub/grass profile (PJ2). A) Classification tree predicting the presence/absence of a nighttime pulse. Blue coloration indicates the prediction of a nighttime pulse event. B) Regression tree predicting the magnitude of the nighttime pulse (ratio of maximum [CO_2] during the nighttime vs. preceding daytime interval). Orange coloration denotes a higher predicted nighttime CO_2 concentration relative to the preceding day.

stimulation of microbial carbon cycling in surficial soils by the delivery of non-precipitation sources of liquid water. The higher rate of nighttime pulse incidence in the JT2 profile than JT1 is also consistent with this mechanism: surficial soils of the under-canopy soil profile likely have a much more substantial litter layer as well as a higher concentration of nutrients (Schlesinger *et al.*, 1996; Titus *et al.*, 2002) relative to the interspace soil profile. At the higher elevation Pinyon Juniper site, however, the PJ1 and PJ2 soil profiles are both located in mixed shrub/grass microsites, yet only 1 nighttime CO_2 pulse was observed at PJ1 over the 2-year monitoring interval while 94 nighttime pulses were identified at PJ2 (Table 4.6). With the current dataset we can only speculate as to the drivers of this disparity, but we offer two potential contributing factors here. First, there are established biological soil crusts adjacent to the PJ2 soil profile, which may provide a source of readily available carbon and nitrogen in the top millimeters of soil (Pointing and Belnap, 2012). It is possible that the frequent nighttime CO_2 production events at PJ2 are related to the transfer of carbon and nutrients between biological soil crusts and plants (Green *et al.*, 2008) or are driven by a unique consortium of microbes and fungi in the vicinity of the crust. Second, it is possible that the PJ2 soil profile receives a comparable litter flux from the surrounding vegetation as the PJ1 profile, but is relatively more exposed due to differences in shrub canopy structure. Less canopy shading would enable higher levels of photo/thermal-degradation that primes the litter chemistry for subsequent microbial degradation (Brandt *et al.*, 2009; Austin *et al.*, 2016; Gliksman *et al.*, 2017).

In all, these findings support calls to better understand and parameterize the role of water vapor and dew deposition as global drivers of litter decomposition and near-surface carbon cycling, especially in water-limited ecosystems like those studied here (McHugh *et al.*, 2015; Gliksman *et al.*, 2017; Evans *et al.*, 2020). As discussed above, while the nighttime CO_2 pulses documented here do not appear to substantially impact surface CO_2 fluxes on an annual timescale, they represent significant perturbations to the local soil biogeochemical environment and have considerable implications for the precise timing of CO_2 production. This suggests that a quantitative understanding of the delivery of non-precipitation sources of water may be required to capture the short-timescale dynamics of coupled soil organic-inorganic carbon cycling in dryland ecosystems.

4.4 Conclusions

Two years of in-situ monitoring of micro-meteorological and soil conditions at a series of soils along a climate gradient in the Mojave Desert provide a window into the primary controls on carbon cycling in arid soil systems. Analysis of in-situ observations of soil CO_2 concentration, water content, and temperature to 125cm depth in a production-diffusion framework reveals that the sensitivity of CO_2 production to environmental conditions is not constant across the soil profile. Shallow soil layers (2.5-15cm depth) are significantly more water sensitive than deeper soil layers. The sensitivity of soil CO_2 production to temperature and water availability also varies with elevation. Respiration at the highest temperature, lowest elevation Creosote site is found to be substantially less temperature sensitive than respiration at the less arid, higher elevation sites, particularly in shallow regions of the soil profile. This may reflect thermal acclimation of soil microbial (and potentially plant) communities to the higher ambient temperatures experienced.

We demonstrate that CO_2 production across the soil profile is well-described by temperature and water content-dependent functions of shallow heterotrophic respiration that declines exponentially with depth and autotrophic respiration that follows the root distribution profile. Production-diffusion models driven by measured soil temperature and water content capture CO_2 dynamics throughout the soil profile, capturing both the pulses of CO_2 production following precipitation events and the soil carbon cycle response to seasonal changes in environmental boundary conditions. In this framework, the autotrophic respiration that dominates the deeper portions of the soil profile is found to be less temperature and water sensitive than near-surface heterotrophic respiration. Additional work aimed at experimentally differentiating between autotrophic and heterotrophic respiration within the context of similar high-resolution in-situ monitoring of soil profiles will help refine the parameterizations developed here (Hanson *et al.*, 2000).

Finally, we document and interrogate the potential mechanistic drivers of significant nighttime CO_2 production events in shallow soils of the higher elevation sites. We show evidence that these nighttime CO_2 pulses may be linked to microbial respiration stimulated by the delivery of non-rainfall moisture to the litter layer and uppermost centimeters of the soil profile. The implications of these nighttime pulse events are found to depend on the timescale of interest. While our results suggest that the nighttime CO_2 production does not substantially impact surface CO_2 fluxes on an annual timescale, the nighttime pulse events represent significant perturbations to the local soil biogeochemical environment, with significant consequences for the short-timescale dynamics of coupled soil organic-inorganic carbon cycling.

In all, our results highlight the utility of high temporal resolution soil profile monitoring as a compliment to measurements of surface flux, which provides an integrated measure of CO_2 production and transport throughout the soil column. The findings presented here emphasize the highly dynamic nature of soil CO_2 production and surface-atmosphere CO_2 exchange in arid ecosystems and provide important quantitative constraints on the response of CO_2 production throughout the soil profile to changing environmental conditions. These insights could help inform our understanding of how soil carbon cycling in dryland systems will evolve in the coming decades in response to predicted changes in temperature and precipitation regimes with changing climate and land use.

Chapter 5

Magnitude and mechanism of CO_2 consumption in Mojave Desert soils

Abstract

Recent reports of CO_2 consumption in highly oxidized desert soils have revealed an enigmatic temporal carbon sink, that appears to have abiotic origins. While arid soils contain relatively low levels of organic carbon, they can contain large amounts of inorganic carbon in the form of pedogenic carbonate. Although a net loss or uptake of soil inorganic carbon requires a significant alkalinity source or sink, the short-timescale dynamics of inorganic carbon speciation and its impact on CO_2 fluxes remain poorly understood. Here we explore the mechanisms and implications of intervals of soil CO_2 uptake observed in a long-term study of a climosequence in the Mojave Desert, including potential links to soil inorganic carbon dynamics. At the most arid site, negative surface fluxes on the order of $-0.1\mu mol/m^2/s$ regularly occur at night during the dry season in inter-canopy soils. These negative surface fluxes are driven by almost continuous nighttime CO_2 consumption in shallow soil layers (0-15cm depth), the magnitude of which is strongly dependent on the amplitude of the diurnal soil temperature oscillation (daily maximum - minimum temperature). We also observe acute consumption events ($-0.2\mu mol/m^2/s$ surface flux) following precipitation in inter-canopy soils. We quantitatively evaluate potential mechanisms for these CO_2 sinks and determine that thermal impacts on the dissolved inorganic carbon system (carbonate mineral solubility and CO_2 gas partitioning into the aqueous phase) alone cannot produce the magnitude of consumption observed, unless higher pH conditions are maintained than predicted for reasonable carbonate mineral saturation states. CO_2 adsorbed on soil minerals, however, possibly represents a much larger accessible CO_2 pool and reasonable assumptions regarding the temperature sensitivity of CO_2 adsorption yields consumption fluxes on the order of that observed in the inter-canopy soils. We thus suggest that temperature dependent CO_2 adsorption onto mineral surfaces could play an important role in driving the large diurnal fluctuations in soil CO_2 surface flux observed in arid systems, but caution that additional work is required to empirically quantify the magnitude of ambient CO_2 adsorption to soil minerals under representative soil conditions. The acute episodes of CO_2 consumption following rain events are consistent with CO_2 uptake driven by carbonate mineral dissolution, potentially augmented

by near-surface biotic carbon fixation. In all, these findings emphasize the importance of accounting for inorganic CO_2 fluxes in interpretations of carbon dynamics in arid systems and highlight the need to develop quantitative predictions of those fluxes.

5.1 Introduction: Complicated drivers of soil-atmosphere CO_2 exchange in arid systems

Recent advances in continuous measurements of soil CO_2 concentrations and fluxes open important unexplored avenues into discovering and understanding previously unrecognized controls on CO_2 dynamics in soils. One of the more surprising of these recent discoveries is the apparent net consumption of CO_2 in arid soil environments that contradicts the long-held assumption that soil CO_2 fluxes are unidirectional, reflecting production by heterotrophic and root respiration. Soils in arid regions have unique characteristics, such as low overall rates of respiration, highly spatially and temporally variable biological processes that respond to brief intervals of adequate moisture followed by extended dry periods, and the visible manifestation of the linkage of biological and non-biological processes in the accumulation of $CaCO_3$ mineral horizons (Monger and Gallegos, 2000; Schlesinger, 1985). Observations of net soil CO_2 consumption have been reported in both hot and cold deserts, across continents including the Mojave (Wohlfahrt *et al.*, 2008), Chihuahuan (Hamerlynck *et al.*, 2013), and Great Basin (Yates *et al.*, 2013) deserts of the southwestern United States; the Mu Us (Liu *et al.*, 2015b; Fa *et al.*, 2016, 2018) and Gurbantunggut (Xie *et al.*, 2009; Ma *et al.*, 2013, 2017; Wang *et al.*, 2020) deserts of Northern China; and the McMurdo Dry-Valleys of Antarctica (Parsons *et al.*, 2004; Ball *et al.*, 2009; Shanhun *et al.*, 2012).

A particularly common observation is negative CO_2 surface fluxes at night (Ma *et al.*, 2013; Hamerlynck *et al.*, 2013). This nocturnal CO_2 uptake has been demonstrated to be abiotic through both laboratory and in-situ sterilization experiments (Parsons *et al.*, 2004; Xie *et al.*, 2009; Yates *et al.*, 2013; Ma *et al.*, 2013; Fa *et al.*, 2018; Wang *et al.*, 2020) and is often observed during extended dry periods. Notably, a majority of these observations of net negative or otherwise anomalous CO_2 fluxes are made in systems with carbonate substrates (e.g. karst ecosystems (Kowalski *et al.*, 2008; Roland *et al.*, 2013; Cueva *et al.*, 2019)) or in saline/alkaline soils (Xie *et al.*, 2009; Shanhun *et al.*, 2012; Yates *et al.*, 2013; Wang *et al.*, 2020). As such, temperature-dependent reactions of the soil carbonate system are often invoked as an explanation for the nocturnal uptake (Ma *et al.*, 2013; Roland *et al.*, 2013; Hamerlynck *et al.*, 2013; Fa *et al.*, 2016; Wang *et al.*, 2020). CO_2 is consumed during carbonate mineral dissolution (Eq. 5.1.1) and produced during carbonate precipitation:

$$CaCO_3 + CO_2 + H_2O \rightleftharpoons Ca^{2+} + 2HCO_3^- \tag{5.1.1}$$

$$K_H(T) = \frac{[CO_{2,aq}]}{P_{CO_2}} \tag{5.1.2}$$

In many ecosystems, the CO_2 fluxes associated with carbonate dissolution-precipitation reactions are small relative to biological fluxes. However, in arid ecosystems the low levels of biotic activity (particularly during dry periods) coupled with the accumulation of

$CaCO_3$ means that CO_2 fluxes from carbonate weathering reactions can be a non-negligible component of overall CO_2 dynamics (Kowalski *et al.*, 2008; Rey, 2015). In particular, calcium carbonate minerals are retrograde soluble, meaning that the mineral is more soluble at lower temperatures (Plummer and Busenberg, 1982). If nighttime temperatures produce soil solution conditions undersaturated with respect to calcium carbonate, the dissolution reaction could contribute to the nocturnal CO_2 uptake observed (Hamerlynck *et al.*, 2013; Fa *et al.*, 2016; Soper *et al.*, 2017). The solubility of CO_2 in water is also temperature sensitive; lower temperatures increase CO_2 partitioning into the soil solution (Wilhelm *et al.*, 1977). Enhanced CO_2 partitioning into the aqueous phase (Eq. 5.1.2) in response to falling temperatures could also drive substantial CO_2 uptake, particularly in high-pH soil solutions (Shanhun *et al.*, 2012; Ma *et al.*, 2013). However, many observations of nocturnal CO_2 consumption occur in soils with very low water contents (including oven-dried soils in the laboratory (Parsons *et al.*, 2004; Yates *et al.*, 2013)), leading to questions of whether the magnitude of consumption observed could be achieved through aqueous-phase reactions with such a limited soil water reservoir. It has also been suggested that CO_2 adsorption to mineral surfaces could play a role in the uptake observed (Parsons *et al.*, 2004; Yates *et al.*, 2013), but the details of such a mechanism have not been quantitatively analyzed.

The specific mechanism underlying the documented CO_2 consumption as well as the broader implications of this abiotic flux thus remain under investigation. Of particular interest is the question of whether the uptake observed represents a net sink of CO_2 over longer timescales or a largely reversible abiotic cycle operating on a diurnal timescale (Schlesinger *et al.*, 2009). Here we document two types of CO_2 consumption occurring predominantly in interspace soils at the most arid site in the Mojave Climosequence, quantitatively explore potential mechanistic underpinnings for this CO_2 uptake, and discuss implications for the interpretation of CO_2 profile and flux data from arid ecosystems.

5.2 Methods

5.2.1 In-situ monitoring of Mojave Desert Climosequence

As detailed in Chapter 4, a series of sites along a climate/elevation gradient in the Mojave National Preserve were sampled and instrumented for long term monitoring of meteorological and soil conditions as part of a broader effort to characterize the controls on coupled organic-inorganic carbon cycling in arid systems. Soil water content, temperature, and CO_2 concentration were measured throughout the profile (surface, 5, 25, 50, and 125cm depth) in both interspace and under-canopy soils adjacent to the dominant vegetation type (e.g. an established creosote shrub). Meteorological and in-situ soil sensor data were logged at ten-minute intervals for a period of over 2 years. Soil horizons were identified, characterized, and sampled in the field; field descriptions as well as complete characterizations of soil physical and chemical properties can be found in Appendix C. Here, we focus solely on the lowest elevation, Creosote site, where the bulk of the net CO_2 consumption behavior was observed.

5.2.2 CO_2 flux and production calculations

Soil CO_2 fluxes were calculated using the flux gradient method as described in Section 4.2.4, making the explicit assumption that CO_2 production (± consumption) and transport via molecular diffusion are the dominant processes controlling CO_2 concentrations in the soil profile (Tang *et al.*, 2005; Vargas and Allen, 2008). In brief, soil CO_2 diffusivity ($D_s, m^2/s$) was calculated at each depth as a function of soil texture, temperature, pressure, and water content following Moldrup *et al.* (1999) (Eq. 7 in that work). The CO_2 flux across various layers in the soil profile, including the surface, was then calculated using flux gradient theory and Fick's first law of diffusion:

$$F = -D_s(z)\frac{\partial C(z)}{\partial z} \tag{5.2.1}$$

$$F_i = -\left(\frac{D_s(z_i) + D_s(z_{i+1})}{2}\right)\frac{C(z_i) - C(z_{i+1})}{z_{i+1} - z_i} \tag{5.2.2}$$

Net CO_2 production was then calculated as the difference in diffusive flux across adjacent layers in the soil profile (Vargas *et al.*, 2010b):

$$P_i = \frac{F_i - F_{i+1}}{z_{i+1} - z_i} \tag{5.2.3}$$

where $\mathrm{P_i}$ is the soil CO_2 production rate ($\mathrm{mol/m^3/s}$) between depths $\mathrm{z_i}$ and $\mathrm{z_{i+1}}$. This assumes an instantaneous steady-state, where CO_2 production in a given depth interval is balanced by CO_2 diffusion into and out of that depth interval.

For the purposes of quantifying CO_2 consumption, we applied a further check on the calculated net production values. In this computational framework, depth-integrated production is equivalent to the net flux out of the soil, i.e. the CO_2 surface flux. In general, the calculated surface flux is in very good agreement with calculated CO_2 production summed across the entire profile, particularly for the bare soil Creosote site where the majority of CO_2 consumption is observed (Figure 5.1A). To produce the most conservative estimate possible of the magnitude of CO_2 consumption in surface soils observed here, we define a 'max production' term, where the difference between the surface flux and depth-integrated production is assigned to the surface horizon (2.5-15cm depth, Figure 5.1B). All production values reported here (and thus calculated consumption magnitudes) reflect this max production term.

5.2.3 Geochemical modeling of nighttime CO_2 consumption

The net CO_2 production calculation described above was used to estimate the magnitude of CO_2 consumption occurring at night in the surface horizons (2.5-15cm depth, constrained by diffusive flux calculations between 0-5cm and 5-25cm depth, Section 5.3.3.1). Two potential mechanisms to explain this CO_2 uptake are explored quantitatively in Section 5.3.4: CO_2 consumption due to temperature-sensitive carbonate system reactions (Henry's law partitioning ± carbonate dissolution) and temperature-sensitive CO_2 adsorption to mineral surfaces. In both, we consider the top 15cm of a 1m x 1m soil column with a bulk density of

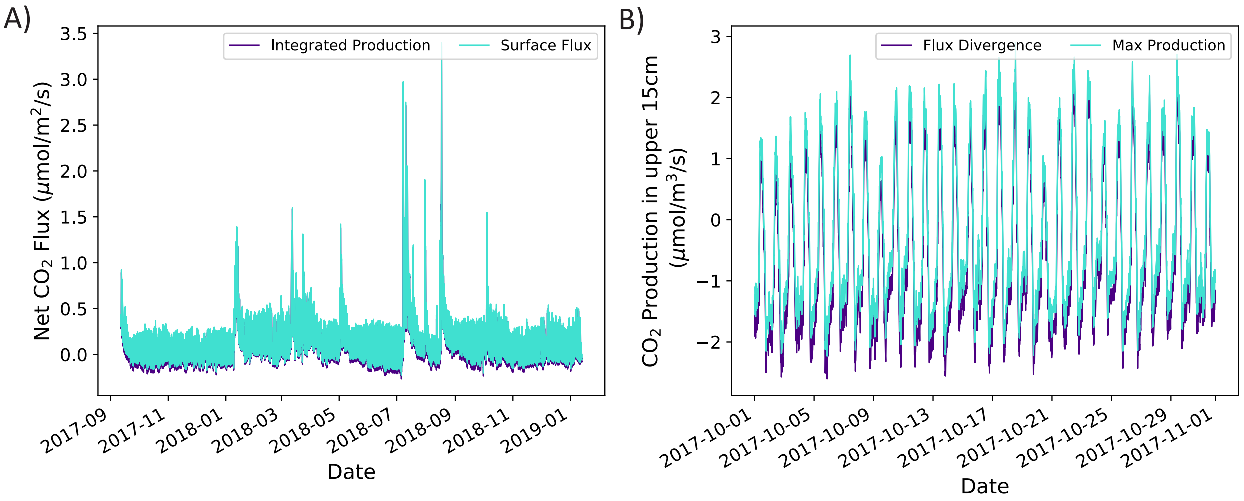

Figure 5.1 – Calculation of conservative 'max production' term for quantifying the magnitude of CO_2 consumption. A) Comparison of CO_2 surface flux (teal) and depth-integrated production (navy) for the bare-soil Creosote profile. B) Comparison of the CO_2 production flux (negative values connote net consumption) calculated by flux-divergence and the 'max production' value used here. In the 'max production', the difference between the surface flux and depth-integrated production is assigned to the surface horizon to provide the most conservative estimate possible for the magnitude of CO_2 uptake in the surface horizon.

1.4g/cm^3 (as measured at 25cm in the Creosote bare soil profile) and porosity of 0.47. This yields a total soil volume of 150,000cm^3 = 150L, total void volume of 71L, and soil water volume dictated by measured volumetric water content (generally under 2%, which would yield 3L water available for CO_2 uptake).

5.2.3.1 CO_2 consumption due to temperature-sensitive carbonate system reactions

Aqueous phase CO_2 partitioning and carbonate mineral solubility are both temperature sensitive: lower temperatures increase $CaCO_3$ solubility and CO_2 partitioning into soil water. We modeled the maximum potential CO_2 uptake due to these effects with PhreeqC (Parkhurst and Apello, 2013), using the reaction_temperature block to run a batch reaction at temperatures ranging from 5-55°C, equilibrating the same starting solution to 500ppm CO_2 and testing the impact of different assumptions regarding calcite supersaturation: equilibrium with an excess of calcite, fixing the supersaturation with respect to calcite at $SI = log_{10}\left(^{\{Ca^{2+}\}\{CO_3^{2-}\}}/_{K_{sp}}\right) = 1.0$, and allowing for an arbitrarily high SI. Solution speciation and calcite saturation were determined using the phreeqC.dat thermodynamic database and calcite equilibrium constant $K_{sp} = 10^{-8.48}$ at 25°C (Plummer and Busenberg, 1982). The maximum nighttime CO_2 uptake (mmol/m^2) was quantified as the difference in total dissolved inorganic carbon between the nighttime minimum temperature and daytime maximum temperature.

The magnitude of CO_2 aqueous-phase partitioning and calcite dissolution is particularly sensitive to solution pH and the total volume of water available for aqueous-phase reactions, the implications of which we explore here (Section 5.3.4.1). Solution chemistry was constrained using saturated paste extract data (Table C5), which yields major ion concentrations at a volumetric water content of ~30%. As a first-order estimate of solution chemistry under field conditions (<1-2% VWC throughout the dry season), we increased the saturation paste extract concentrations by 25x. This yields solution chemistries significantly supersaturated with respect to $CaCO_3$ but no other common sparingly soluble soil mineral phases, so $[Ca^{2+}]$ and carbonate alkalinity are dictated by the assumed supersaturation with respect to calcite (i.e. if calcite equilibrium was assumed, Ca^{2+} and HCO_3^- were removed from solution through calcite precipitation).

5.2.3.2 CO_2 adsorption to mineral surfaces

CO_2 adsorption to mineral surfaces is also temperature dependent. Calculating the potential CO_2 uptake due to solid-phase sorption requires two pieces of information: 1) a reasonable estimate of the moles of CO_2 adsorbed at ambient temperature, pressure, and CO_2 concentration (~400ppm), and 2) the temperature dependence of that adsorption. There is a marked paucity of low-temperature, low-pressure CO_2 adsorption isotherms for soils or individual mineral phases. We thus aim to provide a first-order estimate based on available data. Ravikovitch *et al.* (2005) measured CO_2 BET isotherms of various soils at 0°C (at the low end but within the temperature range experienced by Mojave soils), with CO_2 concentrations as low as ambient pCO_2. They report a maximum CO_2 uptake (for 1atm CO_2) of ~0.1 - 0.15mg/m^2 for soils with low organic carbon contents. At low CO_2 concentrations, the ratio of the measured uptake to maximum uptake was between 0.1-0.3. Thus at 0°C, a conservative estimate of CO_2 adsorption is 0.01 mg CO_2/m^2.

The mineral surface area was calculated from the particle size distribution (Table C7), assuming a surface area for the gravel, sand, silt, and clay size fractions of 11.1, 444.4, 1.11e5, and 7.4e6 cm^2/g, respectively. This yields an estimated surface area of ~40m^2/g for the top 30cm of the soil profile, almost exclusively from the clay size fraction. Thus a first-order estimate of CO_2 adsorbed in the top 15cm of soil is: (0.01 $mgCO_2/m^2$)*(40m^2/g)*(1.4e6g/m^3)* (0.15m) = 84 gCO_2/m^2 = 1.9 mol CO_2/m^2 at 0°C. Note, here m^2 again refers to a 1m x 1m patch of soil (not mineral surface area). A more conservative estimate of 20m^2/g surface area yields an estimated 0.95 mol CO_2 adsorbed.

The temperature dependence of CO_2 adsorption at low partial pressures is again highly under-constrained, but we derive a first-order estimate as follows. Using a Langmuir isotherm framework (Langmuir, 1918), adsorption can be described as:

$$q = q_{sat}\left(\frac{bP}{1+bP}\right) \tag{5.2.4}$$

where q is the amount of gas adsorbed (mol/g), q_{sat} is the sorption capacity, P is the pressure of gas, and b is the temperature-dependent adsorption equilibrium constant. This temperature dependence can be described using the van't Hoff expression (Fianu *et al.*, 2018):

$$b = b_0 \exp\left({}^{\Delta H_{ads}}/_{RT}\right) \tag{5.2.5}$$

where ΔH_{ads} is the enthalpy of adsorption. At low pressures, $1 + bP \sim 1$ and

$$q \sim q_{sat} * b * P = q_{sat} * P * b_0 \exp\left({}^{\Delta H_{ads}}/_{RT}\right) \tag{5.2.6}$$

Thus all else being constant, gas adsorption to solid surfaces scales with temperature roughly as $\exp\left({}^{\Delta H_{ads}}/_{RT}\right)$, and for a given ΔH_{ads}, the ratio of CO_2 adsorbed at two different temperatures can be calculated as:

$$\frac{q_1}{q_2} = \frac{\exp\left({}^{\Delta H_{ads}}/_{RT_1}\right)}{\exp\left({}^{\Delta H_{ads}}/_{RT_2}\right)} = \exp\left(\frac{\Delta H_{ads}}{R}\left(\frac{1}{T_1} - \frac{1}{T_2}\right)\right) \tag{5.2.7}$$

The temperature dependence of CO_2 adsorption to kaolinite reported by Chen and Lu (2015) yields a ΔH_{ads} of 10kJ/mol, a reasonable adsorption enthalpy for physisorption. We use this as a maximum estimate for ΔH_{ads} for the soils considered here.

5.3 Results and Discussion

Two distinct phenomenologies of CO_2 consumption are observed in intercanopy soils of the most arid climosequence site: regular negative nighttime surfaces fluxes during dry intervals, and acute episodes of CO_2 consumption following rain events.

5.3.1 Negative nighttime surface fluxes

Negative nighttime CO_2 surface fluxes are frequently observed in the bare soil profile. Figure 5.2 shows an example from December 2017, at the end of the winter drought period. Every night throughout the month, the CO_2 concentration at 5cm depth drops below the surface CO_2 concentration (Figure 5.2A), yielding a negative surface flux on the order of -0.1μmol/m^2/s (Figure 5.2B). The nighttime surface flux from the bare soil profile is negative during dry intervals throughout the seasonal cycle. The average diurnal cycle in CO_2 surface flux for four representative months between September 2017-2018 is shown in Figure 5.3. During non-monsoon intervals in both the winter and summer (December and June), the average nighttime surface flux from the bare soil profile is between -0.1 and -0.2 μmol/m^2/s while a negligible to positive surface flux is observed for months during wet intervals. These instantaneous rates of nighttime soil CO_2 uptake are similar to those observed in intercanopy soils during a hot and dry interval in the Chihuahuan Desert (Hamerlynck *et al.*, 2013), in saline Antarctic Dry Valley soils (Parsons *et al.*, 2004; Ball *et al.*, 2009; Shanhun *et al.*, 2012), and some saline/alkaline soils from central Asian deserts (Ma *et al.*, 2013; Wang *et al.*, 2020). Substantially higher rates of CO_2 consumption have been observed in hypersaline soils of the Gurbantunggut Desert, with surface fluxes of -1μmol/m^2/s or below reported by Xie *et al.* (2009) and Wang *et al.* (2020).

Notably, the surface flux is infrequently negative in the under-canopy profile adjacent to an established creosote shrub (Figures 5.2, 5.3), echoing the pattern of more frequent and higher magnitude CO_2 uptake in intercanopy soils observed by Hamerlynck *et al.* (2013) and Ma *et al.* (2013). This raises questions regarding the spatial distribution and temporal frequency of nighttime CO_2 consumption in these systems. Is the nightly CO_2 uptake observed driven by nearly continuous gross consumption in all soils, overprinted by higher

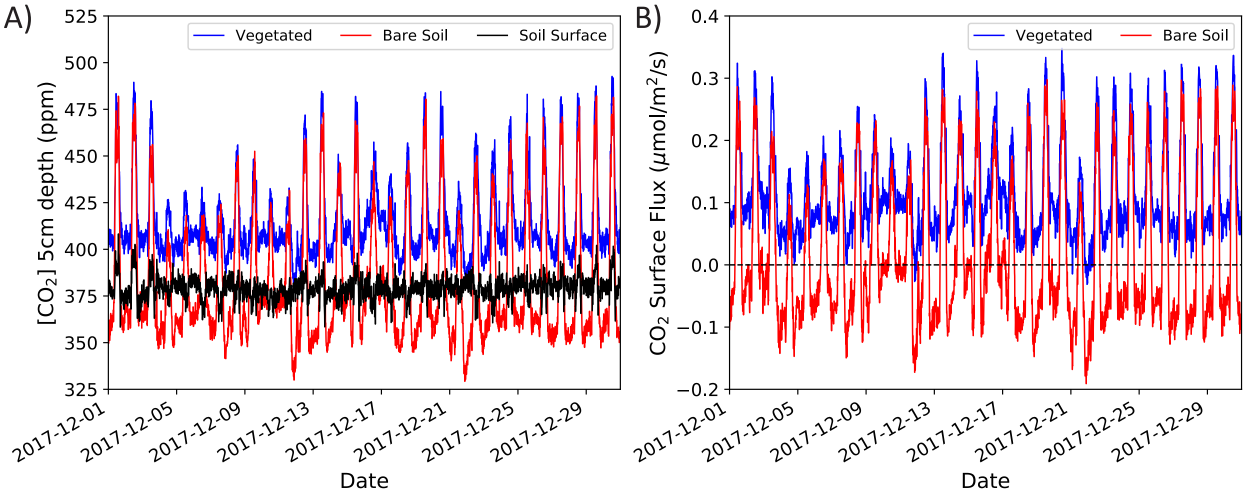

Figure 5.2 – Near-surface CO_2 dynamics during a winter drought interval (3 months without rain) at the Creosote site: A) CO_2 concentration at 5cm depth and B) surface flux. The dashed reference line indicates a surface flux of 0μmol/m^2/s. Regular negative nighttime CO_2 surface fluxes are observed in the intercanopy (bare soil) profile.

levels of biological respiration during wet intervals and in under-canopy soils? Or is the CO_2 consumption flux higher in intercanopy soils, particularly during drought periods, driven by differences in the soil microclimate or biologic activity? We explore these questions in the context of potential mechanistic drivers for this CO_2 uptake in Section 5.3.3.

5.3.2 Acute CO_2 consumption following rain events

In addition to the significant CO_2 uptake indicated by regular negative nighttime surface fluxes, acute CO_2 consumption events (up to -0.2mol/m^2/s surface flux) also occur following precipitation in the intercanopy soils. CO_2 uptake following rain is observed throughout the year in the bare soil profile, both in response to the first rain after extended drought periods (Figure 5.4A,C) and in response to precipitation events within the summer and winter monsoon seasons (Figure 5.4B,D). In many instances, negative surface fluxes are observed, indicative of substantial CO_2 uptake overprinting the pulse of biological respiration observed meters away in the under-canopy profile (Figure 5.4). During other rain events, the bare soil CO_2 response to enhanced water availability is simply muted and delayed relative to the vegetated soil profile (Figure E1).

Figure E2 highlights the temporal relationship between precipitation, delivery of water to the shallow soils, and surficial CO_2 production in the intercanopy and under-canopy soil profiles. A key finding from closer inspection of these acute consumption events is that CO_2 uptake occurs during both day and nighttime hours, meaning that phototrophic C fixation cannot be the sole mechanism driving the uptake (Section 5.3.5). The first rain of the 2018 winter monsoon season (breaking 4 months of drought), occurred from 2am-8am, entirely before dawn (Figure 5.4A, E2A). For the first 1.5 hours, enhanced CO_2 production is observed in intercanopy soils, after which CO_2 production begins to drop. Net CO_2 consumption is observed between 5am and 10am; total production in the upper 15cm is -2.22 mmol/m^2 over

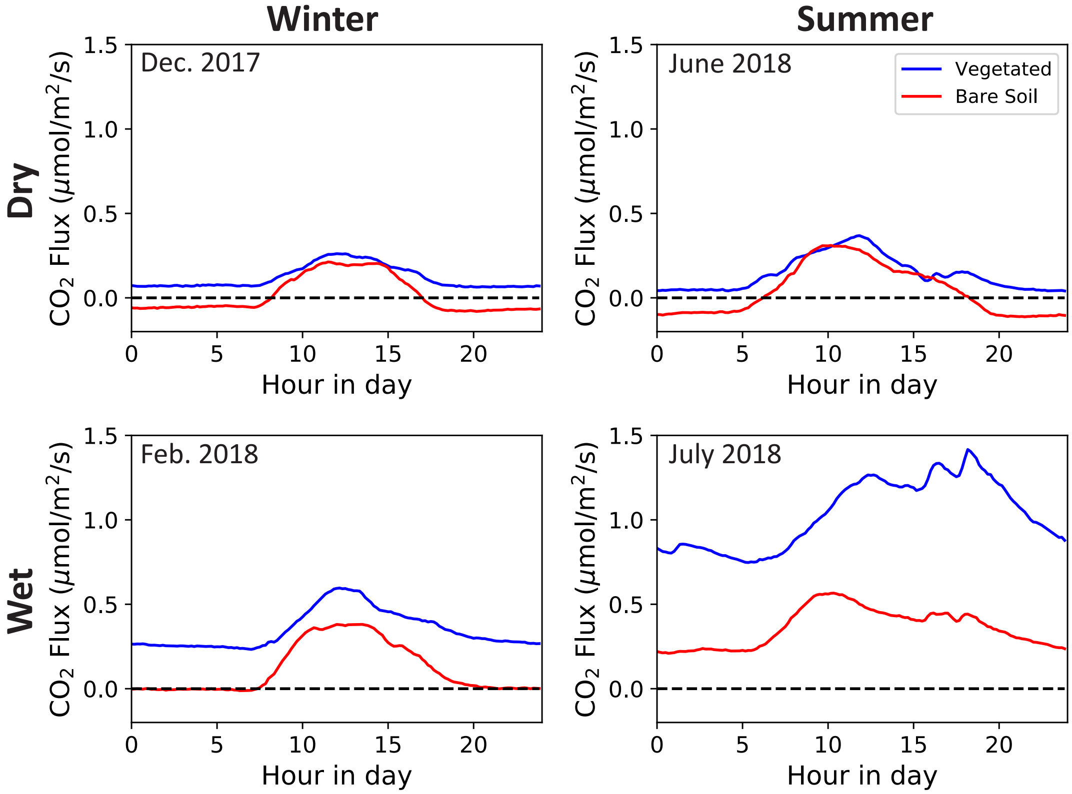

Figure 5.3 – Monthly average diurnal pattern in CO_2 surface flux for four months from September 2017 - September 2018 for under-canopy (blue) and intercanopy (red) soils. The dashed reference line indicates a surface flux of $0\mu\text{mol/m}^2\text{/s}$. Intercanopy soils exhibits negative average nighttime surface fluxes during dry intervals.

Rain Event	Time Interval	Total Production		Total Rain
		Bare Soil	Vegetated	
Units		mmol/m^2	mmol/m^2	mm
8 Jan 2018	24 hours post-rain	9.4	184.3	34
	05:00 - 10:00	-2.2	43.6	
23 Mar 2018	24 hours post-rain	32.2	150.8	6.3
	00:00 - 08:00	-4.8	36.7	
9 May 2019	24 hours post-rain	14.1	331.2	19.4
	20:00-09:00	-13.3	124.2	
15 Aug 2018	24 hours post-rain	68.4	309.3	13.7
	13:00-15:00	-0.83	0.11	
16 Aug 2018	24 hours post-rain	125.8	347.3	36.5
	11:00-18:00	10.8	101.6	

Table 5.1 – Summary of CO_2 uptake in intercanopy soils following precipitation events.

that interval. This places a lower bound on the amount of CO_2 consumed. However, CO_2 production in the intercanopy profile remains significantly muted relative to the vegetated profile throughout the entire diurnal cycle (Figure 5.4A), raising the possibility that gross CO_2 uptake is masking significant biological production in the intercanopy soil. In the 24 hours following the initial rain event, total production in the vegetated soil profile was 189.9 mmol/m^2 but only 9.4 mmol/m^2 in the bare soil profile (Table 5.1). Assuming that CO_2 production in the intercanopy profile in the absence of gross consumption would be approximately half that observed in the vegetated profile (as observed following the initial 24-48 hours after a rain event), gross CO_2 uptake over this interval could be as high as 85.6 mmol/m^2.

This pattern is echoed in subsequent precipitation events. In March 2018 (within the winter monsoon season), a modest rain event occurred from 10pm-1am, leading to net consumption from 12am-8am in intercanopy soils but enhanced CO_2 flux from the vegetated soil profile (Figure 5.4B, E2B). Net consumption in the intercanopy profile coincident with significant production in the vegetated profile is also observed during a nighttime rain event in May 2019 (Figure 5.4C, E2C). Over the 13-hour interval from 8pm-9am, shallow intercanopy soils consumed 13.3mmol/m^2 while under-canopy soils produced 128.6mmol/m^2 (Table 5.1). Two rain events in August 2018 demonstrate the soil's response to daytime precipitation events (Figure 5.4D, E2D). A small afternoon rain on August 15 led to only a slight amount of net consumption but damped CO_2 production relative to the under-canopy profile. A much larger rain event the following day, where 36.5mm of rain was delivered from 10am-1pm, led to substantial CO_2 uptake relative to the diurnal pattern of production.

5.3.3 Potential drivers of nightly CO_2 consumption

5.3.3.1 Magnitude of CO_2 consumption

Before examining potential mechanistic drivers of the nighttime CO_2 consumption, we must quantify the magnitude of CO_2 uptake and its temporal evolution through the seasonal cy-

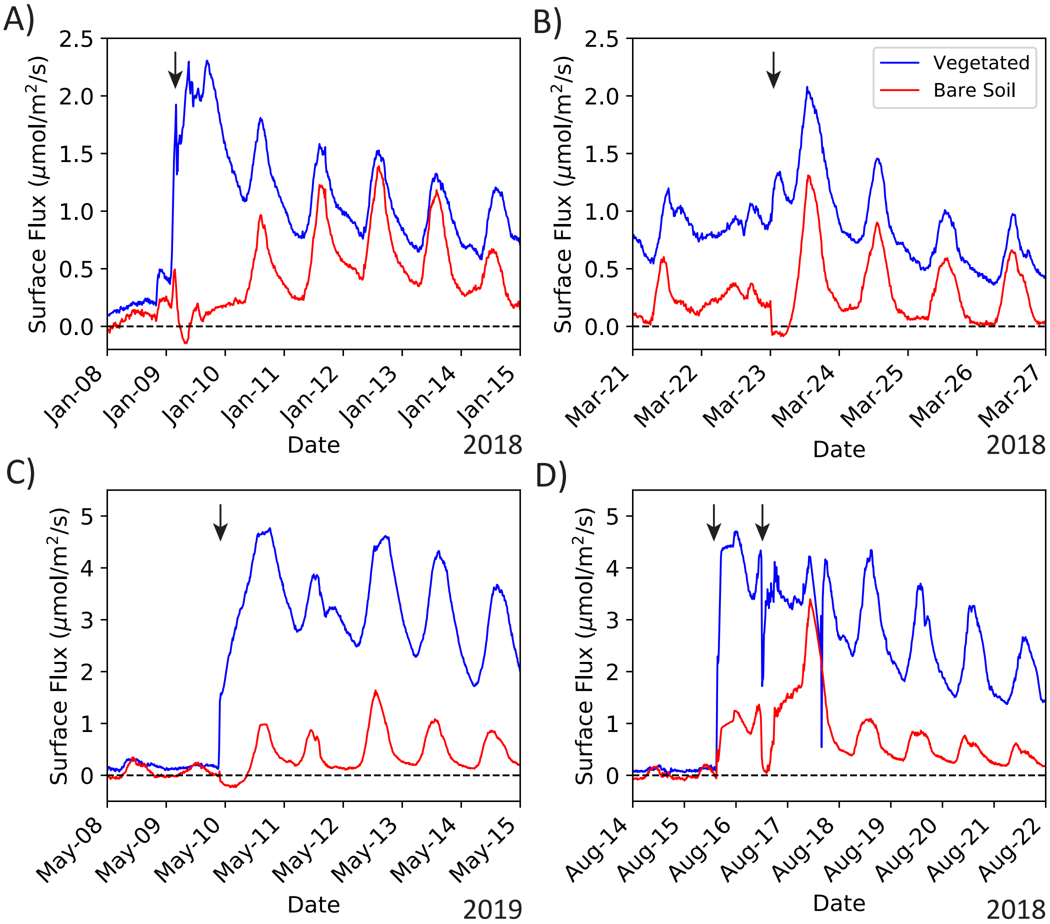

Figure 5.4 – Acute CO_2 consumption in the intercanopy soil profile following rain events. Surface CO_2 flux response to: A) first winter rain after a 4 month dry spell, B) rain event during winter monsoon season, C) summer rain after a 1.5 month dry spell and D) largest recorded rain at end of summer monsoon. Black arrows denote the timing of the rain event and the dashed reference line indicates a surface flux of $0 \mu\text{mol}/\text{m}^2/\text{s}$. Notably CO_2 consumption following rain occurs during both day and nighttime hours.

cle. Importantly, the below-atmospheric CO_2 concentrations observed in shallow soils (5cm depth) are driven by larger magnitude consumption than suggested by the surface flux alone, as CO_2 also diffuses up from the (almost always) higher concentration soils below (Figure 4.2). Figure 5.5 shows the daily integrated surface flux and shallow soil CO_2 production (upper 15cm) across the 2018-2019 seasonal cycle. During dry intervals, the daily integrated surface flux, equivalent to CO_2 production throughout the entire soil profile, is positive but very nearly zero in the bare soil profile (Figure 5.5A), indicative of extremely low levels of biologic respiration. The diurnal cycle in surface flux observed (Figure 5.2) sums to practically zero, suggesting that the diurnal fluctuation is driven by a largely reversible process of CO_2 uptake at night followed by release during the day. The same pattern is generally observed when shallow soil CO_2 production is integrated throughout the day, particularly during winter dry periods (Figure 5.5B), when net production over a diurnal cycle is near-zero. Notably, during some summer drought periods, there is a small amount of net CO_2 consumption on a daily timescale in the upper 15cm of the soil profile. This may reflect net CO_2 uptake via near-surface photosynthesis (e.g. biocrust or other microbial C fixation (Lange, 2003; Pointing and Belnap, 2012)) and/or net dissolution of carbonate minerals, potentially from the dust flux, that are reprecipitated deeper in the soil profile.

Separating this shallow soil CO_2 production into daytime (8am-8pm) and nighttime (8pm-8am) intervals reveals that the negative nighttime surfaces fluxes are driven by nearly continuous nighttime CO_2 consumption in shallow layers of the bare soil profile (Figure 5.6A). The magnitude of nighttime CO_2 consumption varies throughout the year, with the largest CO_2 uptake occurring during the summer months; the interval of regular negative surface flux in December 2017 highlighted in Figure 5.2 actually coincides with some of the lowest magnitude nighttime CO_2 consumption recorded. Notably, the summer months exhibit the largest amplitude diurnal temperature fluctuation (Figure 5.6C), the implications of which are further explored in Section 5.3.3.3. For the purposes of evaluating potential mechanisms driving this nightly CO_2 uptake, we quantified the average amount of shallow soil CO_2 production over the 8pm-8am nighttime interval for three representative months during dry periods: October 2017, December 2017, and June 2018 (Table 5.2). Monthly mean integrated nighttime CO_2 production was -5.58, -3.57, and -10.23 mmol/m^2 during these three intervals, respectively. To place an absolute minimum on the magnitude of CO_2 consumption required by the measured concentrations, the magnitude of CO_2 production implied by the surface flux alone (i.e. assuming there is zero diffusive flux from below) is also tabulated in Table 5.2. This yields significantly lower magnitude CO_2 consumption during the warm periods when deep soil CO_2 concentrations are higher and the diffusive flux from below is non-negligible (Figure 4.2), but is included as an absolute minimum estimate of consumption. Any mechanistic explanation for the CO_2 uptake observed would thus need to be capable of removing a minimum of ~3mmol CO_2/m^2 but up to 10mmol CO_2/m^2 from the soil atmosphere with the available soil water (<1-2%) and observed soil temperature conditions (Table 5.2).

5.3.3.2 Spatial heterogeneity: bare soil versus under-canopy

One of the most striking aspects of both the regular nighttime CO_2 uptake and acute CO_2 consumption in response to rain events documented here is the differential response of the bare soil and under-canopy soil profiles. While negative surface fluxes are observed regularly

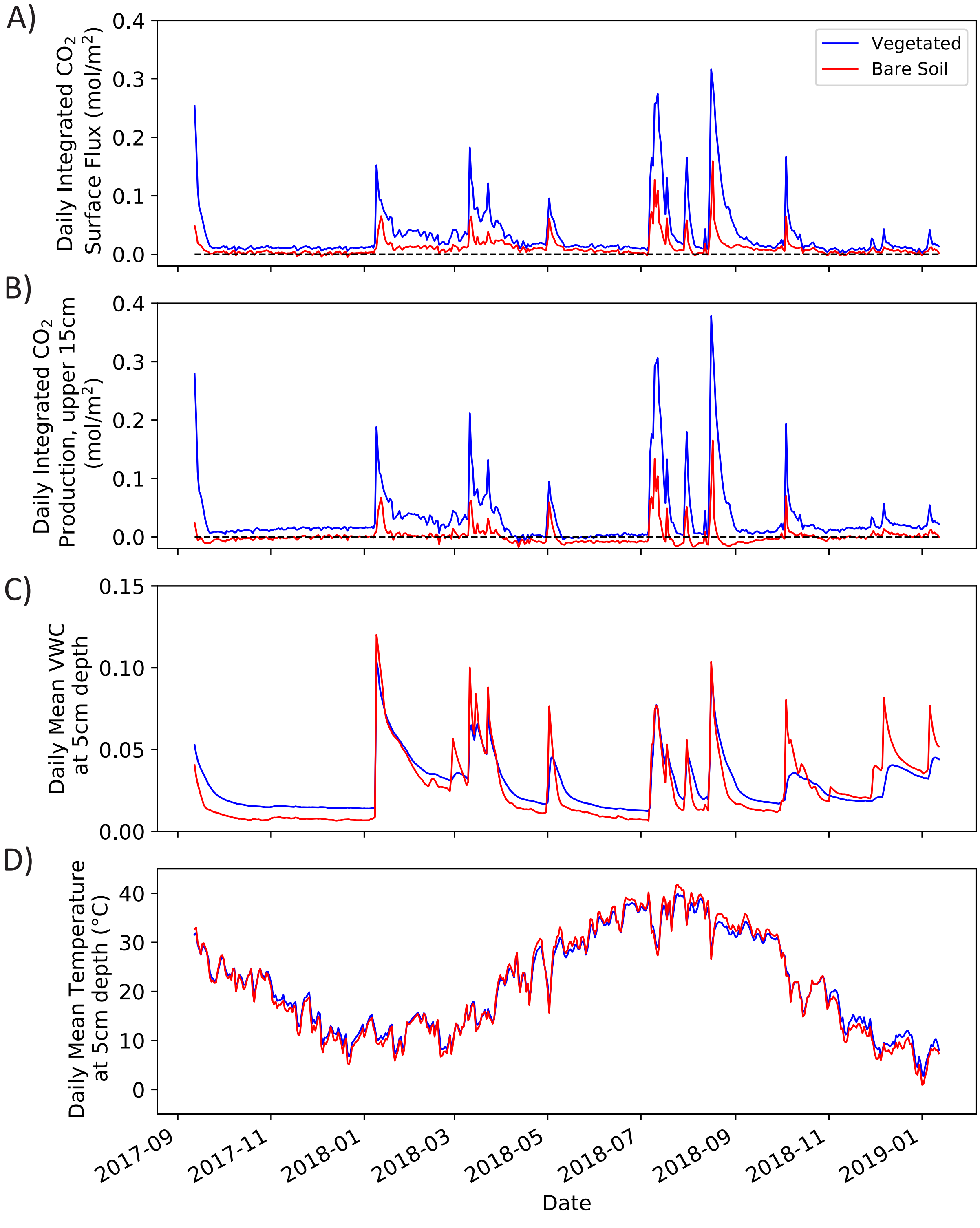

Figure 5.5 – Daily integrated surface flux (A) and shallow soil CO_2 production (upper 15cm, B) across the 2018-2019 seasonal cycle and their relationship to volumetric water content (C) and soil temperature (D). The dashed reference line indicates an integrated surface flux or production rate of 0mol/m^2.

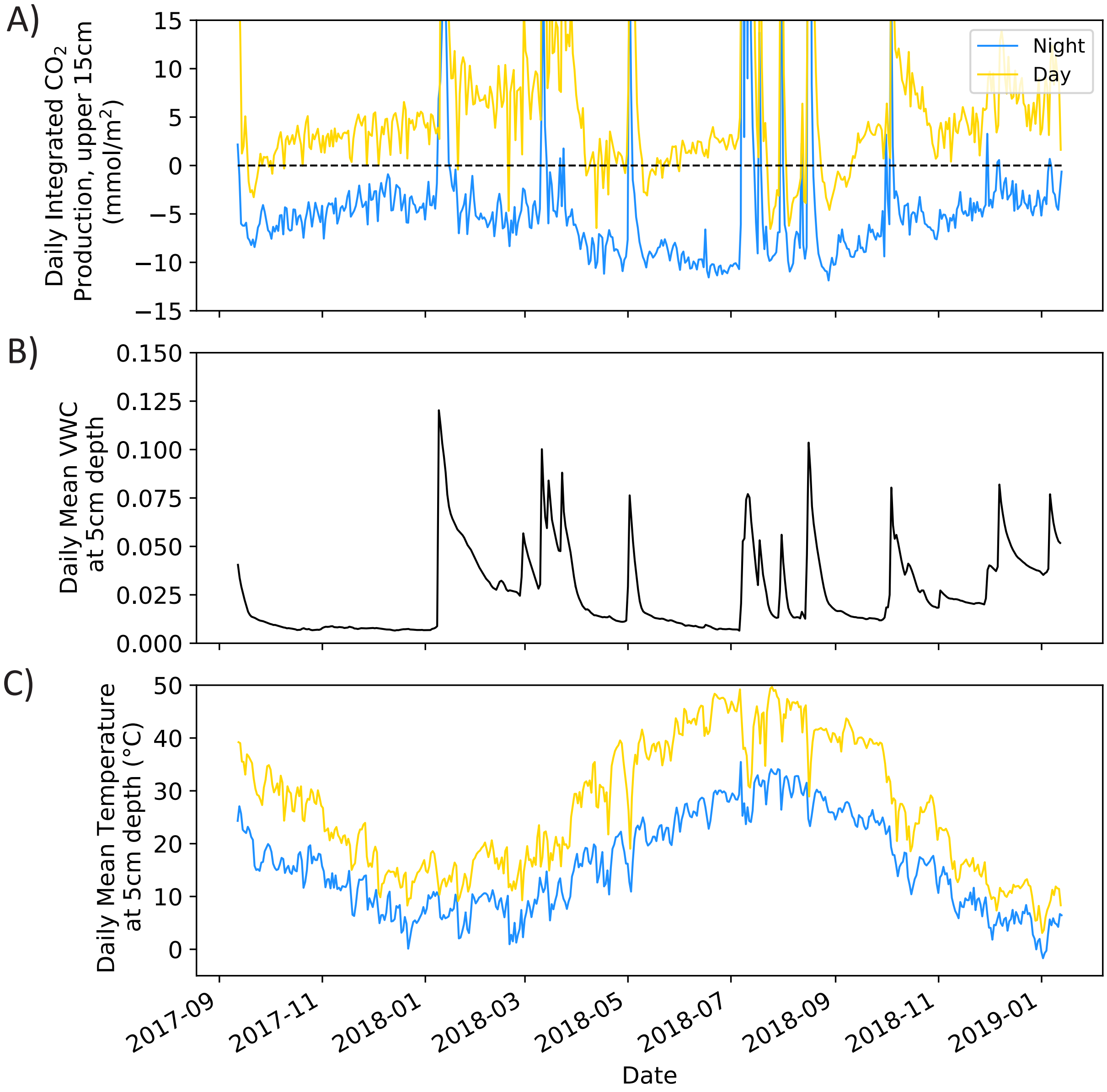

Figure 5.6 – Time series of CO_2 production in the upper 15cm of the bare soil profile, partitioned into daytime and nighttime intervals: A) integrated CO_2 production over day (yellow) and nighttime (blue) hours, B) daily mean volumetric water content at 5cm depth, and C) mean day and nighttime soil temperature at 5cm depth. Note the y axis in A is capped at 15mmol/m^2 to highlight changes in consumption magnitude over time; significantly higher production is observed following rain events (Figure 5.5). The dashed reference line indicates an integrated production rate of 0mmol/m^2.

CO_2 surface flux and shallow-soil production:

Month	Avg. integrated nighttime production*	Avg. integrated nighttime production, solely considering surface flux*	Avg. daily integrated surface flux
Units	mmol/m^2	mmol/m^2	mmol/m^2
Oct 2017	-5.58	-1.68	3.15
Dec 2017	-3.57	-2.59	1.45
June 2018	-10.23	-2.93	3.85

Soil conditions:

Month	Avg. water content		Avg. $[CO_2]$		Avg. magnitude of diurnal T oscillation	Representative daily T range
	5cm	25cm	5cm	25cm	5cm	5cm
Units	cm^3/cm^3	cm^3/cm^3	ppm	ppm	°C	°C
Oct 2017	0.008	0.024	398	568	23.1	15-40
Dec 2017	0.007	0.021	384	445	15	5-25
June 2018	0.008	0.024	451	696	29.4	20-55

Table 5.2 – Monthly average CO_2 production in the Creosote bare soil profile and associated soil conditions for three representative dry intervals. *Production in the upper 15cm of the soil column.

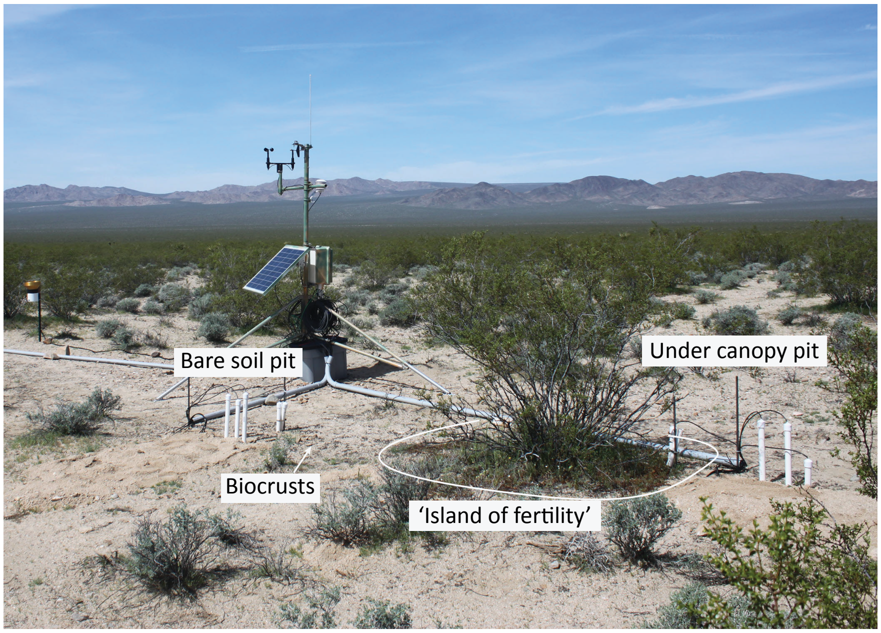

Figure 5.7 – Spatial relationship between the monitored soil pits and 'island of fertility' generated by established creosote shrub.

during dry intervals in the intercanopy soils, negative surface fluxes are far less frequent in the soil adjacent to the canopy of an established creosote shrub, mere meters away (Figure 5.7). Analogously, the intercanopy soils often exhibit net CO_2 consumption immediately following rain events contemporaneous with a large pulse of CO_2 production in under-canopy soils. Desert soils are well known to exhibit a high degree of spatial heterogeneity; 'islands of fertility' or 'resource islands' often develop under shrub canopies with a distinct soil microclimate (D'Odorico *et al.*, 2007; Kidron, 2009), chemistry (Charley and West, 1975; Schlesinger *et al.*, 1996; Titus *et al.*, 2002), biotic community (Herman *et al.*, 1995), and physical characteristics (Wright and Honea, 1986; Wezel *et al.*, 2000). A positive feedback between shrub development and nutrient accumulation arises due to localized litter deposition and nutrient cycling as well as canopy interception of both wind-blown sediment and precipitation (including nutrient-enriched stemflow) (Garner and Steinberger, 1989; Whitford *et al.*, 1997).

In a similar Mojave Desert ecosystem, Titus *et al.* (2002) documented significantly higher N and P concentrations as well as up to a factor of 2 higher soil organic matter content in soils under creosote shrub canopies than interspace sites. The under-canopy soils thus likely support higher levels of biotic activity and respiration throughout the seasonal cycle and particularly in response to rain events (Barron-Gafford *et al.*, 2011), meaning that gross CO_2 consumption could simply be masked by biological CO_2 production. Indeed, net nighttime CO_2 consumption is observed in the top 15cm of the vegetated profile (Figure E3), but only during the summer drought period where the highest magnitude CO_2 consumption is observed in interspace soils (Figure 5.6). The vegetated and bare soil profiles also exhibit potentially important differences in soil microclimate, particularly temperature dynamics (Figure 5.8, Table 5.3). Throughout 2 full seasonal cycles (September 2017-2019), average volumetric water content in the bare soil profile is slightly higher than that in the

Parameter	Soil Depth (cm)	Bare Soil	Vegetated	p value*
Hourly temperature (°C)	5	22.57±13.05	22.55±11.16	0.87
	25	22.24±9.44	22.25±8.97	0.9
Hourly VWC (cm^3/cm^3)	5	0.033±0.026	0.03±0.018	<0.0001
	25	0.034±0.012	0.019±0.008	<0.0001
Diurnal temperature oscillation (°C)	5	20.28±6.04	14.19±3.56	<0.0001
	25	2.57±0.86	1.61±0.64	<0.0001

Table 5.3 – Soil temperature and water content (mean ± standard deviation) of Creosote soil profiles from September 2017-September 2019. *p-value from 2-sided t-test comparing interspace versus vegetated soil profile means.

vegetated profile at 5cm depth, but substantially higher at 25cm depth, possibly due to root water uptake in the vicinity of the vegetated profile (Figure 5.8C). In contrast, average soil temperature is nearly identical both between profiles and with depth (Figure 5.8A). However, this constant average value masks critical differences in the daily temperature extremes experienced across the landscape (Figure 5.8B,D,E). The magnitude of the daily diurnal temperature fluctuation (maximum - minimum temperature) is significantly lower for under-canopy soils, both at 5cm depth and 25cm depth (Table 5.3), and the offset between interspace and under-canopy soils varies seasonally (Figure 5.8E). The daily temperature fluctuation at 5cm depth in under-canopy soils is up to 10°C lower than that experienced by interspace soils during the summer months, largely due canopy shading lowering maximum daily temperatures (Figure 5.8D). But the daily minimum temperature of shallow interspace soils is also consistently lower than that of under-canopy soils, likely driven by differences in radiative cooling and the local energy balance.

5.3.3.3 Relationship to environmental predictors

We now turn to the relationship between nighttime CO_2 consumption and environmental parameters that could influence soil physio-chemical conditions and drive CO_2 uptake. Cross-plots of daily mean CO_2 production in the upper 15cm of the bare soil profile with key environmental parameters, separated into nighttime (blue) and daytime (gold) intervals, are shown in Figure 5.9. Single variable linear regressions of mean nighttime CO_2 production, considering only nights where net CO_2 consumption occurs (452/489 nights in the 15 month period considered) to minimize the influence of extremely high production values associated with rain events, are shown as blue solid lines and tabulated in Table 5.4. Nighttime CO_2 consumption is not strongly correlated with wind speed (Figure 5.9A), in contrast with the dramatic wind speed dependence documented in karst systems where soil-atmosphere CO_2 exchange is thought to be strongly influenced by ventilation-driven CO_2 outgassing (Kowalski *et al.*, 2008; Roland *et al.*, 2013).

The magnitude of CO_2 production is positively correlated with water content during both daytime and nighttime intervals (Figure 5.9B), consistent with the highly water-sensitive production rates documented and discussed in Chapter 4. Notably, these in-situ measurements reflect the net effect of biologic respiration and the CO_2 uptake of interest here; it is impossi-

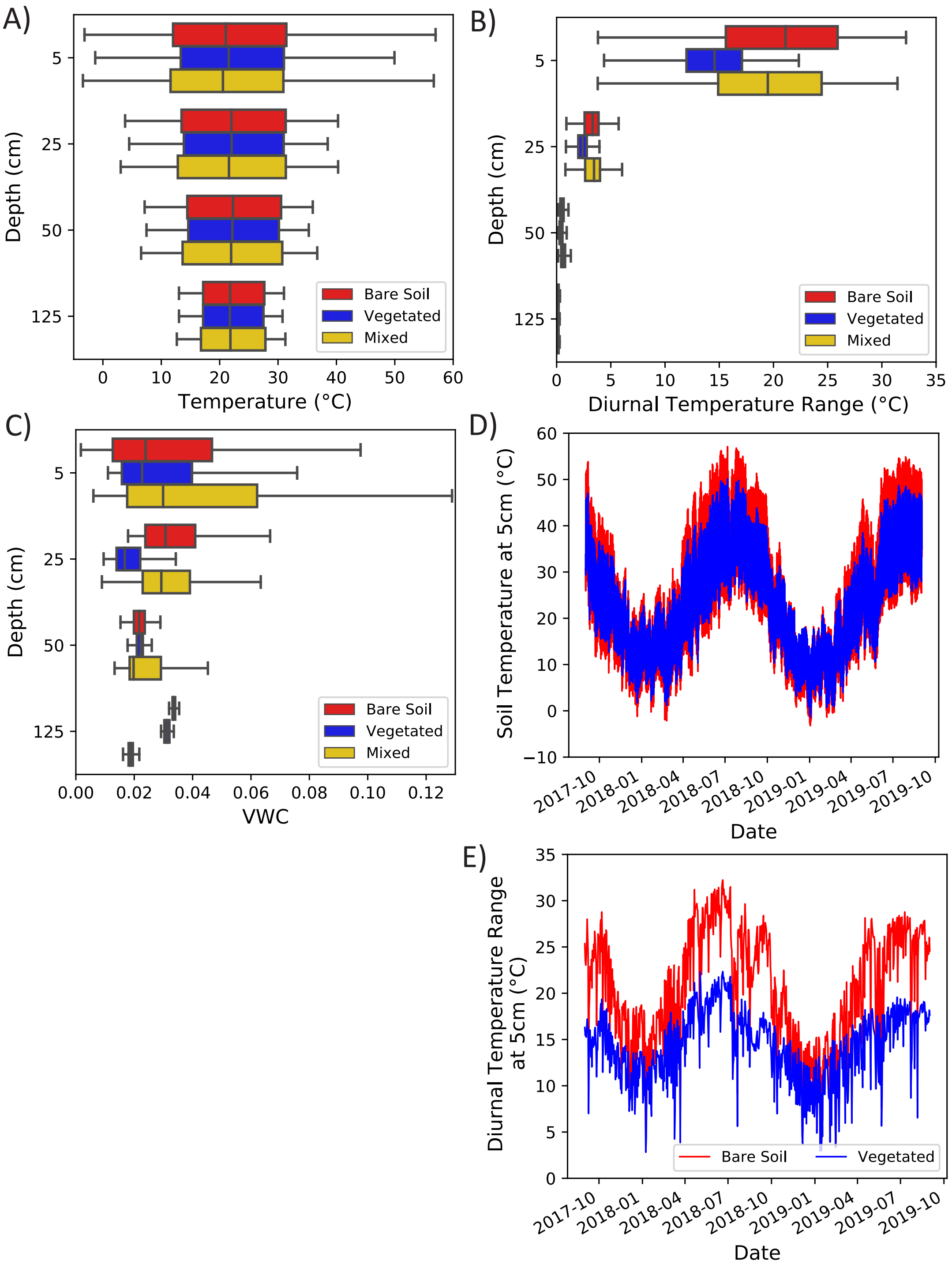

Figure 5.8 – Soil temperature and water dynamics in the vegetated and interspace profiles from September 2017-September 2019. A) Box and whisker plot of hourly soil temperature at 5, 25, 50, and 125cm depth for the three profiles monitored (bare soil = red, vegetated = blue, partially vegetated = gold). B) Box and whisker plot of the diurnal temperature range (daily maximum - minimum temperature). C) Box and whisker plot of hourly volumetric water content. D) Time series of soil temperature at 5cm depth for the bare soil and vegetated profiles. E) Time series of the diurnal temperature range at 5cm depth for the bare soil and vegetated profiles.

Variable	intercept	slope	R^2
Meteorological conditions			
Wind speed (m/s)	-0.17	0.0147	0.067
Relative Humidity	-0.18	0.0011	0.095
Soil conditions			
VWC at 5cm depth (cm^3/cm^3)	-0.18	1.506	0.178
Temperature at 5cm depth (°C)	-0.067	-0.0047	0.474
Magnitude of diurnal T oscillation at 5cm (°C)	0.036	-0.0087	0.731

Table 5.4 – Results of single-variable regression analysis predicting mean nighttime CO_2 production, considering only nights where net CO_2 consumption occurs (452/489 nights in the 15 month period considered). All reported coefficients are significant ($p<0.001$).

ble to separate the influence of water content on respiration from its influence on the (likely largely abiotic) CO_2 consumption flux. The largest magnitude nighttime CO_2 consumption (lowest mean CO_2 production) occurs in dry soils, at <2% volumetric water content (Figure 5.9B). This is consistent with low to negligible levels of respiration in such highly water limited soils (Chapter 4) allowing for the maximum expression of the CO_2 uptake flux, but could also suggest that CO_2 consumption is higher in lower water content soils. Indeed, Xie *et al.* (2009) and Yates *et al.* (2013) both observe a negative correlation between water content and CO_2 consumption in laboratory incubations of *sterilized* soils, suggesting that abiotic CO_2 uptake is reduced at higher water contents. Xie *et al.* (2009) interpreted the lower CO_2 consumption at high water content observed in their laboratory manipulations to reflect lower levels of CO_2 uptake in less saline soil solutions (water content was manipulated through the addition of distilled water). However, Yates *et al.* (2013) also observed that increasing soil water content reduced the rate of CO_2 uptake in their cooling experiments, but found no evidence for a CO_2 flux-salinity relationship. We thus conclude that the nightly CO_2 uptake observed here is in the very least consistent with a mechanism that yields higher levels of uptake in drier soils.

As observed in numerous previous studies, the magnitude of nighttime CO_2 uptake in the interspace soils is strongly correlated with temperature (Figure 5.9C) (Parsons *et al.*, 2004; Xie *et al.*, 2009; Yates *et al.*, 2013; Hamerlynck *et al.*, 2013; Wang *et al.*, 2020). Somewhat counter-intuitively, we find that the magnitude of CO_2 consumption is positively correlated with temperature; as described above, the highest levels of CO_2 consumption occur during the summer months when nighttime soil temperatures range from 20-30°C (Figure 5.6). This is likely driven by 2 main factors. First, soil CO_2 concentrations are higher during the summer months (Figure 4.2), which means there are more moles of CO_2 in the soil atmosphere to be partitioned into the soil solution or sorbed onto soil minerals (Section 5.3.4). Second, our data indicates that the magnitude of the diurnal temperature oscillation (maximum daytime temperature - minimum nighttime temperature) is the more important determinant of the magnitude of nighttime CO_2 uptake (Figure 5.9D); $\Delta T_{diurnal,5cm}$ explains 73% of the variation in the magnitude of nighttime CO_2 consumption (Table 5.4).

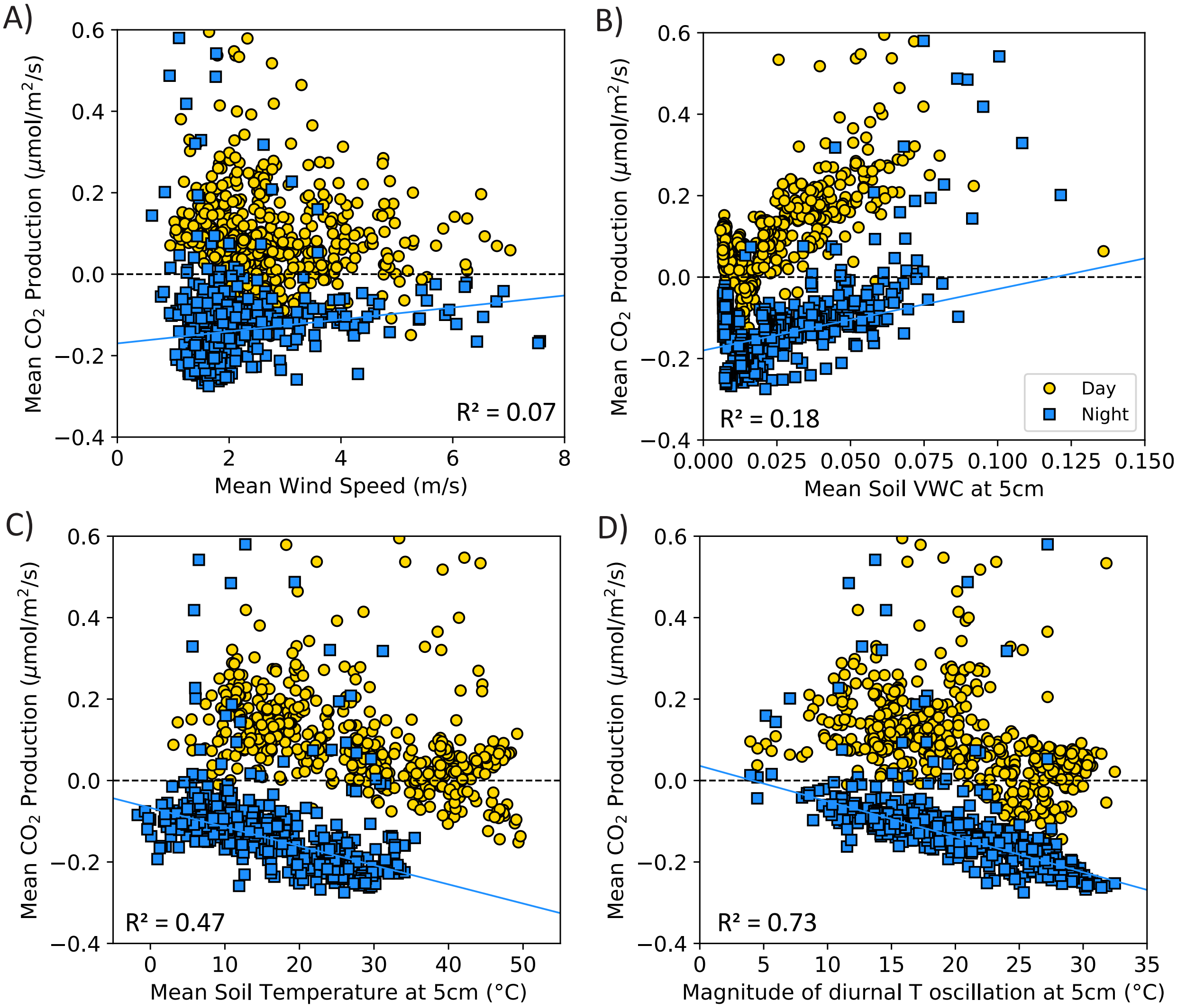

Figure 5.9 – Nighttime CO_2 consumption in intercanopy soils is best described by the amplitude of the diurnal temperature oscillation at 5cm depth. Cross-plots of daily mean CO_2 production in the upper 15cm of the bare soil profile with environmental parameters that could influence soil physio-chemical conditions, broken into daytime (gold) and nighttime (blue) intervals: A) mean wind speed; B) mean soil volumetric water content at 5cm depth; C) mean soil temperature at 5cm depth; D) Magnitude of the diurnal temperature oscillation at 5cm depth (daytime temperature max - nighttime temperature min). The dashed reference line indicates a production rate of $0\mu mol/m^2/s$. The blue solid line and reported R^2 are for a single variable linear regression of the mean nighttime CO_2 production data, considering only nights where net CO_2 consumption occurs (452/489 nights in the 15 month period considered) to minimize the influence of extremely high production values associated with rain events. Note the y axis is capped at $0.6\mu mol/m^2/s$ to highlight the relationship between nighttime consumption and environmental predictors; the full y scale is shown in Figure E4.

5.3.4 Interrogation of potential mechanisms for nighttime consumption

Any potential mechanism for the nightly CO_2 uptake observed here must be consistent with two key trends and plausibly explain the documented magnitude of CO_2 consumption:

1. CO_2 consumption is strongly correlated with the magnitude of the diurnal temperature fluctuation; more CO_2 is consumed when there is a larger difference between the daytime temperature maximum and nighttime temperature minimum.

2. Consumption occurs in very dry soils (<2% VWC) and the magnitude of the CO_2 consumption flux appears to be inversely correlated with volumetric water content (Xie *et al.*, 2009; Yates *et al.*, 2013).

As outlined above, a number of potential mechanisms have been suggested to explain similar observations of nighttime CO_2 uptake in arid systems, though it should be emphasized that many of these observations were made in either carbonate-dominated karst systems or in soils substantially more saline/alkaline than the Mojave soils studied here. Proposed mechanisms include:

1. Continuous carbonate dissolution at night coupled to carbonate precipitation during the day, potentially assisted by convection-driven CO_2 transport (Roland *et al.*, 2013; Hamerlynck *et al.*, 2013; Rey, 2015)

2. Temperature-dependent CO_2 dissolution/exsolution from the soil solution (Henry's law partitioning) (Xie *et al.*, 2009; Shanhun *et al.*, 2012; Ma *et al.*, 2013)

3. Temperature-dependent CO_2 adsorption to mineral surfaces (Parsons *et al.*, 2004; Yates *et al.*, 2013)

We explore these mechanisms in turn, combining mechanisms 1 and 2 under the heading of temperature-dependent carbonate system reactions.

5.3.4.1 Temperature-dependent carbonate system reactions

The solubility of CO_2 gas in water (Wilhelm *et al.*, 1977) and carbonate mineral solubility (Plummer and Busenberg, 1982) are both temperature sensitive: lower temperatures increase calcite solubility and CO_2 partitioning into the soil solution. The nightly CO_2 consumption observed could thus reflect CO_2 uptake due to a combination of carbonate mineral dissolution, which would consume 1 mole of CO_2 per mole of $CaCO_3$ dissolved (Eq. 5.1.1), and enhanced CO_2 partitioning into the aqueous phase (Eq. 5.1.2) in response to falling temperatures. Critically, these are both aqueous-phase reactions, meaning that the magnitude of CO_2 consumption associated with the reaction should scale with the volume of water available to perform the reaction. In addition, unlike many other soils where similar phenomena have been observed, the relatively young Mojave soils studied here are not carbonate-rich. The granitic alluvium parent material has not undergone significant alteration (Table C8) and $CaCO_3$ was not detected in the <2mm size fraction (detection limit ~0.25 wt % carbonate) until >40cm depth (Figure C2), consistent with the lack of effervescence observed with

HCl application in the field (Table C1). However, carbonate is delivered to the soils through the dust flux[1], so it is likely that some quantity of reactive carbonate is present in the upper centimeters of the soil profile. Thus, we calculate a maximum estimate of potential nighttime CO_2 uptake as the difference in dissolved inorganic carbon between a representative soil solution equilibrated with 500ppm CO_2 (Table 5.2) at the two extremes of a typical diurnal temperature fluctuation and test the influence of different assumptions regarding carbonate mineral supersaturation (Section 5.2.3.1). The major ion chemistry of the soil solution is dictated by measured saturated paste extract data, concentrated by a factor of 25 to reflect field volumetric water contents of 1-2%. Notably, this yields solutions highly supersaturated with respect to calcium carbonate minerals, the implications of which we explore here.

Figure 5.10A shows how the total moles of dissolved inorganic carbon (DIC, $CO_{2,aq} + H_2CO_3 + HCO_3^- + CO_3^{2-}$) contained in the soil water of the top 15cm of the soil profile varies as a function of temperature under 3 endmember scenarios of $CaCO_3$ supersaturation, assuming a volumetric water content of 2% in each case. In the first (blue line), the solid $CaCO_3$ phase is not considered, and the solution is allowed to maintain arbitrarily high supersaturations with respect to calcite and aragonite. This represents the temperature dependence of Henry's law partitioning in a high DIC, high pH solution (5.10B,C) reflective of evaporative concentration of the soil solution with no precipitation of carbonate minerals. Importantly, this yields supersaturations in excess of $SI_{calcite} = 3$, which are unrealistically high. Solutions with $SI_{calcite}$ greater than approximately 2.4 are oversaturated with respect to amorphous calcium carbonate (Clarkson *et al.*, 1992), and would almost certainly precipitate rapidly from solution. There is, however, abundant evidence that the soil solution is often somewhat oversaturated with respect to pure calcite (Suarez, 1977; Suarez and Rhoades, 1982; Inskeep and Bloom, 1986a; Amrhein *et al.*, 1993), likely due to kinetic inhibition by inorganic ions and dissolved organic matter (Meyer, 1984; Lebrón and Suárez, 1998; Inskeep and Bloom, 1986b). Suarez and Rhoades (1982) and Inskeep and Bloom (1986a) both report soil solutions with $SI_{calcite}$ up to and slightly exceeding 1.0, so we use $SI_{calcite} = 1.0$ as a representative high but physically reasonable supersaturation for the Mojave soils of interest here. Temperature-driven changes in the total DIC reservoir for solutions where the supersaturation with respect to calcite is fixed at $SI = 1.0$ are shown as a grey line in Figure 5.10A. The calcite precipitation required to achieve this lower supersaturation yields a significantly smaller DIC reservoir and lower pH, which limits the extent of CO_2 dissolution/exsolution with changes in temperature. Analogous changes in total DIC for solutions in equilibrium with calcite are shown as the red line in Figure 5.10A for a volumetric water content of 2%, and for four different water contents in Figure 5.10D. Under the assumptions modeled here, the potential CO_2 uptake for a given temperature change scales linearly with water content such that twice as much CO_2 would be consumed in a soil with 4% VWC as in a soil with 2% VWC.

This analysis reveals that the magnitude of nighttime CO_2 consumption observed could only be explained by the high-pH, high-DIC scenario where the solution supersaturation with respect to $CaCO_3$ minerals is unrealistically high (Table 5.5, 5.2). For that solution chemistry, temperature-driven changes in CO_2 partitioning into the soil solution could drive

---

[1] An average of ~0.8g $CaCO_3/m^2/yr$ was measured by Reheis (2006; 2003) from 1985-2001 at sites monitored in the Eastern Mojave in the vicinity of our climosequence.

nightly CO_2 uptake ranging from 5.8-9.3 mmol/m^2 for the three representative monthly intervals quantified above, accounting for the full magnitude of CO_2 consumption observed (Table 5.2). When $SI_{calcite}$ is capped at 1, the potential nighttime CO_2 uptake drops to 1.8-2.1mmol/m^2, suggesting that upwards of 72% of the CO_2 uptake calculated from the surface flux alone could plausibly be attributed to temperature-dependent carbonate system reactions, but only between 20-56% of the total consumption flux can be accounted for in this manner. Analogously, when the soil solution is assumed to be in equilibrium with calcite, only 0.6-0.7mmol/m^2 CO_2 uptake is predicted in response to the observed diurnal temperature fluctuations, less than 20% of the nighttime consumption observed. Lower DIC concentrations are calculated in this scenario, accompanied by smaller magnitude potential CO_2 uptake, as the high Ca^{2+} concentrations limit the size of the DIC reservoir in equilibrium with calcite and thus decrease carbonate pH buffering, leading to lower pH conditions (Figure 5.10B).

It is thus unlikely that carbonate dissolution and CO_2 partitioning into soil water are the only two CO_2 uptake mechanisms operating in these Mojave desert soils, unless higher pH conditions are maintained than predicted for reasonable carbonate mineral saturation states. This could plausibly be achieved if the Ca^{2+} concentration under field conditions is significantly lower than that predicted from the saturated paste extract data, potentially due to the precipitation of non-carbonate mineral phases (though no common Ca-bearing minerals were found to be supersaturated) or Ca^{2+}-sorption to mineral phases or organic material (Curtin *et al.*, 1998). This highlights the need to develop methods to better constrain in-situ soil solution pH for the highly unsaturated conditions frequently observed in arid systems. Another important caveat to these calculations is that they operate under the inherent assumption that the chemistry of thin films of water in the soil matrix is equivalent to that of a bulk solution. If thin films of water can adsorb substantially more gas than a bulk solution of the same volume, for instance due to the higher surface area in contact with the soil atmosphere, the calculations presented here could be under-estimates.

5.3.4.2 Temperature-dependent CO_2 adsorption to mineral surfaces

Gas adsorption to mineral surfaces is also temperature dependent (Chen and Lu, 2015) and crucially does not require a large aqueous reservoir. In fact, CO_2 adsorption to soil minerals at low nighttime temperatures is a mechanism where lower soil water contents would enhance the magnitude of CO_2 consumption, due to the higher available mineral surface area and lower competition by water vapor. In this section we set out to quantify the amount of CO_2 that could plausibly be reversibly sorbed/desorbed from soil minerals due to the diurnal temperature oscillation. Unfortunately, while there is a rich literature on CO_2 adsorption to solid sorbents at high CO_2 (partial) pressures, including to clay minerals (Chouikhi *et al.*, 2019), data on ambient CO_2 sorption to soil minerals and its temperature dependence is sparse. We thus attempt to provide a first-order estimate of CO_2 adsorption potential based on the best-available information (Section 5.2.3.2).

Working from BET isotherms of CO_2 adsorption to a range of soils measured by Ravikovitch *et al.* (2005), we estimate a CO_2 adsorption capacity of 0.01 mg CO_2/m^2 at 0°C and ambient CO_2 for the organic-poor soils of interest here. Coupling this with an estimated mineral surface area of 20m^2/g based on the measured particle size distribution yields a first-order es-

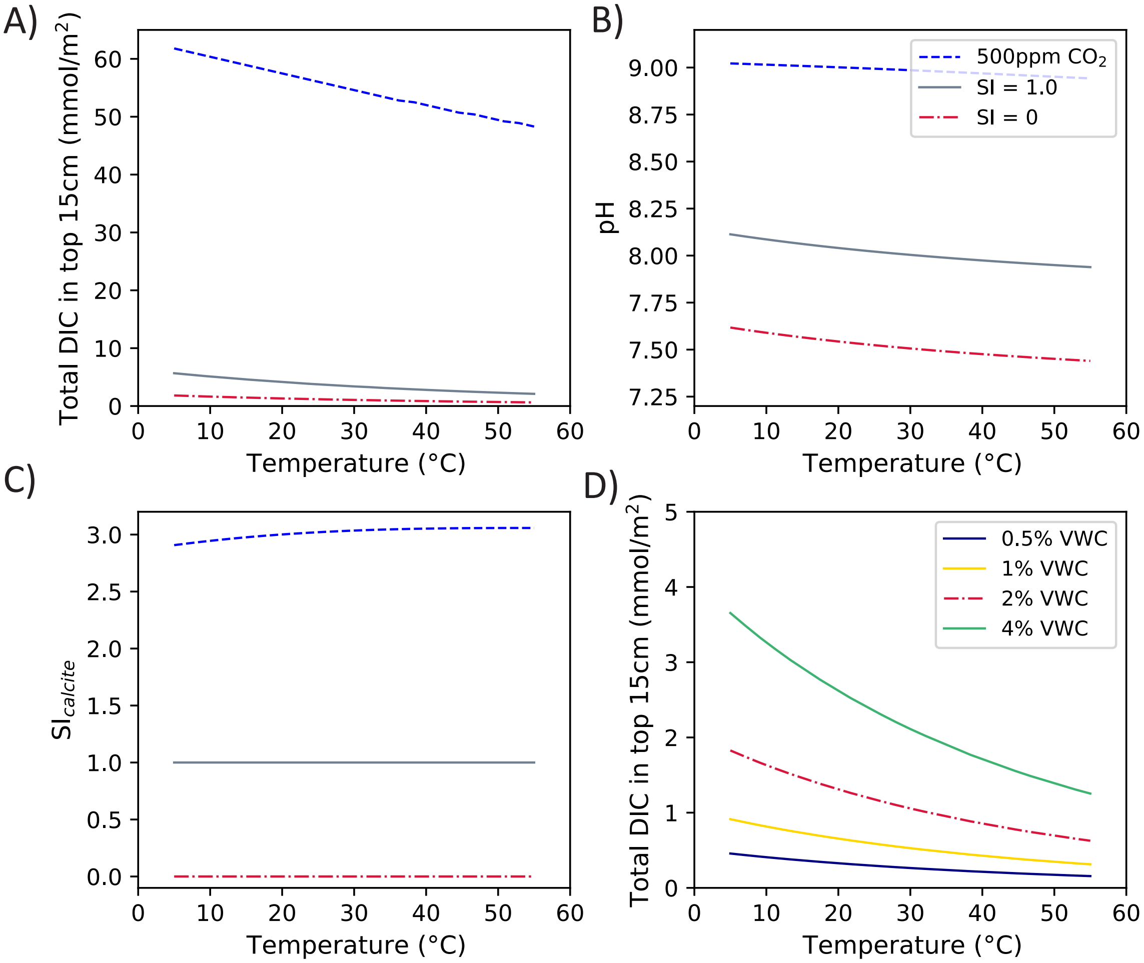

Figure 5.10 – Modeled potential nighttime CO_2 uptake from temperature-dependent carbonate system reactions. A) Modeled total mmol/m^2 dissolved inorganic carbon (DIC) in the top 15cm of soil as a function of temperature under 3 different scenarios of $CaCO_3$ supersaturation: pure Henry's law partitioning of a solution in equilibrium with 500ppm CO_2, allowing for extremely high supersaturation with respect to calcite; equilibration with 500ppm CO_2 while maintaining a calcite saturation index of 1.0; and equilibration with both 500ppm CO_2 and an excess of calcite ($SI_{calcite} = 0$). In all cases, major ion concentrations are derived from the measured saturation extract chemistry, concentrated by a factor of 25 to represent field conditions. DIC quantities reflect a volumetric water content of 2%. B) Solution pH and C) calcite saturation index in each scenario. D) Modeled total mmol/m^2 dissolved inorganic carbon (DIC) in the top 15cm of soil as a function of temperature assuming equilibrium with calcite for four different volumetric water contents.

Condition	Max CO_2 uptake due to diurnal temperature fluctuation (mmol/m^2)		
	Oct 2017 (15-40°C)	Dec 2017 (5-25°C)	June 2018 (20-55°C)
Solely equilibrate with 500ppm CO_2 ($SI_{calcite} > 2.8$, pH 9)	6.99	5.82	9.27
Equilibrate with 500ppm CO_2, $SI_{calcite} = 1.0$	1.80	1.99	2.09
Equilibrate with 500ppm CO_2, $SI_{calcite} = 0$	0.6	0.67	0.70

Table 5.5 – Calculated maximum potential nighttime CO_2 uptake from temperature-dependent carbonate system reactions during three representative dry-season months, assuming a volumetric water content of 2%. In all cases, major ion concentrations are derived from the measured saturation extract chemistry, concentrated by a factor of 25 to represent field conditions. The three scenarios represent different assumptions regarding $CaCO_3$ mineral supersaturation. Associated soil conditions and measured CO_2 uptake are provided in Table 5.2.

timate of CO_2 adsorbed in the top 15cm of soil of: $(0.01\ mgCO_2/m^2)*(20m^2/g)*(1.4e6g/m^3)*(0.15m) = 42\ gCO_2/m^2 = 0.95\ mol\ CO_2/m^2$ at 0°C. Figure 5.11 then shows the calculated temperature dependence of this CO_2 adsorption, using conservative estimates of the enthalpy of adsorption (ΔH_{ads} Section 5.2.3.2) for physisorption of CO_2. These calculations suggest that upwards of 50mmol/m^2 CO_2 could be consumed due to temperature-dependent adsorption to mineral surfaces with the diurnal temperature oscillations documented here, in excess of the 10mmol/m^2 nighttime CO_2 consumption measured during the summer months. While this should be treated as a first-order estimate due to the limited ambient CO_2 adsorption data and potential complicating factors in soil systems, including competitive adsorption by water vapor (Jin and Firoozabadi, 2014; Schaef *et al.*, 2015), we conclude that CO_2 sorbed to soil minerals could represent a non-trivial reservoir of CO_2 that could be reversibly taken up and released by the large thermal fluctuations experienced by shallow soils in these systems.

Is there evidence from the field that thermally driven CO_2 adsorption/desorption from mineral surfaces could play a role in the nightly CO_2 uptake observed in a range of desert environments? Both Ma *et al.* (2013) and Wang *et al.* (2020) report negligible CO_2 uptake in laboratory incubations of dry quartz sand, but the vast majority of the surface area in soils is derived from the clay size fraction and organic material. The quartz sand used in those studies likely had orders of magnitude lower surface area than the Mojave soils of interest here, which would scale the CO_2 uptake potential accordingly. In contrast, Parsons *et al.* (2004) documented substantial CO_2 adsorption and subsequent release in response to temperature changes in laboratory incubations of oven-dry, sterilized soils from Antarctic dry valleys. This, plus the repeated observations that CO_2 uptake declines with increasing water content in laboratory incubations of alkaline soils (Xie *et al.*, 2009; Yates *et al.*, 2013) supports the conjecture that temperature-dependent mineral sorption could play a significant role in the nightly CO_2 uptake observed in arid soils.

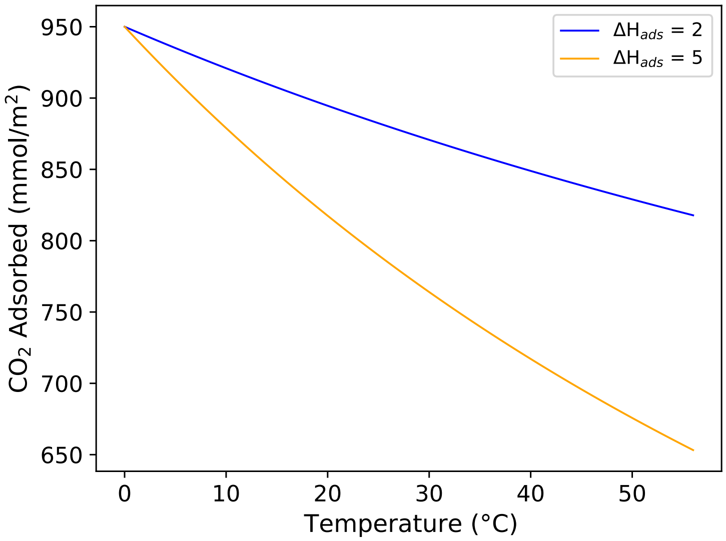

Figure 5.11 – Potential CO_2 consumption due to temperature-dependent adsorption to mineral surfaces. Modeled total mmol/m^2 adsorbed CO_2 in the top 15cm of the soil profile as a function of temperature. Colors denote different assumed enthalpies of adsorption (ΔH_{ads}, kJ/mol). Assumes a CO_2 adsorption capacity of $0.01\text{mgCO}_2/\text{m}^2$ at 0°C (Ravikovitch *et al.*, 2005) and a mineral surface area of $20\text{m}^2/\text{g}$.

5.3.4.3 Alternative explanations: biologic carbon fixation and enhanced transport of CO_2

Additional potential contributors to the nightly CO_2 uptake documented here include biologic carbon fixation and enhanced (i.e. non-diffusive) transport of CO_2. The nighttime CO_2 consumption is obviously not driven by phototrophic carbon fixation, but could be driven in part by dark microbial carbon fixation (Spohn *et al.*, 2020). Chemoautotrophic bacterial may play an important role in carbon fixation in desert soil systems, particularly during extended dry periods (León-Sobrino *et al.*, 2019; Ray *et al.*, 2020). However, it is not immediately clear that biotic CO_2 uptake would scale linearly with soil temperature, more specifically the magnitude of the diurnal temperature fluctuation, and a number of studies have observed similar temperature-driven CO_2 uptake in sterilized soils (Parsons *et al.*, 2004; Xie *et al.*, 2009; Yates *et al.*, 2013; Ma *et al.*, 2013; Fa *et al.*, 2018; Wang *et al.*, 2020). Biotic CO_2 uptake thus likely plays a limited role in the regular nighttime CO_2 consumption observed, but could play an important role in the acute CO_2 consumption observed with precipitation (Section 5.3.5).

Non-diffusive CO_2 transport could also play a role in the CO_2 uptake behavior observed. Atmospheric pumping driven by pressure gradients, particularly those caused by wind, have been demonstrated to be important controls on CO_2 exchange in certain soil systems (Rey *et al.*, 2012; Kowalski *et al.*, 2008; Roland *et al.*, 2013; Rey, 2015). Thermal convective transport of CO_2 can also lead to significantly enhanced CO_2 transfer over typical diffusion rates in high permeability soils which experience large temperature gradients (Ganot *et al.*, 2014). For the Mojave soils of interest here, the permeability is not high enough to expect substantial thermal convective venting (Ganot *et al.*, 2014), and there is a weak correlation between nighttime CO_2 consumption and wind speed (Figure 5.9A). Thus while convective or advective transport could influence surface-atmosphere CO_2 exchange in these soils, we do not find evidence to suggest that non-diffusive transport is a primary driver of the nightly CO_2 uptake observed.

5.3.5 Interpretation of acute consumption following rain

While carbonate dissolution/re-precipitation seems unlikely to be the dominant driver of the regular nighttime CO_2 consumption observed due both to the low soil carbonate content and the limited size of the aqueous reservoir during dry intervals, during precipitation events a substantial volume of rainwater highly undersaturated with respect to $CaCO_3$ is added to the soil system. The acute episodes of CO_2 consumption in interspace soils during and immediately following rain events (Figure 5.4) could thus be driven by carbonate mineral dissolution in shallow soils. The question becomes whether there is enough reactive carbonate in the soil matrix to drive the magnitude of consumption observed (Table 5.1). Again considering a hypothetical 1m x 1m soil column (Section 5.2.3), the top 15cm represents a volume of 150,000cm^3, which at a bulk density of 1.4g/cm^3 equates to 210kg of material. Taking 0.2 wt% $CaCO_3$ as an upper estimate of the carbonate content (no carbonate is detected in the mass spectrometer with a detection limit of ~0.25 wt% $CaCO_3$ and no effervescence was observed in the field), this yields a maximum of 420g or 4.2 moles of $CaCO_3$ total in the upper 15cm. Carbonate dissolution consumes 1mole of CO_2 per mole $CaCO_3$ dissolved (Eq. 5.1.1), meaning that the maximum net CO_2 consumption observed, 13.3mmol/m^2 (Table 5.1), would require the dissolution of 1.33g $CaCO_3$. This is less than 2 years of the carbonate dust flux measured by Reheis (2006; 2003) and well within the potential $CaCO_3$ present in the upper 15cm. Explaining the entirety of the damped intercanopy profile response to rain relative to the under-canopy profile (assuming CO_2 production would be roughly half that of the under-canopy profile in the absence of consumption, Section 5.3.2) would require between 1-4% of the estimated maximum $CaCO_3$ present to dissolve to drive the magnitude of CO_2 consumption observed (Table 5.1). We thus conclude that the net CO_2 consumption in interspace soils following rain events could be driven by the dissolution of carbonate minerals that later reprecipitate deeper in the soil profile as the soil dries out (Breecker *et al.*, 2009; Gallagher and Breecker, 2020).

In addition, there are established, undisturbed, biological soil crusts adjacent to the 'bare soil' profile (Figure 5.7, 5.12). Biotic carbon fixation in surficial soils could thus also contribute to the net CO_2 consumption with rain and subsequent muted respiration response observed in the interspace soils. Rain and the associated CO_2 consumption often occurs at night (Section 5.3.2), meaning that the initial acute CO_2 consumption cannot be solely driven by phototrophic C fixation. However, recovery of full photosynthetic capacity in biocrusts is observed within 10 minutes to 1 hour post-wetting (Garcia-Pichel and Belnap, 1996; Harel *et al.*, 2004; Rajeev *et al.*, 2013), which suggests that near-surface carbon fixation by photosynthetic biocrust communities could be an important driver of the apparent muted CO_2 production for 1-2 days post-rain relative to the under-canopy soil. There is also increasing evidence for microbial chemotrophic carbon fixation in soils, particularly in dry desert environments (León-Sobrino *et al.*, 2019; Ray *et al.*, 2020). Carbon fixation by

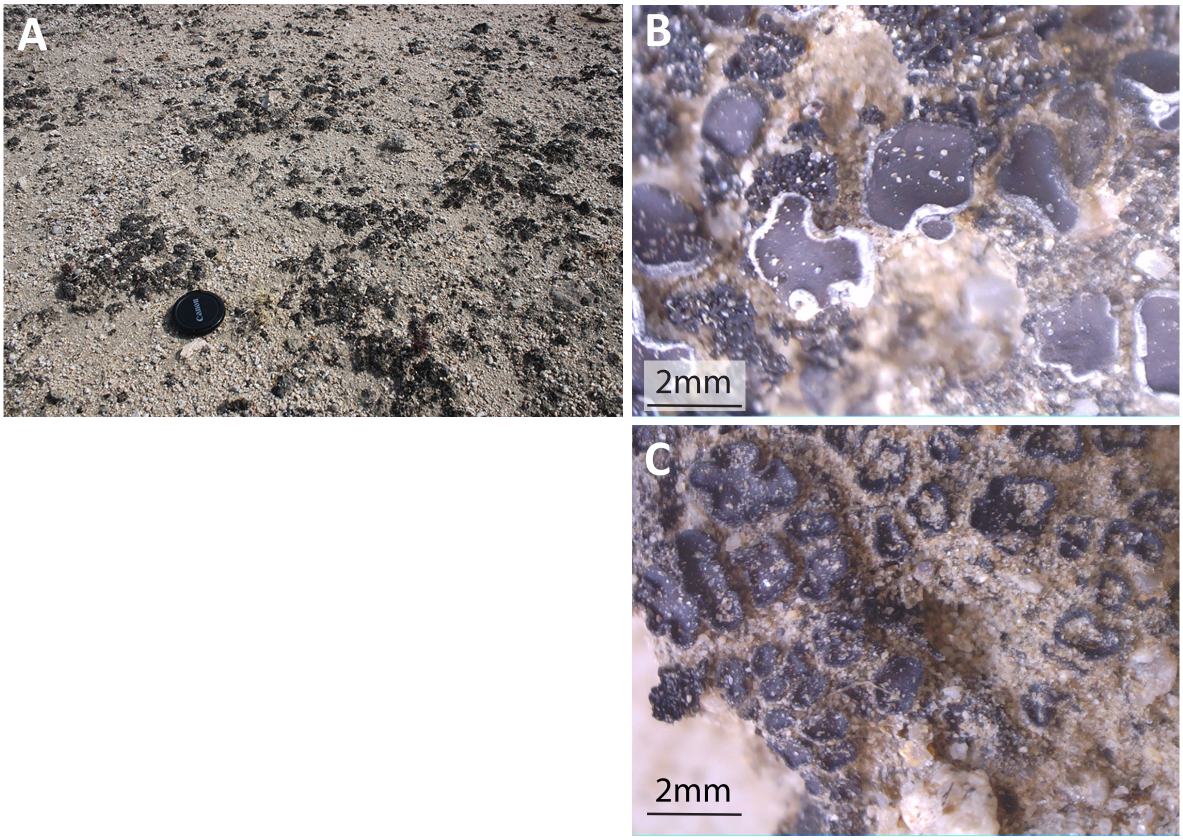

Figure 5.12 – Biocrusts observed at the Creosote, interspace profile. A) Intact soil crusts in the vicinity of the soil profile. B and C) Field microscope images of crusts collected adjacent to the monitored soil pit.

chemoautotrophs in shallow soils could contribute to the initial CO_2 uptake if carbon fixation in these organisms responds on the same timescale as phototrophic crust communities. The acute episodes of CO_2 uptake in interspace soils observed following rain events are thus consistent with CO_2 consumption due to $CaCO_3$ dissolution, potentially augmented by biotic C fixation in shallow soils.

5.3.6 Broader implications for measurements and predictions of CO_2 fluxes in these systems

The nighttime CO_2 consumption documented here represents an abiotic diurnal cycle of CO_2 uptake and release that amplifies the diurnal cycle driven by biologic respiration. This thermally-driven abiotic 'capacitor' for CO_2 is a potential explanation for the inability of a model which only accounts for (presumably biological) CO_2 production and diffusion to capture the magnitude of the diurnal CO_2 fluctuation, particularly during the frequent dry periods between rain events, as observed in Chapter 4. Indeed, our results suggest that most of the diurnal CO_2 oscillation during the dry season is likely driven by this abiotic cycle of CO_2 adsorption at night with falling temperatures followed by release as temperatures rise the following day (Figure 5.5). Notably, our results suggest that the regular CO_2 uptake observed here is not a substantial *net* CO_2 consumption flux, but instead roughly balances on a daily timescale (Figure 5.5). This is in contrast to some previous measurements which suggest significant net CO_2 uptake by the plant-soil system on an annual basis (Jasoni *et al.*, 2005; Wohlfahrt *et al.*, 2008; Liu *et al.*, 2015b) at levels hard to reconcile with our understanding of the size and rate of change of desert carbon pools (Schlesinger *et al.*, 2009).

This additional control on CO_2 dynamics has important implications for the interpretation of soil flux measurements from arid systems. Considering the CO_2 flux at night to be representative of respiration, a common assumption for flux partitioning of eddy covariance measurements (Reichstein *et al.*, 2005), would lead to an under-estimation of respiration as the abiotic CO_2 uptake masks the biologic production. Conversely, soil flux measurements during the day likely provide an over-estimation of respiration, as the net flux reflects CO_2 production from both abiotic and biotic sources. This could significantly impact our understanding of the sensitivity of desert carbon pools to perturbation (Shanhun *et al.*, 2012), as both calculated turnover times and the temperature sensitivity of respiration are often inferred from field and laboratory measurements of CO_2 flux (Sanderman *et al.*, 2003; Bond-Lamberty *et al.*, 2018). Thermally-driven abiotic CO_2 uptake and release, whether underpinned by carbonate system reactions, sorption to soil minerals, or a combination of both, likely has a distinct temperature sensitivity from biologic respiration, as suggested by observations from sterilized and unsterilized soils in the Gurbantunggut Desert (Wang *et al.*, 2020). Homing in on a mechanistic description of these abiotic reactions is thus critical for proper interpretation of existing and future CO_2 measurements from arid ecosystems. Additional work investigating potential CO_2 uptake by soil minerals as a function of relative humidity; additional modeling and potentially experimental work targeting an understanding of the soil carbonate system and pH at low water contents; and empirical studies examining CO_2 dynamics in sterilized and unsterilized soils will all aid in this effort. Diurnal measurements of the carbon isotopic composition of CO_2, as presented by Soper *et al.* (2017) for a similar Mojave soil system, could also help disentangle CO_2 sources in-situ. Notably, Soper *et al.* (2017) report increasing $\delta^{13}C_{CO_2}$ with soil temperature and $\delta^{13}C_{CO_2}$ source values of -7.2‰±2.8‰ in dry interspace soils when soil surface temperatures topped 60°C. This was interpreted as an increasing flux of CO_2 derived from $CaCO_3$ precipitation and CO_2 outgassing as temperatures increase (soil carbonate $\delta^{13}C$ = 0.2‰±0.2‰), but could also represent an increasing contribution from atmospheric CO_2 (∼-8‰) desorbing from mineral surfaces. In-situ measurements will thus need to be coupled with quantitative modeling of the proposed reactions to develop a comprehensive understanding of abiotic CO_2 dynamics.

5.4 Conclusions

Two types of CO_2 consumption are documented in interspace soils of a creosote shrub ecosystem in the Mojave Desert. Nearly continuous nighttime CO_2 consumption in near-surface soils drives regularly negative CO_2 surface fluxes during dry periods and acute episodes of CO_2 consumption occur following rain events. The magnitude of the daily diurnal temperature fluctuation appears to be a key driver of the nightly CO_2 consumption, explaining 73% of the variation in consumption magnitude on nights when net consumption is observed. We quantitatively consider two potential mechanistic explanations for this thermally-driven CO_2 uptake: temperature-dependent carbonate system reactions and CO_2 adsorption/desorption from mineral surfaces. Geochemical modeling of potential CO_2 uptake due to temperature-dependent CO_2 dissolution and dissolved inorganic carbon speciation in the soil solution suggests that these reactions alone cannot account for the magnitude of consumption observed, unless higher pH conditions are maintained than predicted for reasonable carbonate mineral saturation states. Critically, the highest magnitude CO_2 consumption is observed during very dry intervals (<1-2% volumetric water content from 0-25cm depth), where the total volume of water available to perform such aqueous-phase reactions is limited. Changes in CO_2 sorption to soil minerals due to shallow soil temperature fluctuations, in contrast, does not require a large aqueous reservoir, and indeed should be maximized in dry soils with the highest available mineral surface area. First-order calculations suggest that thermally driven CO_2 adsorption/desorption from mineral surfaces could provide a much larger potential CO_2 sink, but data on CO_2 sorption under ambient (low P_{CO2}) conditions is scarce. More data is needed to evaluate CO_2 sorption capacity and its temperature sensitivity under in-situ soil conditions, particularly the influence of competition by water vapor, but we posit that mineral sorption reactions could play a substantial role in driving the large diurnal fluctuations in soil CO_2 flux observed. The CO_2 uptake observed following rain events is consistent with CO_2 consumption due to carbonate mineral dissolution, potentially augmented by shallow-soil carbon fixation via biocrust photosynthesis or microbial autotrophy more broadly. Importantly, the CO_2 consumption documented here occurs in rather pedestrian desert soils on granitic alluvium; the soils are not calcareous or highly saline/alkaline as in many other locations where similar behavior has been observed. This suggests that a thermally-driven abiotic diurnal cycle of CO_2 uptake and release could be a common feature of dryland soils. Further probing the mechanistic underpinnings of this CO_2 uptake and developing quantitative representations of the underlying geochemical processes should be a key emphasis of future work investigating CO_2 dynamics in these important systems.

References

Achal, V., Pan, X., and Zhang, D., 2012. Bioremediation of strontium (Sr) contaminated aquifer quartz sand based on carbonate precipitation induced by Sr resistant Halomonas sp., *Chemosphere*, 89 (6), 764–768.

Agam, N. and Berliner, P.R., 2006. Dew formation and water vapor adsorption in semi-arid environments - A review, *Journal of Arid Environments*, 65 (4), 572–590.

Ahlström, A., Raupach, M.R., Schurgers, G., Smith, B., Arneth, A., Jung, M., Reichstein, M., Canadell, J.G., Friedlingstein, P., Jain, A.K., Kato, E., Poulter, B., Sitch, S., Stocker, B.D., Viovy, N., Wang, Y.P., Wiltshire, A., Zaehle, S., and Zeng, N., 2015. The dominant role of semi-arid ecosystems in the trend and variability of the land CO2 sink, *Science*, 348 (6237), 895 LP – 899.

Ahm, A.S.C., Bjerrum, C.J., Blättler, C.L., Swart, P.K., and Higgins, J.A., 2018. Quantifying early marine diagenesis in shallow-water carbonate sediments, *Geochimica et Cosmochimica Acta*, 236, 140–159.

AlKhatib, M. and Eisenhauer, A., 2017a. Calcium and strontium isotope fractionation during precipitation from aqueous solutions as a function of temperature and reaction rate; II. Aragonite, *Geochimica et Cosmochimica Acta*, 209, 320–342.

AlKhatib, M. and Eisenhauer, A., 2017b. Calcium and strontium isotope fractionation in aqueous solutions as a function of temperature and reaction rate; I. Calcite, *Geochimica et Cosmochimica Acta*, 209, 296–319.

Alvarez, C.C., Quitté, G., Schott, J., and Oelkers, E.H., 2021. Nickel isotope fractionation as a function of carbonate growth rate during Ni coprecipitation with calcite, *Geochimica et Cosmochimica Acta*, 299, 184–198.

Amrhein, C., Zahow, M.F., and Suarez, D.L., 1993. Calcite supersaturation in soil suspensions, *Soil Science*, 156 (3).

Amundson, R., 2001. The Carbon Budget in Soils, *Annual Review of Earth and Planetary Sciences*, 29 (1), 535–562.

Anbeek, C., 1993. The effect of natural weathering on dissolution rates, *Geochimica et Cosmochimica Acta*, 57 (21), 4963–4975.

Anderegg, W.R.L. and Diffenbaugh, N.S., 2015. Observed and projected climate trends and hotspots across the National Ecological Observatory Network regions, *Frontiers in Ecology and the Environment*, 13 (10), 547–552.

Andersson, M.P., Dobberschütz, S., Sand, K.K., Tobler, D.J., Yoreo, J.J.D., and Stipp, S.L.S., 2016. A Microkinetic Model of Calcite Step Growth, *Angewandte Chemie International Edition*, 55 (37), 11086–11090.

Astilleros, J.M., Fernández-Díaz, L., and Putnis, A., 2010. The role of magnesium in the growth of calcite: An AFM study, *Chemical Geology*, 271 (1), 52–58.

Astilleros, J.M., Pina, C.M., Fernndez-daz, L., and Putnis, A., 2002. Molecular-scale surface processes during the growth of calcite in the presence of manganese, *Geochimica et Cosmochimica Acta*, 66 (18), 3177–3189.

Atkin, O.K. and Tjoelker, M.G., 2003. Thermal acclimation and the dynamic response of plant respiration to temperature, *Trends in Plant Science*, 8 (7), 343–351.

Austin, A.T., Méndez, M.S., and Ballaré, C.L., 2016. Photodegradation alleviates the lignin bottleneck for carbon turnover in terrestrial ecosystems, *Proceedings of the National Academy of Sciences*, 113 (16), 4392 LP – 4397.

Austin, A.T. and Vivanco, L., 2006. Plant litter decomposition in a semi-arid ecosystem controlled by photodegradation, *Nature*, 442 (7102), 555–558.

Ball, B.A., Virginia, R.A., Barrett, J.E., Parsons, A.N., and Wall, D.H., 2009. Interactions between physical and biotic factors influence CO2 flux in Antarctic dry valley soils, *Soil Biology and Biochemistry*, 41 (7), 1510–1517.

Barkan, Y., Paris, G., Webb, S.M., Adkins, J.F., and Halevy, I., 2020. Sulfur isotope fractionation between aqueous and carbonate-associated sulfate in abiotic calcite and aragonite, *Geochimica et Cosmochimica Acta*, 280, 317–339.

Barnaby, R.J. and Rimstidt, D.J., 1989. Redox conditions of calcite cementation interpreted from Mn and Fe contents of authigenic calcites, *GSA Bulletin*, 101 (6), 795–804.

Barron-Gafford, G.A., Scott, R.L., Jenerette, G.D., and Huxman, T.E., 2011. The relative controls of temperature, soil moisture, and plant functional group on soil CO2 efflux at diel, seasonal, and annual scales, *Journal of Geophysical Research: Biogeosciences*, 116 (G1).

Batjes, N.H., 2014. Total carbon and nitrogen in the soils of the world, *European Journal of Soil Science*, 65 (1), 10–21.

Beerling, D.J., Kantzas, E.P., Lomas, M.R., Wade, P., Eufrasio, R.M., Renforth, P., Sarkar, B., Andrews, M.G., James, R.H., Pearce, C.R., Mercure, J.F., Pollitt, H., Holden, P.B., Edwards, N.R., Khanna, M., Koh, L., Quegan, S., Pidgeon, N.F., Janssens, I.A., Hansen, J., and Banwart, S.A., 2020. Potential for large-scale CO2 removal via enhanced rock weathering with croplands, *Nature*, 583 (7815), 242–248.

Bénézeth, P., Saldi, G.D., Dandurand, J.L., and Schott, J., 2011. Experimental determination of the solubility product of magnesite at 50 to 200Â°C, *Chemical Geology*, 286 (1), 21–31.

Berner, R.A., 1965. Activity coefficients of bicarbonate, carbonate and calcium ions in sea water, *Geochimica et Cosmochimica Acta*, 29 (8), 947–965.

Berner, R.A., 1975. The role of magnesium in the crystal growth of calcite and aragonite from sea water, *Geochimica et Cosmochimica Acta*, 39 (4), 489–504.

Bhupinderpal-Singh, Nordgren, A., Ottosson Lofvenius, M., Hogberg, M.N., Mellander, P.E., and Hogberg, P., 2003. Tree root and soil heterotrophic respiration as revealed by girdling of boreal Scots pine forest: extending observations beyond the first year, *Plant, Cell & Environment*, 26 (8), 1287–1296.

Birch, H.F., 1964. Mineralisation of plant nitrogen following alternate wet and dry conditions, *Plant and Soil*, 20 (1), 43–49.

Bischoff, W.D., Bishop, F.C., and Mackenzie, F.T., 1983. Biogenically produced magnesian calcite; inhomogeneities in chemical and physical properties; comparison with synthetic phases, *American Mineralogist*, 68 (11-12), 1183–1188.

Blättler, C.L., Henderson, G.M., and Jenkyns, H.C., 2012. Explaining the Phanerozoic Ca isotope history of seawater, *Geology*, 40 (9), 843–846.

Blättler, C.L. and Higgins, J.A., 2017. Testing Urey's carbonate-silicate cycling using the calcium isotopic composition of sedimentary carbonates, *Earth and Planetary Science Letters*, 479, 241–251.

Blume, E., Bischoff, M., Reichert, J.M., Moorman, T., Konopka, A., and Turco, R.F., 2002. Surface and subsurface microbial biomass, community structure and metabolic activity as a function of soil depth and season, *Applied Soil Ecology*, 20 (3), 171–181.

Böhm, F., Eisenhauer, A., Tang, J., Dietzel, M., Krabbenhöft, A., Kisakürek, B., and Horn, C., 2012. Strontium isotope fractionation of planktic foraminifera and inorganic calcite, *Geochimica et Cosmochimica Acta*, 93, 300–314.

Bond-Lamberty, B., Bailey, V.L., Chen, M., Gough, C.M., and Vargas, R., 2018. Globally rising soil heterotrophic respiration over recent decades, *Nature*, 560 (7716), 80–83.

Bond-Lamberty, B. and Thomson, A., 2010. A global database of soil respiration data, *Biogeosciences*, 7 (6), 1915–1926.

Boone, R.D., Nadelhoffer, K.J., Canary, J.D., and Kaye, J.P., 1998. Roots exert a strong influence on the temperature sensitivityof soil respiration, *Nature*, 396 (6711), 570–572.

Bourg, I.C., Beckingham, L.E., and DePaolo, D.J., 2015. The Nanoscale Basis of CO2 Trapping for Geologic Storage, *Environmental Science & Technology*, 49 (17), 10265–10284.

Bourg, I.C., Richter, F.M., Christensen, J.N., and Sposito, G., 2010. Isotopic mass dependence of metal cation diffusion coefficients in liquid water, *Geochimica et Cosmochimica Acta*, 74 (8), 2249–2256.

Bourg, I.C. and Sposito, G., 2007. Molecular dynamics simulations of kinetic isotope fractionation during the diffusion of ionic species in liquid water, *Geochimica et Cosmochimica Acta*, 71 (23), 5583–5589.

Bracco, J.N., Grantham, M.C., and Stack, A.G., 2012. Calcite Growth Rates As a Function of Aqueous Calcium-to-Carbonate Ratio, Saturation Index, and Inhibitor Concentration: Insight into the Mechanism of Reaction and Poisoning by Strontium, *Crystal Growth & Design*, 12 (7), 3540–3548.

Bracco, J.N., Stack, A.G., and Steefel, C.I., 2013. Upscaling Calcite Growth Rates from the Mesoscale to the Macroscale, *Environmental Science & Technology*, 47 (13), 7555–7562.

Bradbury, H.J., Halloran, K.H., Lin, C.Y., and Turchyn, A.V., 2020. Calcium isotope fractionation during microbially induced carbonate mineral precipitation, *Geochimica et Cosmochimica Acta*, 277, 37–51.

Bradbury, H.J. and Turchyn, A.V., 2018. Calcium isotope fractionation in sedimentary pore fluids from ODP Leg 175: Resolving carbonate recrystallization, *Geochimica et Cosmochimica Acta*, 236, 121–139.

Bradford, M.A., McCulley, R.L., Crowther, T.W., Oldfield, E.E., Wood, S.A., and Fierer, N., 2019. Cross-biome patterns in soil microbial respiration predictable from evolutionary theory on thermal adaptation, *Nature Ecology & Evolution*, 3 (2), 223–231.

Bradford, M.A., Wieder, W.R., Bonan, G.B., Fierer, N., Raymond, P.A., and Crowther, T.W., 2016. Managing uncertainty in soil carbon feedbacks to climate change, *Nature Clim. Change*, 6 (8), 751–758.

Brand, U. and Veizer, J., 1980. Chemical diagenesis of a multicomponent carbonate system; 1, Trace elements, *Journal of Sedimentary Research*, 50 (4), 1219–1236.

Brandt, L.A., Bohnet, C., and King, J.Y., 2009. Photochemically induced carbon dioxide production as a mechanism for carbon loss from plant litter in arid ecosystems, *Journal of Geophysical Research: Biogeosciences*, 114 (G2).

Breecker, D.O., Sharp, Z.D., and McFadden, L.D., 2009. Seasonal bias in the formation and stable isotopic composition of pedogenic carbonate in modern soils from central New Mexico, USA, *Geological Society of America Bulletin*, 121 (3-4), 630–640.

Burton, B.P. and Van de Walle, A., 2003. First-principles-based calculations of the CaCO3-MgCO3 and CdCO3-MgCO3 subsolidus phase diagrams, *Physics and Chemistry of Minerals*, 30 (2), 88–97.

Burton, W.K., Cabrera, N., and Frank, F.C., 1951. The growth of crystals and the equilibrium structure of their surfaces, *Philosophical Transactions of the Royal Society of London.*, 243 (866), 299–358.

Cable, J.M., Ogle, K., Lucas, R.W., Huxman, T.E., Loik, M.E., Smith, S.D., Tissue, D.T., Ewers, B.E., Pendall, E., Welker, J.M., Charlet, T.N., Cleary, M., Griffith, A., Nowak, R.S., Rogers, M., Steltzer, H., Sullivan, P.F., and van Gestel, N.C., 2011. The temperature responses of soil respiration in deserts: a seven desert synthesis, *Biogeochemistry*, 103 (1), 71–90.

Cable, J.M., Ogle, K., Tyler, A.P., Pavao-Zuckerman, M.A., and Huxman, T.E., 2009. Woody plant encroachment impacts on soil carbon and microbial processes: results from a hierarchical Bayesian analysis of soil incubation data, *Plant and Soil*, 320 (1), 153–167.

Cabrera, N. and Vermilyea, D.A., 1958. The growth of crystals from solution, *in:* R.H. Doremus, B.W. Roberts, and D. Turnbull, eds., *Growth and Perfection of Crystals: Proceedings of an International Conference on Crystal Growth*, New York, NY: Wiley, 299–358.

Canadell, J., Jackson, R.B., Ehleringer, J.B., Mooney, H.A., Sala, O.E., and Schulze, E.D., 1996. Maximum rooting depth of vegetation types at the global scale, *Oecologia*, 108 (4), 583–595.

Cao, B., Stack, A.G., Steefel, C.I., DePaolo, D.J., Lammers, L.N., and Hu, Y., 2018. Investigating calcite growth rates using a quartz crystal microbalance with dissipation (QCM-D), *Geochimica et Cosmochimica Acta*, 222, 269–283.

Capobianco, C. and Navrotsky, A., 1987. Solid-solution thermodynamics in CaCO3-MnCO3, *American Mineralogist*, 72 (3-4), 312–318.

Charley, J.L. and West, N.E., 1975. Plant-Induced Soil Chemical Patterns in Some Shrub-Dominated Semi-Desert Ecosystems of Utah, *Journal of Ecology*, 63 (3), 945–963.

Chen, Y.H. and Lu, D.L., 2015. CO2 capture by kaolinite and its adsorption mechanism, *Applied Clay Science*, 104, 221–228.

Chou, L., Garrels, R.M., and Wollast, R., 1989. Comparative study of the kinetics and mechanisms of dissolution of carbonate minerals, *Chemical Geology*, 78 (3), 269–282.

Chouikhi, N., Cecilia, J.A., Vilarrasa-García, E., Besghaier, S., Chlendi, M., Franco Duro, F.I., Rodriguez Castellon, E., and Bagane, M., 2019. CO2 Adsorption of Materials Synthesized from Clay Minerals: A Review.

Clark, D.E., Oelkers, E.H., Gunnarsson, I., Sigfússon, B., Snæbjörnsdóttir, S.Ó., Aradóttir, E.S., and Gíslason, S.R., 2020. CarbFix2: CO2 and H2S mineralization during 3.5 years of continuous injection into basaltic rocks at more than 250 Â°C, *Geochimica et Cosmochimica Acta*, 279, 45–66.

Clarkson, J.R., Price, T.J., and Adams, C.J., 1992. Role of metastable phases in the spontaneous precipitation of calcium carbonate, *Journal of the Chemical Society, Faraday Transactions*, 88 (2), 243–249.

Conant, R.T., Steinweg, J.M., Haddix, M.L., Paul, E.A., Plante, A.F., and Six, J., 2008. Experimental warming shows that decomposition temperature sensitivity increases with soil organic matter recalcitrance, *Ecology*, 89 (9), 2384–2391.

Cook, B.I., Ault, T.R., and Smerdon, J.E., 2015. Unprecedented 21st century drought risk in the American Southwest and Central Plains, *Science Advances*, 1 (1), e1400082.

Crowther, T.W., Todd-Brown, K.E.O., Rowe, C.W., Wieder, W.R., Carey, J.C., Machmuller, M.B., Snoek, B.L., Fang, S., Zhou, G., Allison, S.D., Blair, J.M., Bridgham, S.D., Burton, A.J., Carrillo, Y., Reich, P.B., Clark, J.S., Classen, A.T., Dijkstra, F.A., Elberling, B., Emmett, B.A., Estiarte, M., Frey, S.D., Guo, J., Harte, J., Jiang, L., Johnson, B.R., Kröel-Dulay, G., Larsen, K.S., Laudon, H., Lavallee, J.M., Luo, Y., Lupascu, M., Ma, L.N., Marhan, S., Michelsen, A., Mohan, J., Niu, S., Pendall, E., Peñuelas, J., Pfeifer-Meister, L., Poll, C., Reinsch, S., Reynolds, L.L., Schmidt, I.K., Sistla, S., Sokol, N.W., Templer, P.H., Treseder, K.K., Welker, J.M., and Bradford, M.A., 2016. Quantifying global soil carbon losses in response to warming, *Nature*, 540 (7631), 104–108.

Cueva, A., Volkmann, T.H.M., van Haren, J., Troch, P.A., and Meredith, L.K., 2019. Reconciling Negative Soil CO2 Fluxes: Insights from a Large-Scale Experimental Hillslope.

Curtin, D., Selles, F., and Steppuhn, H., 1998. Estimating Calcium-Magnesium Selectivity in Smectitic Soils from Organic Matter and Texture, *Soil Science Society of America Journal*, 62 (5), 1280–1285.

Dacal, M., Bradford, M.A., Plaza, C., Maestre, F.T., and García-Palacios, P., 2019. Soil microbial respiration adapts to ambient temperature in global drylands, *Nature Ecology & Evolution*, 3 (2), 232–238.

Davidson, E.A. and Janssens, I.A., 2006. Temperature sensitivity of soil carbon decomposition and feedbacks to climate change, *Nature*, 440 (7081), 165–173.

Davis, K., 2008. Resolving the nanoscale mechanisms of calcite growth from nonstoichiometric and microbial solutions.

Davis, K.J., Dove, P.M., and De Yoreo, J.J., 2000a. The Role of Mg2+ as an Impurity in Calcite Growth, *Science*, 290 (5494), 1134 LP – 1137.

Davis, K.J., Dove, P.M., Wasylenki, L.E., and De Yoreo, J.J., 2004. Morphological consequences of differential Mg2+incorporation at structurally distinct steps on calcite.

Davis, K.J., Dove, P.M., and Yoreo, J.J.D., 2000b. Resolving the Control of Magnesium on Calcite Growth: Thermodynamic and Kinetic Consequences of Impurity Incorporation for Biomineral Formation, *MRS Proceedings*, 620, M9.5.1.

De La Pierre, M., Raiteri, P., and Gale, J.D., 2016. Structure and Dynamics of Water at Step Edges on the Calcite 1014 Surface, *Crystal Growth & Design*, 16 (10), 5907–5914.

De La Pierre, M., Raiteri, P., Stack, A.G., and Gale, J.D., 2017. Uncovering the Atomistic Mechanism for Calcite Step Growth, *Angewandte Chemie International Edition*, 56 (29), 8464–8467.

De Yoreo, J.J., Gilbert, P.U.P.A., Sommerdijk, N.A.J.M., Penn, R.L., Whitelam, S., Joester, D., Zhang, H., Rimer, J.D., Navrotsky, A., Banfield, J.F., Wallace, A.F., Michel, F.M., Meldrum, F.C., Cölfen, H., and Dove, P.M., 2015. Crystallization by particle attachment in synthetic, biogenic, and geologic environments, *Science*, 349 (6247), aaa6760.

De Yoreo, J.J. and Vekilov, P.G., 2003. Principles of Crystal Nucleation and Growth, *Reviews in Mineralogy and Geochemistry*, 54 (1), 57 LP – 93.

DePaolo, D.J., 2004. Calcium Isotopic Variations Produced by Biological, Kinetic, Radiogenic and Nucleosynthetic Processes, *Reviews in Mineralogy and Geochemistry*, 55 (1), 255–288.

DePaolo, D.J., 2011. Surface kinetic model for isotopic and trace element fractionation during precipitation of calcite from aqueous solutions, *Geochimica et Cosmochimica Acta*, 75 (4), 1039–1056.

Di Tommaso, D., Ruiz-Agudo, E., de Leeuw, N.H., Putnis, A., and Putnis, C.V., 2014. Modelling the effects of salt solutions on the hydration of calcium ions, *Physical Chemistry Chemical Physics*, 16 (17), 7772–7785.

Dirks, I., Navon, Y., Kanas, D., Dumbur, R., and Grunzweig, J.M., 2010. Atmospheric water vapor as driver of litter decomposition in Mediterranean shrubland and grassland during rainless seasons, *Global Change Biology*, 16 (10), 2799–2812.

Dobberschütz, S., Nielsen, M.R., Sand, K.K., Civioc, R., Bovet, N., Stipp, S.L.S., and Andersson, M.P., 2018. The mechanisms of crystal growth inhibition by organic and inorganic inhibitors, *Nature Communications*, 9 (1), 1578.

D'Odorico, P., Caylor, K., Okin, G.S., and Scanlon, T.M., 2007. On soil moisture-vegetation feedbacks and their possible effects on the dynamics of dryland ecosystems, *Journal of Geophysical Research: Biogeosciences*, 112 (G4).

Dove, P.M. and Hochella, M.F., 1993. Calcite precipitation mechanisms and inhibition by orthophosphate: In situ observations by Scanning Force Microscopy, *Geochimica et Cosmochimica Acta*, 57 (3), 705–714.

Dromgoole, E.L. and Walter, L.M., 1990a. Inhibition of calcite growth rates by Mn2+ in CaCl2 solutions at 10, 25, and 50Â°C, *Geochimica et Cosmochimica Acta*, 54 (11), 2991–3000.

Dromgoole, E.L. and Walter, L.M., 1990b. Iron and manganese incorporation into calcite: Effects of growth kinetics, temperature and solution chemistry, *Chemical Geology*, 81 (4), 311–336.

Druhan, J.L., Steefel, C.I., Williams, K.H., and DePaolo, D.J., 2013. Calcium isotope fractionation in groundwater: Molecular scale processes influencing field scale behavior, *Geochimica et Cosmochimica Acta*, 119, 93–116.

Emiliani, C., 1955. Pleistocene Temperatures, *The Journal of Geology*, 63 (6), 538–578.

Eswaran, H., Reich, P.F., Kimble, J.M., Beinroth, F.H., Padmanabhan, R., and Monchareon, P., 2000. Global carbon stocks, *in:* R. Lal, J.M. Kimble, H. Eswaran, and B.A. Stewart, eds., *Global Climate Change and Pedogenic Carbonates.*, Boca Raton, FL: Lewis.

Evans, S., Todd-Brown, K.E.O., Jacobson, K., and Jacobson, P., 2020. Non-rainfall Moisture: A Key Driver of Microbial Respiration from Standing Litter in Arid, Semiarid, and Mesic Grasslands, *Ecosystems*, 23 (6), 1154–1169.

Ewing, S.A., Yang, W., DePaolo, D.J., Michalski, G., Kendall, C., Stewart, B.W., Thiemens, M., and Amundson, R., 2008. Non-biological fractionation of stable Ca isotopes in soils of the Atacama Desert, Chile, *Geochimica et Cosmochimica Acta*, 72 (4), 1096–1110.

Exbrayat, J.F., Pitman, A.J., Abramowitz, G., and Wang, Y.P., 2013. Sensitivity of net ecosystem exchange and heterotrophic respiration to parameterization uncertainty, *Journal of Geophysical Research: Atmospheres*, 118 (4), 1640–1651.

Fa, K., Liu, Z., Zhang, Y., Qin, S., Wu, B., and Liu, J., 2016. Abiotic carbonate dissolution traps carbon in a semiarid desert, *Scientific Reports*, 6 (1), 23570.

Fa, K., Zhang, Y., Lei, G., Wu, B., Qin, S., Liu, J., Feng, W., and Lai, Z., 2018. Underestimation of soil respiration in a desert ecosystem, *CATENA*, 162, 23–28.

Fantle, M.S. and DePaolo, D.J., 2005. Variations in the marine Ca cycle over the past 20 million years, *Earth and Planetary Science Letters*, 237 (1), 102–117.

Fantle, M.S. and DePaolo, D.J., 2007. Ca isotopes in carbonate sediment and pore fluid from ODP Site 807A: The Ca2+ - calcite equilibrium fractionation factor and calcite recrystallization rates in Pleistocene sediments, *Geochimica et Cosmochimica Acta*, 71 (10), 2524–2546.

Fantle, M.S. and Tipper, E.T., 2014. Calcium isotopes in the global biogeochemical Ca cycle: Implications for development of a Ca isotope proxy, *Earth-Science Reviews*, 129, 148–177.

Farkaš, J., Böhm, F., Wallmann, K., Blenkinsop, J., Eisenhauer, A., van Geldern, R., Munnecke, A., Voigt, S., and Veizer, J., 2007. Calcium isotope record of Phanerozoic oceans: Implications for chemical evolution of seawater and its causative mechanisms, *Geochimica et Cosmochimica Acta*, 71 (21), 5117–5134.

Fianu, J., Gholinezhad, J., and Hassan, M., 2018. Comparison of Temperature-Dependent Gas Adsorption Models and Their Application to Shale Gas Reservoirs, *Energy & Fuels*, 32 (4), 4763–4771.

Fierer, N., Allen, A.S., Schimel, J.P., and Holden, P.A., 2003a. Controls on microbial CO2 production: a comparison of surface and subsurface soil horizons, *Global Change Biology*, 9 (9), 1322–1332.

Fierer, N., Colman, B.P., Schimel, J.P., and Jackson, R.B., 2006. Predicting the temperature dependence of microbial respiration in soil: A continental-scale analysis, *Global Biogeochemical Cycles*, 20 (3).

Fierer, N., Schimel, J.P., and Holden, P.A., 2003b. Variations in microbial community composition through two soil depth profiles, *Soil Biology and Biochemistry*, 35 (1), 167–176.

Folk, R.L., 1974. The natural history of crystalline calcium carbonate; effect of magnesium content and salinity, *Journal of Sedimentary Research*, 44 (1), 40–53.

Fuss, S., Lamb, W.F., Callaghan, M.W., Hilaire, J., Creutzig, F., Amann, T., Beringer, T., de Oliveira Garcia, W., Hartmann, J., Khanna, T., Luderer, G., Nemet, G.F., Rogelj, J., Smith, P., Vicente, J.L.V., Wilcox, J., del Mar Zamora Dominguez, M., and Minx, J.C., 2018. Negative emissions - Part 2: Costs, potentials and side effects, *Environmental Research Letters*, 13 (6), 63002.

Gabitov, R.I., Sadekov, A., and Leinweber, A., 2014. Crystal growth rate effect on Mg/Ca and Sr/Ca partitioning between calcite and fluid: An in situ approach, *Chemical Geology*, 367, 70–82.

Gagnon, A., Depaolo, D., and Deyoreo, J., 2010. Calcium Isotope Signature of Amorphous Calcium Carbonate: A Probe of Crystallization Pathway? (Invited), *in: AGU Fall Meeting Abstracts*, vol. 2010, PP22A–08.

Gallagher, T.M. and Breecker, D.O., 2020. The Obscuring Effects of Calcite Dissolution and Formation on Quantifying Soil Respiration, *Global Biogeochemical Cycles*, 34 (12), e2020GB006584.

Ganot, Y., Dragila, M.I., and Weisbrod, N., 2014. Impact of thermal convection on CO2 flux across the earth-atmosphere boundary in high-permeability soils, *Agricultural and Forest Meteorology*, 184, 12–24.

Garcia, C.A., Andraski, B.J., Stonestrom, D.A., Cooper, C.A., ŠimÅ¯nek, J., and Wheatcraft, S.W., 2011. Interacting Vegetative and Thermal Contributions to Water Movement in Desert Soil All rights reserved. No part of this periodical may be reproduced or transmitted in any form or by any means, electronic or mechanical, including photocopying, recording, or, *Vadose Zone Journal*, 10, 552–564.

Garcia-Pichel, F. and Belnap, J., 1996. Microenvironments and microscale productivity of cyanobacterial desert crusts, *Journal of Phycology*, 32 (5), 774–782.

Garner, W. and Steinberger, Y., 1989. A proposed mechanism for the formation of 'Fertile Islands' in the desert ecosystem, *Journal of Arid Environments*, 16 (3), 257–262.

Gebauer, D., Völkel, A., and Cölfen, H., 2008. Stable Prenucleation Calcium Carbonate Clusters, *Science*, 322 (5909), 1819 LP – 1822.

Gebrehiwet, T.A., Redden, G.D., Fujita, Y., Beig, M.S., and Smith, R.W., 2012. The Effect of the CO32- to Ca2+ Ion activity ratio on calcite precipitation kinetics and Sr2+partitioning, *Geochemical Transactions*, 13 (1), 1.

Gerdemann, S.J., O'Connor, W.K., Dahlin, D.C., Penner, L.R., and Rush, H., 2007. Ex Situ Aqueous Mineral Carbonation, *Environmental Science & Technology*, 41 (7), 2587–2593.

Gliksman, D., Rey, A., Seligmann, R., Dumbur, R., Sperling, O., Navon, Y., Haenel, S., De Angelis, P., Arnone III, J.A., and Grünzweig, J.M., 2017. Biotic degradation at night, abiotic degradation at day: positive feedbacks on litter decomposition in drylands, *Global Change Biology*, 23 (4), 1564–1574.

Green, L.E., Porras-Alfaro, A., and Sinsabaugh, R.L., 2008. Translocation of nitrogen and carbon integrates biotic crust and grass production in desert grassland, *Journal of Ecology*, 96 (5), 1076–1085.

Gussone, N., Ahm, A.S.C., Lau, K.V., and Bradbury, H.J., 2020. Calcium isotopes in deep time: Potential and limitations, *Chemical Geology*, 544, 119601.

Gussone, N., Böhm, F., Eisenhauer, A., Dietzel, M., Heuser, A., Teichert, B.M.A., Reitner, J., Wörheide, G., and Dullo, W.C., 2005. Calcium isotope fractionation in calcite and aragonite, *Geochimica et Cosmochimica Acta*, 69 (18), 4485–4494.

Gussone, N., Eisenhauer, A., Heuser, A., Dietzel, M., Bock, B., Böhm, F., Spero, H.J., Lea, D.W., Bijma, J., and Nägler, T.F., 2003. Model for kinetic effects on calcium isotope fractionation (δ44Ca) in inorganic aragonite and cultured planktonic foraminifera, *Geochimica et Cosmochimica Acta*, 67 (7), 1375–1382.

Gussone, N., Hönisch, B., Heuser, A., Eisenhauer, A., Spindler, M., and Hemleben, C., 2009. A critical evaluation of calcium isotope ratios in tests of planktonic foraminifers, *Geochimica et Cosmochimica Acta*, 73 (24), 7241–7255.

Gussone, N., Langer, G., Geisen, M., Steel, B.A., and Riebesell, U., 2007. Calcium isotope fractionation in coccoliths of cultured Calcidiscus leptoporus, Helicosphaera carteri, Syracosphaera pulchra and Umbilicosphaera foliosa, *Earth and Planetary Science Letters*, 260 (3), 505–515.

Gutiérrez-Jurado, H.A., Vivoni, E.R., Harrison, J.B.J., and Guan, H., 2006. Ecohydrology of root zone water fluxes and soil development in complex semiarid rangelands, *Hydrological Processes*, 20 (15), 3289–3316.

Hamerlynck, E.P., Scott, R.L., Sánchez-Cañete, E.P., and Barron-Gafford, G.A., 2013. Nocturnal soil CO2 uptake and its relationship to subsurface soil and ecosystem carbon fluxes in a Chihuahuan Desert shrubland, *Journal of Geophysical Research: Biogeosciences*, 118 (4), 1593–1603.

Hanson, P.J., Edwards, N.T., Garten, C.T., and Andrews, J.A., 2000. Separating root and soil microbial contributions to soil respiration: A review of methods and observations, *Biogeochemistry*, 48 (1), 115–146.

Harel, Y., Ohad, I., and Kaplan, A., 2004. Activation of Photosynthesis and Resistance to Photoinhibition in Cyanobacteria within Biological Desert Crust, *Plant Physiology*, 136 (2), 3070 LP – 3079.

Harouaka, K., Eisenhauer, A., and Fantle, M.S., 2014. Experimental investigation of Ca isotopic fractionation during abiotic gypsum precipitation, *Geochimica et Cosmochimica Acta*, 129, 157–176.

Hartle, R.T., Fernandez, G.C.J., and Nowak, R.S., 2006. Horizontal and vertical zones of influence for root systems of four Mojave Desert shrubs, *Journal of Arid Environments*, 64 (4), 586–603.

Heberling, F., Bosbach, D., Eckhardt, J.D., Fischer, U., Glowacky, J., Haist, M., Kramar, U., Loos, S., Müller, H.S., Neumann, T., Pust, C., Schäfer, T., Stelling, J., Ukrainczyk, M., Vinograd, V., Vučak, M., and Winkler, B., 2014. Reactivity of the calcite-water-interface, from molecular scale processes to geochemical engineering, *Applied Geochemistry*, 45, 158–190.

Hellevang, H., Haile, B.G., and Miri, R., 2016. A Statistical Approach To Explain the Solution Stoichiometry Effect on Crystal Growth Rates, *Crystal Growth & Design*, 16 (3), 1337–1348.

Helm, L. and Merbach, A.E., 1999. Water exchange on metal ions: experiments and simulations, *Coordination Chemistry Reviews*, 187 (1), 151–181.

Hem, J.D., 1963. *Chemical equilibria and rates of manganese oxidation*, 1667, US Government Printing Office.

Henderson, G.M., Chu, N.C., Bayon, G., and Benoit, M., 2006. $\delta44/42$ Ca in gas hydrates, porewaters and authigenic carbonates from Niger Delta sediments, *Geochimica et Cosmochimica Acta*, 70 (18, Supplement), A244.

Herman, R.P., Provencio, K.R., Herrera-Matos, J., and Torrez, R.J., 1995. Resource islands predict the distribution of heterotrophic bacteria in chihuahuan desert soils., *Applied and Environmental Microbiology*, 61 (5), 1816 LP – 1821.

Hernandez, R.R., Hoffacker, M.K., Murphy-Mariscal, M.L., Wu, G.C., and Allen, M.F., 2015. Solar energy development impacts on land cover change and protected areas, *Proceedings of the National Academy of Sciences*, 112 (44), 13579 LP – 13584.

Hicks Pries, C.E., Castanha, C., Porras, R.C., and Torn, M.S., 2017. The whole-soil carbon flux in response to warming, *Science*, 355 (6332), 1420 LP – 1423.

Higgins, J.A., Blättler, C.L., Lundstrom, E.A., Santiago-Ramos, D.P., Akhtar, A.A., Ahm, A.S.C., Bialik, O., Holmden, C., Bradbury, H., Murray, S.T., and Swart, P.K., 2018. Mineralogy, early marine diagenesis, and the chemistry of shallow-water carbonate sediments, *Geochimica et Cosmochimica Acta*, 220, 512–534.

Higgins, S.R. and Hu, X., 2005. Self-limiting growth on dolomite: Experimental observations with in situ atomic force microscopy, *Geochimica et Cosmochimica Acta*, 69 (8), 2085–2094.

Hindshaw, R.S., Reynolds, B.C., Wiederhold, J.G., Kretzschmar, R., and Bourdon, B., 2011. Calcium isotopes in a proglacial weathering environment: Damma glacier, Switzerland, *Geochimica et Cosmochimica Acta*, 75 (1), 106–118.

Hippler, D., Eisenhauer, A., and Nägler, T.F., 2006. Tropical Atlantic SST history inferred from Ca isotope thermometry over the last 140ka, *Geochimica et Cosmochimica Acta*, 70 (1), 90–100.

Hirmas, D.R., Amrhein, C., and Graham, R.C., 2010. Spatial and process-based modeling of soil inorganic carbon storage in an arid piedmont, *Geoderma*, 154 (3-4), 486–494.

Hoffman, P.F., Kaufman, A.J., Halverson, G.P., and Schrag, D.P., 1998. A Neoproterozoic Snowball Earth, *Science*, 281 (5381), 1342 LP – 1346.

Hofmann, A.E., Bourg, I.C., and DePaolo, D.J., 2012. Ion desolvation as a mechanism for kinetic isotope fractionation in aqueous systems, *Proceedings of the National Academy of Sciences*, 109 (46), 18689–18694.

Högberg, P., 2010. Is tree root respiration more sensitive than heterotrophic respiration to changes in soil temperature?, *New Phytologist*, 188 (1), 9–10.

Hong, M. and Teng, H.H., 2014. Implications of solution chemistry effects: Direction-specific restraints on the step kinetics of calcite growth, *Geochimica et Cosmochimica Acta*, 141, 228–239.

Inskeep, W.P. and Bloom, P.R., 1986a. Calcium Carbonate Supersaturation in Soil Solutions of Calciaquolls, *Soil Science Society of America Journal*, 50, 1431–1437.

Inskeep, W.P. and Bloom, P.R., 1986b. Kinetics of Calcite Precipitation in the Presence of Water-soluble Organic Ligands, *Soil Science Society of America Journal*, 50, 1167–1172.

IPCC, 2019. *Climate Change and Land: an IPCC special report on climate change, desertification, land degradation, sustainable land management, food security, and greenhouse gas fluxes in terrestrial ecosystems*, Intergovernmental Panel on Climate Change (IPCC).

Irvine, J., Law, B.E., and Kurpius, M.R., 2005. Coupling of canopy gas exchange with root and rhizosphere respiration in a semi-arid forest, *Biogeochemistry*, 73 (1), 271–282.

Jacobson, A.D. and Holmden, C., 2008. δ44Ca evolution in a carbonate aquifer and its bearing on the equilibrium isotope fractionation factor for calcite, *Earth and Planetary Science Letters*, 270 (3), 349–353.

Janssens, I.A., Dore, S., Epron, D., Lankreijer, H., Buchmann, N., Longdoz, B., Brossaud, J., and Montagnani, L., 2003. Climatic Influences on Seasonal and Spatial Differences in Soil CO2 Efflux BT - Fluxes of Carbon, Water and Energy of European Forests.

Jarvis, P., Rey, A., Petsikos, C., Wingate, L., Rayment, M., Pereira, J., Banza, J., David, J., Miglietta, F., Borghetti, M., Manca, G., and Valentini, R., 2007. Drying and wetting of Mediterranean soils stimulates decomposition and carbon dioxide emission: the "Birch effect", *Tree Physiology*, 27 (7), 929–940.

Jasoni, R.L., Smith, S.D., and Arnone III, J.A., 2005. Net ecosystem CO2 exchange in Mojave Desert shrublands during the eighth year of exposure to elevated CO2, *Global Change Biology*, 11 (5), 749–756.

Jenny, H., 1941. *Factors of soil formation: A system of quantitative pedology*, Dover.

Jiménez-López, C., Romanek, C.S., Huertas, F., Ohmoto, H., and Caballero, E., 2004. Oxygen isotope fractionation in synthetic magnesian calcite, *Geochimica et Cosmochimica Acta*, 68 (16), 3367–3377.

Jin, Z. and Firoozabadi, A., 2014. Effect of water on methane and carbon dioxide sorption in clay minerals by Monte Carlo simulations, *Fluid Phase Equilibria*, 382, 10–20.

Jobbágy, E.G. and Jackson, R.B., 2000. The vertical distribution of soil organic carbon and its relation to climate and vegetation, *Ecological Applications*, 10 (2), 423–436.

Johnson, K.S., 1982. Solubility of rhodochrosite (MnCO3) in water and seawater, *Geochimica et Cosmochimica Acta*, 46 (10), 1805–1809.

Jones, H.G., 1992. *Plants and microclimate: a quantitative approach to environmental plant physiology*, New York, NY: Cambridge University Press.

Jordan, D.N., Zitzer, S.F., Hendrey, G.R., Lewin, K.F., Nagy, J., Nowak, R.S., Smith, S.D., Coleman, J.S., and Seemann, J.R., 1999. Biotic, abiotic and performance aspects of the Nevada Desert Free-Air CO2 Enrichment (FACE) Facility, *Global Change Biology*, 5 (6), 659–668.

Jung, M., Reichstein, M., Schwalm, C.R., Huntingford, C., Sitch, S., Ahlström, A., Arneth, A., Camps-Valls, G., Ciais, P., Friedlingstein, P., Gans, F., Ichii, K., Jain, A.K., Kato, E., Papale, D., Poulter, B., Raduly, B., Rödenbeck, C., Tramontana, G., Viovy, N., Wang, Y.P., Weber, U., Zaehle, S., and Zeng, N., 2017. Compensatory water effects link yearly global land CO2 sink changes to temperature, *Nature*, 541 (7638), 516–520.

Katsikopoulos, D., Fernández-González, Á., and Prieto, M., 2009. Precipitation and mixing properties of the "disordered" (Mn,Ca)CO3 solid solution, *Geochimica et Cosmochimica Acta*, 73 (20), 6147–6161.

Kelemen, P.B., Matter, J., Streit, E.E., Rudge, J.F., Curry, W.B., and Blusztajn, J., 2011. Rates and Mechanisms of Mineral Carbonation in Peridotite: Natural Processes and Recipes for Enhanced, in situ CO2 Capture and Storage, *Annual Review of Earth and Planetary Sciences*, 39 (1), 545–576.

Kelemen, P.B., McQueen, N., Wilcox, J., Renforth, P., Dipple, G., and Vankeuren, A.P., 2020. Engineered carbon mineralization in ultramafic rocks for CO2 removal from air: Review and new insights, *Chemical Geology*, 550, 119628.

Kemp, P.R., Reynolds, J.F., Pachepsky, Y., and Chen, J.L., 1997. A comparative modeling study of soil water dynamics in a desert ecosystem, *Water Resources Research*, 33 (1), 73–90.

Kidron, G.J., 2009. The effect of shrub canopy upon surface temperatures and evaporation in the Negev Desert, *Earth Surface Processes and Landforms*, 34 (1), 123–132.

Kidron, G.J., Herrnstadt, I., and Barzilay, E., 2002. The role of dew as a moisture source for sand microbiotic crusts in the Negev Desert, Israel, *Journal of Arid Environments*, 52 (4), 517–533.

Kisakürek, B., Eisenhauer, A., Böhm, F., Hathorne, E.C., and Erez, J., 2011. Controls on calcium isotope fractionation in cultured planktic foraminifera, Globigerinoides ruber and Globigerinella siphonifera, *Geochimica et Cosmochimica Acta*, 75 (2), 427–443.

Kowalski, A.S., Serrano-Ortiz, P., Janssens, I.A., Sánchez-Moral, S., Cuezva, S., Domingo, F., Were, A., and Alados-Arboledas, L., 2008. Can flux tower research neglect geochemical CO2 exchange?, *Agricultural and Forest Meteorology*, 148 (6), 1045–1054.

Kump, L.R., Brantley, S.L., and Arthur, M.A., 2000. Chemical Weathering, Atmospheric CO2, and Climate, *Annual Review of Earth and Planetary Sciences*, 28 (1), 611–667.

Lal, R., 2004. Soil Carbon Sequestration Impacts on Global Climate Change and Food Security, *Science*, 304 (5677), 1623–1627.

Lammers, L.N., Kulasinski, K., Zarzycki, P., and DePaolo, D.J., 2020. Molecular simulations of kinetic stable calcium isotope fractionation at the calcite-aqueous interface, *Chemical Geology*, 532, 119315.

Lammers, L.N. and Mitnick, E.H., 2019. Magnesian calcite solid solution thermodynamics inferred from authigenic deep-sea carbonate, *Geochimica et Cosmochimica Acta*, 248, 343–355.

Lange, O.L., 2003. Photosynthesis of Soil-Crust Biota as Dependent on Environmental Factors, *in:* J. Belnap and O.L. Lange, eds., *Biological Soil Crusts: Structure, Function, and Management*, Berlin, Heidelberg: Springer Berlin Heidelberg, 217–240.

Langmuir, D., 1979. Techniques of Estimating Thermodynamic Properties for Some Aqueous Complexes of Geochemical Interest.

Langmuir, I., 1918. The adsorption of gases on plane surfaces of glass, mica, and platinum., *Journal of the American Chemical Society*, 40 (9), 1361–1403.

Lardge, J.S., Duffy, D.M., Gillan, M.J., and Watkins, M., 2010. Ab Initio Simulations of the Interaction between Water and Defects on the Calcite (1014) Surface, *The Journal of Physical Chemistry C*, 114 (6), 2664–2668.

Larsen, K., Bechgaard, K., and Stipp, S.L.S., 2010. The effect of the Ca2+ to CO32- activity ratio on spiral growth at the calcite 1014 surface, *Geochimica et Cosmochimica Acta*, 74 (7), 2099–2109.

Lebrón, I. and Suárez, D.L., 1998. Kinetics and Mechanisms of Precipitation of Calcite as Affected by PCO2 and Organic Ligands at 25Â°C, *Geochimica et Cosmochimica Acta*, 62 (3), 405–416.

Lemarchand, D., Wasserburg, G.J., and Papanastassiou, D.A., 2004. Rate-controlled calcium isotope fractionation in synthetic calcite, *Geochimica et Cosmochimica Acta*, 68 (22), 4665–4678.

León-Sobrino, C., Ramond, J.B., Maggs-Kölling, G., and Cowan, D.A., 2019. Nutrient Acquisition, Rather Than Stress Response Over Diel Cycles, Drives Microbial Transcription in a Hyper-Arid Namib Desert Soil .

Lesht, D. and Bauman, J.E., 1978. Thermodynamics of the manganese(II) bicarbonate system, *Inorganic Chemistry*, 17 (12), 3332–3334.

Lin, Y.P. and Singer, P.C., 2009. Effect of Mg2+ on the kinetics of calcite crystal growth, *Journal of Crystal Growth*, 312 (1), 136–140.

Liu, G., Cornwell, W.K., Pan, X., Ye, D., Liu, F., Huang, Z., Dong, M., and Cornelissen, J.H.C., 2015a. Decomposition of 51 semidesert species from wide-ranging phylogeny is faster in standing and sand-buried than in surface leaf litters: implications for carbon and nutrient dynamics, *Plant and Soil*, 396 (1), 175–187.

Liu, J., Fa, K., Zhang, Y., Wu, B., Qin, S., and Jia, X., 2015b. Abiotic CO2 uptake from the atmosphere by semiarid desert soil and its partitioning into soil phases, *Geophysical Research Letters*, 42 (14), 5779–5785.

Lloyd, J. and Taylor, J.A., 1994. On the Temperature Dependence of Soil Respiration, *Functional Ecology*, 8 (3), 315–323.

Lorens, R.B., 1981. Sr, Cd, Mn and Co distribution coefficients in calcite as a function of calcite precipitation rate, *Geochimica et Cosmochimica Acta*, 45 (4), 553–561.

Lukashev, V.K., 1993. Some geochemical and environmental aspects of the Chernobyl nuclear accident, *Applied Geochemistry*, 8 (5), 419–436.

Luo, Y. and Millero, F.J., 2003. Solubility of Rhodochrosite (MnCO3) in NaCl Solutions, *Journal of Solution Chemistry*, 32 (5), 405–416.

Ma, J., Liu, R., and Li, Y., 2017. Abiotic contribution to total soil CO2 flux across a broad range of land-cover types in a desert region, *Journal of Arid Land*, 9 (1), 13–26.

Ma, J., Wang, Z.Y., Stevenson, B.A., Zheng, X.J., and Li, Y., 2013. An inorganic CO2 diffusion and dissolution process explains negative CO2 fluxes in saline/alkaline soils, *Scientific Reports*, 3 (1), 2025.

Maher, K., Johnson, N.C., Jackson, A., Lammers, L.N., Torchinsky, A.B., Weaver, K.L., Bird, D.K., and Brown, G.E., 2016. A spatially resolved surface kinetic model for forsterite dissolution, *Geochimica et Cosmochimica Acta*, 174, 313–334.

Maher, K., Steefel, C.I., DePaolo, D.J., and Viani, B.E., 2006. The mineral dissolution rate conundrum: Insights from reactive transport modeling of U isotopes and pore fluid chemistry in marine sediments, *Geochimica et Cosmochimica Acta*, 70 (2), 337–363.

Malek, E., McCurdy, G., and Giles, B., 1999. Dew contribution to the annual water balances in semi-arid desert valleys, *Journal of Arid Environments*, 42 (2), 71–80.

Manzoni, S., Schimel, J.P., and Porporato, A., 2012. Responses of soil microbial communities to water stress: results from a meta-analysis, *Ecology*, 93 (4), 930–938.

Marriott, C.S., Henderson, G.M., Belshaw, N.S., and Tudhope, A.W., 2004. Temperature dependence of δ7Li, δ44Ca and Li/Ca during growth of calcium carbonate, *Earth and Planetary Science Letters*, 222 (2), 615–624.

Matteodo, M., Grand, S., Sebag, D., Rowley, M.C., Vittoz, P., and Verrecchia, E.P., 2018. Decoupling of topsoil and subsoil controls on organic matter dynamics in the Swiss Alps, *Geoderma*, 330, 41–51.

Mattigod, S.V. and Sposito, G., 1977. Estimated Association Constants for Some Complexes of Trace Metals With Inorganic Ligands, *Soil Science Society of America Journal*, 41 (6).

Mavromatis, V., Gautier, Q., Bosc, O., and Schott, J., 2013. Kinetics of Mg partition and Mg stable isotope fractionation during its incorporation in calcite, *Geochimica et Cosmochimica Acta*, 114 (Supplement C), 188–203.

Mavromatis, V., González, A.G., Dietzel, M., and Schott, J., 2019. Zinc isotope fractionation during the inorganic precipitation of calcite - Towards a new pH proxy, *Geochimica et Cosmochimica Acta*, 244, 99–112.

Mavromatis, V., van Zuilen, K., Blanchard, M., van Zuilen, M., Dietzel, M., and Schott, J., 2020. Experimental and theoretical modelling of kinetic and equilibrium Ba isotope fractionation during calcite and aragonite precipitation, *Geochimica et Cosmochimica Acta*, 269, 566–580.

McBeath, M.K., Rock, P.A., Casey, W.H., and Mandell, G.K., 1998. Gibbs energies of formation of metal-carbonate solid solutions: part 3. The CaxMn1-xCO3 system at 298 K and 1 bar, *Geochimica et Cosmochimica Acta*, 62 (16), 2799–2808.

McHugh, T.A., Morrissey, E.M., Reed, S.C., Hungate, B.A., and Schwartz, E., 2015. Water from air: an overlooked source of moisture in arid and semiarid regions, *Scientific Reports*, 5 (1), 13767.

McQueen, N., Kelemen, P., Dipple, G., Renforth, P., and Wilcox, J., 2020. Ambient weathering of magnesium oxide for CO2 removal from air, *Nature Communications*, 11 (1), 3299.

Mejía, L.M., Paytan, A., Eisenhauer, A., Böhm, F., Kolevica, A., Bolton, C., Méndez-Vicente, A., Abrevaya, L., Isensee, K., and Stoll, H., 2018. Controls over δ44/40Ca and Sr/Ca variations in coccoliths: New perspectives from laboratory cultures and cellular models, *Earth and Planetary Science Letters*, 481, 48–60.

Meyer, H.J., 1984. The influence of impurities on the growth rate of calcite, *Journal of Crystal Growth*, 66 (3), 639–646.

Middelburg, J.J., De Lange, G.J., and van Der Weijden, C.H., 1987. Manganese solubility control in marine pore waters, *Geochimica et Cosmochimica Acta*, 51 (3), 759–763.

Mills, J.V., DePaolo, D.J., and Lammers, L.N., 2021. The influence of Ca:CO3 stoichiometry on Ca isotope fractionation: Implications for process-based models of calcite growth, *Geochimica et Cosmochimica Acta*, 298, 87–111.

Mills, J.V., Lammers, L.N., and Amundson, R., 2020. Carbon Balance with Renewable Energy: Effects of Solar Installations on Desert Soil Carbon Cycle, Tech. rep., California Energy Commission.

Mittemeijer, E.J. and Welzel, U., 2008. The "state of the art" of the diffraction analysis of crystallite size and lattice strain, *Zeitschrift für Kristallographie*, 223 (9), 552–560.

Moldrup, P., Olesen, T., Yamaguchi, T., Schjønning, P., and Rolston, D.E., 1999. Modeling diffusion and reaction in soils: IX. The Buckingham-Burdine-Campbell equation for gas diffusivity in undisturbed soil, *Soil Science*, 164 (8).

Monger, H.C. and Gallegos, R.A., 2000. Biotic and abiotic processes and rates of pedogenic carbonate accumulation in the southwestern United States - relationship to atmospheric CO 2 sequestration., *in:* R. Lal, J.M. Kimbel, H. Eswaran, and B.A. Stewart, eds., *Global climate change and pedogenic carbonates*, Boca Raton, FL: CRC, 273–289.

Morgan, J., 1967. Chemical equilibria and kinetic properties of manganese in natural water, *Principles and applications of water chemistry*, 561–623.

Morgan, J.J., 2005. Kinetics of reaction between O2 and Mn(II) species in aqueous solutions, *Geochimica et Cosmochimica Acta*, 69 (1), 35–48.

Morse, J.W., Andersson, A.J., and Mackenzie, F.T., 2006. Initial responses of carbonate-rich shelf sediments to rising atmospheric pCO2 and "ocean acidification": Role of high Mg-calcites, *Geochimica et Cosmochimica Acta*, 70 (23), 5814–5830.

Morse, J.W., Arvidson, R.S., and Lüttge, A., 2007. Calcium Carbonate Formation and Dissolution, *Chemical Reviews*, 107 (2), 342–381.

Moyano, F.E., Manzoni, S., and Chenu, C., 2013. Responses of soil heterotrophic respiration to moisture availability: An exploration of processes and models, *Soil Biology and Biochemistry*, 59, 72–85.

Moynier, F. and Fujii, T., 2017. Calcium isotope fractionation between aqueous compounds relevant to low-temperature geochemistry, biology and medicine, *Scientific Reports*, 7 (1), 44255.

Mucci, A., 1987. Influence of temperature on the composition of magnesian calcite overgrowths precipitated from seawater, *Geochimica et Cosmochimica Acta*, 51 (7), 1977–1984.

Mucci, A., 1988. Manganese uptake during calcite precipitation from seawater: Conditions leading to the formation of a pseudokutnahorite, *Geochimica et Cosmochimica Acta*, 52 (7), 1859–1868.

Mucci, A. and Morse, J.W., 1983. The incorporation of Mg2+ and Sr2+ into calcite overgrowths: influences of growth rate and solution composition, *Geochimica et Cosmochimica Acta*, 47 (2), 217–233.

Myers, R.J.K., Weier, K.L., and Campbell, C.A., 1982. Quantitative relationship between net nitrogen mineralization and moisture content of soils, *Canadian Journal of Soil Science*, 62 (1), 111–124.

NASEM, 2019. *Negative Emissions Technologies and Reliable Sequestration: A Research Agenda*, Washington, DC: The National Academies Press.

Navrotsky, A. and Capobianco, C., 1987. Enthalpies of formation of dolomite and of magnesian calcites, *American Mineralogist*, 72 (7-8), 782–787.

Nehrke, G., Reichart, G.J., Cappellen, P.V., Meile, C., and Bijma, J., 2007. Dependence of calcite growth rate and Sr partitioning on solution stoichiometry: Non-Kossel crystal growth, *Geochimica et Cosmochimica Acta*, 71 (9), 2240–2249.

Niedermayr, A., Dietzel, M., Kisakurek, B., Bohm, F., Kohler, S.J., Leis, A., and Eisenhauer, A., 2010. Calcium Isotopic Fractionation during Precipitation of Calcium Carbonate Polymorphs and ACC at Low Temperatures, *in: EGU General Assembly Conference Abstracts*, 12448.

Nielsen, A.E., 1984. Electrolyte crystal growth mechanisms, *Journal of Crystal Growth*, 67 (2), 289–310.

Nielsen, L.C., De Yoreo, J.J., and DePaolo, D.J., 2013. General model for calcite growth kinetics in the presence of impurity ions, *Geochimica et Cosmochimica Acta*, 115 (Supplement C), 100–114.

Nielsen, L.C. and DePaolo, D.J., 2013. Ca isotope fractionation in a high-alkalinity lake system: Mono Lake, California, *Geochimica et Cosmochimica Acta*, 118, 276–294.

Nielsen, L.C., DePaolo, D.J., and De Yoreo, J.J., 2012. Self-consistent ion-by-ion growth model for kinetic isotopic fractionation during calcite precipitation, *Geochimica et Cosmochimica Acta*, 86 (Supplement C), 166–181.

Nielsen, M.R., Sand, K.K., Rodriguez-Blanco, J.D., Bovet, N., Generosi, J., Dalby, K.N., and Stipp, S.L.S., 2016. Inhibition of Calcite Growth: Combined Effects of Mg2+ and SO42-, *Crystal Growth & Design*, 16 (11), 6199–6207.

Noy-Meir, I., 1973. Desert Ecosystems: Environment and Producers, *Annual Review of Ecology and Systematics*, 4 (1), 25–51.

Palta, J.A. and Nobel, P.S., 1989. Root Respiration for Agave deserti: Influence of Temperature, Water Status and Root Age on Daily Patterns, *Journal of Experimental Botany*, 40 (2), 181–186.

Paquette, J. and Reeder, R.J., 1990. New type of compositional zoning in calcite: Insights into crystal-growth mechanisms, *Geology*, 18 (12), 1244–1247.

Paquette, J. and Reeder, R.J., 1995. Relationship between surface structure, growth mechanism, and trace element incorporation in calcite, *Geochimica et Cosmochimica Acta*, 59 (4), 735–749.

Parkhurst, D.L. and Apello, C.A.J., 2013. Description of input and examples for PHREEQC version 3 - A computer program for speciation, batch-reaction, one-dimensional transport, and inverse geochemical calculations, *in: U.S. Geological Survey Techniques and Methods, book 6, chap. A43*, 497.

Parsons, A.N., Barrett, J.E., Wall, D.H., and Virginia, R.A., 2004. Soil Carbon Dioxide Flux in Antarctic Dry Valley Ecosystems, *Ecosystems*, 7 (3), 286–295.

Paustian, K., Andrén, O., Janzen, H.H., Lal, R., Smith, P., Tian, G., Tiessen, H., Van Noordwijk, M., and Woomer, P.L., 1997. Agricultural soils as a sink to mitigate CO2 emissions, *Soil Use and Management*, 13 (s4), 230–244.

Paustian, K., Lehmann, J., Ogle, S., Reay, D., Robertson, G.P., and Smith, P., 2016. Climate-smart soils, *Nature*, 532 (7597), 49–57.

Pedregosa, F., Varoquaux, G., Gramfort, A., Michel, V., Thirion, B., Grisel, O., Blondel, M., Prettenhofer, P., Weiss, R., Dubourg, V., Vanderplas, J., Passos, A., Cournapeau, D., Brucher, M., Perrot, M., and Duchesnay, E., 2011. Scikit-learn: Machine Learning in {P}ython, *Journal of Machine Learning Research*, 12, 2825–2830.

Perdikouri, C., Putnis, C.V., Kasioptas, A., and Putnis, A., 2009. An Atomic Force Microscopy Study of the Growth of a Calcite Surface as a Function of Calcium/Total Carbonate Concentration Ratio in Solution at Constant Supersaturation, *Crystal Growth & Design*, 9 (10), 4344–4350.

Pingitore, N.E., Eastman, M.P., Sandidge, M., Oden, K., and Freiha, B., 1988. The coprecipitation of manganese(II) with calcite: an experimental study, *Marine Chemistry*, 25 (2), 107–120.

Plaza, C., Pegoraro, E., Bracho, R., Celis, G., Crummer, K.G., Hutchings, J.A., Hicks Pries, C.E., Mauritz, M., Natali, S.M., Salmon, V.G., Schädel, C., Webb, E.E., and Schuur, E.A.G., 2019. Direct observation of permafrost degradation and rapid soil carbon loss in tundra, *Nature Geoscience*, 12 (8), 627–631.

Plummer, L. and Busenberg, E., 1982. The solubilities of calcite, aragonite and vaterite in CO2-H2O solutions between 0 and 90Â°C, and an evaluation of the aqueous model for the system CaCO3-CO2-H2O, *Geochimica et Cosmochimica Acta*, 46 (6), 1011–1040.

Pockman, W.T. and Sperry, J.S., 2000. Vulnerability to xylem cavitation and the distribution of Sonoran Desert vegetation, *American Journal of Botany*, 87 (9), 1287–1299.

Pointing, S.B. and Belnap, J., 2012. Microbial colonization and controls in dryland systems, *Nature Reviews Microbiology*, 10 (8), 551–562.

Pokrovsky, O.S., Golubev, S.V., Schott, J., and Castillo, A., 2009. Calcite, dolomite and magnesite dissolution kinetics in aqueous solutions at acid to circumneutral pH, 25 to 150Â°C and 1 to 55 atm pCO2: New constraints on CO2 sequestration in sedimentary basins, *Chemical Geology*, 265 (1), 20–32.

Pokrovsky, O.S., Mielczarski, J.A., Barres, O., and Schott, J., 2000. Surface Speciation Models of Calcite and Dolomite/Aqueous Solution Interfaces and Their Spectroscopic Evaluation, *Langmuir*, 16 (6), 2677–2688.

Poulter, B., Frank, D., Ciais, P., Myneni, R.B., Andela, N., Bi, J., Broquet, G., Canadell, J.G., Chevallier, F., Liu, Y.Y., Running, S.W., Sitch, S., and van der Werf, G.R., 2014. Contribution of semi-arid ecosystems to interannual variability of the global carbon cycle, *Nature*, 509 (7502), 600–603.

Prieto, M., 2009. Thermodynamics of Solid Solution-Aqueous Solution Systems, *Reviews in Mineralogy and Geochemistry*, 70 (1), 47–85.

Prieto, M., Astilleros, J.M., and Fernández-Díaz, L., 2013. Environmental Remediation by Crystallization of Solid Solutions, *Elements*, 9 (3), 195–201.

Rajeev, L., da Rocha, U.N., Klitgord, N., Luning, E.G., Fortney, J., Axen, S.D., Shih, P.M., Bouskill, N.J., Bowen, B.P., Kerfeld, C.A., Garcia-Pichel, F., Brodie, E.L., Northen, T.R., and Mukhopadhyay, A., 2013. Dynamic cyanobacterial response to hydration and dehydration in a desert biological soil crust, *The ISME Journal*, 7 (11), 2178–2191.

Ravikovitch, P.I., Bogan, B.W., and Neimark, A.V., 2005. Nitrogen and Carbon Dioxide Adsorption by Soils, *Environmental Science & Technology*, 39 (13), 4990–4995.

Ravizza, G.E. and Zachos, J.C., 2003. Records of Cenozoic ocean chemistry, *Treatise on geochemistry*, 6, 551–581.

Ray, A.E., Zhang, E., Terauds, A., Ji, M., Kong, W., and Ferrari, B.C., 2020. Soil Microbiomes With the Genetic Capacity for Atmospheric Chemosynthesis Are Widespread Across the Poles and Are Associated With Moisture, Carbon, and Nitrogen Limitation, *Frontiers in Microbiology*, 11, 1936.

Reardon, E.J. and Langmuir, D., 1974. Thermodynamic properties of the ion pairs MgCO30 and CaCO30 from 10 to 50 degrees C, *American Journal of Science*, 274 (6), 599–612.

Reddy, M.M. and Wang, K., 1980. Crystallization of calcium carbonate in the presence of metal ions: I. Inhibition by magnesium ion at pH 8.8 and 25Â°C, *Journal of Crystal Growth*, 50 (2), 470–480.

Reed, S.C., Coe, K.K., Sparks, J.P., Housman, D.C., Zelikova, T.J., and Belnap, J., 2012. Changes to dryland rainfall result in rapid moss mortality and altered soil fertility, *Nature Climate Change*, 2 (10), 752–755.

Reeder, R.J., 1996. Interaction of divalent cobalt, zinc, cadmium, and barium with the calcite surface during layer growth, *Geochimica et Cosmochimica Acta*, 60 (9), 1543–1552.

Reeder, R.J. and Grams, J.C., 1987. Sector zoning in calcite cement crystals: Implications for trace element distributions in carbonates, *Geochimica et Cosmochimica Acta*, 51 (2), 187–194.

Reheis, M.C., 2003. Dust deposition in Nevada, California, and Utah, 1984-2002, Tech. rep.

Reheis, M.C., 2006. A 16-year record of eolian dust in Southern Nevada and California, USA: Controls on dust generation and accumulation, *Journal of Arid Environments*, 67 (3), 487–520.

Reichstein, M., Falge, E., Baldocchi, D., Papale, D., Aubinet, M., Berbigier, P., Bernhofer, C., Buchmann, N., Gilmanov, T., Granier, A., Grünwald, T., Havránková, K., Ilvesniemi, H., Janous, D., Knohl, A., Laurila, T., Lohila, A., Loustau, D., Matteucci, G., Meyers, T., Miglietta, F., Ourcival, J.M., Pumpanen, J., Rambal, S., Rotenberg, E., Sanz, M., Tenhunen, J., Seufert, G., Vaccari, F., Vesala, T., Yakir, D., and Valentini, R., 2005. On the separation of net ecosystem exchange into assimilation and ecosystem respiration: review and improved algorithm, *Global Change Biology*, 11 (9), 1424–1439.

Reischl, B., Raiteri, P., Gale, J.D., and Rohl, A.L., 2019. Atomistic Simulation of Atomic Force Microscopy Imaging of Hydration Layers on Calcite, Dolomite, and Magnesite Surfaces, *The Journal of Physical Chemistry C*, 123 (24), 14985–14992.

Renforth, P. and Henderson, G., 2017. Assessing ocean alkalinity for carbon sequestration, *Reviews of Geophysics*, 55 (3), 636–674.

Renforth, P., Manning, D.A.C., and Lopez-Capel, E., 2009. Carbonate precipitation in artificial soils as a sink for atmospheric carbon dioxide, *Applied Geochemistry*, 24 (9), 1757–1764.

Rey, A., 2015. Mind the gap: non-biological processes contributing to soil CO2 efflux, *Global Change Biology*, 21 (5), 1752–1761.

Rey, A., Belelli-Marchesini, L., Were, A., Serrano-ortiz, P., Etiope, G., Papale, D., Domingo, F., and Pegoraro, E., 2012. Wind as a main driver of the net ecosystem carbon balance of a semiarid Mediterranean steppe in the South East of Spain, *Global Change Biology*, 18 (2), 539–554.

Reynard, L.M., Day, C.C., and Henderson, G.M., 2011. Large fractionation of calcium isotopes during cave-analogue calcium carbonate growth, *Geochimica et Cosmochimica Acta*, 75 (13), 3726–3740.

Richter, F.M., Mendybaev, R.A., Christensen, J.N., Hutcheon, I.D., Williams, R.W., Sturchio, N.C., and Beloso, A.D., 2006. Kinetic isotopic fractionation during diffusion of ionic species in water, *Geochimica et Cosmochimica Acta*, 70 (2), 277–289.

Robie, R.A., Haselton Jr., H.T., and Hemingway, B.S., 1984. Heat capacities and entropies of rhodochrosite (MnCO3) and siderite (FeCO3) between 5 and 600 K., *American Mineralogist*, 69 (3-4), 349–357.

Robinson, N.P., Allred, B.W., Smith, W.K., Jones, M.O., Moreno, A., Erickson, T.A., Naugle, D.E., and Running, S.W., 2018. Terrestrial primary production for the conterminous United States derived from Landsat 30 m and MODIS 250 m, *Remote Sensing in Ecology and Conservation*, 4 (3), 264–280.

Rocha, C.L.D.L. and DePaolo, D.J., 2000. Isotopic Evidence for Variations in the Marine Calcium Cycle Over the Cenozoic, *Science*, 289 (5482), 1176 LP —- 1178.

Rodriguez-Navarro, C., Kudlacz, K., Cizer, O., and Ruiz-Agudo, E., 2015. Formation of amorphous calcium carbonate and its transformation into mesostructured calcite, *CrystEngComm*, 17 (1), 58–72.

Roland, M., Serrano-Ortiz, P., Kowalski, A.S., Goddéris, Y., Sánchez-Cañete, E.P., Ciais, P., Domingo, F., Cuezva, S., Sanchez-Moral, S., Longdoz, B., Yakir, D., Van Grieken, R., Schott, J., Cardell, C., and Janssens, I.A., 2013. Atmospheric turbulence triggers pronounced diel pattern in karst carbonate geochemistry, *Biogeosciences*, 10 (7), 5009–5017.

Ruiz-Agudo, E., Kowacz, M., Putnis, C.V., and Putnis, A., 2010. The role of background electrolytes on the kinetics and mechanism of calcite dissolution, *Geochimica et Cosmochimica Acta*, 74 (4), 1256–1267.

Ruiz-Agudo, E., Putnis, C.V., Rodriguez-Navarro, C., and Putnis, A., 2011a. Effect of pH on calcite growth at constant aCa2+/aCO32- ratio and supersaturation, *Geochimica et Cosmochimica Acta*, 75 (1), 284–296.

Ruiz-Agudo, E., Putnis, C.V., Wang, L., and Putnis, A., 2011b. Specific effects of background electrolytes on the kinetics of step propagation during calcite growth, *Geochimica et Cosmochimica Acta*, 75 (13), 3803–3814.

Safavian, S.R. and Landgrebe, D., 1991. A survey of decision tree classifier methodology, *IEEE Transactions on Systems, Man, and Cybernetics*, 21 (3), 660–674.

Saito, T., Fujimaki, H., Yasuda, H., and Inoue, M., 2009. Empirical Temperature Calibration of Capacitance Probes to Measure Soil Water, *Soil Science Society of America Journal*, 73 (6), 1931–1937.

Sand, K.K., Tobler, D.J., Dobberschütz, S., Larsen, K.K., Makovicky, E., Andersson, M.P., Wolthers, M., and Stipp, S.L.S., 2016. Calcite Growth Kinetics: Dependence on Saturation Index, Ca2+:CO32- Activity Ratio, and Surface Atomic Structure, *Crystal Growth {\&} Design*, 16 (7), 3602–3612.

Sanderman, J., Amundson, R.G., and Baldocchi, D.D., 2003. Application of eddy covariance measurements to the temperature dependence of soil organic matter mean residence time, *Global Biogeochemical Cycles*, 17 (2).

Sanderman, J., Hengl, T., and Fiske, G.J., 2017. Soil carbon debt of 12,000 years of human land use, *Proceedings of the National Academy of Sciences*, 114 (36), 9575–9580.

Schaef, H.T., Loring, J.S., Glezakou, V.A., Miller, Q.R.S., Chen, J., Owen, A.T., Lee, M.S., Ilton, E.S., Felmy, A.R., McGrail, B.P., and Thompson, C.J., 2015. Competitive sorption of CO2 and H2O in 2:1 layer phyllosilicates, *Geochimica et Cosmochimica Acta*, 161, 248–257.

Schimel, D.S., 2010. Drylands in the Earth System, *Science*, 327 (5964), 418 LP – 419.

Schindlbacher, A., Zechmeister-Boltenstern, S., and Jandl, R., 2009. Carbon losses due to soil warming: Do autotrophic and heterotrophic soil respiration respond equally?, *Global Change Biology*, 15 (4), 901–913.

Schlesinger, W.H., 1982. Carbon storage in the caliche of arid soils: A cast study from Arizona, *Soil Science*, 133 (4).

Schlesinger, W.H., 1985. The formation of caliche in soils of the Mojave Desert, California, *Geochimica et Cosmochimica Acta*, 49 (1), 57–66.

Schlesinger, W.H., Belnap, J., and Marion, G., 2009. On carbon sequestration in desert ecosystems, *Global Change Biology*, 15 (6), 1488–1490.

Schlesinger, W.H., Raikes, J.A., Hartley, A.E., and Cross, A.F., 1996. On the Spatial Pattern of Soil Nutrients in Desert Ecosystems, *Ecology*, 77 (2), 364–374.

Schott, J., Mavromatis, V., Fujii, T., Pearce, C.R., and Oelkers, E.H., 2016. The control of carbonate mineral Mg isotope composition by aqueous speciation: Theoretical and experimental modeling, *Chemical Geology*, 445, 120–134.

Seager, R., Ting, M., Li, C., Naik, N., Cook, B., Nakamura, J., and Liu, H., 2013. Projections of declining surface-water availability for the southwestern United States, *Nature Climate Change*, 3 (5), 482–486.

Shackleton, N., 1967. Oxygen Isotope Analyses and Pleistocene Temperatures Re-assessed, *Nature*, 215 (5096), 15–17.

Shanhun, F.L., Almond, P.C., Clough, T.J., and Smith, C.M.S., 2012. Abiotic processes dominate CO2 fluxes in Antarctic soils, *Soil Biology and Biochemistry*, 53, 99–111.

Shannon, R.D., 1976. Revised effective ionic radii and systematic studies of interatomic distances in halides and chalcogenides, *Acta Crystallographica Section A*, 32 (5), 751–767.

Sierra, C.A., Trumbore, S.E., Davidson, E.A., Vicca, S., and Janssens, I., 2015. Sensitivity of decomposition rates of soil organic matter with respect to simultaneous changes in temperature and moisture, *Journal of Advances in Modeling Earth Systems*, 7 (1), 335–356.

Sime, N.G., Rocha, C.L.D.L., Tipper, E.T., Tripati, A., Galy, A., and Bickle, M.J., 2007. Interpreting the Ca isotope record of marine biogenic carbonates, *Geochimica et Cosmochimica Acta*, 71 (16), 3979–3989.

Simunek, J. and Suarez, D.L., 1993. Modeling of carbon dioxide transport and production in soil: 1. Model development, *Water Resources Research*, 29 (2), 487–497.

Sø, H.U., Postma, D., Jakobsen, R., and Larsen, F., 2012. Competitive adsorption of arsenate and phosphate onto calcite; experimental results and modeling with CCM and CD-MUSIC, *Geochimica et Cosmochimica Acta*, 93, 1–13.

Söhnel, O. and Mullin, J.W., 1978. A method for the determination of precipitation induction periods, *Journal of Crystal Growth*, 44 (4), 377–382.

Söhnel, O. and Mullin, J.W., 1982. Precipitation of calcium carbonate, *Journal of Crystal Growth*, 60 (2), 239–250.

Son, S., Newton, A.G., Jo, K.n., Lee, J.Y., and Kwon, K.D., 2019. Manganese speciation in Mn-rich CaCO3: A density functional theory study, *Geochimica et Cosmochimica Acta*, 248, 231–241.

Song, J., Zeng, Y., Wang, L., Duan, X., Puerto, M., Chapman, W.G., Biswal, S.L., and Hirasaki, G.J., 2017. Surface complexation modeling of calcite zeta potential measurements in brines with mixed potential determining ions (Ca2+, CO32-, Mg2+, SO42-) for characterizing carbonate wettability, *Journal of Colloid and Interface Science*, 506, 169–179.

Soper, F.M., McCalley, C.K., Sparks, K., and Sparks, J.P., 2017. Soil carbon dioxide emissions from the Mojave desert: Isotopic evidence for a carbonate source, *Geophysical Research Letters*, 44 (1), 245–251.

Soulard, C.E. and Sleeter, B.M., 2012. Late twentieth century land-cover change in the basin and range ecoregions of the United States, *Regional Environmental Change*, 12 (4), 813–823.

Soussana, J.F., Lutfalla, S., Ehrhardt, F., Rosenstock, T., Lamanna, C., Havlík, P., Richards, M., Wollenberg, E.L., Chotte, J.L., Torquebiau, E., Ciais, P., Smith, P., and Lal, R., 2019. Matching policy and science: Rationale for the '4 per 1000 - soils for food security and climate' initiative, *Soil and Tillage Research*, 188, 3–15.

Spohn, M., Müller, K., Höschen, C., Mueller, C.W., and Marhan, S., 2020. Dark microbial CO2 fixation in temperate forest soils increases with CO2 concentration, *Global Change Biology*, 26 (3), 1926–1935.

Stack, A.G. and Grantham, M.C., 2010. Growth Rate of Calcite Steps As a Function of Aqueous Calcium-to-Carbonate Ratio: Independent Attachment and Detachment of Calcium and Carbonate Ions, *Crystal Growth & Design*, 10 (3), 1409–1413.

Staudt, W.J., Reeder, R.J., and Schoonen, M.A.A., 1994. Surface structural controls on compositional zoning of SO2-4 and SeO2-4 in synthetic calcite single crystals, *Geochimica et Cosmochimica Acta*, 58 (9), 2087–2098.

Stephenson, A.E., DeYoreo, J.J., Wu, L., Wu, K.J., Hoyer, J., and Dove, P.M., 2008. Peptides Enhance Magnesium Signature in Calcite: Insights into Origins of Vital Effects, *Science*, 322 (5902), 724 LP – 727.

Stephenson, A.E., Hunter, J.L., Han, N., DeYoreo, J.J., and Dove, P.M., 2011. Effect of ionic strength on the Mg content of calcite: Toward a physical basis for minor element uptake during step growth, *Geochimica et Cosmochimica Acta*, 75 (15), 4340–4350.

Sternbeck, J., 1997. Kinetics of rhodochrosite crystal growth at 25Â°C: The role of surface speciation, *Geochimica et Cosmochimica Acta*, 61 (4), 785–793.

Steuber, T. and Buhl, D., 2006. Calcium-isotope fractionation in selected modern and ancient marine carbonates, *Geochimica et Cosmochimica Acta*, 70 (22), 5507–5521.

Suarez, D.L., 1977. Ion Activity Products of Calcium Carbonate in Waters Below the Root Zone1, *Soil Science Society of America Journal*, 41, 310–315.

Suarez, D.L. and Rhoades, J.D., 1982. The Apparent Solubility of Calcium Carbonate in Soils, *Soil Science Society of America Journal*, 46, 716–722.

Tang, J., Dietzel, M., Bohm, F., Kohler, S.J., and Eisenhauer, A., 2008. Sr2+/Ca2+ and 44Ca/40Ca fractionation during inorganic calcite formation: II. Ca isotopes, *Geochimica et Cosmochimica Acta*, 72 (15), 3733–3745.

Tang, J., Misson, L., Gershenson, A., Cheng, W., and Goldstein, A.H., 2005. Continuous measurements of soil respiration with and without roots in a ponderosa pine plantation in the Sierra Nevada Mountains, *Agricultural and Forest Meteorology*, 132 (3), 212–227.

Tang, J., Niedermayr, A., Kohler, S.J., Bohm, F., Kisakurek, B., Eisenhauer, A., and Dietzel, M., 2012. Sr2+/Ca2+ and 44Ca/40Ca fractionation during inorganic calcite formation: III. Impact of salinity/ionic strength, *Geochimica et Cosmochimica Acta*, 77 (Supplement C), 432–443.

Temmam, M., Paquette, J., and Vali, H., 2000. Mn and Zn incorporation into calcite as a function of chloride aqueous concentration, *Geochimica et Cosmochimica Acta*, 64 (14), 2417–2430.

Teng, H., Dove, P.M., and De Yoreo, J.J., 2000. Kinetics of calcite growth: surface processes and relationships to macroscopic rate laws, *Geochimica et Cosmochimica Acta*, 64 (13), 2255–2266.

Teng, H.H., Dove, P.M., Orme, C.A., and De Yoreo, J.J., 1998. Thermodynamics of Calcite Growth: Baseline for Understanding Biomineral Formation, *Science*, 282 (5389), 724 LP – 727.

Thomey, M.L., Ford, P.L., Reeves, M.C., Finch, D.M., Litvak, M.E., and Collins, S.L., 2014. Climate Change Impacts on Future Carbon Stores and Management of Warm Deserts of the United States, *Rangelands*, 36 (1), 16–24.

Tipper, E.T., Galy, A., and Bickle, M.J., 2006. Riverine evidence for a fractionated reservoir of Ca and Mg on the continents: Implications for the oceanic Ca cycle, *Earth and Planetary Science Letters*, 247 (3), 267–279.

Titus, J.H., Nowak, R.S., and Smith, S.D., 2002. Soil resource heterogeneity in the Mojave Desert, *Journal of Arid Environments*, 52 (3), 269–292.

Tucker, C.L. and Reed, S.C., 2016. Low soil moisture during hot periods drives apparent negative temperature sensitivity of soil respiration in a dryland ecosystem: a multi-model comparison, *Biogeochemistry*, 128 (1), 155–169.

Turner, D.R., Whitfield, M., and Dickson, A.G., 1981. The equilibrium speciation of dissolved components in freshwater and sea water at 25Â°C and 1 atm pressure, *Geochimica et Cosmochimica Acta*, 45 (6), 855–881.

Unger, S., Máguas, C., Pereira, J.S., David, T.S., and Werner, C., 2010. The influence of precipitation pulses on soil respiration - Assessing the "Birch effect" by stable carbon isotopes, *Soil Biology and Biochemistry*, 42 (10), 1800–1810.

Van Cappellen, P., Charlet, L., Stumm, W., and Wersin, P., 1993. A surface complexation model of the carbonate mineral-aqueous solution interface, *Geochimica et Cosmochimica Acta*, 57 (15), 3505–3518.

van der Eerden, J.P., 1993. Crystal Growth Mechanisms, *in: Handbook of Crystal Growth*, Amsterdam: Elsevier, 307–475.

Vargas, R. and Allen, M.F., 2008. Dynamics of Fine Root, Fungal Rhizomorphs, and Soil Respiration in a Mixed Temperate Forest: Integrating Sensors and Observations, *Vadose Zone Journal*, 7, 1055–1064.

Vargas, R., Baldocchi, D.D., Allen, M.F., Bahn, M., Black, T.A., Collins, S.L., Yuste, J.C., Hirano, T., Jassal, R.S., Pumpanen, J., and Tang, J., 2010a. Looking deeper into the soil: biophysical controls and seasonal lags of soil CO2 production and efflux, *Ecological Applications*, 20 (6), 1569–1582.

Vargas, R., Detto, M., Baldocchi, D.D., and Allen, M.F., 2010b. Multiscale analysis of temporal variability of soil CO2 production as influenced by weather and vegetation, *Global Change Biology*, 16 (5), 1589–1605.

Vicca, S., Gilgen, A.K., Camino Serrano, M., Dreesen, F.E., Dukes, J.S., Estiarte, M., Gray, S.B., Guidolotti, G., Hoeppner, S.S., Leakey, A.D.B., Ogaya, R., Ort, D.R., Ostrogovic, M.Z., Rambal, S., Sardans, J., Schmitt, M., Siebers, M., van der Linden, L., van Straaten, O., and Granier, A., 2012. Urgent need for a common metric to make precipitation manipulation experiments comparable, *New Phytologist*, 195 (3), 518–522.

Virtanen, P., Gommers, R., Oliphant, T.E., Haberland, M., Reddy, T., Cournapeau, D., Burovski, E., Peterson, P., Weckesser, W., Bright, J., van der Walt, S.J., Brett, M., Wilson, J., Millman, K.J., Mayorov, N., Nelson, A.R.J., Jones, E., Kern, R., Larson, E., Carey, C.J., Polat, b., Feng, Y., Moore, E.W., VanderPlas, J., Laxalde, D., Perktold, J., Cimrman, R., Henriksen, I., Quintero, E.A., Harris, C.R., Archibald, A.M., Ribeiro, A.H., Pedregosa, F., van Mulbregt, P., and SciPy 1.0 Contributors, 2020. {SciPy} 1.0: Fundamental Algorithms for Scientific Computing in Python, *Nature Methods*, 17, 261–272.

von Allmen, K., Böttcher, M.E., Samankassou, E., and Nägler, T.F., 2010. Barium isotope fractionation in the global barium cycle: First evidence from barium minerals and precipitation experiments, *Chemical Geology*, 277 (1), 70–77.

Wang, B., Zha, T.S., Jia, X., Gong, J.N., Wu, B., Bourque, C.P.A., Zhang, Y., Qin, S.G., Chen, G.P., and Peltola, H., 2015. Microtopographic variation in soil respiration and its controlling factors vary with plant phenophases in a desert-shrub ecosystem, *Biogeosciences*, 12 (19), 5705–5714.

Wang, Q., Grau-Crespo, R., and de Leeuw, N.H., 2011. Mixing Thermodynamics of the Calcite-Structured (Mn,Ca)CO3 Solid Solution: A Computer Simulation Study, *The Journal of Physical Chemistry B*, 115 (47), 13854–13861.

Wang, T., Hamann, A., Spittlehouse, D., and Carroll, C., 2016. Locally downscaled and spatially customizable climate data for historical and future periods for North America, *PloS one*, 11 (6), e0156720.

Wang, Z.Y., Xie, J.B., Wang, Y.G., and Li, Y., 2020. Biotic and Abiotic Contribution to Diurnal Soil CO2 Fluxes from Saline/Alkaline Soils, *Scientific Reports*, 10 (1), 5396.

Wasylenki, L.E., Dove, P.M., Wilson, D.S., and De Yoreo, J.J., 2005a. Nanoscale effects of strontium on calcite growth: An in situ AFM study in the absence of vital effects, *Geochimica et Cosmochimica Acta*, 69 (12), 3017–3027.

Wasylenki, L.E., Dove, P.M., and Yoreo, J.J.D., 2005b. Effects of temperature and transport conditions on calcite growth in the presence of Mg2+: Implications for paleothermometry, *Geochimica et Cosmochimica Acta*, 69 (17), 4227–4236.

Watkins, J.M., Nielsen, L.C., Ryerson, F.J., and DePaolo, D.J., 2013. The influence of kinetics on the oxygen isotope composition of calcium carbonate, *Earth and Planetary Science Letters*, 375 (Supplement C), 349–360.

Wezel, A., Rajot, J.L., and Herbrig, C., 2000. Influence of shrubs on soil characteristics and their function in Sahelian agro-ecosystems in semi-arid Niger, *Journal of Arid Environments*, 44 (4), 383–398.

Whitford, W.G., Anderson, J., and Rice, P.M., 1997. Stemflow contribution to the 'fertile island' effect in creosotebush, Larrea tridentata, *Journal of Arid Environments*, 35 (3), 451–457.

Wilhelm, E., Battino, R., and Wilcock, R.J., 1977. Low-pressure solubility of gases in liquid water, *Chemical Reviews*, 77 (2), 219–262.

Wohlfahrt, G., Fernstermaker, L.F., and Arnone III, J.A., 2008. Large annual net ecosystem CO2 uptake of a Mojave Desert ecosystem, *Global Change Biology*, 14 (7), 1475–1487.

Wolfram, O. and Krupp, R.E., 1996. Hydrothermal solubility of rhodochrosite, Mn (II) speciation, and equilibrium constants, *Geochimica et Cosmochimica Acta*, 60 (21), 3983–3994.

Wolthers, M., Charlet, L., and Cappellen, P.V., 2008. The surface chemistry of divalent metal carbonate minerals; a critical assessment of surface charge and potential data using the charge distribution multi-site ion complexation model, *American Journal of Science*, 308 (8), 905–941.

Wolthers, M., Nehrke, G., Gustafsson, J.P., and Van Cappellen, P., 2012. Calcite growth kinetics: Modeling the effect of solution stoichiometry, *Geochimica et Cosmochimica Acta*, 77 (Supplement C), 121–134.

Wolthers, M., Tommaso, D.D., Du, Z., and de Leeuw, N.H., 2013. Variations in calcite growth kinetics with surface topography: molecular dynamics simulations and process-based growth kinetics modelling, *CrystEngComm*, 15 (27), 5506–5514.

Wright, R.A. and Honea, J.H., 1986. Aspects of desertification in southern New Mexico, U.S.A.: soil properties of a mesquite duneland and a former grassland, *Journal of Arid Environments*, 11 (2), 139–145.

Xie, J., Li, Y., Zhai, C., Li, C., and Lan, Z., 2009. CO2 absorption by alkaline soils and its implication to the global carbon cycle, *Environmental Geology*, 56 (5), 953–961.

Yan, D., Li, J., Pei, J., Cui, J., Nie, M., and Fang, C., 2017. The temperature sensitivity of soil organic carbon decomposition is greater in subsoil than in topsoil during laboratory incubation, *Scientific Reports*, 7 (1), 5181.

Yates, E.L., Detweiler, A.M., Iraci, L.T., Bebout, B.M., McKay, C.P., Schiro, K., Sheffner, E.J., Kelley, C.A., Tadić, J.M., and Loewenstein, M., 2013. Assessing the role of alkaline soils on the carbon cycle at a playa site, *Environmental Earth Sciences*, 70 (3), 1047–1056.

Yoder, C.K. and Nowak, R.S., 1999. Hydraulic lift among native plant species in the Mojave Desert, *Plant and Soil*, 215 (1), 93–102.

Zhang, J. and Nancollas, G.H., 1990. Kink densities along a crystal surface step at low temperatures and under nonequilibrium conditions, *Journal of Crystal Growth*, 106 (2), 181–190.

Zhang, J. and Nancollas, G.H., 1998. Kink Density and Rate of Step Movement during Growth and Dissolution of anABCrystal in a Nonstoichiometric Solution, *Journal of Colloid and Interface Science*, 200 (1), 131–145.

Zhang, X., Niu, G.Y., Elshall, A.S., Ye, M., Barron-Gafford, G.A., and Pavao-Zuckerman, M., 2014. Assessing five evolving microbial enzyme models against field measurements from a semiarid savannah - What are the mechanisms of soil respiration pulses?, *Geophysical Research Letters*, 41 (18), 6428–6434.

Zhang, Y. and Dawe, R.A., 2000. Influence of Mg2+ on the kinetics of calcite precipitation and calcite crystal morphology, *Chemical Geology*, 163 (1), 129–138.

Zhu, G., Yao, S., Zhai, H., Liu, Z., Li, Y., Pan, H., and Tang, R., 2016. Evolution from Classical to Non-classical Aggregation-Based Crystal Growth of Calcite by Organic Additive Control, *Langmuir*, 32 (35), 8999–9004.

Appendix A: Supplementary information for Chapter 2, The influence of Ca^{2+}:$CO_3{}^{2-}$ stoichiometry on Ca isotope fractionation

Nielsen Formulation	Wolthers Formulation
Attachment/Detachment Frequency Relationships	
k_A - fitted k_B - fitted $\nu_A = \sqrt{K_{sp} k_A k_B}$ $\nu_B = \nu_A$	k_{A1} - fitted $k_{A2} = k_{A1}$ $k_{B1} = 2k_{A1}\left(\frac{1+10^{8.6}10^{-pH}}{1+10^{10.33}10^{-pH}}\right)$ $k_{B2} = k_{B1}$ v_{A1} - fitted $\nu_{A2} = \nu_{A1}$ $\nu_{B1} = \frac{K_{sp}\bar{k}_A \bar{k}_B}{\bar{\nu}_A (1+10^{8.6}10^{-pH})}$ $\nu_{B2} = \nu_{B1}$ Effective attachment/detachment coefficients: $\bar{k}_A = k_{A1} + 10^{8.6}10^{-pH} k_{A2}$ $\bar{k}_B = k_{B1} + 10^{10.33}10^{-pH} k_{B2}$ $\bar{\nu}_A = \nu_{A1} + \nu_{A2}$ $\bar{\nu}_B = \nu_{B1} + 10^{8.6}10^{-pH} \nu_{B2}$
Kink Site Probability	
$P_A = \frac{k_A\{A\}+\nu_B}{k_A\{A\}+k_B\{B\}+\nu_A+\nu_B}$ $P_B = 1 - P_A$	$P_{B1} = \frac{\chi(\bar{k}_B\{B_1\}+\bar{\nu}_A)}{\bar{k}_A\{A\}+\bar{\nu}_B+\theta(\bar{k}_B\{B_1\}+\bar{\nu}_A)}$ $\theta = (1 + 10^{8.6}10^{-pH})$ $P_{B2} = 10^{8.6}10^{-pH} P_{B1}$ $P_A = \chi - \theta P_{B1}$
Kink Propagation Rate (s^{-1})	
$u_A = k_A\{A\}P_B - v_A P_A$ $u_B = k_B\{B\}P_A - v_B P_B$	$u_A = \bar{k}_A\{A\}P_B - \bar{v}_A P_A$ $u_B = \bar{k}_B\{B\}P_A - \bar{v}_B P_B$
$u = u_A + u_B$	
Kink Formation Rate (s^{-1}) (Zhang and Nancollas, 1998)	
$i_A = 2exp\left(\frac{-2\epsilon_A}{k_b T}\right)(\Omega - 1)\frac{\nu_B k_A [A]}{k_A[A]+\nu_B}$ $i_B = 2exp\left(\frac{-2\epsilon_B}{k_b T}\right)(\Omega - 1)\frac{\nu_A k_B [B]}{k_B[B]+\nu_A}$	$i_A = 2\chi exp\left(\frac{-2\epsilon_A}{k_b T}\right)(\Omega - 1)\frac{\bar{\nu}_B \bar{k}_A [A]}{\bar{k}_A[A]+\bar{\nu}_B}$ $i_B = 2\chi exp\left(\frac{-2\epsilon_B}{k_b T}\right)(\Omega - 1)\frac{\bar{\nu}_A \bar{k}_B [B]}{\bar{k}_B[B]+\bar{\nu}_A}$
$\Omega = \frac{[A][B]}{K_{sp}}$; $i = \frac{i_A+i_B}{2}$; $\epsilon_A = \epsilon_B = 1.15 * 10^{-20} J$ (Nielsen *et al.*, 2013)	
Steady-State Kink Density	
$\rho = \sqrt{\frac{2i}{u}}$	
Step Velocity (m/s)	
$v_{st} = \rho u a$	
Surface-normal growth rate (mol/m^2/s) - spiral growth	
$R_{net} = \frac{h v_{st} d}{y_0}$	
Surface-normal growth rate (mol/m^2/s) - 2D nucleation	
$R_{net} = 1.137h(I v_{st}^2)^{1/3}$; $I = \frac{v_{st}}{\sigma ab}\left(\frac{\xi_2 \sigma}{\pi ab}\right)^{1/2} \exp\left(\frac{\Delta G^*}{k_b T}\right)$; $\Delta G^* = \frac{\xi ab \psi^2}{k_b T \sigma}$ ψ is the average edge free energy of the nucleus, taken to be 1.49e-10 J/m $\sigma = ln(\Omega)$; $\xi \sim 1/8$; $\xi_2 \sim 4$;	
Ca isotope fractionation	
$\alpha_p = \frac{\alpha_f}{1+\frac{v_A P_A}{k_A\{A\}P_B}\left(\frac{\alpha_f}{\alpha_{eq}}-1\right)}$	$\alpha_p = \frac{\alpha_f}{1+\frac{\bar{v}_A P_A}{\bar{k}_A\{A\}P_{B1}}\left(\frac{\alpha_f}{\alpha_{eq}}-1\right)}$
d = 27100mol/m^3; a = 3.2e-10m; h = 3.1e-10m	

Table A1 – Summary of the key equations of the Nielsen et al. (2012) and Wolthers et al. (2012) ion-by-ion models of calcite growth. In the Wolthers formulation, 1 and 2 subscripts denote CO_3^{2-} and HCO_3^-, respectively.

Fitted model parameters

Attachment/detachment coefficients were fit to available step velocity data (Davis, 2008; Larsen *et al.*, 2010; Bracco *et al.*, 2012; Hong and Teng, 2014; Sand *et al.*, 2016). Best-fit coefficients were largely comparable between datasets; fitted k_A and k_B for various step velocity datasets using the Nielsen et al. (2012) ion-by-ion model are summarized in Figure A1. Kinetic and equilibrium endmember Ca isotope fractionations were fit to the data from this study and the 25°C dataset from Tang et al. (2008); best-fit parameters for both the Nielsen *et al.* (2012) and Wolthers *et al.* (2012) model formulations are summarized in Table A2.

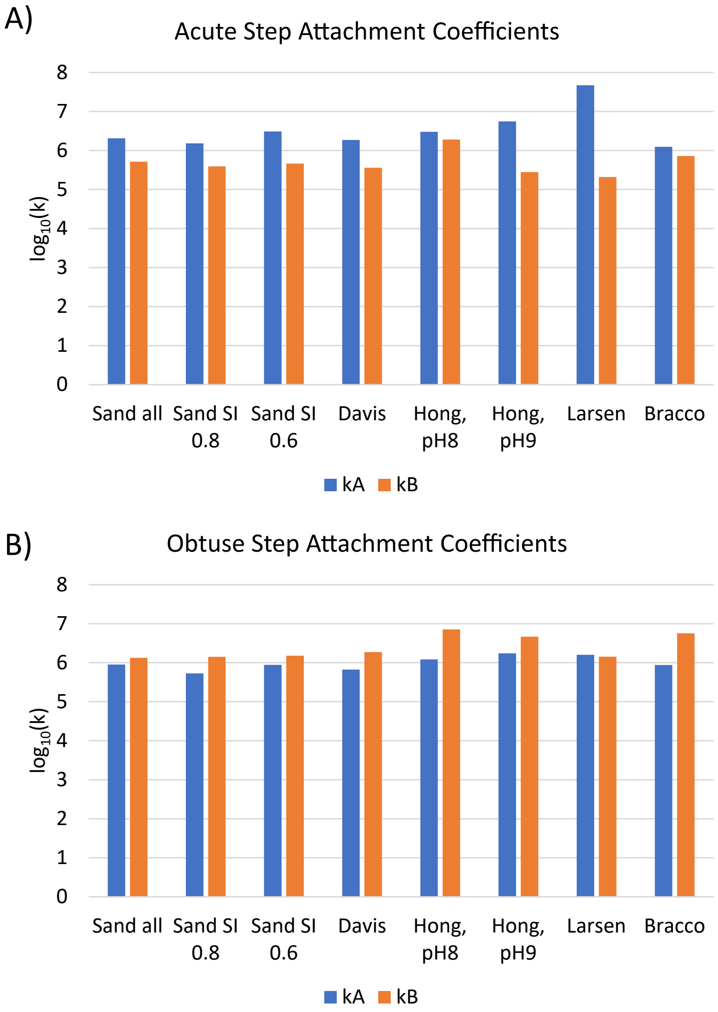

Figure A1 – Best-fit Ca^{2+} (A) and CO_3^{2-} (B) attachment coefficients for various step velocity datasets using the Nielsen et al. (2012) ion-by-ion model. Step velocity datasets: Sand *et al.* (2016); Davis (2008); Hong and Teng (2014); Larsen *et al.* (2010); Bracco *et al.* (2012).

Nielsen et al. (2012) Model						
Step velocity dataset	Step	k_A (s^{-1}M^{-1})	k_B (s^{-1}M^{-1})	α_f*	α_{eq}*	SSE ($\Delta^{44/40}Ca$)
Sand, all SI's	Obtuse	8.945E+05	1.335E+06	0.9974	0.9995	2.79
	Acute	2.050E+06	5.165E+05	0.9970	0.9995	3.06
Sand SI = 0.6	Obtuse	8.792E+05	1.508E+06	0.9974	0.9995	2.59
	Acute	3.071E+06	4.601E+05	0.9970	0.9995	2.93
Davis	Obtuse	6.649E+05	1.866E+06	0.9976	0.9995	2.17
	Acute	1.856E+06	3.618E+05	0.9973	0.9995	2.36
Hong and Teng, pH 8	Obtuse	1.211E+06	7.108E+06	0.9978	0.9995	1.56
	Acute	3.015E+06	1.908E+06	0.9975	0.9995	1.73
Wolthers et al. (2012) Model						
Step Velocity Data	Step	k_A (s^{-1}M^{-1})	ν_A (s^{-1})	α_f*	α_{eq}*	SSE ($\Delta^{44/40}Ca$)
Sand, all SI's	Obtuse	1.859E+07	8.742E+02	0.9979	0.9995	1.06
	Acute	1.560E+07	3.808E+03	0.9975	0.9995	1.16
Sand SI = 0.6	Obtuse	2.672E+07	9.575E+02	0.9980	0.9995	0.83
	Acute	2.428E+07	5.244E+03	0.9976	0.9995	0.89
Davis	Obtuse	1.624E+07	3.428E+02	0.9979	0.9998	0.61
	Acute	1.082E+07	1.933E+03	0.9977	0.9997	0.60

Table A2 – Fitted attachment/detachment coefficients and end member Ca isotope fractionations using different step velocity datasets. *Fitted end member fractionations listed for the obtuse step represent models run only considering the obtuse step while those listed under the acute step account for hillock anisotropy and differing isotope discrimination between the two non-equivalent steps. SSE: sum squared error $\left(\sum_i \left(\Delta^{44/40}Ca_{measured,i} - \Delta^{44/40}Ca_{modeled,i}\right)^2\right)$.

Influence of surface complexation and variable χ (fraction of available growth sites)

For a given set of attachment/detachment coefficients, α_p is independent of χ:

$$\alpha_p = \frac{\alpha_f}{1 + \frac{R^b_{Ca}}{R^f_{Ca}}\left(\frac{\alpha_f}{\alpha_{eq}} - 1\right)} \tag{1}$$

In the Wolthers et al. (2012) ion-by-ion formulation,

$$\frac{R^b_{Ca}}{R^f_{Ca}} = \frac{\bar{v}_A P_A}{\bar{k}_A \{A\} P_{B1}} \tag{2}$$

Noting that $P_A = \chi - \theta P_{B1}$ and $\frac{\bar{v}_A}{\bar{k}_A}$ is a constant at a fixed pH, the solution stoichiometry dependence of α_p is dictated by $\frac{P_A}{P_{B1}}$:

$$\frac{P_A}{P_{B1}} = \frac{\chi - \theta P_{B1}}{P_{B1}} = \frac{\chi}{P_{B1}} - \theta \tag{3}$$

where θ is dependent only on pH ($\theta = \left(1 + 10^{8.6} 10^{-pH}\right)$). Substituting for $\mathrm{P_{B1}}$ (Table A1):

$$\frac{P_A}{P_{B1}} = \frac{\chi}{\frac{\chi\left(\bar{k}_B\{B_1\}+\bar{\nu}_A\right)}{\bar{k}_A\{A\}+\bar{\nu}_B+\theta\left(\bar{k}_B\{B_1\}+\bar{\nu}_A\right)}} - \theta = \frac{\bar{k}_A\{A\} + \bar{\nu}_B + \theta\left(\bar{k}_B\{B_1\} + \bar{\nu}_A\right)}{\bar{k}_B\{B_1\} + \bar{\nu}_A} - \theta \tag{4}$$

Thus the extent of Ca exchange at a given solution chemistry (pH, supersaturation, $Ca^{2+} : CO_3^{2-}$) is dictated only by the best-fit attachment/detachment coefficients.

χ	Step	k_A (s^{-1}M^{-1})	ν_A (s^{-1})	α_f*	α_{eq}*	SSE ($\Delta^{44/40}Ca$)
Variable	Obtuse	1.624e7	3.428e2	0.9979	0.9998	0.61
	Acute	1.082e7	1.933e3	0.9977	0.9997	0.60
Constant	Obtuse	4.431e7	5.675e3	0.9972	0.9995	2.55
	Acute	3.075e7	2.752e4	0.9965	0.9995	2.44

Table A3 – Comparison of best-fit attachment/detachment coefficients and endmember fractionations for Davis (2008) step velocity dataset assuming either a constant fraction of available growth sites ($\chi = 0.01$) or a variable χ set by the Wolthers *et al.* (2008) surface complexation model. SSE: sum squared error $\left(\sum_i \left(\Delta^{44/40}Ca_{measured,i} - \Delta^{44/40}Ca_{modeled,i}\right)^2\right)$.

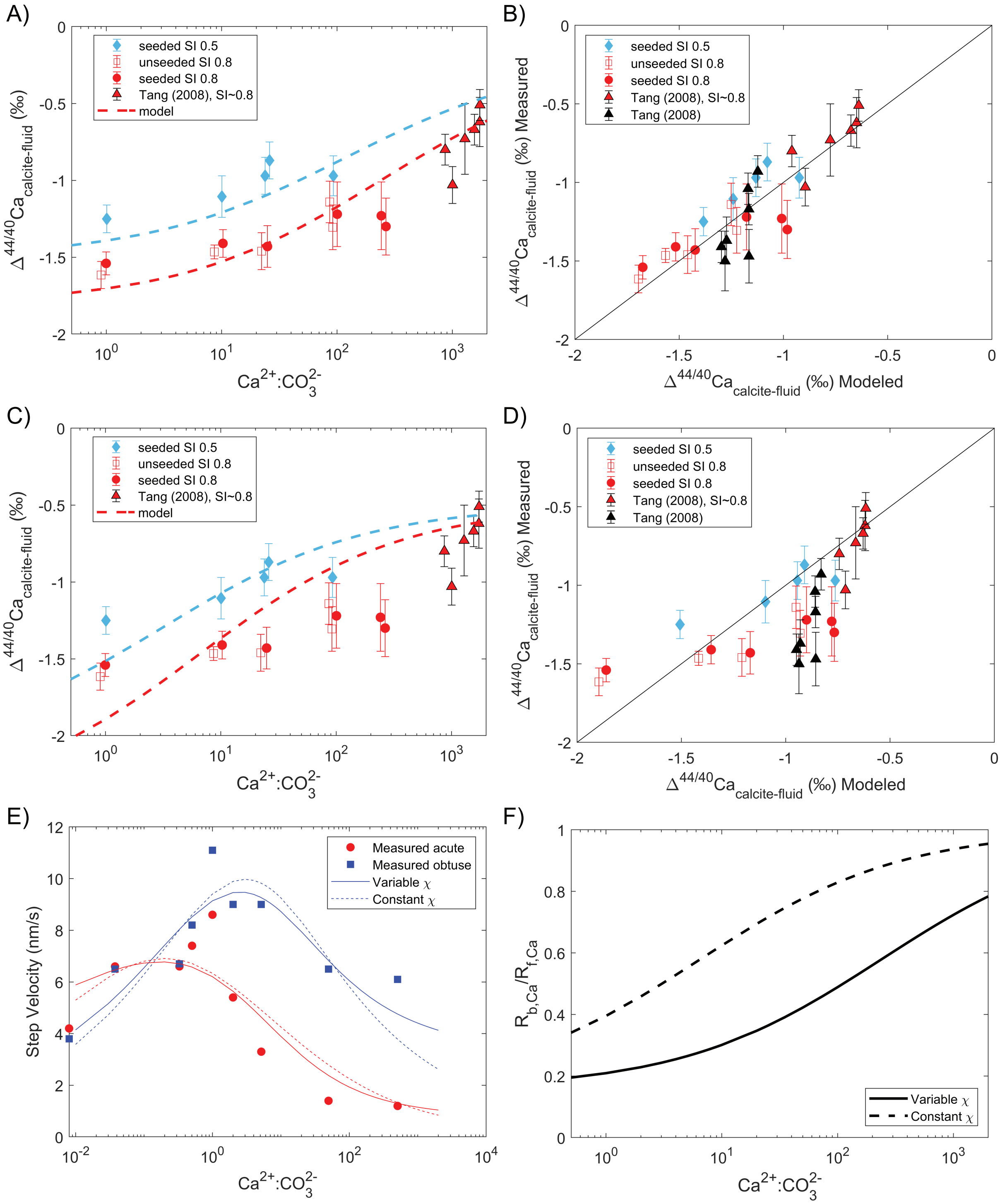

Figure A2 – Influence of accounting for a variable number of growth sites using the CD-MUSIC model of Wolthers *et al.* (2008). A,B) Predicted $\Delta^{44/40}Ca$ assuming a variable χ set by the Wolthers *et al.* (2008) surface complexation model. C,D) Predicted $\Delta^{44/40}Ca$ with a constant fraction of available growth sites ($\chi = 0.01$). E,F) Comparison of modeled step velocities (E) and extent of Ca exchange $\left(\frac{R^b_{Ca}}{R^f_{Ca}}\right)$ assuming either a CD-MUSIC defined χ (solid line) or constant χ (dashed line). In all, attachment/detachment coefficients fit to Davis (2008) obtuse step velocity are used to parameterize the Wolthers et al. (2012) ion-by-ion model.

Fitting attachment/detachment coefficients with measured bulk growth rates

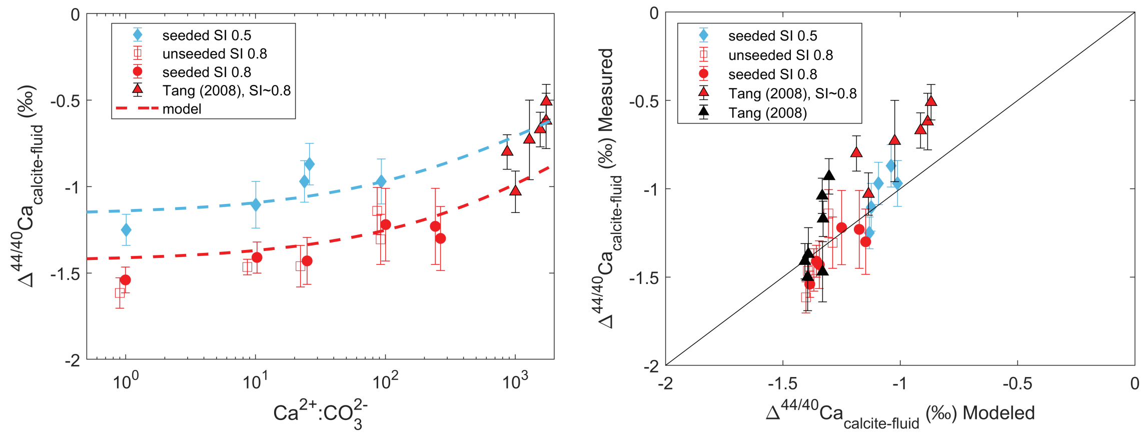
A) Davis y₀ relationship

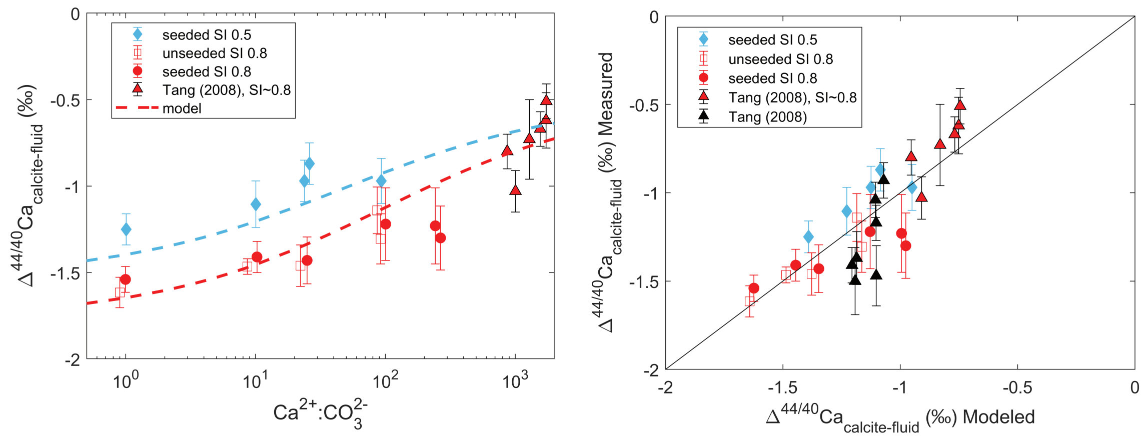
B) Bracco y₀ relationship

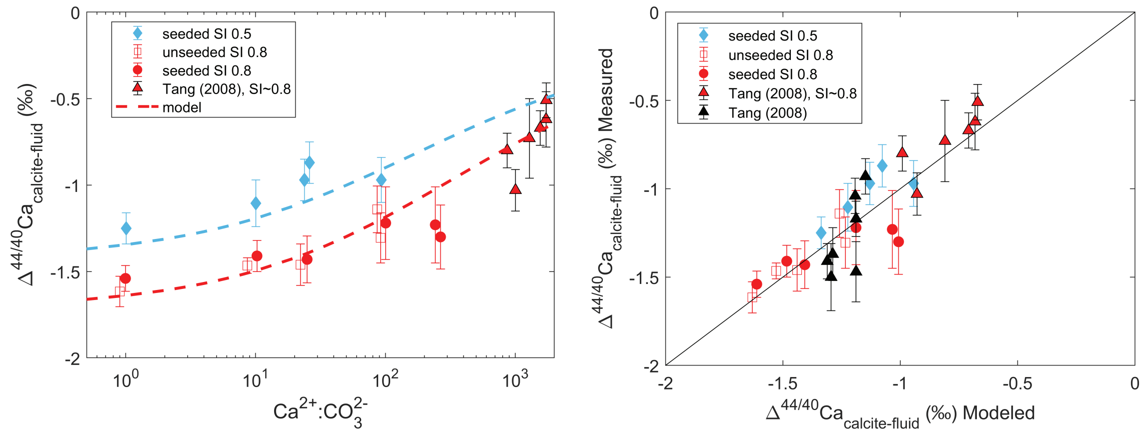
C) Thermo y₀ relationship

Figure A3 – Ion-by-ion model prediction of $\Delta^{44/40}Ca$-$Ca^{2+} : CO_3^{2-}$ relationship using Wolthers et al. (2012) model and Ca attachment/detachment parameters fit directly to the surface-normal growth rates measured here using different step width (y_0) parameterizations: A) Davis (2008), B) Bracco *et al.* (2013), and C) thermodynamic y_0 dependent solely on supersaturation.

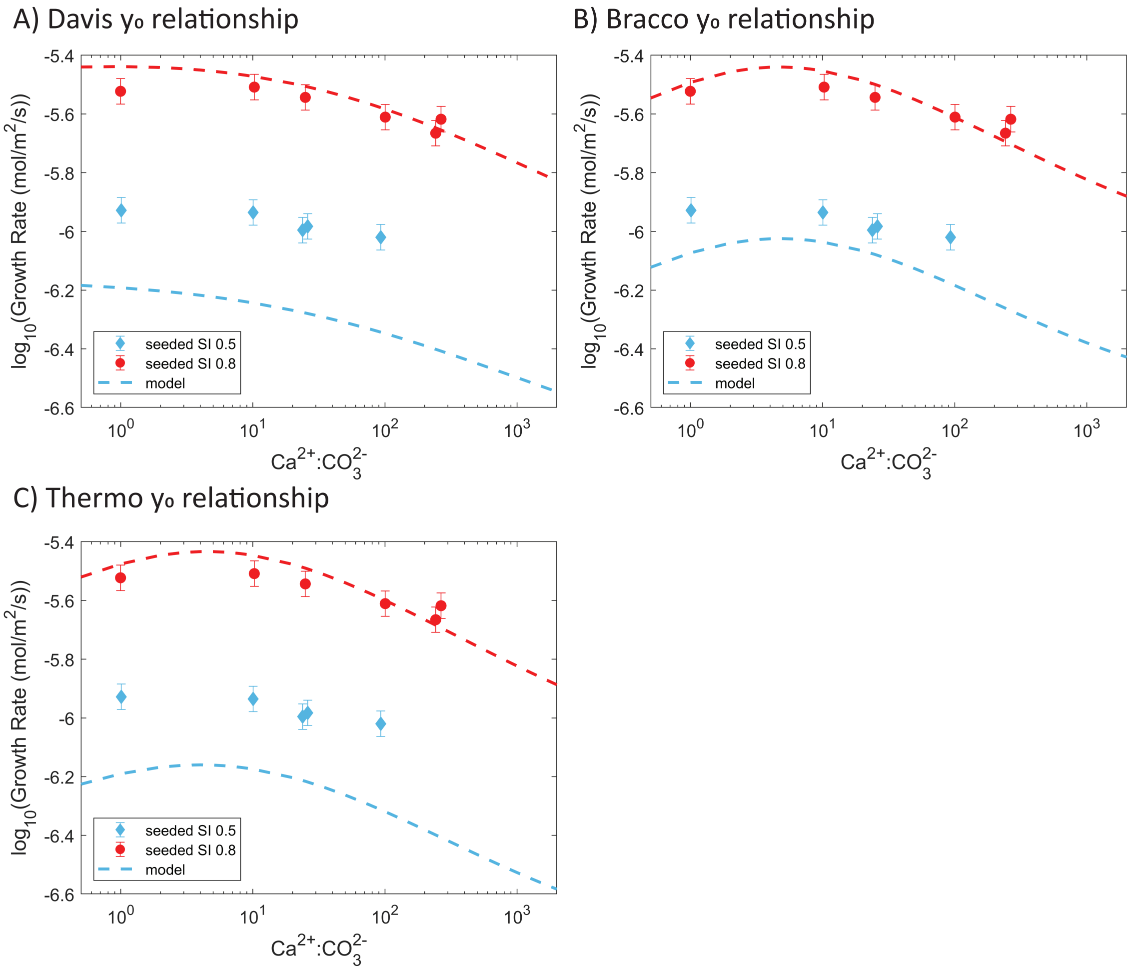

A) Davis y_0 relationship

B) Bracco y_0 relationship

C) Thermo y_0 relationship

Figure A4 – Ion-by-ion model prediction of bulk growth rates using Wolthers (2012) model and Ca attachment/detachment parameters fit directly to the surface-normal growth rates measured here using different step width (y_0) parameterizations: A) Davis (2008), B) Bracco (2013), and C) thermodynamic y_0 dependent solely on supersaturation.

Influence of supersaturation and pH on predicted $\Delta^{44/40}Ca$

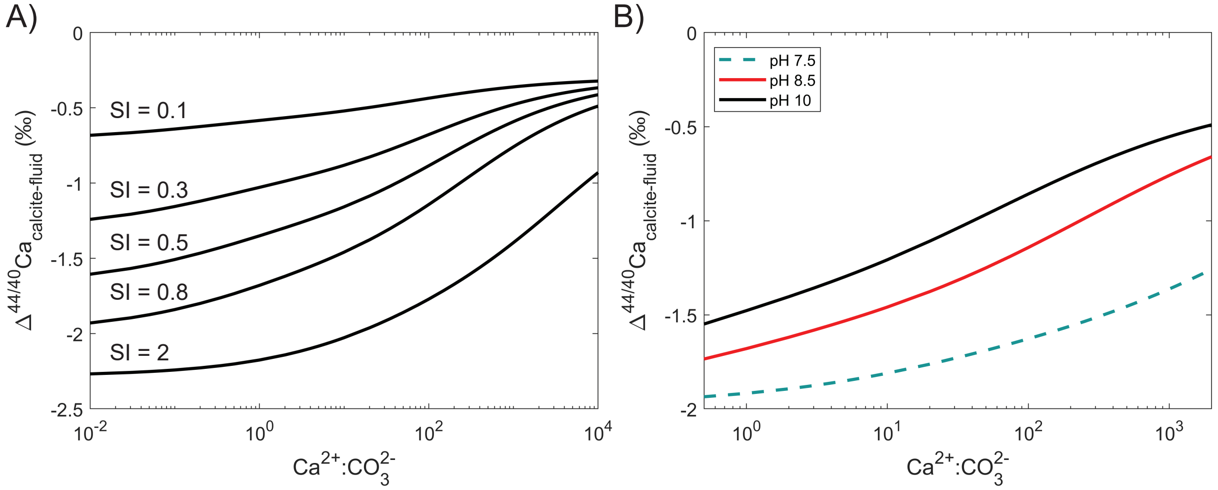

Figure A5 – Influence of supersaturation (A) and pH (B) on predicted $\Delta^{44/40}Ca$. In A, pH is fixed at 8.5 while the supersaturation is varied while in B, the supersaturation is held constant (SI 0.8) while pH is varied. In both, attachment/detachment coefficients fit to Davis (2008) acute and obtuse step velocities are used to parameterize the Wolthers et al. (2012) ion-by-ion model (Table 3). See Figure 2.13 in the main text for comparable plots with attachment/detachment coefficients fit only to Davis (2008) obtuse step velocity data.

Additional experimental data

Experiment	Ca^{2+}:$CO_3{}^{2-}$	SI	$CaCl_2$ (M)	$KHCO_3$ (M)	KCl (M)
1	25	0.5	1.34E-03	1.84E-03	9.41E-02
2	1	0.5	2.90E-04	9.10E-03	9.00E-02
3	10	0.5	8.60E-04	2.90E-03	9.45E-02
4	100	0.5	2.65E-03	9.30E-04	9.11E-02
5	25	0.5	1.34E-03	1.84E-03	9.41E-02
6	1	0.8	4.26E-04	1.28E-02	8.59E-02
7	10	0.8	1.23E-03	4.09E-03	9.22E-02
8	25	0.8	1.91E-03	2.63E-03	9.16E-02
9	100	0.8	3.75E-03	1.34E-03	8.74E-02
10	250	0.8	5.94E-03	8.70E-04	8.13E-02
11	250	0.8	5.94E-03	8.70E-04	8.13E-02
12	1	0.8	4.26E-04	1.28E-02	8.59E-02
13	10	0.8	1.23E-03	4.09E-03	9.22E-02
14	25	0.8	1.91E-03	2.63E-03	9.16E-02
15	100	0.8	3.75E-03	1.34E-03	8.74E-02
16	100	0.8	3.75E-03	1.34E-03	8.74E-02

Table A4 – Summary of reagents used to prepare growth solutions.

Exp.	Surface-normal growth rate	% Change in ionic strength during experiment	$\delta^{44/40}Ca$ measurements (‰ BSE)				Notes
			Fluid T_0*	Fluid T_{int}	Fluid T_{end}	Solid	
Units	mol/m^2/s		(n†, 2σ)	(moles Ca titrated, n†, 2σ)			
1	1.04E-06	5%	0.13 (9, ±0.03)	-	0.88 (4.772e-3, 4, ±0.06)		
2	1.18E-06	5%	0.13 (9, ±0.03)	1.35 (4.02e-3, 1, ±0.12)	1.39 (4.491e-3, 2, ±0.04)		
3	1.16E-06	5%	0.13 (9, ±0.03)	-	1.175 (4.613e-3, 2, ±0.08)		
4	9.55E-07	5%	0.13 (9, ±0.03)	0.59 (3.581e-3, 1, ±0.07)	0.73 (4.406e-3, 4, ±0.05)		
5	1.01E-06	5%	0.13 (9, ±0.03)	0.91 (3.00e-3, 1, ±0.13)	0.925 (4.406e-3, 2, ±0.07)		
6	3.00E-06	5%	0.13 (9, ±0.03)	1.62 (2.518e-3, 2, ±0.06)	1.7 (5.025e-3, 2, ±0.06)		
7	3.10E-06	5%	0.13 (9, ±0.03)	1.05 (2.494e-3, 1, ±0.11)	1.395 (5.016e-3, 2, ±0.06)		
8	2.86E-06	5%	0.13 (9, ±0.03)	0.87 (2.494e-3, 2, ±0.07)	1.24 (4.997e-3, 2, ±0.09)		
9	2.45E-06	5%	0.13 (9, ±0.03)	0.50 (2.485e-3, 2, ±0.07)	0.80 (4.997e-3, 2, ±0.10)		
10	2.16E-06	5%	0.13 (9, ±0.03)	0.50 (3.750e-3, 1, ±0.12)	0.63 (5.00e-3, 2, ±0.07)		
11	2.41E-06	10%	0.18 (3, ±0.04)	0.89 (7.500e-3, 2, ±0.10)	0.98 (1.00e-2, 2, ±0.07)		
12	1.59E-06	2%	0.02 (7, ±0.05)	-	1.65 (2.625e-3, 6, ±0.07)	-0.12 (2, ±0.16)	Only fluid measurement used in $\Delta^{44/40}Ca$ calc.**
13	2.39E-06	3%	0.02 (7, ±0.05)	-	1.19 (2.644e-3, 2, ±0.11)	-0.71 (2, ±0.10)	
14	2.83E-06	2%	0.02 (7, ±0.05)	-	0.72 (1.925e-3, 2, ±0.10)	-1.015 (2, ±0.15)	
15	2.25E-06	2%	0.02 (7, ±0.05)	-	0.44 (1.950e-3, 2, ±0.07)	-0.97 (2, ±0.06)	Only solid measurement
16	2.45E-06	2%	0.02 (7, ±0.05)	-	0.4 (1.500e-3,2, ±0.10)	-1.145 (2, ±0.08)	used in $\Delta^{44/40}Ca$ calc.*†

Table A5 – Supplementary experimental data. †n = number of measurements. *$\delta^{44/40}Ca_{T0}$=$\delta^{44/40}Ca_{titrant}$, dictated by the $CaCl_2$ salt used. **For the unseeded, Ca^{2+}:$CO_3{}^{2-}$ = 1 experiment, only the fluid $\delta^{44/40}Ca$ was used as the solid $\delta^{44/40}Ca$ is highly dependent on recovering all of the precipitated solids given the large change in fluid $\delta^{44/40}Ca$ over the course of the experiment. This is particularly challenging due to nucleation on the sides of the growth chamber, which makes the initial solids preferentially harder to recover. †*For the unseeded, Ca^{2+}:$CO_3{}^{2-}$ = 100 experiments, only the solid $\delta^{44/40}Ca$ was used to calculate $\Delta^{44/40}Ca$ as such a small fraction of the Ca reservoir was precipitated over the course of the experiment.

Appendix B: Supplementary information for Chapter 3, Ca isotope insights into Mn^{2+} and Mg^{2+} inhibition of calcite growth

Mn solution speciation considerations

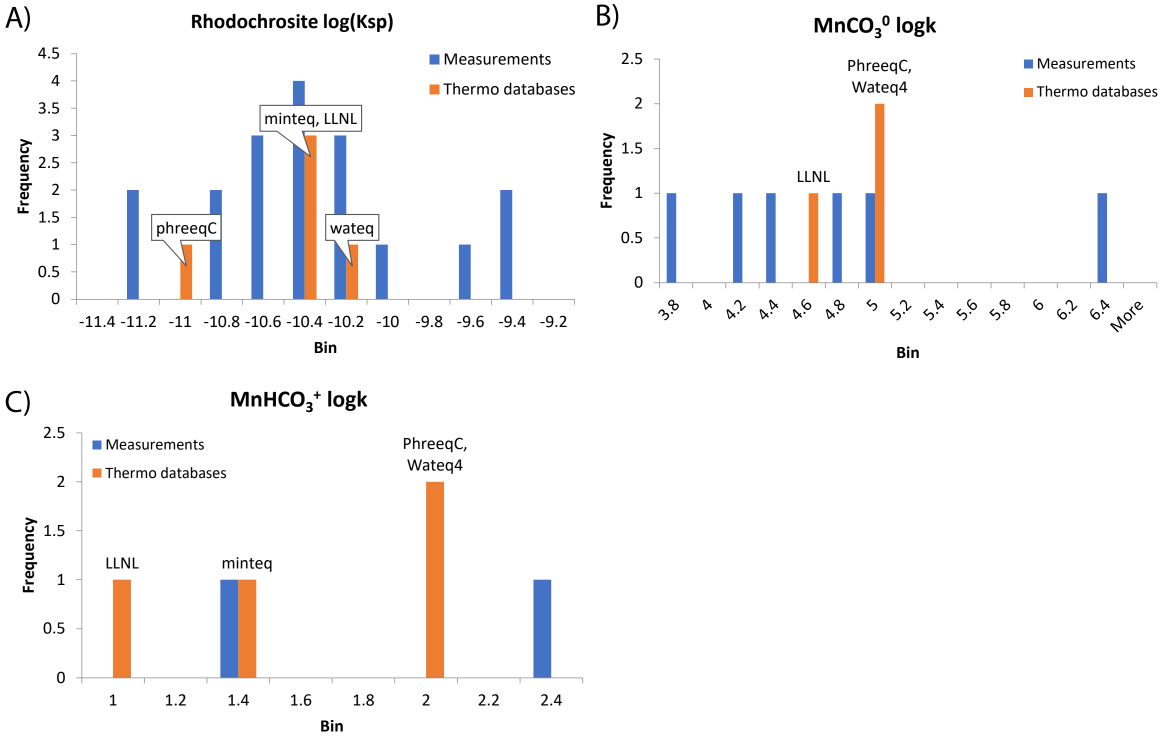

Figure B1 – Histograms of compiled literature measurements (blue) and values from the most common geochemical thermodynamic databases (orange) for key Mn speciation parameters. A) Rhodochrosite solubility (Middelburg *et al.* (1987) and references within), B) $MnCO_3{}^0$ ion pair stability constant (Sternbeck, 1997; Luo and Millero, 2003; Turner *et al.*, 1981; Langmuir, 1979; Wolfram and Krupp, 1996; Mattigod and Sposito, 1977) and C) $MnHCO_3{}^+$ ion pair stability constant (Wolfram and Krupp, 1996; Lesht and Bauman, 1978).

Additional figures for ion-by-ion model investigation of Mn^{2+} inhibition of calcite growth

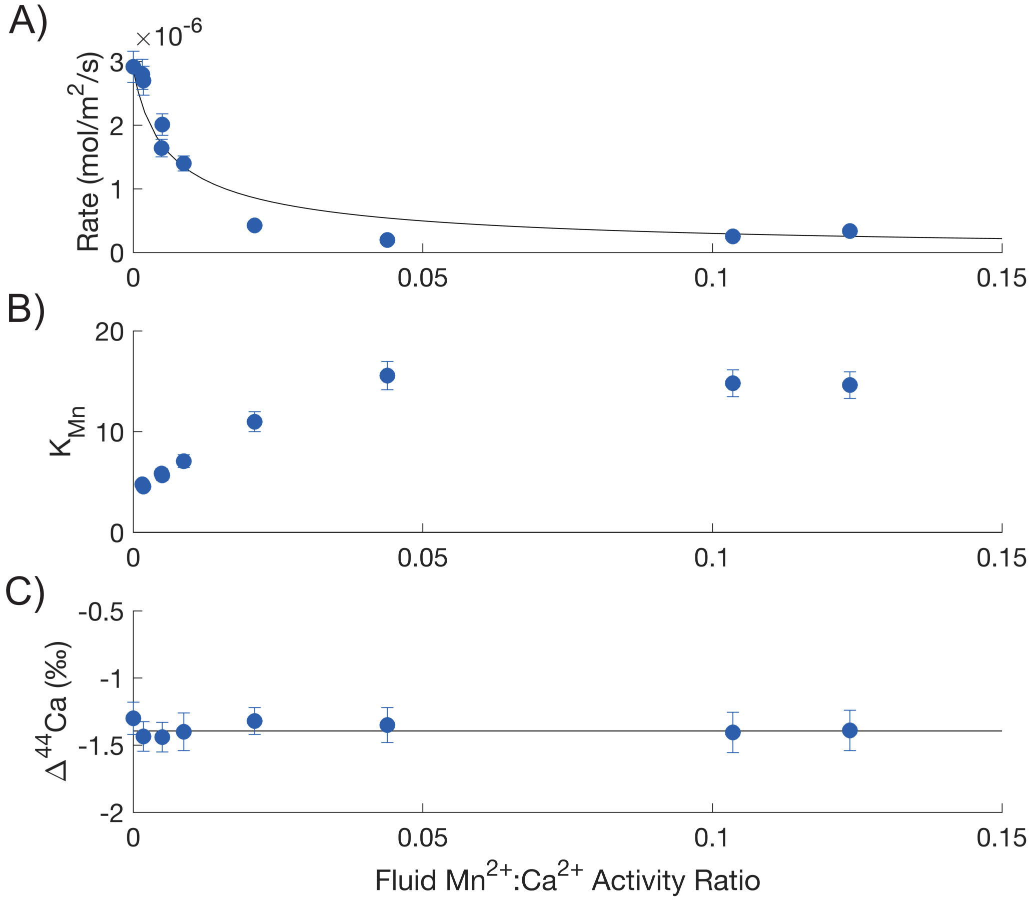

Figure B2 – Ion-by-ion model prediction of bulk growth rate (A), Mn^{2+} partition coefficient (B), and $\Delta^{44/40}Ca_{calcite-fluid}$ (C) as a function of ${}^{\{Mn^{2+}\}}/_{\{Ca^{2+}\}}$ for Mn^{2+} inhibition of calcite growth driven by cation-desolvation limited kink blocking. See Table 3.4 for model parameters.

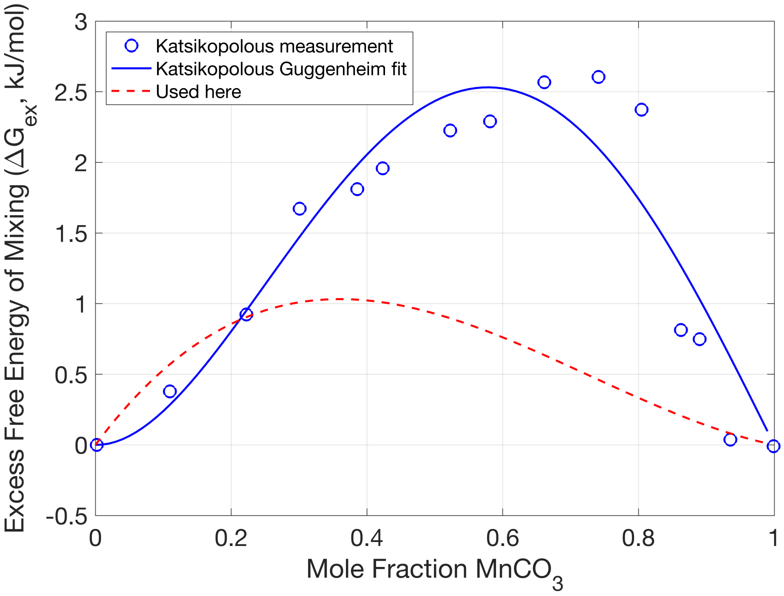

Figure B3 – Comparison of calcite-rhodochrosite solid solution thermodynamic data used here to that measured by Katsikopoulos *et al.* (2009).

Additional figures for ion-by-ion model investigation of Mg^{2+} inhibition of calcite growth

Cation kink blocking with negligible Mg^{2+} detachment rate

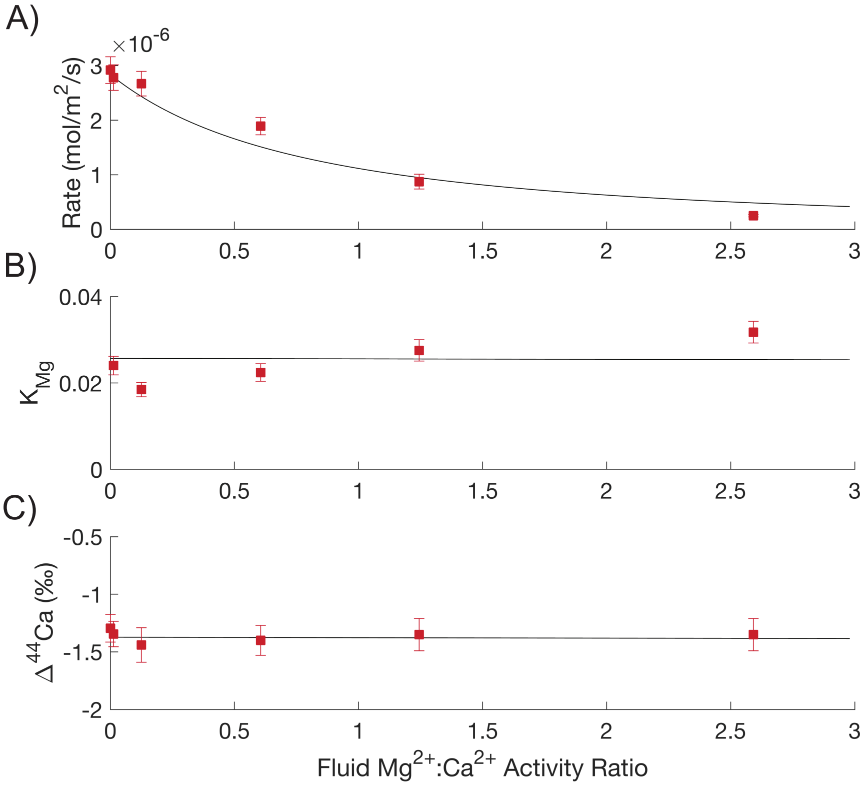

Figure B4 – Ion-by-ion model prediction of bulk growth rate (A), Mg^{2+} partition coefficient (B), and $\Delta^{44/40}Ca_{calcite-fluid}$ (C) as a function of ${\{Mg^{2+}\}}/{\{Ca^{2+}\}}$ for Mg^{2+} inhibition of calcite growth driven by Mg^{2+}-desolvation limited kink blocking with virtually no Mg^{2+} detachment. See Table 3.5 for model parameters (Scenario 2 with y_0 scaled to the observations of Davis *et al.* (2000)).

Cation kink blocking with low Mg^{2+} detachment rate, linked to the solubility of the Mg-calcite lattice

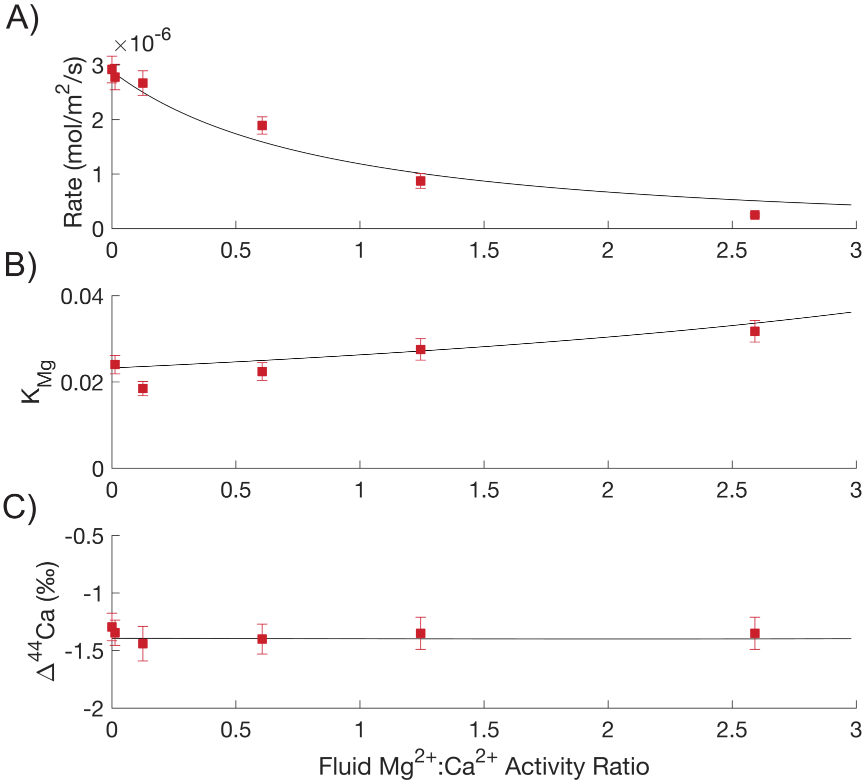

Figure B5 – Ion-by-ion model prediction of bulk growth rate (A), Mg^{2+} partition coefficient (B), and $\Delta^{44/40}Ca_{calcite-fluid}$ (C) as a function of ${}^{\{Mg^{2+}\}}/_{\{Ca^{2+}\}}$ for Mg^{2+} inhibition of calcite growth driven by Mg^{2+}-desolvation limited kink blocking with a low Mg^{2+} detachment flux. See Table 3.5 for model parameters (Scenario 3 with y_0 scaled to the observations of Davis *et al.* (2000)).

Predicted K_{Mg}-growth rate relationship for the different inhibition mechanisms explored

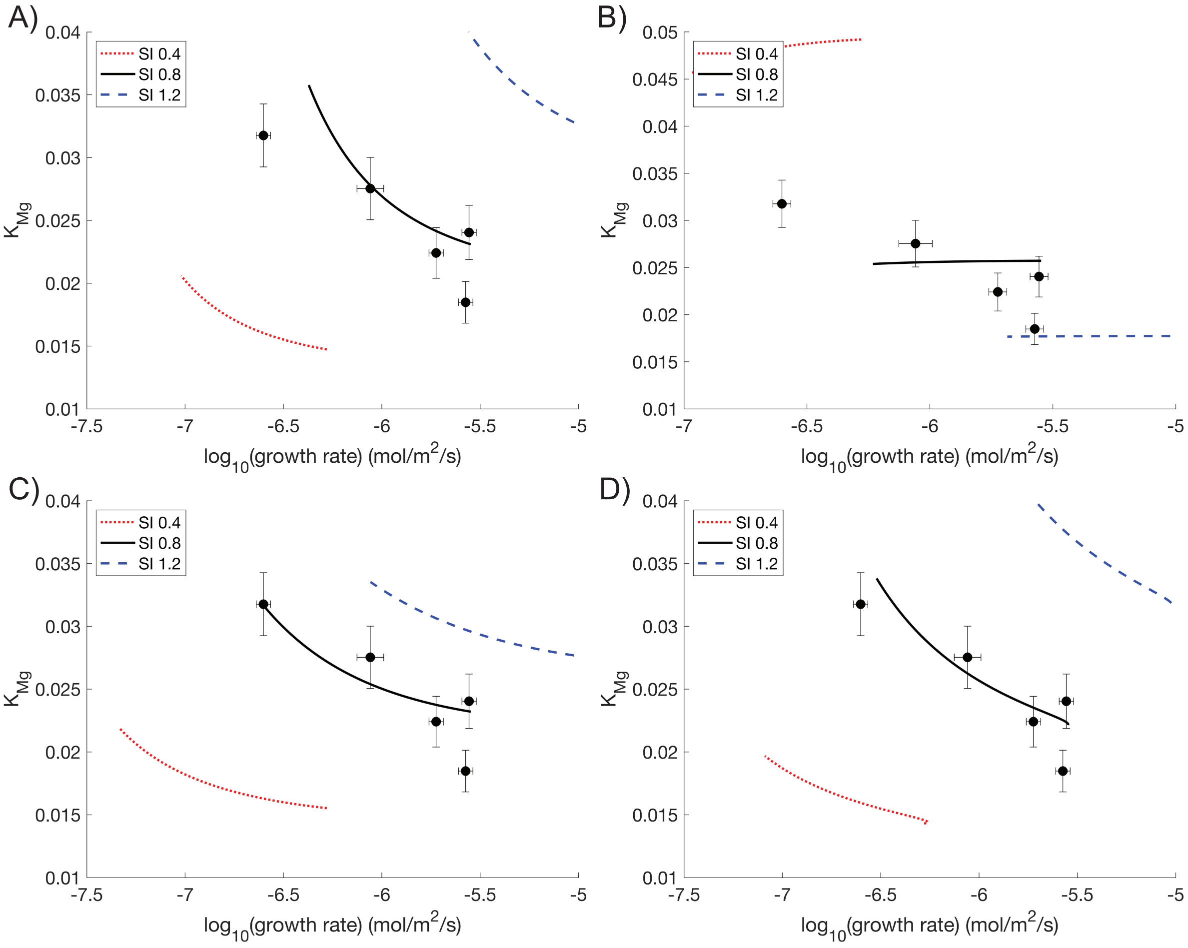

Figure B6 – Predicted growth rate dependence of Mg^{2+} partitioning at different supersaturations for the different inhibition mechanisms explored. K_{Mg} as a function of $\{Mg^{2+}\}/\{Ca^{2+}\}$ for inhibition modeled as cation-desolvation driven kink blocking for A) scenario 1 (y_0 scaled to Davis *et al.* (2000)), B) scenario 2 (thermodynamic y_0), C) scenario 3 (y_0 scaled to Davis *et al.* (2000)), and D) inhibition modeled as Mg^{2+} complex addition + carbonate kink blocking (y_0 scaled to Davis *et al.* (2000)). See Table 3.5 for model parameters.

Assumed calcite-magnesite solid solution thermodynamics dictates the sign of the K_{Mg}-${Mg^{2+}}/{Ca^{2+}}$ relationship

The value of W_{12} dictates the sign of the K_{Mg}-${Mg^{2+}}/{Ca^{2+}}$ relationship. Low values of W_{12} yield an increase in K_{Mg} with fluid ${Mg^{2+}}/{Ca^{2+}}$ while values of W_{12} greater than ~17kJ/mol cause the slope of the K_{Mg}-${Mg^{2+}}/{Ca^{2+}}$ relationship to reverse (Lammers and Mitnick, 2019).

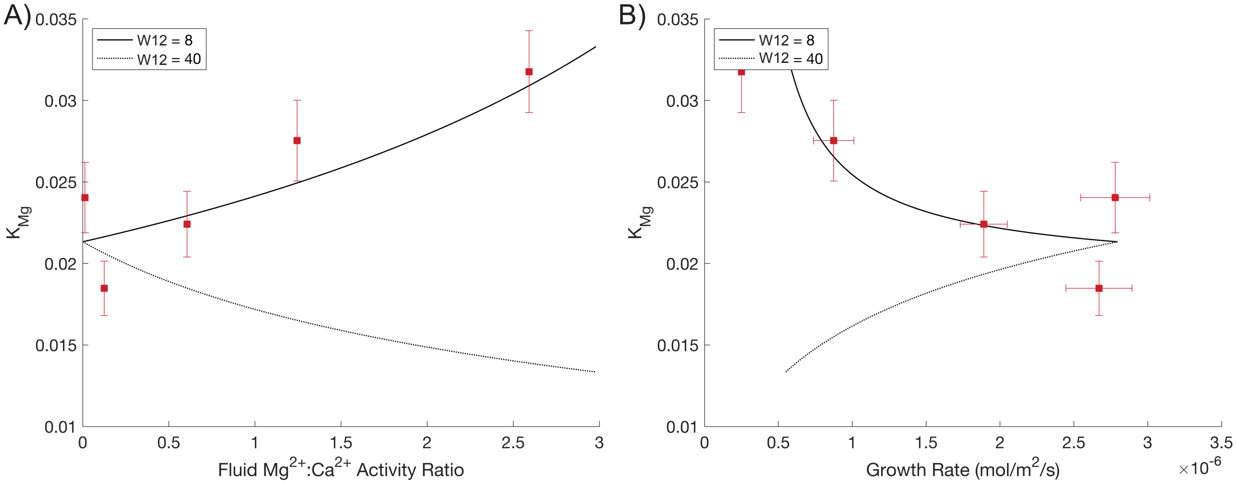

Figure B7 – Assumptions regarding calcite-magnesite solid solution thermodynamics dictate the slope of the K_{Mg}-${Mg^{2+}}/{Ca^{2+}}$ relationship. Ion-by-ion model prediction of Mg partition coefficient vs. ${Mg^{2+}}/{Ca^{2+}}$ (A) and growth rate (B) assuming $W_{12} = 8$kJ/mol (solid line) and $W_{12} = 40$kJ/mol (dotted line).

Solution Preparation

		Growth Solution				Cation Titrant		Carbonate Titrant
Exp.	$\{Me^{2+}\}/\{Ca^{2+}\}$	$CaCl_2$ (M)	$MeCl_2$ (M)	$KHCO_3$ (M)	KCl (M)	$CaCl_2$ (M)	$MeCl_2$ (M)	K_2CO_3 (M)
Mn2	0.005	3.80E-03	1.90E-05	4.12E-03	8.44E-02	2.43E-01	6.63E-03	2.50E-01
Mn3	0.009	3.80E-03	3.80E-05	4.15E-03	8.43E-02	2.36E-01	1.43E-02	2.50E-01
Mn5	0.044	3.80E-03	1.90E-04	4.15E-03	8.60E-02	1.50E-01	1.00E-01	2.50E-01
Mn6	0.104	3.80E-03	3.80E-04	4.25E-03	8.40E-02	9.95E-02	1.51E-01	2.50E-01
Mn7	0.021	3.80E-03	9.50E-05	4.16E-03	8.60E-02	2.03E-01	4.75E-02	2.50E-01
Mn8	0.005	3.80E-03	2.13E-05	4.12E-03	8.50E-02	2.43E-01	6.77E-03	2.50E-01
Mn9	0.002	3.80E-03	6.08E-06	4.11E-03	8.40E-02	2.48E-01	1.85E-03	2.50E-01
Mn11	0.000	3.80E-03	0	4.12E-03	8.70E-02	2.50E-01	0.00E+00	2.50E-01
Mn12	0.002	3.80E-03	7.11E-06	4.11E-03	8.70E-02	2.48E-01	1.85E-03	2.50E-01
Mn13	0.124	3.80E-03	5.70E-04	4.30E-03	8.40E-02	9.17E-02	1.58E-01	2.50E-01
Mg2	0.124	3.80E-03	3.80E-04	4.12E-03	8.40E-02	2.50E-01	5.21E-04	2.50E-01
Mg3	1.243	3.80E-03	3.80E-03	4.20E-03	7.40E-02	2.45E-01	5.12E-03	2.50E-01
Mg4	0.012	3.80E-03	3.80E-05	4.11E-03	8.50E-02	2.50E-01	5.22E-05	2.50E-01
Mg5	0.604	3.80E-03	1.90E-03	4.18E-03	7.90E-02	2.47E-01	2.59E-03	2.50E-01
Mg7	2.589	3.80E-03	9.50E-03	4.35E-03	5.60E-02	2.38E-01	1.24E-02	2.50E-01

Figure B8 – Summary of reagents used to prepare growth and titrant solutions.

Appendix C: Mojave climosequence soil characterization

Soil Description

Soil profiles from three sites along an elevation gradient in the Mojave National Preserve in Southern California were sampled and instrumented for long-term monitoring of meteorological and soil conditions in January, 2017. Each site represents one of the dominant vegetation types in the Mojave: creosote bush at the lowest elevations; joshua trees at mid-elevations; and a mixed pinyon-juniper forest at the highest elevations. At each site three soil pits were excavated; see Table 4.1 for site locations and profile microsite descriptions.

Creosote

Soil Pit	Horizon	Lower Depth (cm)	Roots*	Effervescence**	Weight Percent Gravel (%)
C1	1	3	0	0	26.07
	2	13	1(-)f	0	27.58
	3	28	1vf,f	0	30.42
	4	55	1vf,m,c	me-se	31.70
	5	73	2vf,f	se	71.56
	6	88	1(-)vf	0-me	49.41
	7	104	2vf,f,m	se-ve	60.69
	8	135	2vf,f,m	o-se	38.53
C2	1	3	0		21.00
	2	19	1f,m		28.36
	3	56	1f,m		43.81
	4	61	1vf		52.45
	5	82	2f,1m,co		40.20
	6	88	2f		60.83
	7	98	0		47.85
	8	106	sf		55.25
	9	130	0-1,vf		36.66
C3	1	4	0	0	41.51
	2	16	1f	0	23.76
	3	32	2vf,1f,m	0	35.81
	4	52	1vf,c	0	42.93
	5	58	2vf,1m	0-me	32.46
	6	77	1vf,m	0-me	40.74
	7	89	2vf,1f	se	39.72
	8	106	1vf,f	0-me	32.44
	9	125	0	0-me/se	32.52

Table C1 – Horizon characteristics of lowest elevation, Creosote site soil profiles. *Number indicates quantity of roots; letters describe size of roots: 1 - few, 2 - common, 3 - many, vf - very fine, f - fine, m - medium, c - coarse. **Effervescence: 0 - no effervescence, we - weakly effervescent, me - medium effervescence, se - strongly effervescent, ve - violently effervescent.

Joshua Tree

Soil Pit	Horizon	Lower Depth (cm)	Roots*	Effervescence**	Weight Percent Gravel (%)
JT1	1	4	3vf, 2f	o-me	
	2	14	3vf, 2f	o	23.30
	3	36	2vf, 2f, 1m	o	25.08
	4	49	2vf, 2f, 1m	me	27.66
	5	60	2vf, 2f	se	25.90
	6	76	1vf, 1f	se	29.42
	7	98	1f	ve	43.74
JT2	1	3	1vf	o	20.74
	2	9	1vf,f	o	24.03
	3	22	1vf,f,m	me	26.32
	4	38	1vf,2c	me	26.43
	5	52	1vf,1c	se	28.36
	6	67	1vf,m	se	24.91
	7	87	1vf,m	ve	48.24
	8	126	1vf,f	ve	43.95
	9	138	1f	ve	82.57
	10	145	o	ve	
JT3	1	3	2vf	o	21.05
	2	10	2vf	o	20.63
	3	23	2vf	o	26.91
	4	31	1vf,f	me	25.39
	5	53	1vf,m,c	se	28.12
	6	68	1vf,1c	se	23.97
	7	86	1vf,f	ve	30.41
	8	112	1f,m	ve	40.39
	9	130	1f	ve	45.93
	10	135	1f,2m	ve	34.28

Table C2 – Horizon characteristics of mid-elevation, Joshua Tree site soil profiles. *Number indicates quantity of roots; letters describe size of roots: 1 - few, 2 - common, 3 - many, vf - very fine, f - fine, m - medium, c - coarse. **Effervescence: 0 - no effervescence, we - weakly effervescent, me - medium effervescence, se - strongly effervescent, ve - violently effervescent.

Pinyon Juniper

Soil Pit	Horizon	Lower Depth (cm)	Roots*	Effervescence**	Weight Percent Gravel (%)
PJ1	1	4	1 vf,f	o	20.62
	2	23	3vf,f,1m	o	38.69
	3	38	3vf,f	o	32.65
	4	65	2vf,f	o	23.83
	5	93	2vf, 3f	o	31.71
	6	117	2vf, 2f	me	24.12
	7	136	2vf	se	21.48
PJ2	1	4	1vf,f	o	21.05
	2	17	2vf	o	20.07
	3	35	2vf,1f,m	o	35.27
	4	55	1vf,f,m	o	27.10
	5	72	1vf,f	o	24.77
	6	90	1vf,m	0-me	25.95
	7	114	1vf,f	0-se	
	8	132	o-1,vf	me-se	56.42
	9	155	o	0-se	69.56
PJ3	1	3	o	o	25.52
	2	14	2vf,f,m	o	13.89
	3	26	2vf,f,m	o	17.55
	4	43	1vf,f,2m	o	32.57
	5	56	1vf,f,m	me	39.61
	6	77	o-1f	me-se	59.18
	7	117	0-1f	me-se	49.20
	8	135	o-1c	me-se	36.06

Table C3 – Horizon characteristics of high elevation, Pinyon Juniper site soil profiles. *Number indicates quantity of roots; letters describe size of roots: 1 - few, 2 - common, 3 - many, vf - very fine, f - fine, m - medium, c - coarse. **Effervescence: 0 - no effervescence, we - weakly effervescent, me - medium effervescence, se - strongly effervescent, ve - violently effervescent.

Plant Cover

Ground Cover	Creosote	Joshua Tree	Pinyon Juniper
Bare soil	68.344	56.91	44.77
Burro brush	8.652	1	
Creosote	15.328		
Crust	3.068		0.38
Dead bush	2.432	5.42	
Low grass	3.524	0.34	
Hopsage	0.244		1.39
Amnosia	0.784		
Dead Grass		1.38	
Ephedra		11.82	5.71
Forb		0.05	0.42
Gramma		7.3	6.036
Mendota		0.39	
Muley grass		1.15	3.08
Needle grass		15.35	0.69
Pencil cholla		2.01	
Rubber brush		0.17	
Golden bush			2.04
Silver cholla		0.05	
Desert sage			5.67
Snakeweed			3.29
Banana yucca			1.09
Big sage			8.79
Juniper			4.8
Four wing salt bush			1.17

Table C4 – Vegetation cover and composition at the Mojave climosequence sites in January 2017, quantified as the average of five 50m random line-intercept transects.

Organic C and N content and isotopic composition

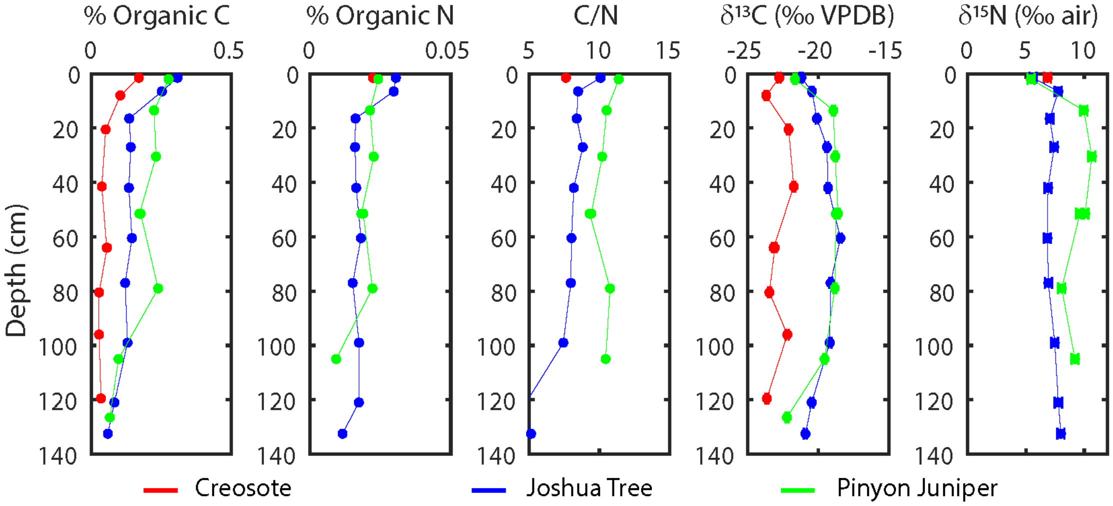

Figure C1 – Soil organic carbon and nitrogen data from intercanopy soil pits at each of the climosequence sites.

Carbonate content and isotopic composition

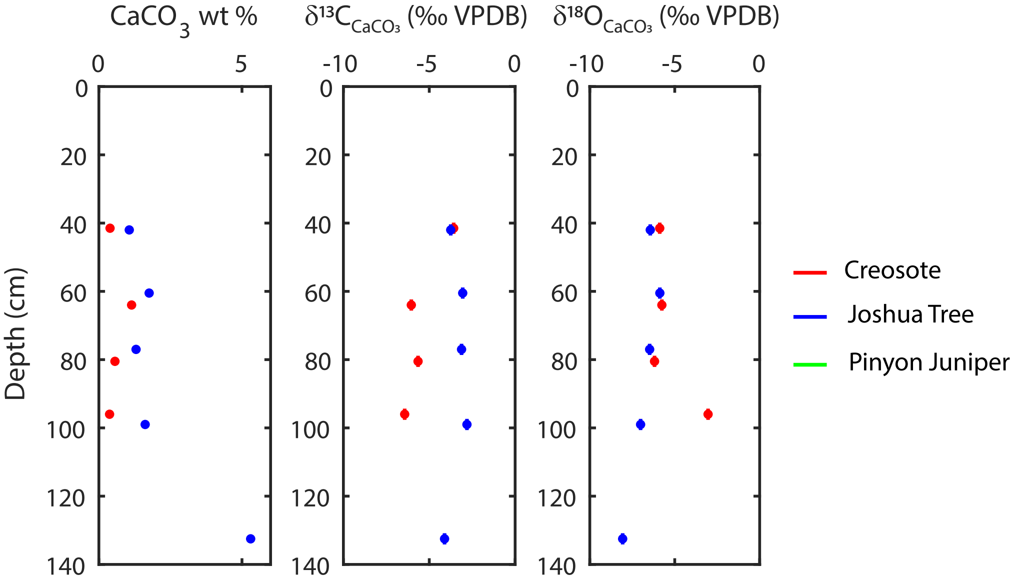

Figure C2 – Soil carbonate data from inter-canopy soil pits at each of the climosequence sites. No measurable carbonate (detection limit ~0.3 wt % carbonate) was found in the highest elevation, Pinyon Juniper profile.

Saturated Paste Extract Data

Soil Pit	Horizon	Lower Depth	Saturation %	pH	EC	Ca	Mg	Na	Cl	B	HCO$_3$	CO$_3$
units		(cm)	%		dS/m	meq/L	meq/L	meq/L	meq/L	mg/L	meq/L	meq/L
Creosote												
C1	1	3	26	7.23	1.31	8.57	2.37	0.31	0.18	0.46	0.6	<0.1
	1 - rep	3		7.22	1.31	8.45	2.33	0.30	0.18	0.46	0.8	<0.1
	2	13	22	8.25	0.22	1.40	0.32	0.17	0.24	0.34	1.1	<0.1
	3	28	22	8.46	0.17	1.20	0.22	0.26	0.18	0.47	0.8	<0.1
	4	55	23	8.42	0.32	2.12	0.27	0.42	1.29	0.56	0.7	<0.1
	5	73	26	8.14	0.68	4.31	0.45	1.32	3.27	0.45	1.0	<0.1
	6	88	26	8.39	0.46	1.89	0.21	2.02	2.80	0.61	1.0	<0.1
	7	104	28	8.82	0.27	0.47	<0.10	2.28	0.59	0.69	1.5	<0.1
	8	135	25	9.17	0.51	0.24	<0.10	4.84	1.01	0.71	2.5	<0.1
Joshua Tree												
JT3	1	3	23	7.08	1.47	9.75	2.67	0.16	2.73	0.31	1.8	<0.1
	2	10	21	7.40	0.48	2.93	0.77	0.16	2.52	0.35	0.5	<0.1
	2 - rep	10		7.40	0.48				2.47		0.6	<0.1
	3	23	21	7.90	0.42	2.88	0.60	0.19	2.58	0.27	0.9	<0.1
	4	31	22	7.88	0.77	5.29	1.12	0.26	5.41	0.29	0.7	<0.1
	5	53	22	8.14	0.55	3.72	0.86	0.24	2.75	0.34	1.0	<0.1
	6	68	22	8.16	0.47	3.19	0.92	0.36	2.06	0.37	1.4	<0.1
	7	86	22	8.18	0.42	2.51	0.89	0.47	2.19	0.37	1.0	<0.1
	8	112	22	8.17	0.35	1.51	0.85	1.02	1.25	0.54	1.3	<0.1
	9	130	24	8.10	0.72	2.09	1.49	2.87	4.37	0.40	1.1	<0.1
	10	135	25	8.47	1.45	1.68	1.62	9.64	9.92	0.70	1.2	<0.1

Table C5 – Saturated paste extract data for low- and mid-elevation sites.

Soil Pit	Horizon	Lower Depth	Saturation %	pH	EC	Ca	Mg	Na	Cl	B	HCO_3	CO_3
units		cm	%		dS/m	meq/L	meq/L	meq/L	meq/L	mg/L	meq/L	meq/L
Pinyon Juniper												
PJ1	1	4	26	5.74	1.14	6.83	2.41	0.20	<0.10	0.21	0.3	<0.1
	2	23	22	7.03	0.11	0.58	0.25	0.22	0.14	0.13	0.4	<0.1
	2 rep	23		7.04	0.11							
	3	38	21	6.96	0.12	0.56	0.26	0.31	0.21	0.12	0.5	<0.1
	4	65	21	6.98	0.24	1.22	0.49	0.45	0.65	0.13	0.4	<0.1
	5	93	21	7.24	0.23	1.15	0.43	0.42	1.39	0.16	0.5	<0.1
	6	117	21	8.01	0.30	1.89	0.49	0.44	1.40	0.14	1.3	<0.1
	7	136	23	8.26	0.19	1.00	0.37	0.46	0.45	0.15	1.2	<0.1
	7 rep	136		8.25	0.19	0.98	0.37	0.45	0.44	0.15		

Table C6 – Saturated paste extract data for highest elevation Pinyon Juniper site.

Particle Size Distribution

Soil Pit	Horizon	Lower Depth (cm)	Sand (%)	Silt (%)	Clay (%)
Creosote					
C1	1	3	71	24	5
	1 - rep	3	72	23	5
	2	13	80	13	7
	3	28	85	9	6
	4	55	90	3	7
	5	73	78	10	12
	6	88	88	6	6
	7	104	85	9	6
	8	135	89	6	5
Joshua Tree					
JT3	1	3	75	18	7
	2	10	74	19	7
	2 - rep	10	75	18	7
	3	23	73	18	9
	4	31	77	15	8
	5	53	79	12	9
	6	68	75	16	9
	7	86	75	14	11
	8	112	77	9	14
	9	130	80	6	14
	10	135	82	6	12
Pinyon Juniper					
PJ1	1	4	71	25	4
	2	23	68	21	11
	2 rep	23	67	21	12
	3	38	70	17	13
	4	65	71	18	11
	5	93	79	11	10
	6	117	87	6	7
	7	136	91	3	6
	7 rep	136	90	4	6

Table C7 – Mojave climosequence particle size distribution.

Bulk Mineralogy

Soil Pit	Horizon	Depth (cm)	Mineral	%
Creosote				
C1	2	3-13	Quartz	30.3
			Na, Ca feldspar	39.4
			K feldspar	23.3
			teepleite (borate)	2
			chlorite	5.1
C1	7	88-104	quartz	20
			Na, Ca feldspar	43
			K feldspar	24
			diopside	11
			CaCO3	1
			mica	1
Joshua Tree				
JT3	4	23-31	Quartz	20.2
			Na, Ca Feldspar	64.6
			K Feldspar	15.2
			vermiculite	<1
JT3	10	130-135	Quartz	23
			Na, Ca Feldspar	41
			K Feldspar	23
			Mg-Calcite	13
Pinyon Juniper				
PJ1	3	23-38	Quartz	24
			Na, Ca Feldspar	51
			K Feldspar	17
			mica	4
			amphibole	4
			vermiculite	1
PJ1	6	93-117	Quartz	21
			Na, Ca Feldspar	26
			K Feldspar	29
			mica	16
			enstatite	5
			hematite	1

Table C8 – Bulk mineralogy of Mojave climosequence soils, derived from XRD analysis of the <2mm size fraction. All samples resemble the granitic parent material.

Appendix D: Supplementary information for Chapter 4, Unpacking controls on soil CO_2 production along a climate gradient in the Mojave Desert

Additional figures for Section 4.2.4: CO_2 flux and production calculations

Comparing continuous CO_2 production calculation to flux divergence method

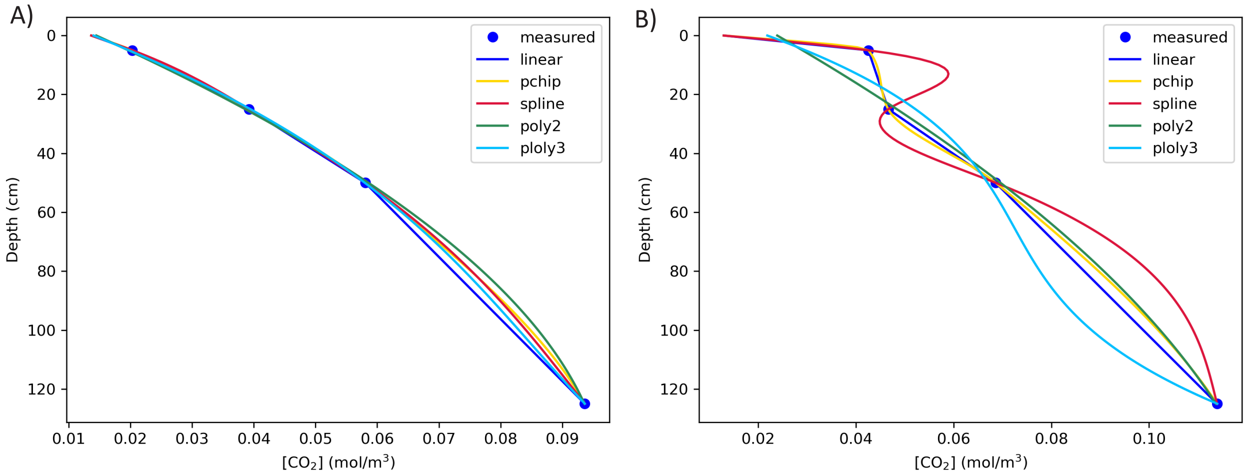

Figure D1 – Comparison of interpolation schemes for producing continuous $[CO_2]$ depth profiles from discrete measurements. A) When the profile resembles a steady-state diffusive profile, as occurs a majority of the time, all interpolation schemes tested (linear, pchip - peacewise cubic hermite interpolation, cubic spline, and second or third order polynomial) yield comparable continuous depth profiles. B) During intervals of increased CO_2 production in near-surface soils (e.g. following rain), all interpolation schemes aside from linear and pchip lead to substantial artifacts. The cubic spline (red) generates unrealistic curvature, the second-order polynomial (green) misses the elevated $[CO_2]$ measured at 5cm depth, and the third-order polynomial misses the high near-surface $[CO_2]$ while also generating unrealistic curvature at depth.

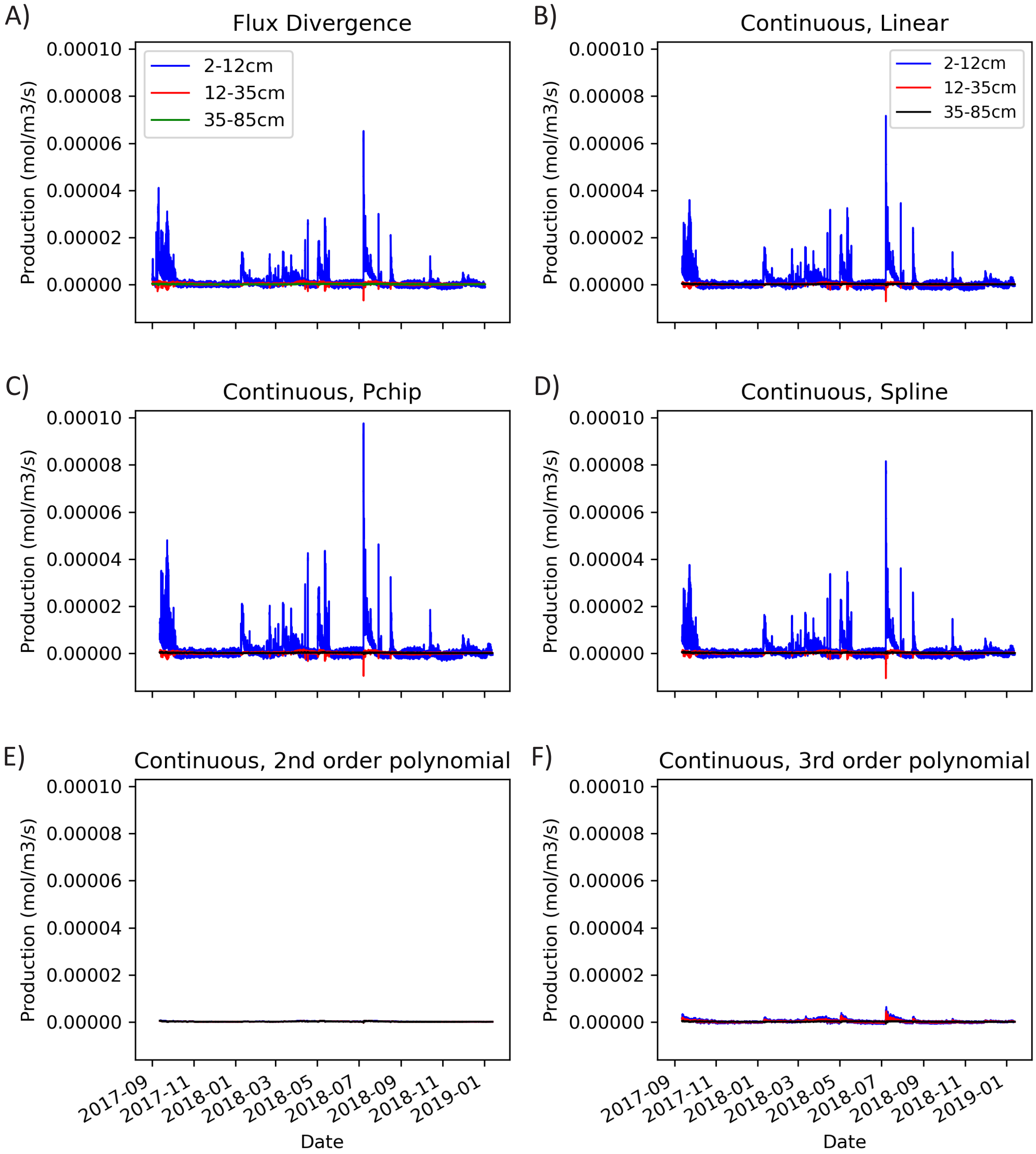

Figure D2 – Time series of calculated CO_2 production, averaged over 3 soil depth intervals, using the flux divergence method and the interpolated profiles demonstrated in Figure D1. The flux divergence method and linear interpolation yield highly comparable results while the polynomial interpolation schemes vastly under-estimate production in the shallow regions of the soil profile.

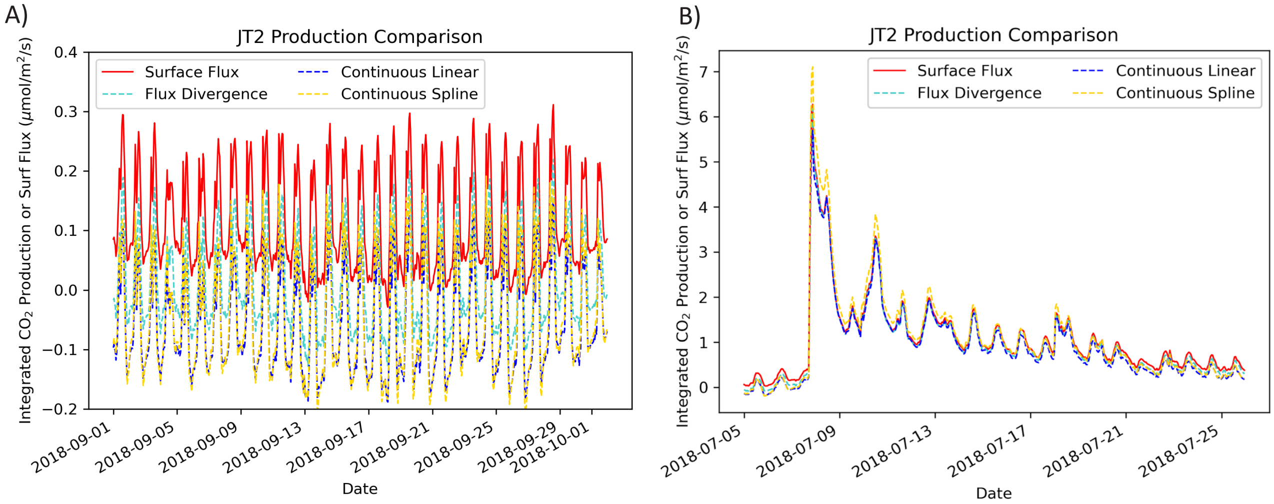

Figure D3 – Comparison of surface CO$_2$ flux (red) with depth-integrated CO2 production calculated using the flux divergence method (green), linear interpolation to produce a continuous profile (blue), and cubic spline interpolation to produce a continuous profile (yellow). Data from the vegetated profile at the mid-elevation Joshua Tree site is shown as an example, during a month-long interval in the dry season (A) and following a significant rain event (B).

Anomalous nighttime CO_2 pulse identification

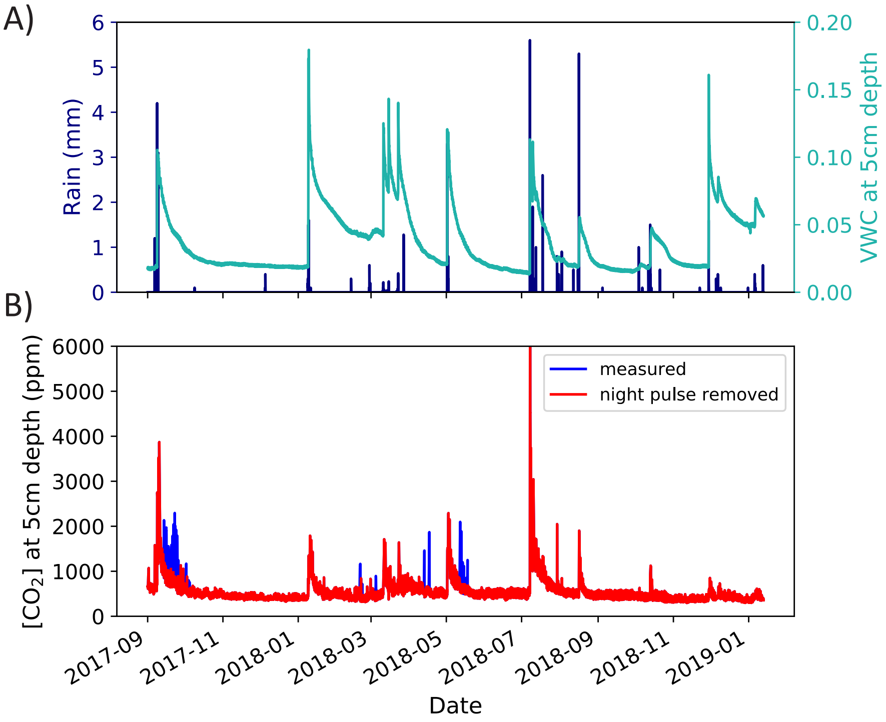

Figure D4 – Identification of anomalous nighttime CO_2 pulses in the Joshua Tree 2 (under-canopy) soil profile. A) Time series of rain (left) and volumetric water content at 5cm depth (right). B) Time series of CO_2 concentration at 5cm depth, with the nighttime pulses identified and removed from the primary dataset shown in blue.

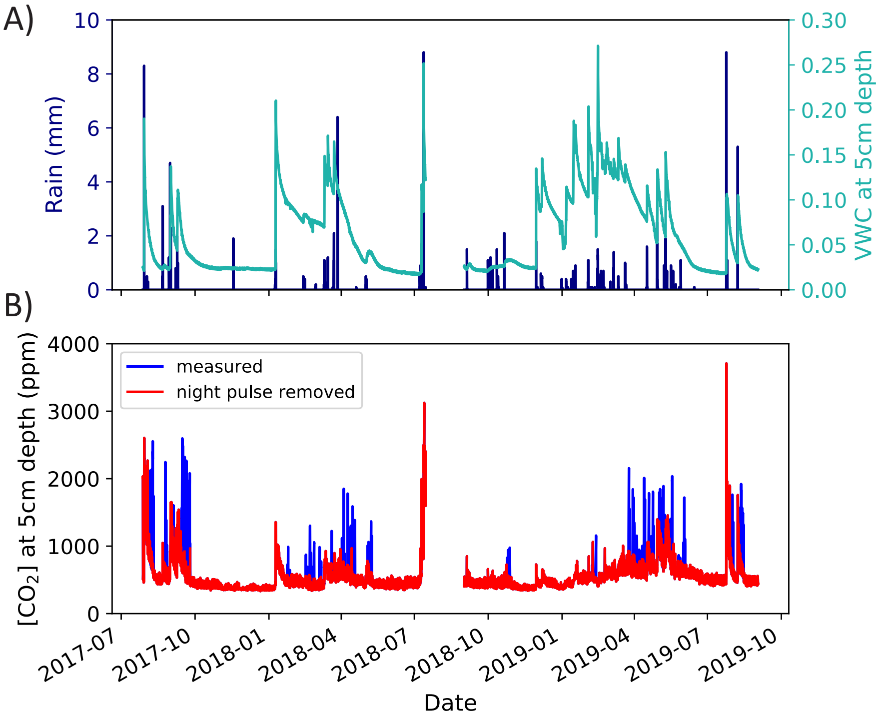

Figure D5 – Identification of anomalous nighttime CO_2 pulses in the Pinyon Juniper 2 (mixed vegetation) soil profile. A) Time series of rain (left) and volumetric water content at 5cm depth (right). B) Time series of CO_2 concentration at 5cm depth, with the nighttime pulses identified and removed from the primary dataset shown in blue.

Additional figures for Section 4.3.1: Site and soil characteristics

Soil CO_2, water content, and temperature data for under-canopy soil profiles

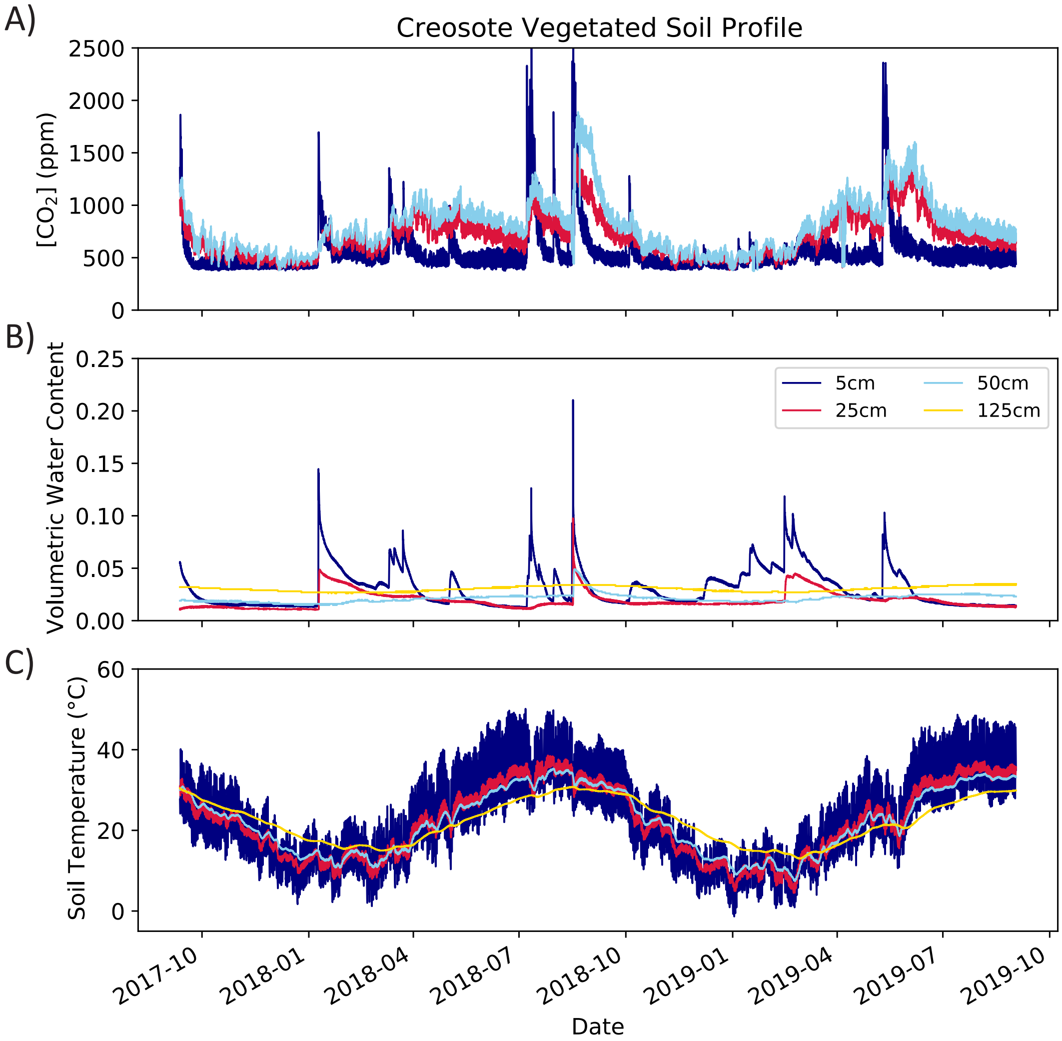

Figure D6 – Two years of in-situ monitoring data (10-minute increments) from the under-canopy profile at the most arid climosequence site, Creosote: A) soil CO_2 concentration, B) volumetric water content, and C) temperature. Colors denote depth in soil profile.

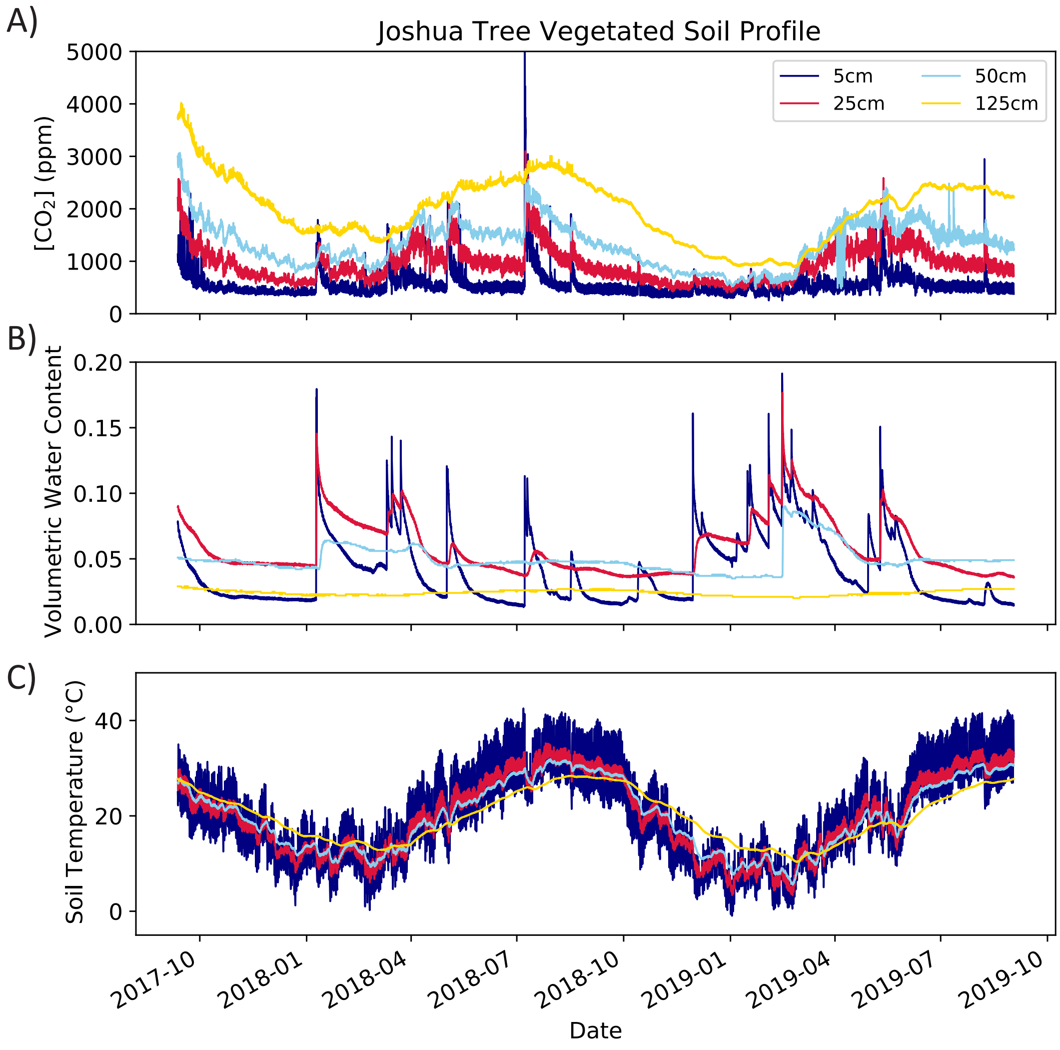

Figure D7 – Two years of in-situ monitoring data (10-minute increments) from the under-canopy profile at the mid-elevation, Joshua Tree, site: A) soil CO_2 concentration, B) volumetric water content, and C) temperature. Colors denote depth in soil profile.

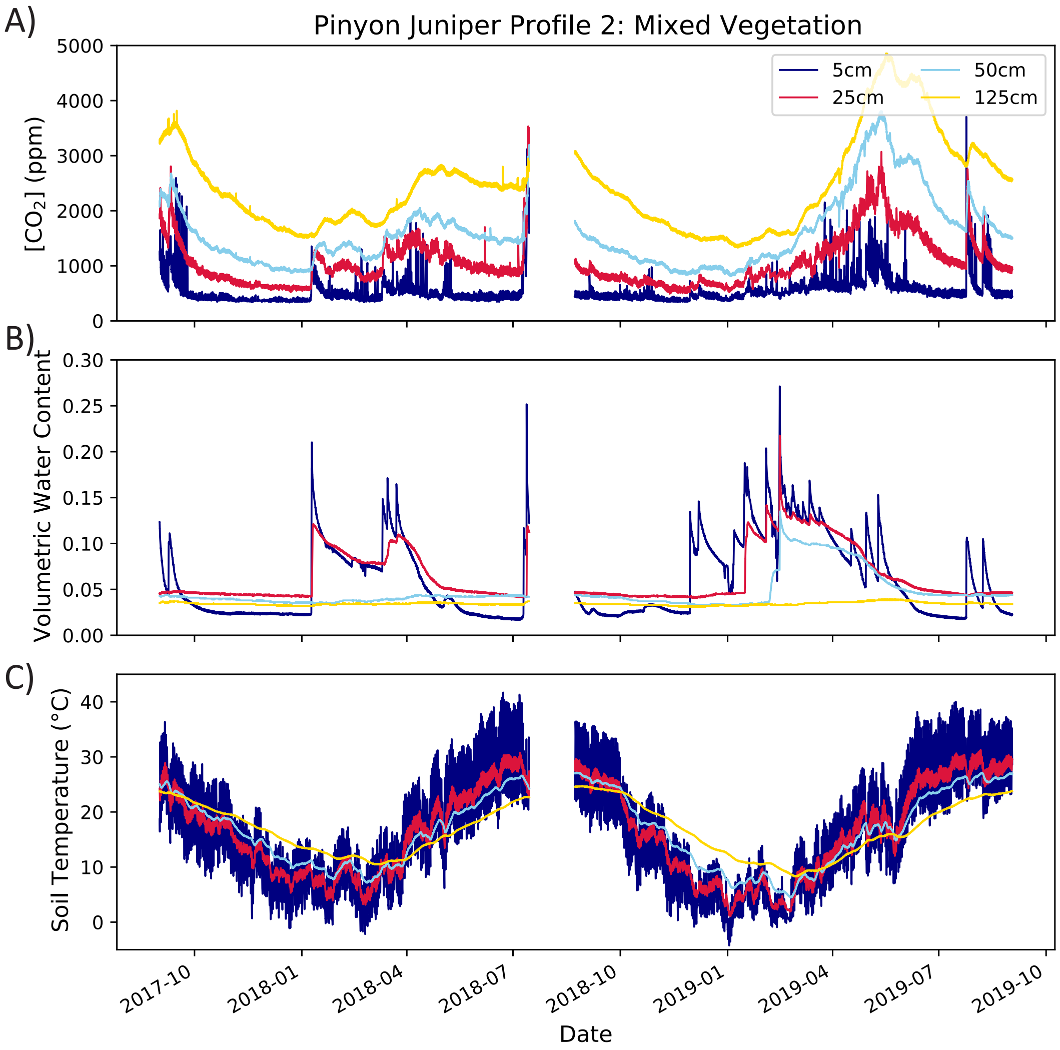

Figure D8 – Two years of in-situ monitoring data (10-minute increments) from the PJ-2 soil profile with mixed vegetation at the highest elevation, Pinyon Juniper site: A) soil CO_2 concentration, B) volumetric water content, and C) temperature. Colors denote depth in soil profile.

	Function	Parameter Description
Temperature Dependence		
Arrhenius	$f(T) = e^{\left(\frac{E_0(T-T_{20})}{RTT_{20}}\right)}$	E_0: activation energy (kJ/mol)
Lloyd and Taylor (modified Arrhenius)	$f(T) = e^{E_0\left(\frac{1}{T_{10}-T_0} - \frac{1}{T-T_0}\right)}$	E_0, T_0: empirical fitting parameters (K)
Water-sensitive Lloyd and Taylor	$E_0 = E_b * \theta/\theta_{max}$	E_b: empirical fitting parameter (K)
Q_{10}	$f(T) = a^{(T-T_{10})/10}$	a: Q_{10}
Sigmoid	$f(T) = a + \left(\frac{1}{b+c\left(\frac{T_{10}-T}{10}\right)}\right)$	a, b, c: empirical fitting parameters
Water Content Dependence		
Linear or curvilinear	$f(\theta) = bx + (1-b)x^2; x = \frac{\theta-\theta_0}{\theta_{max}-\theta_0}$	b: empirical fitting parameter; θ_0: water content at which production ceases θ_{max}: water content which maximizes production
Exponential	$f(\theta) = e^{(a*\theta)}$	a: empirical fitting parameter
Exponential with squared term	$f(\theta) = e^{\left(a*\theta+b*\theta^2\right)}$	a, b: empirical fitting parameters
Gompertz	$f(\theta) = e^{-e^{(a-b*\theta)}}$	a, b: empirical fitting parameters
Antecedent water content dependence	$f(\theta) = e^{(a*moving\ average(\theta,b))}$	a: empirical fitting parameter b: moving average window (days)
Productivity Dependence		
Exponential	$f(GPP) = e^{(a*GPP)}$	a: empirical fitting parameter

Table D1 – Description of parameters for temperature, water content, and productivity scaling functions tested here (Table 4.2).

Additional figures and tables for Section 4.3.4: predictive modeling of CO_2 production throughout the soil profile

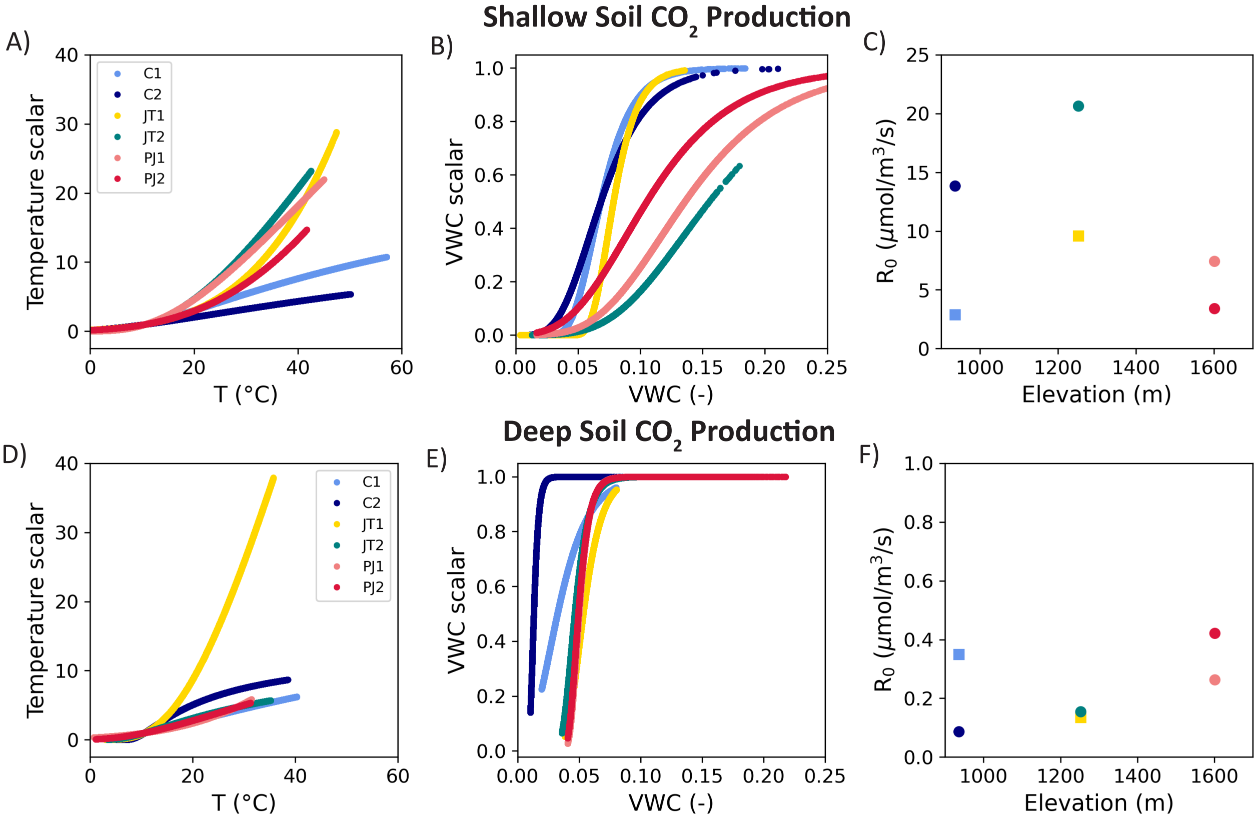

Figure D9 – Regression results for shallow (A-C) and deep (D-F) CO_2 production, using a Lloyd and Taylor temperature dependence and Gompertz water content dependence: temperature scaling factor (A,D), water content scaling factor (B,E), and baseline respiration (C,F). Colors denote the soil profile (Table 4.1).

			Parameters								
			R_0	Temperature		VWC		Antecedent VWC		GPP	
Profile	Functional Form	Depth	(μmol/m^3/s)	E_0	T_0	a	b	a	b (days)	a	R^2
C1	Arrhenius * Gompertz	shallow	8.00	49.46	-	3.86	59.72	-	-	-	0.44
	LT * Gompertz		2.88	63.66	264.74	3.65	58.82	-	-	-	0.46
	LT * $e^{(a*\theta+b*\theta^2)}$		1.44E-04	96.45	258.50	211.24	-1115.59	-	-	-	0.49
	LT * Gompertz*$f(GPP)$		2.58	77.73	262.69	3.60	57.37	-	-	2.79E-03	0.46
	Arrhenius * Gompertz	deep	0.78	43.02	-	1.59	63.28	-	-	-	0.59
	LT * Gompertz		0.35	62.37	263.47	1.56	59.70	-	-	-	0.60
	LT * $e^{(a*\theta+b*\theta^2)}$		0.01	63.71	263.11	127.60	-1199.53	-	-	-	0.62
	LT * Gompertz*$f(GPP)$		0.27	5316.33	38.24	1.36	47.35	-	-	1.21E-02	0.64
	LT * Gompertz*$f(antedecent\,\theta)$		0.22	80.78	260.17	1.18	47.39	11.63	30	-	0.61
	LT * Gompertz*$f(antedecent\,\theta)$*$f(GPP)$		0.14	3383.51	94.41	0.71	26.12	17.40	14	1.23E-02	0.65
C2	Arrhenius * Gompertz	shallow	27.24	35.79	-	2.31	37.97	-	-	-	0.74
	LT * Gompertz		13.83	83.80	254.94	2.34	39.57	-	-	-	0.75
	LT * $e^{(a*\theta+b*\theta^2)}$		0.04	92.17	253.08	113.19	-563.19	-	-	-	0.74
	LT * Gompertz*$f(GPP)$		11.71	145.53	245.66	2.31	37.60	-	-	5.99E-03	0.75
	LT * Gompertz*$f(antedecent\,\theta)$		23.97	85.81	252.07	2.53	48.70	-18.66	14	-	0.78
	LT * Gompertz*$f(antedecent\,\theta)$*$f(GPP)$		19.77	156.06	241.08	2.49	46.05	-18.41	14	6.50E-03	0.78
	Arrhenius * Gompertz	deep	0.36	36.82	4.52	378.67	-	-	-	-	0.36
	LT * Gompertz		0.09	14.67	278.10	4.54	374.31	-	-	-	0.43
	LT * $e^{(a*\theta+b*\theta^2)}$		0.05	15.04	278.10	16.40	-159.98	-	-	-	0.31
	LT * Gompertz*$f(GPP)$		0.05	26.14	276.09	4.01	328.12	-	-	1.08E-02	0.47
	LT * Gompertz*$f(antedecent\,\theta)$		0.20	15.40	278.10	3.50	249.12	-31.58	7	-	0.46
	LT * Gompertz*$f(antedecent\,\theta)$*$f(GPP)$		0.11	30.22	275.07	3.29	233.58	-28.94	7	9.85E-03	0.49

Table D2 – CO_2 production regression analysis results for lowest elevation, Creosote site. See Table 4.2 for functional forms and Table D1 for parameter descriptions.

			Parameters								
			R_0	Temperature		VWC		Antecedent VWC		GPP	
Profile	Functional Form	Depth	(μmol/m^3/s)	E_0	T_0	a	b	a	b (days)	a	R^2
JT1	Arrhenius * Gompertz	shallow	27.89	74.03	-	5.70	77.28	-	-	-	0.66
	LT * Gompertz		9.60	965.79	197.65	5.65	76.70	-	-	-	0.66
	LT * $e^{(a*\theta+b*\theta^2)}$		1.13E-07	721.92	210.05	381.62	-2007.45	-	-	-	0.68
	LT * Gompertz*$f(GPP)$		29.78	140.26	255.10	5.85	82.22	-	-	-2.61E-02	0.69
	LT * Gompertz*$f(antedecent\,\theta)$		22.99	105.24	252.35	7.01	104.15	-25.48	14	-	0.73
	LT * Gompertz*antecedent VWC*$f(GPP)$		29.65	72.34	259.33	6.76	100.37	-22.95	14	-7.31E-03	0.73
	Arrhenius * Gompertz	deep	1.05	99.10	-	5.60	112.66	-	-	-	0.56
	LT * Gompertz		0.13	104.07	266.69	4.89	98.63	-	-	-	0.58
	LT * $e^{(a*\theta+b*\theta^2)}$		2.88E-08	108.50	266.85	450.68	-3321.13	-	-	-	0.59
	LT * Gompertz*$f(GPP)$		0.09	525.64	234.76	5.17	108.93	-	-	9.93E-03	0.60
	LT * Gompertz*$f(antedecent\,\theta)$		0.08	108.98	265.87	5.09	107.15	8.34	30	-	0.58
	LT * Gompertz*$f(antedecent\,\theta)$*$f(GPP)$		0.16	606.23	230.67	4.77	96.04	-10.71	30	9.29E-03	0.60
JT2	Arrhenius * Gompertz	shallow	53.15	81.34	-	2.46	21.51	-	-	-	0.71
	LT * Gompertz		20.65	136.40	259.22	2.31	17.25	-	-	-	0.73
	LT * $e^{(a*\theta+b*\theta^2)}$		2.40E-03	213.09	250.20	119.43	-450.28	-	-	-	0.74
	LT * Gompertz*$f(GPP)$		25.71	90.41	264.71	2.39	21.01	-	-	-1.42E-02	0.75
	LT * Gompertz*$f(antedecent\,\theta)$		15.89	69.37	265.13	2.40	30.50	-17.39	7	-	0.78
	LT * Gompertz*$f(antedecent\,\theta)$*$f(GPP)$		18.56	60.41	266.97	2.42	30.30	-15.62	7	-4.97E-03	0.79
	Arrhenius * Gompertz	deep	0.41	51.87	-	6.01	137.14	-	-	-	0.35
	LT * Gompertz		0.16	30.27	271.97	5.73	131.61	-	-	-	0.37
	LT * $e^{(a*\theta+b*\theta^2)}$		2.00E-04	26.76	272.67	188.08	-1302.37	-	-	-	0.34
	LT * Gompertz*$f(antedecent\,\theta)$		0.01	1822.89	176.20	4.98	113.89	38.70	60	-	0.47
	LT * Gompertz*$f(antedecent\,\theta)$*$f(GPP)$		0.01	347.06	243.33	4.84	107.86	42.41	60	-5.34E-03	0.47

Table D3 – CO_2 production regression analysis results for mid-elevation Joshua Tree site. See Table 4.2 for functional forms and Table D1 for parameter descriptions.

			Parameters								
			R_0	Temperature		VWC		Antecedent VWC		GPP	
Profile	Functional Form	Depth	(μmol/m^3/s)	E_0	T_0	a	b	a	b (days)	a	R^2
PJ1	Arrhenius * Gompertz	shallow	28.80	86.99	2.33	19.81	0.05				0.57
	LT * Gompertz		7.44	106.87	262.40	2.22	19.09				0.61
	LT * $e^{(a*\theta+b*\theta^2)}$		7.13E-03	94.39	264.57	77.94	-230.89				0.64
	LT * Gompertz*$f(GPP)$		12.50	61.90	268.98	2.31	20.10			-5.41E-03	0.63
	LT * Gompertz*$f(antedecent\,\theta)$		29.38	45.21	264.67	2.25	20.63	-27.11	28		0.70
	LT * Gompertz*$f(antedecent\,\theta)$*$f(GPP)$		31.11	42.11	265.75	2.27	20.76	-25.80	28	-9.16E-04	0.70
	Arrhenius * Gompertz	deep	0.62	63.74		8.54	178.17				0.35
	LT * Gompertz		0.26	1024.55	183.63	8.42	175.96				0.35
	LT * $e^{(a*\theta+b*\theta^2)}$		7.61E-04	224.96	240.62	131.12	-709.77				0.30
	LT * Gompertz*$f(GPP)$		0.20	9.76E+08	-1.05E+05	8.29	175.24			2.10E-03	0.35
	LT * Gompertz*$f(antedecent\,\theta)$*$f(GPP)$		0.04	372291.36	-1510.80	14.68	323.37	15.65	7	2.98E-03	0.38
PJ2	Arrhenius * Gompertz	shallow	8.00	80.61		2.55	27.62				0.50
	LT * Gompertz		2.37	340.70	239.16	2.53	27.36				0.51
	LT * $e^{(a*\theta+b*\theta^2)}$		2.62E-03	287.57	243.85	87.33	-283.81				0.49
	LT * Gompertz*$f(GPP)$		3.33	135.35	258.96	2.58	28.50			-4.51E-03	0.52
	LT * Gompertz*$f(antedecent\,\theta)$		8.08	96.31	255.41	2.57	29.51	-24.08	28		0.57
	LT * Gompertz*$f(antedecent\,\theta)$*$f(GPP)$		8.45	84.53	257.97	2.58	29.46	-22.64	28	-9.10E-04	0.57
	Arrhenius * Gompertz	deep	0.97	66.17		7.99	168.22				0.45
	LT * Gompertz		0.38	117.54	254.39	7.86	167.75				0.46
	LT * $e^{(a*\theta+b*\theta^2)}$		1.33E-03	130.11	251.51	137.32	-796.31				0.41
	LT * Gompertz*$f(GPP)$		0.32	211.97	241.37	7.75	167.33			1.51E-03	0.46
	LT * Gompertz*$f(antedecent\,\theta)$		0.60	68.43	261.20	7.53	158.57	-4.39	28		0.46

Table D4 – CO_2 production regression analysis results for highest elevation Pinyon Juniper site. See Table 4.2 for functional forms and Table D1 for parameter descriptions.

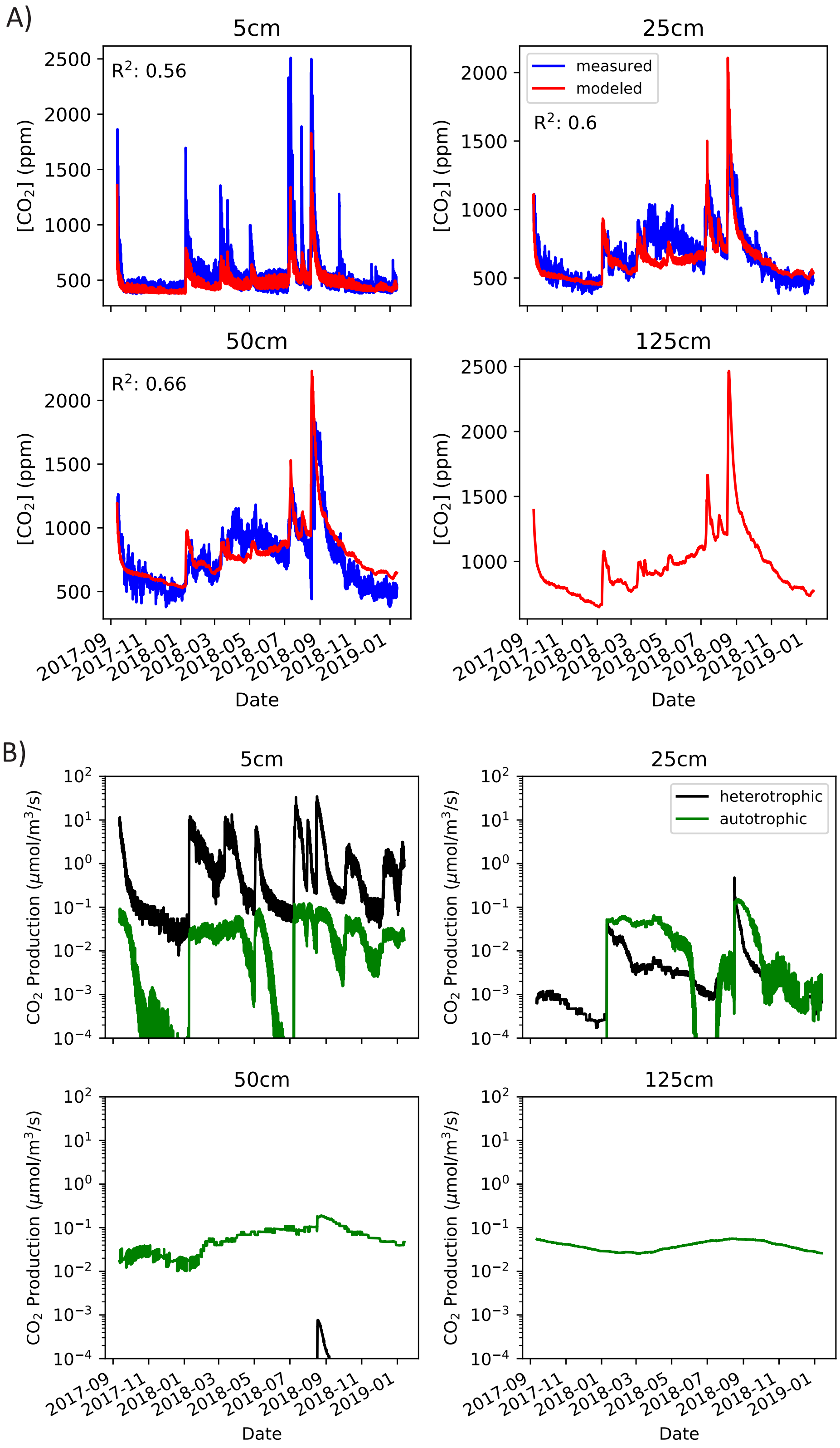

Figure D10 – CO_2 production-diffusion model results for the vegetated profile at Creosote (C2): A) measured (blue) versus modeled (red) CO_2 concentrations and B) modeled heterotrophic (black) and autotrophic (green) respiration functions.

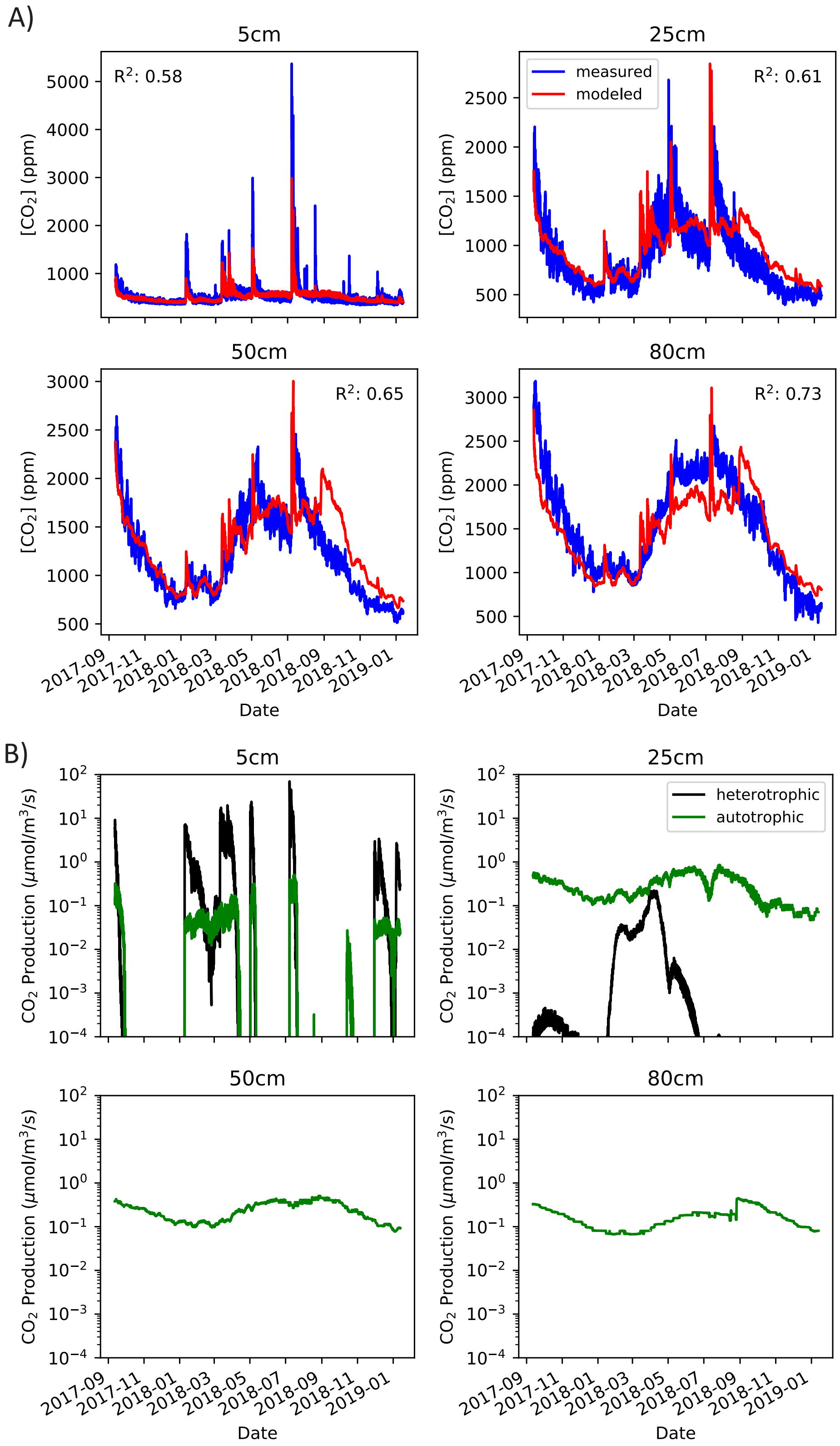

Figure D11 – CO_2 production-diffusion model results for the interspace profile at Joshua Tree (JT1): A) measured (blue) versus modeled (red) CO_2 concentrations and B) modeled heterotrophic (black) and autotrophic (green) respiration functions.

Additional figures for Section 4.3.5, Exploring nighttime pulses of CO_2

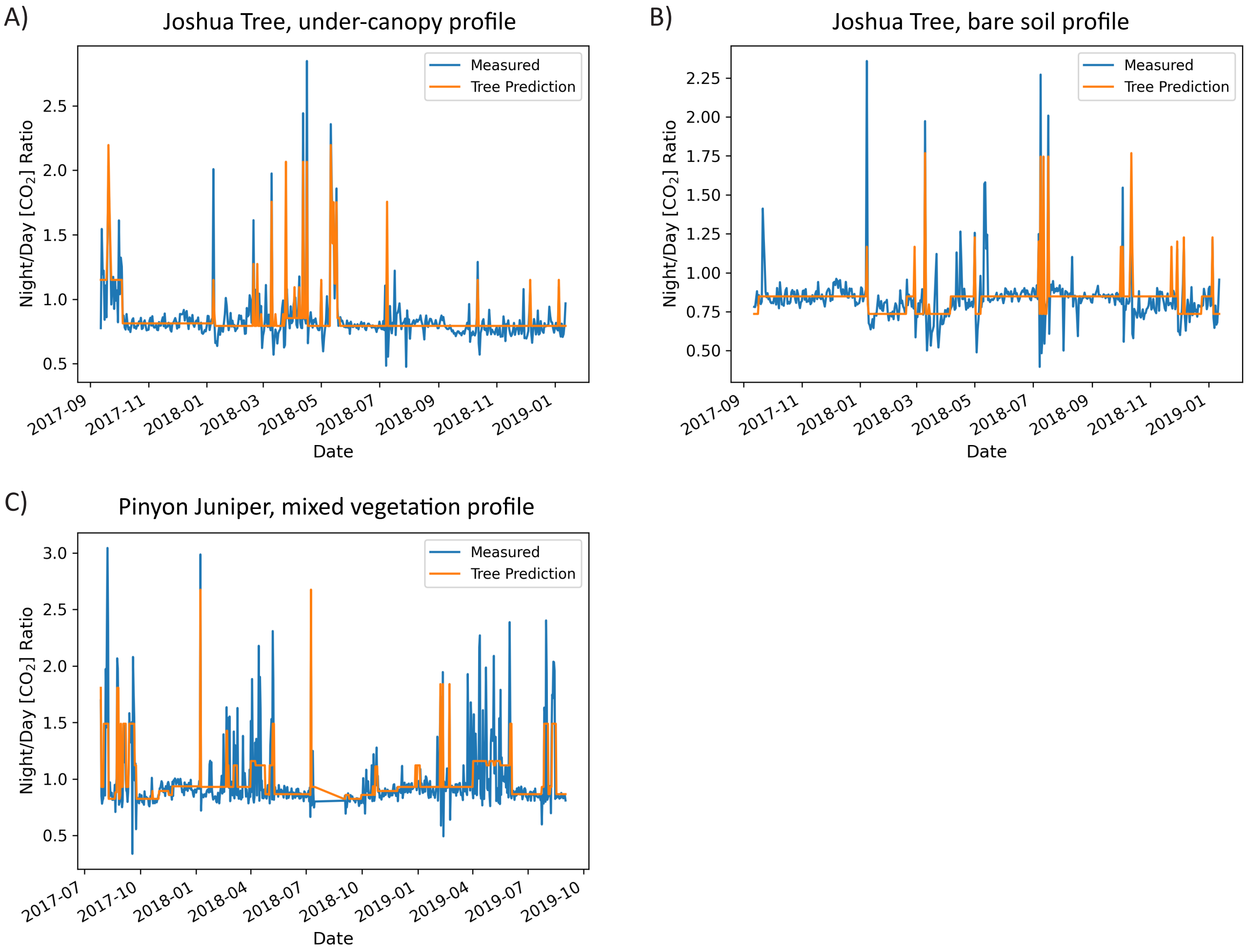

Figure D12 – Regression tree model fits for the prediction of nighttime CO_2 pulse magnitude - the ratio of maximum nighttime to preceding daytime CO_2 concentration - from time-correlative soil and meteorological conditions.

	Mean		Max		Min		
	Pulse	No Pulse	Pulse	No Pulse	Pulse	No Pulse	p value
Avg. GPP	63.00	38.07	74.46	82.55	18.70	0.60	<**.0001**
Max nighttime VPD (kPa)	1.33	1.71	2.13	5.60	0.47	0.05	**0.0010**
Min nighttime VPD (kPa)	0.48	0.80	1.03	2.68	0.12	0.00	<**.0001**
Max nighttime Dew Pt (°C)	1.08	0.38	10.29	21.48	-12.81	-22.70	0.6310
Max nighttime Relative Humidity	57.01	47.08	81.40	100.00	26.23	8.11	**0.0058**
Avg. daytime Air T (°C)	18.72	19.69	30.05	37.44	1.07	-0.53	0.5062
Max nighttime Air T (°C)	18.72	19.69	30.05	37.44	1.07	-0.53	0.5062
Min nighttime Air T (°C)	7.40	10.75	15.79	27.53	-8.02	-7.69	**0.0117**
Avg. daytime soil T at 5cm	24.08	22.08	30.90	37.32	9.22	3.12	0.0981
Avg. nighttime soil T at 5cm	17.83	16.88	24.53	33.59	3.45	0.30	0.4350
Avg. nighttime soil T at 25cm	22.24	20.21	28.24	34.26	8.76	4.67	0.0732
Avg. nighttime soil VWC at 5cm	0.04	0.04	0.07	0.13	0.03	0.01	**0.0148**
Avg. nighttime soil VWC at 25cm	0.07	0.05	0.08	0.13	0.05	0.04	<**.0001**
Time since last rain (days)	12.48	21.02	25.00	86.00	4.00	0.00	<**.0001**
Magnitude of last rain	20.30	11.12	26.50	26.50	1.00	0.00	**0.0001**
Time since last major rain (days)	23.60	56.26	97.00	144.00	4.00	0.00	<**.0001**
Magnitude of last major rain	23.10	19.57	26.50	26.50	16.60	0.00	**0.0004**
Max daytime CO2 production (mol/m3)	1027.98	694.71	2007.37	5455.43	597.48	398.78	**0.0006**
Avg. difference between air T and dew point (°C)	12.82	16.18	23.50	39.20	6.61	0.31	**0.0005**
Min difference between air T and dew point (°C)	13.13	16.10	22.82	38.42	3.65	0.10	**0.0084**

Table D5 – Summary statistics comparing soil and meteorological conditions during nights (and preceding days) with and without nighttime pulse events for the vegetated soil profile at Joshua Tree (JT2). A two-sided t-test was used to determine if the mean of each parameter differed significantly between intervals with and without pulse events.

	Mean		Max		Min		
	Pulse	No Pulse	Pulse	No Pulse	Pulse	No Pulse	p value
Avg. GPP	110.49	73.79	234.30	232.49	13.27	1.28	**<.0001**
Max nighttime VPD (kPa)	1.64	1.47	4.27	4.58	0.32	0.00	0.0772
Min nighttime VPD (kPa)	0.51	0.54	1.61	2.23	0.09	0.00	0.4290
Max nighttime Dew Pt (°C)	-0.87	-0.45	15.58	18.85	-16.82	-26.87	0.6042
Max nighttime Relative Humidity	53.96	56.50	89.20	100.00	19.33	6.57	0.1877
Avg. daytime Air T (°C)	18.01	16.94	32.00	33.73	-1.95	-3.68	0.2467
Max nighttime Air T (°C)	16.93	15.36	31.44	32.48	-1.85	-3.61	0.0950
Min nighttime Air T (°C)	6.62	7.14	18.82	23.21	-9.26	-8.96	0.4984
Avg. daytime soil T at 5cm	21.76	19.18	34.16	37.70	1.91	-0.90	**0.0065**
Avg. nighttime soil T at 5cm	14.93	13.17	28.50	30.35	-0.40	-3.17	**0.0431**
Avg. nighttime soil T at 25cm	18.63	16.77	29.79	30.74	3.02	1.43	**0.0252**
Avg. nighttime soil VWC at 5cm	0.07	0.06	0.14	0.21	0.02	0.02	**0.0098**
Avg. nighttime soil VWC at 25cm	0.07	0.06	0.13	0.17	0.04	0.04	**0.0031**
Time since last rain (days)	7.45	17.37	24.00	68.00	0.00	0.00	**<.0001**
Magnitude of last rain	9.41	8.92	41.60	43.90	0.00	0.60	0.5939
Time since last major rain (days)	34.04	57.31	107.00	163.00	0.00	0.00	**<.0001**
Magnitude of last major rain	24.46	23.59	43.90	43.90	0.00	11.80	0.5355
Max daytime CO2 production (mol/m3)	940.02	625.68	1903.20	3707.74	447.06	370.99	**<.0001**
Avg. difference between air T and dew point (°C)	13.74	13.60	28.75	38.27	5.06	0.00	0.8251
Min difference between air T and dew point (°C)	13.01	13.52	26.11	39.47	2.73	0.00	0.4165

Table D6 – Summary statistics comparing soil and meteorological conditions during nights (and preceding days) with and without nighttime pulse events for the mixed shrub/grass soil profile at Pinyon Juniper (PJ2). A two-sided t-test was used to determine if the mean of each parameter differed significantly between intervals with and without pulse events.

A) Joshua Tree Interspace: presence/absense of nighttime pulse

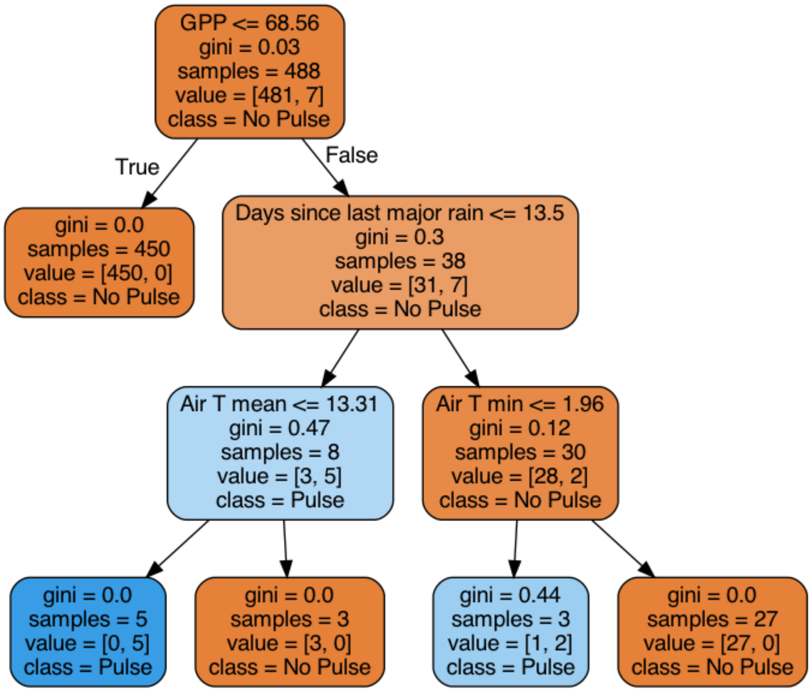

B) Joshua Tree Interspace: magnitude of nighttime pulse

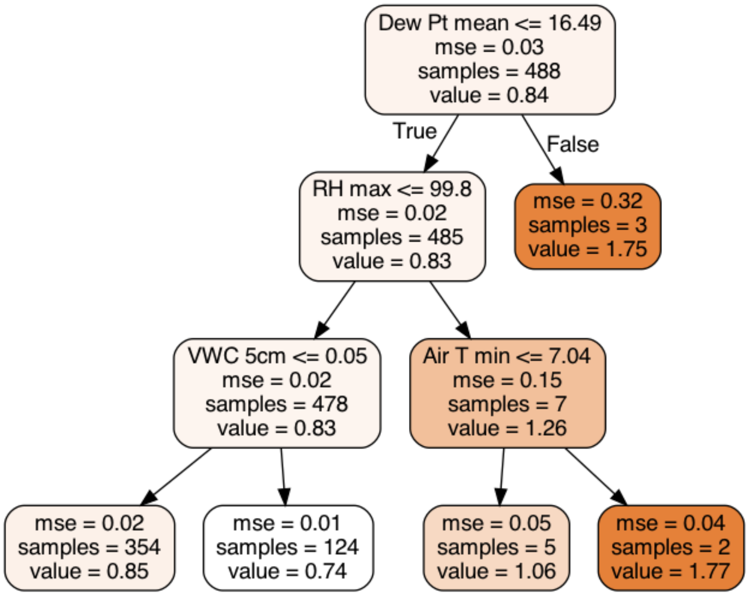

Figure D13 – Decision trees predicting nighttime pulse events at the Joshua Tree interspace profile (JT1). A) Classification tree predicting the presence/absence of a nighttime pulse. Blue coloration indicates the prediction of a nighttime pulse event. B) Regression tree predicting the magnitude of the nighttime pulse (ratio of maximum [CO_2] during the nighttime vs. preceding daytime interval). Orange coloration denotes a higher predicted nighttime CO_2 concentration relative to the preceding day.

Appendix E: Supplementary information for Chapter 5, Magnitude and mechanism of CO_2 consumption in Mojave Desert soils

Additional figures describing acute CO_2 consumption following rain events

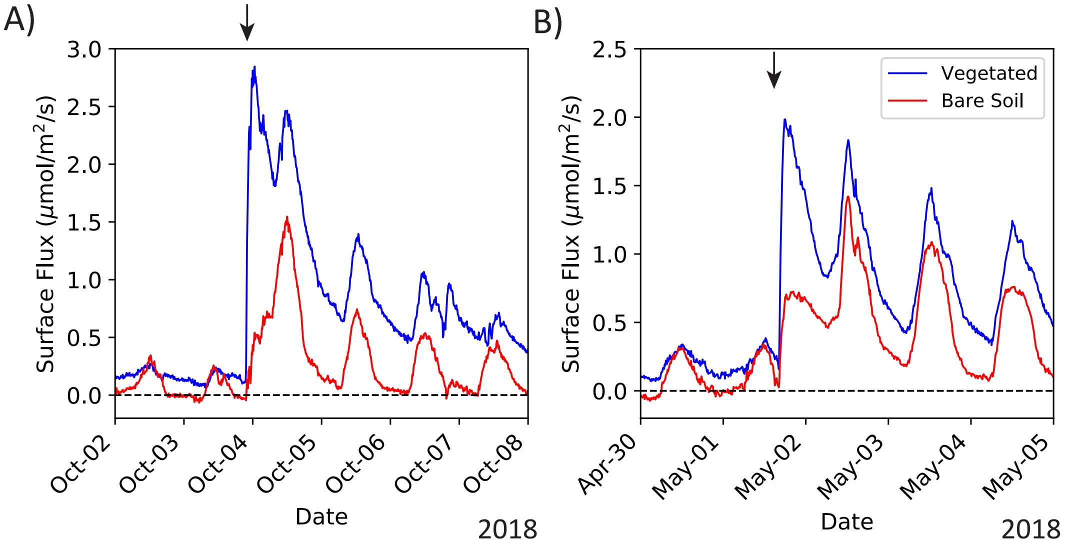

Figure E1 – Creosote site soil CO_2 response to rain events where a muted response to water availability is observed in the bare soil profile but surface fluxes remain positive: A) small rain event (~4mm) during fall drought period, B) afternoon rain event after a 1 month dry spell. Black arrows denote the onset of the rain event and the dashed reference line indicates a surface flux of $0\mu\text{mol}/\text{m}^2/\text{s}$.

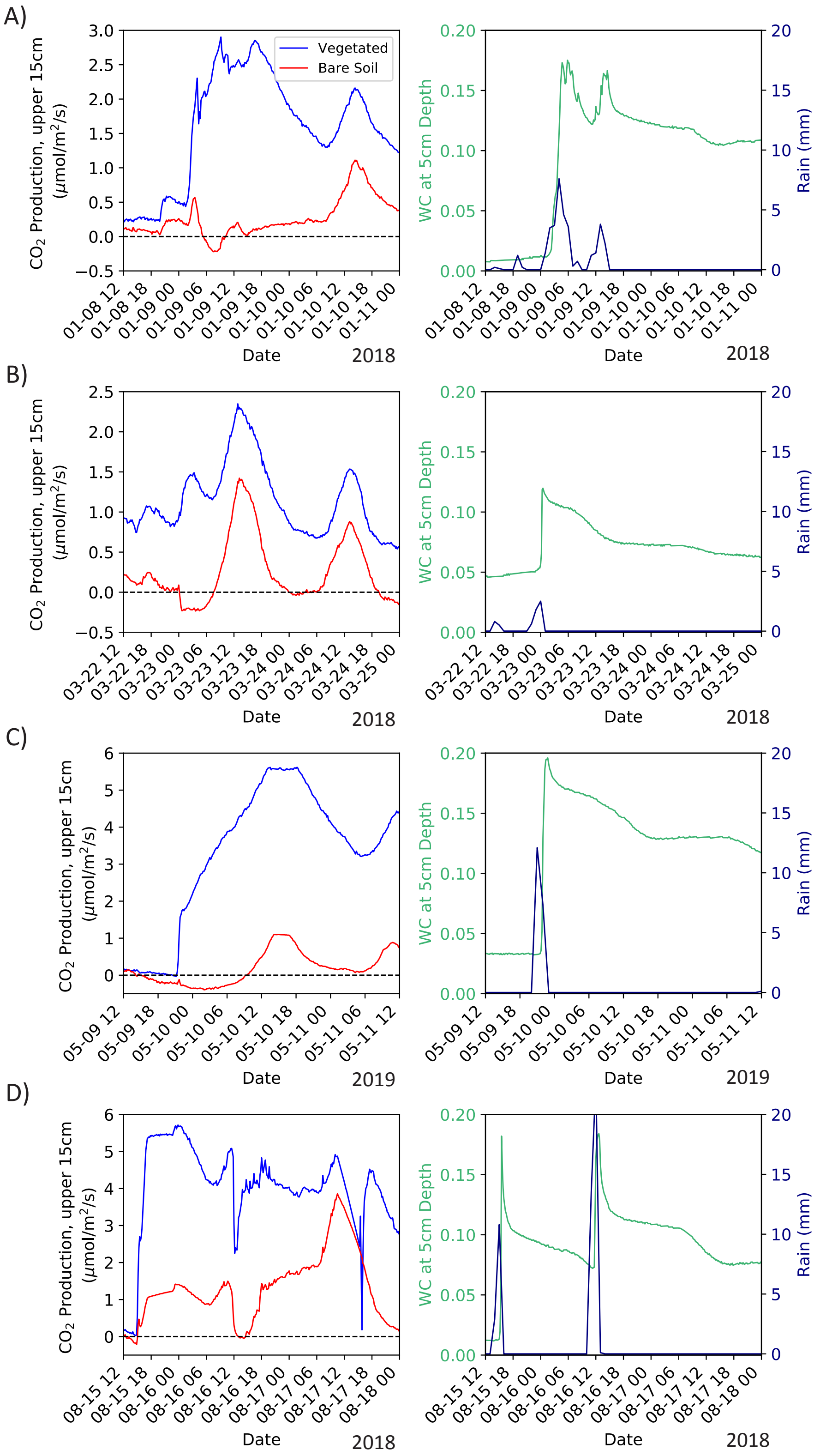

Figure E2 – Time series highlighting the temporal relationship between shallow-soil CO$_2$ production (left) and water delivery to shallow soils (right) for four representative rain events where net CO$_2$ consumption is observed in the intercanopy soil profile.

Additional figures examining potential drivers of nightly CO_2 consumption

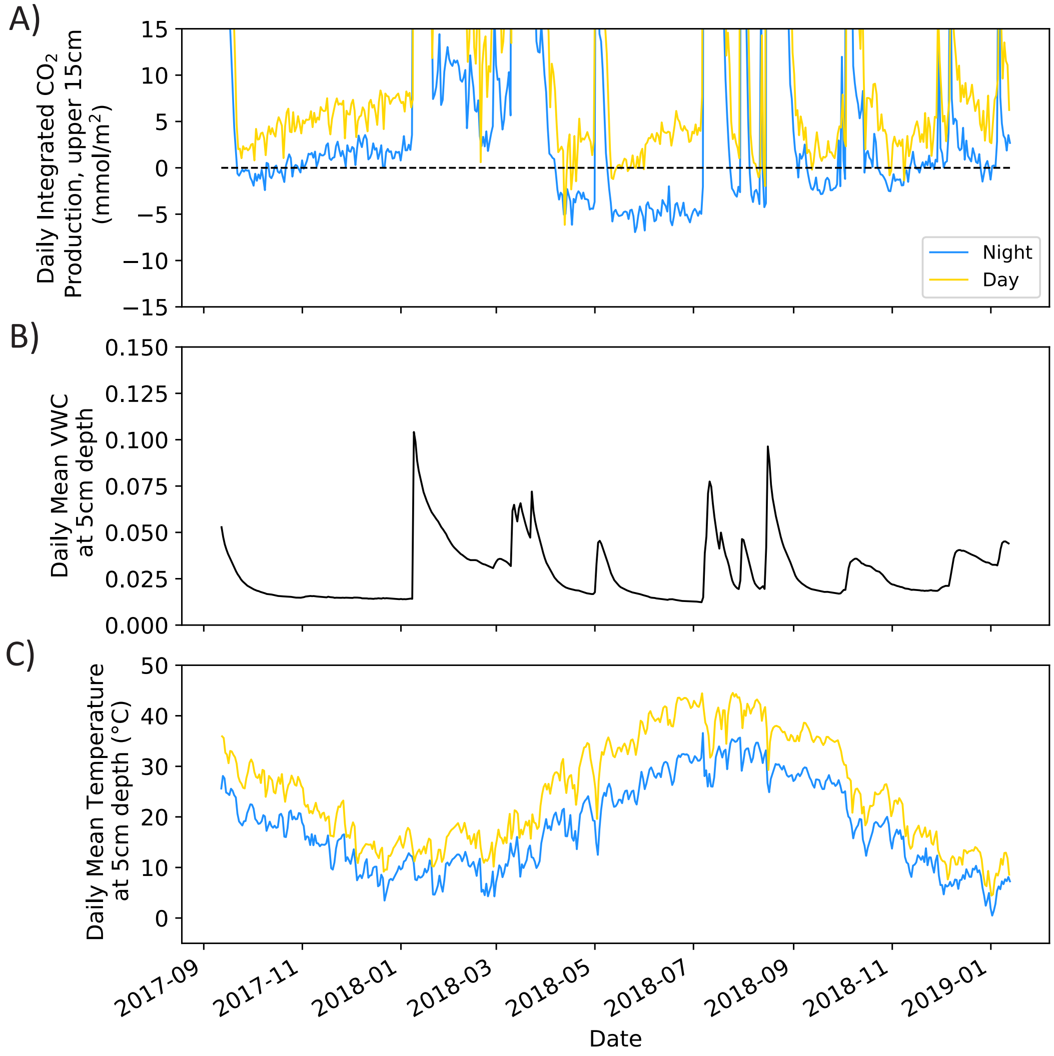

Figure E3 – Time series of CO_2 production in upper 15cm of the vegetated soil profile (C2), partitioned into daytime (8am-8pm) and nighttime (8pm-8am) intervals: A) integrated CO_2 production over day (yellow) and nighttime (blue) hours, B) daily mean volumetric water content at 5cm depth, and C) mean day and nighttime soil temperature at 5cm depth. Note the y axis in A is capped at $15mmol/m^2$ to highlight changes in consumption magnitude over time; significantly higher production is observed following rain events (Figure 5.5).

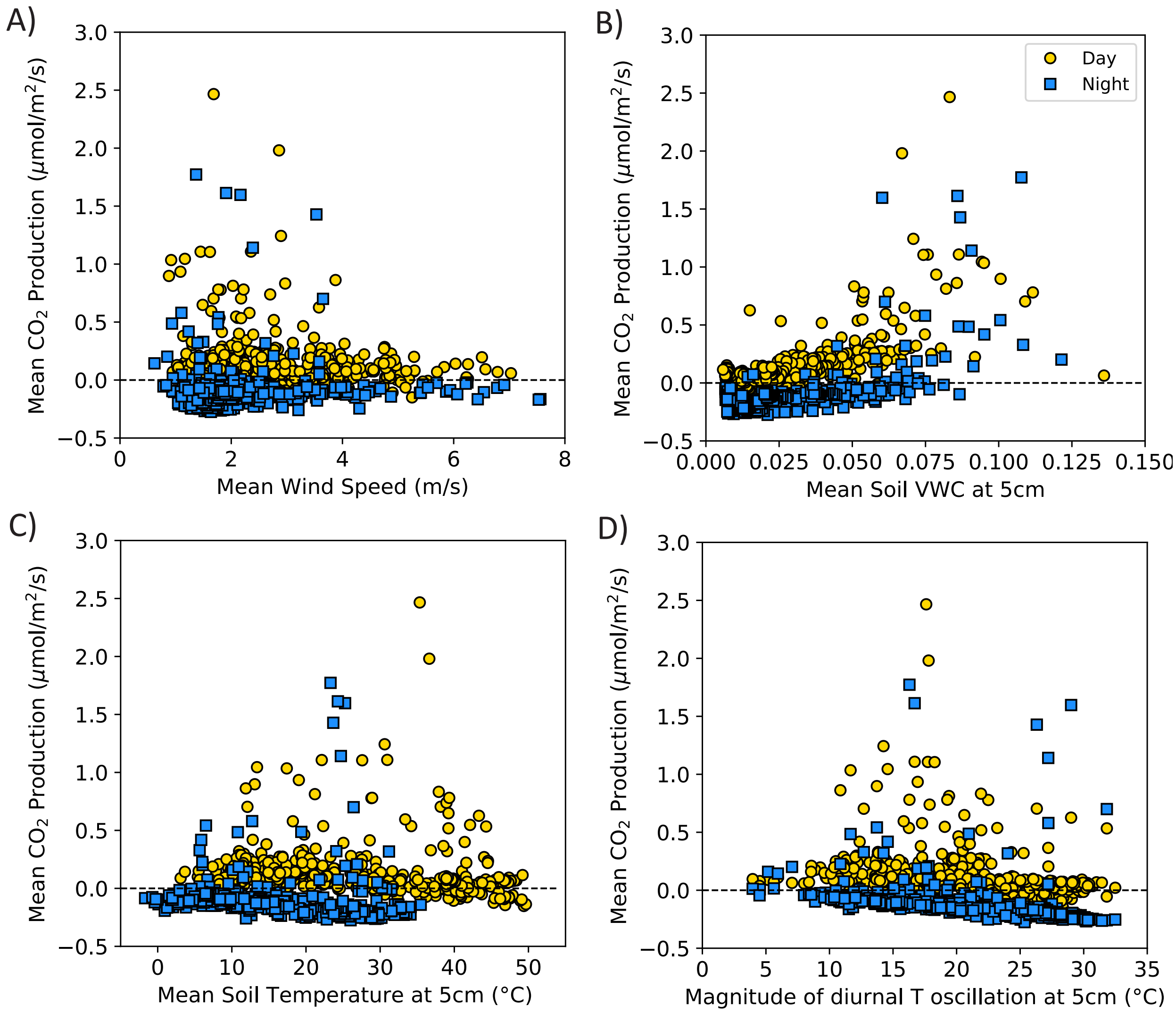

Figure E4 – Cross-plots of daily mean CO$_2$ production in the upper 15cm of the interspace profile with environmental parameters that could influence soil physio-chemical conditions, broken into daytime (gold, 8am-8pm) and nighttime (blue, 8pm-8am) intervals: A) mean wind speed; B) mean soil volumetric water content at 5cm depth; C) mean soil temperature at 5cm depth; D) Magnitude of the diurnal temperature oscillation at 5cm depth (daytime temperature max - nighttime temperature min). The dashed reference line indicates a production rate of 0μmol/m^2/s. Figure 5.9 shows the same data with the y axis capped at 0.6μmol/m^2/s to highlight the relationship between nighttime consumption and environmental predictors.